Transactions of the ASME, Journal of Heat Transfer (ISSN 0022-1481) is published monthly by The American Society of Mechanical Engineers, Three Park Avenue, New York, NY 10016. Periodicals postage paid at New York, NY and additional mailing offices. POSTMASTER: Send address changes to Transactions of the ASME, Journal of Heat Transfer, c/o THE AMERICAN SOCIETY OF MECHANICAL ENGINEERS, 22 Law Drive, Box 2300, Fairfield, NJ 07007-2300. **CHANGES OF ADDRESS** must be received at Society headquarters seven weeks before they are to be effective. Please send old label and new address.

Journal of Heat Transfer

Published Monthly by ASME

VOLUME 130 • NUMBER 11 • NOVEMBER 2008 , pp. 11101-114509

RESEARCH PAPERS

(**Contents continued on inside back cover**)

This journal is printed on acid-free paper, which exceeds the ANSI Z39.48-1992 specification for permanence of paper and library materials. ♾™
♻ 85% recycled content, including 10% post-consumer fibers.

Journal of Heat Transfer Volume 130, Number 11 NOVEMBER 2008

TECHNICAL BRIEFS

The ASME Journal of Heat Transfer is abstracted and indexed in the following:

Applied Science and Technology Index, Chemical Abstracts, Chemical Engineering and Biotechnology Abstracts (Electronic equivalent of Process and Chemical Engineering), Civil Engineering Abstracts, Compendex (The electronic equivalent of Engineering Index), Corrosion Abstracts, Current Contents, E & P Health, Safety, and Environment, Ei EncompassLit, Engineered Materials Abstracts, Engineering Index, Enviroline (The electronic equivalent of Environment Abstracts), Environment Abstracts, Environmental Engineering Abstracts, Environmental Science and Pollution Management, Fluidex, Fuel and Energy Abstracts, Index to Scientific Reviews, INSPEC, International Building Services Abstracts, Mechanical & Transportation Engineering Abstracts, Mechanical Engineering Abstracts, METADEX (The electronic equivalent of Metals Abstracts and Alloys Index), Petroleum Abstracts, Process and Chemical Engineering, Referativnyi Zhurnal, Science Citation Index, SciSearch (The electronic equivalent of Science Citation Index), Theoretical Chemical Engineering

Adiabatic Horizontal and Vertical Pressure Drop of Carbon Dioxide Inside Smooth and Microfin Tubes at Low Temperatures

Yoon Jo Kim
The George W. Woodruff School of Mechanical Engineering,
Georgia Institute of Technology,
Atlanta, GA 30332

Jeremy Jang

Predrag S. Hrnjak

Department of Mechanical Science and Engineering,
University of Illinois at Urbana-Champaign,
Urbana, IL 61801

Min Soo Kim
School of Mechanical and Aerospace Engineering,
Seoul National University,
Seoul 151-742, Korea

This paper presents the pressure drop data and the analysis of adiabatic CO_2 flow in horizontal and vertical smooth and microfin tubes at saturation temperatures around $-20°C$. The test tubes had 3.48 mm inner diameter smooth tube and a 3.51 mm melt-down diameter microfin tube. The test was performed over a mass flux range of 200–800 kg/m^2 s and at saturation temperatures of $-25°C$ and $-15°C$. The effects of various parameters—mass flux, saturated temperature, and tube diameter—on pressure drop were qualitatively analyzed. The analyses showed that the frictional pressure drop characteristics of vertical two-phase flow were much different from that of the horizontal two-phase flow. The microfin tube can be considered as "very rough tube" having the roughness of "fin height." The data were compared with several correlations. The existing frictional pressure drop correlation is sufficient to predict the horizontal pressure drop in smooth tube. For the vertical pressure drop, the simple combination of the frictional pressure drop and void fraction model was in comparatively good agreement. However, the qualitative results showed that there were some limits to cover the different mechanisms related to the interfacial shear stress. The average enhancement factors and penalty factors evidenced that it was not always true that the internally finned geometry guaranteed the superior in-tube condensation performance of microfin tube in refrigeration system and air-conditioning systems. [DOI: 10.1115/1.2957595]

Keywords: carbon dioxide, microfin tube, pressure drop, low temperature, two-phase

1 Introduction

One of the most common techniques for augmenting in-tube condensation in refrigeration and air-conditioning systems is the use of microfin tubes developed at the end of 1970. However, in spite of the recent interest in CO_2, little, if any experimental data or analysis on the pressure drops of CO_2 at sufficiently low temperatures in microfin tube has not been presented. It is partly because the typical condensation (or gas-cooling) operating temperature of refrigeration and air-conditioning system ranges from 30°C to 50°C. However, some applications need a low temperature level, harmless, and odorless working fluids. CO_2, as a natural refrigerant, could be a solution for this application such as a secondary loop or could be used as a refrigerant in low pressure loop in cascade systems. To our best knowledge, this is the first experimental paper that deals with the pressure drop of CO_2 at low temperatures with enhanced tubes.

Typical microfin tubes available for industrial applications are made of copper and have an outside diameter from 4 mm to 15 mm, a single set of 50-70 spiral fins with a helix angle from 6 deg to 30 deg, fin height from 0.1 mm to 0.25 mm, triangular or trapezoidal fin shapes with an apex angle from 25 deg to 90 deg [1]. Although there are some tests showing that the local enhancement factor (EF) (ratio of microfin tube heat transfer coefficient to smooth tube heat transfer coefficient that are obtained from the tests with equivalent diameters at same operating conditions) can be less than 1 at specific operating conditions and the microfin tube geometry [2] microfin tubes generally enhance the heat transfer performance by a factor of 1.5–2.8 with a slight increase of pressure drop, when compared to a smooth tube having an equivalent diameter at the same operating conditions [3]. The enhancement mechanism is generally explained by three major factors: (i) increase in effective area, (ii) liquid drainage due to surface tension, and (iii) turbulence induced in the liquid film by the microfins.

In this paper, the adiabatic horizontal and vertical pressure drop data of CO_2 at low temperatures in smooth and microfin tubes are presented. The two-phase frictional pressure drop characteristics in microfin tube were investigated by the experiment, which was performed in 3.48 mm inner diameter horizontal smooth tube and 3.51 mm melt-down diameter horizontal microfin tube. Similar tests were performed using vertically oriented smooth and microfin tubes having same geometrical configurations. The vertical pressure drop results can be used to observe the gravitational pressure drop and void fraction characteristics of carbon dioxide at low temperature. The pressure drop data from Zilly et al. [4] is used to investigate the effect of diameter on pressure drop. To investigate the effect of various parameters on pressure drop and penalty factor (PF) (ratio of microfin tube pressure drop to smooth tube pressure drop that are obtained from the tests with equivalent diameters at same operating conditions), experiments were performed at several test conditions. Table 1 shows the test conditions of the present study. The experimental data of horizontal pressure drop was compared with the several frictional pressure drop correlations while that of vertical pressure drop was compared with the combinations of frictional pressure drop and void fraction models. A list of the correlations used for comparison with the experimental data is presented in Table 2. The measured pressure drop data can be directly utilized to database for the industry applications as well as to characterize the complex two-phase phenomena inside both smooth and microfin tubes. Also,

Contributed by the Heat Transfer Division for publication in the JOURNAL OF HEAT TRANSFER. Manuscript received August 13, 2007; final manuscript received May 6, 2008; published online September 3, 2008. Review conducted by Satish G. Kandlikar.

Table 1 Test conditions in present study

Description	Present study	Zilly et al. [4]
G (kg/m^2 s)	200, 400, 800	200, 300, 400
T_{sat} (°C)	−25, −15	−25, −15

the strong coupling between heat transfer and pressure drop in two-phase flow, which is commonly symbolized by the parameters such as two-phase multiplier and Martinelli parameter and used in both heat transfer coefficient and pressure drop correlations, requires the pressure drop data for describing two-phase heat transfer characteristics and/or for developing heat transfer coefficient correlations in microfin tubes.

2 Literature Review

2.1 Pressure Drop in Smooth Tubes. Lockhart and Martinelli [5] presented the data for isothermal two-phase, two-component flow in pipes with various diameters and proposed the two-phase multiplier type pressure drop correlation graphically. The authors introduced the parameter X, which is defined as the square root of the ratio of the pressure drop in the pipe if the liquid flowed alone to the pressure drop if the gas flowed alone, and showed that four types of flow exist depending on whether each phase is flowing viscously or turbulently. The two-phase multiplier ϕ_v is graphically correlated with parameter X with respect to the four flow mechanisms [4]. Soliman et al. [6] approximated the graphical results of Lockhart and Martinelli [5]. The formulation of Lockhart–Martinelli was improved by Chisholm [7] with the consideration of the interfacial shear force between the phases. Dukler et al. [8] developed the parameters for two-phase flow corresponding to the Euler and Reynolds numbers for single-phase flow using the similarity analysis for frictional pressure drop in two-phase flow. The authors showed that their correlation gives better agreement than earlier correlations. Chisholm [9] proposed a predictive model for pressure gradient due to friction during evaporation. Based on the correlation of Baroczy [10] and physical property coefficient Γ, the coefficient B was determined and used for considering the effect of the mass flux on the pressure drop in two-phase flow [9]. The predictive model of Friedel [11] was developed for both horizontal and vertical smooth tubes with a data bank of 25,000 data points, which was taken in channels with a diameter over 1 mm. Kuo and Wang [12] reported an interesting fact that the correlation of Friedel [11] can predict the two-phase friction multiplier for both smooth and microfin tubes with success. Some of the researchers have attempted to modify the constant coefficient C in the correlation of Chisholm [7]. Kuo and Wang [12] and Wang et al. [13] correlated the coefficient C with the Martinelli parameter X and the liquid-only Reynolds number ($\mathrm{Re}_{lo}=GD/\mu_l$), which successfully fitted the experimental data. It should be noted that the coefficient C is representative for the interaction between the gas phase and the liquid phase. Therefore, it is possible that more parameters may have relation with the coefficient C and thus the correlation for the coefficient C should be more investigated.

Table 2 The correlations used for comparison in present study

Tube	References
Smooth /horizontal	[8,6,11,12]
Microfin /horizontal	[8,11,12,25]
Smooth /vertical	[8]/[14], [8]/[17], [11]/[14], and [11]/[17]
Microfin /vertical	[8]/[14], [8]/[17], [25]/[14], and [25]/[17]

The gravitational pressure drop can be given by the following equation:

$$\left(\frac{\Delta P}{\Delta L}\right)_g = [\varepsilon\rho_v + (1-\varepsilon)\rho_l]g\sin\varphi \tag{1}$$

where ε, ρ, and φ denote the void fraction, the density, and the angle between the tube axis and the horizontal, respectively. As shown, the gravitational pressure drop significantly depends on the void faction. Thus, the results of the pressure drop in vertical tube can be used to indirectly identify the void fraction of a working fluid. One of the commonly used models for determining the void fraction is void fraction model of Zivi [14], which deduced that an idealized two-phase flow with zero wall friction and zero entrainment equals $(\rho_l/\rho_v)^{1/3}$ using the principle of minimum entropy production. Friedel [15] recommended the use of the void fraction model of Rouhani and Axelsson [16] for determining the mean void fraction and the mean density through the comparative study between several void fraction models and 9009 measurements of the mean void fraction. Hajal et al. [17] mentioned that at very high reduced pressures, the density of the vapor approaches that of the liquid, where the homogeneous void fraction model is applicable, which assumes that the vapor and liquid phases travel at the same velocity in the channel. Hajal et al. [17] developed a new void fraction model (the authors named it as LMε-model), which is the logarithmic mean of the values of homogeneous void fraction and void fraction of Rouhani and Axelsson [16] as given by

$$\varepsilon_{\mathrm{Hajal}} = \frac{\varepsilon_{\mathrm{hom}} - \varepsilon_{\mathrm{RA}}}{\ln\dfrac{\varepsilon_{\mathrm{hom}}}{\varepsilon_{\mathrm{RA}}}} \tag{2}$$

Unlike the other void fraction models, the void fraction predicted by the LMε-model goes toward the limit of the homogenous void fraction as the pressure approaches the critical point [17].

2.2 Pressure Drop in Microfin Tubes. Schlager et al. [18] presented the heat transfer and pressure drop data during the evaporation and the condensation of R22 in horizontal microfin tubes having a 9.5 mm outer diameter and an 8.9 mm maximum inner diameter. The authors showed that the pressure drop in microfin tube was slightly higher than that in smooth tube. Also the penalty factors ranged from 1.1 to 1.4 for the various test conditions and increased with increasing mass flux. The same authors conducted similar experimental test with a microfin tube having a 12.7 mm outer diameter and an 11.7 mm maximum inner diameter [19]. They concluded that no significant differences in performances were observed between 9.52 mm and 12.7 mm microfin tubes. Comparative studies were performed by Eckels and Pate [20] on evaporation and condensation heat transfer coefficients and pressure drop data with R134a and R12 in a smooth tube and a microfin tube. They reported that in the case of R12 and for most conditions with R134a, the penalty factors were less than the enhancement factors but in the case of evaporation of R134a, at the lowest saturation temperature and highest mass flux, the penalty factor slightly exceeded the enhancement factors. Eckels and Tesene [21] also conducted comparative studies on pressure drop during condensation in microfin tube with R22, R134a, R410A, and R407C. Their experimental results revealed that the pressure drop increased with quality and mass flux but decreased with increasing saturation temperature. On the other hand, the highest penalty factors were observed at the mass flux of 250 kg/m^2 s while the penalty factors purely decreased or had the lowest value around the average quality of 0.5. Eckels and Tesene [21] com-

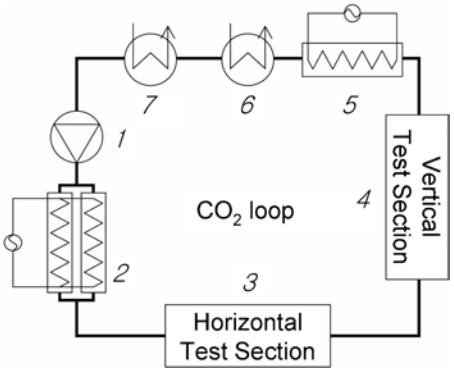

Fig. 1 Simplified schematic diagram of the experimental facility

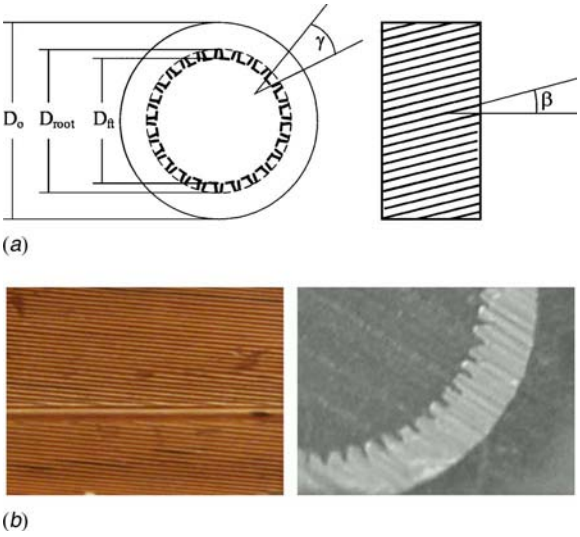

Fig. 2 (*a*) Sketches of common microfin tubes and (*b*) photos of the microfin tube used in present study. (*a*) Sketches of common microfin tubes, (*b*) photos of D_{melt}=3.51 mm microfin tube.

pared the measured pressure drop data with the predictions using the correlations of Dukler et al. [8] and Friedel [11], which were originally developed for smooth tube and generally had good agreement with the experimental data.

Chamra et al. [22,23] presented the heat transfer and pressure drop data for the R22 condensation and evaporation in the microfin and cross-grooved tubes with various helix angles. The test results for the microfin tube showed that the pressure drop slightly increased with increasing helix angle for both evaporation and condensation and the penalty factor had the lowest value at the helix angle of 17.5 deg for evaporation while for the condensation, the penalty factor generally increased with increasing helix angle [22,23].

Zilly et al. [4] conducted experimental studies on condensation of CO_2 at low temperatures in microfin tube in the same laboratory. The experiments were performed in a smooth tube with a diameter of 6.10 mm and a microfin tube with a melt-down diameter of 6.26 mm for mass fluxes ranging from 200 kg/m to 400 kg/m^2 s. The authors showed that the local enhancement factors varied from 2.0 to 3.6 and the local penalty factors varied from 1.1 to 2.2 and from 1.1 to 1.6 for the horizontal and vertical tubes, respectively. Jang and Hrnjak [24] continued and supplemented the work of Zilly et al. [4] with additional experiments and visualization. They showed that the pressure drop correlation of Cavallini et al. [25] was in good agreement with the experimental results.

Based on the pressure drop correlation of Friedel [11] and the void fraction model of Rouhani and Axelsson [16], Cavallini et al. [25] developed a predictive model for two-phase pressure drop in microfin tube. The predictive model of Cavallini et al. [25] gave a mean absolute deviation of 23% with the experimental data of several researchers [1]. Also, various types of predictive models for pressure drop in microfin tubes were proposed by Kaushik and Azer [26], Nozu et al. [27], Newell and Shah [28], and Goto et al. [29]. Unlike the correlations for heat transfer coefficients, most of the pressure drop correlations are applicable for both smooth tube and microfin tube.

3 Experimental Facility

Figure 1 shows a simplified sketch of the testing facility. The flow in the loop is driven by a variable speed gear pump (1). Following the pump, the refrigerant flow is measured by a Coriolis flow meter. A calorimeter (2) is used to bring the subcooled liquid refrigerant to the desired state at the inlet of the test section. The calorimeter has two parallel electrical heaters. Each heater is inside a copper tube with refrigerant flowing through the spirally articulated annulus. By adjusting the power to the calorimeter, the quality of CO_2 at the test section is regulated. The temperature of the CO_2 is measured right before and after the calorimeter, and the saturation pressure is measured with an absolute pressure transducer right before the horizontal pressure drop test section (3). After the calorimeter the refrigerant flows along a horizontal pipe of 1 m length to establish a flow pattern dependent on mass flux and quality. The CO_2 then enters the horizontal (3) and vertical pressure drop test sections (4) having a length of 1 m, in that order. Figure 2 shows the sketches of the common microfin tubes and photos of the microfin tube with the melt-down diameter of 3.51 mm used in the present study. Table 3 reports various dimensions of the tubes used in the experiments of present study and Zilly et al. [4]. The melt-down diameter is the inner diameter of a hypothetical smooth tube with the same outer diameter and cross sectional area of the microfin tube, which is defined by

$$\frac{\pi D_{\text{melt}}^2}{4} = \frac{\pi D_i^2}{4} - A_{\text{fin}} \tag{3}$$

A differential pressure transducer is used to measure the pressure drop in both sections. After leaving the test section, the CO_2 flows through a control heater (5), which evaporates liquid CO_2 in order to keep the pressure of the system at the particular level. This control heater is similar to the calorimeter. The amount of heat to the control heater is regulated by a proportional integral derivative (PID) regulator that uses the pressure measurement as

Table 3 Dimensions of the tubes used in present study

	Microfin tubes	
Description	Zilly et al. [4]	Present study
Outer diameter, D_o	6.98 mm	4.34 mm
Root diameter, D_{root}	6.32 mm	3.74 mm
Fin tip diameter, D_{ft}	5.97 mm	3.30 mm
Melt-down diameter, D_{melt}	6.26 mm	3.51 mm
Fin height	0.18 mm	0.22 mm
Fin base length	0.12 mm	0.17 mm
Gap between fins	0.17 mm	0.04 mm
Number of fins	54	57
Helix anlg, β	14 deg	6 deg
Apex angle, γ	24 deg	30 deg
	Smooth tubes	
Outer diameter, D_o	9.60 mm	5.00 mm
Inner diameter, D_i	6.10 mm	3.48 mm

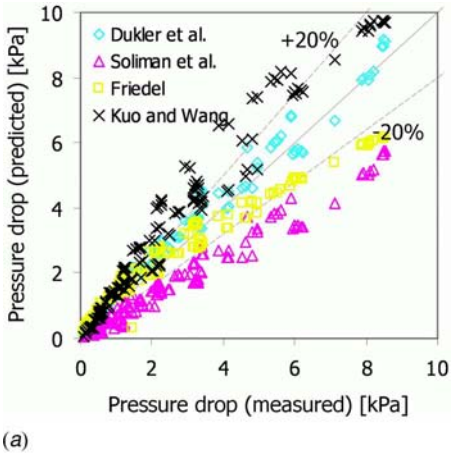

(a)

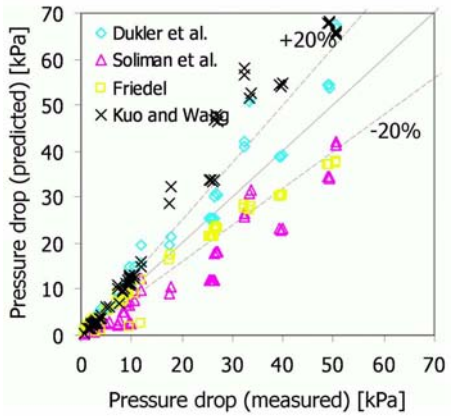

(b)

Fig. 3 Comparisons of horizontal pressure drop data in smooth tube with predictions of Dukler et al. [8], Soliman et al. [6], Friedel [11], and Kuo and Wang [12]. (*a*) Zilly et al. [4] (D_i =6.10 mm), (*b*) present study (D_i=3.48 mm).

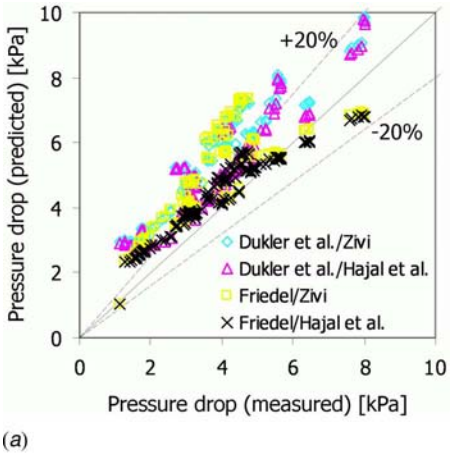

(a)

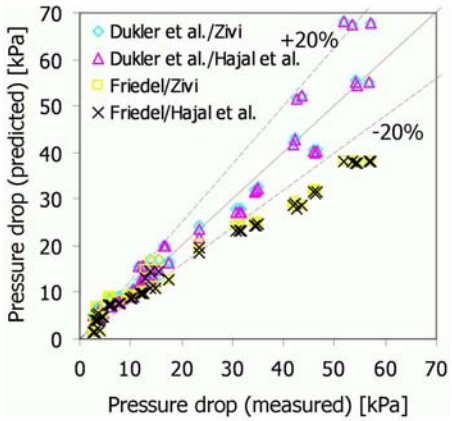

(b)

Fig. 4 Comparisons of vertical pressure drop data in smooth tube with predictions of Dukler et al. [8]/Zivi [14], Dukler et al. [8]/Hajal et al. [17], Friedel [11]/Zivi [14], and Friedel [11]/Hajal et al. [17]. (*a*) Zilly et al. [4] (D_i=6.10 mm), (*b*) present study (D_i=3.48 mm).

input value. The CO_2 is then condensed by the primary heat exchanger (6) with R-404A flowing on the other side, and finally subcooled by the subcooling unit (7) prior to returning to the pump.

4 Data Reduction

The equation used to calculate the calorimeter outlet enthalpy, $h_{cal,o}$, is given by

$$h_{cal,o} = h_{cal,i} + \frac{\dot{Q}_{cal} + \dot{Q}_{cal,amb} + \dot{Q}_{pipe,amb}}{\dot{m}_{CO_2}} \tag{4}$$

where $h_{cal,i}$ is the calorimeter inlet enthalpy, which is calculated by using REFPROP 6.0 [30] with the measured calorimeter inlet temperature and pressure, $\dot{Q}_{cal}$ is the controlled heat input to the calorimeter, $\dot{Q}_{cal,amb}$ and $\dot{Q}_{pipe,cal}$ are the heat transfer losses from the calorimeter and the connecting pipe to ambient and $\dot{m}_{CO_2}$ is the refrigerant mass flow rate. Then, the inlet vapor quality, x, to the horizontal pressure drop test section can be determined by

$$x = \frac{h_{cal,o} - h_{sat,l}}{h_{sat,v} - h_{sat,l}} \tag{5}$$

where $h_{sat,l}$ and $h_{sat,v}$ are the saturated liquid and saturated vapor enthalpies calculated by using REFPROP 6.0 [30] with measured horizontal test section inlet pressure. The saturation temperature, T_{sat}, is also evaluated using REFPROP 6.0 [30] and the horizontal test section inlet pressure. Assuming that the horizontal pressure drop test sections are adiabatic, the calculated x and T_{sat} were used as the representative vapor quality and the saturation temperature of each measured horizontal pressure drop data point. For the vertical pressure drop measurements, the pressure drop through the horizontal test section, which was measured by using a differential pressure transducer, was subtracted from the horizontal test section inlet pressure and thus the vapor quality and the saturation temperature were adjusted as well. However, since the pressure drop was very small compared to the absolute pressure, the adjustments in vapor quality and saturation temperature in vertical pressure drop were mostly negligible.

PF is calculated by following equation:

$$PF = \frac{\Delta P_{en}}{\Delta P_{sm}} \tag{6}$$

where ΔP_{en} and ΔP_{sm} are the measured pressure drops in microfin and smooth tubes having equivalent diameter at same operating conditions, respectively.

The measured parameters are temperature, mass flow rate, absolute pressure, and electrical power input. The uncertainty for temperature reading is 0.1 K for calibrated thermocouples relative to each other. Calibration was done by using the setup of the test rig including cables, datalogger, and reference temperature. The uncertainties of these instruments are therefore included in the uncertainty of the thermocouples. The uncertainty of the Coriolis mass flow meter is almost constant at 0.15% of the reading for mass flow rates above 4% of full scale. The uncertainty in abso-

Table 4 The mean absolute deviations of the pressure drop predictions using several pressure drop correlations from the measured pressure drop in smooth tubes

	Correlations	Zilly et al. [4]	Present study	Total
Horizontal	Dukler et al. [8]	29.0%	23.2%	27.3%
	Soliman et al. [6]	36.2%	37.4%	36.6%
	Friedel [11]	32.4%	23.8%	29.8%
	Kuo and Wang [12]	37.2%	27.0%	34.2%
Vertical	Dukler et al. [8]/Zivi [14]	53.1%	27.9%	44.8%
	Dukler et al. [8]/Hajal et al. [17]	35.7%	19.5%	30.3%
	Friedel [11]/Zivi [14]	39.1%	34.4%	37.5%
	Friedel [11]/Hajal et al. [17]	22.2%	26.9%	23.8%

lute pressure and differential pressure measurements are 0.1% and 0.2% of the full scales (3 MPa and 30 kPa), respectively. The uncertainty in the output value of the electrical power transducer is given as 0.2% of the measured value.

The experimental uncertainties of the vapor quality and saturation temperature reported in this paper were estimated with the Taylor simplification error propagation described in Moffat [31]. All uncertainty data are based on a confidence level of 95%. The estimated vapor quality uncertainty ranges from $\pm 1.8\%$ to $\pm 26.2\%$ (at the lowest vapor quality) and the uncertainty of saturation temperature was estimated to be almost constant at $\pm 0.29\%$ and $\pm 0.39\%$ for each saturation temperatures of $-25\,^{\circ}\mathrm{C}$ and $-15\,^{\circ}\mathrm{C}$, respectively. Also the uncertainty of penalty factors can be calculated with error propagation analysis applied to Eq. (6). The results show that the uncertainty of penalty factors ranges from $\pm 0.31\%$ to $\pm 0.41\%$ for both horizontal and vertical tubes.

5 Results and Discusstion

5.1 Pressure Drop Inside Smooth Tube. The measured horizontal and vertical pressure drop data of the present study and Zilly et al. [4] are compared with several pressure drop correlations in Fig. 3 and 4, respectively. The mean absolute deviations of pressure drop of the present study and Zilly et al. [4] defined as Eq. (7) are listed in Table 4.

$$E_{\mathrm{abs}} = \frac{\sum \frac{|\Delta P_{\mathrm{pred}} - \Delta P_{\mathrm{meas}}|}{\Delta P_{\mathrm{meas}}}}{N} \times 100\ (\%) \tag{7}$$

For the horizontal pressure drop, the predictive models of Dukler et al. [8] and Friedel [11] gave a relatively high accuracy while the predictive model of Soliman et al. [6] and Kuo and Wang [12] significantly under- and overpredicted the data, respectively. The slight superiority of the correlations of Dukler et al. [8] and Friedel [11] is possibly attributed to the universality of those correlations. The predictive model of Dukler et al. [8] was the first approach using the principles of similarity analysis and that of Friedel [11] was developed for both horizontal and vertical smooth tubes with a data bank of 25,000 data points, which was taken in channels with a diameter over 1 mm. Meanwhile, the correlations of Soliman et al. [6] and Kuo and Wang [12] were originated from the correlation of Lockhart and Martinelli [5]. In other words, the theoretical approach of the correlations of Dukler et al. [8] and the substantial data bank of the correlation of Friedel [11] widen the applicable range of those correlations.

For the vertical pressure drop, noticeable fact is that the combined models with the void fraction model of Hajal et al. [17] showed significantly better performance than those with Zivi [14]. The void fraction model and flow regime map of Hajal et al. [17] was developed by slightly modifying the flow pattern map of Kattan et al. [32] that is originally developed for evaporation. Hajal et al. [17] mentioned that the homogenous model was applicable to flows where the vapor and liquid phases traveled at nearly the same velocity, such as near the critical point or at very high mass velocities where the flow regime was either bubbly flow or mist flow. They also indicated that no existing void fraction model was valid over the entire pressure range up to the critical pressure since none tended to the homogeneous model as saturation pressure got close to the critical pressure. This means that existing void fraction models are valid over the typical operating range of reduced pressure, but the void fraction of high pressure refrigerants, which has a higher value of reduced pressure, may not be predicted well by existing void fraction models. Briefly speaking, the carbon dioxide is the representative refrigerant typically operated at high reduced pressure and the void fraction model of Hajal et al. [17] is applicable to the operating range of the system using carbon dioxide as a refrigerant, where commonly used void fraction models usually fail.

The frictional pressure drop mainly depends on the wall shear stress between liquid phase and tube wall and the interfacial shear stress between liquid and vapor phases. Roughly speaking, these shear stresses are strongly affected by the velocity gradient of each phase. The larger bulk velocity of the liquid phase allows the larger velocity gradient of the liquid phase near the tube wall, which results in the increase of wall shear stress. Similarly, since the liquid-vapor interface acts like a tube wall to the vapor phase, the increase of velocity difference between the liquid and vapor phases causes the increase of interfacial shear stress. Figure 5(*a*) clearly evidences these mechanisms. As the mass flux and vapor quality increase, the liquid phase velocity and the velocity difference between the phases increase. Consequently, the pressure drop as well as the shear stresses increase. The exceptional case is the lowest mass flux ($200\ \mathrm{kg/m^2\,s}$) in the vertical pressure drop, where the effect of the gravitational pressure drop is more dominant and the pressure drop remains nearly constant with increasing vapor quality.

When the vertical pressure drop is compared with the horizontal pressure drop, the effect of the gravity (or gravitational pressure drop) showed various aspects with respect to the mass flux and vapor quality. At the lowest mass flux ($200\ \mathrm{kg/m^2\,s}$), the gravitational pressure drop played very important role that allows more pressure drop, about 3–5 kPa, to the vertical pressure drop. However, as the vapor quality increases, the difference between the horizontal and vertical pressure drops shrinks. Finally, at the very high quality, the difference becomes almost insignificant. On the other hand, at the middle mass flux ($400\ \mathrm{kg/m^2\,s}$), the gravitational pressure drop shows nearly no change with the increase of the vapor quality, and at the highest mass flux ($800\ \mathrm{kg/m^2\,s}$), the trend is finally reversed, which means the gravitational pressure drop does not decrease but slightly increases with increasing vapor quality. According to the Eq. (1), due to the significantly higher density of the liquid phase than the vapor phase the gravitational pressure drop mostly depends on the weight of the liquid phase. Moreover, as the vapor quality increases, the amount of the liquid phase diminishes. Consequently, at the very high vapor quality, the cross sectional area of the tube is mostly occupied by the vapor phase of the refrigerant, and then the vertical pressure drop has almost same value with the horizontal pressure drop, as shown in the lowest mass flux ($200\ \mathrm{kg/m^2\,s}$) case. However, as seen in Fig. 5(*a*), at sufficiently high mass flux, the trend does not follow the Eq. (1). In the case of vertical two-phase flow, additional waves are generated on the liquid film due to the gravity. The waves on the liquid film act much like surface roughness in single-phase flow, causing increased friction due to the form drag [33]. Wongwises and Kongkiatwanitch [34] observed that in annular two-phase upward cocurrent flow in a vertical circular pipe, the interfacial shear stress increased with increasing vapor Reynolds number ($\mathrm{Re}_v = GDx/\mu_v$), which is proportional to the vapor quality and mass flux. Accordingly, in the vertical two-phase flow, the liquid film surface is rougher and the surface wave frequency

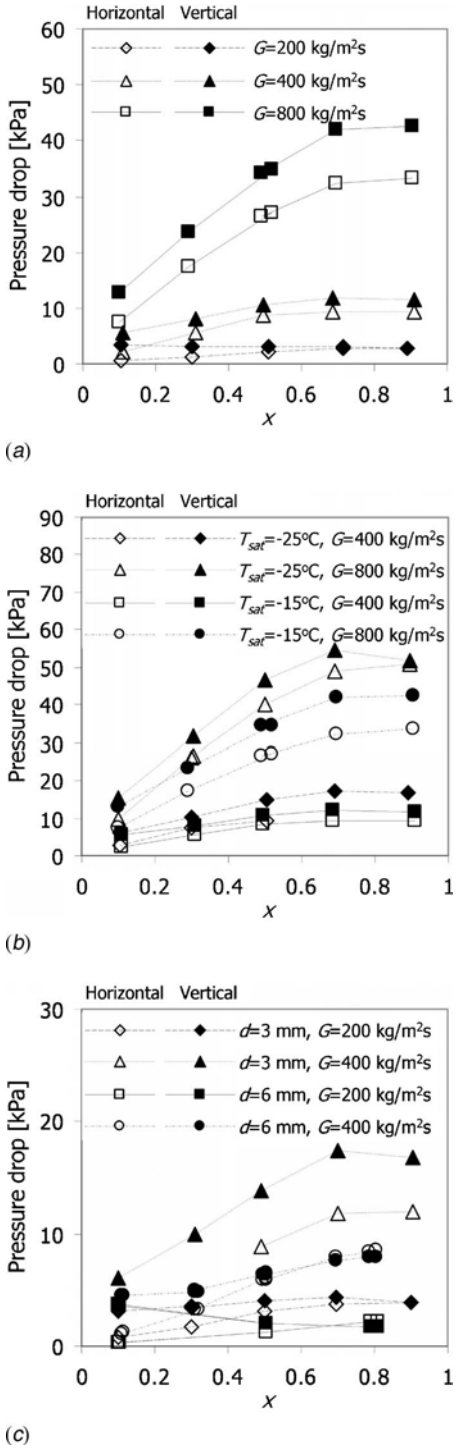

Fig. 5 Effects of (*a*) mass flux, (*b*) saturation temperature, and (*c*) diameter on adiabatic horizontal and vertical pressure drop in smooth tube. (*a*) Mass flux (D_i=3.48 mm, T_{sat}=−15 °C), (*b*) saturation temperature (D_i=3.48 mm), (*c*) diameter (T_{sat}=−25 °C).

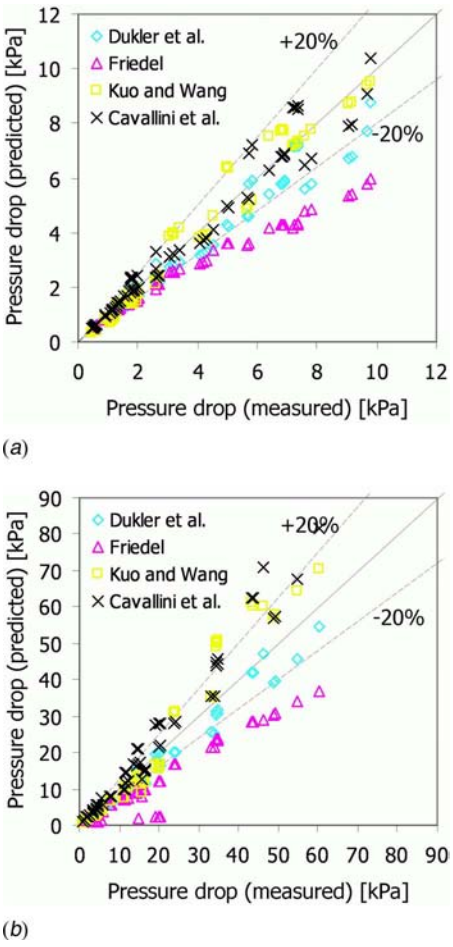

Fig. 6 Comparisons of horizontal pressure drop data in micro tube with predictions of Dukler et al. [8], Friedel [11], Kuo and Wang [12] and Cavallini et al. [25]. (*a*) Zilly et al. [4] (D_{melt}=6.26 mm), (*b*) present study (D_{melt}=3.51 mm).

is higher so that the interfacial shear stress is larger than those in the horizontal two-phase flow. In addition, this phenomenon proportionally depends on the mass flux and vapor quality, causing the results in Fig. 5(*a*).

The effect of the saturation temperature on pressure drop in smooth tube is depicted in Fig. 5(*b*). The increase of saturation temperature leads to the increase of the reduced pressure, which means that the flow is losing its two-phase flow characteristics, i.e., a decrease of the difference between vapor and liquid velocities, density, viscosity, and so on. Moreover, the reduction in liquid density also resulted from the increase of saturation temperature. Therefore, the wall shear stress and the interfacial shear stress decrease and thus the pressure drop decreases with increasing saturation temperature, as shown in Fig. 5(*b*).

Figure 5(*c*) shows the effect of tube diameter for two mass fluxes on pressure drop in smooth tubes. The pressure drop data in smooth tube with D_i=6.10 mm measured by Zilly et al. [4] is plotted in Fig. 5(*c*) as well. As expected, the pressure drop decreases when the diameter of tube is increased. Frictional pressure drop can be expressed as

$$-\left(\frac{\Delta P}{\Delta L}\right)_f = -\left(\frac{\Delta P}{\Delta L}\right)_{f,\mathrm{lo}} \phi_{\mathrm{lo}}^2 = \frac{f_{\mathrm{lo}} G^2}{2D\rho_l}\phi_{\mathrm{lo}}^2 \tag{8}$$

Considering that $f_{\mathrm{lo}} \sim D^{-0.25}$ in turbulent flow and from the definition $\phi_{\mathrm{lo}}^2 = (\Delta P/\Delta L)_{\mathrm{TP}}/(\Delta P/\Delta L)_{\mathrm{lo}}$ can be roughly assumed to be a weak function of diameter, Eq. (8) shows that the pressure drop is almost inversely proportional to the diameter, which can be the evidence for the diameter effect on pressure drop in Fig. 5(*c*). Additionally, indirect effect of tube diameter on the pressure drop exists. Since the wall shear and interfacial shear stresses are affected by the way how the liquid phase is in contact with the tube wall and the liquid and vapor phases are distributed inside the tube cross section, the flow regime should have an influence on the two-phase pressure drop characteristics. As observed by Dobson and Chato [35], the tube diameter affected the flow regime

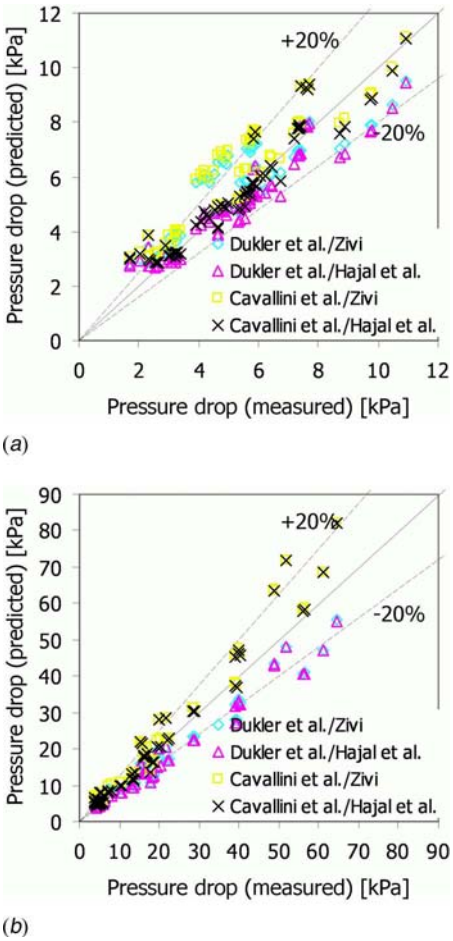

Fig. 7 Comparisons of vertical pressure drop data in microtube with predictions of Dukler et al. [8]/Zivi [14], Dukler et al. [8]/Hajal et al. [17], Cavallini et al. [25]/Zivi [14], and Cavallini et al. [25]/Hajal et al. [17]. (*a*) Zilly et al. [4] (D_{melt}=6.26 mm), (*b*) present study (D_{melt}=3.51 mm).

transitions. As the tube diameter was reduced at a fixed mass flux, the transition from wavy flow to wavy-annular flow and the transition from wavy-annular flow to annular flow shifted to lower qualities. In short, the results shown in Fig. 5(*c*) are caused by the combinations of the direct and indirect effects of the tube diameter on pressure drop.

5.2 Pressure Drop Inside Microfin Tube. In Figs. 6 and 7, the comparison of the horizontal and vertical pressure drops in microfin tubes of the present study and Zilly et al. [4] with the several correlations is shown. The mean absolute deviations are listed in Table 5. The melt-down diameter was used as an equivalent diameter for calculating the frictional pressure drop in microfin tube using the correlations of Dukler et al. [8] and Friedel [11], which were originally developed for smooth tube only. It is interesting that the correlations of Dukler et al. [8] and Friedel [11] happen to show better performance to predict the pressure drop in microfin tubes than that in smooth tubes even developed for smooth tubes. However, both correlations mostly underpredicted the measured pressure drop, which means that the melt-down diameter is not satisfactory to consider the finned geometry of the microfin tube wall. The correlation of Cavallini et al. [25] showed superior accuracy with total deviations of 12.4% and 14.7% for the horizontal and vertical pressure drops, respectively. The correlation of Cavallini et al. [25] was originally developed for the pressure drop during condensation in microfin and cross-grooved tubes with the correction factor of Mickley et al. [36] to account for the mass transfer on the interfacial shear stress [1]. In present study, the correction factor of Mickley et al. [36] was not considered for calculating the adiabatic pressure drop. The distinctive feature of the correlation of Cavallini et al. [25] is that the microfin tube is considered as rough tube that has roughness of fin height. Moreover, the fictitious roughness is used to determine the friction factor for microfin tube instead using the melt-down diameter, which may result in the prominent accuracy of the pressure drop correlation of Cavallini et al. [25]. The void fraction model of Hajal et al. [17] shows better performance to predict the vertical pressure drop, which may be resulted from the same reason with the smooth tube. The smallest deviation was produced by the combination of the pressure drop correlation of Cavallini et al. [25] and void fraction model of Hajal et al. [17], which gives E_{abs} of 12.8%, 16.7%, and 14.7% for the experimental data in microfin tubes of Zilly et al. [4], present study, and total, respectively.

The horizontal and vertical pressure drop data of adiabatic two-phase flow in microfin tubes are plotted versus quality with the variations of mass flux in Fig. 8(*a*). As shown, the trend is not much different from that of smooth tubes. The pressure drop increases with increasing quality and mass flux. Exceptionally, the vertical pressure drop at the lowest mass flux (200 $kg/m^2 s$) seems to be nearly irrespective of the vapor quality change, which means that the reduction of the gravitational pressure drop due to the diminishing amount of liquid phase is almost equally compensated by the increase of the frictional pressure drop and thus remains constant with increasing vapor quality. However, at the higher mass fluxes, the trend shown in the lowest mass flux does not appear. At the highest mass flux (800 $kg/m^2 s$), the vertical pressure drop increases with respect to the vapor quality following the variations of horizontal pressure drop, and thus the difference between the vertical and horizontal pressure drops is almost invariant. These phenomena are similar with the smooth tubes, which is caused by the increased interfacial shear stress due to gravity in vertical two-phase flow.

The vertical pressure drop predictions using the simple combination of the frictional pressure drop correlation and void fraction model may not be satisfactory to predict the pressure drop in vertical two-phase flow because the frictional pressure drop in

Table 5 The mean absolute deviations of the pressure drop the predictions using several pressure drop correlations from the measured pressure drop in microfin tubes

	Correlations	Zilly et al. [4]	Present study	Total
Horizontal	Dukler et al. [8]	14.6%	17.4%	16.0%
	Friedel [11]	26.0%	35.5%	30.7%
	Kuo and Wang [12]	13.7%	28.8%	21.1%
	Cavallini et al. [25]	8.3%	16.6%	12.4%
Vertical	Dukler et al. [8]/Zivi [14]	20.4%	19.8%	20.1%
	Dukler et al. [8]/Hajal et al. [17]	13.2%	18.3%	15.7%
	Cavallini et al. [25]/Zivi [14]	24.8%	23.3%	24.0%
	Cavallini et al. [25]/Hajal et al. [17]	12.8%	16.7%	14.7%

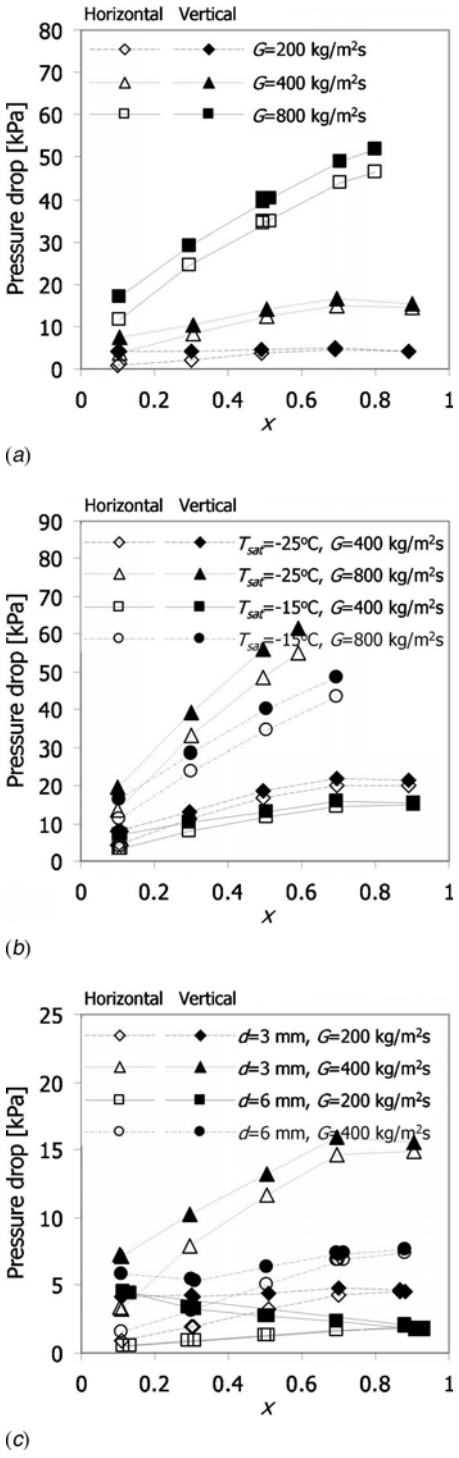

Fig. 8 Effects of (*a*) mass flux, (*b*) saturation temperature, and (*c*) diameter on adiabatic horizontal and vertical pressure drop in microfin tube. (*a*) Mass flux (D_{melt}=3.51 mm, T_{sat}=−15 °C), (*b*) saturation temperature (D_{melt}=3.51 mm), (*c*) diameter (T_{sat}=−15 °C).

vertical two-phase flow is considerably different from that in horizontal two-phase flow due to the form drag. However, the comparisons in Figs. 4 and 7 evidenced that the simple combinations were fairly accurate to predict the vertical pressure drop. This may be because the correlation of Friedel [11] were developed based on the extensive databank, which includes the vertical tube data and the correlation of Dukler et al. [8] was developed with very theoretical basis using the similarity analysis. The correlation of Cavallini et al. [25] was developed by modifying the correlation of Friedel [11].

Figures 8(*b*) and 8(*c*) show the effects of saturation temperature and tube diameter on pressure drop in microfin tubes, respectively. As seen in Figs. 8(*b*) and 8(*c*), both the horizontal and vertical pressure drops in microfin tube are similar to the results of smooth tubes. The finned geometry has nearly no significant effect on the pressure drop mechanisms except that the pressure drop in microfin tube has higher value than that in smooth tube. This means that the microfin tube can be considered as "very rough tube" having the roughness of the fin height and thus existing frictional pressure drop correlations can be successfully used with slightly modified microfin tube friction factor. Kedzierski and Goncalves [2] also observed that the exponent of Reynolds number on their correlation was consistent with that obtained from the Moody chart, which supports the results in Figs. 8(*b*) and 8(*c*).

Table 6 shows the average enhancement factors and average penalty factors at various operating conditions. Temperature difference between the inner wall and the refrigerant (ΔT) is included as one of the operating conditions, which is only applicable to the enhancement factor. The enhancement factor data are obtained from the experiment that was accompanied with present pressure drop experiment by the same authors of the present study [37]. The average enhancement factors of the present study and Zilly et al. [4] range from 1.1 to 1.8 and from 1.9 to 2.8, respectively. For the horizontal two-phase flow, the average penalty factors of the present study and Zilly et al. [4] range from 1.3 to 1.7 and from 1.3 to 1.6, respectively while the vertical pressure drop penalty factors of the present study and Zilly et al. [4] range from 1.2 to 1.4 and from 1.1 to 1.4, respectively. Since the vertical pressure drop mostly had larger value than the horizontal pressure drop, the penalty factor of vertical two-phase flow was smaller. Generally, D_{melt}=6.26 mm microfin tube had better performance than D_{melt}=3.51 mm microfin tube. When the ratio of enhancement factor to penalty factor is merely compared, at operating conditions of the saturation temperature of −25 °C, the temperature difference of 3 °C, the mass flux of 200 kg/m^2 s, and the diameter of 6 mm, the microfin tube shows the best performance.

6 Conclusion

In this study, the pressure drop data of adiabatic flow of CO_2 at saturation temperatures around −20 °C in smooth and microfin tubes in horizontal and vertical orientations were presented. Qualitative analysis was discussed such as the analysis of the effect of several parameters on pressure drop in smooth tubes and microfin tubes with refrigerant CO_2.

The thermophysical properties of carbon dioxide at the saturation temperature around −20 °C are similar with the other commonly used refrigerants in regular condensation conditions. Accordingly, the investigated characteristics of the horizontal pressure drop of carbon dioxide in smooth tube were qualitatively analogous to those of commonly used refrigerants. However, the frictional pressure drop in vertical two-phase flow was different from that in horizontal flow, which was caused by the difference in flow regime and the gravitational effects. Therefore, the simple combination of the frictional pressure drop correlation and void fraction model is not satisfactory to cover the whole operating ranges of usual applications. In the case of gravitational pressure drop, the void fraction model of Hajal et al. [17] showed relatively better performance that resulted from the considerations of the homogeneous state at the critical point.

The experimental results showed that the effects of the saturation temperature and the tube diameter were identical between smooth tubes and microfin tubes. In other words, microfin tube can be considered as very rough tube having the roughness of the fin height and thus existing frictional pressure drop correlations can be successfully used with slightly modified microfin tube friction factor.

Table 6 Average enhancement and penalty factors

D_{melt} (mm)	T_{sat} (°C)	G (kg/m^2 s)	ΔT (°C)	EF	PF (Horizontal)	PF (Vertical)
(6.26 Zilly et al. [4])	−15	200	3	2.5	1.6	1.4
	−15	200	6	2.6		
	−15	400	3	2.0	1.4	1.3
	−15	400	6	1.9		
	−25	200	3	2.8	1.5	1.1
	−25	300	3	2.4	1.4	1.3
	−25	400	3	2.1	1.3	1.3
	−25	400	6	2.1		
(3.51 Present study)	−15	200	3	1.8	1.6	1.4
	−15	200	6	1.8		
	−15	400	3	1.5	1.5	1.3
	−15	400	6	1.5		
	−15	800	3	1.2	1.4	1.2
	−15	800	6	1.2		
	−25	200	3	1.8	1.5	1.4
	−25	200	6	1.8		
	−25	400	3	1.5	1.7	1.3
	−25	400	6	1.5		
	−25	800	3	1.1	1.3	1.3
	−25	800	6	1.2		

The rough comparison between the enhancement factors and the penalty factors of the present study shows that it is not true that the heat transfer enhancement by the internally finned geometry is always a superior mechanism to the pressure drop penalty, which means that under specific operating conditions with unoptimized fin geometry, the microfin tube could degrade the in-tube condensation performance in the refrigeration and air-conditioning systems using CO_2 as refrigerant. It is necessary to make a quantitative and fine investigation into the relations between the diameter of microfin tube and its usefulness.

Acknowledgment

The authors are grateful to ACRC consortium and Wolverine for their help in realization of this project. This work is jointly supported by the Micro Thermal System Research Center of Seoul National University and BK21 program of the Ministry of Education.

Nomenclature

A_{fin} = cross-sectional area occupied by fin inside microfin tube (m^2)
C = coefficient in the correlation of Chisholm [7]
D = diameter (m)
D_i = inner diameter of smooth tube (m)
D_o = outer diameter (m)
E_{abs} = mean absolute deviation
f = friction factor
g = acceleration of gravity, 9.8 m/s^2
i = enthalpy (J/kg)
G = mass flux (kg/m^2 s)
L = length (m)
N = the number of data
P = pressure (kPa)
ΔP = pressure drop (kPa)
$\dot{Q}$ = heat transfer (W)
Re = Reynolds number, GD/μ
T = temperature (°C)
ΔT = temperature difference between tube inner wall and refrigerant (°C)
X = Martinelli parameter, $\sqrt{(\Delta P/\Delta L)_l/(\Delta P/\Delta L)_v}$
x = vapor quality

Greek Symbols

ε = void fraction
β = helix angle (deg)
ρ = density (kg/m^3)
γ = apex angle (deg)
μ = viscosity (kg/m s)
ϕ_v = two-phase multiplier for gas phase, $\sqrt{(\Delta P/\Delta L)_{TP}/(\Delta P/\Delta L)_v}$
ϕ_{lo} = two-phase multiplier for liquid phase flows with total mass flux, $\sqrt{(\Delta P/\Delta L)_{TP}/(\Delta P/\Delta L)_{lo}}$
Γ = physical property coefficient, $\sqrt{\Delta P_{vo}/\Delta P_{lo}}$
φ = angle between tube and horizontal (deg)

Subscripts

amb = ambient
cal = calorimeter
CO_2 = refrigerant carbon dioxide
en = enhanced (microfin) tube
f = frictional
ft = fin-tip of microfin
g = gravitational
Hajal = Hajal et al. [17]
hom = homogeneous
i = inlet
l = liquid phase or liquid phase flows with its own mass flux
lo = liquid phase flows with total mass flux
meas = measured
melt = melt-down
o = outlet
pipe = pipe
pred = predicted
RA = Rouhani and Axelsson
root = fin root
sat = saturated
sm = smooth tube
TP = two-phase
v = gas phase or gas phase flows with its own mass flux
vo = gas phase flows with total mass flux

References

[1] Cavallini, A., Del Col, D., Doretti, L., Longo, G. A., and Rossetto, L., 2000, "Heat Transfer and Pressure Drop During Condensation of Refrigerants Inside Horizontal Enhanced Tubes," Int. J. Refrig. **23**, pp. 4–25.

[2] Kedzierski, M. A., and Goncalves, J. M., 1999, "Horizontal Convective Condensation of Alternative Refrigerants Within a Micro-Fin Tube," J. Enhanced Heat Transfer, **6**, pp. 161–178.

[3] Cavallini, A., Censi, G., Del Col, D., Doretti, L., Longo, G. A., Rossetto, L., and Zilio, C., 2003, "Condensation Inside and Outside Smooth and Enhanced Tubes—A Review of Recent Research," Int. J. Refrig., **26**, pp. 373–392.

[4] Zilly, J., Jang, J., and Hrnjak, P. S., 2003, "Condensation of CO_2 at Low Temperatures in Micro-Fin Horizontal Tubes," University of Illinois at Urbana-Champaign, ACRC Technical Report 49.

[5] Lockhart, R. W., and Martinelli, R. C., 1949, "Proposed Correlation of Data for Isothermal Two-Phase, Two-Component Flow in Pipes," Chem. Eng. Prog., **45**(1), pp. 39–48.

[6] Soliman, M., Schuster, J. R., and Berenson, P. J., 1968, "A General Heat Transfer Correlation for Annular Flow Condensation," ASME J. Heat Transfer, **90**, pp. 267–276.

[7] Chisholm, D., 1967, "A Theoretical Basis for the Lockhart–Martinelli Correlation for Two-Phase Flow," Int. J. Heat Mass Transfer, **10**, pp. 1767–1778.

[8] Dukler, A. E., Wicks, M., III, and Cleveland, R. G., 1964, "Frictional Pressure Drop in Two-Phase Flow: B. An Approach Through Similarity Analysis," AIChE J., **10**, pp. 44–51.

[9] Chisholm, D., 1973, "Pressure Gradients Due to Friction During the Flow of Evaporating Two-Phase Mixtures in Smooth Tubes and Channels," Int. J. Heat Mass Transfer, **16**, pp. 347–358.

[10] Baroczy, C. J., 1966, "A Systematic Correlation for Two-Phase Pressure Drop," Chem. Eng. Prog., Symp. Ser., **62**, pp. 232–249.

[11] Friedel, L., 1979, "Improved Friction Pressure Drop Correlations for Horizontal and Vertical Two-Phase Pipe Flow," European Two-Phase Flow Group Meeting, Paper No. E2.

[12] Kuo, C. S., and Wang, C. C., 1996, "In-Tube Evaporation of HCFC-22 in a 9.52 mm Micro-Fin/Smooth Tube," Int. J. Heat Mass Transfer, **39**(12), pp. 2559–2569.

[13] Wang, C. C., Chiang, C. S., and Yu, J. G., 1998, "An Experimental Study of In-Tube Evaporation of R-22 Inside a 6.5-mm Smooth Tube," Int. J. Heat Fluid Flow, **19**, pp. 259–269.

[14] Zivi, S. M., 1964, "Estimation of Steady-State Steam Void-Fraction by Means of the Principle of Minimum Entropy Production," ASME J. Heat Transfer, **86**, pp. 247–252.

[15] Friedel, L., 1980, "Pressure Drop During Gas/Vapor-Liquid Flow in Pipes," Int. Chem. Eng., **20**(3), pp. 352–367.

[16] Rouhani, Z., and Axelsson, E., 1970, "Calculation of Void Volume Fraction in the Subcooled and Quality Boiling Region," Int. J. Heat Mass Transfer, **13**, pp. 383–393.

[17] Hajal, J. E., Thome, J. R., and Cavallini, A., 2003, "Condensation in Horizontal Tubes, Part 1: Two-Phase Flow Pattern Map," Int. J. Heat Mass Transfer, **46**, pp. 3349–3363.

[18] Schlager, L. M., Pate, M. B., and Bergles, A. E., 1989, "Heat Transfer and Pressure Drop During Evaporation and Condensation of R22 in Horizontal Micro-Fin Tubes," Int. J. Refrig., **12**, pp. 6–14.

[19] Schlager, L. M., Pate, M. B., and Bergles, A. E., 1990, "Evaporation and Condensation Heat Transfer and Pressure Drop on Horizontal, 12.7-mm Microfin Tubes With Refrigerant 22," ASME J. Heat Transfer **112**, pp. 1041–1047.

[20] Eckels, S. J., and Pate, M. B., 1991, "Evaporation and Condensation of HFC-134a and CFC-12 in a Smooth Tube and a Micro-Fin Tube," ASHRAE Trans., **97**, pp. 71–81.

[21] Eckels, S. J., and Tesene, B. A., 1999, "A comparison of R-22, R-134a, R-410a, and R-407C Condensation Performance in Smooth and Enhanced Tubes: Part II, Pressure Drop," ASHRAE Trans., **105**, pp. 442–452.

[22] Chamra, L. M., Webb, R. L., and Randlett, M. R., 1996, "Advanced Micro-Fin Tubes for Evaporation," Int. J. Heat Mass Transfer, **39**(9), pp. 1827–1838.

[23] Chamra, L. M., Webb, R. L., and Randlett, M. R., 1996b, "Advanced Micro-Fin Tubes for Condensation," Int. J. Heat Mass Transfer, **39**(9), pp. 1839–1846.

[24] Jang, J., and Hrnjak, P. S., 2004, "Condensation of CO_2 at Low Temperatures," Technical Report ACRC CR-56.

[25] Cavallini, A., Del Col, D., Doretti, L., Longo, G. A., and Rossetto, L., 1997, "Pressure Drop During Condensation and Vaporisation of Refrigerants Inside Enhanced Tubes," Heat Technol., **15**(1), pp. 3–10.

[26] Kaushik, N., and Azer, N. Z., 1990, "A General Pressure Drop Correlation for Condensation Inside Internally Finned Tubes," ASHRAE Trans., **96**, pp. 242–250.

[27] Nozu, S., Katayama, H., Nakata, H., and Honda, H., 1998, "Condensation of a Refrigerant CHC11 in Horizontal Microfin Tubes (Proposal of a Correlation Equation for Frictional Pressure Gradient)," Exp. Therm. Fluid Sci., **18**, pp. 82–96.

[28] Newell, T. A., and Shah, R. K., 1999, "Refrigerant Heat Transfer, Pressure Drop, and Void Fraction Effects in Microfin Tubes," *Proceedings of the Second International Symposium Experimentation*, on Two-Phase Flow and Experimentation, Edizioni ETS, Italy, Vol. 3, pp. 1623–1639.

[29] Goto, M., Inoue, N., and Ishiwatari, N., 2001, "Condensation and Evaporation Heat Transfer of R410A Inside Internally Grooved Horizontal Tubes," Int. J. Refrig., **24**(7), pp. 628–638.

[30] McLinden, M. O., Klein, S., Lemmon, E., and Peskin, A., 1998, NIST Thermodynamic and Transport Properties of Refrigerants and Refrigerant Mixtures Database (REFPROP), Version 6.0, National Institute of Standards and Technology, Gaithersburg, MD.

[31] Moffat, R. J., 1988, "Describing the Uncertainties in Experimental Results," Exp. Therm. Fluid Sci., **1**, pp. 3–17.

[32] Kattan, N., Thome, J. R., and Favrat, D., 1998, "Flow Boiling in Horizontal Tubes: Part I—Development of a Diabatic Two-Phase Flow Pattern Map," ASME J. Heat Transfer, **120**, pp. 140–147.

[33] Bergelin, O. P., Kegel, P. K., Carpenter, F. G., and Gazley, C., Jr., 1949, "Co-Current Gas Liquid Flow. II. Flow in Vertical Tubes," Proceedings of Heat Transfer and Fluid Mechanics Institute, pp. 19–28.

[34] Wongwises, S., and Kongkiatwanitch, W., 2001, "Interfacial Friction Factor in Vertical Upward Gas-Liquid Annular Two-Phase Flow," Int. Commun. Heat Mass Transfer, **28**(3), pp. 323–336.

[35] Dobson, M. K., and Chato, J. C., 1998, "Condensation in Smooth Horizontal Tubes," ASME J. Heat Transfer, **120**, pp. 193–213.

[36] Mickley, H. S., Ross, R. C., Squyers, A. L., and Stewart, W. E., 1954, "Heat, Mass and Momentum Transfer for Flow Over a Flat Plate With Blowing or Suction," Report No. NACA-TN-3208.

[37] Kim, Y. J., Jang, J., Hrnjak, P. S., and Kim, M. S., 2007, "Condensation Heat Transfer of Carbon Dioxide Inside Horizontal Smooth and Micro-Fin Tubes at Low Temperatures," ASME J. Heat Transfer, submitted.

Akira Nakayama

Yusuke Kuwahara

Department of Mechanical Engineering,
Shizuoka University,
3-5-1 Johoku,
Hamamatsu 432-8561, Japan

Kansei Iwata
DGS Computer Ltd.,
2-7 Minami-Ohsawa,
Hachioji 162-0393, Japan

Masafumi Kawamura
School of Medicine,
Keio University,
35 Shinanomachi, Shinjuku,
Tokyo 160-8582, Japan

The Limiting Radius for Freezing a Tumor During Percutaneous Cryoablation

The freezing front in a tumor during percutaneous cryoablation therapy was traced both analytically and numerically exploiting a bioheat equation. It has been shown that there exists a limiting size of the tumor, which one single cryoprobe can freeze at the maximum. The freezing front moves radially outward from the cryoprobe and reaches the end, where the heat from the surrounding tissue to the frozen tissue balances with the heat being absorbed by the cryoprobe. An excellent agreement between the analytical and numerical results has been achieved for the time required to freeze the tumor using the cryoprobe of a single needle. An analytical expression for estimating the limiting radius has been derived to give useful information for cryotherapy treatment plans.
[DOI: 10.1115/1.2969759]

Keywords: bioheat transfer, cryoablation, porous media, freezing

Introduction

Cryotherapy is often preferred to more traditional kinds of surgical therapy because of its minimal pain, scarring, and cost. The therapy has been gaining significant acceptance as a minimally invasive therapy for treatments of various malignant cancers. In a cryosurgical treatment, a single or multiprobe metal system is placed in contact with the target tissue through the skin. We have placed the emphasis of this paper on the treatment of a malignant lung tumor, since its application to lung cancer has been practiced on a trial basis for some years in Japanese medical schools [1].

The cryoprobe in consideration houses a small coaxial nozzle internally. A high-pressure gas supply line is connected to the probe so as to supply argon gas, which expands through the nozzle to the probe tip and then flows backwards through the internal channel leading to the cryoprobe outlet. Due to the Joule–Thompson effect, the outer surface temperature of the probe decreases below $-135\,^{\circ}\mathrm{C}$. As the tissue temperature is lowered, an ellipsoidal ice ball forms around each probe that is increasing in size, eventually encompassing and invading the entire tumor. This freezing process continues for 5–15 min. Then, the thawing process takes place as helium gas is supplied. Because of the difference in the inversion temperature, the probe temperature during this process increases to about $20\,^{\circ}\mathrm{C}$ to thaw the frozen tissue. This freezing-thawing sequence is repeated several times to kill abnormal cells or tissues, such as those found in malignant tumors. Cryoinjury is believed to be due to two primary mechanisms: one is the direct injury to the cells from the freeze-thaw cycle and the other is the indirect injury that results from the biological response to the damage caused by freezing, primarily the vasculature of the tumor.

As with any medical treatment, there are risks involved, primarily that of damage to nearby healthy tissue [2]. We must know the exact time required to freeze the entire cancer without damaging its surrounding healthy tissue. However, some standards for setting clinical parameters such as freezing rate and time are quite empirical today. Therefore, improvements in cryosurgery depend on developing reliable mathematical models and pre-operational simulation tools based on them.

Perhaps, Bischof et al. [3] were the first to predict ice ball formation around a single cryosurgical probe. They used a cylindrical model to predict the interface location and the temperature profile. Rewcastle et al. [4] proposed a finite difference model for single probe freezing and generated isotherms within the ice ball during its growth. Keanini and Rubinsky [5] and Baissalov et al. [6] dealt with the problem of optimization in cryosurgery regarding the placement of cryoprobes and the freezing protocol design. Wan et al. [7] appealed to finite element methodology to simulate ice ball formation in a multiprobe cryosurgery. Rabin and Shitzer [8] and Rossi et al. [9] introduced fairly sophisticated numerical techniques for freezing an angioma, while Rossi and Rabin [10] developed an elegant experimental technique to create a two-dimensional freezing problem associated with prostate cryosurgery with urethral warming. However, none of them considered the case of lung cancer or are concerned with the effects of the blood perfusion on the temporal evolution of ice formation, which leads to the fact, namely, that there exists the limiting size of the tumor, which one single cryoprobe can freeze at the maximum. No attempts were made to estimate the limiting radius for freezing tumors.

In this paper, we shall appeal to a bioheat equation recently developed by Nakayama and Kuwahara [11] and solve it both numerically and analytically to simulate the ice ball evolution and to locate the freezing front as time goes by. The analytical results based on the integral method agree very well with the numerical results based on the enthalpy method. Thus, the present analytical expression may be exploited for estimating the time for freezing a cancer of a given size. It will also be pointed out that there exists the limiting size of the cancer, which one single cryoprobe can freeze at the maximum. It is believed that the present results lend quantitative support to the current empirical standards for cryosurgical clinical applications.

Bioheat Equation

Pennes [12] proposed a simple bioheat equation for living tissue in which the perfusion heat source was introduced as follows:

$$\rho_s c_s \frac{\partial T}{\partial t} = \frac{\partial}{\partial x_j}\left(k_s \frac{\partial T}{\partial x_j}\right) + \rho_f c_{p_f} \omega_{\mathrm{Pennes}} (T_{a0} - T) + S_m \qquad (1)$$

where T is the tissue temperature, while T_{a0} is the mean brachial artery temperature. k, ρ, and c are the thermal conductivity, den-

Contributed by the Heat Transfer Division of ASME for publication in the JOURNAL OF HEAT TRANSFER. Manuscript received July 19, 2007; final manuscript received May 7, 2008; published online August 28, 2008. Review conducted by Ben Q. Li.

sity, and specific heat capacity, whose subscripts s and f refer to tissue and blood, respectively. Moreover, ω_{Pennes} $(1/s)$ is Pennes' blood perfusion rate (i.e., the rate of perfusion to the tissue per unit volume of tissue), while S_m is the metabolic heat generation rate. Pennes' model is often adequate for roughly describing the effect of blood flow on the tissue temperature. Nevertheless, a considerable number of modifications have been proposed by various researchers. Wulff [13] and Klinger [14] considered the local blood mass flux to account for the blood flow direction, while Chen and Holmes [15] examined the effect of thermal equilibration length on the blood temperature and added the dispersion and microcirculatory perfusion terms to the Klinger equation. Furthermore, Xuan and Roetzel [16] replaced the perfusion rate with the interfacial convection term. On the other hand, Nakayama and Kuwahara [11] have exploited the volume averaging theory in porous media, and showed that all these existing bioheat equations are included in their general bioheat equation. The general bioheat equation, for the case of isolated blood vessels, runs as

$$\rho_s c_s \frac{\partial T}{\partial t} = \frac{\partial}{\partial x_j}\left(k_s \frac{\partial T}{\partial x_j}\right) + \rho_f c_{p_f} \omega (T_f - T) + a_f h (T_f - T) + S_m \quad (2)$$

where the second time and the third term on the right-hand side correspond to the blood perfusion on the tissue and the interfacial heat transfer from the blood to the tissue through the vessel wall, respectively. Similarity between our equation and Pennes' equation is obvious as we rewrite the foregoing equation as

$$\rho_s c_s \frac{\partial T}{\partial t} = \frac{\partial}{\partial x_j}\left(k_s \frac{\partial T}{\partial x_j}\right) + \rho_f c_{p_f} \omega_{\text{eff}} (T_f - T) + S_m \quad (3)$$

where

$$\omega_{\text{eff}} = \omega + \frac{a_f h}{\rho_f c_{p_f}} \quad (4)$$

is the effective perfusion rate. However, ω_{eff} conceptually differs from Pennes' perfusion rate ω_{Pennes}, which is purely empirical. It should also be noted that T_f in $(T_f - T)$ is the local blood temperature, whereas T_{a0} in Eq. (1) is the mean brachial artery temperature. Perhaps Pennes considered that the blood perfusion is the predominant heat source for the tissue and did not bother to describe the interfacial convective heat transfer between the blood and tissue via the vascular wall. Instead, he introduced T_{a0} to adjust the total heat transfer, which takes place as the blood enters and leaves the tissue. However, the interfacial convective heat transfer between the blood and tissue can never be insignificant for the countercurrent bioheat transfer. Even when there is no perfusion, i.e., $\omega_{\text{Pennes}}=0$, the effective perfusion rate never vanishes since $\omega_{\text{eff}}=a_f h/\rho_f c_{p_f}$. Thus, Eq. (4) must always be used for countercurrent bioheat transfer for the case of closely aligned pairs of vessels.

Numerical Analysis Based on Enthalpy Method

The enthalpy method is often used for locating an interface in phase change problems, since it allows us to use a fixed mesh. An easy approach to implement this method is to include the latent heat by artificially increasing the specific heat capacity around the freezing point, thus making it a function of temperature as illustrated in Fig. 1.

This simple temperature function satisfies the obvious relationship among the latent heat of solidification h_{sf}, artificial maximum heat capacity $c_{\max}$, and artificial temperature band ΔT, namely, $h_{\text{sf}}=c_{\max}(2\Delta T)$. The temperature band ΔT should be set according to the mesh resolution. Naturally, a finer grid system allows us to use a smaller ΔT, which provides us with a sharper freezing front where $T=T_i$. In this study, ΔT was set from 1 °C to 5 °C. The temporal development of the freezing front is found fairly insensitive to ΔT in this range.

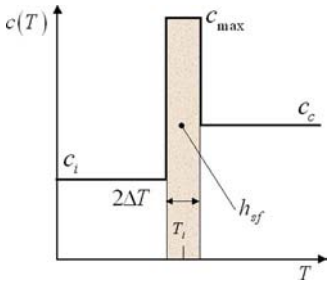

Fig. 1 Effective specific heat capacity

Any standard scheme may be used to discretize the governing equation (3). We shall use a finite volume method as proposed by Patankar [17] to obtain a two-dimensional finite volume expression. We consider a control volume of size $\Delta x \Delta y$ centering the node P (pole), as shown in Fig. 2, and let the uppercase letters E (east), W (west), N (north), and S (south) denote its neighboring nodes. Furthermore, we let the lowercase versions of the same letters e, w, n, and s denote the four faces of the control volume, and $(\delta x)_e$, $(\delta x)_w$, $(\delta y)_n$, and $(\delta y)_s$ denote the distances between the nodes. Then, the discretized version of the bioheat equation may be written as follows (see Ref. [18] for details):

$$a_P T_P = a_E T_E + a_W T_W + a_N T_N + a_S T_S + b \quad (5)$$

where

$$a_E = \left(\frac{\Delta y}{\delta x_e}\right)\frac{1}{T_E - T_P}\int_{T_P}^{T_E} k(T)dT \quad (6a)$$

$$a_W = \left(\frac{\Delta y}{\delta x_w}\right)\frac{1}{T_P - T_W}\int_{T_W}^{T_P} k(T)dT \quad (6b)$$

$$a_N = \left(\frac{\Delta x}{\delta y_n}\right)\frac{1}{T_N - T_P}\int_{T_P}^{T_N} k(T)dT \quad (6c)$$

$$a_S = \left(\frac{\Delta x}{\delta y_s}\right)\frac{1}{T_P - T_S}\int_{T_S}^{T_P} k(T)dT \quad (6d)$$

$$a_P = \left(\frac{\Delta x \Delta y}{\Delta t}\right)\overline{\rho c} + a_E + a_W + a_N + a_S + \rho_f c_{p_f} \omega_{\text{eff}} \Delta x \Delta y \quad (6e)$$

$$b = \left(\frac{\Delta x \Delta y}{\Delta t}\right)\overline{\rho c} T_P^o + (\rho_f c_{p_f} \omega_{\text{eff}} T_f + S_m)\Delta x \Delta y \quad (6f)$$

$$\overline{\rho c} = \frac{1}{T_P - T_P^o}\int_{T_P^o}^{T_P} \rho c(T)dT \quad (6g)$$

The superscript o indicates the value at the *old* time t, whereas no superscript is assigned for the value at the new time $t+\Delta t$.

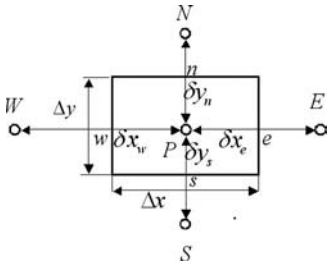

Fig. 2 Grid nomenclatures

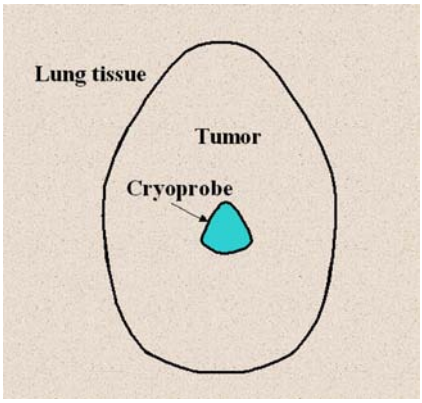

Fig. 3 Numerical model for cryoablation

The present computer code is capable of dealing with arbitrary two-dimensional shapes of the cryoprobe and tumor, as illustrated in Fig. 3. The initial and boundary conditions for the freezing process using the cryoprobe of outer radius R_p are given as follows:

$t=0$:

$$T = T_f \quad \text{(everywhere)} \tag{7}$$

$t>0$:

$$T|_{x^2+y^2=R_P{}^2} = T_p \quad \text{(cryoprobe outer surface)} \tag{8a}$$

$$T|_{x^2+y^2\to\infty} = T_f \quad \text{(deep tissue region)} \tag{8b}$$

Computations were carried out using highly nonuniform grid systems, namely, (250×500) to cover the right half domain 30×60 mm^2 for the case of the longitudinal tumor of 20×27 mm^2, and (350×700) to cover the right half domain 160×160 mm^2 for the case of determining the limiting radius. The results associated with the limiting radius are found to be independent of any additional expansion of the calculation domain. Grid nodes are laid out densely around the probe. Grid refinement tests were carried out to ensure that the results are independent of grid systems. Convergence was measured in terms of the maximum change in temperature during an iteration, which was set to 10^{-5}.

Analytical Treatment Based on Integral Method

In what follows, we shall exploit an integral method to derive an analytical expression for the limiting radius of the tumor, which one single cryoprobe can freeze at the maximum. For the sake of simplicity in this analytical treatment, we shall assume that the probe is a circular cylinder and that the tumor is so large that heat transfer to the healthy lung tissue is negligible.

The temperature around the cryoprobe is schematically shown in Fig. 4, where T_p and T_i are the temperatures of the probe and the freezing front, respectively, while T_0 is the body temperature. Upon referring to the figure, we may introduce the energy balance relationship at the freezing front at $r=R_i$ as follows:

$$\rho_i h_{sf} R_i \frac{dR_i}{dt} = R_i k_i \left.\frac{\partial T}{\partial r}\right|_{r=R_i} - R_i k_c \left.\frac{\partial T}{\partial r}\right|_{r=R_i} - \rho_c c_c (T_0 - T_i) R_i \frac{dR_i}{dt}: \quad r = R_i \tag{9}$$

where the subscripts i and c refer to the frozen and unfrozen regions, respectively. The first, second, and third terms on the right-hand side correspond to the conduction heat flux evaluated at the ice side, the conduction heat flux evaluated at the unfrozen side, and the sensible heat entering the interface as the interface

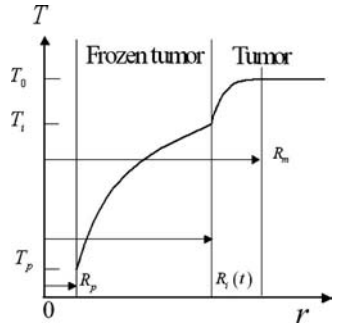

Fig. 4 Temperature profile around a probe

(freezing front) at $r=R_i(t)$ moves radially outward from the cryoprobe, respectively.

The freezing front moves so slowly that a quasisteady approximation may be valid. Thus, assuming that the temperature profile within the frozen region follows that obtained at the steady state, namely,

$$\frac{T - T_p}{T_i - T_p} = \frac{\ln(r/R_p)}{\ln(R_i/R_p)}: \quad R_p \le r \le R_i \tag{10}$$

where we may estimate the first term on the right-hand side as

$$R_i k_i \left.\frac{\partial T}{\partial r}\right|_{r=R_i} = k_i \frac{T_i - T_p}{\ln(R_i/R_p)} \tag{11}$$

In order to estimate the second term on the right-hand side (representing the heat flux from the unfrozen tumor to the interface), we write the bioheat equation (2) for the unfrozen tumor region using the cylindrical coordinate system, which, under the quasisteady approximation, may be integrated to give

$$-k_c R_i \left.\frac{dT}{dr}\right|_{r=R_i} - \rho_c c_c \omega_{\text{eff}} \int_{R_i}^{R_m} r(T - T_0) dr + S_m \int_{R_i}^{R_m} r dr = 0 \tag{12}$$

Let us assume that the temperature in this unfrozen region follows

$$\frac{T - T_0}{T_i - T_0} = \left(1 - \frac{r - R_i}{R_m - R_i}\right)^2: \quad R_i \le r \le R_m \tag{13}$$

The equation satisfies $T=T_i$ at $r=R_i$ and $T=T_0$ and $\partial T/\partial r=0$ at $r=R_m$ such that the boundary condition given by Eq. (8*b*) is satisfied in an approximate sense. Then substituting this temperature profile into Eq. (12), we have

$$2k_c R_i \frac{T_i - T_0}{R_m - R_i} - \rho_c c_c \omega_{\text{eff}} (T_i - T_0)\left(\frac{1}{3}(R_m - R_i)R_i + \frac{1}{12}(R_m - R_i)^2\right) + S_m \frac{R_m{}^2 - R_i^2}{2} = 0 \tag{14}$$

which forms a cubic equation for $R_i/(R_m-R_i)$. The root of the cubic equation is quite complex. However, it is found that the following explicit expression based on Newton's shooting method gives a quite accurate value for the root:

$$\frac{R_i}{R_m - R_i} = R_i \sqrt{\frac{1}{6}\left(\frac{\omega_{\text{eff}}}{\alpha_c} + 3\frac{S_m}{k_c(T_0 - T_i)}\right)} + \frac{1}{8}\left(\frac{\dfrac{\omega_{\text{eff}}}{\alpha_c} + 6\dfrac{S_m}{k_c(T_0 - T_i)}}{\dfrac{\omega_{\text{eff}}}{\alpha_c} + 3\dfrac{S_m}{k_c(T_0 - T_i)}}\right) \tag{15}$$

where $\alpha_c = k_c/\rho_c c_c$ is the thermal diffusivity of the unfrozen tumor. Thus, the second term on the right-hand side of Eq. (9) may be estimated as

$$R_i k_c \left.\frac{\partial T}{\partial r}\right|_{r=R_i} = 2k_c(T_0 - T_i)\left(R_i\sqrt{\frac{1}{6}\left(\frac{\omega_{\text{eff}}}{\alpha_c} + 3\frac{S_m}{k_c(T_0 - T_i)}\right)} + \frac{1}{8}\left(\frac{\frac{\omega_{\text{eff}}}{\alpha_c} + 6\frac{S_m}{k_c(T_0 - T_i)}}{\frac{\omega_{\text{eff}}}{\alpha_c} + 3\frac{S_m}{k_c(T_0 - T_i)}}\right)\right) \tag{16}$$

Upon substituting Eqs. (11) and (16) into Eq. (9), we have

$$(\rho_i h_{\text{sf}} + \rho_c c_c(T_0 - T_i))R_i\frac{dR_i}{dt} = k_i\frac{T_i - T_p}{\ln\left(\frac{R_i}{R_p}\right)} - 2k_c(T_0 - T_i)\left(R_i\sqrt{\frac{1}{6}\left(\frac{\omega_{\text{eff}}}{\alpha_c} + 3\frac{S_m}{k_c(T_0 - T_i)}\right)} + \frac{1}{8}\left(\frac{\frac{\omega_{\text{eff}}}{\alpha_c} + 6\frac{S_m}{k_c(T_0 - T_i)}}{\frac{\omega_{\text{eff}}}{\alpha_c} + 3\frac{S_m}{k_c(T_0 - T_i)}}\right)\right) \tag{17}$$

which reduces to

$$dt^* = \frac{1 + \text{Sr}}{\text{Ste}} \times \frac{R_i^* \ln R_i^*}{1 - \frac{\ln R_i^*}{\text{Cr}}\left(\sqrt{\frac{2}{3}}(\omega^* + 3\text{Met})^{1/2}R_i^* + \frac{\omega^* + 6\text{Met}}{4(\omega^* + 3\text{Met})}\right)} dR_i^* \tag{18}$$

where

$$R_i^* = R_i/R_p \tag{19a}$$

and

$$t^* = \alpha_i t/R_p^2 \tag{19b}$$

is the Fourier number and where $\alpha_i = k_i/\rho_i c_i$ is the thermal diffusivity of the ice. Moreover, the following dimensionless parameters are introduced:

$$\text{Ste} = \frac{c_i(T_i - T_p)}{h_{\text{sf}}}: \quad \text{Stefan number} \tag{20a}$$

$$\text{Sr} = \frac{\rho_c c_c(T_0 - T_i)}{\rho_i h_{\text{sf}}} \tag{20b}$$

$$\omega^* = \frac{\omega_{\text{eff}} R_p^2}{\alpha_c} \tag{20c}$$

$$\text{Cr} = \frac{k_i(T_i - T_p)}{k_c(T_0 - T_i)} \tag{20d}$$

$$\text{Met} = \frac{S_m R_p^2}{k_c(T_0 - T_i)} \tag{20e}$$

The foregoing ordinary differential equation (18) may readily be integrated using any standard integration scheme such as Runge–Kutta–Gill, to find the dimensionless time $t^* = \alpha_c t/R_p^2$ required for freezing the tumor of a given dimensionless radius $R_i^* = R_i/R_p$. Obviously, the quasisteady assumption is valid when $t^*\text{Ste}/(1+\text{Sr}) > 1$, which roughly gives $t > 1$ s. Thus, the assumption holds for most parts of the freezing process except at its initial short period.

Table 1 Thermal properties

Subscript	Frozen tumor i	Tumor c	Lung l
k[W/mK]	2.20	0.52	0.281
ρ[kg/m^3]	1000	1000	550
c[J/kg K]	2000	4000	3710
α[m^2/s]	1.10×10^{-6}	1.30×10^{-7}	1.38×10^{-7}
$h_{\text{sf}} = 3.34\times10^5$ J/kg			

It is interesting to note that there exists the limiting radius R_{lim} of the tumor that one single cryoprobe can freeze at the maximum. Its dimensionless value $R_{\text{lim}}^* = R_{\text{lim}}/R_p$ may be obtained by setting $dR_{\text{lim}}^*/dt^* = 0$, for which Eq. (18) yields

$$\frac{\ln R_{\text{lim}}^*}{\text{Cr}}\left(\sqrt{\frac{2}{3}}(\omega^* + 3\text{Met})^{1/2}R_{\text{lim}}^* + \frac{\omega^* + 6\text{Met}}{4(\omega^* + 3\text{Met})}\right) = 1 \tag{21}$$

This implicit equation gives the dimensionless limiting radius R_{lim}^* for a given set of the dimensionless values, Met, Cr, and ω^*. Usually, ω^* is much larger than Met. For such cases, the following explicit expression based on Newton's shooting method may be used to give a reasonably accurate value for R_{lim}^*:

$$R_{\text{lim}}^* = \frac{\left(\sqrt{\frac{3}{2\omega^*}}\text{Cr} + R_0^*\right)R_0^* + \sqrt{\frac{3}{32\omega^*}}R_0^*(1 - \ln R_0^*)}{R_0^*(1 + \ln R_0^*) + \sqrt{\frac{3}{32\omega^*}}} \tag{22}$$

where

$$R_0^* = \frac{\frac{3\text{Cr}^2}{\omega^*} + \frac{3\text{Cr}}{8\omega^*}\left(1 - \ln\left(\sqrt{\frac{3}{2\omega^*}}\text{Cr}\right)\right)}{\sqrt{\frac{3}{2\omega^*}}\text{Cr}\left(1 + \ln\left(\sqrt{\frac{3}{2\omega^*}}\text{Cr}\right)\right) + \sqrt{\frac{3}{32\omega^*}}} \tag{23}$$

For the present case of Cr=15.4, Eq. (22) along with Eq. (23) gives $R_{\text{lim}}^* = 29.9$ and 12.9 for $\omega^* = 0.031$ ($\omega = 0.004$/s) and 0.310 ($\omega = 0.04$/s), respectively.

Results and Discussion

Some tissues freeze over a fairly large range of temperatures. However, for the case of lung cancer, the blood comes out from the vessels during the freezing-thawing sequence. The subsequent freezing takes place around the probe surrounded by the blood as a conducting medium. To a first approximation, we may use a single temperature for the phase change. Numerical calculations based on the enthalpy method were carried out for the case in which the cryosurgical and biological parameters are given by

$$R_p = 1 \text{ mm} \quad , T_p = -135\,^\circ\text{C}, \quad T_i = -0\,^\circ\text{C}$$

$$T_f = T_0 \text{ (body temperature)} = 37\,^\circ\text{C}$$

and

$$S_m = 1200 \text{ W/m}^3$$

The effective perfusion rate ω_{eff} within the tumor can be quite high since some blood vessels are connected to the tumor. Here, we assume the effective perfusion rate in the range of $\omega_{\text{eff}} = 0.004 - 0.04$/s. Moreover, the thermophysical properties for frozen and unfrozen tissues in the lung are listed in Table 1, according to Ref. [19].

For the case in which $T_p=-135\,^\circ\mathrm{C}$, $T_i=0\,^\circ\mathrm{C}$, $T_0=37\,^\circ\mathrm{C}$, $S_m=1200\ \mathrm{W/m^3}$, $\omega_{\mathrm{eff}}=0.004/\mathrm{s}$, and $R_p=1$ mm, we have Ste $=0.808$, Sr$=0.443$, Met$=6.24\times10^{-5}$, Cr$=15.4$, and $\omega^*=0.031$. A typical evolution of the isotherms obtained for a longitudinal tumor of $20\times27\ \mathrm{mm^2}$ is presented in Figs. 5(*a*)–5(*c*). The outermost isotherm in each figure corresponds to the freezing front (i.e., $T=T_i=0\,^\circ\mathrm{C}$). Figure 5(*c*) clearly indicates that ill-placement of the probe may result in a substantial damage to the surrounding healthy tissue.

Let us consider the freezing process when the probe is placed in a large tumor. The temporal evolutions of the freezing front for the cases of $\omega_{\mathrm{eff}}=0.004/\mathrm{s}$ (low perfusion) and 0.040/s (high perfusion) are illustrated in Figs. 6(*a*) and 6(*b*), respectively, along with the curve analytically obtained by integrating the ordinary differential equation (18). The figures may also be used to know the time required to kill the circular tumor of radius R_i. The numerical results obtained for these two cases in the figures clearly show that the limiting radii R_{lim} for $\omega_{\mathrm{eff}}=0.004/\mathrm{s}$ and 0.040/s are around 29.9 mm and 12.8 mm, respectively, which are estimated on the basis of the analytical expression (22).

Finally, the curve representing the limiting radius is generated from Eq. (22) and plotted against the effective perfusion rate in Fig. 7. We learn from the figure that a single probe, even when placed in the center of the target, is capable of freezing only the size of a tumor whose equivalent radius is less than the limiting radius R_{lim}. The figure indicates that, for the case of comparatively high perfusion rate, a single probe of radius 1 mm can freeze a tumor only within a radius of 20 mm or less. This is consistent with the fact reported by Nakatsuka et al. [1]. In practice, we may introduce a factor λ and estimate the range of the killed tissue by $r\leqslant\lambda R_{\mathrm{lim}}$. The factor λ has to be chosen carefully, depending on

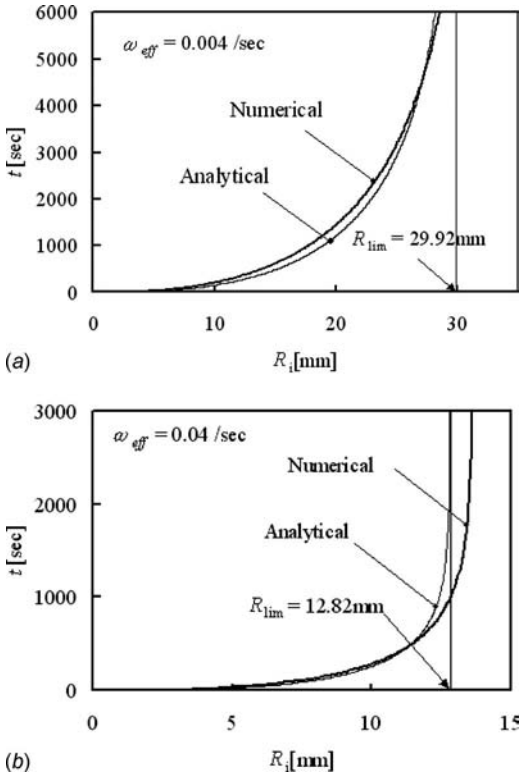

Fig. 6 Time required for freezing the tumor

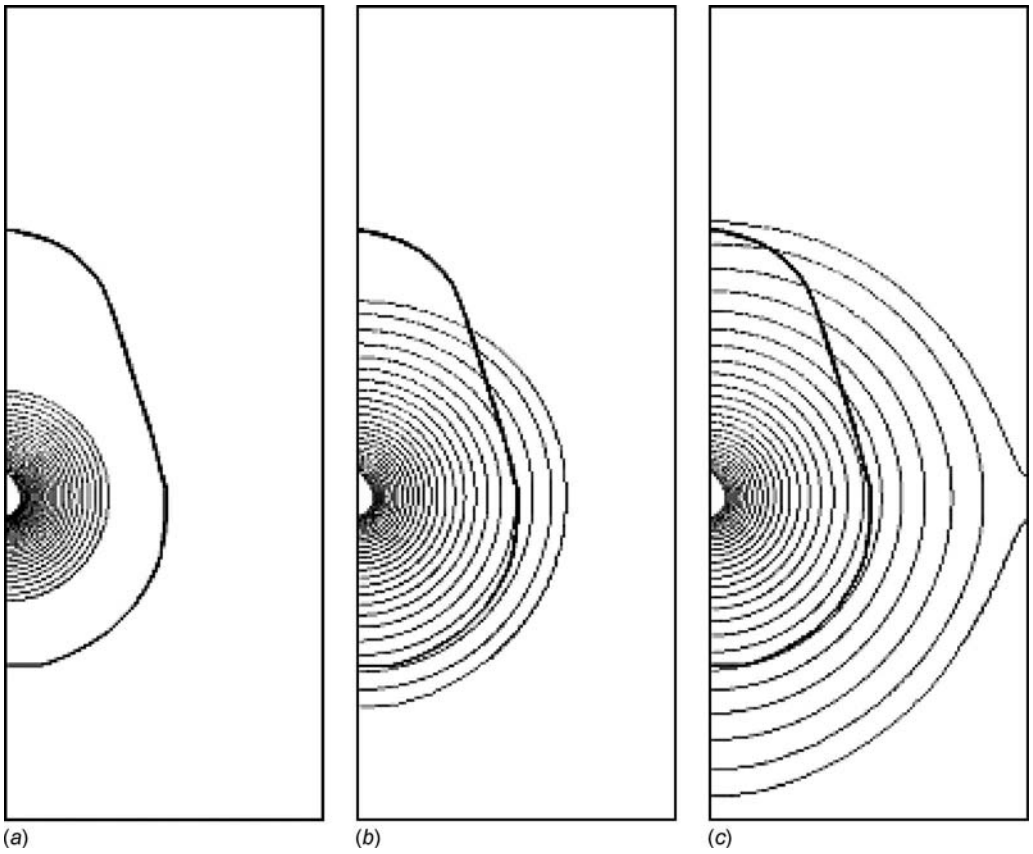

Fig. 5 Temporal evolution of isotherms

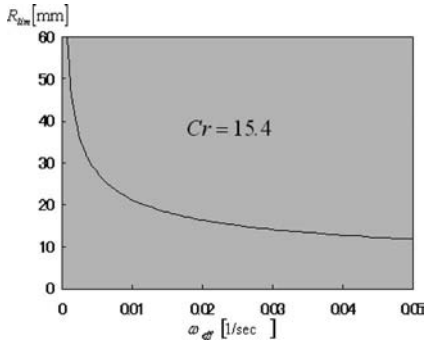

Fig. 7 Effects of the perfusion rate on the limiting radius

the specific clinical and surgical constraints such as the number of cryoprobes available, the time set for a single freezing process, and the level of malignancy.

Conclusions

The bioheat equation recently proposed by Nakayama and Kuwahara to account for the blood perfusion has been exploited to find the freezing front in a tumor during percutaneous cryoablation therapy. Two-dimensional numerical calculations based on the enthalpy method were conducted to simulate the ice formation around the cryoprobe. Using a cylindrical coordinate system, an analytical treatment was also made to estimate the time required to kill the entire tumor. Both sets of the results are found to be in good accord with each other. The analysis reveals that there exists a limiting size of the tumor, which one single cryoprobe can freeze at the maximum, as the heat flowing from the surrounding tissue to frozen region compensates for the heat absorbed by the cryoprobe. An explicit expression is obtained for estimating the limiting radius, which is believed to provide useful information for the preliminary planning of cryotherapy treatment. In reality, a multiprobe system may be used. Thus, future work needs to be done before real clinic applications.

Nomenclature

a_f = specific surface area
c = specific heat
Cr = dimensionless parameter associated with the thermal conductivity ratio
h_f = interfacial heat transfer coefficient
h_{sf} = latent heat of solidification
k = thermal conductivity
Met = dimensionless number associated with metabolic reaction rate
r = radial coordinate
R_i = radius of the freezing front
R_{lim} = limiting radius
S_m = metabolic reaction rate
Ste = Stephan number
t^* = Fourier number
T = temperature
T_i = phase change tempearture
T_p = probe temperature
T_0 = body temperature
x_i = Cartesian coordinates
a = thermal diffusivity
ρ = density
ω = perfusion rate
ω_{eff} = effective perfusion rate
ω^* = dimensionless perfusion rate

Subscripts and Superscripts

c = unfrozen tumor
i = ice, interface
p = cryoprobe
$*$ = dimensionless

References

[1] Nakatsuka, S., Kawamura, M., Sugiura, H., Nakano, K., Izumi, Y., Kobayashi, K., Jinzaki, M., Hashimoto, S., Kuribayashi, S., Wakabayashi, G., and Kitajima, M., 2004, "Preliminary Experience With Percutaneous Cryoablation for Malignant Lung Tumors Under CT Fluoroscopic Guidance," Low Temp. Med., **30**(1), pp. 9–15.

[2] Butz, T., Warfield, S. K., Tuncali, K., Silverman, S. G., van Sonnenberg, E., Jolesz, F. A., and Kikinis, R., 2000, "Pre- and Intra-Operative Planning and Simulation of Percutaneous Tumor Ablation," *Proceedings of the Medical Image Computing and Computer Assisted Intervention (MICCAI)*, Pittsburgh, PA, Oct. 11–14, pp. 317–326.

[3] Bischof, J. C., Smith, D., Pazhayannur, P. V., Manivel, C., Hulbert, J., and Roberts, K. P., 1997, "Cryosurgery of Dunning AT-1 Rat Prostate Tumor: Thermal, Biophysical, and Viability Response at the Cellular and Tissue Level," Cryobiology, **34**, pp. 42–69.

[4] Rewcastle, J., Sandison, G., Hahn, L., Saliken, J., McKinnon, J., and Donnelly, B., 1998, "A Model for the Time-Dependent Thermal Distribution Within an Ice Ball Surrounding a Cryoprobe," Phys. Med. Biol., **43**, pp. 3519–3534.

[5] Keanini, R. G., and Rubinsky, B., 1992, "Optimization of Multi-Probe Cryosurgery," ASME Trans. J. Heat Transfer, **114**, pp. 796–802.

[6] Baissalov, R., Sandison, G. A., Reynolds, D., and Muldrew, K., 2001, "Simultaneous Optimization of Cryoprobe Placement and Thermal Protocol for Cryosurgery," Phys. Med. Biol., **46**, pp. 1799–1814.

[7] Wan, R., Liu, Z., Muldrew, K., and Rewcastle, J., 2003, "A Finite Element Model for Ice Ball Evolution in a Multi-Probe Cryosurgery," Comput. Methods Biomech. Biomed. Eng., **6–3**, pp. 197–208.

[8] Rabin, Y., and Shitzer, A., 1998, "Numerical Solution of the Multidimensional Freezing Problem During Cryosurgery," ASME Trans. J. Heat Transfer, **120**, pp. 32–37.

[9] Rossi, M. R., Tanaka, D., Shimada, K., and Rabin, Y., 2007, "An Efficient Numerical Technique for Bioheat Simulations and its Application to Computerized Cryosurgery Planning," Comput. Methods Programs Biomed., **85**, pp. 41–50.

[10] Rossi, M. R., and Rabin, Y., 2007, "Experimental Verification of Numerical Simulations of Cryosurgery With Application to Computerized Planning," Phys. Med. Biol., **52**, pp. 4553–4567.

[11] Nakayama, A., and Kuwahara, F., 2008, "A General Bioheat Transfer Model Based on the Theory of Porous Media," Int. J. Heat Mass Transfer, **51**, pp. 3190–3199.

[12] Pennes, H. H., 1948, "Analysis of Tissue and Arterial Blood Temperature Blood Temperature in the Resting Human Forearm," J. Appl. Physiol., **1**, pp. 93–122.

[13] Wulff, W., 1974, "The Energy Conservation Equation for Living Tissue," IEEE Trans. Biomed. Eng., **BME 21**, pp. 494–495.

[14] Klinger, H. G., 1978, "Heat Transfer in Perfused Biological Tissue. II. The 'Macroscopic' Temperature Distribution in Tissue," Bull. Math. Biol., **40**, pp. 183–199.

[15] Chen, M. M., and Holmes, K. R., 1980, "Microvascular Contributions in Tissue Heat Transfer," Ann. N.Y. Acad. Sci., **335**, pp. 137–150.

[16] Xuan, Y., and Roetzel, W., 1997, "Bioheat Equation of the Human Thermal System," Chem. Eng. Technol., **20**, pp. 268–276.

[17] Patankar, S. V., 1980, *Numerical Heat Transfer and Fluid Flow*, Hemisphere, Washington, D.C.

[18] Nakayama, A., 1995, *PC-Aided Numerical Heat Transfer and Convective Flow*, CRC, Boca Raton, FL.

[19] Yokoyama, S., 1993, *Bioheat Transfer Phenomena (in Japanese)*, Hokkaido University Press, Hokkaido, Japan.

Solutions for Transient Heat Conduction With Solid Body Motion and Convective Boundary Conditions

Robert L. McMasters
Department of Mechanical Engineering,
Virginia Military Institute,
Lexington, VA 24450
e-mail: mcmastersrl@vmi.edu

James V. Beck
Department of Mechanical Engineering,
Michigan State University,
East Lansing, MI 48824
e-mail: beck@egr.msu.edu

The analytical solution for the problem of transient thermal conduction with solid body movement is developed for a parallelepiped with convective boundary conditions. An effective transformation scheme is used to eliminate the flow terms. The solution uses Green's functions containing convolution-type integrals, which involve integration over a dummy time, referred to as "cotime." Two types of Green's functions are used: one for short cotimes comes from the Laplace transform and the other for long cotimes from the method of separation of variables. A primary advantage of this method is that it incorporates internal verification of the numerical results by varying the partition time between the short and long components. In some cases, the long-time solution requires a zeroth term in the summation, which does not occur when solid body motion is not present. The existence of this zeroth term depends on the magnitude of the heat transfer coefficient associated with the convective boundary condition. An example is given for a two-dimensional case involving both prescribed temperature and convective boundary conditions. Comprehensive tables are also provided for the nine possible combinations of boundary conditions in each dimension. [DOI: 10.1115/1.2944243]

Keywords: conduction, eigenvalue, cotime, series, Green's functions

1 Introduction

A primary motivation for the development of the analytical solutions described in this paper is rooted in the verification of numerical heat transfer codes. This is accomplished by the development of a framework for exact solutions for multidimensional heat conduction in moving solids; this approach is in contrast to the generation of manufactured solutions [1–3]. Methods for solving the heat conduction equation for solid body flow, using a transformation, are given in both Refs. [4,5]. Reference [5] also provides a general method for solving transient heat conduction problems using Green's functions (GFs), including those addressing solid body motion. The use of these methods for application in verification work is discussed in Refs. [6,7]. In particular, the method of time partitioning is introduced in Ref. [7]. Solutions for problems involving solid body motion are given in Ref. [8], with emphasis on transient boundary conditions of the first kind (that is, prescribed temperatures). References for exact solutions for layered slabs are Refs. [9–13]. A necessary component of a computer code, which calculates exact solutions for heat conduction problems, is an efficient routine for computing eigenvalues, which is given in Ref. [14]. A formulation for analytical solutions involving moving boundaries, similar to the solution generated in the present research, is given in Ref. [15]. However, the "zeroth" term in the infinite series solution is not given in Ref. [15]; its omission can greatly affect the solution under certain conditions. Reference [16] also addresses moving body problems with one convective boundary and introduces the zeroth term in the series solution.

The present paper gives a derivation of the transformed heat conduction equation for moving boundary conditions in a two-dimensional problem with convective boundary conditions on two sides and prescribed temperature boundary conditions on the other two sides. Using this example as a template, a system for generating general solutions for three-dimensional parallelepipeds with solid body motion, having any combination of boundary conditions, is given. Moreover, the components of these solutions are summarized in tabular form to provide a systematic way of building the general solutions.

In developing these solutions using the time-partitioning method mentioned above, two different types of GFs are used. The first type comes from the Laplace transform method and is known as the "short cotime" solution. (We define "cotime" to be the difference between the time of interest and the dummy time variable in the GF; see Nomenclature.) The other type of GF comes from the separation-of-variables method and is known as the "long cotime" solution. Both are used together in solving multidimensional heat conduction problems when time partitioning is used. Time partitioning is usually used for two- and three-dimensional problems but is not needed for one-dimensional problems.

In general, the transformation of boundary conditions does not introduce fundamental problems in the solution using GFs based on the Laplace transform. However, for the separation-of-variables-based GFs, all the eigenvalues (for a given direction and boundary conditions of the second and third kinds) are changed for solid body flow in that direction and might cause the introduction of a zeroth boundary condition.

An outline of the paper is now given. First, the general differential equation is addressed for 2D Cartesian coordinates in an isotropic body. A transformation removes the solid body flow terms. The boundary conditions are also transformed. This is followed by the solution of the equation for the transformed variable and the implications of the product of the 1D GFs for a parallelepiped. Next the 1D GFs are given for boundary conditions of

Contributed by the Heat Transfer Division of ASME for publication in the JOURNAL OF HEAT TRANSFER. Manuscript received July 14, 2007; final manuscript received November 27, 2007; published August 28, 2008. Review conducted by Louis C. Burmeister. Paper presented at the 2007 ASME-JSME Thermal Engineering Conference and Summer Heat Transfer Conference (HT2007), Vancouver, British Columbia, Canada, July 8–12, 2007.

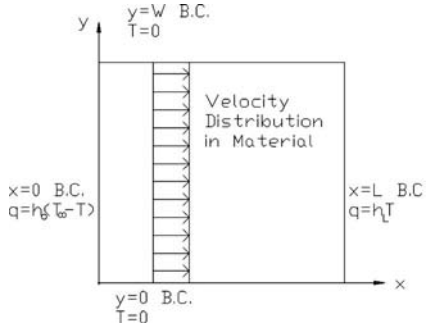

Fig. 1 Schematic diagram of moving body with convective boundary conditions

second and third kinds. Finally results are given in summary form for nine different combinations of boundary conditions using solid body motion.

2 Problem Statement and Transformation Equations

The transient heat conduction equation for an isotropic body with constant thermal properties and solid body flow in the x direction is

$$\frac{\partial^2 T}{\partial x^2}+\frac{\partial^2 T}{\partial y^2}=\frac{1}{\alpha}\left[\frac{\partial T}{\partial t}+U\frac{\partial T}{\partial x}\right],\quad 0<x<L,\quad 0<y<W,\quad t>0 \tag{1}$$

where α is the thermal diffusivity. The U term is the uniform velocity in the x direction, quantifying the solid body velocity, and is constant. The boundary and initial conditions for this problem are

$$-k\frac{\partial T}{\partial x}(0,y,t)=h_0(T_\infty-T(0,y,t))$$

$$-k\frac{\partial T}{\partial x}(L,y,t)=h_L T(L,y,t)$$

$$T(x,0,t)=0,\quad T(x,W,t)=0$$

$$T(x,y,0)=0 \tag{2}$$

The first two boundary conditions might be modified for equilibrium conditions for heat transfer with flow in a porous media; these conditions may be discussed in a future paper.

Figure 1 provides a schematic diagram of the moving body, showing the boundary conditions. It is necessary to transform Eq. (1) to eliminate the $U\partial T/\partial x$ term. A derivation is given in Ref. [5]. Let the temperature be related to the new variable ψ by

$$T(x,y,t)=\psi(x,y,t)e^{Ux/2\alpha-U^2t/4\alpha} \tag{3}$$

Substituting this expression into the differential equation and boundary conditions,

$$\frac{\partial^2\psi}{\partial x^2}+\frac{\partial^2\psi}{\partial y^2}=\frac{1}{\alpha}\frac{\partial\psi}{\partial t},\quad 0<x<L,\quad 0<y<W,\quad t>0$$

$$-k\frac{\partial\psi}{\partial x}(0,y,t)=h_0T_\infty e^{U^2t/4\alpha}-\left(h_0-\frac{kU}{2\alpha}\right)\psi(0,y,t)$$

$$-k\frac{\partial\psi}{\partial x}(L,y,t)=\left(h_L+\frac{kU}{2\alpha}\right)\psi(L,y,t)$$

$$\psi(x,0,t)=0,\quad \psi(x,W,t)=0$$

$$\psi(x,y,0)=0 \tag{4}$$

It is convenient use some "effective" convection coefficients. On the left side of the body, the convection coefficient becomes

$$h_{e0}=h_0-\frac{kU}{2\alpha} \tag{5}$$

and on the right side

$$h_{eL}=h_L+\frac{kU}{2\alpha} \tag{6}$$

Note that these effective convection coefficients can be either negative or positive because the flow velocity can be positive (positive x direction) or negative (negative x direction). It is also convenient to write these coefficients in dimensionless form,

$$\mathrm{Bi}_{e0}\equiv\frac{h_0L}{k}-\frac{1}{2}\mathrm{Pe},\quad \mathrm{Pe}\equiv\frac{UL}{\alpha} \tag{7}$$

Equation (7) addresses the $x=0$ side of the body; matching expressions can be written for the $x=L$ side by changing the 0 subscript to L.

3 Green's Function Solution Equation for the Transformed Variable, ψ

The solution for ψ in terms of GFs [5] is given by

$$\psi(x,y,t)=\psi_{\mathrm{ic}}(x,y,t)+\psi_{\mathrm{bc}}(x,y,t) \tag{8}$$

which has terms for the initial condition and boundary conditions. The initial condition term [5] becomes

$$\psi_{\mathrm{ic}}(x,y,t)=\int_{x=0}^{L}\int_{y=0}^{W}G_\psi(x,t;x',0)G_\psi(y,t;y',0)\times e^{Ux'/2\alpha}F(x',y')dx'dy' \tag{9}$$

where function $F(x',y')$ is the initial temperature distribution in the body, which is zero in this problem. Therefore, Eq. (9) does not provide a nonzero contribution to the solution. The boundary condition term is

$$\psi_{\mathrm{bc}}(x,y,t)=\frac{1}{\rho c}\int_{\tau=0}^{t}G_{\psi X33}(x,t|0,\tau)\int_{y'=0}^{W}G_{\psi Y11}(y,t|y',\tau)\times f(y',\tau)dy'd\tau \tag{10}$$

In this example, the right hand boundary condition is homogeneous, so Eq. (10) includes only a contribution from the left boundary condition. This boundary condition is described as

$$f(y',\tau)=h_0T_\infty e^{U^2\tau/4\alpha}=f(\tau) \tag{11}$$

The GF for the x-direction component of the ψ problem can be written as

$$G^L_{\psi X33}(x,t|x',\tau)=\sum_{m=0}^{\infty}e^{-\beta_m^2\alpha(t-\tau)/L^2}\frac{X_m(x)X_m(x')}{N_m} \tag{12}$$

where X_m are the eigenfunctions and are defined as

$$X_m(x)=\beta_m\cos(\beta_m x/L)+\mathrm{Bi}_{e0}\sin(\beta_m x/L) \tag{13}$$

for m equal to 1 and greater. The eigenfunctions for the various cases are given by Table 1 for both the zeroth and other eigenfunctions. The norms for $m=1,2,3,\ldots$ are simply the same as those for the $X33$ case, using the effective Biot numbers. The eigencondition for $m=1,2,\ldots$ is

$$\tan(\beta_m)=\frac{\beta_m(\mathrm{Bi}_{e0}+\mathrm{Bi}_{eL})}{\beta_m^2-\mathrm{Bi}_{e0}\mathrm{Bi}_{eL}} \tag{14a}$$

and the eigencondition for the zeroth eigenvalue (if it is present) is given by

Table 1 Eigenfunctions for the ψ differential equation

Case	Zeroth term	$m=1,2,\ldots$
XU11	—	$\sin(\beta_m x^+)$
XU12	$\sinh(\beta_0 x^+)$	$\sin(\beta_m x^+)$
XU13	$\sinh(\beta_0 x^+)$	$\sin(\beta_m x^+)$
XU21	$\sinh[\beta_0(1-x^+)]$	$\sin[\beta_m(1-x^+)]$
XU22	$\lvert\mathrm{Pe}/2\rvert\exp(-\mathrm{Pe}\,x/(2L))$	$m\pi\cos(m\pi x^+)$ $-(\mathrm{Pe}/2)\sin(m\pi x^+)$
XU23	$\beta_0\cosh(\beta_0 x^+)+\mathrm{Bi}_{e0}\sinh(\beta_0 x^+)$	$\beta_m\cos(\beta_m x^+)+\mathrm{Bi}_{e0}\sin(\beta_m x^+)$
XU31	$\sinh[\beta_0(1-x^+)]$	$\sin[\beta_m(1-x^+)]$
XU32	$\beta_0\cosh(\beta_0 x^+)+\mathrm{Bi}_{e0}\sinh(\beta_0 x^+)$	$\beta_m\cos(\beta_m x^+)+\mathrm{Bi}_{e0}\sin(\beta_m x^+)$
XU33	$\beta_0\cosh(\beta_0 x^+)+\mathrm{Bi}_{e0}\sinh(\beta_0 x^+)$	$\beta_m\cos(\beta_m x^+)+\mathrm{Bi}_{e0}\sin(\beta_m x^+)$

$$\tanh(\beta_0)=-\frac{\beta_0(\mathrm{Bi}_{e0}+\mathrm{Bi}_{eL})}{\beta_0^2+\mathrm{Bi}_{e0}\mathrm{Bi}_{eL}}=-\frac{\beta_0(\mathrm{Bi}_0+\mathrm{Bi}_L)}{\beta_0^2+\left(\mathrm{Bi}_0-\frac{\mathrm{Pe}}{2}\right)\left(\mathrm{Bi}_L+\frac{\mathrm{Pe}}{2}\right)} \tag{14b}$$

The reason for the tangent function in the eigencondition becoming a hyperbolic tangent for the zeroth term is rooted in the derivation of the eigencondition. Although the complete derivation is beyond the scope of this paper, the eigenvalue normally arises in a separation-of-variables solution by setting a negative constant equal to two functions. One of these is a function of time only and one is a function of space only. This gives rise to orthogonal eigenfunctions, from which the eigenvalues are derived. Instead of assuming a negative constant term, the zeroth term comes about when a positive constant is chosen, hence the nonorthogonal eigenfunctions of hyperbolic tangent. Other individual cases can be seen in Table 2. Moving on to the GF for the y dimension, the $Y11$ case is prescribed as

$$G^L_{\psi Y11}(y,t|y',\tau)=\frac{2}{W}\sum_{n=1}^{\infty}e^{-(n\pi/W)^2\alpha(t-\tau)}\sin(n\pi y/W)\sin(n\pi y'/W) \tag{15}$$

and the integration over y' needed in Eq. (10) is

$$\int_{y'=0}^{W}G_{\psi Y11}(y,t|y',\tau)dy'=4\sum_{n-1}^{\infty}\frac{\sin(\eta_n y^+)}{\eta_n}e^{-(\eta_n/W)^2\alpha u},$$

$$y^+\equiv\frac{y}{W},\quad \eta_n=(2n-1)\pi,\quad u=t-\tau \tag{16}$$

The solution of Eq. (10) can be written in two parts, one for $m=0$ and the other for $m=1,2,\ldots$ and is symbolically written as

$$\psi_{\mathrm{bc}}(x,y,t)=\psi_{\mathrm{bc},0}(x,y,t)+\psi_{\mathrm{bc},m}(x,y,t) \tag{17}$$

The first component using Eqs. (10)–(12) and (16) is

$$\begin{aligned}\psi_{\mathrm{bc},0}(x,y,t)&=\frac{1}{\rho c}\int_{\tau=0}^{t}h_0T_\infty e^{U^2\tau/4\alpha}e^{-(\beta_0/L)^2\alpha u}\frac{X_0(x)X_0(0)}{N_0}4\sum_{n-1}^{\infty}\frac{\sin(\eta_n y^+)}{\eta_n}e^{-(\eta_n/W)^2\alpha u}d\tau\\&=\frac{h_0T_\infty}{\rho c}e^{U^2t/4\alpha}\int_{u=0}^{t}e^{-U^2u/4\alpha}e^{-(\beta_0/L)^2\alpha u}\frac{X_0(x)X_0(0)}{N_0}4\sum_{n-1}^{\infty}\frac{\sin(\eta_n y^+)}{\eta_n}e^{-(\eta_n/W)^2\alpha u}du\\&=\frac{h_0T_\infty}{\rho c}e^{U^2t/4\alpha}4\sum_{n-1}^{\infty}\frac{\sin(\eta_n y^+)}{\eta_n}\frac{X_0(x)X_0(0)}{N_0}\int_{u=0}^{t}e^{-R_0^2\alpha u}du\end{aligned} \tag{18a}$$

where

$$R_0^2\equiv\left(\frac{U}{2\alpha}\right)^2+\left(\frac{\beta_0}{L}\right)^2+\left(\frac{\eta_n}{W}\right)^2 \tag{18b}$$

Performing the integration over the cotime u in Eq. (18a) gives

$$\psi_{\mathrm{bc},0}(x,y,t)=\frac{h_0T_\infty}{k}e^{U^2t/4\alpha}4\frac{X_0(x)X_0(0)}{N_0}\sum_{n=1}^{\infty}\frac{\sin(\eta_n y^+)}{\eta_n R_0^2}[1-e^{-R_0^2\alpha t}] \tag{19}$$

The same procedure used to obtain Eq. (19) can be repeated for the second term in Eq. (17) to get

Table 2 Eigenconditions for the $m=1,2,\ldots$ terms in the long-time GFs found from the ψ transformation

Temperature problem type	Goes to the ψ problem	Bi_{e0}	Bi_{eL}	$m=1,2,\ldots$, eigenvalue or eigencondition for the ψ problem
XU11	X11			$m\pi$
XU12	X13		$\mathrm{Pe}/2$	$\tan(\beta_m)=-2\beta_m/\mathrm{Pe}$
XU13	X13		$\mathrm{Bi}_L+\mathrm{Pe}/2$	$\tan(\beta_m)=-2\beta_m/(2\mathrm{Bi}_L+\mathrm{Pe})$
XU21	X31	$-\mathrm{Pe}/2$		$\tan(\beta_m)=2\beta_m/\mathrm{Pe}$
XU22	X33	$-\mathrm{Pe}/2$	$\mathrm{Pe}/2$	$m\pi$
XU23	X33	$-\mathrm{Pe}/2$	$\mathrm{Bi}_L+\mathrm{Pe}/2$	$\tan(\beta_m)=4\beta_m\mathrm{Bi}_L/(4\beta_0^2+\mathrm{Pe}(2\mathrm{Bi}_L+\mathrm{Pe}))$
XU31	X31	$\mathrm{Bi}_0-\mathrm{Pe}/2$	∞	$\tan(\beta_m)=-2\beta_m/(2\mathrm{Bi}_0-\mathrm{Pe})$
XU32	X33	$\mathrm{Bi}_0-\mathrm{Pe}/2$	$\mathrm{Pe}/2$	$\tan(\beta_m)=4\beta_m\mathrm{Bi}_0/(4\beta_m^2-\mathrm{Pe}(2\mathrm{Bi}_0-\mathrm{Pe}))$
XU33	X33	$\mathrm{Bi}_0-\mathrm{Pe}/2$	$\mathrm{Bi}_L+\mathrm{Pe}/2$	$\tan(\beta_m)=4\beta_m(\mathrm{Bi}_0+\mathrm{Bi}_L)/(4\beta_m^2-(2\mathrm{Bi}_0-\mathrm{Pe})(2\mathrm{Bi}_L+\mathrm{Pe}))$

$$\psi_{\mathrm{bc},m}(x,y,t) = \frac{h_0 T_\infty}{k} e^{U^2 t/4\alpha} 4 \sum_{m=1}^{\infty} \frac{X_m(x) X_m(0)}{N_m} \times \sum_{n=1}^{\infty} \frac{\sin(\eta_n y^+)}{\eta_n R_m^2} [1 - e^{-R_m^2 \alpha t}] \tag{20a}$$

where

$$R_m^2 \equiv \left(\frac{U}{2\alpha}\right)^2 + \left(\frac{\beta_m}{L}\right)^2 + \left(\frac{\eta_n}{W}\right)^2 \tag{20b}$$

There are two problems with the solution given by Eqs. (19) and (20*a*). First, they converge very slowly, and second, the eigenvalues may be difficult to obtain. Fortunately both of these problems can be solved. The first is solved using the time-partitioning method, and the second can be efficiently solved using the solution in Ref. [14], and it is discussed more in the next section. Before discussing the eigenvalues, the solution is presented in a different form below, which is more appropriate for time partitioning.

The solution for the temperature given by the sum of Eqs. (19) and (20*a*) is multiplied, as indicated by Eq. (3). This solution can also be obtained by using using both the short time GFs for $u=0$ to t_p in Eq. (10) and the long cotime GFs from t_p to t. Equations (19) and (20*a*) each contain two components, a steady state and what is called a complementary transient. The steady state component is associated with the terms multiplied by the "1" in the brackets; it is the part that converges slowly and causes a problem in obtaining accurate values. The second part is the complementary transient and converges exponentially, provided that t is not equal to zero. The complementary transient component of Eq. (20*a*) is

$$\psi_{\mathrm{ct},m}(x,y,t) = -\frac{h_0 T_\infty}{k} e^{U^2 t/4\alpha} 4 \sum_{m=1}^{\infty} \frac{X_m(x) X_m(0)}{N_m} \sum_{n=1}^{\infty} \frac{\sin(\eta_n y^+)}{\eta_n R_m^2} e^{-R_m^2 \alpha t} \tag{21}$$

Notice that it is defined to be negative; the subscript "ct" denotes complementary transient.

When the time-partitioning method is used, the solution can be written as

$$T(x,y,t) = T^S(x,y,t_p) + T^L_{\mathrm{ct}}(x,y,t) - T^L_{\mathrm{ct}}(x,y,t_p) \tag{22}$$

The first term on the right side is obtained using the short cotime GFs integrated from $u=0$ to t_p, and the other terms are obtained from the complementary transient components, which, as noted above, converge exponentially. These equations are integrated, as shown in Eq. (10), to produce the solution $\psi(x,y,t)$, and this solution is then transformed back into a temperature solution using the transformation given in Eq. (3).

4 Eigencondition for the Zeroth Eigenvalue

The eigencondition for the zeroth eigenvalue (if one exists) for the ψ problem is found using Eq. (14*b*). The zeroth eigenvalue, β_0, only exists when the right side of Eq. (14*b*) is positive and less than 1. We consider two cases. One is for β_0 greater than about 3 (where the hyperbolic tangent is equal to unity), and the other is for β_0 very nearly equal to zero. For "large" β_0 values, replace the left side of Eq. (14*b*) by 1 to get

$$\beta_0^2 + (\mathrm{Bi}_{e0} + \mathrm{Bi}_{eL})\beta_0 + \mathrm{Bi}_{e0}\mathrm{Bi}_{eL} = 0 \tag{23}$$

The roots of this equation are

$$\beta_0 = -\mathrm{Bi}_{e0}, \quad \beta_0 = -\mathrm{Bi}_{eL} \tag{24}$$

Only one of these conditions can be satisfied, and the root must be positive and greater than about 3 to be valid using Eq. (24). For the root to be positive, it means that one of the effective Biot numbers must be negative. Suppose that the velocity is in the positive x direction. Then we must have

$$\mathrm{Bi}_{e0} < -3 \tag{25}$$

for flow in the positive direction and for large values of β_0. For these large values of β_0, Eq. (24) indicates that β_0 is a linear function of Pe.

For "small" magnitudes of the eigenvalues, the hyperbolic tangent can be approximated with the first term of the small argument approximation to get

$$\beta_0^2 + \mathrm{Bi}_{e0}\mathrm{Bi}_{eL} + \mathrm{Bi}_{e0} + \mathrm{Bi}_{eL} = 0 \tag{26}$$

Solving this equation for β_0 gives

$$\beta_0 = [-\mathrm{Bi}_{e0}\mathrm{Bi}_{eL} - \mathrm{Bi}_{e0} - \mathrm{Bi}_{eL}]^{1/2} \tag{27}$$

This expression can also be expanded in terms of the true Biot numbers, as opposed to the effective Biot numbers. In this case, we have

$$\beta_0 = \left[-\mathrm{Bi}_0\mathrm{Bi}_L + \left(\frac{\mathrm{Pe}}{2}\right)^2 + \frac{\mathrm{Pe}}{2}(\mathrm{Bi}_L - \mathrm{Bi}_0) - \mathrm{Bi}_0 - \mathrm{Bi}_L\right]^{1/2} \tag{28}$$

Since the expression in the brackets must be positive, from Eq. (28) we conclude that

$$-\mathrm{Bi}_0\mathrm{Bi}_L + \left(\frac{\mathrm{Pe}}{2}\right)^2 + \frac{\mathrm{Pe}}{2}(\mathrm{Bi}_L - \mathrm{Bi}_0) - \mathrm{Bi}_0 - \mathrm{Bi}_L > 0 \tag{29}$$

Setting this equation equal to zero and solving for Pe/2 gives the minimum Pe as

$$\mathrm{Pe}_{\min} = \mathrm{Bi}_0 - \mathrm{Bi}_L + [(\mathrm{Bi}_0 + \mathrm{Bi}_L)^2 + 4(\mathrm{Bi}_0 + \mathrm{Bi}_L)]^{1/2} \tag{30}$$

for flow in the positive x direction, that is, $\mathrm{Pe} > 0$. This expression is valid only for small values of the eigenvalue. For negative maximum Pe values, a negative sign would replace the positive sign before the first bracket in Eq. (30); interchanging the Biot numbers gives the same magnitude as given by Eq. (30) for the positive Pe numbers. See Table 3 for the positive $\mathrm{Pe}_{\min}$ values. The first column gives the Bi_L values, and the second column gives $\mathrm{Pe}_{\min}$ for $\mathrm{Bi}_0 = 0$. For both Biot numbers equal to zero, the minimum is equal to zero, which is consistent with the XU22 case. For larger Bi_0 values, the minimum Pe is nearly independent of Pe. In principle, Eq. (30) can be used for all the cases. However, it is only needed for the XU33 case because simpler expressions are available for the other cases.

Eigenconditions for the zeroth eigenvalue are given in Table 4. Table 2 gives similar eigenconditions for the remaining eigenvalues, and Table 1 gives the eigenfunctions for the zero eigenfunction for the transformed variable ψ. Table 5 gives limiting conditions for the existence of a zeroth eigenvalue for all of the possible combinations of boundary conditions. Table 6 gives the norms for each of the boundary condition combinations. The zeroth term in the long-time portion of the solution can be found whenever the conditions given in Table 5 indicate that the zeroth term exists. Figure 2 plots curves for the zeroth eigenvalue as a function of Pe. The use of Table 5 and Fig. 2 for the XU13 case can be illustrated by an example; let $\mathrm{Bi}_L = 5$ and $\mathrm{Pe} = -15$ so that $2\mathrm{Bi}_L + \mathrm{Pe} = -5$, which gives 2.464 for the value of Bi_{eL}. Notice that XU12 and XU13 are associated with negative Pe values, while XU21 and XU31 are associated with positive Pe values. Figure 3 is a similar plot to Fig. 2, except that it addresses the existence of the zeroth eigenvalue for the XU23 and XU32 cases.

Since Eq. (30) gives the minimum value of Bi at each side of the body, which will generate a zeroth term in the series solution for the XU33 case, it can be seen that a zeroth term can be generated for all combinations of positive Bi. Figure 4 shows a plot of the minimum Pe, which will generate a zeroth term for various combinations of Bi_0 and Bi_L. Unlike the XU23 and XU32 cases, the zeroth term can exist for XU33 at very small values of Pe.

Table 3 Minimum positive Pe values for which the zeroth term in the long-time form of the GFs appears. The values are found using Eq. (19). The negative of these Pe values are the values for negative Pe, provided that Bi_0 and Bi_L are interchanged.

Bi_L	$Bi_0=0$	$Bi_0=1$	$Bi_0=2$	$Bi_0=5$	$Bi_0=10$
0.00	0	3.236068	5.464102	11.7082	21.83216
0.25	0.780776	3.311738	5.500000	11.71868	21.83563
0.5	1.000000	3.372281	5.531129	11.72842	21.83896
0.75	1.137459	3.422144	5.558422	11.73749	21.84216
1	1.236068	3.464102	5.582576	11.74597	21.84523
1.5	1.372281	3.531129	5.623475	11.76136	21.85103
2	1.464102	3.582576	5.656854	11.77496	21.85641
3	1.582576	3.656854	5.708204	11.79796	21.86607
4	1.656854	3.708204	5.745967	11.81665	21.87451
5	1.708204	3.745967	5.774964	11.83216	21.88194
10	1.83216	3.845233	5.856407	11.88194	21.90890

5 Short Cotime Green's Functions

The GFs given above are known as the long cotime GFs. The term cotime is defined in Refs. [5–8] as $u=t-\tau$, which appears, for example, in Eq. (12). As mentioned in Refs. [5–8], two expressions are available for the GF. Equation (12) above gives the long-time GF. These long-time GFs are used in conjunction with the short time GFs, each contributing a portion of the solution. Using the long-time functions alone, there are often tens of thousands of terms required in order to obtain four or five digits of accuracy. As noted in Refs. [5–8], the number of terms is significantly reduced with time partitioning, with a very high accuracy often obtainable with fewer than ten terms. For the $X11$ case the short cotime expression is

$$G^S_{\psi}(y,t;y',\tau) = \sum_{n=-\infty}^{n=\infty} (K(2nW + y - y', t-\tau) - K(2nL + y + y', t-\tau)) \tag{31}$$

where

$$K(y,\theta) \equiv \frac{1}{\sqrt{4\pi\alpha\theta}} e^{-y^2/4\alpha\theta} \tag{32}$$

Equation (31) is for the short time form and has an S superscript; this form comes from the Laplace transform. The boundary conditions of the first kind on the $y=0$ and $y=W$ boundaries are the simplest because the transformation, Eq. (3), does not change the boundary conditions.

In addition to Eq. (31) for the Y11 GF, short cotime GFs are needed for the X33 problem. These can be difficult to obtain in exact form, but it is only necessary to find expressions for small dimensionless times when the temperature change only near the heated surface is needed. Reference [6] gives expressions accurate until $\alpha t/L^2=0.05$. For the present solution, a simpler expression is chosen, and the computation is restricted to $x=0$. This GF is the same as for a semi-infinite body and is given by

Table 4 Eigenconditions for the zeroth term in the long-time GFs found from the ψ transformation

Case for T	Goes to the ψ problem	Bi_{e0}	Bi_{eL}	Zeroth eigenvalue or eigencondition for the ψ problem
XU11	X11			None
XU12	X13		Pe/2	$\tanh(\beta_0)=-2\beta_0/\mathrm{Pe}$ (only $\mathrm{Pe}<-2$)
XU13	X13		$Bi_L+Pe/2$	$\tanh(\beta_0)=-2\beta_0/(2Bi_L+Pe)(Pe<-2(1+Bi_L))$
XU21	X31	−Pe/2		$\tanh(\beta_0)=2\beta_0/\mathrm{Pe}$ (only $\mathrm{Pe}>2$)
XU22	X33	−Pe/2	Pe/2	$\beta_0=\lvert Pe\rvert/2$ (all Pe values)
XU23	X33	−Pe/2	$Bi_L+Pe/2$	$\tanh(\beta_0)=-4\beta_0 Bi_L/(4\beta_0^2-Pe(2Bi_L+Pe))$
XU31	X31	$Bi_0-Pe/2$		$\tanh(\beta_0)=-2\beta_0/(2Bi_0-Pe)$, $(Pe>2(1+Bi_0))$
XU32	X33	$Bi_0-Pe/2$	Pe/2	$\tanh(\beta_0)=-4\beta_0 Bi_0/(4\beta_0^2+Pe(2Bi_0-Pe))$
XU33	X33	$Bi_0-Pe/2$	$Bi_L+Pe/2$	$\tanh(\beta_0)=-4\beta_0(Bi_0+Bi_L)/(4\beta_0^2+(2Bi_0-Pe)(2Bi_L+Pe))$

Table 5 Limiting conditions for the zeroth term for long-time GFs

Case	Criteria for positive Pe	Criteria for negative Pe
XU11	None	None
XU12	None	$\mathrm{Pe}<-2$
XU13	None	$\mathrm{Pe}<-2(1+Bi_L)$
XU21	$\mathrm{Pe}>2$	None
XU22	$\mathrm{Pe}>0$	$\mathrm{Pe}<0$
XU23	$\mathrm{Pe}>-Bi_L+[Bi_L^2+4Bi_L]^{1/2}$	$\mathrm{Pe}<-Bi_L-[Bi_L^2+4Bi_L]^{1/2}$
XU31	$\mathrm{Pe}<2(1+Bi_0)$	None
XU32	$\mathrm{Pe}>Bi_0+[Bi_0^2+4Bi_0]^{1/2}$	$\mathrm{Pe}<Bi_0-[Bi_0^2+4Bi_0]^{1/2}$
XU33	$\mathrm{Pe}>Bi_0-Bi_L+[(Bi_0+Bi_L)^2+4(Bi_0+Bi_L)]^{1/2}$	$\mathrm{Pe}<Bi_0-Bi_L-[(Bi_0+Bi_L)^2+4(Bi_0+Bi_L)]^{1/2}$

Table 6 Norms for the zeroth term for long-time GFs

Case	Norm[a]
XU11	None
XU12	$L[(-1/2)+\sinh(2\beta_0)/4\beta_0]$
XU13	$L[(-1/2)+\sinh(2\beta_0)/4\beta_0]$
XU21	$L[(-1/2)+\sinh(2\beta_0)/4\beta_0]$
XU22	N_{33}
XU23	N_{33}
XU31	$L[(-1/2)+\sinh(2\beta_0)/4\beta_0]$
XU32	N_{33}
XU33	N_{33}

[a]The norm N_{33} is $N_{33}=L/2[\beta_0^2-B_{e0}[1+B_{e0}-\cosh(2\beta_0)]]+L[(\beta_0^2+B_{e0}^2)\sinh(2\beta_0)]/4\beta_0$.

$$G^S_{\psi X30}(0,t|0,\tau)=\frac{1}{\sqrt{\pi\alpha(t-\tau)}}-\frac{h_{eo}}{k}e^{\alpha(t-\tau)h_{eo}^2/k^2}\,\mathrm{erfc}\left(\frac{h_{eo}}{k}\sqrt{\alpha(t-\tau)}\right) \tag{33}$$

For the same values of x, x', t, and τ, Eqs. (12) and (31) give the same numerical answer. However, the required number of terms to get the desired accuracy can be quite different in the two expressions. For small values of dimensionless cotime $\alpha u/L^2$, e.g., less than 0.05, only a few terms are needed in Eq. (12) and only a few are needed in Eq. (31) for $\alpha u/L^2$ greater than 0.05. Conversely, for large values of $\alpha u/L^2$, e.g., 1, many terms are needed using Eq. (31) and the same is true for Eq. (12) for that dimensionless group going to zero. In the time-partitioning method both of these forms are used. Each is used in its most

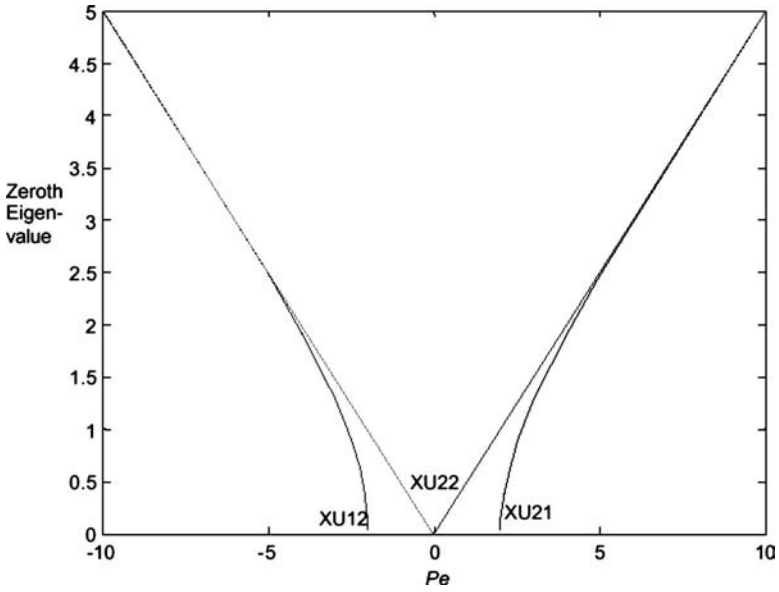

Fig. 2 Zeroth eigenvalues for XU12, XU22, and XU22 cases as a function of Pe. This figure is also valid for the XU13 case by using the XU12 curve with the Pe on the abscissa replaced by $2Bi_L+Pe$ and also for the XU31 case by using the XU21 curve with the Pe on the abscissa replaced by $Pe-2Bi_0$.

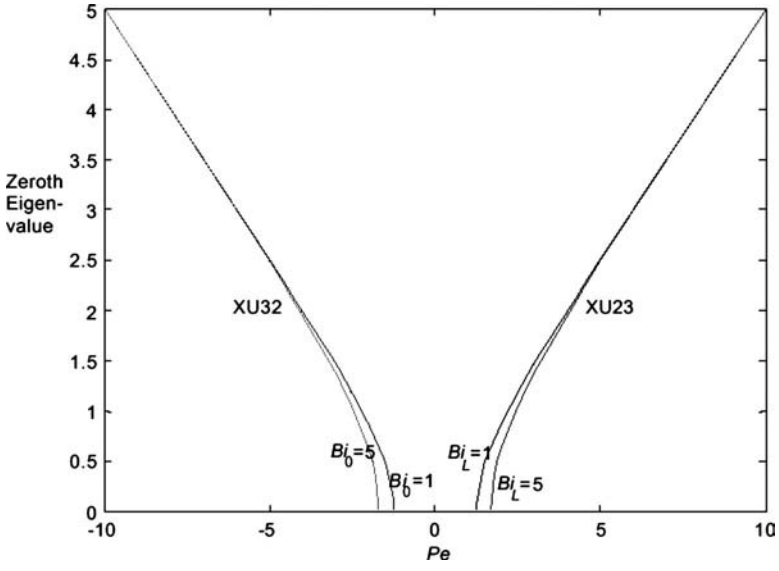

Fig. 3 Zeroth eigenvalues for XU23 and XU32 cases as a function of Pe. For the XU23 case, $Bi_L=1$ and 5 and for the XU32 case, $Bi_0=1$ and 5.

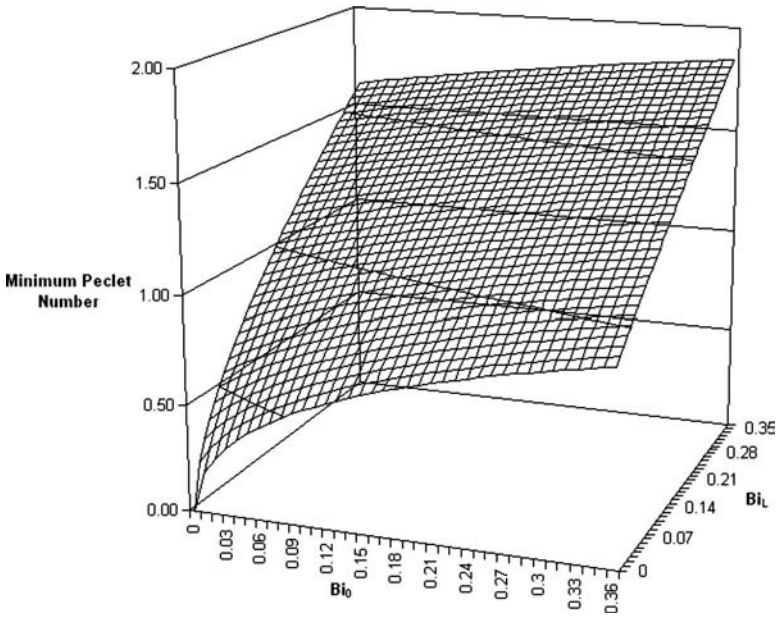

Fig. 4 Minimum Pe for the existence of a zeroth term for the XU33 case, as a function of Bi at the right and left hand boundaries of the body. Unlike the XU23 and XU32 cases, the zeroth term can exist for XU33 at very small values of Pe.

efficient region, resulting in only a few terms being needed in each summation. This is true for 1D, 2D, and 3D cases, with and without solid body flow.

An efficient and rapidly converging form of the solution can be obtained by using the solution for the short cotime and the long cotime, as indicated by Eq. (29). A relatively simple application is for small dimensionless times, $x=$ and y not near 0 or W. In that case, the problem is a semi-infinite one-dimensional problem. The temperature for this 1D problem can be found and is now considered known. Note that this temperature is the same as for the 2D problem because the time is sufficiently small so that the edge effects are not present. The difficult part to find in Eq. (29) is the steady state part, which is obtained by letting t go to zero, which gives

$$T(x,y,\infty) = T_{SS}(x,y) = T^S(x,y,t_p) - T^L_{\text{ct}}(x,y,t_p) \tag{34}$$

Notice that the two terms on the right side are not difficult to obtain. The first term is obtained from the small time solution and the second term has exponential convergence.

Since the 3D GF for the present problem can be formed by a product of the 1D GFs, the GF solution equation can be written in a relatively simple manner for product forms of initial conditions, volumetric energy generation, and boundary conditions. Due to space limitations this topic is explored briefly. Using the current example, the X33 GF is multiplied by the X11 GF. This is because the body under consideration has boundary conditions of the third kind (convective) in the x direction and boundary conditions of the first kind (prescribed temperature) in the y direction.

6 Summary and Conclusions

This paper gives a derivation for exact solutions of the transient heat conduction equation for solid body flow in a rectangle. The method can be expanded to include a parallelepiped. One objective is to develop a general method for providing extremely accurate and efficient solutions for the verification of large multidimensional computer codes using finite element, control volume, and other related approximate methods. A transformation is used to obtain the standard form of the transient heat conduction equation. This transformed equation does not contain the flow terms. GFs are available for solving this standard equation. Using the example given here as a template, a system for generating general solutions for three-dimensional parallelepipeds with solid body motion, having any combination of boundary conditions, is given. Moreover, the components of these solutions are summarized in tabular form to provide a systematic way of building the general solutions.

Nomenclature

- Bi = Biot number (hL/k)
- c = specific heat (J/kg °C)
- $G^S(\,)$ = short cotime GF
- $G^L(\,)$ = long cotime GF
- h_0 = heat transfer coefficient for the left hand side (W/m^2 °C)
- h_L = heat transfer coefficient for the right hand side (W/m^2 °C)
- k = thermal conductivity (W/m °C)
- $K(\,)$ = component of short cotime GF
- L = overall length of the body in the x direction (m)
- Pe = Peclet number (UL/α)
- q = heat flux (W/m^2)
- R_o = dimensionless number, $(\text{Pe}/2)^2+\beta_o^2$
- T = temperature (°C)
- U = uniform velocity in the x direction (m/s)
- u = cotime, $t-\tau$ (s)
- W = overall length of the body in the y direction (m)
- X11 = designation for conduction with prescribed temperature on both x boundaries
- X33 = designation for conduction with convection on both boundaries
- XU22 = designation for conduction with both boundaries insulated and solid body motion
- XU33 = designation for conduction with convection on both boundaries and solid body motion

x, y = spatial variables (m)
Y11 = designation for conduction with prescribed temperature on both y boundaries

Greek

α = thermal diffusivity (m^2/s)
β = eigenvalue
ρ = density (kg/m^3)
ψ = transformed temperature variable, Eq. (2)

Acknowledgment

We appreciate the support of this research by Sandia National Laboratories, Albuquerque, NM. Dr. Kevin Dowding was the project manager at Sandia. The support and insights of Professor David Yen, Professor Emeritus, Department of Mathematics, Michigan State University (MSU), for many parts of this research is appreciated. The authors would also like to thank Professor Charles Macleur of the MSU Mathematics Department for his insightful contribution regarding the zeroth eigenvalue.

References

[1] Roach, P. J., 1998, *Verification and Validation in Computational Science and Engineering*, Hermosa, Albuquerque, NM, Chaps. 3–8.
[2] McMasters, R. L., Zhou, Z., Dowding, K. J., Somerton, C., and Beck, J. V., 2002, "Exact Solution for Nonlinear Thermal Diffusion and Its Use for Verification," J. Thermophys. Heat Transfer, **16**, pp. 366–372.
[3] Oberkampf, W. L., Sindir, M. N., and Conlisk, A. T., 1998 "Guide for the Verification and Validation in Computational Fluid Dynamics Simulation," Paper No. AIAA-G-077-1998.
[4] Ozisik, M., 1980, *Heat Conduction*, Wiley, New York.
[5] Beck, J., Cole, K., Haji-Sheikh, A., and Litkouhi, B., 1992, *Heat Conduction Using Green's Functions*, Hemisphere, Washington, DC.
[6] McMasters, R., Dowding, K., Beck, J., and Yen, D., 2002, "Methodology to Generate Accurate Solutions for Verification in Transient Three-Dimensional Heat Conduction," Numer. Heat Transfer, Part B, **41**, pp. 521–541.
[7] Yen, D. H. Y., Beck, J., McMasters, R., and Amos, D. E., 2002, "Solution of an Initial-Boundary Value Problem for Heat Conduction in a Parallelepiped by Time Partitioning," Int. J. Heat Mass Transfer, **45**, pp. 4267–4279.
[8] Beck, J., and McMasters, R., 2002, "Verification Solutions for Heat Conduction With Solid Body Motion and Isothermal Boundary Conditions," Arabian J. Sci. Eng., **27**, pp. 49–65.
[9] Haji-Sheikh, A., and Beck, J. V., 2002, "Temperature Solution in Multi-Dimensional Multi-Layer Bodies," Int. J. Heat Mass Transfer, **45**, pp. 1865–1877.
[10] Haji-Sheikh, A., Beck, J. V., and Agonafer, D., 2003, "Steady-State Heat Conduction in Multi-Layer Bodies," Int. J. Heat Mass Transfer, **46**, pp. 2363–2379.
[11] Yen, D. H. Y., and Beck, J. V., 2003, "Small Time Approximations of Green's Functions for One-Dimensional Heat Conduction Problems With Convective Boundaries," Z. Angew. Math. Mech., **83**, pp. 549–558.
[12] de Monte, F., 2003, "Unsteady Heat Conduction in Two-Dimensional Two Slab-Shaped Regions: Exact Closed-Form Solution and Results," Int. J. Heat Mass Transfer, **46**, pp. 1455–1469.
[13] de Monte, F., 2004, "Transverse Eigenproblem of Steady-State Heat Conduction for Multi-Dimensional Two-Layered Slabs With Automatic Computation of Eigenvalues," Int. J. Heat Mass Transfer, **47**, pp. 191–201.
[14] Haji-Sheikh, A., and Beck, J. V., 2000, "An Efficient Method of Computing Eigenvalues in Heat Conduction," Numer. Heat Transfer, Part B, **38**, pp. 133–156.
[15] Polyanin, A. D., 2002, *Handbook of Linear Partial Differential Equations for Engineers and Scientists*, Chapman and Hall, London, p. 62.
[16] Beck, J., and McMasters, R., 2004, "Solutions for Multi-Dimensional Transient Heat Conduction With Solid Body Motion," Int. J. Heat Mass Transfer, **47**, pp. 3757–3768.

Ground Heat Transfer From a Varying Line Source With Seasonal Temperature Fluctuations

X. Duan
Department of Mechanical and Manufacturing Engineering,
University of Manitoba,
75A Chancellors Circle,
Winnipeg, MB, R3T 5V6, Canada

G. F. Naterer
Professor and Canada Research Chair
Director of Research, Graduate Studies, and Development,
Faculty of Engineering and Applied Science,
University of Ontario Institute of Technology,
2000 Simcoe Street North,
Oshawa, ON, L1H 7K4, Canada

In this paper, transient heat conduction between a line heat source and a semi-infinite medium (representing a foundation of a power transmission tower and the surrounding ground) is analyzed numerically and experimentally. The tower foundation is represented by a metal rod buried in a semi-infinite medium. Using an experimental test cell with a data acquisition system, heat transfer and temperature measurements within the domain are collected. The experimental studies are first applied to unidirectional heat conduction, wherein the analytical solutions are compared against measured temperature responses. Then two transient heat transfer cases are studied: one case with a steady heat input provided by an electrical heater and another with sinusoidal temperature variations achieved by temperature-controlled fluid in a heat exchanger. The analysis shows that a metal tower footing has significant thermal effects on the temperature response of the local half-space around the footing in the foundation. This thermal effect varies with time, as well as spatially at different positions around the tower footing. In particular, measured results from the case of sinusoidal temperature variations show that the tower footing introduces additional temperature increases in the "summer" periods and temperature decreases in the "winter" periods. [DOI: 10.1115/1.2955467]

Keywords: transient heat conduction, varying line heat source, power transmission tower foundation, ground thermal response

1 Introduction

With climate change and global warming, construction and maintenance of power transmission infrastructure in northern climates are becoming increasingly costly and difficult. Permafrost, or permanently frozen ground, refers to a thermal condition of ground soil with a temperature that remains at or below 0°C continuously for a significantly long period of time [1]. Above the permafrost is an active layer (see Fig. 1), which remains frozen in winter and melted in summer due to seasonal changes in the air temperature. With the thermal equilibrium of the ground, any heat transferred into the region during the thaw season is removed during the freezing season to maintain the permafrost level. However when a heated object or any structure is buried over permafrost to change the thermal regime, a continuous addition of excess thermal energy into the local permafrost may eventually cause thawing of the foundation and structure. This article presents analytical and experimental studies that investigate the effects of a varying line heat source (representing a buried vertical tower foundation) on a surrounding half-space.

A danger of ground thawing in northern regions lies in the potential settling, tilting, heaving, and loss of mechanical strength of structures, which can lead to the failure of a foundation. Bond strengths between permafrost and piles or tower footings are significantly reduced by higher ground temperatures. Increases in the thickness of the active layer can cause frost heaving of structures. In the permafrost areas in Northern Canada, there are many structures that are being affected by permafrost retreat due to climate change, such as pipelines, roads, power transmission lines, and community infrastructures like solid waste facilities, electrical generating facilities, towers, and fuel storage tanks. The potential for severe thaw induced disruptions to engineered structures has been reported for each of these cases [2]. For example, the ground thawing problem has led to significant financial costs for the maintenance of power transmission structures in Northern Manitoba [3]. Due to the freezing/thawing cycle and local degradation of permafrost due to climate change, the original frozen ground near the tower footing retreats or even disappears over time. The resulting heave, settlement, or tilting can break the tower legs, tilt whole towers, buckle tower members, or bend footing members. Often a tower must be abandoned or completely replaced.

Many past studies have investigated ground heat transfer and temperature variations near the foundation of a structure. Sivanbaev [4] examined thawing of permafrost subjected to a steady heat source. Structures with temperatures above 100°C inside rooms of furnaces or electrical power plants were studied. It was proposed to divide the foundation into four zones: (1) desiccated ground, (2) intensely vaporized ground, (3) thawed ground, and (4) frozen ground. Taking the thermal effects of the heat source into account, the depth of ground thawing was calculated and found to be about one-half of the Neumann solution [4]. Khrustalev et al. [5] developed a method of extrapolating the ground temperature at holes located in the bed of a structure. A group of extrapolation functions reduced the three-dimensional problem of heat conduction to a set of one-dimensional problems. However, this method did not account for seasonal variations in soil temperature. Thus, it was only applicable to the prediction of mean/annual temperatures, not detailed seasonal temperature variations. Khrustalev and Shumilishskii [6] showed that a natural historical variation in climate leads to a variation in the bearing capacity of permafrost beds. If these variations are not taken into consideration in the structural design, then deformations of structures may occur.

The objective of this paper is to analyze the transient thermal

Contributed by the Heat Transfer Division of ASME for publication in the JOURNAL OF HEAT TRANSFER. Manuscript received November 18, 2007; final manuscript received February 22, 2008; published online August 29, 2008. Review conducted by A. Haji-Sheikh.

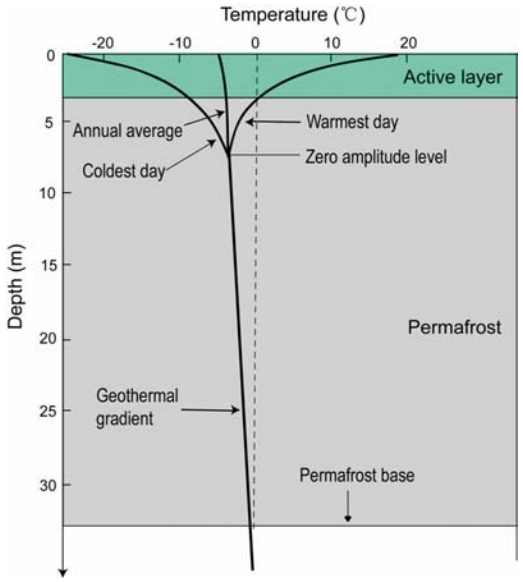

Fig. 1 Annual temperature variations in the ground

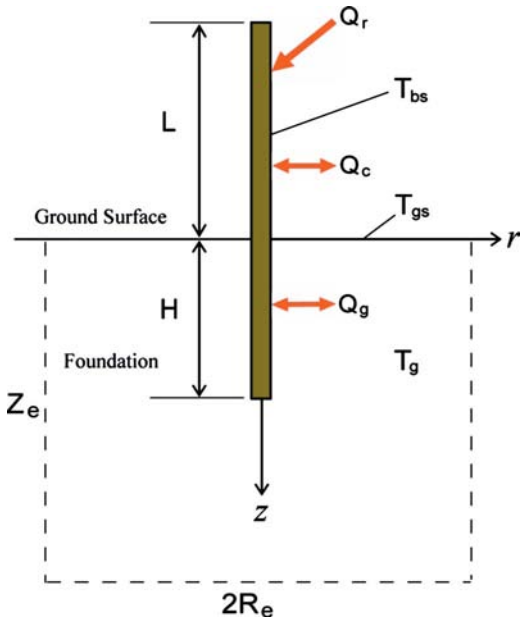

Fig. 2 Schematic of a simplified tower foundation—a metal rod buried in the ground

response of ground soil to a varying line heat source that represents a buried power transmission line tower. In particular, it examines how the temperature varies around the foundation in different seasons, as well as the effects of the presence of the tower foundation on the ground temperature. In the summer, the air temperature is usually higher than the ground temperature and heat is conducted through the tower downward into the ground. This leads to local thawing around the tower foundation. To the best knowledge of the authors, there is no past literature that has analyzed, predicted, or measured these phenomena. This paper addresses this shortcoming by formulating and solving the problem of transient heat conduction from a varying line heat source into a semi-infinite half-space. A single metal rod is used to approximate a tower footing. The ground is approximated as a semi-infinite medium, only heat conduction is modeled, and the medium is assumed dry.

Several past studies have been reported on ground heat transfer from buried vertical structures. An analytical solution was developed for steady-state heat transfer from a finite rod buried in a semi-infinite medium [7]. Anteby and Shai [8] developed a modified shape factor for isothermal surfaces embedded in a semi-infinite medium. Deng and Fedler [9] predicted the heat transfer in a multilayer ground material with a vertical ground heat exchanger (GHE) using a two-dimensional model of unsteady heat conduction. Yavuzturk and Spitler [10] used a step response factor model for vertical ground loop heat exchangers. Bi et al. [11] analyzed the temperature distribution in a GHE and performed measurements.

There have also been numerical studies on transient heat transfer with underground energy storage, such as Refs. [12,13]. There is a significant difference between a GHE and the current problem of heat transfer from a buried vertical tower. For example, fluid flow and convection occur inside the tubes of a GHE, but only heat conduction through the tower footing. In Ref. [7], a heat source method was used to obtain the analytical solution. Most past models of transient heat conduction in a semi-infinite medium have used a point heat source (Carslaw and Jaeger [14]). A buried vertical structure can be approximated as a line heat source through a series of point heat sources. A one-dimensional infinite line-source model was developed by Ingersoll et al. [15] and was later applied to earth-coupled heat transfer problems by Hart and Couvillion [16]. Zeng et al. [17] presented a 2D finite line-source model to predict axial heat flow in the ground for a long-term performance of ground-source heat pumps (GSHPs). Recently, the model was extended by Duan et al. [18] and Duan and Naterer [19] to transient heat conduction from a buried power transmission line tower.

This paper extends a previous finite line-source model [17] to a nonuniform line heat source that varies both spatially and temporally. The model will be used to analyze the ground thermal response to a tower footing with a time-dependent ground surface temperature. Also, experimental studies will be conducted to determine the ground temperatures near a buried tower foundation, both for validation purposes and sensitivity studies with different ground materials. Various heat conduction cases will be analyzed, from which comparisons will be made between the mathematical models and experimental data. This paper will present the detailed temperature response of the ground to the presence of a tower foundation, as well as the seasonal thermal effects of the tower footing on temperature variations near the foundation. These new data will provide key insights for developing mitigation strategies to overcome seasonal thawing problems of tower foundations in the northern regions.

2 Formulation of Ground Heat Transfer

Figure 1 shows a typical ground temperature profile in the northern region without the presence of a tower foundation (based on Refs. [20,21]). It has the same temperature profile as the ground far from a tower footing (called the "far-field" temperature). A typical annual range of ground temperatures is shown by the warmest and coldest temperatures at each depth. With increasing depth into the ground, the seasonal difference of temperature decreases. The point where there is no discerniable change in temperature is called the "depth of zero annual amplitude." Below this depth, temperature changes are very small throughout the year.

When a power transmission line tower is buried under the ground, the annual ground temperature variations must be modified by the thermal effects of the tower footing. Figure 2 shows a simplified tower foundation with a metal rod approximation. The simplified tower has an above-ground part, L, and an underground part, H. The main energy exchange components on the tower include solar radiation, Q_r, convective heat transfer at the tower surface caused by wind, Q_c, and heat transfer with the ground, Q_g, through the tower footing. Radiative heat transfer between the

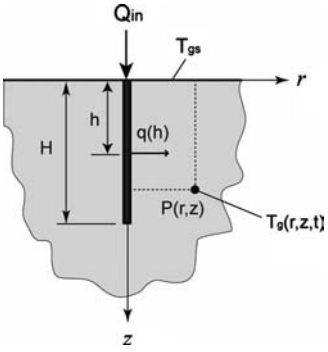

Fig. 3 Schematic of a line heat source in a semi-infinite half-space

tower and the ground surface is neglected in the illustration. The surface temperature of the tower, T_{bs}, and the ground surface temperature, T_{gs}, are assumed close to the air temperature. The purpose of this study is to analyze the transient heat conduction within the tower foundation by examining the annual variation of the foundation temperature, T_g. In particular, the thermal effects of the tower on the ground temperature profile can be found by examining the foundation temperature variations with or without the presence of the tower.

This section will first analyze the long-term thermal response in the local half-space around the tower footing to the yearly averaged net heat input to the foundation through the tower. In Fig. 2, the tower itself has no net heat gain or loss. The net heat input through the tower (including solar radiation and convective heat transfer to the tower) can be expressed as

$$Q_{in} = Q_g = Q_r + Q_c \tag{1}$$

The foundation is assumed to have a uniform initial temperature of T_i. In this case, the ground surface is further assumed to remain at a constant temperature, which is the same as the initial foundation temperature. Defining a temperature difference, $\theta = T - T_i$, makes the temperature difference of the ground surface and the initial temperature difference zero. The temperature difference of point $P(r,z)$ in the foundation becomes $\theta_g(r,z,t) = T_g(r,z,t) - T_i$.

As shown in Fig. 3, the buried rod is approximated by a finite line heat source, with a heating strength of $q(h)$, where h is the distance from the top end. Different distributions of the heating strength along the line heat source will be considered: (1) a uniform distribution, $q(h) = Q_{in}/H$, (2) a linear distribution with zero heating strength at the lower end of the rod, $q(h) = 2Q_{in}/H(1 - h/H)$, and (3) a variable heating strength (VHS) distribution,

$$q(h) = m_b Q_{in}[\coth(m_b H)\cosh(m_b h) - \sinh(m_b h)] \tag{2}$$

where $m_b = \sqrt{2k_g/k_b R_b^2 \ln(2H_b/R_b)}$ and R_b and k_b are the radius and thermal conductivity of the rod, respectively. This heating strength distribution considers heat conduction through the metal rod itself and assumes that the strength is proportional to the temperature difference between the rod and the ground surface. The derivation of Eq. (2) was detailed in Ref. [18], where an adiabatic boundary condition at the bottom tip of the rod was assumed. In terms of the thermal response to this steady line heat source, the foundation temperature response can be calculated by the line heat source formulation of Zeng et al. [17] as follows:

$$\theta_g(r,z,t) = \frac{1}{4\pi k_g}\int_0^H q(h)\left[\operatorname{erfc}\left(\frac{D_1}{2\sqrt{\alpha_g t}}\right)\Big/ D_1 - \operatorname{erfc}\left(\frac{D_2}{2\sqrt{\alpha_g t}}\right)\Big/ D_2\right]dh \tag{3}$$

where $D_1 = \sqrt{r^2 + (z-h)^2}$ and $D_2 = \sqrt{r^2 + (z+h)^2}$. This model will be used to calculate the maximum temperature response to the tower foundation.

Secondly, this section extends the previous formulation by allowing the heat input and ground surface temperatures to vary with time, i.e., $Q_{in}(t)$ and $\theta_{gs}(t) = T_{gs}(t) - T_i$. This case more closely resembles the actual heat transfer process in a real tower foundation, where both the metal tower and the ground surface undergo seasonal temperature variations. The buried rod is approximated by a finite line heat source with a varying heating strength of $q(h,t)$. Using a superposition method detailed in Ref. [19], the total temperature difference in the ground becomes the superposition of a temperature response to a continuous infinite plane doublet of strength $2\alpha_g\theta_{gs}(t)$ at the plane of $z=0$ [14,15], denoted as θ_{gp}, and the response to a finite line heat source of strength $q(h,t)$ buried in the ground on the centerline of $r=0$, denoted as θ_{gl}. In a two-dimensional system, the total temperature difference at point $P(r,z)$ becomes

$$\theta_g = \theta_{gp} + \theta_{gl} \tag{4}$$

The thermal response to the plane doublet is [15]

$$\theta_{gp} = \frac{2}{\pi^{0.5}}\int_{z/2\sqrt{\alpha_g t}}^{\infty} \theta_{gs}\left(t - \frac{z^2}{4\alpha_g \beta^2}\right)e^{-\beta^2}d\beta \tag{5}$$

The thermal response to the finite line heat source is obtained by a method of images and an integration of a series of time-varying point heat sources to simulate a finite line heat source as follows [19]:

$$\theta_{gl} = \frac{1}{8\pi^{1.5}k_g\sqrt{\alpha_g}}\int_0^H\int_0^t \frac{q(h,t')}{(t-t')^{1.5}}\left\{\exp\left[-\frac{D_1^2}{4\alpha_g(t-t')}\right] - \exp\left[-\frac{D_2^2}{4\alpha_g(t-t')}\right]\right\}dt'dh \tag{6}$$

Defining new variables, i.e., $\lambda = (t-t')^{-0.5}$, $\beta_1 = D_1\lambda/2\sqrt{\alpha_g}$, and $\beta_2 = D_2\lambda/2\sqrt{\alpha_g}$, and rearranging, the result in Eq. (6) can also be expressed as

$$\theta_{gl} = \frac{1}{2\pi^{1.5}k_g}\int_0^H\left[\frac{1}{D_1}\int_{D_1/2\sqrt{\alpha_g t}}^{\infty} q\left(h, t - \frac{D_1^2}{4\alpha_g\beta_1^2}\right)e^{-\beta_1^2}d\beta_1 - \frac{1}{D_2}\int_{D_2/2\sqrt{\alpha_g t}}^{\infty} q\left(h, t - \frac{D_2^2}{4\alpha_g\beta_2^2}\right)e^{-\beta_2^2}d\beta_2\right]dh \tag{7}$$

Equation (7) reduces to the steady line-source model of Ref. [17] under the special case of a constant heat strength, i.e., $q(h,t) = q(h)$. This comparison against an existing formulation provides a useful validation of the current transient formulation.

The annual variations of the ground surface temperature and the strength of the line heat source will be approximated by the following sinusoidal expressions:

$$\theta_{gs}(t) = \theta_m + A_\theta \sin(w_1 t + \phi_1) \tag{8}$$

$$q(h,t) = q_m + A_q \sin(w_2 t + \phi_2) \tag{9}$$

Using these sinusoidal variations, the following analytical form of the long-term temperature response in the ground is obtained:

$$\theta_{gp} = \theta_m \operatorname{erfc}\left(\frac{z}{2\sqrt{\alpha_g t}}\right) + A_\theta e^{-z\sqrt{w_1/2\alpha_g}} \sin\left[w_1 t - z\sqrt{\frac{w_1}{2\alpha_g}} + \phi_1\right] \tag{10}$$

$$\theta_{gl} = \frac{q_m}{4k_g\pi}\int_0^H \left[\frac{1}{D_1}\operatorname{erfc}\left(\frac{D_1}{2\sqrt{\alpha_g t}}\right) - \frac{1}{D_2}\operatorname{erfc}\left(\frac{D_2}{2\sqrt{\alpha_g t}}\right)\right] dh + \frac{A_q}{4\pi k_g}\int_0^H \left\{\left[\frac{e^{-D_1\sqrt{w_2/2\alpha_g}}}{D_1}\sin\left(w_2 t - D_1\sqrt{\frac{w_2}{2\alpha_g}} + \phi_2\right)\right] - \left[\frac{e^{-D_2\sqrt{w_2/2\alpha_g}}}{D_2}\sin\left(w_2 t - D_2\sqrt{\frac{w_2}{2\alpha_g}} + \phi_2\right)\right]\right\} dh \tag{11}$$

This approximate solution requires much less computational time than conventional methods of full numerical simulations with finite elements or differences. In the following section, an experimental study will be presented for this ground heat transfer problem.

3 Experimental Apparatus and Procedures

In the tower foundation problem, the domain is approximately a semi-infinite half-space, which is infinite in the lateral (r coordinate) direction and semi-infinite in the depth (z coordinate) direction. This paper will examine an equivalent "effective area" (or examined area) of heat transfer, expressed as $R_e \times Z_e$ in a two-dimensional system (depicted in Fig. 2). Two criteria will be used to determine the appropriate dimensions of the examined area. First, in order to determine the thermal response to the tower footing, the examined area must not be less than the "local area," within which the tower footing induces a significant temperature response. Second, in order to examine the seasonal variation of the ground temperature, the depth of the examined area must not be less than the "zero amplitude level" in the ground (shown in Fig. 1). For both criteria, a threshold temperature variation of 0.1°C will be used.

The local area around the buried rod was established in the following way. A maximum possible incoming heat flow was obtained from actual peak summer weather data (at the highest air temperature and solar heating) for a tower foundation in Northern Manitoba, Canada (Q_{in}=80 W, Ref. [18]). Substituting this incoming heat flow into the line heat source model, Eq. (3), gives the maximum temperature response (reached at a steady state) at any point in the ground. When r=6 m, the maximum temperature increase is less than 0.1°C. Beyond this radial distance, the temperature increases can be assumed negligible. Also, when z =12 m, the maximum temperature increase is less than 0.1°C. Beyond this depth, temperature increases can also be assumed negligible. This gives a local area of R_l=6 m and Z_l=12 m. For the second criterion, a far-field ground temperature model [22] was used for the Northern Manitoba site. The amplitude of temperature variations can be calculated as

$$T_A = 16.97e^{-0.576z} \tag{12}$$

At a depth of 11 m, the annual amplitude of the temperature variation is less than 0.1°C. Combining the calculated results for both criteria yields the following dimensions of the examined area: Z_e=12 m and R_e=6 m.

The dimensions of the experimental test cell were then obtained by scaling down the dimensions of the examined area and simplified tower footing (a metal rod with a diameter of 0.4 m and a buried depth of 4 m). The scaling factor was determined from a dimensional analysis of heat conduction in the ground, which yielded a temperature scale of 1:1, a length scale of 1:60, and a time scale of 1:3600. With this method, the experimental test cell was designed with the following dimensions: examined area of 200 mm in depth, 200 mm in diameter centered on a metal rod of 6.67 mm in diameter, and 66.67 mm buried in the half-space. The annual cycle of temperature variations in the foundation for 365 d/yr was then simulated in the test cell over a time of 146 min.

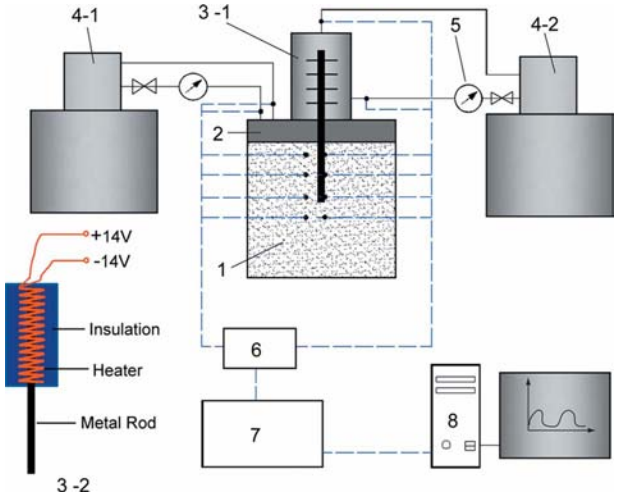

Fig. 4 Overview of the experimental system 1: container, 2: plate heat exchanger, 3-1: circular heat exchanger and metal rod, 3-2: electrical heater and metal rod, 4: Neslab temperature-controlled baths, 5: FTB603B flow sensors, 6: TAI module NI9211, 7: USB chassis for cDAQ-9172, 8: Computer and data logger program, ●: TCs

The test cell was constructed as a cubic enclosure with four side walls tangential to the outer surface of the scaled examined area. Figure 4 shows the experimental setup. The container is made with 2.54 cm thick Plexiglas and an inner volume of 200×200 ×200 mm^3 to simulate the examined area of the simplified tower foundation. Initially it was filled with dry wheat flour as the heat transfer medium to ensure only heat conduction in the container. An additional layer of a composite fabric was used for insulation purposes. A multipass plate heat exchanger, with temperature-controlled fluid circulating within it, was installed on the top of the enclosure to provide the desired top surface boundary conditions. The bottom plate of the heat exchanger was made from aluminum, while the cover was made of stainless steel. The inner surfaces of this heat exchanger were coated with a thin layer of epoxy for protection against corrosion. The plate heat exchanger was well enclosed by the walls of the container and the Plexiglas cover of 20 mm thickness.

A metal rod was then buried into the heat transfer medium to simulate the tower footing. It can be inserted into the container through a hole located at the center of the cover. In this study, two heat sources were designed for the metal rod, corresponding to the two heat input cases discussed in Sec. 2. First, an electrical heater was wrapped around a steel rod (part 3-2 in Fig. 4) to provide a steady input heat. A 15 mm thick layer of a carbon fiber sheet was used around the heater for thermal insulation. The second type was a circular heat exchanger designed together with an aluminum rod. A temperature-controlled fluid then circulates around the finned part of the rod inside the circular heat exchanger. This was designed to simulate the annual variation of the air temperature around the above-ground portion of a tower. The shell of this heat exchanger was made with Acrylonitrile butadiene styrene (ABS) for insulation purposes. The 3 mm thick ABS shell was wrapped with another layer of composite fabric of 8 mm thickness to provide additional thermal insulation.

The circulating fluids for both the plate and circular heat exchangers were supplied by Neslab RTE 140 heating/refrigerating baths. RTE 140 can provide a temperature range of −40°C to +150°C, with a stability of ±0.05°C. Constant or variable bath temperatures were realized by programming the baths through a

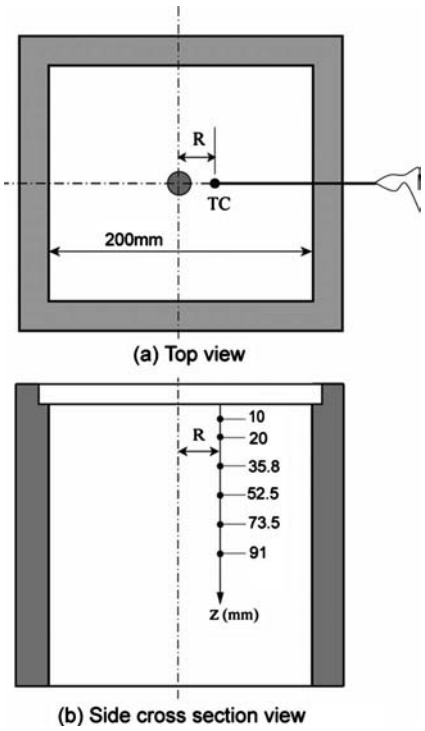

Fig. 5 Installation positions of the TCs

microcontroller. The circulating fluid in this study was water, and the flow rates of the circulating water were measured with the Omega FTB603B flow sensors.

The total mass of materials in the test cell was measured with a Starfrit electric scale. This mass was then divided by the total volume of the test cell to find the density. The thermal conductivity and diffusivity of the dry flour were measured with a Hukseflux TP01 thermal sensor. For temperature measurements in the test cell, 18 *T*-type thermocouple (TC) probes (SCPSS-G-062, from Omega) were inserted horizontally into the enclosure through three sides of the Plexiglas walls, with six TCs on each side. The radial distance, *R*, between the TCs and the metal rod was the same for each side, but it varied for different sides, as shown in Fig. 5 (depicting only one side).

A computer data acquisition system was used (see Fig. 6). The TCs were connected to six thermocouple analog input (TAI) modules [National Instrument (NI) 9211] with a differential connection mode. Each TAI module provided four channel inputs. The input modules were connected to a cDAQ-9172 (National Instrument) chassis, which has an eight-slot chassis designed for use with C series input/output (I/O) modules. I/O channels were accessible using the NI-DAQmx software. The data acquisition system allowed for a maximum sampling rate of 15 samples/s with a resolution of 24 bits.

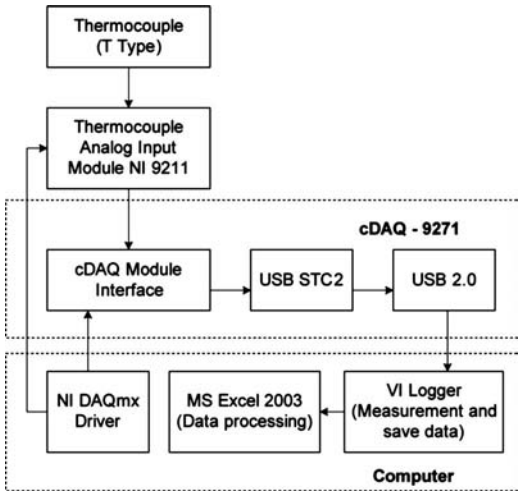

Fig. 6 Computer data acquisition system

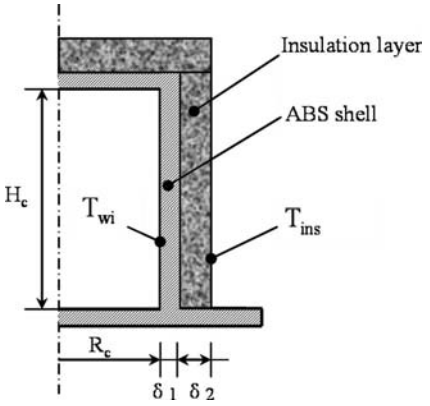

Fig. 7 Schematic of insulation for the circular heat exchanger and heat losses/gains

Three TCs were installed at the inlet of the circular heat exchanger and another three at the outlet to measure the mean controlled fluid temperatures, $T_{f_{\text{in}}}$ and $T_{f_{\text{out}}}$. The FTB603B flow sensor measured the flow rate, $\dot{V}_f$, of the circulating water. When the aluminum rod was buried into the enclosure, an energy balance for the heat exchanger revealed that the total heat dissipated to the enclosure equals the amount of heat transferred by the circulating water, which is calculated by

$$Q_{\text{inf}} = \rho_f \dot{V}_f c_f (T_{f_{\text{in}}} - T_{f_{\text{out}}}) \tag{13}$$

The density, ρ_f, and specific heat, c_f, of water depend on the average temperature through the heat exchanger, $T_f \approx 0.5(T_{f_{\text{in}}} + T_{f_{\text{out}}})$. To calculate the heat input most accurately, the dependence of the density and specific heat of the circulating water was fitted to second-order functions in the temperature range of the experiments: $\rho_f = (-0.0051T_f^2 + 0.0123T_f + 999.93)$ kg/m^3 and $c_f = (0.0286T_f^2 - 2.0873T_f + 4214)$ J/kg °C, in the range of 0.01–50 °C. Also, the electrical heat source provided a steady heat input as follows:

$$Q_{\text{in}e} = \frac{U_e^2}{R_{\text{el}}} \tag{14}$$

where U_e is the voltage provided to the heater and R_{el} is the resistance of the heater. These two parameters were measured with an Omega HHM93 multimeter. It should be noted that the actual heat input to the enclosure is different than the amounts calculated from Eqs. (13) and (14) since heat losses/gains from the experiment are inevitable, although as much effort as possible was taken to minimize these losses. The heat losses/gains were estimated in the following way. Taking the circular heat exchanger as an example, the inner surface temperature of the ABS shell, T_{w_i}, and the outer surface temperature of the fabric insulation layer, T_{ins}, were both monitored (see Fig. 7). By assuming a quasisteady heat conduction through a two-layered cylinder, the heat loss/gain was estimated as [23]

Table 1 Summary of the measurement uncertainties

Parameter	Uncertainty
Temperature, T	$\pm 1.3\,^{\circ}$C
TC positions: radial distance, R vertical distance, z	± 1.2 mm
Diameter of the metal rod, R_b	± 0.5 mm
Thickness of insulation sheets, σ	± 0.7 mm
Buried length of the metal rods, H_b	± 1.1 mm
Density of flour, ρ_{flr}	$\pm 2.37\%$
Conductivity of flour, k_{flr}	$\pm 5\%$
Diffusivity of flour, α_{flr}	$\pm 20\%$
Specific heat of circulating fluid, c_f	$\pm 0.5\%$
Density of circulating fluid, ρ_f	$\pm 0.5\%$
Flow rate of circulating fluid, $\dot{V}_f$	$\pm 1\%$
Circular heat exchanger heat input, Q_{inf}	$\pm 28.3\%$
Voltage of electric heater, U_e	± 0.09 V
Electrical resistance of heater, R_{el}	$\pm 1.5\ \Omega$
Electrical heater power, Q_{ine}	0.03 W

$$\dot{Q}_{\text{loss}} = \pi R_c^2 \frac{T_{w_i} - T_{\text{ins}}}{\dfrac{\delta_1}{k_{\text{ABS}}} + \dfrac{\delta_2}{k_{\text{ins}}}} + 2\pi H_c \frac{T_{w_i} - T_{\text{ins}}}{\dfrac{\ln[(R_c+\delta_1)/R_c]}{k_{\text{ABS}}} + \dfrac{\ln[(R_c+\delta_1+\delta_2)/(R_c+\delta_1)]}{k_{\text{ins}}}} \tag{15}$$

The ABS shell and the composite fabric insulation layer have similar thermal conductivity values, and therefore the thermal bridge effect was neglected in the calculation. A similar method was used to estimate heat losses from the electrical heater.

Efforts were taken to minimize experimental errors and uncertainties as much as possible. *T*-type TC wires were used to connect the inserted TC probes and the input modules. These wires were made as short as possible to reduce the uncertainty in the measured temperature, which was the most important parameter in this study. A detailed uncertainty analysis was conducted by the method of Kline and McClintock [24], and the results are summarized in Table 1. The uncertainty of the measured temperature includes the cold-junction compensation sensor accuracy, errors caused by the NI9211 modules (including gain errors, offset errors, differential and integral nonlinearities, noise errors, and isothermal errors), as well as the accuracy of the TC probe itself. These uncertainty components were combined by the root-sum-square method, as outlined by Kline and McClintock [24]. Time was recorded in the VI logger by the CPU time for transient temperature and flow rate measurements. The precision limit was assumed to be negligible. A bias limit came from the inaccuracy of defining the starting time of the heat transfer process, which lies in the range of 5 s. Uncertainties in the dimensions of the test cell involved errors caused by both the manufacturer and the imperfect insulation of the metal rod along the centerline of the enclosure. The results of the uncertainty analysis are summarized in Table 1. In the next section, results from the analytical and experimental studies will be presented.

4 Results and Discussion

The previous analysis and experiments will be used to examine the temperature variations around a simplified tower foundation under different operating conditions. The ground test material has the following properties: density of $\rho_{\text{flr}}=780$ kg/m^3, thermal conductivity of $k_{\text{flr}}=0.24$ W/m K, and thermal diffusivity of $\alpha_{\text{flr}}=1.6\times10^{-7}$ m^2/s. Before each experiment, the test cell was left unused for more than 12 h to set a uniform initial temperature. This was confirmed by measuring temperatures at various positions within the enclosure.

4.1 Model Validation for 1D Transient Heat Conduction. In order to validate the experimental setup, 1D heat conduction problems were first considered and measurements were compared to the analytical solutions. Without any heat source, the test cell only has a plate heat exchanger at the top boundary. The temperature bath is heated to 50°C before the valve is opened to provide a circulating liquid to the plate heat exchanger. Careful measurements of the inlet and outlet temperatures of the plate heat exchanger showed that the actual temperature of the circulating fluid is 49°C, forming the top boundary of the 1D heat conduction problem. The analytical solution for the temperature in the enclosure is

$$T_g(z,t) - T_i = \text{erfc}\left(\frac{z}{2\sqrt{\alpha_{\text{flr}}t}}\right)(T_s - T_i) \tag{16}$$

where T_i is the initial temperature, 22.1°C, and T_s is the top boundary temperature, 49°C.

The second validation case involves a sinusoidal surface temperature at the top surface, wherein the circulating fluid temperature is controlled in the following manner:

$$T_f = T_i + 16\sin\left(\frac{2\pi t}{P} + \frac{2\pi}{3} - 2\right) \tag{17}$$

where the cyclic period, P, of the temperature variation of the controlling fluid is 146 min in this study. This leads to a top boundary temperature of $\theta_s(t)=16\sin(2\pi t/P+2\pi/3-2)$, and the thermal response in the test cell can be predicted by the model in Eq. (10).

Figure 8(*a*) shows the results for the measured temperatures (T_g) from all TC probes after 60 min, compared to the analytical solution. A good agreement between analytical and measured data can be observed. These results suggest a one dimensionality of the measurements since measured results from all positions lie on the analytical solution curve. Also, the results suggest that the enclosure can be regarded as semi-infinite since there is almost no temperature increase further than the depth of 90 mm (less than half of the total depth of the enclosure). A similarly good agreement was also obtained for the sinusoidal surface temperature case, shown in Fig. 8(*b*). The results show the decrease in temperature variation amplitude with depth in the ground. It will be shown that these temperature variations will be influenced by thermal effects of a buried tower footing (forthcoming results in the following subsections).

4.2 Thermal Response to a Steady Heat Input. The metal rod with an electrical heater was inserted into the enclosure to study temperature responses to a steady heat input to the tower foundation. The heat generated by the heater is conducted downward through the metal rod. In the meantime, heat is conducted from the rod to the surrounding medium, thereby leading to a thermal response. The top boundary of the enclosure is maintained at a constant temperature of 20.6°C, which is the same as the initial temperature of the material in the enclosure. The voltage for the heater is measured to be 14 V, and the electrical resistance of the heater is 121 Ω. These parameters lead to a heating power of 1.62 W through Eq. (14), with 30% of the heat loss through the carbon fiber insulation, estimated by Eq. (15). This leads to the actual heat input to the buried rod of $Q_{\text{in}}=1.13$ W.

Figure 9 shows the measured temperature variations in the test cell as a response to the buried metal rod. It can be observed from Fig. 9(*a*) that the medium temperature increases continuously with time, but the slope of the temperature curve decreases. At the same depth, the thermal response is higher for positions closer to the line heat source. This difference increases with time. Figure 9(*b*) shows the vertical variations in the thermal response. Since

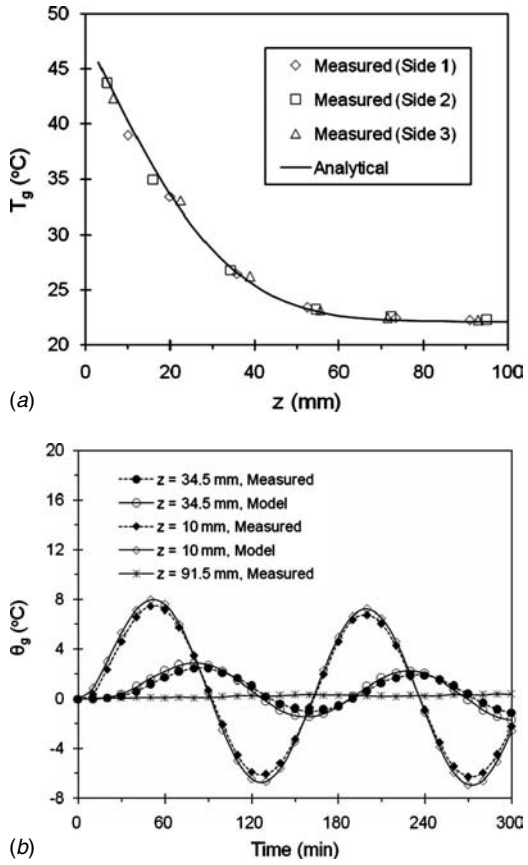

Fig. 8 Measured and analytical results for a one-dimensional transient heat conduction

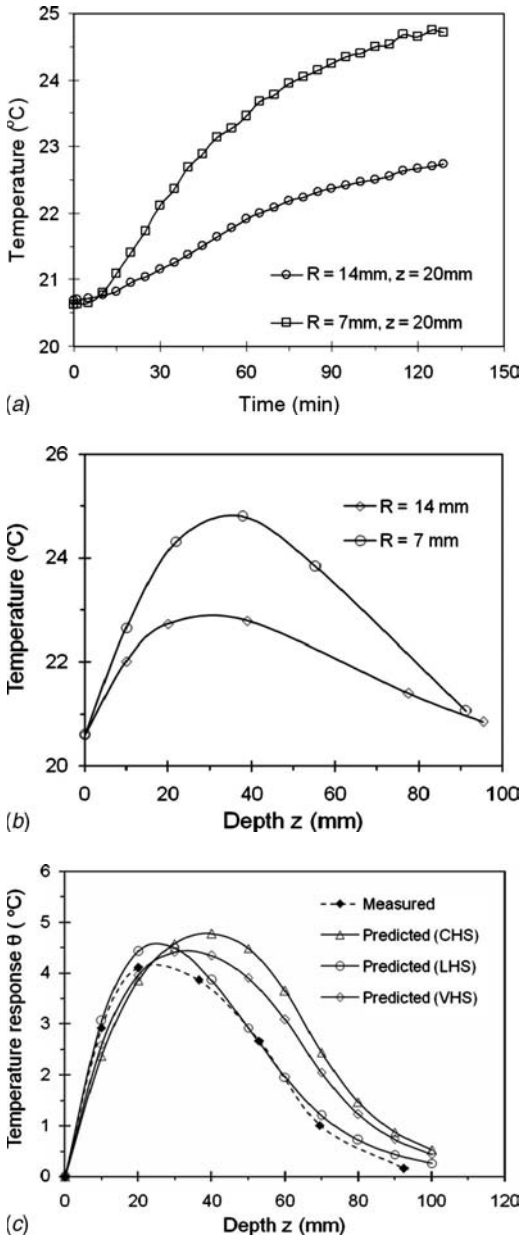

Fig. 9 Measured temperatures with a steady line heat source: (*a*) thermal response at two locations, (*b*) 127.5 min after the heater is turned on, and (*c*) comparison with the model

the top boundary is maintained at the initial temperature, the temperature response increases from zero to a peak amplitude at a certain depth (a different depth for varying radial distances from the rod), then it drops to zero at another depth. These results confirm that the thermal response to the tower footing only exists within a limited space around it.

The predictive model from Sec. 2 is used for the present conditions. Figure 9(*c*) shows a comparison between measured and predicted thermal responses. Three different line heat source models were used: (1) constant/uniform heating strength (CHS) model, (2) linear distribution of heating strength (LHS), and (3) the VHS, as expressed in Eq. (2). All of the models give reasonable predictions with Eq. (3). The LHS model gives the best prediction, while the CHS model shows the lowest accuracy for a varying line heat source. This occurs because the CHS model assumes a constant heating strength, while actually it decreases along the length of the rod.

4.3 Thermal Response to Sinusoidal Temperature Variations. In this section, the circular heat exchanger is fitted, with the aluminum rod buried in the enclosure, in order to approximate a tower footing. Both the circular heat exchanger and the plate heat exchanger have temperature-controlled circulating fluids with a sinusoidal temperature variation expressed in Eq. (17) to simulate the seasonal temperature variation of air around a power transmission tower. The initial temperature, T_i, is 23 °C. Using Eq. (13), the input heat from the circular heat exchanger was measured, and the results are shown in Fig. 10. It can be observed that the heating rate fluctuates, but it forms a general sinusoidal trend. Comparing the mean temperature of the circulating water through the circular heat exchanger and the sinusoidal fitting of the input heat rate, one can find a "phase lag" between the two variations, which is about 30.5 min for this experiment. It was expected that the thermal effects of the tower footing would be highest in the warmest summer days. However this study indicates a phase lag as heat conduction through the tower to the foundation reaches a maximum positive value, sometime earlier than the time when the highest air temperature is reached in the summer.

The heat losses/gains from the circular heat exchanger to the ambient air are estimated by the method discussed in Sec. 3 (Eq. (15)). Temperatures at the outer surface of the insulation layer and inner wall of the ABS shell are measured and shown in Fig. 11. They are fitted to sinusoidal functions as follows: $T_{\text{ins}}(t)=24.3+5\sin(2\pi t/146+2\pi/3-2.25)$ and $T_{w_i}(t)=23.5+13\sin(2\pi t/146+2\pi/3-2.25)$. The thermal conductivity of the ABS shell and the composite fabric insulation layer are $k_{\text{ABS}}=0.19$ W/m K and $k_{\text{ins}}=0.16$ W/m K, respectively. Using these parameters in Eq. (15) leads to a resulting heat loss/gain of $Q_{\text{loss}}=-1.5+14\sin(2\pi t/146+0.18)$. It was found that variations in amplitude of this

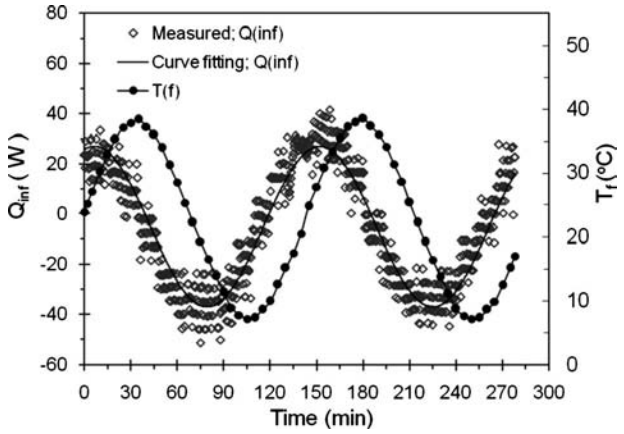

Fig. 10 Measured temperature variations of circulating water through the heat exchangers and heat input to the circular heat exchanger (note: *T*(*f*) and *Q*(inf) refer to T_f and Q_{inf})

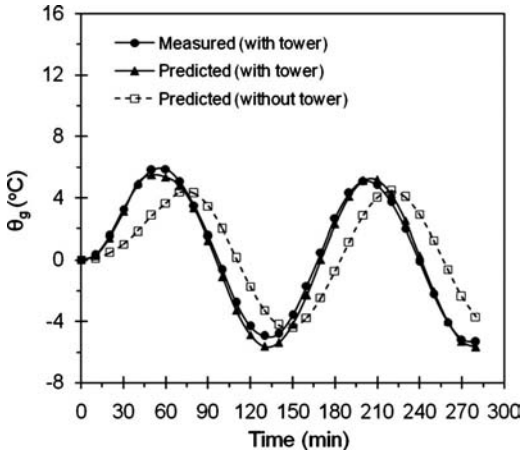

Fig. 12 Comparison between predicted and measured temperatures at a point in the test cell

heat loss/gain were approximately 50% of the total heat input through the circular heat exchanger. The combined values of the measured Q_{inf} and Q_{loss}, along with other parameters of the test cell, were placed into the extended VHS model discussed in Sec. 2 (a uniform distribution of heat strength was assumed) to predict the temperature response in the simplified foundation. Figure 12 shows the temperature response at a point of $R=6$ mm and $z=20$ mm in the test cell within the first two cycles (292 min). The measured thermal responses were obtained by subtracting the measured temperatures in the test cell by the initial temperature. The predicted results compare well with the measured data.

The thermal effects of the tower can be observed by comparing the temperature responses with or without the tower. The results in Fig. 12 indicate that during each "summer" period, the tower footing introduces an additional positive temperature response, making the foundation material near the tower footing warmer. In the "winter" period, the tower footing causes an additional negative temperature response, making the local space cooler. With this thermal effect, the amplitude of "seasonal" temperature variations at locations near the tower footing becomes larger than those far away from it. This effect of the tower footing also makes the phase lag of temperature variation decrease, wherein the surrounding soil becomes warm earlier in summer and cold earlier in winter.

Figure 13 shows the measured temperature responses at several locations in the container at two typical times, $t=212$ min and $t=280$ min, which approximately correspond to a particular time in winter and another time in summer. It can be observed that a significant temperature response exists only up to a certain depth within the semi-infinite medium, around 90 mm in the enclosure. Figure 13 also shows the thermal effects of the tower footing in an alternative way. At $t=212$ min (early winter), there is an additional cooling effect, making the surrounding medium colder. At $t=280$ min (early summer), it makes the surrounding medium warmer. Further analysis shows that the thermal effect caused by the tower footing is not uniform within the foundation. It varies not only with time, but also at different positions around the tower footing. At the same radial distance from the heat source, the response starts from zero at the surface and increases to a maximum level at a certain depth (about 42 mm for the current example). Then it decreases to zero at another depth beyond the buried depth of the tower footing. Comparing the results of $R=7$ mm and those of $R=14$ mm, one can find that the effect of the line heat source increases at locations closer to the line source (as expected).

The seasonal thermal effects of the tower footing on the temperature variations in the foundation are caused by variations in air temperature and the difference between the thermal properties of the metal tower and the foundation. For example, a transmis-

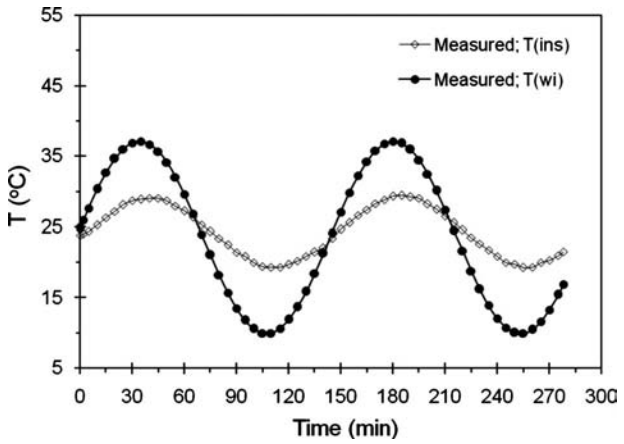

Fig. 11 Measured temperature variations at the inner wall of the circular heat exchanger and outer surface of the insulation layer (note: *T*(ins) and *T*(wi) refer to T_{ins} and T_{w_i})

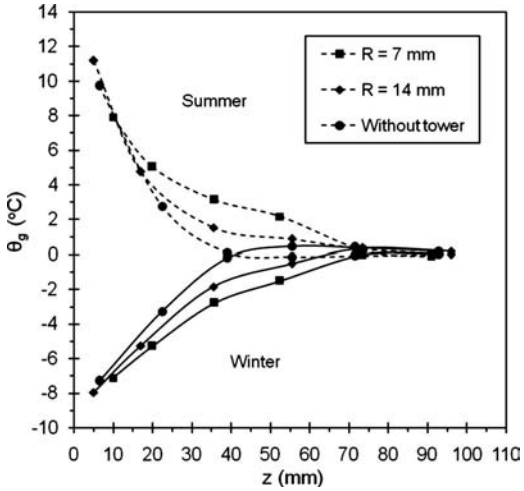

Fig. 13 Temperature response in summer (*t*=280 min; curves with dashed lines) and winter (*t*=212 min; curves with solid lines) at different positions around the buried rod

sion tower made from carbon steel (plain carbon, Mn$\leqslant$1%, Si $\leqslant$0.1%) has a thermal conductivity around 60 W/m K and a thermal diffusivity around 1.8×10^{-5} m^2/s. However, the thermal conductivity of typical dry soil is 1.0 W/m K (2.0 for wet soil) and the thermal diffusivity is about 0.35×10^{-6} m^2/s (0.48×10^{-6} m^2/s for wet soil). So the metal tower has a much higher thermal conductivity and diffusivity than soil in the tower foundation. In summer, the air temperature is usually higher than the ground temperature and heat is conducted through the tower downward into the ground. This leads to an additional temperature increase of the surrounding soil. In the winter, the air temperature is usually colder than the ground temperature, thereby causing heat flow from the ground to the surrounding air. This seasonal thermal effect enhances the possibility of ground thawing in summer and freezing in winter if the tower foundation lies in permafrost regions. These results provide important new insights for the design and construction of power transmission line towers and other structures in northern climates, such as northern regions of Canada.

5 Conclusions

In this paper, analytical and experimental studies were conducted for transient heat conduction from a line heat source to a semi-infinite half-space (representing a tower footing buried in the ground). Temperature and heat transfer measurements were collected from the experimental test cell over a range of operating conditions. The experimental data were analyzed for steady and sinusoidal heat inputs, with heat sources provided by an electrical heater and circulating fluids through a circular heat exchanger. The measured temperature responses were successfully compared against results from analytical models. This study has found that a buried metal tower footing introduces additional temperature increases in summer and temperature decreases in winter. The thermal response varies cyclically and also spatially at different positions throughout the medium. These results provide valuable new insights for the design, maintenance, and development of new foundations of power transmission line towers and other structures in northern regions.

Acknowledgment

Support of this research from Manitoba Hydro, the Natural Sciences and Research Council of Canada (NSERC), and a University of Manitoba Graduate Fellowship (X.D.) is gratefully acknowledged.

Nomenclature

A = amplitude
c = specific heat (J/kg °C)
D = distance, diameter (m or mm)
H = height (m or mm)
k = thermal conductivity (W/m °C)
L = length (m or mm)
P = cyclic period (or min.)
q = heating strength (W/m)
Q = heat flow rate (W)
r = radial coordinate (m or mm)
R = radius (m or mm)
R_{el} = electric resistance (Ω)
T = temperature (°C)
t = time (s or min)
U = voltage (V)
$\dot{V}_f$ = volumetric flow rate (lpm or m^3/s)
w = frequency
z = vertical coordinate (m or mm)

Greek

α = thermal diffusivity (m^2/s)
β = integration variable
ρ = density (kg/m^3)
θ = temperature response or difference (°C)
δ = thickness (mm)
ϕ = phase lag

Subscripts

b = buried metal rod or tower footing
c = circular heat exchanger
f = circulating fluid (water)
flr = flour
g = ground
gp = plane doublet heat source
gl = line heat source
i = initial condition
ins = insulation
in = input
m = mean
s = surface
w_i = inner wall

References

[1] Lunardini, V. J., 1981, *Heat Transfer in Cold Climates*, Van Nostrand Reinhold, New York.
[2] U.S. Arctic Research Commission Permafrost Task Force 2003, "Climate Change, Permafrost, and Impacts on Civil Infrastructure," U.S. Arctic Research Commission, Special Report No. 01-03.
[3] Staudzs, A., 1982, "Frost and Permafrost: Effects and Remedial Work on Transmission Tower Foundations," Manitoba Hydro, report, Winnipeg, Manitoba, Canada.
[4] Sivanbaev, V., 1971, "Thawing of Permafrost Under a High Temperature Heat Source," Soil Mech. Found. Eng. (Engl. Transl.), **8**(1), pp. 50–53.
[5] Khrustalev, L. N., Pustovoit, G. P., and Emel'yanova, L. V., 1994, "Prediction of Permafrost Temperature in Bed of Structure From Field Data," Soil Mech. Found. Eng. (Engl. Transl.), **31**(6), pp. 200–204.
[6] Khrustalev, L. N. and Shumilishskii, M. V., 1997, "Consideration of Temperature Variation in Determining the Bearing Capacity of Permafrost Beds," Soil Mech. Found. Eng. (Engl. Transl.), **34**(5), pp. 167–169.
[7] Eckert, E. R. G., and Drake, R. M., Jr., 1972, *Analysis of Heat and Mass Transfer*, McGraw-Hill, New York.
[8] Anteby, I., and Shai, I., 1993, "Modified Conduction Shape Factors for Isothermal Bodies Embedded in a Semi-Infinite Medium," Numer. Heat Transfer, Part A, **23**(2), pp. 233–245.
[9] Deng, Y., Fedler, C. B., 1992 "Multi-Layered Soil Effects on Vertical Ground-Coupled Heat Pump Design," Trans. ASAE, **35**(2), pp. 687–694.
[10] Yavuzturk, C., and Spitler, J. D., 1999, "A Short Time Step Response Factor Model for Vertical Ground Loop Heat Exchangers," ASHRAE Trans., **105**(2), pp. 475–485.
[11] Bi, Y., Chen, L., and Wu, C., 2002, "Ground Heat Exchanger Temperature Distribution Analysis and Experimental Verification," Appl. Therm. Eng., **22**(2), pp. 183–189.
[12] Lund, P. D., and Ostman, M. B., 1985, "A Numerical Model for Seasonal Storage of Solar Heat in the Ground by Vertical Pipes," Sol. Energy, **34**(4), pp. 351–366.
[13] Breger, D. S., Hubbell, J. E., El Hasnaoui, H., and Sunderland, J. E., 1996, "Thermal Energy Storage in the Ground: Comparative Analysis of Heat Transfer Modeling Using U-Tubes and Boreholes," Sol. Energy, **56**(6), pp. 493–503.
[14] Carslaw, H. S., and Jaeger, J. C., 1993, *Conduction of Heat in Solids*, 2nd ed., Oxford University Press, New York.
[15] Ingersoll, L. R., Zobe, O. J., and Ingersoll, A. C., 1954, *Heat Conduction With Engineering, Geological and Other Applications*, rev. ed., University of Wisconsin Press, Madison.
[16] Hart, D. P., and Couvillion, R., 1986, *Earth-Coupled Heat Transfer*, National Water Well Association, Dublin, OH.
[17] Zeng, H. Y., Diao, N. R., and Fang, Z. H., 2002, "A Finite Line-Source Model for Boreholes in Geothermal Heat Exchangers," Heat Transfer Asian Res., **31**(7), pp. 558–567.
[18] Duan, X., Naterer, G. F., Lu, M., and Mueller, W., 2007, "Transient Heat Conduction from a Vertical Rod Buried in a Semi-Infinite Medium With Variable Heating Strength," Heat Mass Transfer, **43**(6), pp. 547–557.

[19] Duan, X., and Naterer, G. F., 2007, "Temperature Response to the Time-Varying Strength of a Line Heat Source in a Half-Space," AIAA Paper No. 2007-3898.
[20] Permafrost, Natural Resource of Canada (http://gsc.nrcan.gc.ca/permafrost/whatis_e.php).
[21] Hammer, T. A., Ryan, W. L., and Zirjacks, W. L., 1985, "Ground Temperature Observations," *Thermal Design Considerations in Frozen Ground Engineering*, T. G. Krzewinski and R. G. Tart, Jr., eds., ASCE, Reston, VA.
[22] Duan, X., and Naterer, G. F., 2007, "Ground Temperature Estimation With an Energy Balance Method," 21st Canadian Congress of Applied Mechanics, Toronto, Ontario, June 3–7.
[23] Incropera, F. P., Dewitt, D. P., Bergman, T. L., and Lavine, A. S., 2007, *Introduction to Heat Transfer*, 5th ed., Wiley, Hoboken, NJ, pp. 100–118.
[24] Kline, S. J., and McClintock, F. A., 1953, "Describing Uncertainties in Single Sample Experiments," Mech. Eng. (Am. Soc. Mech. Eng.), **75**, pp. 3–8.

The Thickness of the Liquid Microlayer Between a Sliding Bubble and a Heated Wall: Comparison of Models to Experimental Data

D. Keith Hollingsworth

Xin Li

Larry C. Witte

Department of Mechanical Engineering,
University of Houston,
Houston, TX 77204-4006

Sliding vapor bubbles are known to create high heat transfer coefficients along the surfaces against which they slide. The details of this process remain unclear and depend, in part, on the evolution of the liquid microlayer that forms between the bubble and the surface, as the bubble grows by evaporation. A mechanistic model of the microlayer thickness verified by direct observation of the microlayer thickness is needed. This paper describes a comparison of measurements from a recent set of experiments to the results of microlayer models from literature and to the predictions of a new model presented here for the first time. The measurements were produced by a laser-based method developed to measure the thickness of the liquid microlayer between a cap-shaped sliding bubble and an inclined heated wall. Microlayer thicknesses of 22–55 μm were obtained for saturated FC-87 and a uniform-temperature surface inclined at 2–15 deg from the horizontal. The basis of each model, input requirements, limitations, and performance relative to this data set is discussed. A correlation is developed based on the structure of the lubrication theory. It collects the measured microlayer thickness presented as a microlayer Reynolds number to within $\pm$10%. This correlation depends only on bubble volume, inclination, and a bubble shape factor, all of which can be determined experimentally to within reasonable accuracy. [DOI: 10.1115/1.2957485]

Keywords: bubbles, microlayers, enhancement

1 Introduction

There are many convective situations where bubbles, once nucleated at an upstream position, will slide downstream along a heated surface. Cornwell and Schüller [1] found that sliding bubbles can sustain high local heat transfer rates in two-phase shell-and-tube heat exchangers. They observed that with all the tubes in an industrial heat exchanger at the same heat flux, the upstream tubes were in nucleate flow-boiling while no bubbles were nucleated on the downstream tubes. Cornwell and Schüller postulated that the high flux on the downstream tubes was sustained by bubbles that nucleated on the upstream tubes and slid around the downstream tubes. This kindled an interest in the mechanisms by which sliding bubbles remove heat from the surfaces against which they move.

A companion paper, Li et al. [2], provides a more detailed review of the past work on sliding bubbles. Three candidate mechanisms for sustaining the observed heat flux have been established: As the bubble moves, (1) it displaces liquid in its path so that a local enhancement in convection around the bubble can occur; (2) a thin liquid microlayer between the bubble and the surface evaporates and is continually replenished by liquid trapped under the upstream edge of the bubble; and (3) the bubble induces substantial mixing in its wake, and there is an attendant, and sustained increase in surface heat flux behind the bubble.

Li et al. [2] reported direct measurements of microlayer thickness, $\delta(x)$, adjacent to sliding bubbles. They compared those measurements with the results of various predictive models. Figure 1 is a sketch of the geometry of the cap-shaped sliding bubbles discussed here, based on high-speed images from Refs. [2,3] of typical bubbles shown as image collages in plan view in Fig. 2 (at 2 deg inclination) and side view in Fig. 3 (at 10 deg inclination). Figure 1(*a*) can be thought of as a slice along the centerline of the bubble, as seen in the plan view in Fig. 2. The velocity field $u(x,y)$ within the microlayer with thickness $\delta(x)$ is drawn in the reference frame of the bubble. With these images as a guide, the experiments of Li et al. will be briefly introduced. Then, past attempts to model the liquid microlayer will be described and each model will exercised with respect to the data of Li. Finally, a new model will be introduced and evaluated against the data.

1.1 Direct Measurement of Microlayer Thickness.

A brief description of the apparatus used by Li [3] for the direct measurement of liquid microlayer thickness is presented here as a framework for the modeling investigation. A more detailed description of the apparatus, calibration procedures, and basic results is given in Refs. [2,3]. A chamber containing FC-87 could be rotated around a pivot, which allowed the test surface at the top to be positioned at different angles to the horizontal. Glass windows allowed optical access to the test surface.

The test surface was a 9.5 mm thick, 254×174 mm^2 aluminum plate heated by microfoil heaters. A fiber-optic microlayer thickness probe was mounted in the center of the test plate. Two optical fibers were glued side by side in a 1.7 mm diameter glass tube. The single-receiving-fiber design used here was selected over designs using multiple receiving fibers based on the simulations of Yu and Tso [4] who suggest that a smaller minimum δ can be resolved with the monofiber design.

Digital images at 1000 frames/s were acquired with an IDT

Contributed by the Heat Transfer Division of ASME for publication in the JOURNAL OF HEAT TRANSFER. Manuscript received August 21, 2007; final manuscript received February 12, 2008; published online September 3, 2008. Review conducted by Raj M. Manglik.

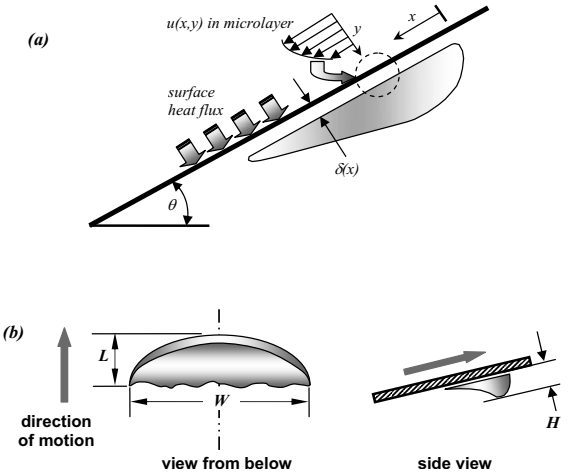

Fig. 1 (*a*) Sketch of the bubble geometry. The velocity distribution in the microlayer is shown in the reference frame of the bubble. (*b*) Definitions of bubble width (*W*), length (*L*), and height (*H*).

X-Stream VISION XS-4 monochrome complementary metal oxide semiconductor (CMOS) camera. Both side and plan views of the sliding bubble could be captured simultaneously by the camera system. These image sequences allow measurements of bubble size, speed, and acceleration, but they do not resolve the microlayer itself. Figures 2 and 3 show example images.

Typical measurements are shown in Fig. 4 for runs at 2 deg and 15 deg of surface inclination. The complete data set, when graphed against the bubble length, is shown in Fig. 5. The uncertainty bars shown give ± 2 standard deviations for the data for each bubble. Bubble-averaged microlayer thickness for these cap-shaped bubbles in FC-87 ranged from 25 μm to 48 μm and decreased with increasing inclination angle. Details of several runs are given in Table 1.

2 Previous Analytical Models

The literature reveals few attempts at modeling this phenomenon. One approach is to infer a microlayer thickness that is required to match the thermal history caused by bubble passage, see Cornwell and Schüller [1], Kenning et al. [5], and Bayazit et al. [6,7]. Another approach, taken by Addlesee and Cornwell [8] and Addlesee and Kew [9], is based on the fluid mechanics of the interaction between the bubble, the surrounding fluid, and the wall. Some of the models will be revisited here as we compare their results to the direct measurements of Li et al. [2,3], and modifications to these models will be explored where appropriate.

2.1 Models Based on Thermal Measurements. Cornwell and Shüller [1] performed an analysis to find the δ adjacent to a growing bubble sliding up a vertical surface at constant velocity. They assumed that a bubble grows because of evaporation of the microlayer only. This assumption ignores the transient cooling of the surface, vapor condensation at the outer surface of the bubble, and sensible heat content of the layer. They assumed dry-out of the microlayer over a portion of the bubble length, that the temperature distribution across the microlayer is linear, and that the effects of bubble pressure on T_{sat} and local surface cooling on T_w could be ignored. They found the resulting δ to be 3–6 μm for water vapor bubbles sliding on a vertical surface. This is one to two orders of magnitude smaller than the measurements and other predictions discussed here for surfaces inclined much closer to the

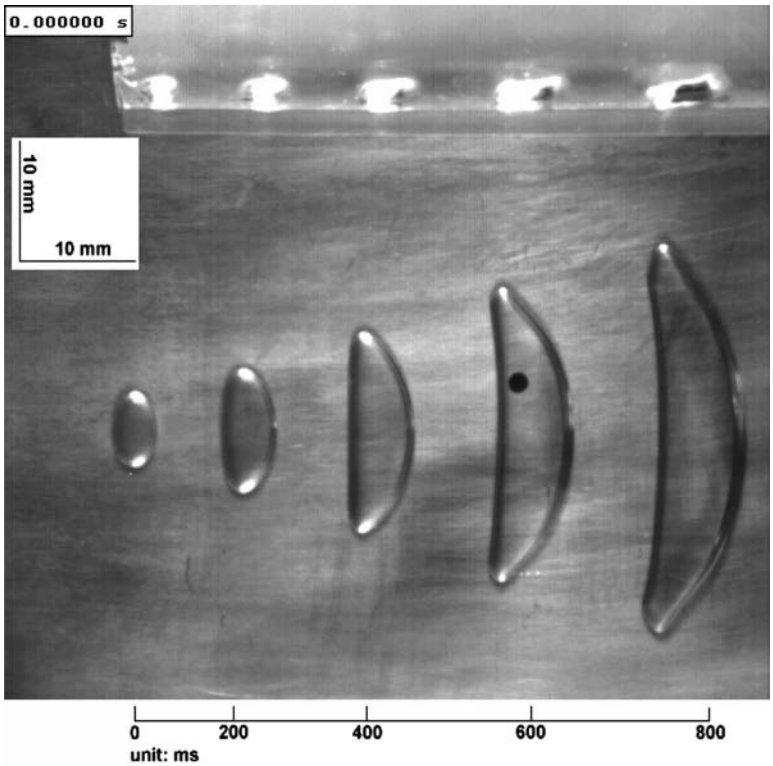

Fig. 2 A collage of images of a single bubble moving from left to right under a heated wall inclined at 2 deg. The black spot is the fiber-optic film thickness probe. Side views of the bubbles are shown at the top of the figure. The scale at the bottom shows time measured from the first image on the left.

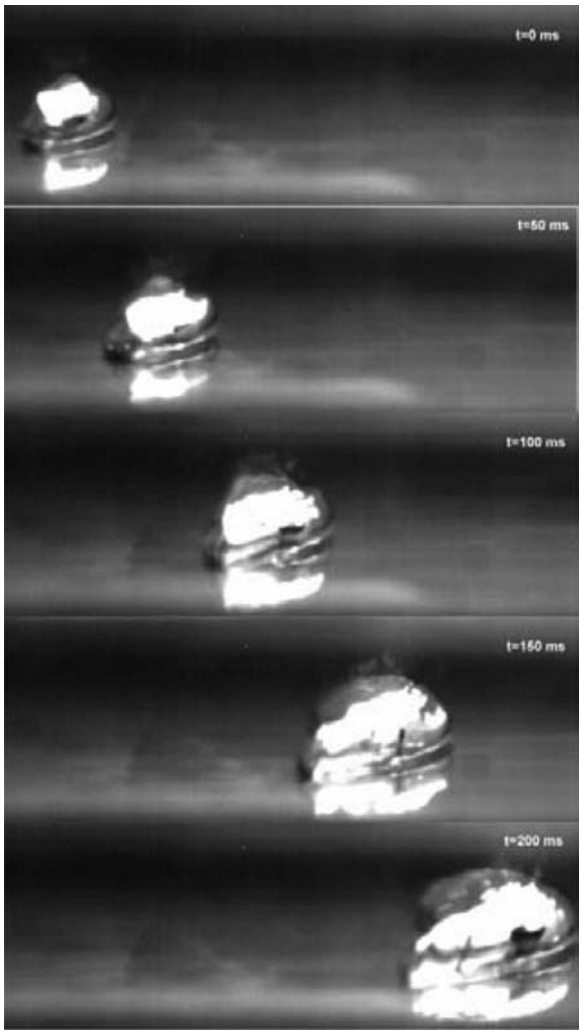

Fig. 3 Side view of a sliding bubble undergoing transition from a small to a large cap-shaped bubble at 10 deg inclination. Bubble motion is left to right. Picture is inverted: The heated surface is at the bottom of the frames.

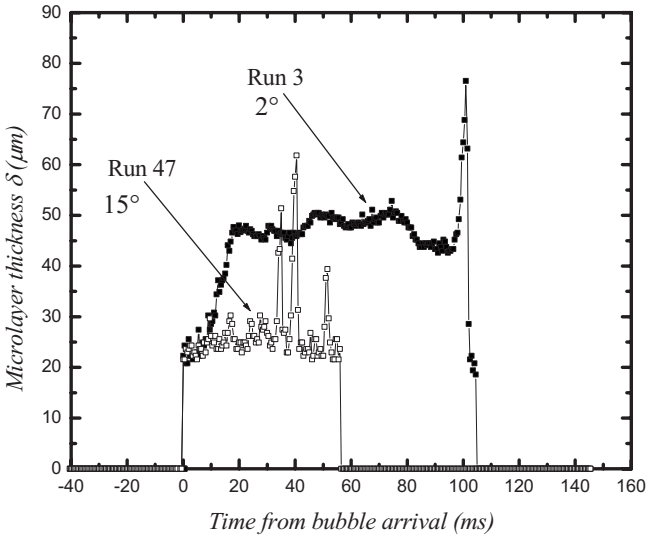

Fig. 4 Example traces of microlayer thickness for bubbles at inclinations of 2 deg and 15 deg

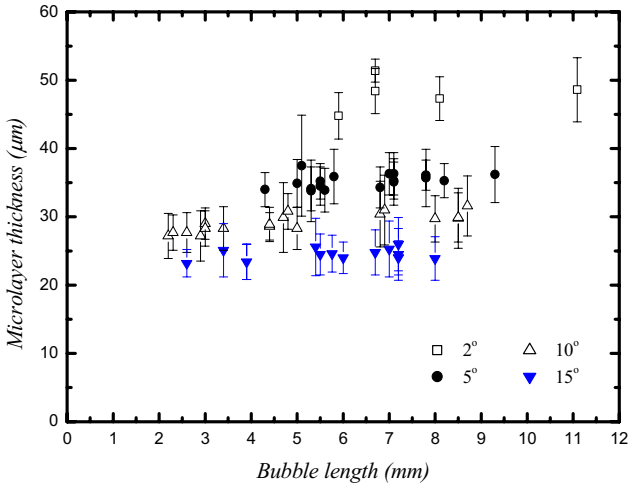

Fig. 5 Microlayer thickness versus bubble length from Li et al. [2,3]

horizontal.

Bayazit et al. [6,7] developed a numerical model to analyze the heat transfer through the microlayer above a sliding vapor bubble based on thermochromic liquid crystal images. The flow in the microlayer was assumed to a steady two-dimensional Couette flow with a no-slip condition at the bubble surface. In this model, the wall heat flux has two sources: that which results from the uniform electrical generation in the heater foil and the local depletion of the foil's internal energy. Bayazit showed that the release of energy stored within the foil dominates the wall heat flux: It is roughly five times the steady generation flux over most of the bubble's length. δ is not predicted directly by this method. Rather, a δ must be selected that matches the temperature distribution in the heated foil above the bubble.

Bayazit applied his solution to two FC-87 bubbles, one a smaller bubble with a passage time of 280 ms, and the other a larger bubble with a passage time of 420 ms. This technique yielded $\delta=40\pm5$ μm for the smaller bubble and $\delta=50\pm5$ μm for the larger bubble, which compares reasonably well to Li's direct measurements for FC-87 bubbles, as shown in Table 1.

Kenning et al. [5] used thermochromic liquid crystals to study a sliding vapor bubble at 15 deg inclination using water. They modeled the heat transfer by transient conduction through a stationary δ in contact with the heater. The thermal capacity of the wall was accounted for, as well as heat generated in the wall. δ was selected to create a best match between the computed and measured wall temperature distributions. Their calculated values are approximately half of those predicted by the correlation based on bubble velocity and height given by Addlesee and Cornwell [8].

2.2 Models Based on Fluid Dynamics. Addlesee and Kew [9] treated the bubble as a hemisphere sliding against the wall. The geometry is shown in Fig. 1 except that the bubble shape is assumed to be hemispherical and unchanging. They assumed that the bubble is fixed and the wall moves downward at u_{wall}, equal and opposite to u_{bubble}. The liquid motion ahead of the bubble is treated as a potential flow except for a thin laminar boundary layer on the wall. The mass flow in this boundary layer becomes the liquid microlayer above the bubble. The problem is analogous to liquid films flowing down inclined surfaces, and their analysis follows closely the work on falling films by Cerro and Whitaker [10] and Anderson [11].

The boundary layer in front of the bubble is driven by a freestream velocity that was obtained on a plane of symmetry in the flow past a sphere of radius r_h in a uniform stream at u_{bubble}. The integral momentum equation for a two-dimensional boundary of thickness δ_f is used to estimate the boundary layer thickness at

the nose of the bubble. They found the volume flow in the boundary layer in front of the bubble by integrating the velocity profile and, likewise, the wall shear stress could be found from the velocity profile. The pressure gradient was given by Bernoulli's equation.

An integral equation for a falling film was adapted by Addlesee and Kew to describe the evolution of momentum in the microlayer,

$$\frac{d}{dx}\int_{\delta}\rho(u(y))^2 dy = -\tau + \rho g \sin\theta\cdot\delta + \rho g\cos\theta\cdot\delta\frac{d\delta}{dx} \quad (1)$$

The gravity terms in Eq. (1) account for the component of the fluid weight acting down the sloping wall and the hydrostatic pressure distribution in the film. Surface tension is not included as the film is assumed to be thin compared with the bubble dimensions. The velocity profile across the microlayer assumed by Addlesee and Kew is

$$u/u_{\text{bubble}} = 1 - 3\left(1 - \frac{1}{\lambda}\right)\left(\eta_f - \frac{\eta_f^2}{2}\right) \quad (2)$$

where $\lambda \equiv u_{\text{bubble}}\delta/q$, $\eta_f \equiv y/\delta$, and q is the volume flow per unit width. Equation (2) meets the boundary conditions of no slip at the wall and no shear at the bubble surface.

The initial film thickness was obtained by assuming that the film originates at the nose of the bubble where, at the stagnation point, the velocity on the bubble surface is zero,

$$\lambda = 3, \text{ or } \delta = 3q/u_{\text{bubble}} \quad (3)$$

The wall shear stress and the momentum flux are evaluated in terms of the velocity profile and introduced into Eq. (1), which can be written nondimensionally as

$$\frac{d\lambda}{d\xi}\left(\frac{\lambda^2 - 6}{5} - \frac{\lambda^3}{\text{Fr}^2\,\text{Re}^{1/2}\tan\theta}\right) = 3(\lambda - 1) + \frac{\lambda^3}{\text{Fr}^2} \quad (4)$$

where

$$\text{Fr} \equiv \frac{u_{\text{bubble}}}{(gD\sin\theta)^{1/2}}, \quad \text{Re} \equiv \frac{u_{\text{bubble}}D}{\nu}, \quad \xi \equiv \frac{x}{D} \quad (5)$$

In Eq. (5), D is defined in keeping with Addlesee and Kew's definition: the diameter of a sphere of equal volume to a hemispherical bubble of radius $L/2$: $D \equiv 4^{1/3}L/2$.

In a fully developed condition, λ_∞ depends only on the Froude number,

$$\lambda_\infty^3/3(1 - \lambda_\infty) = \text{Fr}^2 \quad (6)$$

The roots of Eq. (6) can be obtained numerically, and δ can be found from the definition of λ.

δ was computed using Addlesee and Kew's model for all the cases of Table 1, as shown in Fig. 6. The curves are terminated at the measured length of the bubbles. The δ levels off to values on the order of 100 μm. The direct measurements in Table 1 are on the order of 35 μm. These results show that δ approaches a constant value after 3–4 mm of microlayer development. Li's direct measurements yield a much shorter development length.

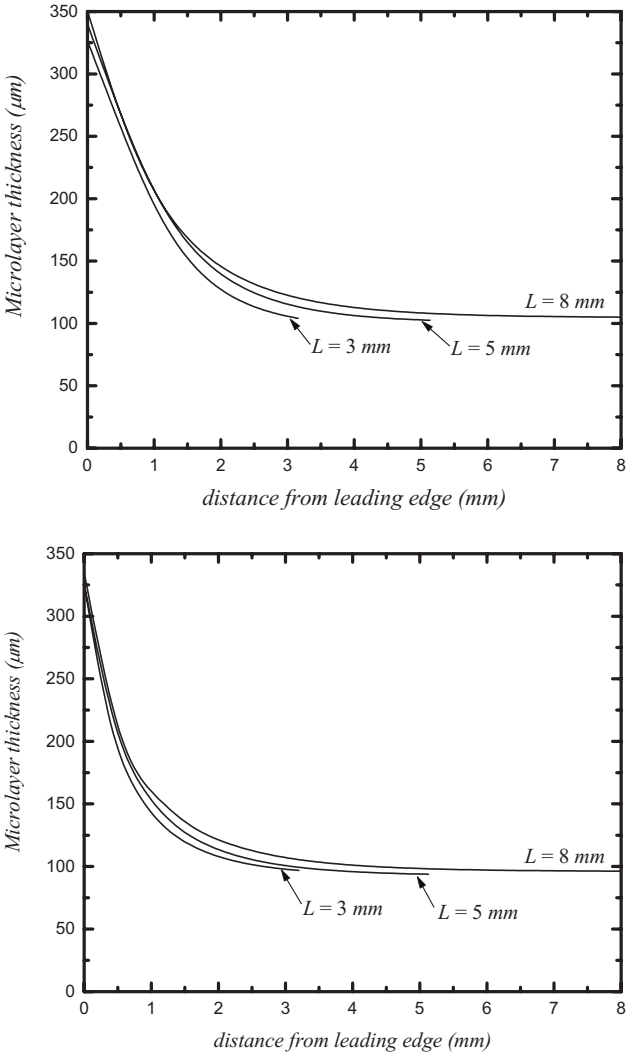

Fig. 6 Microlayer thickness calculations for sliding bubbles at inclinations of (top) 5 deg and (bottom) 10 deg using Addlesee and Kew's model

3 Modification of the Addlesee and Kew Model

Addlesee and Kew treated the volume flux into the microlayer as a constant and assumed that the total volume flux within the boundary layer in front of the bubble enters the microlayer. However, it can be assumed that only *part* of that volume flux enters the microlayer and, because evaporation may be a major contribution to the enhancement of heat transfer, some fraction of the volume flux q is evaporated in the microlayer. Therefore, a modification of Addlesee and Kew's model is proposed wherein a q function is postulated as

Table 1 Data for six sliding bubbles from Li et al. [2,3]

	θ (deg)	L (mm)	u_{bubble} (mm/s)	Growth rate (mm^3/s)	T_w (°C)	Re	Fr	δ (μm)
I	5	3	70	220	33.0	819	1.35	34
II	5	5	82	520	34.0	1199	1.41	35
III	5	8	105	1100	34.5	1843	1.65	37
IV	10	3	85	320	33.0	1243	1.04	28
V	10	5	105	1000	35.0	1781	1.19	30
VI	10	8	125	2000	36.0	2413	1.33	32

$$q = q(\xi) = cq_{\text{initial}} f(\xi) \tag{7a}$$

where

$$f(\xi) \equiv 1 + d(e^{-n\xi} - 1) \tag{7b}$$

q_{initial} is the volume flux predicted by direct application of Addlesee and Kew's model, c is the fraction of q_{initial} that will enter the microlayer, and d and n set the rate of evaporation as the flow progresses down the microlayer. Equation (7*b*) assumes that evaporation behaves exponentially with distance along the microlayer and also assumes that the entire bubble volume growth is attributed to microlayer evaporation. If Eqs. (7*a*) and (7*b*) are inserted into Eq. (1), a modified equation is obtained in terms of dimensionless quantities,

$$\frac{d\lambda}{d\xi}\left(\frac{\lambda^2 - 6}{5} - \frac{cf(\xi)\cdot\lambda^3}{\text{Fr}^2\,\text{Re}^{1/2}\tan\theta}\right) = \frac{3(\lambda-1)}{p^2 f(\xi)} + \frac{\lambda^3}{\text{Fr}^2} + \left[\frac{c\cdot\lambda^4}{\text{Fr}^2\,\text{Re}^{1/2}\tan\theta} - \frac{1}{5f(\xi)}(\lambda^3 + 6\lambda - 2\lambda^2)\right]\frac{df(\xi)}{d\xi} \tag{8}$$

where the definitions of Fr and Re are unchanged.

Data for the bubble growth rate for the runs described in Table 1 were used to determine the constants c and d in Eqs. (7*a*) and (7*b*). The measured bubble width, W, is used to calculate the bubble volume growth per unit width, G,

$$G = q_{\text{initial}}\rho_{\text{liquid}}\frac{cd}{\rho_{\text{vapor}}} \quad \text{or} \quad c = G\frac{\rho_{\text{vapor}}}{\rho_{\text{liquid}}}\cdot\frac{1}{dq_{\text{initial}}} \tag{9}$$

By combining Eqs. (8) and (9), the following is obtained:

$$\frac{d\lambda}{d\xi}\left(\frac{\lambda^2-6}{5} - u_{\text{bubble}}G\frac{\rho_{\text{vapor}}}{\rho_{\text{liquid}}}\cdot\frac{1}{dq_{\text{initial}}}\cdot\frac{f(\xi)\lambda^3}{\text{Fr}^2\,\text{Re}^{1/2}\tan\theta}\right) = \left(u_{\text{bubble}}G\frac{\rho_{\text{vapor}}}{\rho_{\text{liquid}}}\cdot\frac{1}{dq_{\text{initial}}}\right)^{-2}\frac{3(\lambda-1)}{f(\xi)} + \frac{\lambda^3}{\text{Fr}^2} + \frac{df(\xi)}{d\xi}\left[u_{\text{bubble}}G\frac{\rho_{\text{vapor}}}{\rho_{\text{liquid}}}\cdot\frac{1}{d\,q_{\text{initial}}}\cdot\frac{\lambda^4}{\text{Fr}^2\,\text{Re}^{1/2}\tan\theta} - \frac{1}{5f(\xi)}(\lambda^3+6\lambda-2\lambda^2)\right] \tag{10}$$

By choosing appropriate coefficients c, d, and n, Eq. (10) can be solved numerically. Figure 7 shows the results from the modified model for the bubbles in Table 1. The corresponding values of c, d, and n are shown in Table 2. If about 30–37% of q_{initial} enters the microlayer and about 4–10% of the flux that enters evaporates in the microlayer, Li's direct measurements of δ can be matched well.

Addlesee and Kew's model, both as initially developed and as modified herein, shows that δ decreases as θ increases. This trend is also observed in Li's measurements.

In Fig. 7, δ decreases from 100 μm to 200 μm to about 27–37 μm within 0.5 mm of travel in the x direction. A length of 0.5 mm requires about 5 ms of the bubble passage time. This rise time to a plateau value matches well the general tendency of Li's optical probe signals to obtain a plateau value rapidly. Figure 4 shows a rise time of about 20 ms for a 2 deg inclination and no perceptible rise time at 15 deg. The 5 deg data show at most single-digit rise times.

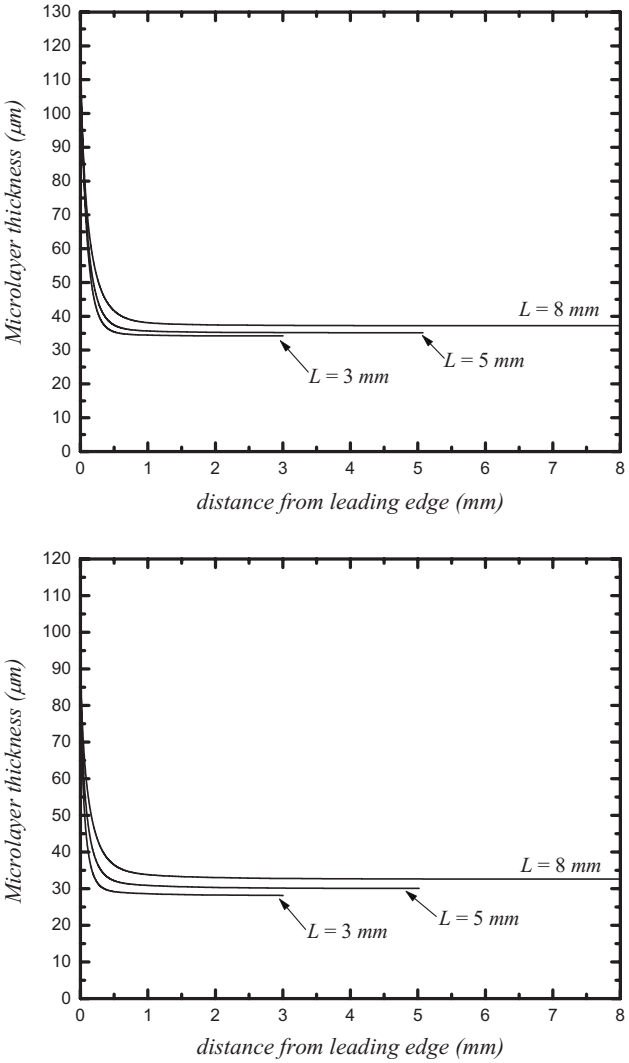

Fig. 7 Microlayer thickness calculations for sliding bubbles at inclinations of (top) 5 deg and (bottom) 10 deg using the modified Addlesee and Kew model

The modified analysis demonstrates that if approximately 1/3 of the flux predicted by Addlessee and Kew enters the microlayer and a single-digit percentage evaporates, a flat microlayer of the measured thickness results. This analysis makes no attempt to independently verify the values selected for these constants. It demonstrates only that physically reasonable values can match the measured results.

4 New Model Based on Lubrication Theory

The sliding of a bubble under an inclined surface may also be cast as a two-dimensional internal lubrication problem: The

Table 2 *c*, *d*, and *n* values for bubbles in Table 1

Run number from Table 1	I	II	III	IV	V	VI
Fraction of volume flux entering microlayer, c (%)	33	34	37	30	34	35
Fraction of volume flux evaporated, d (%)	4.5	6	6.5	7	9	10
Evaporation rate coefficient, n			5			

Table 3 Microlayer curvature parameters for four inclination angles

θ (deg)	u_{bubble} (mm/s)	L (mm)	H (mm)	Volume (mm^3)	a (mm)	b (mm)	δ (μm)
2	75	8	3.6	217	1.3	1250	47
5	100	8	3.2	381	1.6	1550	34
10	125	8	3.4	381	1.7	1860	29
10	136	8	3.8	367	1.9	2180	23

bubble forms one of two bearing surfaces such that the pressure force developed in the microlayer offsets the component of the buoyancy of the bubble that is normal to the test surface. The pressure force developed is a function of δ and the streamwise gradient in the thickness. A model function for the streamwise evolution of δ is used to drive the computation. Given that the modified Addlesee and Kew model infers that a single-digit percentage of the volume flux evaporates, a fixed q through the microlayer (no evaporation) is assumed. The result is a set of constants for the thickness function that produces a vapor interface shape that both satisfies the force balance and produces a plateau value of δ that matches the measurements.

For the analysis, the microlayer is assumed to be approximately two dimensional as the bubble width W is generally three to five times larger than the bubble length L. The analysis takes place in a reference frame where the bubble is stationary and the wall moves with u_{bubble}. The fluid is incompressible and laminar and δ is much less than the bubble length. The equations for continuity and for momentum in the x and y directions in the liquid film are

$$\frac{\partial u}{\partial x} + \frac{\partial v}{\partial y} = 0 \tag{11a}$$

$$\frac{\partial p}{\partial x} = \mu \frac{\partial^2 u}{\partial y^2} \tag{11b}$$

$$\frac{\partial p}{\partial y} = 0 \tag{11c}$$

where p is the pressure and the x and y directions lie along and normal to the bubble, respectively. The bubble surface and the wall are not parallel, and therefore the streamlines are not parallel, so $\partial v/\partial y \neq 0$ and so $u=u(x,y)$. We further assume a no-shear boundary condition at the vapor interface. This condition approximates a continuous shear across the interface with the additional condition that shear exerted by the vapor is negligible. The corresponding boundary conditions are

$$y = 0, \quad u = u_{bubble} \tag{12a}$$

$$y = \delta(x), \quad \frac{\partial u}{\partial y} = 0 \tag{12b}$$

$$x = 0, \quad p = p_0 \tag{12c}$$

and

$$x = L, \quad p = p_0 \tag{12d}$$

By using these boundary conditions, the (constant) volume flow per unit bubble width, q, and pressure in the microlayer can be derived:

$$q = u_{bubble}\Delta \tag{13}$$

$$p(x) = p_0 + 3\mu u_{bubble}\gamma_1 - 3\mu q \gamma_2 \tag{14}$$

where γ_1 and γ_2 are

$$\gamma_1(x) \equiv \int_0^x \frac{dx}{\delta^2}, \quad \text{and} \quad \gamma_2(x) \equiv \int_0^x \frac{dx}{\delta^3} \tag{15}$$

and the characteristic thickness, Δ, is defined based on γ_1 and γ_2 at $x=L$:

$$\Delta \equiv \frac{\gamma_1(L)}{\gamma_2(L)} \tag{16}$$

δ is assumed to be an exponential function,

$$\delta(x) = a\exp(-bx) + \delta_\infty \tag{17}$$

The exponential shape agrees reasonably well with the photographs of Li [3] of the leading edge of typical cap-shaped bubbles moving under the plate, as illustrated in the sketch in Fig. 1 and by the sequence of bubble images in Fig. 2. Using this function, the microlayer is divided into two regions: the entrance region, where δ decreases from an initial value, $a+\delta_\infty$, at $x=0$ to a uniform thickness, δ_∞, in the plateau region.

The pressure force generated by the microlayer balances the buoyancy of the bubble normal to the heated surface. That is, the bubble does not generate a lift force on its lower (sloping) surface. Using the expression developed for the pressure in the microlayer, the force balance is

$$\frac{F}{W} = (\rho_{liq} - \rho_{vap})g\frac{V}{W}\cos(\theta) = \int_0^L p(x)dx - p_0 L$$

$$= \int_0^L (3\mu u_{bubble}\gamma_1 - 3\mu q\gamma_2)dx. \tag{18}$$

In Eq. (18), the force depends on u_{bubble}, fluid viscosity, and microlayer geometry.

Four bubbles at 2 deg, 5 deg, 10 deg, and 15 deg and $L=8$ mm were chosen to test this model and the corresponding data related to the bubble are shown in Table 3. As bubble dimensions, velocity, and δ were obtained from Li's experimental observations as described previously, a and b are the only parameters required in Eq. (17). Because a is related to the initial height of the microlayer, we assume that height begins at the start of curvature for the upper side of the bubble: $a=H/2$, where $H/2 \gg \delta_\infty$. The bubble height, H, is given in Table 3. The constant, b, controls the length of the entrance region. It has been observed from Li's videos that the length of the entrance region is different for each θ. In addition, the length of the entrance region decreases with θ, as observed from optical probe signals. Based on these observations, values of b related to θ are chosen to drive the solution of Eq. (18). The values of a, b and the measured values of δ (matched by the computation) are shown in Table 3.

The microlayer shapes for the four bubbles at different δ are shown in Fig. 8. The corresponding pressure distribution was computed from Eq. (14). Figure 9 shows the pressure distribution in the microlayer for the four bubbles. The peak pressure within the microlayer increases with θ. Furthermore, the position of pressure peak moves toward the front of the bubble as θ increases.

The resulting values of b show a monotonic progression: The curvature at the front of the bubble sharpens as θ increases. How-

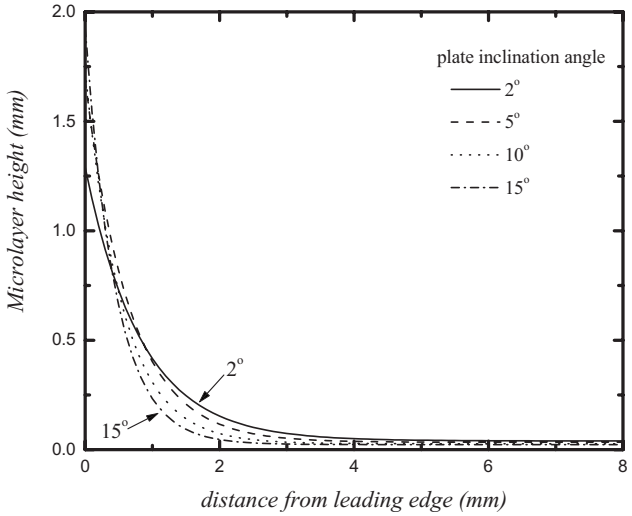

Fig. 8 Assumed microlayer curvature

ever, the slope is much gentler than that given by the modified falling-film model. This computation considers one bubble at each θ and selects a value of b that produces the measured d for that bubble. All measured bubbles can be made to fit the model by selecting somewhat different values of b as this coefficient is likely to be a function of parameters that vary at fixed θ such as speed, acceleration, volume, Reynolds number, Weber number, or drag coefficient. This analysis ignores these possibilities as its purpose is to show that lubrication theory, given a reasonable general assumption for the shape of the interface bounding the microlayer, can produce the force magnitudes required to offset the bubble buoyancy across all the measured inclinations.

5 Microlayer Thickness Correlation Based on Lubrication Theory

While the development of the lubrication-based theory for sliding bubbles required the selection of appropriate values of factors that control the shape of the bubble, and thus does not produce a direct value of δ, it provides the basis for a direct correlation of experimental data in terms of parameters that naturally arise in the model.

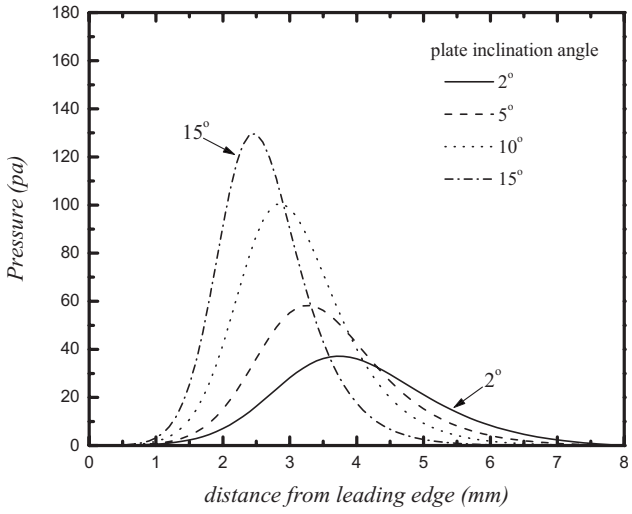

Fig. 9 Pressure developed under bubbles of various inclinations

The development of the correlation starts with the result from the lubrication model, Eq. (18), written as

$$\text{force}/(WL) = \rho_l g(V/WL)\cos\,\theta = \int_0^1 (6\mu u_b \lambda_1 - 12\mu q \lambda_2) d(x/L) \tag{19}$$

The volume flux per unit width is assumed to be proportional to the product of bubble velocity and microlayer thickness: $q \equiv \dot{V}/W \sim u_{\text{bubble}}\delta$. Equation (19) is rewritten as

$$\rho_l g(V/WL)\cos\,\theta \sim \frac{6\mu u_{\text{bubble}}}{\delta}\int_0^1 (\delta\lambda_1 - 2\delta^2\lambda_2) d(x/L) \tag{20}$$

The integral in Eq. (20) is dimensionless and is a function of the shape of the interface (the λ's). The shape was shown in the lubrication model to be a function of θ. For these reasons the integral is modeled as

$$\int_0^1 (\delta\lambda_1 - 2\delta^2\lambda_2) d(x/L) \sim f(\theta) \sim \theta^m \tag{21}$$

We now have

$$\rho_l g(V/WL)\cos\,\theta \sim \mu u_{\text{bubble}}\delta^{-1}\theta^m \tag{22}$$

Rearranging into dimensionless groups guided by the emergence of a microlayer Reynolds number, Re_δ, we have

$$\frac{g(V/WL)\cos\,\theta}{u_{\text{bubble}}^2}\theta^{-m} \sim \frac{\nu}{\delta u_{\text{bubble}}} \tag{23}$$

or

$$\frac{u_{\text{bubble}}\delta}{\nu} \sim \frac{u_{\text{bubble}}^2}{g(V/WL)\cos\,\theta}\theta^m \tag{24}$$

Re_δ contains the thickness measurement and is defined as

$$\text{Re}_\delta \equiv \frac{u_{\text{bubble}}\delta}{\nu} \tag{25}$$

The right side of Eq. (24) contains a type of Froude number, defined here as Fr_2:

$$\text{Fr}_2 \equiv \left[\frac{u_{\text{bubble}}^2}{g(V/WL)\cos\,\theta}\right]^{1/2} \tag{26}$$

With these definitions, the suggested correlation is

$$\text{Re}_\delta \sim \text{Fr}_2^2\theta^m \tag{27}$$

For a cap-shaped bubble, $V/WL = (\pi/6)WLH/WL = (\pi/6)H$. The volume is assumed equivalent to 1/8 of the volume of an ellipse with radii of L, $W/2$, and $2H$, and follows the practice established in Refs. [2,3,6,7]. Figure 10 illustrates the relationship between Re_δ and Fr_2^2 for each θ. Figure 11 shows a collapse on θ with $m = -1/3$. Figure 11 suggests a reasonable fit to be

$$\text{Re}_\delta = 0.850\,\text{Fr}_2^2\theta^{-1/3} \tag{28}$$

with a scatter band of approximately $\pm 15\%$. Some degree of failure of the underlying assumptions may cause part of the scatter. Among these assumptions are ignoring any hydrodynamic lift force that counteracts part of the buoyancy and assuming that the dimensions from imaged bubbles match the dimensions of bubbles for which the microlayer was measured.

The trends are right: For a fixed velocity and θ, as the buoyant force against the microlayer increases, the δ decreases. The decrease in δ with increasing inclination is also captured. It is also interesting to note that the Re_δ values are very near unity.

A better correlation can be obtained if one keeps in mind that the kinematics of the bubbles in this one fluid apparently depend

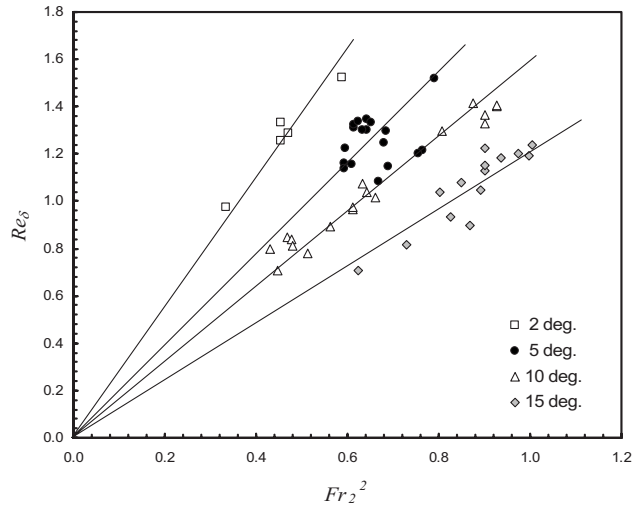

Fig. 10 The dependence of Re_δ on Fr_2^2 for various inclination angles

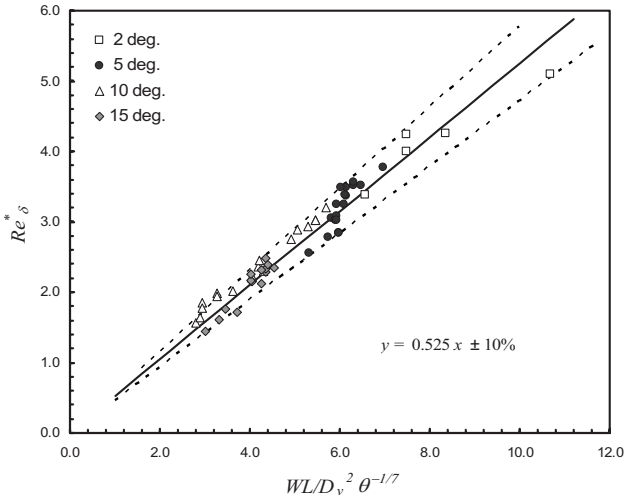

Fig. 12 The dependence of Re^*_δ on a shape factor and inclination angle

only on volume and θ. There should therefore be a velocity scale that depends on only these measurands. Such a scale is

$$U^* \equiv \sqrt{gD_v}, \quad \text{where} \quad D_v \equiv V^{1/3} \tag{29}$$

It can be shown from the data of Li et al. [2] that the observed velocity is dependent on this velocity scale and θ:

$$u_{\text{bubble}} = U^* G(\theta) \tag{30}$$

Going back to Eq. (22), we can write

$$\rho_l g(V/WL)\cos\,\theta \sim \mu u_{\text{bubble}} \delta^{-1} \theta^m \tag{31}$$

$$(gD_v)\left(\frac{D_v^2}{WL}\right)\cos\,\theta \sim \frac{\nu u_{\text{bubble}}}{\delta}\theta^m \tag{32}$$

$$\frac{U^*\delta}{\nu} \sim \frac{u_{\text{bubble}}}{U^*}\left(\frac{WL}{D_v^2}\right)\cos\,\theta \cdot \theta^m \tag{33}$$

$$\frac{U^*\delta}{\nu} \sim \left(\frac{WL}{D_v^2}\right)G(\theta)\cdot\cos\,\theta\cdot\theta^m \tag{34}$$

In Eq. (34), a new microlayer Reynolds number is defined:

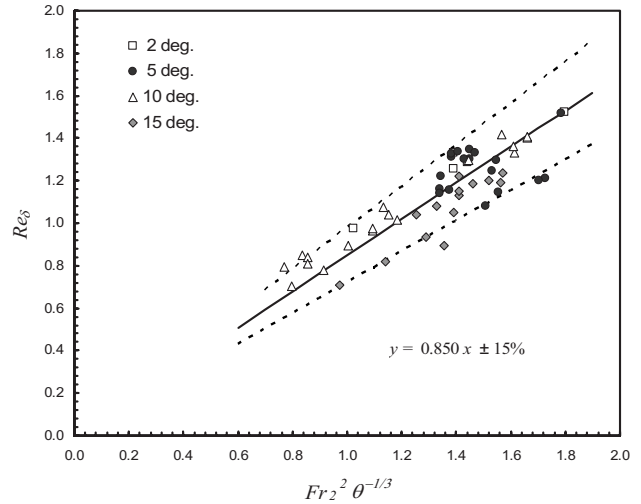

Fig. 11 A curve fit for Re_δ in terms of Froude number and inclination angle

$$\text{Re}^*_\delta \equiv \frac{U^*\delta}{\nu} \tag{35}$$

and Eq. (34) can be written simply as

$$\text{Re}^*_\delta \sim \left(\frac{WL}{D_v^2}\right)F(\theta) \tag{36}$$

Figure 12 gives the results for

$$\text{Re}^*_\delta = 0.525\left(\frac{WL}{D_v^2}\right)\cdot\theta^{-1/7} \tag{37}$$

The experimental data presented as Re^*_δ are captured very nicely within $\pm 10\%$—near the level of the measurement uncertainty and the resulting correlation depends only on volume, θ, and a bubble shape factor (WL/D_v^2, or $WL/V^{2/3}$), all of which can be determined experimentally to within reasonable accuracy.

6 Summary

Direct measurements of microlayer thicknesses under sliding FC-87 bubbles are compared with the results of various models. Models found in literature are based on two different approaches: one in which δ is inferred from a thermal analysis of the microlayer, and the other is based on the hydrodynamics of the bubble motion along the surface. The falling-film-inspired model of Addlesee and Kew predicts a plateau δ that is about three times that observed by Li et al. This model yields a longer development length than observed, but it does predict the trend observed by Li of decreasing δ with increasing θ. Reasonable agreement with Li's measured values of δ could be obtained by modifying the model of Addlesee and Kew to allow for a smaller q entering the microlayer and to account for partial evaporation of the microlayer under the bubble. However, new constants were introduced as part of the modification, and the improved results are purely "postdictive,"

A model based on classical internal-flow lubrication theory was developed. It balances the pressure force generated in the microlayer and the buoyancy force of the bubble. This model requires that the shape of the developing microlayer be known and a number of constants to be specified to describe that shape. The photographs of bubble behavior from Li were used to develop a shape that approximates those observations. This shape function results in good (again, postdictive) agreement with Li's direct measurements of δ. The basic structure of the lubrication theory yields a correlation that captures experimental data presented as Re_δ very nicely within $\pm 10\%$. This correlation depends only on volume, θ,

and a bubble shape factor ($WL/V^{2/3}$), all of which can be determined experimentally to within reasonable accuracy.

Nomenclature

a = fraction of bubble height, mm
b = rate of microlayer height decrease, mm^{-1}
c = volume flux fraction entering microlayer, %
D = equivalent diameter defined by Addlesee and Kew model, mm
D_v = bubble length scale, $\equiv V^{1/3}$, mm
d = volume flux fraction evaporated in microlayer, %
F = buoyancy force, N
f = volume flux fraction in microlayer, dimensionless
Fr = Froude number $\equiv u_{\text{bubble}}/(gD \sin \theta)^{1/2}$, dimensionless
Fr_2 = Froude number, $\equiv u_{\text{bubble}}/(g(V/WL)\sin \theta)^{1/2}$, dimensionless
G = bubble growth rate per unit width, mm^2/s
g = gravitational acceleration, m/s^2
H = bubble height, mm
L = bubble length, mm
m = exponent on θ, dimensionless
n = evaporation rate coefficient, dimensionless
q = volume flow rate per unit width, mm^2/s
p = pressure in the microlayer, Pa
p_0 = pressure external to the microlayer, Pa
r_h = radius of hemispherical bubble, mm
Re = Reynolds number $\equiv u_{\text{bubble}} \cdot D_{\text{eq}}/\nu$, dimensionless
Re_δ = microlayer Reynolds number $\equiv u_{\text{bubble}}\delta/\nu$, dimensionless
Re^*_δ = microlayer Reynolds number $\equiv U^*\delta/\nu$, dimensionless
T_{sat} = saturation temperature of working fluid, °C
T_w = temperature of test surface, °C
U^* = bubble velocity scale, $U^* \equiv \sqrt{g(V^{1/3})}$, mm/s
u = velocity relative to bubble in the microlayer, mm/s
u_{bubble} = bubble velocity, mm/s
u_{wall} = test surface velocity relative to bubble, mm/s
v = y-direction velocity in the microlayer, mm/s
V = bubble volume, $\equiv(\pi/6)WLH$, mm^3
W = bubble width, mm
x, y = coordinates, x along wall, y normal to wall, mm

Greek

Δ = characteristic thickness, μm
δ = microlayer thickness, μm
δ_f = boundary layer thickness ahead of the bubble, μm
γ_1 = microlayer thickness parameter, μm^{-1}
γ_2 = microlayer thickness parameters, μm^{-2}
η_f = dimensionless coordinate, $\equiv y/\delta_f$
λ = dimensionless microlayer thickness, $\equiv u_{\text{bubble}}\delta/q$
μ = absolute viscosity, kg/s·m
υ = kinematic viscosity, m^2/s
θ = heating surface inclination angle, arc degrees
ρ = density, kg/m^3
τ = shear stress, N/m^2
ξ = dimensionless distance from the bubble nose, $\equiv x/D$

Acknowledgment

This work was supported in part by a state of Texas Advanced Research Program grant, Grant No. ARP 003652-762.

References

[1] Cornwell, K., and Schüller, R. B., 1982, "A Study of Boiling Outside a Tube Bundle Using High Speed Photography," Int. J. Heat Mass Transfer, **25**(5), pp. 683–690.
[2] Li, X., Keith Hollingsworth, D., and Witte, L. C., 2006, "The Thickness of the Liquid Microlayer Between a Cap-Shaped Sliding Bubble and a Heated Wall: Experimental Measurements," ASME J. Heat Transfer, **128**, pp. 934–944.
[3] Li, X., 2005, "Measurement of the Microlayer Thickness Between a Sliding Bubble and an Inclined Wall," Ph.D. thesis, University of Houston, Houston, TX.
[4] Yu, S. C. M., and Tso, C. P., 1995, "Simulation of Fiber Optic Sensors in Determination of Thin Liquid Film Thickness," Adv. Eng. Software, **22**, pp. 55–62.
[5] Kenning, D. B. R., Bustnes, O. E., and Yan, Y., 2000, "Heat Transfer to a Sliding Vapor Bubble," Multiphase Sci. Technol., **14**(1), pp. 75–94.
[6] Bayazit, B. B., Hollingsworth, D. K., and Witte, L. C., 2003, "Heat Transfer Enhancement Caused by Sliding Bubbles," ASME J. Heat Transfer, **125**(3), pp. 503–509.
[7] Bayazit, B. B., 2000, "A Thermographic Analysis of the Heat Transfer Mechanisms Generated by a Sliding Bubble," M.S. thesis, University of Houston, Houston, TX.
[8] Addlesee, A. J., and Cornwell, K., 1997, "Liquid Film Thickness Above a Bubble Rising Under an Inclined Plate," Trans. IChemE, Part C, **75**, pp. 663–667.
[9] Addlesee, A. J., and Kew, P. A., 2002, "Development of the Liquid Film Above a Sliding Bubble," Trans. IChemE, Part C, **80**(A3), pp. 272–277.
[10] Cerro, R. L., and Whitaker, S., 1971, "Entrance Region Flows With a Free Surface: the Falling Liquid Film," Chem. Eng. Sci., **26**, pp. 785–798.
[11] Anderson, H. I., 1984, "On Integral Method Predictions of Laminar Film Flow," Chem. Eng. Sci., **39**(6), pp. 1005–1100.

Flush-Mounted Steady-Periodic Heated Film With Application to Shear-Stress Measurement

Kevin D. Cole
Mechanical Engineering Department,
University of Nebraska-Lincoln,
Lincoln, NE 68588-0656
e-mail: kcole1@unl.edu

Surface-mounted heated films have been used for fluid-flow measurement for many years. Recently unsteady heating of such surface films has been explored experimentally. In this paper steady-periodic heating of a surface-mounted film is studied analytically. Wall effects and axial heat conduction in the fluid are included. The temperature is found as an exact integral expression constructed from separate Green's function formulations in the fluid flow and in the solid wall that are matched at the fluid-solid interface. Results for temperature, obtained by quadrature, are reported for several flow speeds and several steady-periodic frequencies. The results show that steady-periodic heating has potential for shear-stress measurement because the heating frequency may be tuned to maximize the temperature response at the shear stress of interest. Thermal calibration of these sensors is discussed, and simulated calibration curves are given.
[DOI: 10.1115/1.2955472]

Keywords: hot-film anemometer, gas flow, frequency response, conjugate heat transfer, thermal wave

Introduction

Flush-mounted thermal sensors have been used for shear-stress measurements for many years with steady heating [1]. Recently pulsed heating has been investigated experimentally for obtaining quantitative shear-stress values [2] and observing shear-stress direction [3].

The purpose of this paper is to explore steady-periodic heating of flush-mounted hot-film sensors with application to shear-stress measurement. The pertinent literature will be discussed next in the areas of flush-mounted heated films, conjugate heat transfer, and periodic heating applied for thermal measurements.

There have been several theoretical studies of heat/mass transfer from flush-mounted sensors to a fluid with no participating wall, which exactly describes mass-transfer sensors and is a good approximation for thermal sensors in liquids. The steady response of a circular mass-transfer sensor was studied with a boundary-element solution by Stone [4] and with an asymptotic method by Phillips [5]. Soliman and Chambre [6] used a double Laplace transform to find the response of a steady fluid flow to a step change in boundary heating; Geshev [7] reported theoretical results for the response of a strip-shaped sensor to a fluid flow containing a small sinusoidal oscillation; Steenhoven and van de Beucken [8] reported numerical results for a strip-shaped sensor and experimental results were reported for a mass-transfer sensor, which was circular in shape. The flow contained a low-frequency oscillating component over a range of amplitudes, the largest of which caused flow reversals.

The phrase "conjugate heat transfer" is used to describe convection heat transfer with a participating wall. The temperature and heat flux at the fluid-solid boundary are initially unknown and must be determined from the solution of the entire problem. The author has previously investigated steady conjugate heat transfer from a flush-mounted film [9]. Although the work was limited to high Peclet number (axial conduction in the fluid was neglected), a wide variety of flow conditions, fluid-solid property ratios, and wall thicknesses were studied. The solution involved distinct Green's function (GF) descriptions of the temperature in the fluid and the solid, matched numerically at the interface. In a later study, axial heat conduction in the fluid was included and an exact integral expression was found for the steady-temperature solution [10]. Quadrature was used to obtain numerical results. An asymptotic method was used by Stein et al. [11] to study the steady-temperature decay downstream of a strip heater on a slab wall. Chao et al. [12] used a finite-difference method to compute temperature and velocity contours near a very small heater ($a = 0.2$ mm) on a silicon substrate cooled by airflow. Axial conduction of the fluid is important when the heater is very small.

There have been several studies of unsteady conjugate heat transfer. Cole and Beck [13] simulated a strip-shaped film and a single on-off pulse of heat. Later Liang and Cole [14] extended this work to a 3D rectangular flush-mounted sensor. In these studies a simplified fluid-side theory was used to represent flow with large Peclet number (axial heat conduction neglected in the fluid) and low-frequency thermal transients (as the fluid heat transfer was quasisteady). A later study by the author included axial heat conduction in the fluid and a rapid heating event [15]. Dinu et al. [16] simulated the wall-side heat conduction from a flush-mounted heater for use as a heat flux sensor. The fluid flow was modeled as a convection boundary condition on the wall. Frequency-response results show that the phase depends only on the excitation frequency and not on the signal size. Several papers report studies of a heater with specified temperature (such as provided by a constant-temperature anemometer circuit) with a transient caused by variations in the flow velocity [17–20]. The intent of these papers was to find the frequency response of the sensor to fluid-flow transients. Of particular note in this group is Tardu and Pham [20] whose two-dimensional numerical study showed that axial fluid conduction must be included when the sensor is small and when the fluid flow is small. They also showed that measurements in gas flows are the most challenging because of heat transfer to the wall.

There have been many studies of steady-periodic heating applied to measurement of thermal properties in solids, including the thermal hot-strip method [21,22], the 3-omega method [23], and photothermal methods [24,25].

Contributed by the Heat Transfer Division of ASME for publication in the JOURNAL OF HEAT TRANSFER. Manuscript received September 10, 2007; final manuscript received January 16, 2008; published online August 29, 2008. Review conducted by Minking Chyu. Paper presented at the 2006 ASME International Mechanical Engineering Congress (IMECE2006), Chicago, IL, November 5–10, 2006.

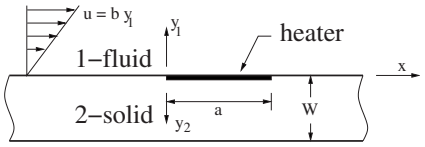

Fig. 1 Geometry for a flush-mounted heated film cooled by a fluid flow

Recently there have been a few studies of steady-periodic heating effects applied to fluid-flow measurement. Bonne and Kubisiak [26] have developed a mechanical actuator combined with two identical flush-mounted thermal sensors. The mechanical actuator produces steady-periodic reversing flow over one thermal sensor to calibrate the main thermal sensor for measurement of flow velocity for any flowing liquid. Al-Salaymeh and Durst [27] studied gas flow and Chung et al. [28] studied liquid flow using a single-wire sensor energized by a periodic heating signal. The same wire is also used as a temperature sensor, and the phase lag of the temperature response is combined with a transient model of the heated wire to deduce the fluid-flow velocity around the wire. This type of sensor has a wider velocity range than a wire energized by a traditional constant-temperature anemometer circuit. Rachalski [29] used a three-wire system with one periodically heated wire and two temperature-sensing wires. The temperature signal was analyzed using a GF solution for the heat transfer in a uniform-velocity flow.

To the author's knowledge steady-periodic heating has not been applied for the measurement of wall shear stress. This paper is a theoretical study of a periodically heated film, flush mounted on a solid wall, applied to the measurement of shear stress. This paper is divided into sections on the temperature equations, the GF, theory for two regions in contact, numerical results, and a summary.

Temperature Equations

The equations describing the temperature in the fluid and the solid are given in this section. The temperature distribution $\tilde{T}(x,y,t)$ satisfies

$$\frac{\partial^2 \tilde{T}_1}{\partial x^2} + \frac{\partial^2 \tilde{T}_1}{\partial y_1^2} = \frac{by_1}{\alpha_1}\frac{\partial \tilde{T}_1}{\partial x} + \frac{1}{\alpha_1}\frac{\partial \tilde{T}_1}{\partial t}, \quad 0 < y_1 < \infty \tag{1}$$

$$\frac{\partial^2 \tilde{T}_2}{\partial x^2} + \frac{\partial^2 \tilde{T}_2}{\partial y_2^2} = -\frac{1}{k_2}\tilde{g}(x,y_2,t) + \frac{1}{\alpha_2}\frac{\partial \tilde{T}_2}{\partial t} \quad \text{in domain } \Omega_2 \tag{2}$$

The fluid velocity is described by a linear distribution by_1 because the thermal boundary layer is contained in the near-wall portion of the fluid velocity boundary layer [9]. Quantity $\tilde{g}$ is the volume energy source in Region 2 that describes any heating condition including a flush-mounted heated film. Domain Ω_2 can include the slab body $(0<y_2<W)$ as shown in Fig. 1 or the semi-infinite body $(0<y_2<\infty)$.

The boundary conditions for the combined domain are the following:

$$\text{at } x \to \pm\infty, \quad \tilde{T}_i \text{ is bounded}, \quad i = 1,2$$

$$\text{at } y_1 \to \infty, \quad \tilde{T}_1 \text{ is bounded}$$

$$\text{at } y_2 = W, \quad k\frac{\partial \tilde{T}_2}{\partial y_2} + h\tilde{T}_2 = \tilde{f}_2(x,t) \tag{3}$$

The boundary condition at $y_2=W$ may be one of the three types depending on the values of coefficients k and h: boundary type 1 is specified temperature for $k=0$ and $h=1$, boundary type 2 is specified heat flux for $h=0$, and boundary type 3 is specified convection.

Since in this paper the applications are limited to steady-periodic heating, we take the heating terms $\tilde{g}$ and $\tilde{f}$ and the resulting temperature $\tilde{T}_i(x,y,t)$ to be steady periodic at a single frequency. That is, let

$$\tilde{g}(x,y,t) = \text{Re}[g(x,y,\omega)e^{j\omega t}]$$

$$\tilde{f}(x,t) = \text{Re}[f(x,\omega)e^{j\omega t}]$$

$$\tilde{T}_i(x,y,t) = \text{Re}[T_i(x,y,\omega)e^{j\omega t}] \tag{4}$$

Now in Eqs. (1)–(3) we replace $\tilde{g}$, $\tilde{f}$, and $\tilde{T}_i$ with $ge^{j\omega t}$, $fe^{j\omega t}$, and $T_i e^{j\omega t}$, respectively, to find the steady-periodic equations

$$\frac{\partial^2 T_1}{\partial x^2} + \frac{\partial^2 T_1}{\partial y_1^2} = \frac{by_1}{\alpha_1}\frac{\partial T_1}{\partial x} + \frac{j\omega}{\alpha_1}T_1 \tag{5}$$

$$\frac{\partial^2 T_2}{\partial x^2} + \frac{\partial^2 T_2}{\partial y_2^2} = -\frac{1}{k_2}g(x,y_2,\omega) + \frac{j\omega}{\alpha_2}T_2 \tag{6}$$

$$k\left.\frac{\partial T_2}{\partial y_2}\right|_{y_2=W} + h\,T_2|_{y_2=W} = f(x,\omega) \tag{7}$$

In this paper complex-valued $T_i(x,y,\omega)$ is interpreted as the steady-periodic temperature (Kelvin) in the ith body ($i=1$ or 2) at a single frequency ω. For further discussion of this point, see Ref. [30], pp. 2 and 3. Later in the paper, results will be discussed in the form of amplitude and phase of this temperature.

GF Solution in Each Region

The steady-periodic temperature will be stated formally with the GF method. Assume for the moment that the GF in frequency space, G, is known. Then the steady-periodic temperature is given by the following integral equation (see Ref. [31], pp. 40–43):

$$T_i(x,y,\omega) = \frac{\alpha_i}{k_i}\int g(x',y_i',\omega)G_i(x-x',y_i,y_i',\omega)dx'dy_i'$$

(for volume heating)

$$+\alpha_i\int_S f\begin{bmatrix} -\partial G_i/\partial n' & \text{(type 1 only)} \\ \dfrac{1}{k_i}G_i & \text{(type 2 or 3)} \end{bmatrix} ds'$$

(at the boundaries) (8)

for regions $i=1,2$. Here S is the surface area and n is the outward normal unit vector on the boundary. The same GF appears in each integral term but it is evaluated at locations appropriate for each integral. The GF's needed in the above equation are discussed in detail in the appendixes. Next the temperature solution for two regions in contact will be examined.

Two Regions in Contact

In this section the thermal response of two regions in contact will be studied to model conjugate heat transfer with application to shear-stress measurement. Consider two regions in contact as shown in Fig. 1.

Let Region 2 be a stationary solid heated by a known volume energy source, $g(x,y,\omega)$, and let Region 1 be a flowing fluid, which is heated by contact with Region 2. Then the temperatures in each region may be formally stated with the GF solution equation given in Eq. (8), in terms of known functions G_1 and G_2 and unknown interface heat fluxes q_1 and q_2, as follows:

$$T_1(x,y_1,\omega) = \frac{\alpha_1}{k_1}\int q_1(x',\omega)G_1(x-x'y_1,\omega)dx'$$

$$T_2(x,y_2,\omega)=\frac{\alpha_2}{k_2}\int q_2(x',\omega)G_2(x-x',y_2,\omega)dx'+B_2(y_2) \quad (9)$$

where

$$B_2(y_2)=\frac{\alpha_2}{k_2}\int\int g(x',y_2',\omega)G_2(x-x',y_2,y_2')dx'dy_2' \quad (10)$$

Here B_2 is the contribution to the temperature caused by the volume energy source. The volume energy source, g, could represent any spatial distribution, such as from a thin heater at the surface.

Next consider matching conditions at the interface between the regions. The heat flux entering Region 1 leaves Region 2, and the temperatures match at the interface. That is,

$$q_1(x,\omega)=-q_2(x,\omega) \quad (11)$$

$$T_1(x,0,\omega)=T_2(x,0,\omega) \quad (12)$$

The temperature solution will be sought with a spatial-Fourier transform defined by the following transform pair:

$$\bar{T}(\beta)=\int_{-\infty}^{\infty}T(x)e^{-j\beta x}dx \quad (13)$$

$$T(x)=\frac{1}{2\pi}\int_{-\infty}^{\infty}\bar{T}(\beta)e^{j\beta x}d\beta \quad (14)$$

Apply the integral transform to Eqs. (9)–(12) to obtain

$$\bar{T}_1(\beta,y_1,\omega)=\frac{\alpha_1}{k_1}\bar{q}_1(\beta,\omega)\bar{G}_1(\beta,y_1,y_1'=0,\omega) \quad (15)$$

$$\bar{T}_2(\beta,y_2,\omega)=\frac{\alpha_2}{k_2}\bar{q}_2(\beta,\omega)\bar{G}_2(\beta,y_2,y_2'=0,\omega)+\bar{B}_2(y_2) \quad (16)$$

$$\bar{q}_1(\beta,\omega)=-\bar{q}_2(\beta,\omega) \quad (17)$$

$$\bar{T}_1(\beta,0,\omega)=\bar{T}_2(\beta,0,\omega) \quad (18)$$

Note that the convolution rule has been used to strip away the integral over x'. Now evaluate temperatures $\bar{T}_1$ and $\bar{T}_2$ at the interface and substitute them into Eq. (18). Supressing the dependence on β and ω, Eq. (18) becomes

$$\frac{\alpha_1}{k_1}\bar{q}_1\bar{G}_1=\frac{\alpha_2}{k_2}\bar{q}_2\bar{G}_2+\bar{B}_2(0) \quad (19)$$

Now define $\phi_i=(\alpha_i/k_i)\bar{G}_i(y_i=y_i'=0)$, eliminate $\bar{q}_2$ with Eq. (17), and solve the above equation for $\bar{q}_1$ as follows:

$$\bar{q}_1=\frac{\bar{B}_2(0)}{\phi_1+\phi_2} \quad (20)$$

The above expression for $\bar{q}_1$ represents an exact solution to the problem in β-space, because it can be replaced with Eqs. (15) or (16) to give the temperature solution anywhere in either region in β-space. Of course, the appropriate inverse transform is needed to evaluate the temperature in x-space. The above example has treated two regions in contact, however, this approach can be extended to any number of layers in contact for an exact solution in β-space (see, for example, Ref. [24]).

Response of Flush-Mounted Heater. In the special case of a thin, flush-mounted heater, the volume generation term takes the form $g(x,y_2,\omega)=q_h(x,\omega)\delta(y_2)$ where q_h is the heater flux and δ is the Dirac delta function. Now replace this form of g with the expression for B_2, evaluate the integral over y_2 with the sifting property of the Dirac delta function, and strip off the integral over x' with the spatial-Fourier transform

$$\bar{B}_2(\beta,y_2,\omega)=\frac{\alpha_2}{k_2}\bar{q}_h(\beta,\omega)\bar{G}_2(\beta,y_2,\omega) \quad (21)$$

Then, evaluate $\bar{B}_2$ at $y_2=0$ and replace the expression for the heat flux with the fluid, Eq. (20),

$$\bar{q}_1=\frac{\bar{q}_h\phi_2}{\phi_1+\phi_2} \quad (22)$$

Finally, replace this value for $\bar{q}_1$ with the expression for the fluid temperature as follows:

$$\bar{T}_1(\beta,y_1,\omega)=\frac{\alpha_1}{k_1}\left(\frac{\bar{q}_h\phi_2}{\phi_1+\phi_2}\right)\bar{G}_1(\beta,y_1,\omega) \quad (23)$$

This is the β-space temperature in the fluid caused by a flush-mounted heater. The real-space temperature in the fluid is found with the inversion integral, Eq. (14),

$$T_1(x,y_1,\omega)=\frac{1}{2\pi}\int_{-\infty}^{\infty}\bar{T}_1(\beta,y_1,\omega)e^{j\beta x}d\beta \quad (24)$$

Spatial Average on the Heater. The average temperature on the heater is a practical means to extract information from a heated film because the average temperature can be measured with suitable electronics such as that developed for pulse-heated thermal conductivity measurements [21]. The spatial-average temperature on the heater may be computed from the surface temperature by

$$T_{\mathrm{av}}(\omega)=\frac{1}{a}\int_0^a T_1(x,0,\omega)dx=\frac{1}{a}\int_0^a\left[\frac{1}{2\pi}\int_{-\infty}^{\infty}\bar{T}_1(\beta,0,\omega)e^{j\beta x}d\beta\right]dx$$

$$=\frac{1}{2\pi}\int_{-\infty}^{\infty}\bar{T}_1(\beta,0,\omega)\left[\frac{(e^{j\beta a}-1)}{j\beta a}\right]d\beta \quad (25)$$

Note that the spatial integral on x has been carried out in closed form. Quantity T_{av} is actually easier to evaluate numerically, compared to $T_1(x)$, because the added factor of $1/\beta$ causes the integrand to vanish more rapidly as $\beta\rightarrow\pm\infty$.

Numerical Results

In this section numerical results are given for heating caused by a flush-mounted, spatially uniform heater. Spatially uniform heating describes a thin metallic sensor whose temperature rise is small enough so that variation in the sensor electrical resistivity is likewise small. Another possible boundary condition, that of a spatially uniform temperature on the sensor, is not treated here. Let the spatially uniform heat-flux distribution be described by

$$q_h(x,\omega)=\begin{cases}q_0, & 0<x<a\\ 0 & \text{otherwise}\end{cases} \quad (26)$$

where q_0 is a constant. The spatial-Fourier transform of this heat flux is needed, found by applying Eq. (13) as follows:

$$\bar{q}_h(\beta)=\int_0^a q_h(x,\omega)e^{-j\beta x}dx=q_0\frac{1-e^{-j\beta a}}{j\beta} \quad (27)$$

This heating function is used for the numerical results discussed below.

Fluid Flow Alone. In this section calculations are reported for a fluid flow adjacent to a wall, which does not participate in the heat transfer. This is a useful limiting case, which can be checked against fluid-flow theory, and it also has application, by analogy, to certain mass-transfer sensors.

The temperature for the fluid-only case can be found from the two-region solution, Eq. (23), by taking the limit as $k_2\rightarrow 0$, which

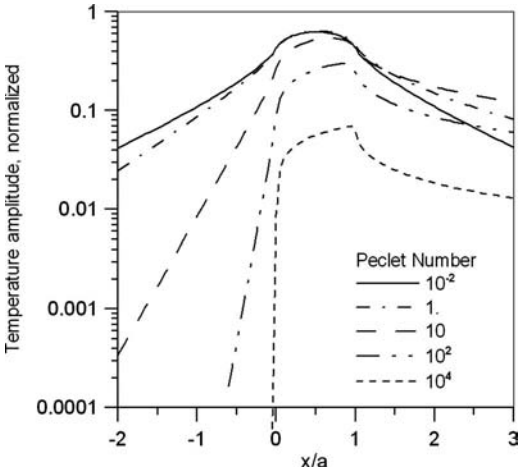

Fig. 2 Amplitude of temperature along the boundary of a flowing fluid heated over $0<x/a<1$ and insulated elsewhere for various flow values, at frequency $\omega^+=1$. No wall effects are present.

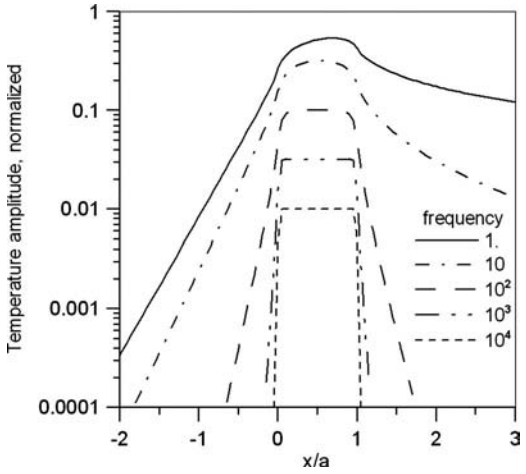

Fig. 3 Amplitude of temperature along the boundary of a flowing fluid heated over $0<x/a<1$ and insulated elsewhere for various frequencies, at fluid flow Pe=10. No wall effects are present.

is consistent with no heat entering or leaving the wall. This causes ϕ_2 to be much larger than ϕ_1. Taking this limit in the temperature expression gives

$$\lim_{\phi_2\to\infty}[\bar{T}_1(\beta,y_1,\omega)]=\frac{\alpha_1}{k_1}\left(\frac{\bar{q}_h\phi_2}{0+\phi_2}\right)\bar{G}_1(\beta,y_1,\omega) \tag{28}$$

$$=\frac{\alpha_1}{k_1}\bar{q}_h\bar{G}_1(\beta,y_1,\omega) \tag{29}$$

That is, the temperature reduces to that given by heating of the fluid alone.

Using the above expression for spatially uniform $\bar{q}_h$ and the expression for $\bar{G}_1$ from Appendix A, the β-space fluid temperature is given by

$$\bar{T}_1(\beta,y_1,\omega)=\frac{\alpha_1}{k_1}\frac{q_0(e^{-j\beta a}-1)}{j\beta\alpha_1 p^{1/3}}\frac{\mathrm{Ai}[(j\omega/\alpha_1+\beta^2+py)/p^{2/3}]}{\mathrm{Ai}'[(j\omega/\alpha_1+\beta^2)/p^{2/3}]} \tag{30}$$

where Ai is the Airy function and where $p=b\beta j/\alpha_1$. The real-space temperature is obtained with the inverse-Fourier transform given by Eq. (24), which must be evaluated numerically.

Normalized parameters are used for presenting the results, as follows: The temperature is normalized as $T^+=(Tk_1)/(q_0a)$ the frequency is normalized as $\omega^+=\omega a^2/\alpha_1$ and the normalized shear stress is given by the Peclet number ($\mathrm{Pe}=ba^2/\alpha_1$). The Peclet number is defined with velocity gradient b, which is proportional to shear stress μb where μ is viscosity. Using these parameters, Fig. 2 shows the amplitude of the temperature along the wall for a range of shear-stress values (Peclet number) and at frequency $\omega^+=1$. The fluid flow is from left to right. At $\mathrm{Pe}=10^{-2}$, the temperature amplitude is symmetric about the heated region, indicating that the x-direction heat conduction dominates the heat transfer and convection is negligible. One of the contributions of the present work is the retention of the axial conduction in the fluid, which allows for study of small-Pe conditions. The amplitude plot for the $\mathrm{Pe}=10^{-2}$ case shown in Fig. 2 has the same shape as that in earlier work by the author for heating of stationary solids [32].

As the Peclet number increases, the temperature on the heater decreases slightly, the upstream temperature falls precipitously, and the downstream temperature rises, all because of increasing convection heat transfer. At large Peclet number the fluid temperature is dominated by convection and x-direction conduction is negligible. Further, because frequency is small in Fig. 2, the results shown for $\mathrm{Pe}=10^4$ agree to four digits with steady convection-only theory [9], providing another check on the present results. This occurs because for Pe large and for small frequency, the time scale for convection is much shorter than the time scale for heating fluctuations.

Figure 3 shows the temperature amplitude at Pe=10 for several heating frequencies. At $\omega^+=1$ the fluid temperature is quasisteady. The upstream region of the wall is dominated by conduction heat transfer and the warm region downstream represents a strong convection component. At $\omega^+=10$ the temperature amplitude drops slightly on the heater, but the temperature drops rapidly downstream where the convection component is much smaller. One explanation is that the higher frequency decreases the thermal penetration into the fluid so the steady-periodic thermal boundary layer is much thinner.

As the frequency increases to $\omega^+=10^2$, the downstream convection dissappears; however, x-direction conduction is still evident from the rounded temperature distribution at the edges of the heater. At $\omega^+=10^3$ and 10^4 the temperature on the heater is flat, indicating that only y-direction conduction remains. That is, at high frequency, there remains only one-dimensional heat conduction perpendicular to the plane of the heater.

Next the spatial-average temperature on the heater will be discussed. Figure 4 shows the amplitude of average temperature on the heater versus Peclet number for several heating frequencies. At every frequency there is a range of low Peclet numbers for which the amplitude is flat. As Peclet increases, there is a point where the amplitude begins to vary with Peclet number. Note that the edge of the flat region occurs at higher Peclet numbers for higher frequency curves. This suggests that the shear-stress sensitivity for a particular sensor geometry can be tuned, by heating frequency, to the shear-stress level (Peclet level) of interest. An upper limit exists, however, as at higher frequencies the signal amplitude becomes smaller and smaller. As frequency increases in Fig. 4, a slight upward bump appears in the amplitude curve at the transition between flat and falling amplitudes. An echo of this feature also appears in the phase plot (Fig. 5) in the $\omega^+=100$ curve. At the present time the reason for this frequency-dependent feature is not understood.

Figure 5 shows the phase of the average heater temperature for the same conditions as for Fig. 4. The phase is important for several reasons. First, like the amplitude, the phase varies with the Peclet number in a clearly defined range determined by frequency. Second, and most important, the phase is an absolute quantity for which no calibration is needed. Phase measurements are not af-

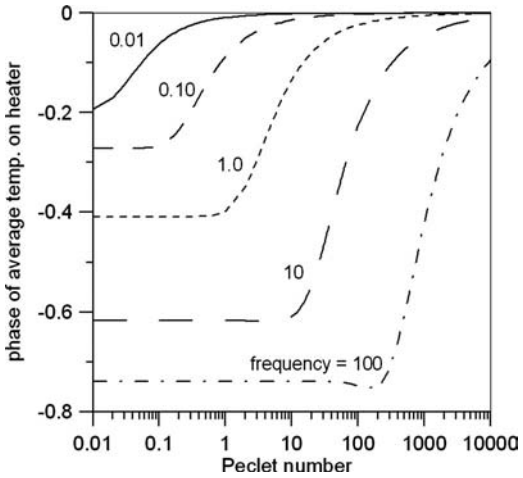

Fig. 5 Phase of spatial-average temperature on the heater for fluid flow alone, for various frequencies

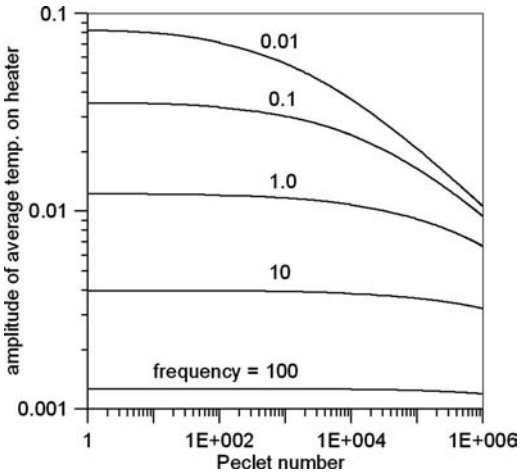

Fig. 6 Amplitude of spatial-average temperature on the heater for airflow over a polymer wall ($k_1/k_2=0.22$, $\alpha_1/\alpha_2=291$) for various frequencies

fected by the "zero drift," which occurs in electronic amplifiers and which often appears in constant-temperature hot-film techniques. Finally, the sensitivity to Peclet number (slope of the curves in Fig. 5) actually increases with increasing frequency. In contrast, the amplitude sensitivity (slope in Fig. 4) is the same for every frequency. Clearly, the phase response is important for the flow-sensor application, especially at higher Peclet number.

The results given in this section have been for heat transfer in the fluid alone. In the next section the effects of heat conduction in the wall are included.

Gas Flow With Participating Wall. For thermal measurement of shear stress, gas flows are the most challenging because most of the introduced heat enters the wall, and only a small portion of the heat directly enters the fluid flow. For gas flows, then, the sensor signal contains a large wall-sensitive portion and a very small fluid-sensitive portion. Every steadily heated sensor design is limited by this wall-dominated response. Steady-periodic heating, however, combined with the use of the phase response of the sensor, can completely remove the steady signal from the measured response. The steady signal, which is removed, is primarily the wall response, greatly improving the sensitivity of the measurement to the fluid shear stress.

In this section, the two-body theory presented earlier is applied to find the steady-periodic temperature for a strip heater on a thermally participating wall. Specifically, the interface temperature given by Eq. (25) is evaluated. Figure 6 shows the amplitude of the spatial-average temperature on the heater for $\alpha_1/\alpha_2=291$ and $k_1/k_2=0.22$ to simulate air flow over a kapton (polymer) substrate. The most prominent feature of Fig. 6 is the smaller amplitude, about ten times smaller than for air alone (Fig. 4) at $\omega^+=1$. This indicates that most of the introduced heat flows directly to the wall. In addition, as the frequency varies, the spacing between the amplitude curves is more uniform in Fig. 6 compared to air alone (Fig. 4). This is another indication that the wall dominates the heat transfer, as frequency defines the thermal penetration perpendicular to the heater. The fluid side is nonuniform with respect to heat penetration because of the velocity distribution. Finally, each curve of Fig. 6 contains a flat portion at low frequency and a falling region at higher frequency. This overall shape is similar to air alone; however, for the air-polymer case, the location of the transition from flat amplitude to falling amplitude occurs at higher Peclet number than for air alone (see Fig. 4). That is, more vigorous convection is needed in order for the heater mounted on a participating wall to be affected by the shear stress.

Figure 7 shows the phase of the spatial-average heater temperature for the air/kapton case plotted versus Peclet number. This is a simulated calibration curve for shear stress by measuring phase. Compared to the phase for the fluid-only case (Fig. 5), the range

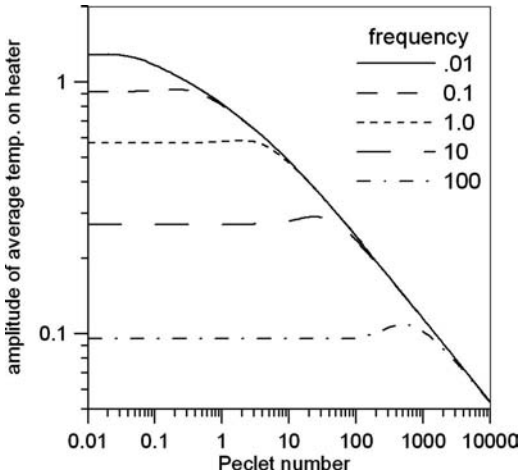

Fig. 4 Amplitude of spatial-average temperature on the heater for fluid flow alone, for various frequencies

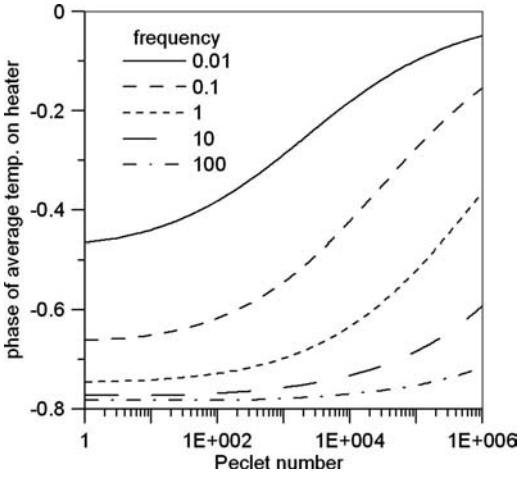

Fig. 7 Phase of spatial-average temperature on the heater for airflow over a polymer wall ($k_1/k_2=0.22$, $\alpha_1/\alpha_2=291$) for various frequencies

Table 1 Typical values of Reynolds and Peclet numbers associated with airflow (Pr=0.69) in a flat-plate boundary layer, and associated frequency values drawn from Fig. 7

Re_x	x (m)	a (m)	$\mathrm{Pe}=ba^2/\alpha_f$	u_∞ (m/s)	ω^+	f (Hz)
Laminar[a]						
10^3	0.1	0.001	$7.24(10^{-1})$	$1.59(10^{-1})$	0.01	0.0366
10^4	0.1	0.001	$2.29(10^{+1})$	1.59	0.10	0.3660
10^5	0.1	0.001	$7.24(10^2)$	$1.59(10^1)$	1.00	3.6600
Turbulent[b]						
10^6	1.0	0.001	$1.29(10^3)$	$1.59(10^1)$	0.1	0.366
10^7	1.0	0.001	$9.31(10^4)$	$1.59(10^2)$	1.0	3.660
10^8	1.0	0.001	$6.70(10^6)$	$1.59(10^3)$	10.0	36.600

[a] $c_f=0.664\,\mathrm{Re}_x^{-1/2}$.
[b] $c_f=0.027\,\mathrm{Re}_x^{-1/7}$ (Ref. [33], Chap. 7).

of Pe-sensitive behavior begins at a much higher Peclet number, and the Peclet-sensitive range is much wider. Note the low frequencies involved at a given Peclet number. For frequency $\omega^+=1$ the phase varies strongly only for $\mathrm{Pe}>10^4$. This normalized frequency corresponds to $\omega=\omega^+\alpha_1/a^2$, which represents $f=\omega/(2\pi)=3.58$ Hz for a heater with $a=1$ mm in airflow. Making the heater larger should help by increasing the Peclet number (recall $\mathrm{Pe}=ba^2/\alpha_1$); however, increasing the heater size also increases ω^+ by the same factor, leaving the phase relationship unchanged. Increasing the heater size should, however, have the effect of increasing the signal size.

A rough estimate of the precision of the phase-based shear-stress measurement can be inferred from Fig. 7. At frequency $\omega^+=1$, over the shear-stress range $(10^4<\mathrm{Pe}<10^5)$, the phase varies over the range $(-0.64,-0.52)$ rad or $(-36.6,-29.8)$ deg. The average slope over this region is $d(\mathrm{Pe})/d(\mathrm{phase})\approx 13{,}000\ \mathrm{deg}^{-1}$. If the phase can be measured to within ± 0.01 deg with a lock-in amplifier, a conservative value [28], then the precision of the shear-stress measurement is approximately $13{,}000\times(\pm 0.01)/10^5\times 100\%=\pm 0.13\%$ at $\mathrm{Pe}=10^5$. As the calibration curve (Fig. 7) is nonlinear, the precision will vary somewhat with frequency and flow range.

The relationship between dimensionless parameters and a specific airflow geometry is given next. Table 1 contains values for Reynolds and Peclet numbers associated with airflow in a flat-plate boundary layer in both laminar and turbulent regimes. The Peclet number depends on the velocity gradient b at the plate surface, which is found from the skin-friction correlations given below the table. The assumed heater size is 1 mm. For each flow situation given in Table 1, a representative frequency is given, drawn from Fig. 7, at which the phase of the observed sensor signal is sensitive to the shear stress. The values in Table 1 show that higher frequencies are associated with higher shear-stress values. The range of frequencies associated with the airflows shown in the table are attainable with conventional electronic equipment.

As indicated above, Fig. 7 is a simulated calibration curve for shear stress found from phase angle. For most sensors such a calibration curve is found from a flow calibration. In the next section a thermal calibration procedure is discussed.

Thermal Calibration. In gas flows, the flow calibration of thermal shear-stress sensors is installation dependent, because the sensor creates a large "heat island" on the wall in which it is mounted [19]. Several researchers have studied in situ flow calibrations [17,18] in an attempt to experimentally compensate for the effects of the wall on the sensor. This section contains a discussion of thermal calibration, which involves analyzing the sensor response without the presence of fluid flow to determine the sensor thermal properties. This is analogous to obtaining the tare weight on a scale or the null reading in a gage. Once the thermal properties of the sensor are obtained, then the sensor flow response can be interpreted with suitable data-analysis techniques. This idea has previously been explored with a steadily heated sensor [13].

The thermal calibration procedure is essentially the measurement of the thermal properties of the sensor substrate; that the thermal properties of a solid can be reliably measured with a small, periodically heated region is well documented [34,35]. The thermal calibration procedure is the following: Energize the in situ sensor with a steady-periodic signal at Peclet=0 (no fluid flow) at several frequencies, measure the sensor response at each frequency, and systematically compare the actual response to the two-body simulated response to determine the wall thermal properties. The wall conductivity k_2 and the wall diffusivity α_2 are to be sought.

This procedure for measuring thermal properties is a type of inverse problem. An important part of every multiple-parameter inverse problem are the sensitivity coefficients. For successful estimation of multiple parameters, the sensitivity coefficients must be large and linearly independent (equivalently they must have different shapes when plotted) [36]. For measurement of wall properties, the sensitivity coefficients are derivatives of the data with respect to the sought-after parameters. Let X be the sensitivity coefficient, given by

$$X_i=m_i\frac{\partial T}{\partial m_i} \tag{31}$$

where $m_i=k_2$ or α_2. The sensitivity coefficients have been computed from the temperature simulation by a finite difference as follows:

$$X_i\approx m_i\frac{T(m_i(1+\epsilon))-T(m_i)}{\epsilon m_i} \tag{32}$$

and are plotted in Figs. 8 and 9 for the air/polymer case. To repeat, the sensitivities must be large and linearly independent for a successful inverse calculation. The amplitudes of the sensitivities, Fig. 8, become small at higer frequencies, which indicates that there is an upper limit on useful frequencies. Also, at higher frequency, the amplitide of sensitivity tends to have the same descending shape, which is another indication that higher frequencies are not useful. At smaller frequency, the amplitude of the sensitivity has a limiting value, indicating that there is also a lower bound on useful frequencies.

The phases of sensitivities, Fig. 9, are large and of differing shape, especially at the middle-to-higher freqencies shown. Frequencies above $\omega^+=100$ probably will not contribute further because both curves flatten out, and any region where the curves have the same shape indicates a lack of linear independence. Frequencies below $\omega^+=0.001$ probably do not contribute further be-

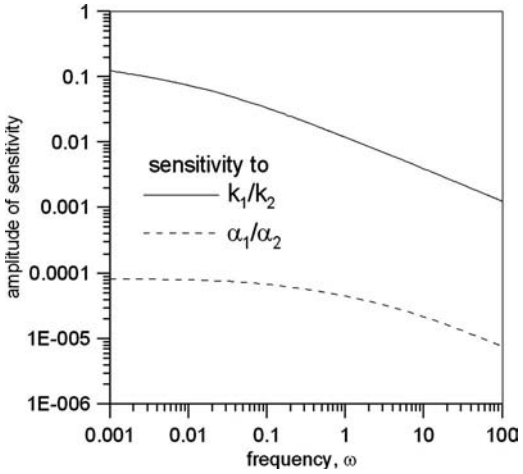

Fig. 8 Amplitude of sensitivity of temperature to thermal properties, computed for the air/polymer case with Pe=0 (no air velocity)

cause one curve approaches zero. These sensitivity curves suggest that for successful measurement of wall properties, data would need to be collected from several frequencies over the range shown.

The sensitivity curves shown here suggest that both conductivity and diffusivity of the wall could be found from both amplitude and phase data. Phase data are probably more important because the phase sensitivity is large, especially at higher frequencies. For further discussion of thermal-property measurements based on phase data, see Refs. [34,37].

There are several ways that thermal calibration could change the way shear-stress sensors are used. For example, some hot-film sensors are factory-built units, which are installed in a cavity on the fluid-flow boundary. If the wall thermal properties are measured pre-install and postinstall, and are unchanged, then the factory calibration could be used for the fluid-flow measurement. As another example, if the in situ wall thermal properties are unchanged before and after a fluid-flow test, then the flow calibration could not have changed during the test. Finally, for situations where flow calibration is inconvenient, such as for high speed, high altitude conditions, the thermal calibration could be combined with the analytical methods discussed in this paper to construct simulated calibration curves. The fluid-flow values inferred from this approach would, however, be limited by the veracity of the thermal model of the sensor.

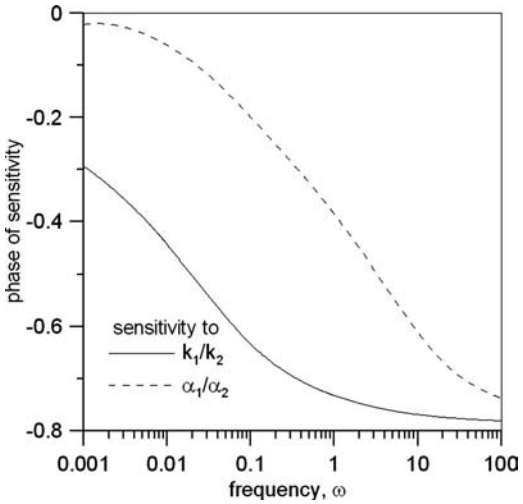

Fig. 9 Phase of sensitivity of temperature to thermal properties, computed for the air/polymer case with Pe=0 (no air velocity)

Computing Issues. Considerable programming effort was needed to obtain efficient evaluation of the β-inversion integral in Eqs. (24) and (25). The CPU time required for the numerical integration was greatly decreased by the recognition that the integrand contains a sinusoidal factor, with zero crossings at 0, $\pm 2\pi$, $\pm 4\pi$, and so on. The integrand has a maximum magnitude at $\beta = 0$ and the magnitude shrinks towards zero as $\beta \rightarrow \pm\infty$. To take advantage of this form, the improper integral on $0 < \beta < \infty$ was replaced with a summation of proper integrals, each of width 2π, beginning at $\beta = 0$. Additional terms of this series were added until the fractional change in the magnitude of the running sum was less than a tolerance to provide five-digit precision. The integral over $-\infty < \beta < 0$ was handled in a similar way.

Computations were carried out on a Sun Blade 2000 with dual 900 MHz processors running the Solaris operating system. The theory was coded in FORTRAN 77 with variables of type double-precision complex. As an example of the computer time required for numerical results, about 20 min was required to compute each curve in Fig. 3, which is composed of 300 points.

Athough the numerical results presented here are based on exact theory, they have been found from numerical integration. Two comments are in order as to whether the results could have been found from a fully numeric calculation (such as finite-difference or finite-element methods). First, fully numeric methods are ill suited to geometries with widely diverse length scales such as this one (thin, small heater on a large domain). A very large number of nodes would be needed near the edges of the heater and many nodes would be needed far from the heater to fill the large domain. Further, since the spatial extent of the thermal boundary layer is both velocity and frequency dependent (see Figs. 2 and 3) the nodal mesh would have to be regenerated many times, consuming considerable computer resources, to cover the same range of results given here. Second, the numerical-integration results have been checked against independent limiting cases to four-digit accuracy and were repeatable to five-digit precision; similar accuracy from a fully numeric calculation, if possible at all, would be prohibitively time consuming.

Summary

The steady-periodic heated film discussed in this paper has several distinct advantages over traditional steadily heated sensors. First, the periodic-heated sensor can be tuned, via frequency, to the shear-stress level of interest. Second, if a lock-in amplifier is used to measure the sensor response, the phase response alone can be used to measure the fluid shear stress, which is important because phase measurements are less sensitive to signal drift caused by electronic amplifiers compared to amplitude measurements. Third, the same lock-in amplifier that gives the flow response can be used for in situ measurement of the sensor thermal properties. This thermal calibration could be used before and after an experiment to verify that the flow calibration has not changed. Finally, for situations where flow calibration is difficult or impossible, the thermal calibration could be used to construct simulated flow-calibration curves based on the analytical techniques presented here.

The present work is limited to steady shear stress. Considerable effort would be needed to include an arbitrary time-varying shear stress, because the analytical advantage of steady-periodic behavior would be lost. One approach is a hybrid scheme in which an analytic solution in the wall could be matched to a fully numeric solution in the fluid flow.

Acknowledgment

The author gratefully acknowledges support from NASA,, Washington DC, under EPSCOR Program Contract No. NCC5-

165. Thanks also go to Gregg Noffz at NASA Dryden for several valuable discussions of hot-film sensors.

Nomenclature

- Ai = Airy function, Eq. (30)
- a = size of heated region
- b = fluid velocity gradient (s^{-1})
- B_2 = effect of volume generation, Eq. (10)
- c = specific heat ($J\,kg^{-1}\,K^{-1}$)
- f = known effect at boundary i
- g = internal heating at frequency ω
- G = steady-periodic GF ($s\,m^{-2}$)
- h = heat transfer coefficient ($W\,m^{-2}\,K^{-1}$)
- j = imaginary number, $\sqrt{-1}$
- k = thermal conductivity ($W\,m^{-1}\,K^{-1}$)
- m = parameter, Eq. (31)
- n = outward-facing unit normal vector on a boundary
- q = steady-periodic heat flux ($W\,m^{-2}$)
- Pe = Peclet number, ba^2/α_1
- s_i = surface area of boundary i
- S_M = coefficient for kernel function in Eq. (B6)
- t = time (s)
- T = steady-periodic temperature (K)
- X = sensitivity coefficient, Eq. (31)
- z = defined above Eq. (A7)

Greek

- α = thermal diffusivity ($m^2\,s^{-1}$)
- β = wave number, Eq. (14) (m^{-1})
- δ = Dirac delta function
- ν = defined for Eq. (B5)
- ρ = defined above Eq. (A6)
- ϕ = influence function, Eq. (20)
- ω = frequency ($rad\,s^{-1}$)
- Ω = domain

Superscripts

- $\sim$ = time-domain quantity
- $-$ = spatial Fourier transform, Eq. (13)

Subscripts

- 1 = fluid
- 2 = solid
- h = heater
- i = index

Appendix A: Fluid-Side Green's Function

In this appendix the GF for the steady-periodic temperature in a shear flow is developed. The GF associated with the time-periodic problem satisfies the following energy equation (subscript 1 has been supressed in this section):

$$\frac{j\omega}{\alpha}G + by\frac{\partial G}{\partial x} = \frac{\partial^2 G}{\partial x^2} + \frac{\partial^2 G}{\partial y^2} + \frac{1}{\alpha}\delta(x-x')\,\delta(y-y') \tag{A1}$$

The boundary conditions are as follows:

$$\text{at } y = 0, \quad \frac{\partial G}{\partial y} = 0 \tag{A2}$$

$$\text{at } y \to \infty, \quad \partial G \text{ is bounded} \tag{A3}$$

and

$$\text{at } x \to \pm\infty, \quad \partial G \text{ is bounded} \tag{A4}$$

A Type 2 boundary (specified flux) is used at $y=0$ to be consistent with the flux condition used in Eq. (10). The solution for G will be found with a Fourier transform along x. First, use a simple change of variable to replace $(x-x')$ with x. Then apply Eq. (13) to the above differential equation and boundary conditions to find

$$\frac{d^2\bar{G}}{\partial y^2} - \left(\frac{j\omega}{\alpha} + \beta^2 + \frac{byj\beta}{\alpha}\right)\bar{G} = -\frac{1}{\alpha}\delta(y-y') \tag{A5}$$

Let $p = b\beta j/\alpha$, $\rho = j\omega/\alpha + \beta^2 + py$. Then the differential equation can be written as

$$\frac{d^2\bar{G}}{\partial y^2} - \rho\bar{G} = -\frac{1}{\alpha}\delta(y-y') \tag{A6}$$

This second-order, ordinary differential equation can be transformed into the Airy equation with a change of variable to $z = \rho/p^{2/3}$. The solution to this equation will be sought by splitting the domain at $z=z'$ into two regions. That is, we seek solutions

$$\frac{d^2\bar{G}_a}{\partial z^2} - z\bar{G}_a = 0, \quad z_0 < z < z' \tag{A7}$$

$$\frac{d^2\bar{G}_b}{\partial z^2} - z\bar{G}_b = 0, \quad z' < z < \infty \tag{A8}$$

$$\text{where } z_0 = z|_{y=0} \tag{A9}$$

$$\text{and } z' = z|_{y=y'} \tag{A10}$$

The general solution is given by

$$\bar{G}_a(z) = C_1\,\mathrm{Ai}(z) + C_2\,\mathrm{Bi}(z) \tag{A11}$$

$$\bar{G}_b(z) = C_3\,\mathrm{Ai}(z) + C_4\,\mathrm{Bi}(z) \tag{A12}$$

where $\mathrm{Ai}(z)$ and $\mathrm{Bi}(z)$ are Airy functions (Ref. [38], p. 448) and C_j are constants. As there are four undetermined constants, four conditions are needed. Two are boundary conditions on y, restated here in terms of z,

$$\text{at } z = z_0, \quad \frac{\partial\bar{G}_a}{\partial z} = 0 \tag{A13}$$

$$\text{at } z \to \infty, \quad \bar{G}_b \text{ is bounded} \tag{A14}$$

A matching condition is required at $z=z'$, that is,

$$\bar{G}_a(z') = \bar{G}_b(z') \tag{A15}$$

There is also a jump condition at $z=z'$, found by integrating Eq. (A6) over $(y'-\epsilon, y'+\epsilon)$, taking the limit as $\epsilon \to 0$, and converting d/dy to d/dz with the chain rule as follows:

$$\left.\frac{d\bar{G}_b}{\partial z}\right|_{z=z'} - \left.\frac{d\bar{G}_a}{\partial z}\right|_{z=z'} = -\frac{1}{\alpha p^{1/3}} \tag{A16}$$

With these four conditions the four constants may be determined algebraically and substituted into the general solution. The GF for a Type 2 boundary at $y=0$ is given by

$$\bar{G}(z,z') = \begin{cases} [\mathrm{Ai}'(z_0)\mathrm{Bi}(z) - \mathrm{Bi}'(z_0)\mathrm{Ai}(z)]\dfrac{\mathrm{Ai}(z')}{\alpha p^{1/3} D}, & z < z' \\ [\mathrm{Ai}'(z_0)\mathrm{Bi}(z') - \mathrm{Bi}'(z_0)\mathrm{Ai}(z')]\dfrac{\mathrm{Ai}(z)}{\alpha p^{1/3} D}, & z > z' \end{cases}$$

where

$$D = [\mathrm{Bi}'(z')\mathrm{Ai}(z') - \mathrm{Ai}'(z')\mathrm{Bi}(z')]\mathrm{Ai}'(z_0)$$

As expected, this GF satisfies reciprocity: $\bar{G}(z,z') = \bar{G}(z',z)$.

Special case for heating at the wall. The special case of the fluid response to heating at the wall has been published previously [7]. In this case, $z' \to z_o$, and the expression for $\bar{G}$ simplifies to

$$\bar{G}(z,z_0) = -\frac{1}{\alpha p^{1/3}} \frac{\mathrm{Ai}(z)}{\mathrm{Ai}'(z_0)} \tag{A17}$$

This is the fluid-side GF used in the numerical examples.

The complex-valued Airy function needed for this GF was computed from series expressions. Expressions for $\mathrm{Ai}(z)$ and $\mathrm{Ai}'(z)$ for small-z and large-z values (Ref. [38], pp. 446–448) were coded in FORTRAN and spot-checked against a commercial mathematics code. Numerical values were highly accurate at small-$|z|$ and large-$|z|$, with a minimum of five-digit accuracy at intermediate values near $|z|=5$.

Appendix B: Solid-Side Green's Function

The GF for the steady-periodic temperature in the solid satisfies the following differential equation (subscript 2 has been suppressed in this section):

$$\frac{j\omega}{\alpha} G = \frac{\partial^2 G}{\partial x^2} + \frac{\partial^2 G}{\partial y^2} + \frac{1}{\alpha}\delta(x-x')\delta(y-y') \tag{B1}$$

The boundary conditions are as follows:

$$\text{at } x \to \pm\infty, \quad \partial G \text{ is bounded} \tag{B2}$$

$$\text{at } y = 0, \quad \frac{\partial G}{\partial y} = 0 \tag{B3}$$

$$\text{at } y = W, \quad k\frac{\partial G}{\partial y} + hG = 0 \tag{B4}$$

For the semi-infinite body, replace the condition at $y=W$ with a boundedness condition at $(y\to\infty)$. For the present work, the spatial-Fourier transform of this GF is needed. First use a simple change of variable to replace $(x-x')$ with x. Then apply the Fourier transform, Eq. (13), to the above differential equation, to find

$$\frac{d^2\bar{G}}{\partial y^2} - \nu^2\bar{G} = -\frac{1}{\alpha}\delta(y-y') \tag{B5}$$

where $\nu^2=\beta^2+j\omega/\alpha$. The solution for this GF in Fourier space is given by [32]

$$\bar{G}(y,y',\nu) = \frac{S_2^-(e^{-\nu(2W-|y-y'|)} + e^{-\nu(2W-y-y')})}{2\alpha\nu(S_2^+ - S_2^- e^{-2\nu W})} + \frac{S_2^+(e^{-\nu(|y-y'|)} + e^{-\nu(y+y')})}{2\alpha\nu(S_2^+ - S_2^- e^{-2\nu W})} \tag{B6}$$

Coefficients S_2^+ and S_2^- depend on the type of boundary condition at Side 2 $(y=W)$ and are given by

$$S_2^+ = \begin{cases} 1 & \text{Type 0, Type 1, or Type 2} \\ k\nu + h & \text{Type 3} \end{cases}$$

$$S_2^- = \begin{cases} 0 & \text{Type 0} \\ -1 & \text{Type 1} \\ 1 & \text{Type 2} \\ k\nu - h & \text{Type 3} \end{cases}$$

To find the GF in x-space an inverse-Fourier transform is needed. However, in the present work the GF is used to find the temperature in Fourier transform space and then the inverse-Fourier transform is applied to the temperature solution.

Special case for heating at $y=0$. In the special case with localized heating at the fluid-solid surface, the GF may be simplified. Replace $y'=0$ with the above expression to find

$$\bar{G}(y,0,\nu) = \frac{S_2^-(e^{-\nu(2W-|y|)} + e^{-\nu(2W-y)})}{2\alpha\nu(S_2^+ - S_2^- e^{-2\nu W})} + \frac{S_2^+(e^{-\nu(|y|)} + e^{-\nu y})}{2\alpha\nu(S_2^+ - S_2^- e^{-2\nu W})} \tag{B7}$$

Finally, for the solution to the conjugate problem, the temperature is also evaluated at the fluid-solid interface. Replace $y=0$ with the above expression to obtain

$$\bar{G}(0,0,\nu) = \frac{S_2^+ + S_2^- e^{-2\nu W}}{\alpha\nu(S_2^+ - S_2^- e^{-2\nu W})} \tag{B8}$$

This expression, with the appropriate coefficients given above, is the solid-side GF used in the numerical examples.

References

[1] Ludwieg, H., 1950, "Instrument for Measuring the Wall Shearing Stress of Turbulent Boundary Layers," NACA Report No. TN 1284.

[2] Mayer, R., Henkes, R. A. W. M, and Van Ingen, J. L., 1988, "Quantitative Infrared Thermography for Wall Shear Stress Measurement in Laminar Flow," Int. J. Heat Mass Transfer, **41**, pp. 2347–2360.

[3] Baughn, J. W., Mayhew, J. E., Butler, R. J., Byerley, A. R., and Rivir, R. B., 1999, "Turbine Blade Flow Separation and Reattachment at Low Reynolds Number," ASME J. Heat Transfer, **121**(3), poster insert.

[4] Stone, H. A., 1989, "Heat/Mass Transfer From Surface Films to Shear Flows at Arbitrary Peclet Numbers," Phys. Fluids A, **1**(7), pp. 1112–1122.

[5] Phillips, C. G., 1990, "Heat and Mass Transfer From a Film Into Steady Shear Flow," Q. J. Mech. Appl. Math., **43**, pp. 135–160.

[6] Soliman, M., and Chambre, P. L., 1967, "On the Time-Dependent Leveque Problem," Int. J. Heat Mass Transfer, **10**, pp. 169–179.

[7] Geshev, P. I., 1996, "The Green Function Method for Calculating Characteristics of a Small Strip-Shaped Shear Stress Probe," J. Electroanal. Chem., **410**, pp. 1–8.

[8] Steenhoven, A. A., and van de Beuken, F. J. H. M., 1991, "Dynamical Analysis of Electrochemical Wall Shear Rate Measurements," J. Fluid Mech., **231**, pp. 599–614.

[9] Cole, K. D., 1997, "Conjugate Heat Transfer From a Small Heated Strip," Int. J. Heat Mass Transfer, **40**(11), pp. 2709–2719.

[10] Harman, S., 1998, "Conjugate Heat Transfer: Effects of Axial Conduction and the Layered Wall," MS thesis, University of Nebraska, Mechanical Engineering Department, Lincoln, NE.

[11] Stein, C. F., Johansson, P., Bergh, J., Löfdahl, L., Sen, M., and Gad-el-Hak, M., 2002, "An Analytical Solution to a Conjugate Heat Transfer Problem," Int. J. Heat Mass Transfer, **45**(12), pp. 2485–2500.

[12] Chao, J. H., Shyy, W., Thakur, S. S., Sheplak, M., and Mei, R. W., 2005, "Effect of Conjugate Heat Transfer on MEMS-Based Thermal Shear Stress Sensor," Numer. Heat Transfer, Part A, **48**(3), pp. 197–217.

[13] Cole, K. D., and Beck, J. V., 1988, "Conjugated Heat Transfer From a Hot Film Probe for Transient Air Flow," ASME J. Heat Transfer, **110**, pp. 290–296.

[14] Liang, P. W., and Cole, K. D., 1992, "Conjugated Heat Transfer From a Rectangular Hot-Film With the Unsteady Surface Element Method," J. Thermophys. Heat Transfer, **6**, pp. 349–355.

[15] Cole, K. D., 2002, "Analysis of Pulse Heating on a Fluid-Cooled Surface for Fluid Shear Stress," *Proceedings, International Mechanical Engineering Congress and Exposition*, New Orleans, LA, Paper No. 2-20-5-5.

[16] Dinu, C., Beasley, D. E., and Figliola, R. S., 1998, "Frequency Response Characteristics of an Active Heat Flux Gage," ASME J. Heat Transfer, **120**, pp. 557–582.

[17] Bellhouse, D. J., and Schultz, D. S., 1967, "The Determination of Flucuating Velocity in Air With Heated Thin-Film Gages," Phys. Fluids, **29**, pp. 289–295.

[18] Alfredsson, P. H., Johansson, A. V., Haritonidis, J. H., and Eckelmann, H., 1988, "On the Fluctuating Wall Shear Stress and the Velocity Field in the Viscous Sublayer," Phys. Fluids, **31**, pp. 1026–1033.

[19] Reda, D. C., 1991, "Rise-Time Response of Nickel-Foil-on-Kapton-Substrate, Hot-Film Shear-Stress Sensors," *Proceedings of the 29th Aerospace Sciences Meeting*, Reno, NV, Paper No. AIAA-91-0169.

[20] Tardu, F. S., and Pham, C. T., 2005, "Response of Wall Hot-Film Gages With Longitudinal Diffussion and Heat Conduction to the Substrate," ASME J. Heat Transfer, **127**, pp. 812–819.

[21] Gustafsson, S. E., Chohan, M. A., Ahmed, K., and Maqsood, A., 1984, "Thermal Properties of Thin Insulating Layers Using Pulse Transient Hot Strip Measurements," J. Appl. Phys., **55**(9), pp. 3348–3353.

[22] Zhong, Q. Y., Favro, L. D., and Thomas, R. L., 2000, "Thermal Wave Reflections of a Pulsed Stripe Heat Source From a Plane Boundary," J. Appl. Phys., **87**, pp. 3999–4004.

[23] Cahill, D. G., 1990, "Thermal Conductivity Measurement From 30 to 750 K: the 3ω Method," Rev. Sci. Instrum., **61**, pp. 802–808.

[24] Cole, K. D., and McGahan, W. A., 1993, Theory of Multilayers Heated by Laser Absorption, ASME J. Heat Transfer, **115**, pp. 767–771.

[25] Hu, H., Wang, X., and Xu, X., 1999, "Generalized Theory of the Photoacoustic Effect in a Layered Material," J. Appl. Phys., **86**, pp. 3953–3958.

[26] Bonne, U., and Kubisiak, D., 2001, "Actuation-Based Microsensors," Smart

Mater. Struct., **10**(6), pp. 1185–1195.
[27] Al-Salaymeh, A., and Durst, F., 2004, "Development and Testing of a Novel Single-Wire Sensor for Wide Range Flow Velocity Measurements," Meas. Sci. Technol., **15**(5), pp. 777–788.
[28] Chung, W. S., Kwon, O., Choi, D. S., Park, S., Choi, Y. K., and Lee, J. S., 2004, "Tunable AC Thermal Anemometry," Superlattices Microstruct., **35**(3–6), pp. 325–338.
[29] Rachalski, A., 2006, "High-Precision Anemometer With Thermal Wave," Rev. Sci. Instrum., **77**(9), p. 095107.
[30] Mandelis, A., 2001, *Diffusion-Wave Fields, Mathematical Methods and Green's Functions*, Springer, New York.
[31] Beck, J. V., Cole, K. D., Haji-Sheikh, A., and Litkouhi, B., 1992, *Heat Conduction Using Green's Functions*, Hemisphere, New York.
[32] Cole, K. D., 2006, "Steady-Periodic Green's Functions and Thermal-Measurement Applications in Rectangular Coordinates," ASME J. Heat Transfer, **128**(7), pp. 709–716.
[33] White, F. M., 1999, *Fluid Mechanics*, 4th ed., McGraw-Hill, New York.
[34] Haji-Shiekh, A., Hong, Y. S., You, S. M., and Beck, J. V., 1998, "Sensitivity Analysis for Thermophysical Property Measurements Using the Periodic Method," ASME J. Heat Transfer, **120**(3), pp. 568–576.
[35] Aviles-Ramos, C., Haji-Shiekh, A., Beck, J. V., and Dowding, K. J., 2001, "Estimation of Thermophysical Properties by the Spectral Method-Development and Evaluation," ASME J. Heat Transfer, **123**(1), pp. 24–30.
[36] Dowding, K. J., and Blackwell, B. F., 2001, "Sensitivity Analysis for Nonlinear Heat Conduction," ASME J. Heat Transfer, **123**, pp. 1–10.
[37] Cole, K. D., 2004, "Analysis of Photothermal Characterization of Layered Materials—Design of Optimal Experiments," Int. J. Thermophys., **25**, pp. 1567–1584.
[38] Abramowitz, M., and Stegun, I., 1964, *Handbook of Mathematical Functions*, Dover, New York.

Large-Scale Pulsation Detection by Means of Temperature Measurements

N. Silin

V. Masson

Consejo Nacional de Investigaciones Científicas y Técnicas,
Avenida Bustillo 9500 CAB, Bariloche,
Río Negro 8400, Argentina

A. Rauschert

Comisión Nacional de Energía Atómica,
Avenida del Libertador 8250,
Buenos Aires 1429, Argentina

In the present work we explore the potential of time-resolved temperature measurements to obtain information on large-scale pulsations in a rod bundle geometry with axial flow. Large-scale flow pulsation is the phenomenon that dominates the turbulent mixing between the subchannels of rod bundles, which explains why it is of great importance for the design or assessment of nuclear fuel elements. The objective of the present work is to determine the characteristics of large-scale pulsations that can be used for the verification or validation of computational fluid dynamics code results. The method proposed is to generate a temperature gradient across the location of flow pulsations and to measure the time-varying temperature field downstream. Pulsation characteristic times, lengths, and traveling speed have been obtained. This study has been performed in a rod bundle similar to a nuclear fuel assembly and the results obtained are in good agreement with previous works on similar geometries. The technique can be applied to obtain additional large-scale structure information in test sections designed for thermal measurements, in situations where convection is dominated by these structures. [DOI: 10.1115/1.2969262]

Keywords: large-scale structures, pulsations, time-resolved thermometry, subchannels, turbulent mixing

1 Introduction

The cores of nuclear power reactors generally consist of parallel nuclear fuel rods arranged in a fuel bundle refrigerated by a coolant that flows in the axial direction. The coolant flows through the open areas between the rods, called subchannels, and mixes mass, momentum, and enthalpy with neighboring subchannels through the gaps between the rods. The distributions of enthalpy and refrigerating flow in a fuel bundle are therefore highly dependent on this mixing process.

Various experiments for estimating the turbulent mixing rate between subchannels showed that turbulent mixing is higher than expected by isotropic turbulence models, and independent of gap size [1]. Further investigations revealed the existence of large-scale and almost periodic pulsations through the gap [2] and showed that these pulsations were the dominating phenomenon in the mixing process [3]. Pulsations occur through the gaps between two rods and form trains of alternating vortices [4], as shown in Fig. 1(*a*). Similar pulsations have been found under a variety of other geometries including channels with longitudinal fins, rectangular channels connected by a slot, and rivers or channels with lateral flooding planes [5] (Fig. 1(*b*)). In all these cases the large-scale pulsations dominate the mixing process. It has also been shown that when modeling these kinds of flows, realistic results can only be achieved if large-scale pulsations are taken into account [6]. These pulsations may also have other important effects on the fuel element. For example, they can produce flow-induced vibrations that, in the long term, could compromise the fuel element integrity.

Measurements related to the large-scale pulsation phenomenon have been usually performed in adiabatic test sections to provide information on the fluid-dynamic aspect. Only a few measurements, particularly those performed by Meyer [7] and Krauss and Meyer [8,9], include the use of heated rods and time-resolved temperature measurements. Yet these measurements have been performed in conditions such that the temperature gradients across the gaps are zero, thus making it not possible to calculate the azimuthal eddy diffusivities of heat in the gap. However, the measurements presented by Krauss and Meyer [8] do show increasing values of azimuthal eddy diffusivity of heat toward the gap between rods. He also analyzed the power spectra of velocity and temperature fluctuations next to the gap. The maxima of the autopower spectrum of velocity and temperature fluctuations are located at the same frequency, corresponding to the flow-pulsation characteristic frequency. He also presented the cross power spectrum of azimuthal velocity and temperature fluctuations, which also shows a maximum at the same frequency, clearly indicating the relationship between the involved transport processes.

It is worth mentioning that the large-scale pulsations have an almost periodic nature, i.e., the size of the structures producing the pulsations is not constant but varies within certain limits, and the

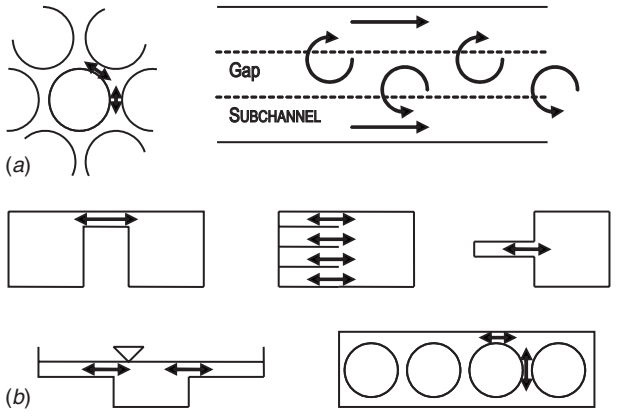

Fig. 1 Large-scale pulsations (*a*) in a rod bundle and (*b*) in rectangular channels connected by a gap, in a channel with fins, in a channel with a lateral slot, in a river with flooded planes, and in rods inside a duct

Contributed by the Heat Transfer Division of ASME for publication in the JOURNAL OF HEAT TRANSFER. Manuscript received April 4, 2007; final manuscript received April 17, 2008; published online September 4, 2008. Review conducted by Bengt Sunden.

sequence of pulsations may also be interrupted occasionally. These factors make the peak in the auto- and cross power spectra broader, being broadest for a larger rod spacing [10].

The existence of this macroscopic flow process, i.e., flow pulsations, dominating the turbulent mixing of heat across the gaps between rods has thus various implications. The first one is that large-scale pulsations become more intense for smaller rod spacings, which causes the mixing rate to have high values and to be nearly independent of the gap width, as was mentioned above. The second implication is that as flow pulsations are a macroscopic flow process involving the regions adjacent to the gaps, and as this process is almost periodic, fluctuating components of velocity and temperature show high auto- and cross-correlation values in this area and share the same periodicity.

Because of the importance of rod bundle heat transfer, in terms of nuclear power plant economics as well as in terms of safety, it is necessary that the model used in its assessment predicts accurately the occurrence of these large-scale pulsations at different flow rates and in different geometrical arrangements. This is a difficult task because pulsations in different gaps connected to the same subchannel have a strong interaction [7,11], making models based on local conditions alone not reliable. In other words, mixing rates and other flow data obtained on a simplified geometry may not reflect what is happening in a complete fuel bundle.

Most experimental works on the subject are based on anemometric data, either thermal anemometry or laser Doppler anemometry, providing very comprehensive experimental data on the flow field and the turbulent transport. These methods are quite costly and difficult to apply to the diverse geometries found in nuclear fuel elements, which include nonhomogeneous arrangements and a large number of different spacers and end-plates. In this context a simpler and more versatile experimental technique would be useful for the evaluation of mixing and pulsation behavior in nuclear fuel prototypes.

In some early works on nuclear fuel bundles using heated experimental devices, temperature fluctuations have been reported. These fluctuations were presumably caused by the passage of large-scale pulsations [12]. Temperature measurements have also been used in the study of Rayleigh–Bénard convection cavities, where temperature fluctuations are analyzed for the detection of large-scale coherent flow patterns and the identification of different turbulent states [13]. These experiments suggest the possibility of detecting large-scale structures through the measurement of temperature fluctuations.

The technique proposed here is to generate a temperature gradient across the mixing area, i.e., the gap between rods, and to measure the temperature fluctuations caused by large-scale pulsations. As mentioned above in rod bundles the mixing is dominated by large-scale pulsations that have a high correlation between temperature and velocity fluctuations in the gap area. In this situation temperature measurements reflect the periodicity of the flow pulsations in the gap. This opens the possibility to retrieve additional flow information in experimental devices that do not allow for velocity measurements, which is very common in test sections meant for heat transfer coefficient measurements.

As a result we have been able to obtain the pulsation frequency, convection velocity, and streamwise length scale of large-scale pulsations. In the same experimental device we have also measured the mixing rate between subchannels [14]. We have added these measurements for the conditions corresponding to pulsation measurements, finding some interesting tendencies. The pulsation frequency, convection velocity, and mixing rate taken together are very useful information for numerical simulation verification.

2 Experimental Technique

The experimental rig is shown in Fig. 2 and consists of a water tank, a pump, control valves, piping, and a stainless steel test section. The test section has three 10 mm diameter stainless steel rods inside a circular tube of 26.5 mm internal diameter, generating one central and three peripheral subchannels with 120 deg symmetry (Fig. 3(*a*)). The rods' pitch to diameter ratio is 1.205 and the wall gap to diameter ratio is 0.120. The experimental rig is described in detail by Silin and Juanicó [15]. The working fluid is water at room temperature (22°C).

Each rod has a ceramic substrate part with a superficial electrical heater deposited electrochemically (Fig. 4) and forms a continuous surface with the rods to minimize flow perturbation. These heaters face the central subchannel and generate a small temperature gradient between the central and peripheral subchannels (Fig. 3(*b*)). The heating area for each heater is a longitudinal strap 4.5 mm wide and 100 mm long as shown in Fig. 4. The heating of the flow can be thought as the introduction of a passive contaminant: a "thermal trace," similar to the introduction of hot water as described by Chiu and Todreas [16]. The electrical power was supplied by three direct current power sources and adjusted for symmetrical power within 5%. Temperature gradients have also to be kept small to avoid buoyancy effects, so a very sensible thermometric system had to be used. In the present work mean temperature increases were between 0.25 K and 0.6 K.

An attractive characteristic of the present approach in comparison to other tracing methods is that the tracer concentration (temperature) field generated resembles that of the application case, in which the heat is introduced to the flow from the rods walls.

For the measurement of mixing between subchannels a first temperature sensor is located at the test section inlet, upstream the heaters, for a reference temperature. A second sensor is positioned downstream the heaters at different axial distances and then it is

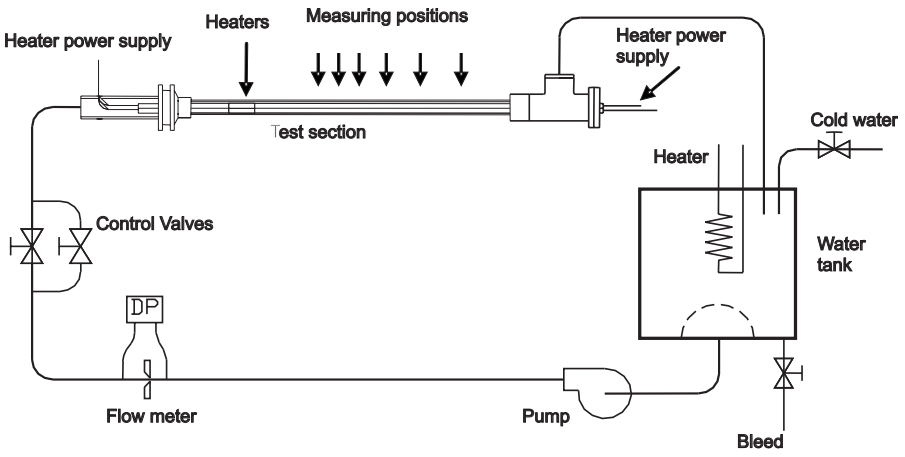

Fig. 2 Experimental loop

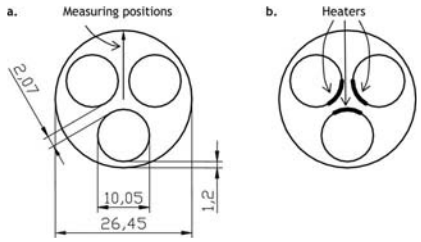

Fig. 3 Test section: (*a*) main dimensions and (*b*) heater strip locations

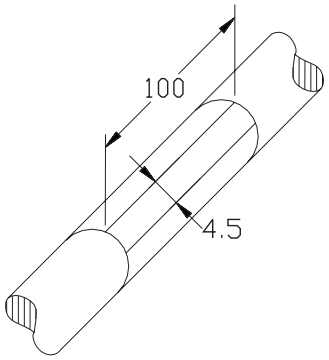

Fig. 4 Superficial strip heaters' dimensions

transversed to measure the temperatures of the central and peripheral subchannels. The transversal measurement line across the superior gap is represented in Fig. 3(*a*). From the decay of the temperature difference between the central and peripheral subchannels we calculate the mixing rate. Details of the experimental technique and calculation procedures can be found in Ref. [14].

For the time-resolved measurements we use two GE thermoprobe model P20 thermistor sensors. These small thermistors provide a relatively rapid response, about 20 ms, in a rugged package and produce a low disturbance. The thermistors can be introduced to the test section through several holes in the outer stainless steel tube. For the pulsation characterization the first thermistor was located at 175 mm downstream the heaters' end and at 4 mm from the test section center in the gap area. The second sensor was located at 50 mm downstream from the first sensor. The thermistors were driven by a homemade electronic circuit that provided a linear response for the temperature range of interest, i.e., between 20°C and 24°C [17]. The signal was amplified and acquired at 1000 samples/s into a personal computer for further processing.

3 Data Processing

The data processing for mixing rate determination is described in detail by Silin et al. [14]. The mixing rate is obtained from the exponential decay of the temperature difference between the central and peripheral subchannels for a hydraulically and thermally developed flow in adiabatic conditions. Adiabatic conditions can be assumed because the fluid is kept at room temperature and viscous dissipation can be neglected. The mixing rate is then calculated from the coefficient of decay of the temperature difference and the calorific capacity of the subchannels. To obtain the flow rates of the central and peripheral subchannels, needed for the mixing rate calculation, we applied the pressure drop coefficients for triangular arrays measured as by Rehme [18]. It is interesting to notice that the pressure drop in this geometry does not present a drag crisis and is smooth in the transition regime.

Data processing for large-scale pulsation detection were based on autocorrelations and cross-correlations of temperature signals. The fluctuating temperature signals carry variations caused not only by large-scale pulsations but also by other phenomena. Besides, flow pulsations through the gap have a quasiperiodic nature, i.e., they may present variations in the periods and pulsation trains that are out of phase. We will discuss the most common analysis techniques for time-resolved turbulent measurements: autocorrelation coefficients, cross-correlation coefficients for two points at different axial positions, and the power spectra for both cases [19].

The cross-correlation of two signals $x(t)$ and $y(t)$ is the expected value of their product as a function of a time lag τ between them. Here we calculate the cross-correlation value as

$$R_{xy}(\tau) = \lim_{T\to\infty} \int_0^T x(t)y(t+\tau)dt \tag{1}$$

In the present work we use the cross-correlation normalized by the standard deviations of the signals, i.e., the cross-correlation coefficient, which is a nondimensional quantity.

$$r_{xy}(\tau) = \frac{R_{xy}(\tau)}{\sigma_x \sigma_y} \tag{2}$$

The cross-correlation coefficient analysis will be applied to the temperature signals from two temperature sensors located one downstream the other. Let us remind that a maximum value for a given delay τ means that there is a high expectancy that the signal in the first sensor will be repeated in the second sensor a time τ later. The autocorrelation is a special case of the cross-correlation of the signal with itself, in the present case the signal of the first sensor. A minimum value for a given delay τ means that there is a high expectancy that for that sensor the signal will be repeated with an opposite sign a time τ later. In all cases the constant (mean) value is subtracted from the signals as we are only concerned with the fluctuations caused by the fluid-dynamic phenomena.

The cross-spectra is obtained as the Fourier transform of the cross-correlation.

$$P_{xy}(\omega) = \frac{1}{2\pi} \int_{-\infty}^{\infty} R_{xy}(\tau) e^{-i\omega\tau} d\tau$$

The power spectrum of a single sensor signal is a particular case in which the autocorrelation is used in place of the cross-correlation.

4 Sensor Response Time

Even though the sensors chosen for the time-resolved temperature measurements are among the fastest commercially available, the thermal time constant of the sensors is not small enough to be neglected. This delay produces a low-pass filtering of the signal in a frequency range close to the large-scale pulsation frequencies, affecting the correlations as well as the power spectra. To overcome this difficulty, a signal enhancement was performed based on the measured time response of the sensors. With this processing the cut-off frequencies of the measurements were extended in one decade.

The sensor relaxation time was measured by means of water plunge tests at different fluid velocities. The results were fitted by the equation

$$\tau_s = C_1 + C_2 u^{-0.6} \tag{3}$$

as suggested by Kerlin et al. [20]. The results for the two sensors used are shown in Fig. 5.

5 Preliminary Results

The objective of the work is to measure large-scale pulsation properties by means of temperature measurements downstream

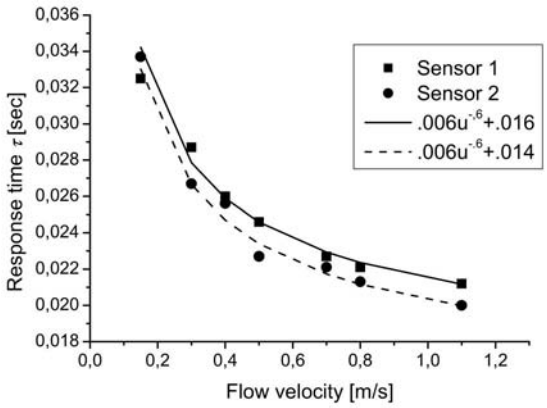

Fig. 5 Time constant of the sensors at different flow velocities as measured by water plunge and fitting curves by Eq. (3)

localized heaters. We performed preliminary measurements to decide the locations of the sensors that would provide the best results. The measurements were performed at a Reynolds number of 2700.

The first measurement series was done with one sensor located in the gap area at different distances downstream the heaters' end. The autocorrelations of these measurements are shown in Fig. 6. It is clear from that figure that the sensor located in position 2, 175 mm downstream from the heaters' end, is the one that best captures the periodic passage of the pulsations. The mixing process downstream makes the autocorrelation broaden and lose the evidence of periodicity.

With one sensor located in the gap at 175 mm from the heaters' end we studied the cross-correlations for the second sensor located in the gap at different distances downstream. The results are shown in Fig. 7. As expected closer the sensors give higher cross-correlation coefficients. For the large-scale pulsation measurements we have adopted a distance of 50 mm to reduce the relative error due to sensor positioning and sensor response time uncertainties.

The flow in the test section is hydrodynamically developed before reaching the heaters; therefore, measurements have to be independent of downstream distance, even though measurement error will vary. To verify this condition we measured the cross-correlations for two sensors separated by 100 mm at different axial positions, as shown in Figs. 8 and 9, and the corresponding cross-spectra (Fig. 10). It can be seen that for far downstream positions the periodic character of the cross-correlation fades but the lag to the maximum stays constant within 2%.

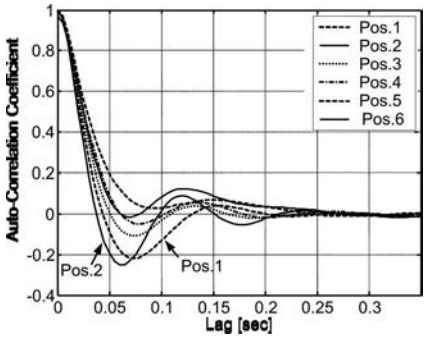

Fig. 6 Autocorrelation coefficient for temperature measurements in the gap area at the following positions: (1) 75 mm, (2) 175 mm, (3) 275 mm, (4) 375 mm, (5) 475 mm, (6) 575 mm, and (7) 675 mm, downstream from the heaters' end

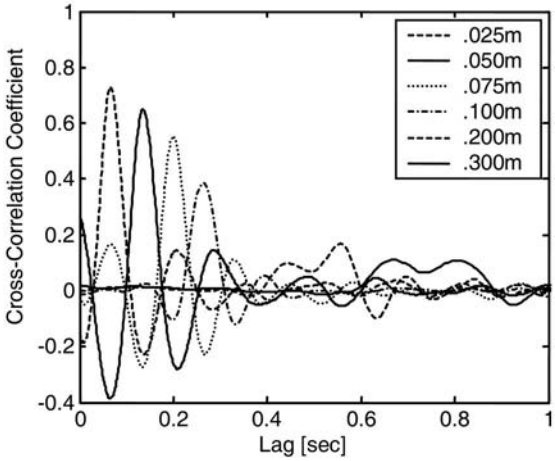

Fig. 7 Cross-correlation coefficient for temperature measurements in the gap area. First sensor at 175 mm from the heaters' end, and second sensor at different positions downstream in the gap.

In Fig. 10 we see that the cross-spectrum spreads as we move downstream but it keeps the general aspect. Only for the measurements at distances larger than 575 mm (80 hydraulic diameters) from the heaters the spectrum gets clearly distorted.

The periodic nature of the pulsations is clear from the oscillatory behavior of the autocorrelation (Fig. 6) and also in the cross-correlations. This periodic nature is reflected in the power spectrum and in the cross-spectrum. In Fig. 11 we see the power

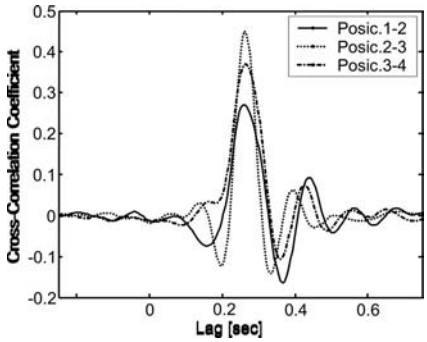

Fig. 8 Cross-correlation coefficient for temperature measurements in the gap area. Sensor positions: (1) 75 mm, (2) 175 mm, (3) 275 mm, and (4) 375 mm, downstream from the heaters' ends.

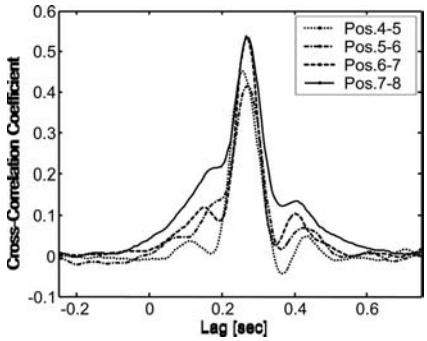

Fig. 9 Cross-correlation coefficient for temperature measurements in the gap area. Sensor positions: (4) 375 mm, (5) 475 mm, (6) 575 mm, (7) 675 mm, and (8) 775 mm, downstream from the heaters' ends.

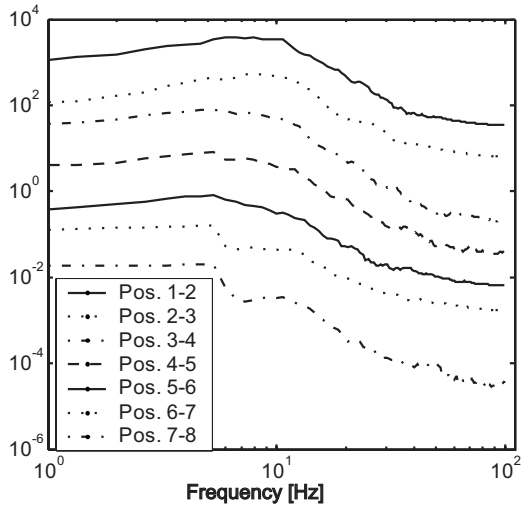

Fig. 10 Cross-spectrum for measurements in the gap area. Sensor positions: (1) 75 mm, (2) 175 mm, (3) 275 mm, (4) 375 mm, (5) 475 mm, (6) 575 mm, (7) 675 mm, and (8) 775 mm.

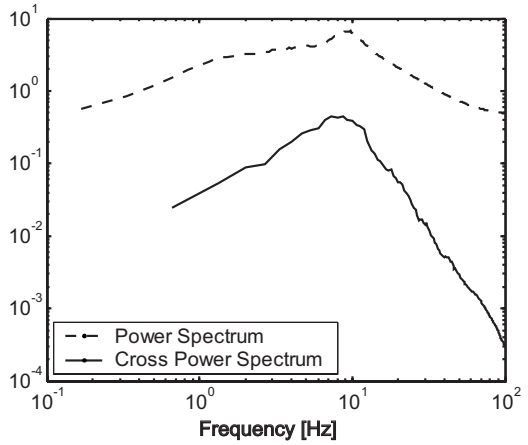

Fig. 11 Power spectrum and cross-spectrum for measurements in the gap area with sensors separated 100 mm

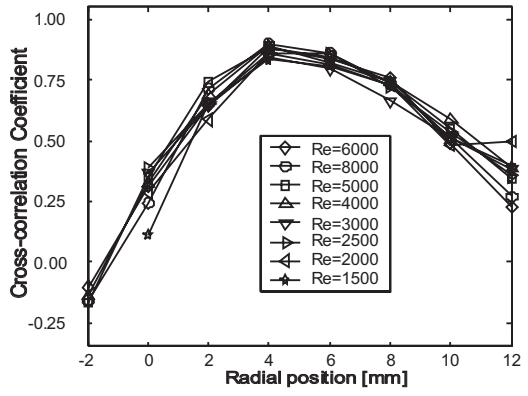

Fig. 12 Maximum cross-correlation coefficients for different Re numbers

spectrum and in the cross-spectrum of a single sensor at position 2 and for a couple of sensors separated 100 mm streamwise at positions 2 and 3, respectively. The cross-spectrum shows a narrower peak because it only accounts for fluctuations that show good correlation between the two sensors, as is the case for large scale pulsations. In this sense the cross-spectrum gives better information on pulsations than the power spectrum.

In Fig. 12 we show the maxima of the cross-correlation coefficients for various Reynolds numbers and radial positions of the downstream sensor. We can see that the maximum values of the correlation coefficients are independent of the Reynolds number. The maximum correlation is found for the radial position at 4 mm from the subchannel center, i.e., in the gap area, but values in the peripheral ($r=10$) and central ($r=0$) subchannels stay relatively high. This is consistent with the assumption that temperature fluctuations are dominated by large-scale pulsations, which are more intense in the gap area but extend into the subchannels.

6 Results

We first analyze the autocorrelations of the temperature signal. In Fig. 13 we can see the autocorrelation coefficients for different Reynolds numbers. The typical method for obtaining an integral time scale is to integrate the autocorrelation coefficient for positive delays, giving a characteristic autocorrelation decay time [19]. In our case, we expect a train of alternating pulsations, caused by the alternating vortices or flow pulsations [21]. Thus we chose to take the time delay to the first local minimum as the macroscopic characteristic time, which can be regarded as half the pulsation period $1/2\tau_P$. The half pulsation periods so obtained are shown in the second column of Table 1 for different Reynolds numbers.

The pulsation passing frequency, f_P, is calculated as the inverse of τ_P. This frequency is shown in Fig. 14, as a function of the Reynolds number. The pulsation frequency shows a linear dependency on the bulk velocity (fluid properties were kept constant). This linear dependency of passing frequency on bulk velocity has been reported in previous works on different experimental geometries [3,12,22].

A typical dimensionless form of the passing frequency is the Strouhal number.

$$\mathrm{Str} = f_p D_h / u^*$$

This number takes into account the velocity gradient that participates in the pulsation generation though the shear velocity u^*. In Fig. 15 we can see that the Strouhal number remains approximately constant within the range of Reynolds numbers measured, but shows a decreasing tendency for smaller Reynolds numbers.

The second analysis we made is the cross-correlation of two temperatures sensors located at a distance $L=50\ \mathrm{mm} \pm 1\ \mathrm{mm}$ from each other in the flow direction. These results are shown in Fig. 16 for different Reynolds numbers. The delay time to the first maximum can be regarded as the pulsation convection (or "propagation") time, τ_{12} (third column of Table 1). The pulsation convection velocity

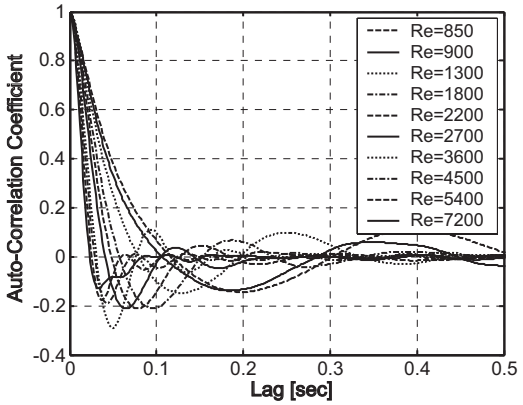

Fig. 13 Autocorrelation coefficient for temperature measurements at 175 mm downstream from the heaters in the gap area

Table 1 Parameters of large-scale pulsations obtained from thermal measurements

Reynolds Nos.	$1/2\tau_P$ (s) ± 0.005	τ_{12} (s) ± 0.003	Convection velocity U_C (m/s)	U_C/U_M	Pulsation characteristic length L (m)	Stanton (St)
7200	0.033	0.051	0.980 ± 0.16	0.99	0.065 ± 0.03	
5400	0.038	0.068	0.735 ± 0.09	0.99	0.056 ± 0.02	0.013 ± 0.002
4500	0.043	0.082	0.610 ± 0.07	0.99	0.052 ± 0.02	
3600	0.05	0.102	0.490 ± 0.05	0.99	0.049 ± 0.02	0.015 ± 0.002
2700	0.065	0.134	0.373 ± 0.03	1.01	0.049 ± 0.02	0.017 ± 0.002
2200	0.078	0.16	0.312 ± 0.02	1.02	0.049 ± 0.02	
1800	0.096	0.196	0.255 ± 0.015	1.04	0.049 ± 0.015	0.021 ± 0.003
1300	0.129	0.242	0.207 ± 0.015	1.14	0.053 ± 0.012	0.015 ± 0.006
900	0.184	0.346	0.145 ± 0.010	1.17	0.053 ± 0.010	
850	0.197	0.367	0.136 ± 0.010	1.17	0.054 ± 0.010	

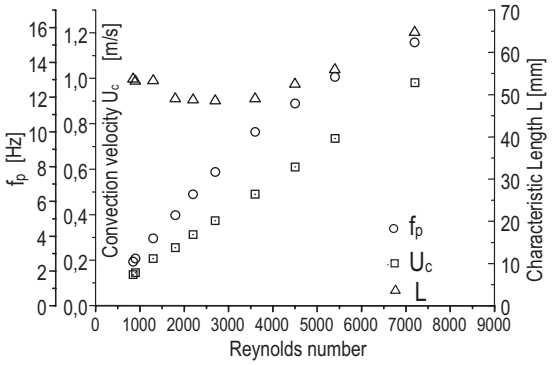

Fig. 14 f_p, U_C, and characteristic length L as function of the Reynolds number

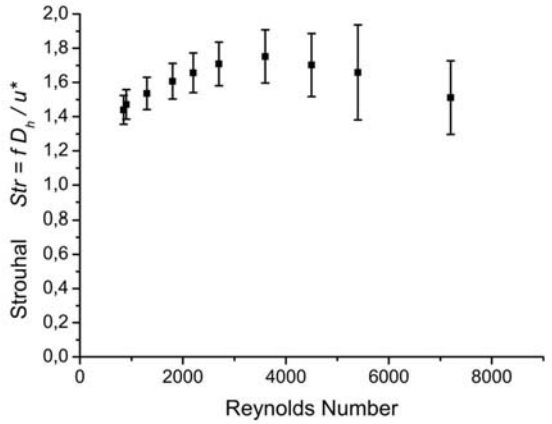

Fig. 15 Strouhal number of pulsations as function of the Reynolds number

$$U_C = \frac{L}{\tau_{12}}$$

is shown in the fourth column of Table 1 and in Fig. 14. In this manner, with this simple measurement, we can obtain the pulsation convection velocity, which is an important parameter of this phenomenon.

It is interesting to calculate the rate of pulsation convection velocity to the bulk velocity U_C/U_M (fifth column of Table 1). It is clear that U_C is equal to or larger than U_M, even though the mean axial velocity in the gap is smaller than U_M. This is in agreement with previously published results that show pulsation propagation velocities larger than local mean velocities [21].

From pulsation frequency and the convection time we can calculate the axial length of the structure, the structure size L. The

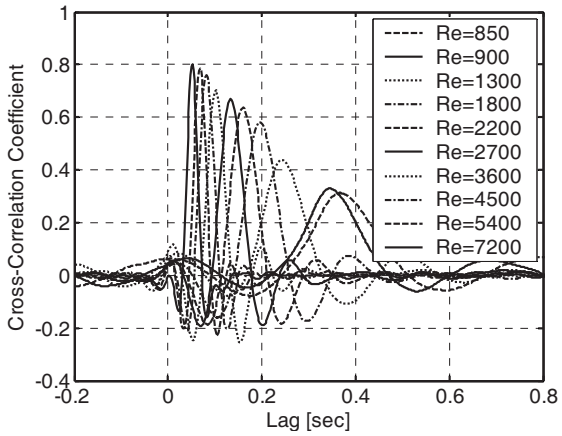

Fig. 16 Cross-correlations for two sensors in the gap separated 50 mm streamwise

values of the structure size at different Reynolds numbers are shown in column 6 of Table 1 and in Fig. 14. For the considered conditions the structure size remains approximately constant. Changes in structure size as reported by Lexmond et al. [21] for low Reynolds numbers were not found for our measurement range.

As we mentioned before the pulsation periodic nature is reflected not only in the autocorrelation but also in the cross-correlation. We have compared the time difference between the cross-correlation maximum and minimum with half the pulsation period $1/2\tau_P$ obtained from autocorrelations; differences are within 6% except for Re 850 that shows a difference of 12%.

7 Comparison With Mixing Measurements

Pulsations are the dominating phenomenon in the turbulent interchange of heat between subchannels and therefore determine the mixing rate and its nondimensional form, the Stanton number. The Stanton number is thus an indirect measurement of the pulsation intensities and effectiveness, as is shown in the work of Lexmond et al. [21]. The mixing rate was measured and the Stanton number was calculated for various Reynolds numbers. The results are shown in the last column of Table 1 that shows that though the mixing Stanton number increases from Reynolds 5400 to 1800, the structure characteristic length (Fig. 14) and Strouhal number (Fig. 15) stay constant within error.

These results indicate that the Stanton number (mixing rate) can vary while the Strouhal number remains constant. A related result is provided by Baratto et al. [11], who measured the flow while varying the rod-wall distance and obtained a large variation of velocity fluctuations while the pulsation frequency stayed relatively constant. This evidence shows the weakness of models

based on pulsation data alone such as the model proposed by Kim and Park [6], and show the need to include the pulsation intensity in models like the one proposed by Rehme [23].

8 Conclusions

We have shown that relatively simple temperature measurements in an imposed temperature gradient field can provide reliable time and length scales for large-scale flow structures, i.e., quasiperiodic flow pulsations. The general condition for this to be possible is that these structures cause a strong convection across the imposed temperature gradient [24].

The proposed method is based on the transport of heat, which is a scalar quantity, and therefore can certainly not offer detailed information on the vectorial flow field. In the flow studied, turbulent mixing of heat between subchannels is dominated by large-scale pulsations with a well defined spatial location, large length scales, and a relatively low pulsation frequency. In this context the method can effectively obtain the pulsation frequencies, convection velocities, and characteristic streamwise length scales. This information together with the turbulent mixing rate make a good set for model verification or numerical simulation validation. It is worth noting that this method can be applied relatively effortlessly in experimental devices originally built for lumped heat transfer measurements.

All measurement results are compatible with the idea that auto- and cross-correlation maxima and minima for temperature signals are a good indication of large-scale pulsations. Two examples are that auto- and cross-correlations show a similar spectral distribution and that the Strouhal number for the pulsations is a constant. The measurement results are in good agreement with previous works on the matter both qualitatively and quantitatively. In particular, we have shown the linear dependence of pulsation passing frequency on the flow bulk velocity and the invariance of the characteristic axial length even at low Reynolds numbers. Changes in structure size as reported by Lexmond et al. [21] for low Reynolds numbers were not found in our geometry and measurement range.

From the present measurement results it is worth noting that the Stanton number has a maximum for a Reynolds number around 2000. This variation is not associated with a change either in the pulsation characteristic axial length or in the pulsation Strouhal number, precluding the use of mixing models based on pulsation frequencies alone [6].

We think that this simple method can be very useful to obtain additional large-scale structure information on experimental facilities designed for thermal measurements, provided that large-scale structures generate strong turbulent mixing. This is actually the case in various flows, e.g., the flows described in Sec. 1. The general idea is to create a thermal gradient across the geometrical location of the passing large-scale structures and to measure the temperature fluctuations downstream. This may be achieved by the same heat transfer mechanism that is being studied or it may need a minor modification to generate the required temperature gradient. The present experimental setup is an example of this last case. In the real application the whole nuclear fuel rod is heated, while to obtain an adequate thermal gradient in the experiment only a 100 mm long strip of the rod facing the central subchannel is heated. Both thermal gradient generation and temperature measurement are techniques that are normally available in most thermal experimental setups, which makes the present technique relatively simple to apply.

Acknowledgment

The authors would like to acknowledge Mr. D. Mateos for the construction of the experimental setup, Dr. José Barbero for the construction of the heaters, and the personnel of the Leo Falicov Library of Centro Atómico Bariloche for their assistance. This research was sponsored by CONICET and CNEA.

Nomenclature

D_h = hydraulic diameter (m)
f_P = pulsation passing frequency (Hz)
L = characteristic length (m)
L_{12} = distance between sensors (mm)
R_{xy} = cross-correlation value
r_{xy} = normalized cross-correlation
Re = Reynolds number
St = Stanton number
Str = Strouhal number
t = time (s)
U_C = pulsation convection velocity (m/s)
U_M = bulk velocity (m/s)
u^* = shear velocity (m/s)

Greek

s_x = standard deviation of the x signal
s_y = standard deviation of the y signal
t = time between two signals (s)
t_{12} = pulsation convection time (s)
t_P = pulsation period (s)

References

[1] Rogers, J. T., and Rosehart, R. G., 1972, "Mixing by Turbulent Interchange in Fuel Bundles, Correlations and Inferences," ASME Paper No. 72-HT-53.
[2] Rowe, D. S., Johnson, B. M., and Knudsen, J. G., 1974, "Implications Concerning Rod Bundle Crossflow Mixing Based on Measurements of Turbulent Flow Structure," Int. J. Heat Mass Transfer, **17**, pp. 407–419.
[3] Hooper, J. D., and Wood, D. H., 1984, "Fully Developed Rod Bundle Flow Over a Large Range of Reynolds Number," Nucl. Eng. Des., **83**, pp. 31–46.
[4] Guellouz, M. S., and Tavoularis, S., 2000, "The Structure of Turbulent Flow in a Rectangular Channel Containing a Cylindrical Rod–Part 1: Reynolds-Averaged Measurements," Exp. Therm. Fluid Sci., **23**, pp. 59–73.
[5] Meyer, L., and Rehme, K., 1995, "Periodic Vortices in Flow Through Channels With Longitudinal Slots or Fins," *Proceedings of the Tenth Symposium on Turbulent Shear Flows*, Pennsylvania State University, Aug. 14–16, University Park, PA.
[6] Kim, S., and Park, G. C., 1997, "Estimation of Anisotropic Factor and Turbulent Mixing Rate in Rod Bundles Based on the Flow Pulsation Phenomenon," Nucl. Technol., **117**, pp. 340–352.
[7] Meyer, L., 1994, "Measurements of Turbulent Velocity and Temperature in Axial Flow Through a Heated Rod Bundle," Nucl. Eng. Des., **146**, pp. 71–82.
[8] Krauss, T., and Meyer, L., 1996, "Characteristics of Turbulent Velocity and Temperature in a Wall Channel of Heated Rod Bundle," Exp. Therm. Fluid Sci., **12**, pp. 75–86.
[9] Krauss, T., and Meyer, L., 1998, "Experimental Investigation of Turbulent Transport of Momentum and Energy in a Heated Rod Bundle," Nucl. Eng. Des., **180**, pp. 185–206.
[10] Guellouz, M. S., and Tavoularis, S., 2000, "The Structure of Turbulent Flow in a Rectangular Channel Containing a Cylindrical Rod. Part 1: Reynolds-Averaged Measurements," Exp. Therm. Fluid Sci., **23**, pp. 59–73.
[11] Baratto, F., Bailey, S. C. C., and Tavoularis, S., 2006, "Measurements of Frequencies and Spatial Correlations of Coherent Structures in Rod Bundle Flows," Nucl. Eng. Des., **236**, pp. 1830–1837.
[12] Van Der Ros, T., and Bogaardt, M., 1970, "Mass and Heat Exchange Between Adjacent Channels in Liquid-Cooled Rod Bundles," Nucl. Eng. Des., **12**, pp. 259–268.
[13] Sano, M., Wu, X. Z., and Libchaber, A., 1989, "Turbulence in Helium-Gas Free Convection," Phys. Rev. A, **40**, pp. 6421–6430.
[14] Silin, N., Juanico, L., and Delmastro, D., 2004, "A Method for the Measurement of Thermal Mixing Between Subchannels," Nucl. Eng. Des., **227**(1), pp. 51–63.
[15] Silin, N., and Juanicó, L. E., 2006, "Experimental Study on the Reynolds Number Dependence of Turbulent Mixing in a Rod Bundle," Nucl. Eng. Des., **236**, pp. 1860–1866.
[16] Chiu, C., and Todreas, N., 1980, "Experimental Techniques for Liquid Metal Cooled Fast Breeder Reactor Fuel Assembly Thermal/Hydraulic Tests," Nucl. Eng. Des., **62**, pp. 253–270.
[17] Horowitz, P., and Hill, W., 1989, *The Art of Electronics*, Cambridge University Press, Cambridge, UK, Chap. 15.
[18] Rehme, K., 1972, "Pressure Drop Performance of Rod Bundles in Hexagonal Arrangements," Int. J. Heat Mass Transfer, **15**, pp. 2499–2517.
[19] Smolyakov, A. V., and Tkachenko, V. M., 1983, *The Measurement of Turbulent Fluctuations*, Springer-Verlag, Berlin, Chap. 1, p. 2.
[20] Kerlin, T. W., Shepard, R. L., Hashemian, H. M., and Petersen, K. M., 1982, "Response of Installed Temperature Sensors," *Temperature, Its Measurement*

and Control in Science and Industry, Vol. 5, American Institute of Physics, New York, pp. 1357–1366.
[21] Lexmond, A. S., Mudde, R. F., and van der Hagen, T. H. J. J., 2005, "Visualisation of The Vortex Street and Characterization of the Cross Flow in the Gap Between Two Sub-Channels," *Proceedings of the 11th International Topical Meeting on Nuclear Reactor Thermal-Hydraulics* (NURETH-11), Pope's Palace Conference Center, Avignon, France, Oct. 2–6, Paper No. 122.
[22] Möller, S. V., 1991, "On Phenomena of Turbulent Flow Through Rod Bundles," Exp. Therm. Fluid Sci., **4**, pp. 25–35.
[23] Rehme, K., 1992, "The Structure of Turbulence in Rod Bundles and the Implications on Natural Mixing Between the Subchannels," Int. J. Heat Mass Transfer, **35**(2), pp. 567–581.
[24] Hussain, A. K. M. F., 1986, "Coherent Structures and Turbulence," J. Fluid Mech., **173**, pp. 303–356.

Three-Dimensional Numerical Simulation on the Laminar Flow and Heat Transfer in Four Basic Fins of Plate-Fin Heat Exchangers

Yinhai Zhu

Yanzhong Li[1]
e-mail: yzli-epe@mail.xjtu.edu.cn

School of Energy and Power Engineering,
Xi'an Jiaotong University,
Xi'an 710049, P.R.C.

In this paper, four basic fins of the plate-fin heat exchangers, rectangular plain fin, strip offset fin, perforated fin, and wavy fin, are modeled and simulated by taking account of fin thickness, thermal entry effect, and end effect. Three-dimensional numerical simulations on the flow and heat transfer in the four fins are investigated and carried out at laminar flow regime. Validity of the modeling technique is verified by comparing computational results with both corresponding experimental data and three empirical correlations from literatures. Global average Colburn factor (j factor) and friction factor (f factor) and their local 1D streamwise-average distributions along the fins are presented by introducing data reduction method. The heat transfer behaviors in both the developing and developed regions are analyzed by examining variations of the local Nusselt number along the flow direction. It is found that the thermal entry length of the four fins might be expressed in the format of $L_e = c_1\, Re^{c2}\, Pr\, D_h$, *which has the same form as the one in a circular tube.* [DOI: 10.1115/1.2970072]

Keywords: strip offset fin, perforated fin, wavy fin, plate-fin heat exchanger, CFD modeling, heat transfer

1 Introduction

Compact heat exchangers are used for heat transfer in a wide variety of engineering applications, including aerospace, chemical engineering, and industrial process because of their high efficiency, light weight, and small size. The plate-fin heat exchanger (PFHE) as a widely used compact heat exchanger has various forms of fin passages, which can be plain fins, strip offset fins, perforated fins, wavy fins, pin fins, and louvered fins. As a general rule, surface interruptions enhance the heat transfer coefficient but increase the flow friction. In order to best match the heat transfer and pressure drop in PFHE, many experimental and theoretical studies have been performed to understand the heat transfer and flow behaviors in various fin geometries and working conditions.

Kays and London [1] carried out early experimental investigations on various fin geometries. Later the experimental studies were extended by Kays [2], Briggs and London [3], London and Shah [4], Waiters [5], Mochizuki and Yagi [6], Shah et al. [7], Manglik and Bergles [8,9], Hu and Herold [10], and Rush et al. [11]. The monograph by Kays and London [12] was perhaps the most comprehensive design sourcebook. These experimental data provided the basis for later theoretical and numerical investigations. Many empirical correlations were carried out and most were for the strip offset fins [12–15]. In contrast to the empirical correlations, numerical study based on the computational fluid dynamics (CFD) technique has the ability to describe the flow and heat transfer behaviors in depth. Sparrow et al. [16] investigated a case of offset strip fin with zero fin thickness. Patankar and Prakash [17] investigated the effect of fin thickness, but its validity was not established by comparison with experimental data. That investigation was extended by Xi et al. [18], Saidi and Sundén [19], Beale [20], and Wang et al. [21].

The laminar flow and heat transfer in wavy fins were studied by two-dimensional numerical simulation [22–26]. By employing three-dimensional modeling technique, Asako et al. [27] studied heat transfer characteristics of laminar air flow ($10 \le \mathrm{Re} \le 2000$) in sinusoidal wavy flow channels. Later, Manglik et al. [28] considered the steady forced convection in periodically developed air flows in three-dimensional wavy-plate-fin cores with low Reynolds number in the range of $10 \le \mathrm{Re} \le 1000$.

To the best of the authors' knowledge, complete three-dimensional flow and heat transfer in the perforated fins have received scant attention in literature. In addition, most of the previous studies are based on simple models with very short computational fins in length, i.e., only one periodic flow length and fully developed region with periodically flow conditions are considered [17,19,25,28]. It is well known that the heat transfer coefficient in the thermal entry region is much higher than that in the fully developed region. The results based on the simplified model with short computational fin length cannot properly reflect the overall heat transfer coefficient of a practical PFHE. Moreover, in order to best match the heat transfer coefficient and pressure loss in the PFHE fins, the local distributions of j and f factors along the fins, especially at flow-interrupted locations, need to be well understood.

The purpose of this paper is to study the laminar flow and heat transfer in the four basic PFHE fins by considering the thermal entry effect and the end effect. The four fin models are created in proper three-dimensional calculation domains and finely meshed. These models are validated by comparing the simulation results of the strip offset fin with the corresponding experimental data and also with three empirical correlations. Based on those models, numerical simulations are then carried out for a wide range of laminar flow ($132.3 \le \mathrm{Re} \le 1323$). The flow and heat transfer process in the four fins are obtained and represented with the local pattern and distribution of the j and f factors and the Nusselt number. The behaviors of heat transfer enhancement in the three flow-interrupted fins are carefully illustrated and discussed.

[1]Corresponding author.

Contributed by the Heat Transfer Division of ASME for publication in the JOURNAL OF HEAT TRANSFER. Manuscript received August 31, 2007; final manuscript received May 14, 2008; published online September 4, 2008. Review conducted by Gautam Biswas.

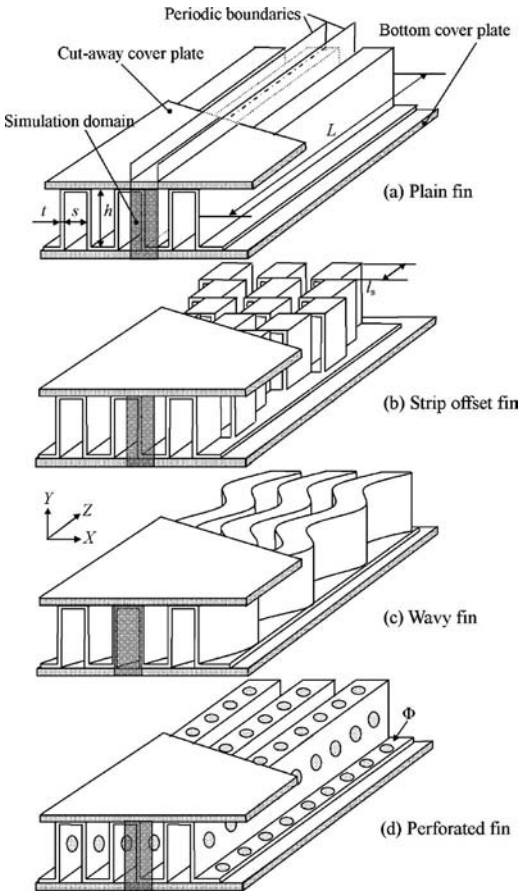

Fig. 1 Perspective view of four basic fins in PFHE

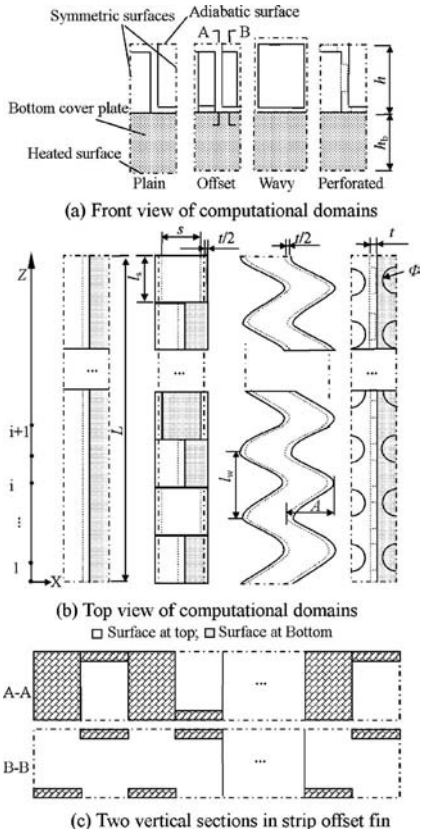

Fig. 2 CFD models of the four fins

2 Model Approach

CFD models. The perspective view of three-dimensional structures of the four basic PFHE fins, plain fin, strip offset fin, wavy fin, and perforated fin, is shown in Fig. 1. In order to study the heat transfer and flow behaviors and make a comparison among those four fins, some dimensions are equal such as the fin thickness, fin height, fin spacing distance, and total fin array length, and they are listed in Table 1 in detail.

To accurately simulate the characteristics of heat transfer and pressure drop and at the same time simplify the modeling and computation processes, the following considerations are made in the present work.

(1) A proper fin length of 0.306 m is selected: The length is not very long so as to simplify the modeling and computation, but it is longer than its thermal entry length. For example, the studied strip offset fin has 50 periodic offset fins and the thermal entry region is about 3–9 periodic offset fins long with $132.3 \leq \mathrm{Re} \leq 1323$. Therefore, the flow and heat transfer behaviors in both thermal entry and fully developed regions can be investigated.
(2) Symmetry boundaries, as shown in Fig. 1(*a*), are used to reduce the extent of each computational model to a symmetric subsection of the overall fin.
(3) Not only the fin thickness in the *X*-direction but also the thickness of top and bottom fins in the *Y*-direction is considered in creating fin models.

The four fin models are created in three-dimensional domains, as schematically shown in Fig. 2. The perforated fin is meshed with a hybrid grid of structured hexahedral grids and unstructured tetrahedral grids, while other fins are meshed with a hexahedral grid in GAMBIT Version 2.2. In order to obtain faster computation speed, only the locations with significant flow changes such as velocity boundaries and flow-interrupted places are with concentrated grid density. Each fin model is initially made at about 2,400,000 elements. For the perforated and strip offset fins, the grids later adapt to about 2,800,000 elements to confirm that the results are grid independent.

Solution algorithm. The working fluid is water, thermodynamics properties of which are assumed constant in the present studies: density, $\rho = 983\ \mathrm{kg/m^3}$, viscosity, $\mu = 4.7 \times 10^{-4}$ Pa s, thermal conductivity, $k = 0.655\ \mathrm{W/(m\,K)}$, and specific heat, $c_p = 4180\ \mathrm{J/(kg\,K)}$. The Reynolds number in the present work

Table 1 Fin geometries

Fin type	Fin thickness, t (mm)	Fin height, h (mm)	Fin spacing distance, s (mm)	Fin array length, L (mm)	Specification
Plain fin	0.152	2.26	1.52	306	—
Strip offset fin	0.152	2.26	1.52	306	$l_s = 6.12$ mm
Wavy fin	0.152	2.26	1.52	306	$A = 1.52$ mm; $l_w = 7.6$ mm
Perforated fin	0.152	2.26	1.52	306	$\Phi = 0.8$ mm (16% open)

Table 2 Inlet conditions of four fins

Re	Fluid inlet velocity, v (m s^{-1})			
	Plain fin	Strip offset fin	Wavy fin	Perforated fin
132.3	0.0348	0.0353	0.0366	0.0341
285	0.075	0.076	0.0788	0.0735
614	0.161	0.164	0.170	0.158
1323	0.348	0.353	0.366	0.341

ranges from 132.3 to 1323, while the Prandtl number is fixed at 3. Both fins and bottom cover plates are made of aluminum with a thermal conductivity of 206 W/(m K). The height of the bottom cover plate is 2.5 mm.

On inlets of the four fins, the "velocity inlet" condition with an inlet temperature of 60°C is applied and listed in Table 2. The "pressure outlet" condition is adopted on the fin outlets. The bottom surface of the cover plate is modeled in the constant heat flux boundary condition with a constant heat flux of 30,000 W/m^2. No slip wall condition is used and the symmetry boundary condition is applied on the two side surfaces of the fins.

The commercial code FLUENT Version 6.2 is employed in the present numerical simulation. The well-known SIMPLE algorithm is applied to obtain the pressure field [29]. The plain fin is easy to be meshed with a hexahedral grid to make sure that the flow is aligned with the grid so that the first-order upwind scheme is selected for the plain fin. For other three fins, the third order QUICK scheme is adopted to obtain more accurate results. A model with steady-state three-dimensional incompressible laminar flow is employed for the solution of the problem [30]. The maximum residual tolerance of the conservation equations is kept at less than $1e^{-5}$.

Data reduction method. To analyze the heat transfer and flow behaviors in the four fins, Colburn factor, j, and Fanning friction factor, f, are computed from the CFD simulation results by the following procedure.

The hydraulic diameters of the four fins based on $D_h = 4A_cL/A$ defined in Ref. [12] are given as follows.

For plain fin,

$$D_h = \frac{2sh}{s+h} \tag{1a}$$

For strip offset fin,

$$D_h = \frac{2shl}{sl+hl+th} \tag{1b}$$

For perforated fin

$$D_h = \frac{4shL}{2sL+2hL-2n_{\text{row}}\pi r^2+2n_{\text{row}}\pi 2rt} \tag{1c}$$

For wavy fin,

$$D_h = \frac{2sh}{s+\zeta_w h} \tag{1d}$$

The Reynolds number is evaluated based on D_h, ν, ρ, and μ, which is defined as

$$\text{Re} = \frac{\rho D_h \nu}{\mu} \tag{2}$$

Different from an air-cooled application, the resistance of the bottom aluminum cover plate cannot be ignored since the liquid water has significantly higher heat transfer coefficient than that of air. So the cross-section-averaged local heat transfer coefficient, h_i, is written as [10]

$$h_i = \frac{1}{\eta_i}\frac{1}{(1/U_i)-(h_b A_i/k_A A_{2_i})} \tag{3}$$

U_i is calculated by

$$U_i = \frac{Q_i}{\Delta T_i A_i} \tag{4}$$

where ΔT_i is the arithmetic-mean temperature difference between the heated surface and the fluid from cross section i to $i+1$ defined as

$$\Delta T_i = \frac{(T_{s_{i+1}}-T_{f_{i+1}})+(T_{s_i}-T_{f_i})}{2} \tag{5}$$

the average fluid temperature in each section is calculated by section mass-weighted average method as follows:

$$T_f = \frac{\int T\rho u dV}{\int \rho u dV} \tag{6}$$

The average heat transfer surface efficiency, η_i, is related to the fin efficiency according to

$$\eta_i = 1 - \frac{A_{F_i}}{A_i}(1-\eta_{F_i}) \tag{7}$$

The average fin efficiency η_{F_i} is computed based on a one-dimensional fin model, where the effective fin height is chosen as $h+s$ as the unheated plate is lumped together with the fin area [10]. η_{F_i} is then expressed by

$$\eta_{F_i} = \frac{\tanh[m_i(h+s)]}{m_i(h+s)} \tag{8}$$

where $m_i=(2h_i/k_A t)^{0.5}$ is the average fin effectiveness parameter from cross section i to $i+1$.

From Eqs. (1*a*)–(1*d*) and (2)–(8), h_i can be determined by an iterative calculation, where the required areas of the four fins from cross section i to $i+1$ are defined according to Kays and London [12] as follows.

For plain fin,

$$A_{F_i} = (2h+s)L_i, \quad A_{2_i} = (s+t)L_i, \quad A_i = A_{F_i} + sL_i \tag{9a}$$

For strip offset fin,

$$A_{F_i} = [4(l_s h + th) + 2l_s s]\frac{L_i}{2l_s}, \quad A_{2_i} = (s+t)L_i, \quad A_i = A_{F_i} + sL_i \tag{9b}$$

For perforated fin,

$$A_{F_i} = [(2h+s)L - 3n_{\text{row}}\pi r^2 + 2n_{\text{row}}\pi 2rt]\frac{L_i}{L}, \quad A_{2_i} = (s+t)L_i \tag{9c}$$

$$A_i = A_{F_i} + (sL + n_{\text{row}}\pi r^2)\frac{L_i}{L}$$

For wavy fin,

$$A_{F_i} = (2\zeta_w h + s)L_i, \quad A_{2_i} = (s+t)L_i, \quad A_i = A_{F_i} + sL_i \tag{9d}$$

By transforming the h_i into a Nusselt number Nu_i, the local Colburn factor, j_i, used for the evaluation on heat transfer performance, is defined as

$$j_i = \frac{\text{Nu}_i}{\text{Re Pr}^{1/3}} \tag{10}$$

the pressure drop can be expressed in terms of the friction factor, f, defined as

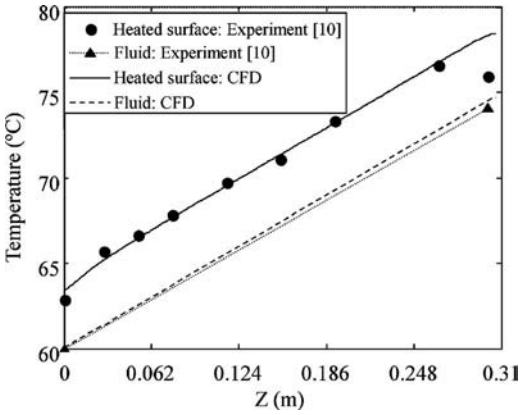

Fig. 3 Comparisons of fluid and fin surface temperature between CFD and experiment at Re=285

$$f = \frac{\Delta P_L D_h}{2\rho u^2 L} \tag{11}$$

where ΔP_L is the pressure drop of the fin array in the flow direction.

3 Model Validation

Since the strip offset fin in this work has the same geometries as the cold plate 3 tested in Ref. [10], experimental data of the cold plate 3 are chosen to compare with the present CFD simulation results. In addition, three existing empirical correlations of the *j* and *f* factors from Kays [13], Wieting [14], and Joshi and Webb [15] are used to validate the effectiveness of the present CFD modeling method.

Figure 3 depicts the comparison of fluid and fin surface temperatures between CFD and experiment. The deviation of the fluid outlet temperature between the CFD results and the experimental data is only 0.91%. The experimental fin surface temperature coincides fairly well with the simulation results along the fin array except two ends due to conduction effect by thermal spreading to unheated end sections during experimental test [10]. In contrast with the experimental test, the end conduction effect can be easily avoided in the CFD simulation by setting insulated boundary condition at two surfaces of fin ends.

In Fig. 4, *j* and *f* factors of the strip offset fin calculated from the three different empirical correlations are used to compare with the CFD results. From Fig. 4, *f* factors obtained from CFD method fit the correlations well in all Re range. Average absolute deviations of the *j* factor between the present CFD simulation and correlations from Kays [13] and Wieting [14] are 10.52% and 6.32%, respectively. All the above comparisons show that the present CFD modeling method provides reliable results in simulation on the flow and heat transfer process.

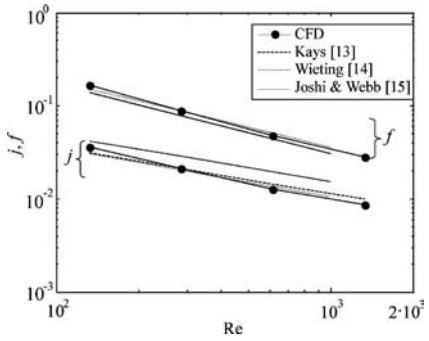

Fig. 4 Comparisons of *j* and *f* factors between CFD and correlations

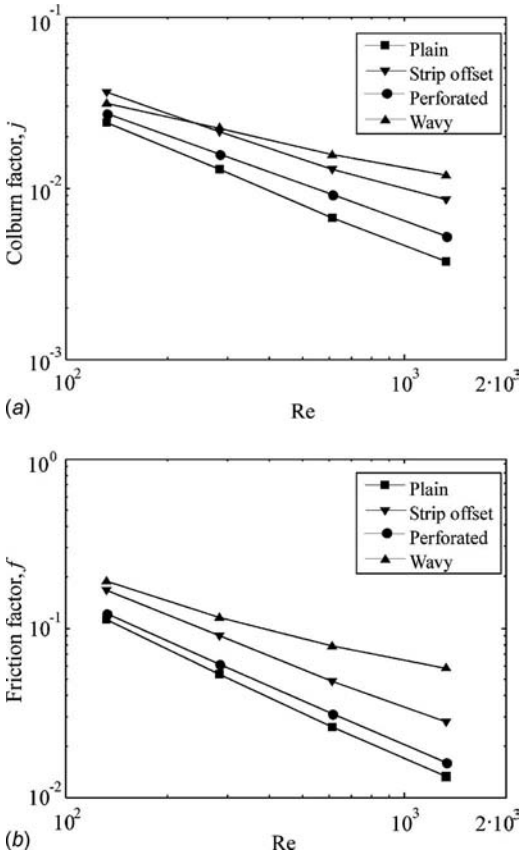

Fig. 5 Comparisons of *j* and *f* factors among the four fins: (*a*) *j* factor and (*b*) *f* factor

4 Results and Discussions

Global average j and f factors. The global average *j* factors of the four fins are calculated by Eqs. (1*a*)–(1*d*), (9*a*)–(9*d*), and (10) and depicted in Fig. 5(*a*). The plain fin has the lowest *j* in all tested Re due to the heat transfer in other three flow-interrupted fins enhanced by thermal boundary layer interruption with offset strip fins, holes, or corrugated walls. Results show that *j* factors of the strip offset and wavy fins are close at small Re (Re$<$300), and the wavy fin has the highest *j* factor at Re$>$300. Figure 5(*b*) shows a comparison of *f* factors with the four basic fins. The wavy fin has the greatest pressure loss especially at large values of Re.

Local heat transfer and flow behaviors. Further insights into the heat transfer behaviors in the four fins are carried out by examining variations of the local streamwise-average *j* factors along the flow direction, as presented in Fig. 6 in detail. In all cases, heat transfer is enhanced at both the fin entrance and exit due to the thermal entry effect and end effect. As Re increases, the thermal entry effect enhances but the end effect becomes weak.

Local *j* factor distributions along the strip offset fin from *Z* =0.12 to 0.17 m at Re=285 are depicted in Fig. 6(*b*). The fluid is blocked by leading surfaces and separated by tailing surfaces, resulting in *j* factor increases at these locations. As we know from results in previous two-dimensional models, the flow in the strip offset fin is not periodic in two strip fin lengths but four strip fin lengths, obviously because the fin thickness in the *Y*-direction is considered in the present simulation.

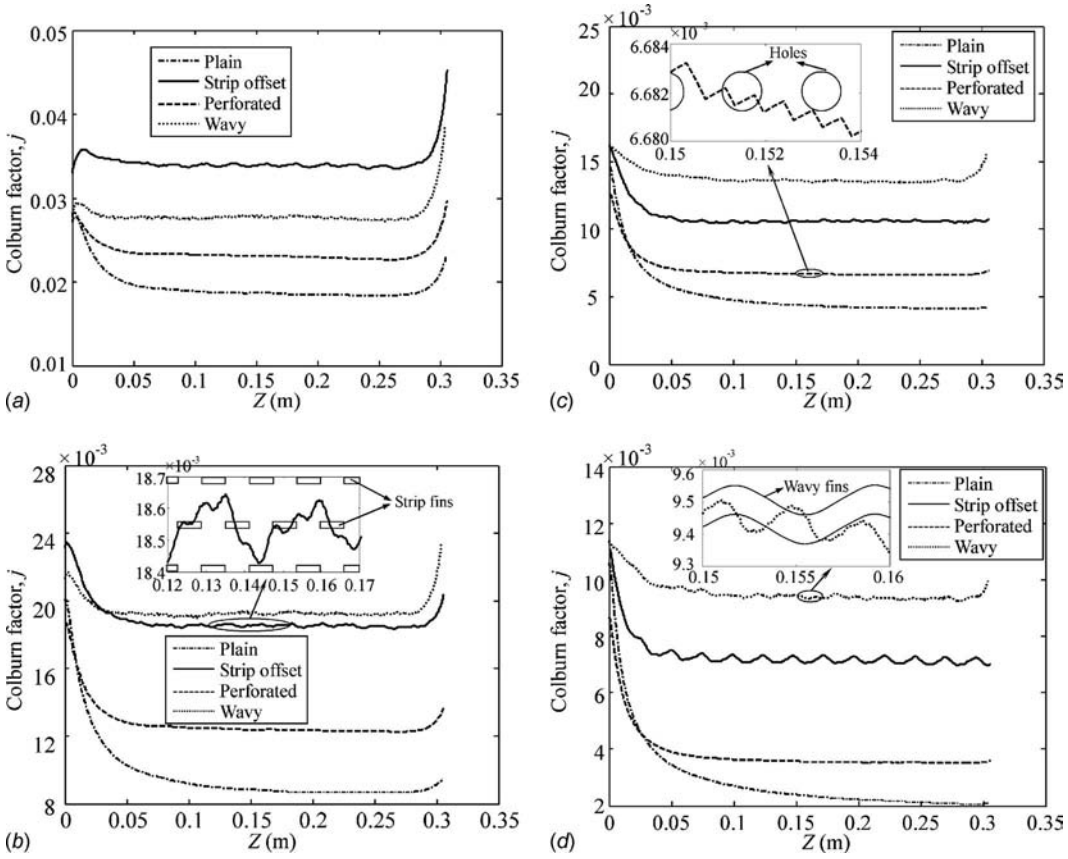

Fig. 6 Local streamwise-average *j* factor distributions along the four fins at different Re: (*a*) Re =132.3, (*b*) Re=285, (*c*) Re=614, and (*d*) Re=1323

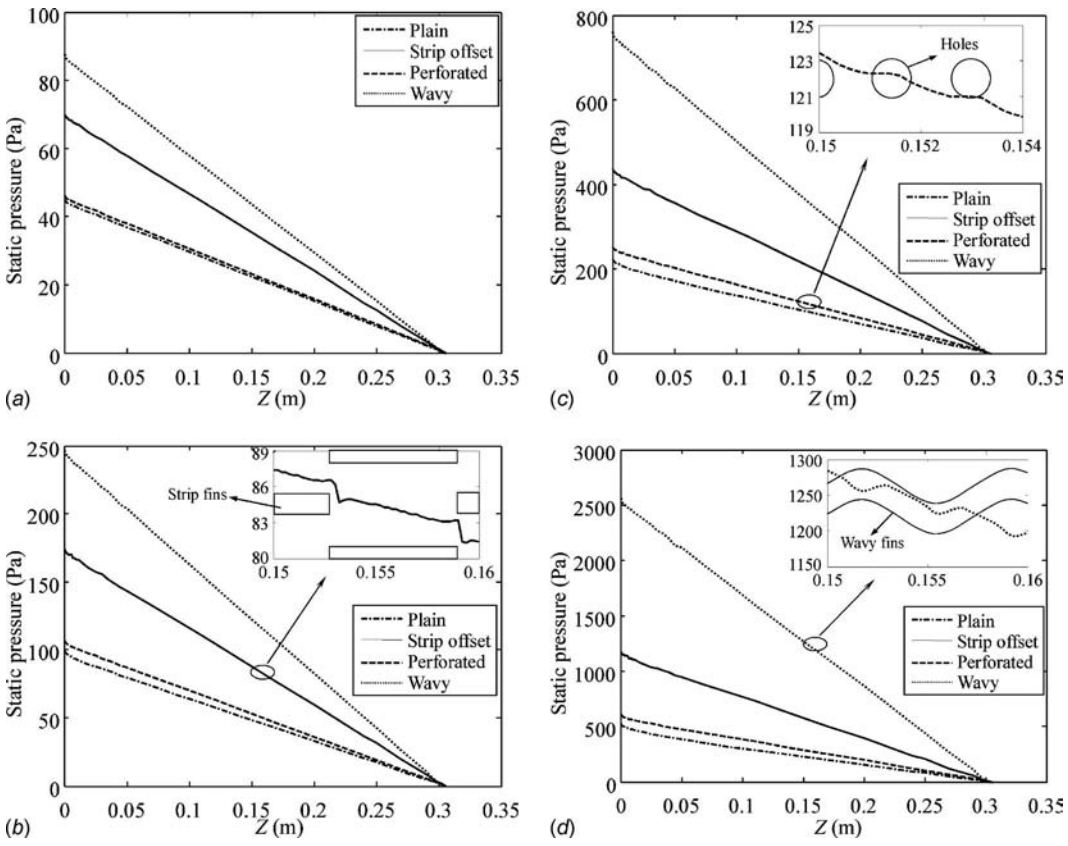

Fig. 7 Pressure distributions along the flow direction of four fins at different Re: (*a*) Re=132.3, (*b*) Re =285, (*c*) Re=614, and (*d*) Re=1323

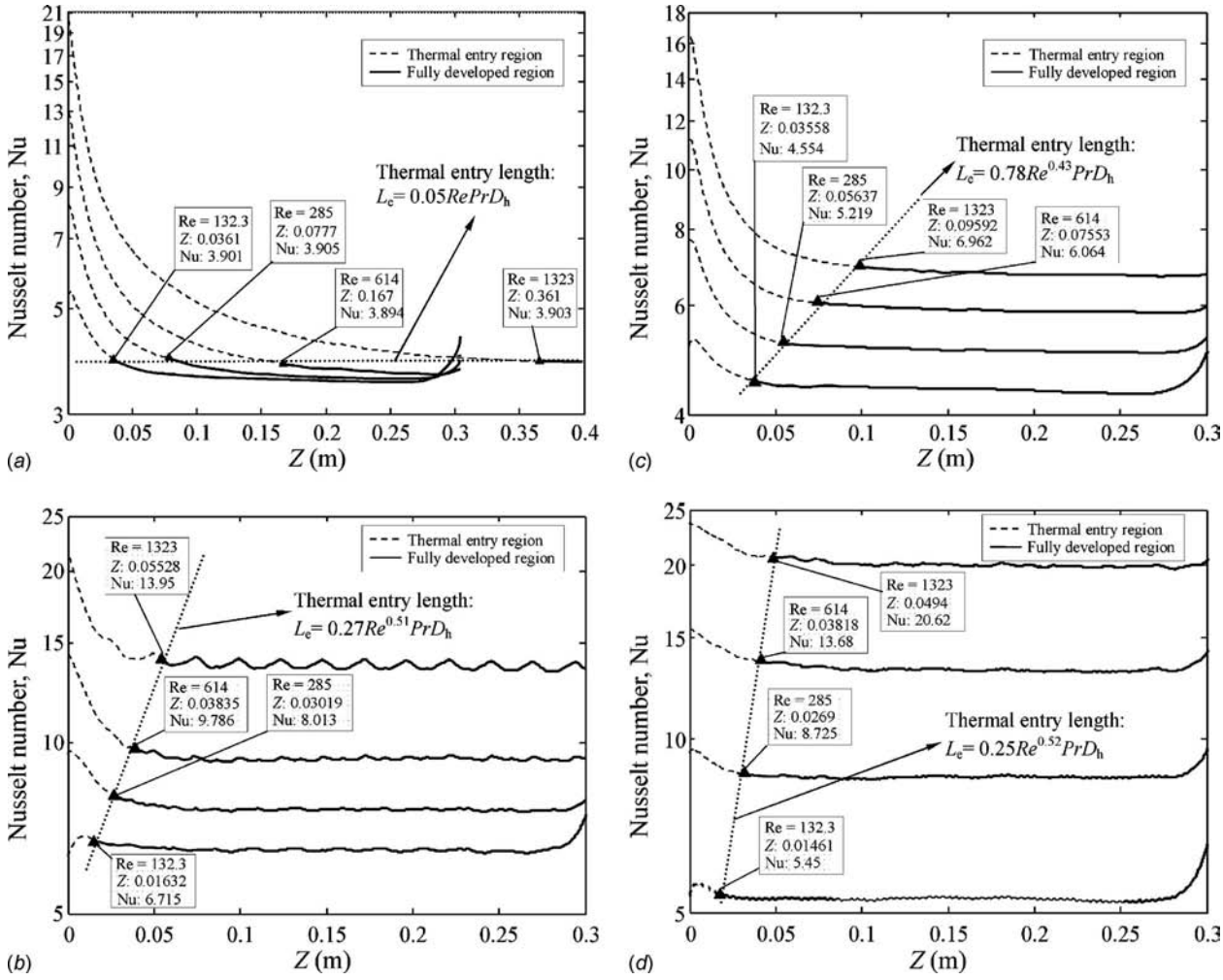

Fig. 8 Local Nusselt number distributions along flow direction: (*a*) plain fin, (*b*) strip offset fin (*c*) perforated fin, and (*d*) wavy fin

Figure 6(*c*) shows local *j* factor of the perforated fin from $Z=0.15$ to 0.154 m at Re=614. It is observed that the holes have two opposite effects on *j* factor: When the fluid flow approaches a hole, there is an increase in *j* because the flow and thermal boundary layer are interrupted there; then *j* drops rapidly through that hole due to the local heat transfer area reduced by the hole. As a result, the perforated fin does not enhance the overall heat transfer coefficient as much as the strip offset and wavy fins do.

Local *j* factor distributions along the wavy fin from $Z=0.15$ to 0.16 m at Re=1323 are shown in Fig. 6(*d*). In the wavy fin, the flow is blocked by each wall-corrugation peak causing the thermal boundary disturbed and reattached, resulting in an increase in the *j* factor at each peak.

An enhancement of the heat transfer always associates with an increase in the pressure drop. Some details of the pressure distribution along the three flow-interrupted fins are depicted in Figs. 7(*b*)–7(*d*), respectively. In Fig. 7(*b*), the pressure rapidly drops at leading surfaces due to the blockage of the flow. In contrast with strip fins and wavy passages, the impact of holes is relatively small, as shown in Fig. 7(*c*). In the wavy fin, wavy passages increase the flow friction, resulting in a great pressure drop at each wall-corrugation peak, as shown in Fig. 7(*d*).

From the representation of the local *j* factor and local pressure distribution in the strip offset, perforated, and wavy fins in Figs. 6 and 7, it is clear that a bigger interruption of the flow always corresponds to a higher heat transfer coefficient and a greater pressure drop.

Thermal entry length. Due to the thermal boundary layer thickness that is zero at the fin entrance, the heat transfer coefficient and Nusselt number are extremely large at $Z=0$. The variation of local Nu in the flow distance of the four fins is presented in Fig. 8, where the thermal entry region and the fully developed region are given as dashed and real lines, respectively. In Fig. 8(*a*), details of the local Nu along the flow distance of the plain fin at different Re are depicted. At all the tested Re, Nu is about 3.9 in the fully developed region.

The thermal entry lengths, L_e, of the four fins are derived from the local Nu. As shown in Fig. 8, L_e is linear with Nusselt number when it is in logarithm coordinate and the distance Z is in linear coordinate. A fitting correlation of L_e in the plain fin, $L_e = 0.05\ \mathrm{Re\ Pr}\ D_h$, is obtained by regression analysis. It completely agrees to the expression of the thermal entry length for laminar flow in Ref. [31]. In the same way, correlations of L_e for other three fins are established as follows.

For strip offset fin,

$$L_e = 0.27\ \mathrm{Re}^{0.51}\ \mathrm{Pr}\ D_h \tag{12a}$$

For perforated fin,

$$L_e = 0.78\ \mathrm{Re}^{0.43}\ \mathrm{Pr}\ D_h \tag{12b}$$

For wavy fin,

$$L_e = 0.25\ \mathrm{Re}^{0.52}\ \mathrm{Pr}\ D_h \tag{12c}$$

L_e in the three flow-interrupted fins is much shorter than that in the plain fin, especially at larger values of Re. For example, the L_e of the plain fin is about two times that of the strip offset fin at Re=132.3 but near seven times of that at Re=1323. The correlations of L_e provide a simple way to calculate the thermal entry length of the four PFHE fins. In practice, by taking account of the thermal entry effect, the average Nusselt number for computing the overall heat transfer coefficient may be calculated in this way:

$$\mathrm{Nu}_{\mathrm{ave}} = \mathrm{Nu}_{\mathrm{developed}} + \frac{L_e}{2L_{\mathrm{total}}}\Delta\mathrm{Nu} \tag{13}$$

where $\mathrm{Nu}_{\mathrm{ave}}$ and $\mathrm{Nu}_{\mathrm{developed}}$ represent the average value of the Nu number at a whole fin and the one at the fully developed region, respectively. ΔNu expresses the Nu drop in the thermal entry region. L_{total} is the total length of a fin.

5 Conclusions

Flow and heat transfer in complete three-dimensional geometries of the plain fin, strip offset fin, perforated fin, and wavy fin are carefully investigated, in which the fin thickness, thermal entry effect, and end effect are taken into account in this work. CFD simulations are carried out for the four basic fins of PFHE at Reynolds number ranges of 132.3–1323. The validity of the simulation models is verified by comparing the computed results of the strip offset fin with both the corresponding experimental data and three empirical correlations from literatures. Good agreement has been obtained between the computations and the experiments or the correlations.

Furthermore, data reduction method for calculation of the local Nusselt numbers, j factor, and f factor is presented, based on which, the heat transfer and pressure drop characteristics in the four fins are obtained and analyzed in detail. Influences of the offset fins in the strip fin, holes in the perforated fin, and corrugated walls in the wavy fin on the flow and heat transfer are investigated. Correlations of the thermal entry length for the four PFHE fins are obtained by analyzing the variation of the local Nusselt number along the flow direction.

Acknowledgment

The authors are thankful to the National Natural Science Foundation of China for the support (Grant No. 50676074).

Nomenclature

A = amplitude in wavy fin and total heat transfer area (m^2)
A_2 = heated area at the bottom cover plate (m^2)
A_c = minimum free-flow area (m^2)
A_F = total fin area (m^2)
c_p = specific heat at constant pressure (J/kg K)
D_h = hydraulic diameters, m
f = Fanning friction factor
h = fin height and heat transfer coefficient
h_b = thickness of the bottom aluminum cover plate
j = Colburn factor
k = thermal conductivity of the fluid (W/m K)
k_A = thermal conductivity of aluminum (W/m K)
L = fin array length
L_e = thermal entry length
l_s = strip offset fin length
l_w = pitch of wavy fin waviness
m = fin effectiveness parameter
n_{row} = row number of holes in perforated fin array in the z-direction
Nu = Nusselt number ($=hD_h/k$)
Pr = Prandtl number ($=\mu c_p/k$)
Q = heat (W)
r = radius (m)
Re = Reynolds number based on hydraulic diameters ($=\rho D_h \nu/\mu$)
s = fin spacing distance
T = temperature (K)
t = fin thickness
ν = fluid velocity (m/s)
V = volume (m^3)
U = average overall heat transfer coefficient
X, Y, Z = Cartesian coordinates

Greek Symbols

Φ = hole diameter in the perforated fin
ρ = density (kg/m^3)
μ = dynamic viscosity (Pa s)
η = heat transfer surface efficiency
η_F = fin efficiency
ζ_w = ratio of the wavy fin passage length to the wavy fin length in the z-direction

Subscripts

i = computational node index in the z-direction
f = working fluid
s = fin surface

References

[1] Kays, W. M., and London, A. L., 1950, "Heat Transfer and Flow Friction Characteristics of Some Compact Heat-Exchanger Surfaces, Part I. Test System and Procedure," ASME J. Heat Transfer, **72**, pp. 1075–1085.
[2] Kays, W. M., 1960, "The Basic Heat Transfer and Flow Friction Characteristics of Six Compact High-Performance Heat Transfer Surfaces," ASME J. Eng. Power, **82**, pp. 27–34.
[3] Briggs, D. C., and London, A. L., 1961, "The Heat Transfer and Flow Friction Characteristics of Five Offset Rectangular Duct and Six Plain Triangular Plate-Fin Heat Transfer Surfaces," *International Developments in Heat Transfer*, American Society of Mechanical Engineers, New York, August, pp. 122–134.
[4] London, A. L., and Shah, R. K., 1968, "Offset Rectangular Plate-Fin Surfaces-Heat Transfer and Flow Friction Characteristics," ASME J. Eng. Power, **90**, pp. 218–228.
[5] Waiters, F. M., 1969, "Hypersonic Research Engine Project—Phase IIA, Category I Test Report on Fin Heat Transfer and Pressure Drop Testing," Data Item No. 63.02, AiResearch Manufacturing Company, Document No. AP-69-5348.
[6] Mochizuki, S., and Yagi, Y., 1977, "Heat Transfer and Friction Characteristics of Strip Fins," Heat Transfer-Jpn. Res., **6**, pp. 36–59.
[7] Shah, R. K., Kraus, A. D., and Metzger, D., 1990, "Compact Heat Exchangers," *A Festschrift for A.L. London*, Hemisphere, New York.
[8] Manglik, R. M., and Bergles, A. E., 1990, "The Thermal-Hydraulic Design of the Rectangular Offset-Strip-Fin Compact Heat Exchanger," *Compact Heat Exchangers*, R. K. Shah, A. D. Kraus, and D. Metzger, eds., Hemisphere, New York, pp. 123–149.
[9] Manglik, R. M., and Bergles, A. E., 1995, "Heat Transfer and Pressure Drop Correlations for the Rectangular Offset-Strip-Fin Compact Heat Exchanger," Exp. Therm. Fluid Sci., **10**(2), pp. 171–180.
[10] Hu, S., and Herold, K., 1995, "Prandtl Number Effect on Offset Fin Heat Exchanger Performance: Experimental Results," Int. J. Heat Mass Transfer, **38**(6), pp. 1053–1061.
[11] Rush, T. A., Newell, T. A., and Jacobi, A. M., 1999, "An Experimental Study of Flow and Heat Transfer in Sinusoidal Wavy Passages," Int. J. Heat Mass Transfer, **42**, pp. 1541–1553.
[12] Kays, W. M., and London, A. L., 1984, *Compact Heat Exchangers*, 3rd ed., McGraw-Hill, New York.
[13] Kays, W. M., 1972, "Compact Heat Exchangers," *AGARD Lecture Series on Heat Exchangers* No. 57, NATO, Paris, January, Paper No. AGARD-LS-57-72.
[14] Wieting, A. R., 1975, "Empirical Correlations for Heat Transfer and Flow Friction Characteristics of Rectangular Offset-Fin Plate-Fin Heat Exchangers," Trans. ASME, Ser. C: J. Heat Transfer, **97**, pp. 488–490.
[15] Joshi, H. M., and Webb, R. L., 1987, "Heat Transfer and Friction in the Offset Trip-Fin Heat Exchanger," Int. J. Heat Mass Transfer, **30**, pp. 69–84.
[16] Sparrow, E. M., Baliga, B. R., and Patankar, S. V., 1977, "Heat Transfer-and Fluid Flow Analysis of Interrupted Wall Channels With Application to Heat Exchangers," ASME J. Heat Transfer, **99**, pp. 4–11.
[17] Patankar, S. V., and Prakash, C., 1981, "An Analysis of the Effect of Plate Thickness on Laminar Flow and Heat Transfer in Interrupted-Plate Passages," Int. J. Heat Mass Transfer, **24**, pp. 1801–1810.
[18] Xi, G., Hagiwara, Y., Suzuki, K., and Kaneda, T., 1992, "Effect of Fin Thickness on Flow and Heat Transfer Characteristics of Fin Arrays-An Offset-Fin Array in the Low Reynolds Number Range," Heat Transfer-Jpn. Res., **22**, pp.

1–19.
[19] Saidi, A., and Sundén, B., 2001, "A Numerical Investigation of Heat Transfer Enhancement in Offset Strip Fin Heat Exchangers in Self-Sustained Oscillatory Flows," Int. J. Numer. Methods Heat Fluid Flow, **11**(7), pp. 699–716.
[20] Beale, S. B., 2007, "Use of Streamwise Periodic Boundary Conditions for Problems in Heat and Mass Transfer," ASME J. Heat Transfer, **129**, pp. 601–605.
[21] Wang, Q. W., Lin M., Zeng M., and Tian L., 2008, "Investigation of Turbulent Flow and Heat Transfer in Periodic Wavy Channel of Internally Finned Tube With Blocked Core Tube," ASME J. Heat Transfer, **130**, pp. 061801.
[22] De Losier, C. R., Subramanian, S., Ponyavin, V., Chen, Y., Hechanova, A. E., and Peterson, P. F., 2007, "The Parametric Study of an Innovative Offset Strip-Fin Heat Exchanger," ASME J. Heat Transfer, **129**, pp. 1453–1458.
[23] Nishimura, T., Murakami, S., Arakawa, S., and Kawamura, Y., 1990, "Flow Observation and Mass Transfer Characteristics in Symmetrical Wavy-Walled Channels at Moderate Reynolds Number for Steady Flow," Int. J. Heat Mass Transfer, **33**(5), pp. 835–845.
[24] Asako, Y., and Faghri, M., 1987, "Finite-Volume Solutions for Laminar Flow and Heat Transfer in a Corrugated Duct," ASME J. Heat Transfer, **109**(3), pp. 627–634.
[25] Zhang, J., Kundu, J., and Manglik, R. M., 2004, "Effect of Fin Waviness and Spacing On the Lateral Vortex Structure and Laminar Heat Transfer in Wavy-Plate-Fin Cores," Int. J. Heat Mass Transfer, **47**(8-9), pp. 1719–1730.
[26] Dalal, A., and Das, M. K., 2006, "Natural Convection in a Cavity With a Wavy Wall Heated From Below and Uniformly Cooled From the Top and Both Sides," ASME J. Heat Transfer, **128**, pp. 717–725.
[27] Asako, Y., Faghri, M., and Sundén, B., 1998, "Three-Dimensional Laminar Forced Convection Characteristics of Wavy Ducts With Trapezoidal Cross Section for Plate-Fin Heat Exchangers," *Computational Simulation in Compact Heat Exchangers*, B. Sundén and M. Faghri, eds., Computational Mechanics, Southampton, UK, pp. 49–75.
[28] Manglik, R. M., Zhang, J., and Muley, A., 2005, "Low Reynolds Number Forced Convection in Three-Dimensional Wavy-Plate-Fin Compact Channels: Fin Density Effects," Int. J. Heat Mass Transfer, **48**, pp. 1439–1449.
[29] Patankar, S. V., and Spalding, D. B., 1972, "A Calculation Procedure for Heat, Mass and Momentum Transfer in Three-Dimensional Parabolic Flows," Int. J. Heat Mass Transfer, **15**, pp. 1787–1806.
[30] Batchelor, G. K., 1967, *An Introduction to Fluid Dynamics*, Cambridge University Press, Cambridge, England.
[31] Kays, W. M., and Crawford, M. E., 1980, *Convective Heat and Mass Transfer*, McGraw-Hill, New York.

Numerical Simulation of Transient Multiphase Field During Hybrid Plasma-Laser Deposition Manufacturing

Fanrong Kong

Haiou Zhang[1]
e-mail: zholab@mail.hust.edu.cn

State Key Laboratory of Digital Manufacturing Equipment and Technology,
Huazhong University of Science and Technology,
Wuhan City 430074, P.R.C.

Guilan Wang
State Key Laboratory of Material Forming and Die and Mould Technology,
Huazhong University of Science and Technology,
Wuhan City 430074, P.R.C.

The hybrid plasma-laser deposition manufacturing (PLDM) process is developed based on the plasma deposition manufacturing (PDM) technology. PLDM belongs to the three-dimensional (3D) welding technology and involves the laser power as an augmented heat resource. Compared to PDM technology, the PLDM process has many advantages such as a higher power density, higher processing precision, refined microstructure, and improved mechanical performance of forming components. There exist complicated physical and metallurgical interaction mechanisms due to the combination of PLDM along with the rapid melting and solidification process. Moreover, the interaction between the laser and plasma arc also directly influences the forming quality and precision of the 3D metal components. Therefore, the proposed work is a preliminary attempt to study the transport phenomena in the PLDM process, in which the heat transfer, fluid flow, and molten powder depositing processes have been investigated in detail. The numerical study is performed by using a pressure-based finite volume difference technique after making appropriate modifications of the algorithm. The associated solid/liquid phase transformation process is involved by using an enthalpy-porosity method, and the level-set approach is introduced to track the evolution of weld surface of the deposition layer with powder feeding. An experimentally based hybrid heat input model is developed to involve the influence of the interaction of laser and arc plasma on the redistributed energy absorption by the material. Corresponding experiments of the PLDM process are performed using the same parameters as in the computations, showing a good qualitative agreement. [DOI: 10.1115/1.2969749]

Keywords: hybrid plasma-laser deposition manufacturing, heat transfer, finite volume difference technique, level-set approach

1 Introduction

The plasma deposition with powder injection technique [1–3], as well as the laser cladding technique, has been widely used in many industrial applications, such as surface coating, rapid prototyping, direct metal deposition, and molds and dies repairing. Laser cladding is a very promising technology from a metallurgical point of view, and its benefits include low heat input into the substrate, rapid cooling rates with a fine microstructure of the coating, and an excellent metallurgical bonding with the substrate. The main disadvantage of laser cladding is the poor process efficiency that causes a high manufacturing cost. An optimization of the energy management to reduce the power loss due to thermal conduction is necessary to gain interest at the industrial level. An improved manufacturing efficiency with a shorter manufacturing cycle can be achieved by applying a novel deposition forming technology of coupling a laser with a plasma arc; that is, hybrid plasma-laser deposition manufacturing (PLDM) [4–6]. As a newly developed direct metal fabrication process based on the plasma deposition manufacturing (PDM) technology, PLDM still belongs to the three-dimensional (3D) welding technique. The main idea of PLDM is that the processing area as well as the fed powders are preheated and melted by a transferred arc. The laser power is mainly used for heating up the feedstock material until melted and deposited into a desired shape. Compared to laser cladding, an increase in cladding speed and a lower energy input are reached by applying the PLDM method. With this method, the efficiency of the material can be nearly doubled, with a much lower cost to stock the material. The heat-affected zone is also reduced, which offers the possibility to process crack sensitive materials [7]. Shelyagin et al. [8] also considered the peculiarities of these processes occurring from a combined utilization of a laser beam and a consumable-electrode arc or a plasma jet. Shelyagin et al. [8] developed fundamentally new approaches for one- and multipass hybrid laser-arc weldings, as well as a combined and hybrid laser-microplasma deposition of coatings including diamond and diamondlike thin coatings.

Due to PLDM essentially belonging to a fusion and solidification process, there involve complicated physical and metallurgical interactions that occur between the plasma arc, the laser beam, the metal powders, the base material (substrate), and the shielding gas. Many processing parameters influence the surface characteristics and manufacturing quality of the metal components. Some of those parameters are strongly coupled with each other. It is necessary to optimize these processing parameters to obtain the desired dimensional accuracy and material integrity of the 3D parts. Due to the limits of the previous level of research, few effective experimental investigations have been obtained. Numerical simulation offers a cost-efficient means to better investigate the related complex physics in the PLDM process.

Mainly investigated were the simulation works on the heat and mass transfer and thermal stress evolution in the laser welding,

[1]Corresponding author.

Contributed by the Heat Transfer Division of ASME for publication in the JOURNAL OF HEAT TRANSFER. Manuscript received May 23, 2007; final manuscript received May 12, 2008; published online September 2, 2008. Review conducted by Ben Q. Li. Paper presented at the 15th International Symposium on Electromachining (ISEM XV), Pittsburgh, PA.

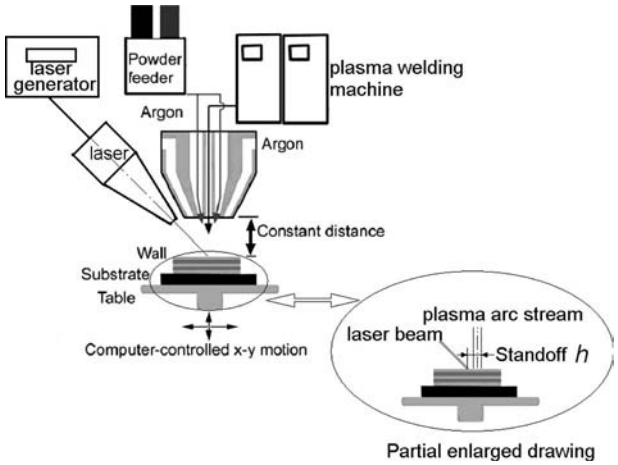

Fig. 1 Sketch map of the PLDM process

laser cladding and surface remelting, electric arc welding, and hybrid high beam welding processes. At an earlier age, Kar and Mazumder [9] presented a one-dimensional diffusion model for determining the composition of an extended solid solution formed due to rapid cooling in the laser cladding. This model considered a diffusion mechanism for mass transport in a one-dimensional semi-infinite molten pool of the cladding material from which heat is removed by conduction through a one-dimensional semi-infinite solid substrate. However, the surface profile of the cladding strip in this model was assumed to be semicylindrical. Subsequently, Zeng [10] developed a two-dimensional quasistate numerical model of fluid flow and heat transfer process in the molten pool for the laser cladding, taking into account the deformation of the free surface. The height of the deposition layer that did not coincide with a practical situation has been presumed by Zeng. Recently, Han et al. [11] developed a mathematical model to predict the thermal behavior and geometry of the melt pool in the laser cladding process; moreover, a level-set approach was applied in this model to track the evolution of the melt pool shape. Yoon et al. [12] added plasma arc welding (PAW) to the existing single laser heat source to join the conventional *V*-grooved butt joint of thin stainless steel tubes. The effect of the welding speed enhancement was also investigated in this study by experiments and finite element analysis. So far, few of the investigations on the heat and mass transfer process in the PLDM have been seen in public. In this paper, a two-dimensional model of the transport phenomena occurring in the PLDM process is developed based on the previous research of Kong and co-workers [13,14]. The effects of the hybrid power model on heat and mass transfer of the molten pool are investigated based on the simulation and experiments in the proposed study.

2 Physical Models

A schematic of the PLDM process with coaxial powder feeding is shown in Fig. 1. The computational domain is initially composed of the substrate (solid phase) and the air (vapor phase) above the substrate. Powders are delivered onto the substrate concentrically with the plasma arc. A small area of the surface of substrate or the present deposited layers is heated and melted under the burning of the plasma arc, and forms a molten pool. A metal part is formed into the designed shape with the multilayer scanning of the plasma arc torch controlled by a computer numerical control (CNC) machine tool and the continuous addition of powder.

The interactions between the laser beam, plasma arc, powder flow, and substrate in the PLDM process are very complicated, and more influencing factors exist for the formation of quality of metal components. To establish the mathematical model that describes the whole deposition process, some fundamental assumptions are presented as follows.

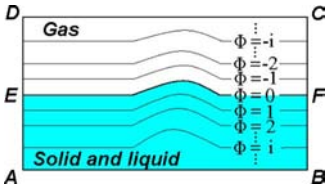

Fig. 2 Schematic of the level-set approach

(1) The plasma power intensity, laser power intensity, and powder flow distribution, respectively, are assumed to be the Gaussian distribution in this study. Considering that the physical mechanisms of interaction between the plasma arc and the laser beam are much more complex, we describe this interaction in detail in another paper [14]. Here, we adopt the energy distribution models of the present references [13] and consider the effect of the interaction of laser and plasma arc on the energy redistribution by the experimental investigations.
(2) The gas flow is assumed to be incompressible.
(3) The liquid flow is assumed to be incompressible and a laminar flow.
(4) The mixture region of the solid phase and liquid phase is regarded as a mushy region.
(5) The interaction of the shield gas pressure on the surface profile and fluid flow of the molten pool has been ignored.

3 Mathematical Modeling

3.1 Tracking of the Deposited Layer Surface: Level-Set Approach. To consider the evolvement of the free surface of the molten pool in the deposited layers, and involving the related physical process of powder deposition (Fig. 2), a level-set approach is adopted to track the free surface [15]

$$\frac{\partial \phi}{\partial t} + F|\nabla \phi| = 0 \tag{1}$$

$$F = F_{\text{prop}} + F_{\text{curv}} + F_{\text{adv}} \tag{2}$$

where F_{prop} is the propagation expansion speed, $F_{\text{curv}} = -\in \kappa$ is the dependence of the speed on the curvature, and $F_{\text{adv}} = U(x,y,t)\cdot\vec{n}$ is the advection speed. Thus, we obtain

$$\frac{\partial \phi}{\partial t} + F_0(x,y,t)\cdot|\nabla \phi| + U(x,y,t)\cdot\nabla\phi = \in \kappa|\nabla\phi| \tag{3}$$

where $U(x,y,t)$ is the convection velocity of the fluid flow and $F_0(x,y,t)$ is the function of the powder feed rate distribution

$$F_0(x,y,t) = \begin{cases} \dfrac{\eta' m}{\pi R'^2}\exp\left(-\dfrac{r'^2}{R'^2}\right)\Big/(\rho_l V_s), & r' \leqslant R' \\ 0, & r' > R' \end{cases} \tag{4}$$

Here, η' is the efficiency of powders used, m is the powder feeding rate, R' is the diameter of the powder flow beam, V_s is the scanning speed, and r' is the distance of a certain powder from the centerline of the powder flow. The influence of the term $\in \kappa|\nabla\phi|$ has been ignored in this study. So, the equation below yields from Eq. (3)

$$\frac{\partial \phi}{\partial t} + F_0(x,y,t)\cdot|\nabla \phi| + U(x,y,t)\cdot\nabla\phi = 0 \tag{5}$$

To extend the zero level set to the entire domain, the level-set function should be well defined, and the signed distance function is initially chosen as the standard

$$\phi(x,y,t) = \pm d \tag{6}$$

where d is the actual distance from the zero level set ϕ_0 and the plus (minus) sign denotes the outside (inside) of the value ϕ_0. In this paper, $\phi(x,y,t)<0$ exists while in the vapor region and $\phi(x,y,t)>0$ exists while in the solid and liquid mixture region.

3.2 Governing Equation. In this study, the phase change is modeled using an enthalpy-porosity technique [16]. Latent heat absorbed or released along with melting or solidification process has been considered by using a temperature-controlled approach. When material is in the process of melting or solidifying, the temperature is assumed to be kept as constant until the latent heat has been entirely absorbed or released; the temperature, then, goes on changing according to the energy equilibrium law. All of the boundary conditions mentioned above have been involved into source terms of governing equations.

The resulting governing equations for mass, momentum, and energy equations are as follows. Continuity:

$$\frac{\partial \rho}{\partial t} + \frac{\partial}{\partial x}(\rho u) + \frac{\partial}{\partial y}(\rho v) = 0 \tag{7}$$

Momentum:

$$\frac{\partial}{\partial t}(\rho u) + \frac{\partial}{\partial x}(\rho u u) + \frac{\partial}{\partial y}(\rho v u) = \frac{\partial}{\partial x}\left(\mu \frac{\partial u}{\partial x}\right) + \frac{\partial}{\partial y}\left(\mu \frac{\partial u}{\partial y}\right) - \frac{\partial P}{\partial x} + S_x \tag{8}$$

$$\frac{\partial}{\partial t}(\rho v) + \frac{\partial}{\partial x}(\rho u v) + \frac{\partial}{\partial y}(\rho v v) = \frac{\partial}{\partial x}\left(\mu \frac{\partial v}{\partial x}\right) + \frac{\partial}{\partial y}\left(\mu \frac{\partial v}{\partial y}\right) - \frac{\partial P}{\partial y} + S_y \tag{9}$$

Energy:

$$\frac{\partial}{\partial t}(\rho H) + \frac{\partial}{\partial x}(\rho u H) + \frac{\partial}{\partial y}(\rho v H) = \frac{\partial}{\partial x}\left(k \frac{\partial T}{\partial x}\right) + \frac{\partial}{\partial y}\left(k \frac{\partial T}{\partial y}\right) + S_h \tag{10}$$

The above source terms according to our enthalpy-porosity formulation and physically coupling with level-set approach are expressed as follows:

$$S_x = e_x \cdot \left(-\tau\kappa(\phi)\,\nabla\,\phi + \nabla_s T \frac{d\tau}{dT} - P_v\right) \cdot \delta(\phi) - \left[C\frac{(1-f_l)^2}{f_l^3 + b}\right] u \tag{11}$$

$$S_y = e_y \cdot \left(-\tau\kappa(\phi)\,\nabla\,\phi + \nabla_s T \frac{d\tau}{dT} - P_v\right) \cdot \delta(\phi) - \left[C\frac{(1-f_l)^2}{f_l^3 + b}\right] v + \rho g \beta (T - T_0) \tag{12}$$

where C is a dependent constant on an arborescent structure of the mushy region and b is a small number to avoid a zero denominator. The values for τ, $\kappa(\Phi)$, and ∇_s are the surface tension coefficient, surface curvature, and surface nabla, respectively. The values for e_x and e_y are unit vectors in the x and y directions, respectively. The value for g is the acceleration of gravity, β is the thermal expanding coefficient, T_0 is the reference temperature, and f_s and f_l refer to the mass fraction of the solid and liquid phases, where $f_l=1$ in the liquid phase region, $0<f_l<1$ in the mushy region of the two phases, and $f_l=0$ in the solid phase region. The delta function is given by

$$\delta(x) = \begin{cases} 1, & x = 0 \\ 0 & \text{otherwise} \end{cases} \tag{13}$$

The thermal boundary conditions, including the heat input q_{plasma} and q_{laser}, and heat loss due to radiation and convection, are involved into the source term S_h of Eq. (10).

$$S_h = (q_{\text{plasma}} + q_{\text{laser}})\,\delta_\varepsilon(\phi) - \sigma \ni (T^4 - T_\infty^4) \cdot \delta(\phi) - \frac{\partial}{\partial t}(\rho \Delta H) - A_h(T - T_\infty) \tag{14}$$

where

$$q_{\text{plasma}}(x,y) = \eta_p \frac{P_{\text{plasma}}}{\pi R_p^2} \exp\left(-\frac{2(x - V_s t - x_a)^2}{R_p^2}\right) \tag{15}$$

$$q_{\text{laser}}(x,y) = \eta_l \frac{P_{\text{laser}} \cos\theta}{\pi R_l^2} \exp\left(-\frac{2(x - V_s t - x_l)^2 \cos^2\theta}{R_l^2}\right) \tag{16}$$

Here, η_p and η_l denote the absorption coefficients of the plasma arc and laser beam, respectively, by which the effect of the field interaction of the plasma arc and laser beam on the hybrid heat source redistribution has been considered. The values for R_p and R_l denote the effective radii of the plasma arc and laser beam action on the substrate, respectively. The value for θ is the inclined angle of the laser beam from the vertical direction, i.e., the deflection angle from the centerline of the laser beam to that of the plasma arc, as shown in the partial enlarged drawing of Fig. 1. In this study, θ is set as 30 deg. The values for x and y are two-dimensional coordinates, respectively. The values for x_a and x_l are the initial locations at the x-direction of the plasma torch and laser head, respectively. So the standoff distance of laser-to-arc, h, equals to the difference of x_a minus x_l. H is enthalpy. The value for ΔH is latent heat due to solidification or melting.

$$H = (1 - f_l)c_s T + f_l c_l T \tag{17}$$

$$\Delta H = \begin{cases} L, & T > T_l \\ f_l L, & T_s \leqslant T \leqslant T_l \\ 0, & T < T_s \end{cases} \tag{18}$$

3.3 Boundary and Initial Conditions. At time $t=0$, the entire domain is in the solid state at room temperature. At time $t>0$, the following boundary conditions are applied. In the proposed study, it is assumed that the gas phase boundaries, *DC*, *DE*, and *CF*, are with thermal insulated boundaries; however, there exists a combined convection and radiation heat transfer between the solid phase boundaries, *AB*, *AE*, *BF*, and ambient, as shown in Fig. 2. At the top surface of the work piece, two heat fluxes with Gaussian distributions are applied.

3.4 Numerical Procedure. The material for the substrate and powders used in the present study are the nickel-based alloy K163. The physical parameters of K163 are listed in Table 1. The whole dimension of the simulation region is 60×30 mm^2, in which the dimension of the substrate is 60×15 mm^2, and the other region out of the substrate and the deposited layers is air. In this study, the input current of the plasma arc is 70 A, the electric voltage is 34 V, the effective diameter of the plasma arc is 6 mm, the diameter of the powder flow beam is 5 mm, the powder feed rate is 0.25 g/s, the scanning speed is 6 mm/s, the nominal laser power is 700 W, and the effective diameter of the laser beam is 0.6 mm.

The two-dimensional coupled continuity, momentum, energy, and level-set equations along with the boundary conditions are solved numerically by using a finite volume differential technique. The general framework of the numerical solution rests on the SIMPLEC algorithm [17], modified appropriately to accommodate the phase change process and the tracking of the liquid and vapor interface. Transient studies are carried out in order to entirely investigate the heat and mass transfer process of the molten pool and deposition layer during the PLDM. Figure 3 shows the flowchart of the solution procedure in each time step. A nonuniform grid of 90×80 is used to discretize the computational do-

Table 1 Main physical parameters of K163

Property	Symbol	Value (unit)
Ambient temperature	T_∞	25°C
Solid viscosity	μ_s	1 m^2/s
Kinematic viscosity	μ_l	1.0×10^{-3} m^2/s
Solid specific heat	C_s	461 $J\,kg^{-1}\,°C^{-1}$
Liquid specific heat	C_l	461 $J\,kg^{-1}\,°C^{-1}$
Solid thermal conductivity	k_s	$(11.21+0.017*T)$ $W\,m^{-1}\,°C^{-1}$
Liquid thermal conductivity	k_l	33.31 $W\,m^{-1}\,°C^{-1}$
Solid density	ρ_s	8360 kg/m^3
Liquid density	ρ_l	8360 kg/m^3
Latent heat of fusion	L_m	3.1×10^5 $J\,kg^{-1}$
Solidus temperature	T_S	1300°C
Liquidus temperature	T_l	1355°C
Dynamic viscosity	μ_l	5.0×10^{-3} $kg\,m^{-1}\,s^{-1}$
Radiation emissivity	∋	0.1
Plasma beam radius	r	3 mm
Surface tension coefficient	τ	0.860 kg/s^2 (at 660°C)
Surface tension coefficient	$\frac{\partial\tau}{\partial T}$	-0.35×10^{-3} $kg\,s^{-2}\,°C^{-1}$
Stefan–Boltzmann's constant	σ	5.67×10^{-8} $W/m^2\,K^4$
Heat transfer coefficient	h_c	40 $m^{-2}\,s^{-1}\,°C^{-1}$

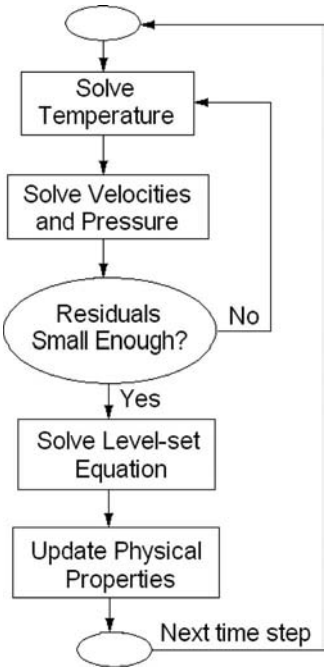

Fig. 3 Flowchart of the solution procedure in each time step

main, with finer grids inside the molten pool. The grid mesh is also used in a previous study [13], and the numerical results have a good agreement with the experimental measurement.

4 Results and Discussion

A series of numerical analyses investigates the heat and mass transfer mechanism in the PLDM process. The transient temperature evolution during the PLDM with the standoff of 0 mm is listed in Fig. 4. It can be known that the temperature field reaches a steady state in a short time after the start of the deposition process, and the fluid flow in the molten pool also shows the same trend (Fig. 5).

According to previous experiment investigations [18], the standoff distance of the laser-to-arc has a sensitive influence on the plasma shapes of hybrid laser-arc welding (Fig. 6). So, it is

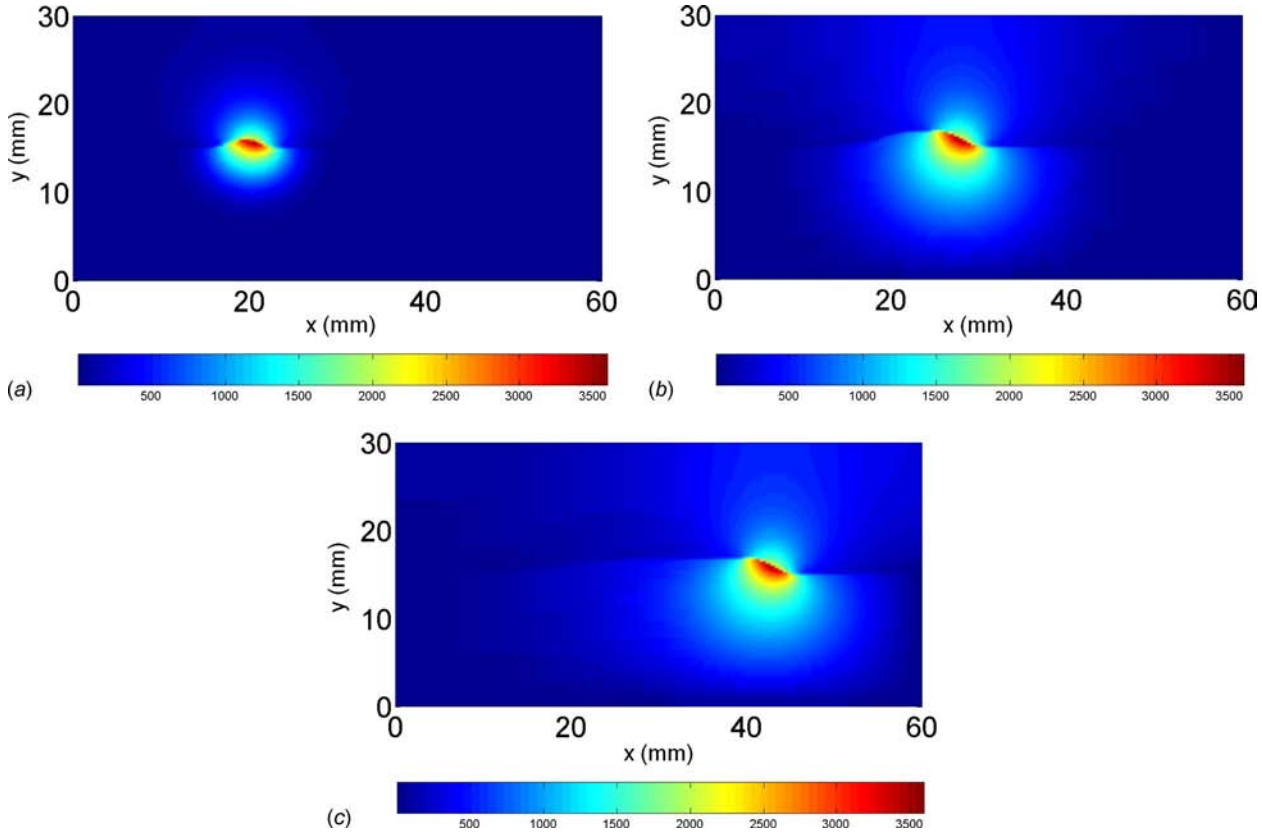

Fig. 4 Transient temperature distribution during PLDM (h=0 mm): (a) t=0.5 s, (b) t=2 s, and (c) t=5 s

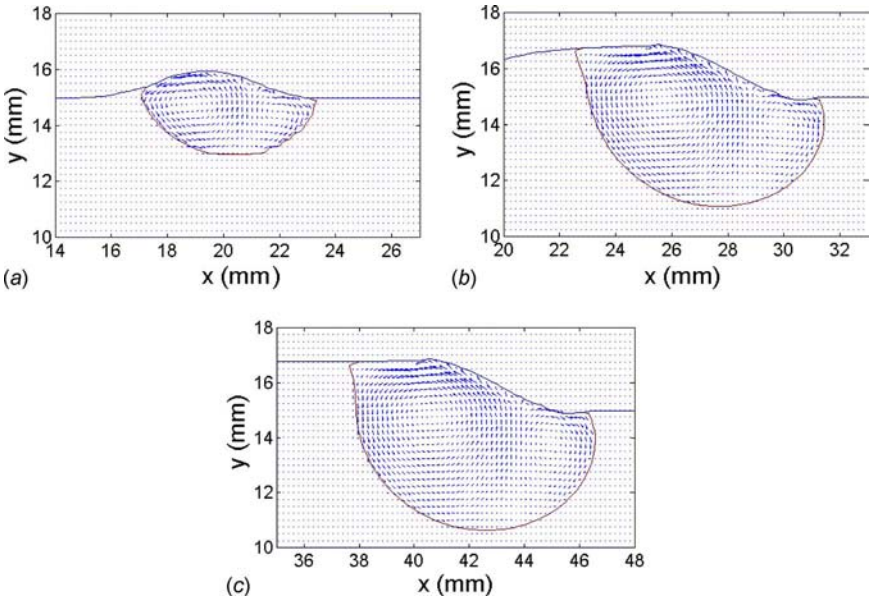

Fig. 5 Fluid flow in the molten pool during the PLDM (h=0 mm): (a) t=0.5 s, (b) t=2 s, and (c) t=5 s

very interesting and necessary to understand the influence of the laser-to-arc distance on the temperature distribution and the profile of the molten pool in the PLDM process. In this study, according to the distance from the center of the laser beam to that of the plasma arc, the numerical experiments of the PLDM are implemented in three cases (Fig. 7): (1) The laser beam spot area acting on the deposited layer surface is set away from and outside of the plasma arc region acting on the surface of the deposited layers, h=0 mm; (2) the laser beam spot area acting on the deposited layer surface is set away from and partly inside of the plasma arc region acting on the deposited layer surface, h=3 mm; and (3) the center of the laser beam spot area acting on the deposited layer surface is set the same as that of the plasma arc region acting on the deposited layer surface, h=6 mm.

Fig. 6 Plasma shapes of hybrid welding with different standoff distances D_{LA}=1 mm, 2 mm, 3 mm, 4 mm, 5 mm, and 6 mm, respectively (see Ref. [18])

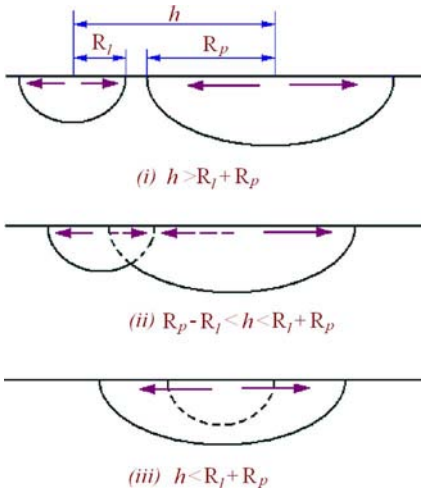

Fig. 7 Sketch map of the PLDM process with different hybrid heat source distributions

Figure 8 shows the evolution of the temperature distribution of the deposition layer and substrate during the PLDM process with three different standoff distances of the laser-to-arc at the moment t=0.2 s, and Fig. 9 shows the fluid flow in the molten pool during the PLDM process with three different standoff distances at the moment t=0.4 s. It can be found that the temperature field and the geometry of the molten pool sensitively depend on the standoff distance of the laser-to-arc. The longitudinal length of the molten pool is obviously elongated with the increase in the standoff distance of the laser-to-arc. The convection circles in the common molten pool are also disordered.

It is seen that the standoff distance from the center of the laser beam to that of the plasma arc directly influences the trajectory of the convection and the profile of the molten pool as well as the flow velocity of the liquid phase in the molten pool. The simulation results also show that the hybrid heat sources induce the depth of the molten pool to enlarge enough to make metallurgical bonding between the deposition layer and the adjacent one.

With the increase in the standoff distance of the laser-to-arc, the maximum temperature of the molten pool almost has no change (Fig. 10). The depth of the molten pool also has a slight increase and increases with the process time until the depth approaches an equilibrium state (Fig. 11). The length of the molten pool increases with the standoff distance of the laser-to-arc due to the enlargement of the acting area of the hybrid heat sources, as shown in Fig. 12.

To further investigate the effects of the laser parameters on the plasma arc, and the width and depth of the molten pool, the corresponding experiments are implemented with the hybrid laser and plasma heat sources. Specimens are cut along their vertical sections and then finished. According to relative experiments [4], the mean value of the molten pool depth is compared to the simulation results based on the same material properties and processing parameters. The average powers of laser are 70 W, 117 W, and 225 W, respectively, and the power of the plasma arc is kept as 2380 W. A good agreement exists between the experiment and simulation, as shown in Fig. 13.

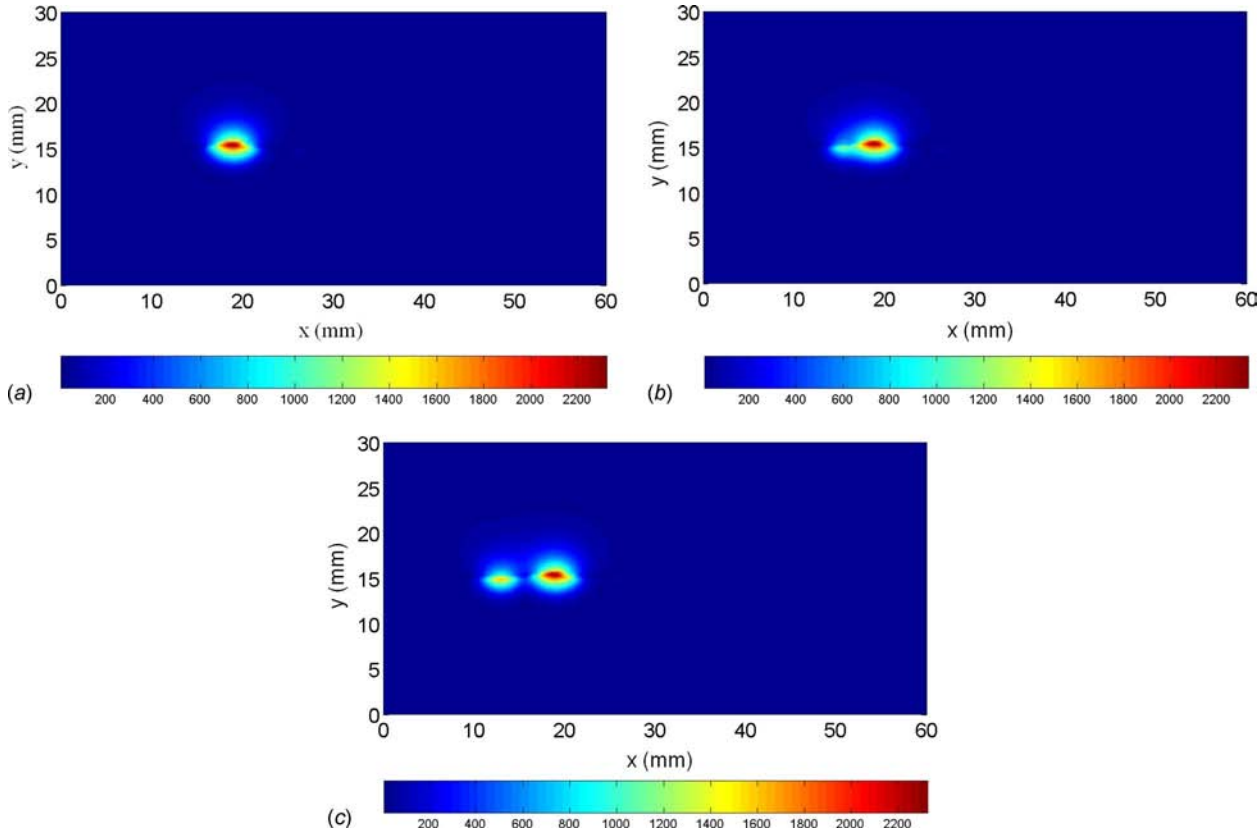

Fig. 8 Temperature distribution in the PLDM with different off-distances at the moment t=0.2 s: (a) h=0 mm, (b) h =3 mm, and (c) h=6 mm

5 Conclusions

A transient solid, liquid, and vapor unified mathematical model during the PLDM process is presented in the proposed study. The model introduces a level-set approach to track the evolution of the molten pool surface, involving the physical boundary conditions at the liquid-vapor interface and solid-liquid interface into the source terms of the governing equation. The numerical results show that convection plays a significant role in influencing the heat dissipation and the molten pool shape. Compared with the previous assumption of a flat free surface, tracking the surface profile of the deposition layer by the level-set approach may cause an apparent improvement toward the real situation. The computa-

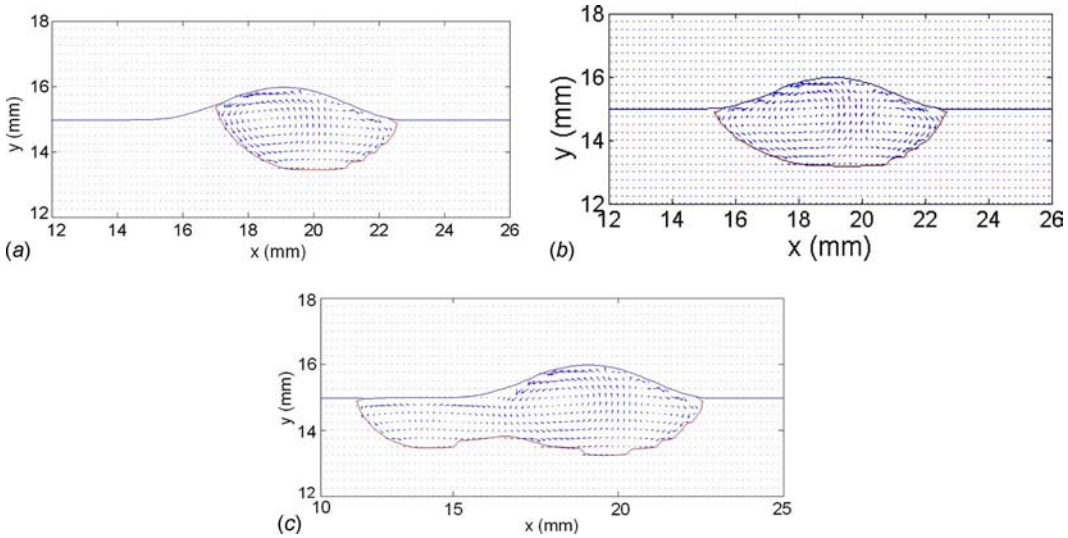

Fig. 9 Fluid flow in the molten pool during the PLDM process with different off-distances at the moment t=0.4 s: (a) h=0 mm, (b) h=3 mm, and (c) h=6 mm

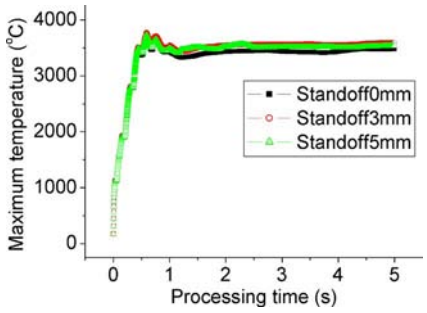

Fig. 10 Evolution of maximum temperature in the molten pool during the PLDM

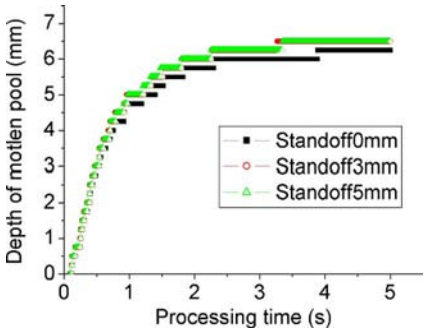

Fig. 11 Evolution of the depth of molten pool during the PLDM

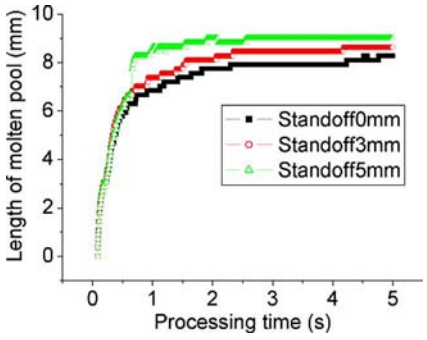

Fig. 12 Evolution of the length of the molten pool during the PLDM

tional results show that the standoff distance of the laser beam to the plasma arc directly influences the length of the molten pool due to the enlarged action area of the hybrid heat sources. Since the underlying mechanisms investigated could also occur in other high-energy beam processes, such as hybrid laser-arc welding, the results of this study will give some insight into the practical applications. There are complicated mechanisms existing in the hybrid laser and arc processing material, such as welding, cutting,

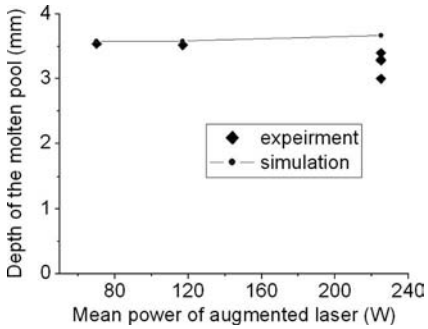

Fig. 13 Measurement values [4] and numerical simulation of the molten pool depth during the PLDM (h=0 mm)

cladding, and so on. Most of these mechanisms have to be further studied based on the numerical methods and experiments.

References

[1] Zhang, H., Xu, J., and Wang, G., 2003, "Fundamental Study on Plasma Deposition Manufacturing," Surf. Coat. Technol., **171**(1–3), pp. 112–118.

[2] Chen, Y., Wang, G., and Zhang, H., 2001, "Numerical Simulation of Coating Growth and Pore Formation in Rapid Plasma Spray Tooling," Thin Solid Films, **390**(1–2), pp. 13–19.

[3] Zhang, H., Wang, G., Yunhua, L., and Takeo, N., 2001, "Rapid Hard Tooling by Plasma Spraying for Injection Molding and Sheet Metal Forming," Thin Solid Films, **390**(1–2), pp. 7–12.

[4] Qian, Y., Zhang, H., and Wang, G., 2006, "Research on Techniques of High-Temperature Alloy Powder Deposition by Hybrid Plasma-Laser," Chin. J. Mech. Eng., **17**(3), pp. 315–317.

[5] Qian, Y., Zhang, H., and Wang, G., 2006, "Research of Rapid and Direct Thick Coatings Deposition by Hybrid Plasma-Laser," Appl. Surf. Sci., **252**(18), pp. 6173–6178.

[6] Zhang, H., Qian, Y., Wang, G., and Zheng, Q., 2006, "The Characteristics of Arc Beam Shaping in Hybrid Plasma and Laser Deposition Manufacturing," Sci. China, Ser. E: Technol. Sci., **49**(2), pp. 238–247.

[7] Wilden, J., Emmel, A., Bergmann, J. P., and Dolles, M., 2004, "Optimisation of Energy Management Through Plasma-Augmented-Laser Cladding (PALC)," *Proceedings of the International Thermal Spray Conference, ITSC 2004*, Osaka, Japan, May 10–12, pp. 5–11.

[8] Shelyagin, V. D., Krivtsun, I. V., Borisov, Yu. S., Khaskin, V. Yu., Nabok, T. N., Siora, A. V., Bernatsky, A. V., Vojnarovich, S. G., Kislitsa, A. N., and Nedej, T. N., 2005, "Laser-Arc and Laser-Plasma Welding and Coating Technologies," Avtomaticheskaya Svarka, **8**, pp. 49–54.

[9] Kar, A., and Mazumder, J., 1987, "One-Dimensional Diffusion Model for Extended Solid Solution in Laser Cladding," J. Appl. Phys., **61**, pp. 2645–2655.

[10] Zeng, D., 1998, "Numerical Analysis of Fluid Flow Field, Temperature Field and Concentration Field in the Laser Melting Pool," Ph.D. thesis, Huazhong University of Science and Technology, China.

[11] Han, L., Phatak, K. M., and Liou, F. W., 2004, "Modeling of Laser Cladding With Powder Injection," Metall. Mater. Trans. B, **35**(6), pp. 1139–1150.

[12] Yoon, S. H., Hwang, J. R., and Na, S. J., 2007, "A Study on the Plasma-Augmented Laser Welding for Small-Diameter STS Tubes," Int. J. Adv. Manuf. Technol., **32**(11–12), pp. 1134–1143.

[13] Zhang, H., Kong, F., Wang, G., and Zeng, L., 2006, "Numerical Simulation of Multiphase Transient Field During Plasma Deposition Manufacturing," J. Appl. Phys., **100**, pp. 123522.

[14] Kong, F., Lin, D., Yang, S., and Kovacevic, R., 2008, "Numerical Analysis of a Hybrid Laser-Arc Welding Process by Using 3D Nonlinear Finite Element Model," *COM2008*, Canada, Aug.

[15] Osher, S., and Sethian, J. A., 1988, "Fronts Propagating With Curvature Dependent Speed: Algorithms Based on Hamilton-Jacobi Formulations," J. Comput. Phys., **79**, pp. 12–49.

[16] Brent, A. D., Voller, V. R., and Reid, K. J., 1988, "Enthalpy-Porosity Technique for Modeling Convection-Diffusion Phase Change: Application to the Melting of a Pure Metal," Numer. Heat Transfer, **13**(3), pp. 297–318.

[17] Tao, W., 2001, *Numerical Heat Transfer*, 2nd ed., Xi'an Jiaotong University Press, Xi'an, China.

[18] Gao, M., Zeng, X. Y., and Hu, Q. W., 2006, "Effects of Welding Parameters on Melting Energy of CO_2 Laser-GMA Hybrid Welding," Sci. Technol. Weld. Joining, **11**(5), pp. 517–522.

Extraordinary Coherent Thermal Emission From SiC Due to Coupled Resonant Cavities

Nir Dahan
Avi Niv
Gabriel Biener
Yuri Gorodetski
Vladimir Kleiner
Erez Hasman
e-mail: mehasman@tx.technion.ac.il

Faculty of Mechanical Engineering,
Micro and Nanooptics Laboratory,
Russell Berrie Nanotechnology Institute,
Technion-Israel Institute of Technology,
Haifa 32000, Israel

In high temperature and vacuum applications, when heat transfer is predominantly by radiation, the material's surface texture is of substantial importance. Several micro- and nanostructure designs have been proposed to enhance a material's emissivity and its radiative coherence, as control of thermal emission is of crucial concern in the design of infrared sources, optical filters, and sensing devices. In this research, an extraordinary coherent thermal emission from an anisotropic microstructure is experimentally and theoretically presented. The enhanced coherency is due to coherent coupling between resonant cavities obtained by surface standing waves, wherein each cavity supports a localized field that is attributed to coupled surface phonon polaritons. We show that it is possible to obtain a polarized quasimonochromatic thermal source from a SiC microstructure with a high quality factor of 600 at the resonant frequency of the cavity and a spatial coherence length of 716 wavelengths, which corresponds to an angular divergence of 1.4 mrad. In the experimental results, we measured a quality factor of 200 and a spatial coherence length of 143 wavelengths. We attribute the deviation in the experimental results to imperfections in the fabrication of the high quality factor cavities.
[DOI: 10.1115/1.2955475]

Keywords: coherence, thermal emission, resonators, surface waves

1 Introduction

The thermal emission of absorbing materials is affected by surface morphology as well as the excitation of surface waves, surface plasmon polaritons in metal, or surface phonon polaritons (SPPs) in polar crystal [1–3]. Surface waves are confined electromagnetic waves due to collective oscillations of the free electrons in metal or the resonant collective lattice vibrations in polar crystal, which propagate along the interface and decay exponentially with increasing the distance from the interface [4,5]. The electromagnetic energy density associated with surface waves has been widely investigated. It has been shown that thermal emission can be quasimonochromatic in the vicinity of a flat surface, in a distance that is of the order of a wavelength, due to the excitation of resonant surface waves [6]. Furthermore, surface modes yield a long-range spatial coherence length, L_c, on a scale of the surface wave propagation length, $L_{\|}$, which may be much larger than the emitted wavelength, $L_c \approx L_{\|} \gg \lambda$ [7,8]. To transmit these surface waves along with their coherency to the far field, several configurations were suggested to design thermal sources, such as gratings [9,10], multilayer structure [11,12], photonic crystals [13–15], and resonant cavities [16,17]. In the far field, the spatial coherence can be evaluated by the directivity of the emitted wave via $l_c \sim \lambda/(\Delta\theta \cos\theta)$, where $\Delta\theta$ is the angular lobe. In the case of introducing a shallow grating coupler ($h \ll \lambda$), a smooth perturbation is caused to the surface [1]; therefore, the emission pattern had a rainbowlike behavior, and the coherence length in the far field, l_c, was found to be limited by that of the delocalized surface waves ($l_c \leq L_c$) [7,9].

An alternative way of analyzing thermal emission, according to Kirchhoff's law, is by determining the absorptivity of a structure. Using a relatively deep grating ($h \sim \lambda$), strong radiation absorption was obtained over a broad range of incident angles due to localized field enhancement. This absorption was attributed to the excitation of standing wave coupled surface plasmons in narrow grating cavities [18].

In this paper, we investigate theoretically and experimentally an extraordinary coherent thermal radiation of coupled resonant cavity (CRC) structure that was etched on a silicon carbide (SiC-6*H* polytype) substrate. Herein, the implementation of CRC is extended to crystalline material where the delocalized SPPs have a long-range coherency in the near field ($L_c = 55\lambda$), consecutive to our recent work on amorphous fused silica, where the spatial coherence of the radiative field was enhanced by an order of magnitude compared to the small delocalized SPP coherency ($l_c = 32\lambda \gg L_c = 2\lambda$) [17]. Here, we show that it is possible to obtain a quasimonochromatic thermal source with a high quality factor $Q = \omega/\Delta\omega \approx 600$, which corresponds to highly temporal coherence and a spatial coherence length of the radiative field $l_c \approx 716\lambda$. This coherence length is enhanced compared with the coherency of the delocalized SPPs and therefore is encouraged to design highly coherent and unidirectional infrared (IR) sources, e.g., for spectroscopy or selective detectors. Moreover, our source has a peculiar behavior: It supports a thermal emission at a single resonant frequency and in a well-defined direction. Note that this emission distribution is fundamentally different than coupling delocalized SPPs using a prism or grating coupler whereby each frequency is emitted in a different direction according to the dispersion relation of the delocalized SPPs. This resonant enhancement could be obtained for a TM polarized wave (as illustrated in Fig. 1(*a*)) due to CRC structure in the spectral range where SiC supports SPPs. The CRC structure consists of periodic cavities in which each cavity supports standing waves and adjacent cavities are coupled by surface standing waves.

2 Theoretical Analysis and Experimental Results

The coherent thermal emission can be viewed as the interplay between two mechanisms. The first is a localized field inside the cavity. A single resonant frequency is supported by the cavity according to its geometry, i.e., width, depth, shape, and the nature

Contributed by the Heat Transfer Division of ASME for publication in the JOURNAL OF HEAT TRANSFER. Manuscript received October 10, 2007; final manuscript received March 26, 2008; published online September 3, 2008. Review conducted by Jayathi Murthy.

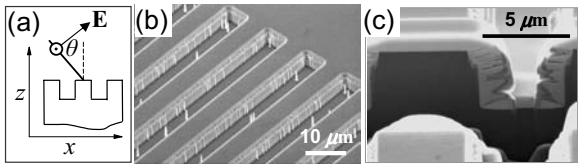

Fig. 1 (*a*) CRCs geometry with a coordinate system. (*b*) SEM image of CRC structure. (*c*) SEM image of a single cavity cross section embedded in SiC with periodicity $\Lambda=11.6$ μm, fill factor $q=0.56$, and depth $h=4.6$ μm; to observe the cavity profile in a high contrast (the dark region indicates SiC), a Pt was deposited and ion milling with a focused ion beam was performed.

of the substrate material. The magnitude of the TM polarized electric field was calculated by a finite difference time domain (FDTD) algorithm, as shown in Fig. 2(*a*) for deep resonant cavities. Standing waves are clearly discerned inside the cavities, which originate from coupled SPPs that decay from the inner cavity walls; this results in a greater energy density being observed along the walls. Each isolated cavity can be regarded as a localized source supporting a broad angular emission. In order to obtain a directional emission, a coherent coupling mechanism between the cavities is required. Otherwise, the emission behavior would be according to the localized field, which is omnidirectional [19]. By choosing the periodicity of the cavities according to Rayleigh's anomaly, a surface standing wave is excited by the first diffraction order, as shown in Fig. 2(*b*), which correlates adjacent resonant cavities. As a result, we obtained a resonant frequency having a coherency for a longer distance than that of the delocalized SPPs, yielding a highly directional emission.

We studied the thermal emission by realizing a CRC structure embedded in SiC substrate. SiC is an interesting candidate as a thermal source since it has a high melting temperature, a low thermal expansion, and specialized by a high mechanical strength. As a polar crystal, SiC supports SPPs in the spectral range where $\tilde{\varepsilon}'<-1$, corresponding to the IR spectra between 10.6 μm and 12.6 μm, having a complex dielectric constant of $\tilde{\varepsilon}(\lambda_0=11.6\ \mu\text{m})=\tilde{\varepsilon}'+i\tilde{\varepsilon}''=-11.9+i0.62$ [20]. Our structure was designed to support directional thermal emission at $\lambda_0=11.6$ μm wavelength in the normal direction. For this purpose, the periodicity was set to be equal to the wavelength $\Lambda=\lambda_0$. Because of the high Q, the resonant frequency is sensitive to the cavity shape; therefore, the final depth h was fine-tuned accordingly to be $h=4.6$ μm with a filling factor $q=0.56$. We fabricated a 15 mm square CRC structure by standard photolithographic technique using a negative photoresist. After developing the photoresist, a NiCr of thickness 1300 Å was deposited and afterward lift-off was performed. The substrate was etched through the NiCr mask by reactive ion etching at a power of 250 W and a pressure of

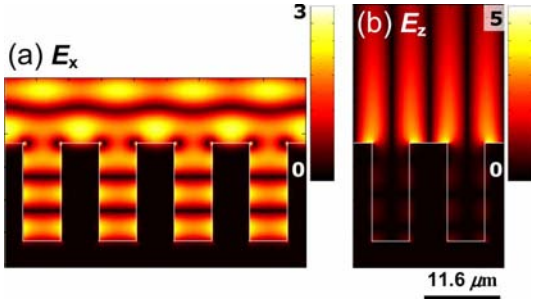

Fig. 2 The magnitude of the electric field components in the *x-z* plane, (*a*) $|E_x|$ and (*b*) $|E_z|$, for normal incident wavelength $\lambda_0=11.6$ μm. The calculations were performed for a SiC CRC with periodicity $\Lambda=11.6$ μm, fill factor $q=0.5$, and depth $h=14.85$ μm.

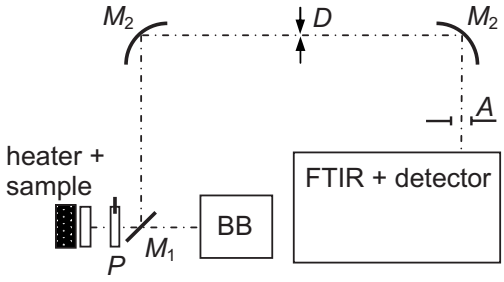

Fig. 3 Experimental setup used to measure spectral directional emissivity. *P*-polarizer; BB-blackbody; M_1-flat mirror on rotating stage; M_2-parabolic mirror, focal length=250 mm; *D*-angular resolution diaphragm in the focal plane of M_2, diameter=1 mm; *A*-field of view aperture; diameter=10 mm.

10 mTorr with SF_6 and O_2 gases at flow rates of 19 SCCM and 1 SCCM, respectively (SCCM denotes cubic centimeter per minute at STP). The etching was performed at a rate of 600 Å/min at room temperature until the desired depth was reached. As a final step, the remaining NiCr was removed with a Cr etchant. Scanning electron microscope (SEM) images of the structure and the cavity cross section are shown in Figs. 1(*b*) and 1(*c*), respectively. Submicron rods remained after the etching process inside the cavities, as shown in Fig. 1(*b*). They are located randomly inside the cavities and upon the sample with a typical diameter of 400 nm, which is much smaller than the emitted wavelength. Thus, we neglect them in our calculations.

The experimental setup that was used to measure the spectral directional emissivity is illustrated in Fig. 3. The sample and the blackbody (CI-Systems, Model SR-80-4HT) were heated to $T=770\pm1$ K to increase the radiative flux and improve the signal-to-noise ratio. The sample temperature was measured with a K-type thermocouple and controlled by a temperature controller (HeatWave Labs, Model 101303-04B). Measurements of the emission spectra were performed using a Fourier transform IR spectrometer (FTIR, Bruker-Vertex 70) equipped with a cooled HgCdTe detector. The spectral resolution was set to $\delta\omega=1$ cm^{-1}, the field of view $A=10$ mm, and an angular resolution $\Omega=2.4\times10^{-6}$ sr (corresponding to $\delta\theta=0.1$ deg). Note that the measured emissivity ($\bar{\varepsilon}$) is actually an averaged emissivity over the solid angle Ω, i.e., $\bar{\varepsilon}(\omega\pm\delta\omega/2,\theta\pm\delta\theta/2,T)=\int_\Omega\varepsilon(\omega\pm\delta\omega/2,\theta,T)d\Omega'$. The calculated emissivity was derived from the calculations of the reflectivity using rigorous coupled wave analysis (RCWA). Figure 4(*a*) shows the emissivity distribution in the (θ,ω) plane calculated for a rectangular cavity configuration shown in Fig. 1(*a*). The measured emissivity (normalized to a blackbody) is given in Fig. 4(*b*). Both figures are for TM polarization state at the spectral range that supports SPPs. A bright spot is observed in the center, which indicates high emission. This thermal source is quasimonochromatic—it supports only a very narrow spectral band—and is highly directional. Although a signature pattern of frequencies emitted in off-axis directions is observed in Fig. 4, the image confirms a low emissivity, resulting from less effective support by the cavity. The measured and the calculated spectral emissivity near the normal direction at $\theta=0$ deg and $\theta=1$ deg are shown in Fig. 5(*a*) for the realized cavity profile, as depicted in the inset of Fig. 5(*a*). A narrow spectral peak, $\Delta\omega=1.41$ cm^{-1} (corresponding to $\Delta\lambda=20$ nm) at half maximum, is theoretically observed around $\omega_0=862$ cm^{-1} (11.6 μm) having a quality factor $Q=\omega_0/\Delta\omega\approx600$. Figure 5(*b*) shows measured and calculated angular emissivities at the peak frequencies observed in Fig. 5(*a*). As can be seen, there is a single resonance peak at the frequency that is supported by the cavity and satisfies the standing wave between the cavities (black). At nearby frequency (red), the emissivity drops and the angular lobes are much broader, which corresponds to smaller spatial coherency. The calculated lobe width at half

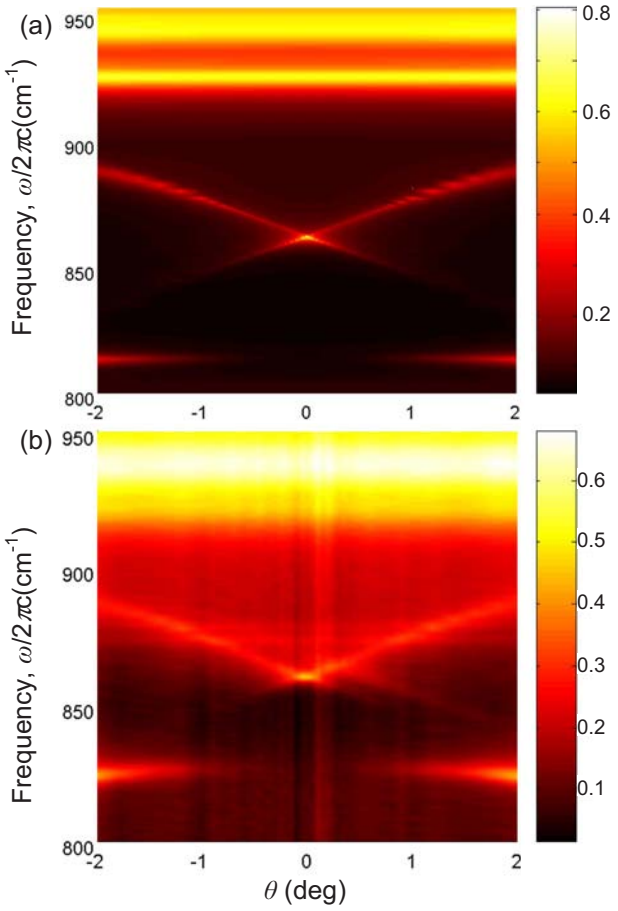

Fig. 4 (***a***) **Calculated emissivity, ε, for rectangular cavity profile shown in Fig. 1(*a*) and (*b*) measured emissivity, $\bar{\varepsilon}$, distribution as a function of frequency in the spectral range in which SiC supports SPPs, and the observation angle near the normal direction. The bright colors represent high emissivity.**

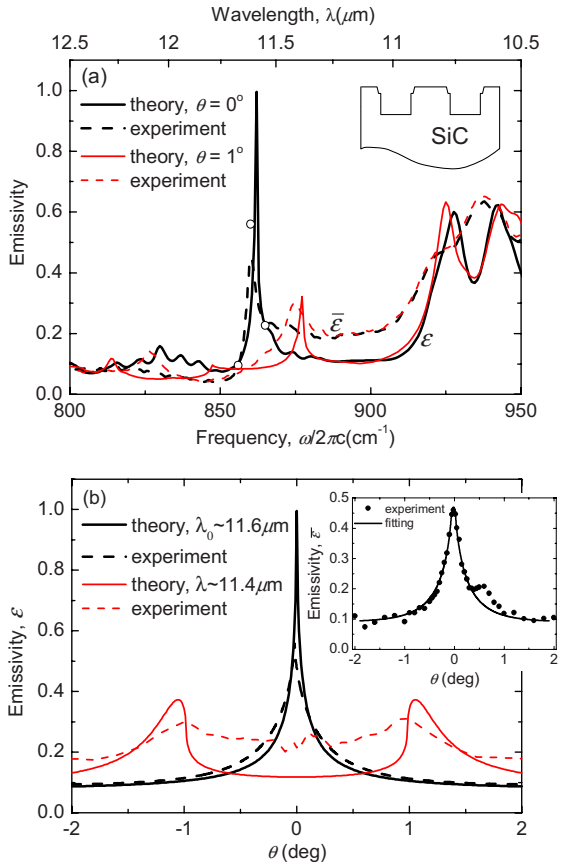

Fig. 5 (***a***) **Spectral emissivity observed in (thick line) a normal direction and in (thin line) θ=1 deg for TM polarized wave; (solid) calculated emissivity for the realized cavity profile as illustrated in the inset, (dash) experiment, and (circle) corrected emissivity obtained from (*b*). (*b*) Angular emissivity at the peak wavelengths obtained in (*a*); (solid) theory and (dash) experiment obtained by deconvolution analysis. The inset shows (dots) the measured emissivity and the (solid) curve fitting to the experimental results obtained by convolving the dash curve in (*b*) and the angular resolution.**

maximum, $\Delta\theta$=0.08 deg=1.4 mrad, is a signature to the spatial coherence length of the thermal radiation. The relation between the angular deviation of the beam and the spatial coherence length is known as $l_c \approx \lambda/\Delta\theta$, herein, $l_c \approx 716\lambda_0 \approx 8.3$ mm; slightly smaller than Aperture *A*. Note that this spatial coherence length is significantly higher than the propagation length of SPPs on a flat SiC-vacuum interface, which equals approximately the coherence length of the delocalized surface waves, $L_{\|} \approx 1/\mathrm{Im}(k_{\|}) \approx 55$ μm, where $k_{\|}=(\omega/c)\sqrt{\tilde{\varepsilon}(\omega)/(\tilde{\varepsilon}(\omega)+1)}$ is the SPPs' wave number [7]. The experimental results depicted in Fig. 5(*a*) and 5(*b*) show a reasonable agreement with the calculation. Herein, the theoretical lobe width is of the order of the angular resolution we have used in our experiment ($\Delta\theta \sim \delta\theta$). As a result, the measured emissivity ($\bar{\varepsilon}(\omega \pm \delta\omega/2, \theta \pm \delta\theta/2, T)$) is smaller than the real emissivity ($\varepsilon(\omega \pm \delta\omega/2, \theta, T)$) at the resonance frequency near the normal direction (see inset in Fig. 5(*b*)). In order to retrieve the emissivity distribution we have used deconvolution analysis. The emissivity peak shown in Fig. 5(*b*) equals 0.56 with an angular width at half maximum $\Delta\theta$=0.4 deg, which corresponds to a spatial coherence $L_c \approx 143\lambda_0$. Using this result, we corrected the spectral emissivity at the peak frequency in Fig. 5(*a*) to be 0.56 as well (circle), with an estimated quality factor $Q \sim 200$. We attribute the deviation in the coherency values to the high sensitivity of the structure in the cavity geometry, roughness, and defects due to the behavior of the high Q cavity.

In order to understand the physical origin of the enhanced coherency, we calculated the reflectivity as a function of the cavity depth for the actual cavity profile shown in Fig. 1(*c*). Figure 6 shows the reflectivity for TM polarized light at 11.6 μm wavelength using RCWA. The sharp dips resemble a Fabry–Pérot-like resonator, which indicates its high Q. The difference between two successive depths $h_{m+1}-h_m$ is equal to half of the wavelength of the standing wave inside the cavity, λ^{sw} [18]. In our case, for incident vacuum wavelength of 11.6 μm, we obtained λ^{sw} =10.4 μm with the corresponding wave number $k^{sw}=2\pi/\lambda^{sw}$.

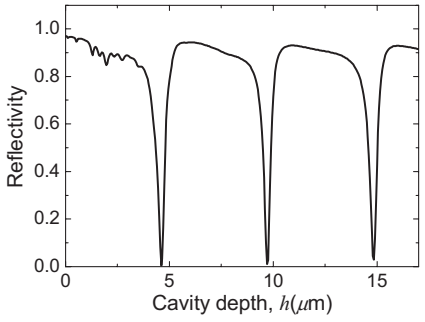

Fig. 6 Calculated reflectivity of CRC as a function of the cavity depth, for normal incident wavelength λ_0=11.6 μm

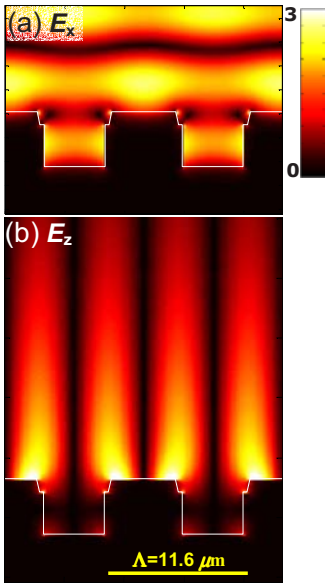

Fig. 7 The magnitude of the electric field components in the *x-z* plane, (*a*) $|E_x|$ and (*b*) $|E_z|$, for normal incident wavelength λ_0=11.6 μm. The calculations were performed for the realized cavity profile as shown in Fig. 1(*c*): periodicity Λ=11.6 μm, fill factor q=0.56, and depth h=4.6 μm.

The depth of the realized cavity was determined to be the first dip due to fabrication considerations. Figure 7 shows the calculated field distribution using FDTD algorithm for the realized structure having the cavity parameters, as shown in Fig. 1(*c*). Figure 7(*a*) shows the electric field localized inside the cavity whereas Fig. 7(*b*) shows the horizontal standing wave between adjacent cavities. We confirmed that the observed standing waves inside the cavity are due to the coupled SPPs from the vertical walls inside the cavity by solving the characteristic equation of an infinite slab waveguide [21], an air gap between two semi-infinite layers of lossy material, herein SiC. The wave number of the coupled surface wave is calculated as

$$\beta = \left\{ k_0^2 + \frac{2}{\tilde{\varepsilon}^2 d^2}\left[1 + \sqrt{1 + k_0^2 \tilde{\varepsilon}^2 d^2 (1+\tilde{\varepsilon})}\right] \right\}^{1/2} \quad (1)$$

where $k_0 = 2\pi/\lambda_0$ is the wave number of the incident wave in a vacuum and d is the width of the slab, which equals the cavity width $d = \Lambda(1-q) \approx 5.1$ μm. Equation (1) is valid under the approximation that $d \ll 2\delta_{air}$, where δ_{air} is the decay length of the SPPs in air, which is evaluated by $\delta_{air} = 1/|\mathrm{Im}\sqrt{k_0^2 - k_\parallel^2}| \approx 5.7$ μm. The dispersion relation of the waveguide mode wave number, β, given by Eq. (1) is shown in Fig. 8(*a*) along with k^{sw} and the

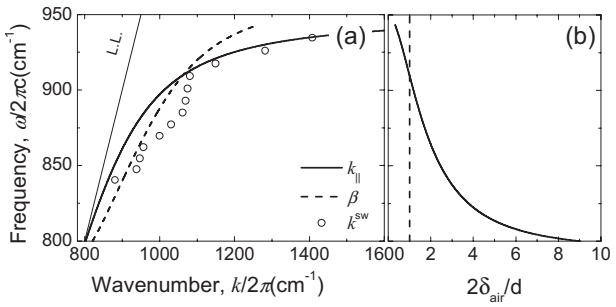

Fig. 8 (*a*) Dispersion relation of SPPs at SiC flat surface $k_\parallel$, i.e., delocalized (solid); slab waveguide β (dashed); standing waves inside the cavity k^{sw} (dots). (*b*) Decay length of delocalized SPPs in air as a function of frequency.

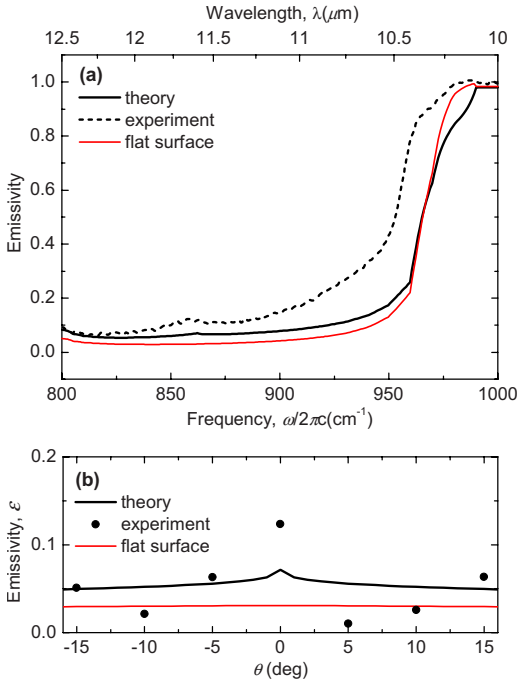

Fig. 9 (*a*) Spectral emissivity observed in normal direction for TE polarized wave and (*b*) angular emissivity at the peak wavelength at 11.6 μm, obtained in (*a*).

delocalized SPPs $k_\parallel$. Two regimes are discerned: above and beneath the intersection of $k_\parallel$ and β. Beneath the intersection point, k^{sw} behaves like β, whereas above it behaves like $k_\parallel$. It can be understood according to the decay length of SPP in air as shown in Fig. 8(*b*), where the intersection point corresponds to a decay length of half the cavity width. Our calculations showed an enhanced coherent emission at frequencies below the intersection point, while above it the coherency was similar to that of the delocalized SPPs. Thus, coupled SPPs inside the cavity are necessary to obtain enhanced coherency. A horizontal standing wave at the same frequency is excited on the rib between the cavities (see Fig. 7(*b*)), designated to link adjacent cavities for a long distance on the interface; evidence of the high directivity of the spontaneous emission. The CRC structure can also be understood as a coherent coupled antenna array; each cavity can be regarded as an IR antenna consisting of a wire with a length of a half-wavelength ($\lambda^{sw}/2$) at the operating frequency [22].

Finally, the thermal emission from CRC structure was characterized for TE polarization state. SPPs do not exist in SiC at TE polarized light; hence, no emission enhancement is expected. We measured and calculated the spectral emissivity in the normal direction (Fig. 9(*a*)) and the directional emissivity at 11.6 μm (Fig. 9(*b*)). A low omnidirectional emissivity was observed close to that of a flat surface. The small enhancement is obtained due to a guided mode mechanism, which is affected by the cavity dimension (geometric resonance). The geometric resonance appears as long as the cavity width is larger than the cutoff width $d_c \sim (\lambda/\pi)\tan^{-1}\sqrt{-\tilde{\varepsilon}'}$, for a lossy infinite waveguide [23]. In our structure d_c=4.76 μm, slightly smaller than the cavity width, which confirms the existence of geometric resonance. These resonances become the dominant mechanism for enhanced emission in very deep cavities. For example, the emissivity for a TE wave can reach 0.8 at ~100 μm cavity depth.

3 Conclusions

In conclusion, by utilizing periodic CRCs, a very highly coherent and polarized thermal source can be designed, e.g., for IR

spectrometers, that is not limited by the coherence of the delocalized SPPs. This enhancement is obtained due to the increasing photonic density of states inside the cavity by localized surface waves, coupling adjacent cavities by horizontal standing wave, and coherent coupling into radiative. The high resonance structure might be utilized also in absorption mechanism for multispectral thermal detectors as well as for IR sensing devices.

Nomenclature

c = speed of light in vacuum
d = cavity width
d_c = cutoff width
h = cavity height
k = wave number
$k_{\|}$ = SPPs wave number
l_c = spatial coherence length in the far field
$L_{\|}$ = surface wave propagation length
L_c = spatial coherence length in the near field
q = filling factor
Q = quality factor
β = waveguide wave number
δ = decay length, $\delta = 1/\mathrm{Im}(k_z)$
ε = theoretical spectral directional emissivity
$\bar{\varepsilon}$ = experimental spectral directional emissivity
$\tilde{\varepsilon}$ = dielectric constant, relative electric permittivity
λ = wavelength
λ^{sw} = wavelength of a standing wave
Λ = periodicity of CRC structure
θ = polar emission angle
ω = angular frequency
Ω = solid angle

References

[1] Greffet, J.-J., Carminati, R., Joulain, K., Mulet, J.-P., Mainguy, S., and Chen, Y., 2002, "Coherent Emission of Light by Thermal Sources," Nature (London), **416**, pp. 61–63.

[2] Fu, C. J., Zhang, Z. M., and Tanner, D. B., 2005, "Planar Heterogeneous Structures for Coherent Emission of Radiation," Opt. Lett., **30**, pp. 1873–1875.

[3] Sai, H., Yugami, H., Akiyama, Y., Kanamori, Y., and Hane, K., 2001, "Spectral Control of Thermal Emission by Periodic Microstructured Surfaces in the Near-Infrared Region," J. Opt. Soc. Am. A, **18**, pp. 1471–1476.

[4] Boardman, A. D., 1982, *Electromagnetic Surface Modes*, Wiley, Belfast, Ireland.

[5] Raether, H., 1988, *Surface Plasmons*, Springer-Verlag, Berlin.

[6] Shchegrov, A. V., Joulain, K., Carminati, R., and Greffet, J.-J., 2000, "Near-Field Spectral Effects Due to Electromagnetic Surface Excitations," Phys. Rev. Lett., **85**, pp. 1548–1551.

[7] Carminati, R., and Greffet, J.-J., 1999, "Near-Field Effects in Spatial Coherence of Thermal Sources," Phys. Rev. Lett., **82**, pp. 1660–1663.

[8] Setälä, T., Kaivola, M., and Friberg, A. T., 2002, "Degree of Polarization in Near Fields of Thermal Sources: Effects of Surface Waves," Phys. Rev. Lett., **88**, p. 123902.

[9] Laroche, M., Arnold, C., Marquier, F., Carminati, R., Greffet, J.-J., Collin, S., Bardou, N., and Pelouard, J.-L., 2005, "Highly Directional Radiation Generated by a Tungsten Thermal Source," Opt. Lett., **30**, pp. 2623–2625.

[10] Hesketh, P. J., Zemel, J. N., and Gebhart, B., 1988, "Polarized Spectral Emittance From Periodic Micromachined Surfaces. I. Doped Silicon: The Normal Direction," Phys. Rev. B, **37**, pp. 10795–10802.

[11] Lee, B. J., and Zhang, Z. M., 2007, "Coherent Thermal Emission From Modified Periodic Multilayer Structures," ASME J. Heat Transfer, **129**, pp. 17–26.

[12] Ben-Abdallah, P., 2004, "Thermal Antenna Behavior for Thin-Film Structures," J. Opt. Soc. Am. A, **21**, pp. 1368–1371.

[13] Yablonovitch, E., 1987, "Inhibited Spontaneous Emission in Solid-State Physics and Electronics," Phys. Rev. Lett., **58**, pp. 2059–2062.

[14] Chan, D. L. C., Soljačić, M., and Joannopolous, J. D., 2006, "Thermal Emission and Design in 2D-Periodic Metallic Photonic Crystal Slabs," Opt. Express, **14**, pp. 8785–8796.

[15] El-Kady, I., Chow, W. W., and Fleming, J. G., 2005, "Emission From an Active Photonic Crystal," Phys. Rev. B, **72**, p. 195110.

[16] Celanovic, I., Perreault, D., and Kassakian, J., 2005, "Resonant-Cavity Enhanced Thermal Emission," Phys. Rev. B, **72**, p. 075127.

[17] Dahan, N., Niv, A., Biener, G., Gorodetski, Y., Kleiner, V., and Hasman, E., 2007, "Enhanced Coherency of Thermal Emission: Beyond the Limitation Imposed by Delocalized Surface Waves," Phys. Rev. B, **76**, p. 045427.

[18] Sobnack, M. B., Tan, W. C., Wanstall, N. P., Preist, T. W., and Sambles, J. R., 1998, "Stationary Surface Plasmons on a Zero-Order Metal Grating," Phys. Rev. Lett., **80**, pp. 5667–5670.

[19] Dahan, N., Niv, A., Biener, G., Kleiner, V., and Hasman, E., 2005, "Space-Variant Polarization Manipulation of a Thermal Emission by a SiO_2 Subwavelength Grating Supporting Surface Phonon-Polaritons," Appl. Phys. Lett., **86**, p. 191102.

[20] Palik, E. D., 1985, *Handbook of Optical Constants of Solids*, Academic, Orlando, FL.

[21] Yang, F., Sambles, J. R., and Bradberry, G. W., 1991, "Long-Range Surface Modes Supported by Thin Films," Phys. Rev. B, **44**, pp. 5855–5872.

[22] Mühlschlegel, P., Eisler, H.-J., Martin, O. J. F., Hecht, B., and Pohl, D. W., 2005, "Resonant Optical Antennas," Science, **308**, pp. 1607–1609.

[23] Gordon, R., and Brolo, A. G., 2005, "Increased Cut-Off Wavelength for a Subwavelength Hole in a Real Metal," Opt. Express, **13**, pp. 1933–1938.

Effect of Channel Geometry Variations on the Performance of a Constrained Microscale-Film Ammonia-Water Bubble Absorber

Jeromy Jenks

Vinod Narayanan[1]
e-mail: vinod.narayanan@oregonstate.edu

Department of Mechanical Engineering,
Oregon State University,
204 Rogers Hall,
Corvallis, OR 97331-6001

An experimental study of the absorption of ammonia vapor in a constrained thin film of ammonia-water solution is presented. A large aspect ratio microchannel with one of its walls formed of a porous material is used to constrain the thickness of the liquid film. Experiments are performed at a pressure of 2.5 bar absolute and 4 bar absolute and at a fixed weak solution inlet temperature. Weak solution flow rates are varied from 10 g/min to 30 g/min (corresponding to the weak solution Reynolds number, Re, from 15 to 45), inlet mass concentrations are varied from 0% to 15%, and gas flow rates are varied between 1 g/min and 3 g/min (corresponding to the vapor Re from 160 to 520). Six geometries, including three smooth-bottom-walled channels of differing depths and three channels with structured bottom walls, are considered. Results indicate that, for identical rates of vapor absorption, the overall heat transfer coefficient of the 400 μm absorber is in most cases significantly larger than that of other absorbers. For the 150 μm and 400 μm absorbers, a trade-off between the high overall heat and mass transfer coefficients is achieved for the highest vapor to solution flow rate ratio.
[DOI: 10.1115/1.2970065]

Keywords: microchannel, absorption refrigeration, absorber, mass transfer, heat transfer coefficient, thin film

1 Introduction

Ammonia-water absorption refrigeration cycles are appealing due to their environmentally benign working fluids in addition to the requirement of less electrical power compared with vapor compression cycles. The size of the absorber in a heat-actuated refrigeration system significantly impacts its overall size; hence, several designs to reduce its size have been proposed. Thus far, the vast majority of studies has been devoted to two major absorption methods, namely, falling-film and bubble absorption [1].

Meachum and Garimella [2] designed and characterized a NH_3-H_2O microchannel falling-film absorber with small diameter cooling tubes and with the solution film forming around the tubes. They reported a cooling load of 15.1 kW with a 0.456 m^2 exchange surface area. Analytical studies by Goel and Goswami [3] suggest a further reduction in absorber size with the addition of a mesh/fabric screen woven between the unused spacing of the tubes. Recently, Goel and Goswami [4] found good agreement of their numerical model with an experimental study.

Bubble absorption has been recommended by several researchers over the better part of the past decade due to its enhanced mass transfer performance over falling-film absorption, while still maintaining a high heat transfer coefficient for some configurations. Staicovici [5] developed a phenomenological theory of absorption for multicomponent mixtures and concluded that the bubble absorber was an efficient means of absorption. Helbing et al. [6] compared film and bubble/slug flow absorbers and found the latter to have improved the heat and mass transfer. Kang et al. [7] analytically compared falling-film and bubble absorbers and found the local absorption rates to be higher in the bubble mode, resulting in a 48.7% smaller absorber size. Lee et al. [8] performed an experimental study on both absorber types and found that the mass transfer rates in a bubble absorber were larger than that for a falling-film absorber. In a subsequent study, Lee et al. [9] presented experimental results on a bubble absorber with a plate-type heat exchanger. They found that increasing the weak solution flow rate seldom affected the mass transfer but improved the heat transfer. Also, increasing the gas flow rate was found to produce slug flow in the bubble mode.

1.1 Motivation and Objectives. Presented here is a study of NH_3-H_2O bubble-mode absorption within a microchannel. Ammonia vapor is injected through a porous top plate into the microchannel, where it gets absorbed into the solution that flows along the channel (see Fig. 1). A coolant microchannel removes heat from the bottom side of the solution microchannel. Thus, the overall heat transfer rate from the bubble-liquid interface, where the heat of absorption is generated, to the coolant, where the heat is dissipated, can be enhanced. In addition, the mass transfer resistance is low due to the high interfacial area in bubble absorption.

The present study seeks to characterize the heat and mass transfer attributes of the constrained-thin-film absorber through the variation of various fluid and geometrical parameters. Experiments are performed at a fixed inlet temperature of the weak solution and vapor. Fluid flow variables include the mass flow rates of the weak solution and vapor. Geometrical variables include smooth channel depths of 150 μm, 400 μm, and 1500 μm and three different structured microchannels. Cross ribs (CRs), angled cross ribs (ACRs), and streamwise fins (SFs) on the channel's bottom wall are the structural variations that were studied. Both the weak solution and ammonia vapor flow rates are varied, and these fluid streams enter the absorber nominally at 25°C. Data presented in this paper are not at the operating conditions typically

[1]Corresponding author.

Contributed by the Heat Transfer Division of ASME for publication in the JOURNAL OF HEAT TRANSFER. Manuscript received August 8, 2007; final manuscript received April 8, 2008; published online September 5, 2008. Review conducted by Jamal Seyed Yagoobi. Paper Presented at the 2007 ASME-JSME Thermal Engineering and Summer Heat Transfer Conference (HT2007), Vancouver, BC, Canada, July 8–12, 2007.

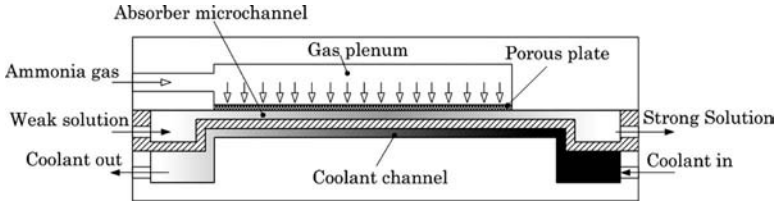

Fig. 1 Schematic of the absorber test section

encountered in absorption systems due to limitations in the experimental facility; however, they serve as an indicator of the relative performance of the various absorber geometries.

2 Experimental Facility and Test Section

Figure 1 shows a schematic of the test section. Anhydrous ammonia entered the gas plenum that was fabricated using polyetheretherketone (PEEK) through both sides of the plenum. The weak solution entered the absorber at the inlet plenum and flowed along the microchannel to the exit plenum. The gas flowed through a stainless-steel sintered porous plate of 0.5 μm pore size and impinged upon the liquid solution that flowed in a 10 cm long $\times 2$ cm wide stainless-steel microchannel. The latter third of the gas plenum was blocked to prevent ammonia gas from bubbling through the sintered plate into the microchannel in this section. This design mitigated the presence of vapor bubbles at the exit of the test section that was observed using the original absorber design [10], thereby ensuring complete absorption within the microchannel test section. The major dimensions of the absorber were $0.145 \times 0.09 \times 0.06$ m^3 ; these dimensions would be significantly reduced in the absence of measurement devices within the test section. The heat released during absorption was removed by the coolant (water) flowing in a counter arrangement to the solution flow.

Table 1 summarizes the six basic microchannel geometries used in this study. A porous plate was used as the top channel wall for all geometries. For all microchannel geometries, the coolant side channel dimensions (at $10 \times 2 \times 0.88$ cm^3) and flow conditions (at 269 g/min and at $T_{in} = 10.6°$C) were kept fixed in order to determine the effect of structured surfaces on the absorber microchannel heat transfer coefficient. The overall heat transfer coefficient for the heat exchanger was based on the heat exchange area on the coolant side, which remained at 10×2 cm^2.

The first three channel geometries were of depth 150 μm, 400 μm, and 1500 μm and had a flat bottom wall. In order to potentially enhance the heat and mass transfer characteristics of the microchannel absorber, microstructures were introduced on the channel's bottom wall. The other three channels had a nominal depth of 150 μm and had on their bottom walls either cross ribs, 45-deg angled cross ribs, or streamwise fins; these geometries are indicated in the photographs in Figs. 2(*a*)–2(*c*), respectively. The intent of the CR and ACR structured surface designs were twofold: (a) to provide an increase in the residence time for absorption within the microchannel by pinning the vapor bubbles in the valleys between ribs, and (b) to enhance heat transfer by the periodic renewal of the thermal boundary layer. The latter intent was motivated by single-phase flow results on the internal gas turbine blade cooling that have indicated an enhancement in the heat transfer coefficient due to the presence of ribs (for example, see Ref. [11]).

The CR absorber consisted of 23 cross ribs, each of width 500 μm. The cross ribs were cut 250 μm deep into a nominal base channel depth of 150 μm. This resulted in a rib-height to inter-rib-spacing ratio of 16:1. Also for the present configuration, the addition of the ribs increased the effective heat exchange area on the solution side by 11% compared with the smooth channel walled absorbers. The ACR absorber was studied to potentially enhance heat transfer through the presence of a secondary flow. It consisted of 45-deg ACRs, which increased the effective heat exchange area on the solution side by 9% over the smooth channel walled absorbers. The SF channel was designed with the intent of increasing the heat transfer surface area. For this absorber, longitudinal fins of a height of approximately 150 μm were machined to the bottom surface in a 150 μm absorber. This resulted effectively in ten parallel microchannels (fins), each of width 1.6 mm, and in a 9% decrease in the hydraulic diameter of each channel compared with the smooth 150 μm channel. Because the tip of the fins was not sealed to the porous plate, there was a possibility for leakage of the flow across the fin tips. A preliminary estimation of the fin effectiveness of a 150-μm-long stainless-steel fin, based on a Nu of 5.39 (that corresponded to a heat transfer coefficient of 1815 W/m^2 K), indicated that the fin efficiency was unity. Hence the entire fin area can be treated to be at the same temperature as the bottom wall.

Figure 3 shows a schematic of the experimental facility used in this study. A regulated flow of anhydrous ammonia was supplied from a gas tank to the gas plenum of the absorber through a mass flow controller (Model C100L, Sierra Instruments, Monterey, CA). This mass flow controller also measured the gas flow rate. The system pressure was maintained by pressurizing the inlet and exit solution reservoirs using compressed air. The flow rate of the inlet weak solution was controlled using a variable speed gear pump. A Coriolis flowmeter (CF010 sensor and 2700 transmitter, Micromotion, Boulder, CO) was used to measure the mass flow rate and the density of the incoming weak solution. A translucent Teflon® perfluoroalkoxy (PFA) visualization section was located

Table 1 Microchannel Geometry

Channel type	Nominal channel depth (μm)	Additional geometry information
1-Smooth	150	none
2-Smooth	400	none
3-Smooth	1500	none
4-Cross ribbed (CR)	400	Twenty-two 250 μm steps machined into the 150 μm base surface of the microchannel
5-Angled cross ribbed (ACR)	400	Thirteen 250 μm steps machined into the 150 μm base surface of the microchannel
6-Streamwise finned (SF)	150	Ten approximately 150 μm tall fins protruding from the base of the microchannel

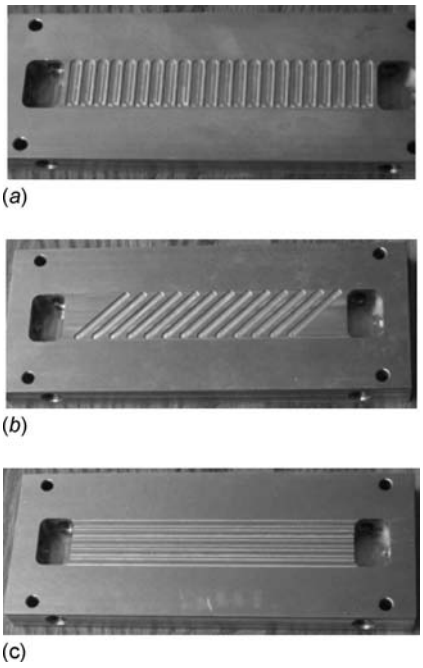

Fig. 2 Photographs of the three structured microchannels: (*a*) the CR channel, (*b*) the 45-deg ACR channel, and (*c*) the SF channel

at the exit of the absorber to monitor the level of absorption within the test section. A computer-controlled three-way solenoid valve, located at the exit of this visualization section, was used to divert the strong solution into alternate paths. During data collection at steady state, the valve directed the flow to a sample reservoir, which was a closed container, to prevent evaporative loss. At all other times, the strong solution was directed to a discharge reservoir. A recirculation chiller (ThermoHaake C30P) supplied the coolant water. The mass flow rate of the water was measured by a correlated rotameter (Gilmont GF1360).

The temperature and pressure were monitored at the absorber inlet and exit for the solution, the gas inlet, and the Coriolis flowmeter, as indicated in Fig. 3. The temperatures were measured using calibrated *T*-type thermocouples, while the pressures were measured using calibrated capacitance-type absolute pressure transducers (Models PX302 and PX32B1, Omegadyne Engineering, Stamford, CT). Data from all instruments were recorded through data acquisition boards using a LabVIEW® (National Instruments, Austin, TX) program.

3 Experimental Procedure

The test facility was first pressurized using a compressed air supply to the reservoirs. Cooling water was then supplied to the test section. A weak solution at a fixed flow rate and a fixed mass concentration of ammonia was introduced into the absorber. At steady state, the three-way solenoid valve was opened to permit the strong solution to flow into the sample reservoir. Steady state was considered attained when the inlet and exit solution temperatures were constant. The strong solution was collected in the sample reservoir for the duration of the steady–state run. The strong solution flow was diverted into the Coriolis flowmeter using the three-way solenoid valve upon completion of each experiment. Upon attainment of a steady value for the pressure, temperature, and density of the strong solution, these data were recorded to determine the strong solution concentration.

4 Data Reduction and Analysis

An overall mass balance for the absorber was used to determine the mass flow rate of the exiting strong solution

$$\dot{m}_{\rm ss} = \dot{m}_{ws} + \dot{m}_v \tag{1}$$

Inlet and exit concentrations were determined from the measurements of the strong solution density, pressure, and temperature using the NH_3-H_2O call function in engineering equation solver (EES) (F-Chart Software, Madison, WI), which utilizes correlations from Ibrahim and Klein [12]. A species mass balance yielded a check for the measured exit concentration

$$X_{\rm ss} = \frac{\dot{m}_{ws}X_{ws} + \dot{m}_v}{\dot{m}_{\rm ss}} \tag{2}$$

The heat transferred to the coolant, or heat duty, was determined from an energy balance

$$\dot{q}_{\rm abs} = \dot{m}_{ws}h_{ws} + \dot{m}_v h_v - \dot{m}_{\rm ss}h_{\rm ss} \tag{3}$$

Equivalently, it was also calculated from the coolant side energy balance

$$\dot{q}_c = \dot{m}_c c_{pc}(T_{ce} - T_{ci}) \tag{4}$$

The overall heat transfer coefficient, U, with the absorber as the hot side and the coolant flow as the cold side of the heat exchanger was given by

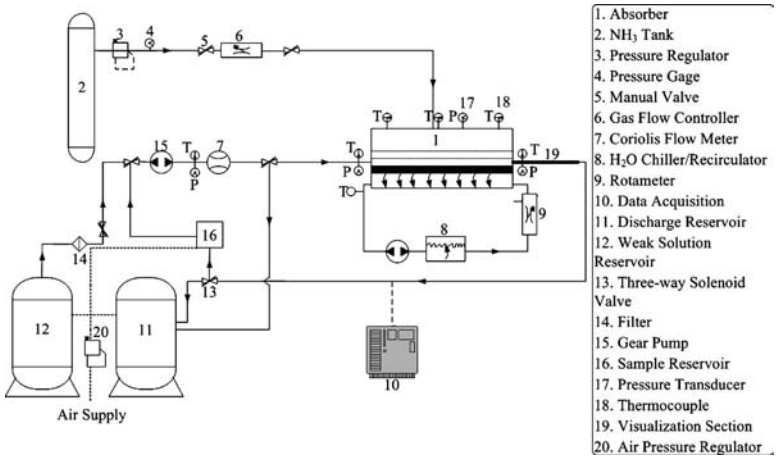

Fig. 3 Schematic of the experimental facility

Table 2 Range of Flow Conditions

Channel geometry	Vapor Reynolds number, Re_v (for 1/2/3 g/min)	Superficial vapor velocity, V_{VS} (m/s, for 1/2/3 g/min)	Weak solution Reynolds number Re_{ws} (for 10/20/30 g/min)	Superficial liquid velocity, V_{LS} (m/s, for 10/20/30 g/min)
150 μm	173/346/520	2.03/4.06/6.09	15/30/45	0.062/0.124/0.186
400 μm	171/342/514	0.76/1.52/2.28	15/30/45	0.023/0.047/0.07
1500 μm	162/324/486	0.20/0.41/0.61	14/28/43	0.006/0.012/0.019
CR	172/343/515	1.22/2.44/3.66	15/30/45	0.037/0.074/0.112
ACR	158/317/475	1.39/2.78/4.18	14/28/41	0.043/0.085/0.128
SF	192/383/575	2.47/4.06/6.09	17/33/50	0.074/0.149/0.223

$$U = \frac{\dot{q}_{abs}}{A\Delta T_{lm}} \tag{5}$$

where the log-mean temperature difference, ΔT_{lm}, was determined as

$$\Delta T_{lm} = \frac{(T_{ws} - T_{ce}) - (T_{ss} - T_{ci})}{\ln\left(\frac{(T_{ws} - T_{ce})}{(T_{ss} - T_{ci})}\right)} \tag{6}$$

Note that the heat exchanger analysis performed in this study is based on the traditional heat exchanger analysis definition of U, to be consistent with current work on absorbers in literature. However, it should be noted that unlike typical heat exchangers, there is a source term, that of heat of absorption, which caused conditions under which the temperature of the hot stream increased along the length of the absorber despite the removal of heat by the counterflowing coolant. A modified heat exchanger analysis to account for this aspect is discussed in detail elsewhere [13].

The overall mass transfer coefficient was determined using the vapor flow rate and the heat exchange surface area

$$h_m = \frac{\dot{m}_v}{\Delta X_{lm} A} \tag{7}$$

where ΔX_{lm} denotes the nominal log-mean concentration difference along the absorber microchannel

$$\Delta X_{lm} = \frac{(X_{ws,sat} - X_{ws}) - (X_{ss,sat} - X_{ss})}{\ln\left(\frac{X_{ws,sat} - X_{ws}}{X_{ss,sat} - X_{ss}}\right)} \tag{8}$$

The saturation concentrations in Eq. (8) were determined based on the measured temperatures and pressures using the relation from Ibrahim and Klein [12].

4.1 Uncertainty Analysis. Uncertainty analysis was performed on all measured variables and propagated through the calculations to the reported variables for all experimental conditions. Values of uncertainty are represented as error bars in the figures presented in Sec. 5. Thermocouples and pressure transducers were calibrated using a National Institute on Standards and Technology (NIST)-traceable reference standard. The Coriolis mass flowmeter flow rate measurement was calibrated using a computer-controlled catch-and-weigh method. The manufacturer's calibration was used to determine the bias error in the gas flow controller and the Coriolis flowmeter density. Uncertainty in mass concentration and ΔT_{lm} was determined using a sequential perturbation technique [14] in EES based on the measurement uncertainties in temperatures, pressures, and densities. The propagation of errors method [14] was used to determine uncertainties in other calculated quantities. Uncertainty in the $\dot{q}_{abs}$ was determined using Eq. (3) and includes uncertainties in the mass flow rates and enthalpies. The preceding errors were then finally propagated into Eqs. (5) and (7) to find the uncertainty in U and h_m, respectively. The average difference between $\dot{q}_{abs}$ and $\dot{q}_c$ for the 110 experimental conditions presented in this paper was 7.5%. On average, a 6.7% difference in the exit concentration determined from experiments and from using Eq. (2) was noted. Results are presented based on the exit concentrations determined from experiments.

5 Results and Discussion

Preliminary studies [15] were performed to qualitatively document the effect of hole patterns in the top porous plate on bubble formation within the microchannel. Three types of plates were considered: a 0.5 μm-pore size sintered stainless-steel plate of approximately 50% porosity (Mott Corporation, Farmington, CT), a plate with a triangular hole pattern, and a plate with a staggered hole pattern. Visualization indicated that a larger number of smaller bubbles was generated using the sintered plate and hence this plate was henceforth used for quantitative studies.

For data presented in this section, flow variables included the weak solution flow rate, which was varied from 10 g/min to 30 g/min, and the vapor flow rate, which was varied from 1 g/min to 3 g/min. The corresponding Reynolds number ranges for the weak solution and vapor flows for all geometries are indicated in Table 2 along with an estimate of the superficial liquid and vapor velocities. For the structured microchannels, the Reynolds number (Re) and velocity calculations were based on the area-averaged channel dimensions that are dependent on the geometry of the structures.

Experiments were performed at a nominal pressure of 4 bar absolute unless mentioned otherwise. Reference to pressure henceforth will be made with an absolute reference without explicit mention. The coolant side flow rate was held fixed at 269 g/min, corresponding to a Re of 370, while the coolant inlet temperature was held nominally fixed at 10.6°C. The inlet temperature of the weak solution was measured at the Coriolis flowmeter and was held nominally constant at 22.5°C. The inlet temperature of the ammonia vapor was measured in the gas plenum and held nominally fixed at 22.4°C. In the data reported in this paper, the weak solution inlet mass concentration was held fixed at 15% for all absorber geometries. The effect of the weak solution concentration on the heat and mass transfer coefficients for the 150 μm absorber is documented elsewhere [15].

Representative average uncertainty estimates are indicated for each series of plots in the graphs in order to preserve clarity of presentation. Some graphs do not have error bars for data; these graphs are largely cross-plots from other graphs in which error estimates are already indicated. Results are typically presented for the vapor to weak solution flow rate ratios, $\dot{m}_v/\dot{m}_{ws}$, henceforth referred to as flow rate ratios. These mass flow rate ratios are proportional to the ratios of vapor to liquid Re and also to the vapor to liquid superficial velocities indicated in Table 2. For example, the largest flow rate ratio, $\dot{m}_v/\dot{m}_{ws}$ of 3/10 corresponds to the largest Reynolds number ratio, Re_v/Re_{ws} of 520/15 (=34.6) and the largest superficial velocity ratio, V_{VS}/V_{LS} of 6.09/0.062 (=98) for the 150 μm absorber. Data presented in Sec. 5 are for conditions of complete absorption within the test

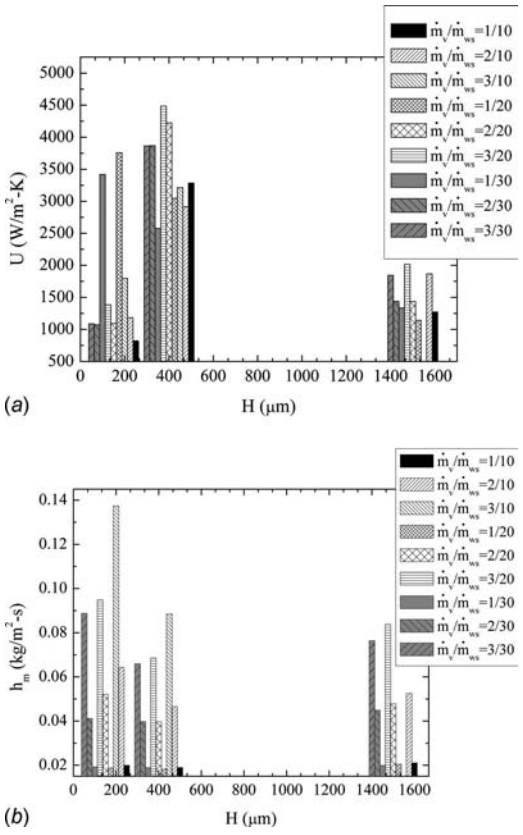

Fig. 4 Effect of the channel depth on the absorber performance for various flow rate ratios: (*a*) overall heat transfer coefficient and (*b*) mass transfer coefficient. The nominal absorber pressure is 4.0 bars and X_{ws}=0.15. The absorbers are of discrete nominal depths of 150 μm, 400 μm, and 1500 μm.

section, as verified by visual observations of the exiting strong solution flow in the visualization section downstream of the absorber.

5.1 Effect of Microchannel Depth. Figure 4(*a*) shows the variation of the overall heat transfer coefficient with the microchannel depth with flow rate ratios as a parameter. The experiments were performed at a pressure of 4 bars and at an inlet mass concentration of weak solution of 15%. At the lowest flow ratios of 1/20 and 1/30, the overall heat transfer coefficient decreases with an increase in channel depth. Because the coolant side resistance remains constant for different solution microchannels, a decrease in the overall heat transfer coefficient is directly proportional to a decrease in the solution-side convective heat transfer coefficient. Interestingly, for mass flow rate ratios larger than 1/20, a substantial increase in U is observed from the 150 μm to the 400 μm absorber, after which U drops for the 1500 μm absorber. For example, for the mass flow ratio of 3/30, U increases from 1090 W/m^2 K for the 150 μm absorber to 3850 W/m^2 K for the 400 μm absorber and then decreases to a value of 1760 W/m^2 K for a 1500 μm absorber. This suggests that there may exist an optimum channel depth for flow rate ratios larger than 1/20. The causes for this trend are not completely clear; however, one plausible explanation is put forth here. From a heat transport perspective, two competing effects can be envisioned to explain the variation of U with the absorber channel depth: (a) a reduction in the net heat exchange area due to vapor contact upon its impingement on the bottom microchannel wall and (b) a reduction in the heat transport rate within the solution from the liquid-vapor interface to the heat exchange surface due to the increased liquid layer thickness and the corresponding heat transfer resistance. It is not possible to conclusively distinguish between their individual effects on U based on the global measurements presented in this study.

Consider a situation in which there exists identical vapor and weak solution flow rates for all three microchannel absorbers (say, for example, a flow rate ratio of 3/30). On an average over the entire absorber, a fixed vapor flow rate implies that there will be a larger amount of vapor in contact with the heat exchange surface for a 150 μm absorber compared with the 400 μm and 1500 μm absorbers based on volume constraints for incompressible fluids. Thus, the area for heat exchange is reduced, and hence U for a 150 μm absorber is lower than that for the 400 μm absorber. For the 1500 μm absorber, although the vapor contact area with the heat exchange area is expected to be lower than that for the 400 μm absorber, there is an added resistance to heat transfer due to the on-average larger thickness of the liquid layer between the liquid-vapor bubble interface and the heat exchange surface. From the results in Fig. 4(*a*), it is seen that this increased liquid resistance has a greater effect than the competing effect of the reduced vapor contact with the heat exchange area. Hence a net decrease in the solution-side heat transfer coefficient and hence a decrease in U compared with the 400 μm absorber is observed.

Figure 4(*b*) shows the effect of the channel depth on the mass transfer coefficient, h_m, for the same conditions as those in Fig. 4(*a*). Two distinct trends are observed. For the low vapor flow rates of 1 g/min, h_m is small and the variation with the channel depth is negligible. Note that these are the conditions for which U decreases with the increase in channel depth (see Fig. 4(*a*)). For vapor flow rates larger than 2 g/min and flow rate ratios larger than 2/30, h_m decreases quite rapidly from the 150 μm to the 400 μm absorber and increases more gradually from the 400 μm to the 1500 μm absorber. This trend is in contrast with that seen in U in Fig. 4(*a*) and is a result of the difference in the temperature change from the inlet to exit of the absorbers. For the lower flow rate ratios, this temperature change is not substantial; hence, the saturation concentration at the exit does not vary significantly from that at the inlet. For the higher flow rate ratios, a smaller mass transfer driving potential exists for the 150 μm absorber compared with the 400 μm absorber due to the higher temperature at the exit for this absorber, and thereby, a lower exit saturation concentration. Consequently, it follows from Eq. (8) that a net lower mass transfer coefficient for the 400 μm absorber results due to the fixed flow rate of the vapor and the chosen area for both absorbers.

A comparison of U and h_m trends (Figs. 4(*a*) and 4(*b*), respectively) indicates that for a fixed h_m and vapor flow rate, the corresponding U is higher for the 400 μm absorber. For example, consider a h_m of approximately 0.09 kg/m^2 s. This includes the flow rate ratio of 3/10 for the 400 μm absorber, as well as the flow rate ratios of 3/20 and 3/30 for the 150 μm absorber. For these conditions, Fig. 4(*a*) indicates that the U for the 400 μm absorber is considerably larger than that for the 150 μm absorber. The flow ratio of 3/10 yields the most desirable flow conditions for both the 150 μm and 400 μm absorbers. Whereas h_m at this flow rate ratio for the 400 μm absorber is 64% lower, the corresponding U is 79% larger compared with the 150 μm absorber. The 400 μm absorber seems to be the more desirable geometry among the absorber dimensions presented here considering both the heat and mass transfer attributes. Perhaps a microchannel depth that has more desirable heat and mass transfer characteristics lies in between these two channel depths for this flow rate ratio.

5.2 Comparison of Smooth Surface and Microstructured Surface Absorbers. Figure 5(*a*) shows the effect of the vapor flow rate on U of structured microchannels for a weak solution flow rate of 10 g/min. Also shown for comparison is the U of the 150 μm, 400 μm, and 1500 μm absorbers. Note that the vapor

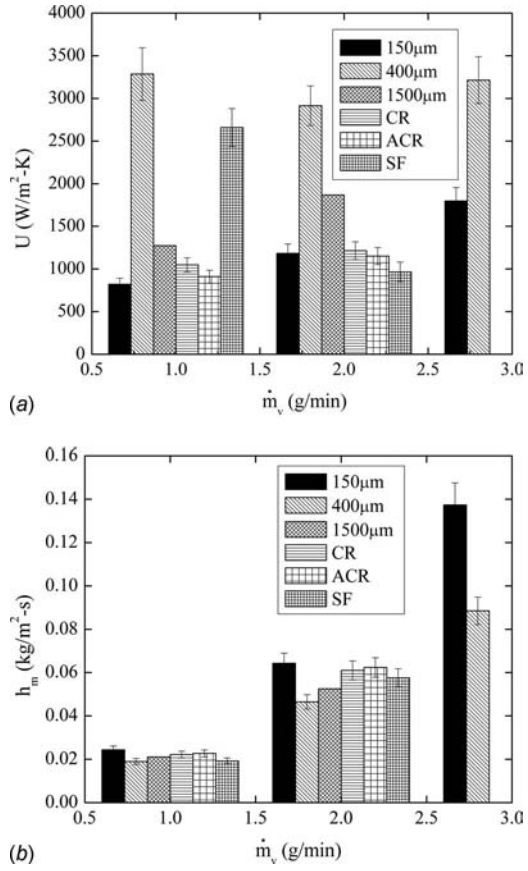

Fig. 5 Effect of the vapor flow rate on the absorber performance for various channel geometries and at a fixed inlet flow rate of 10 g/min: (*a*) overall heat transfer coefficient and (*b*) mass transfer coefficient. The nominal absorber pressure is 4.0 bars and X_{ws}=0.15. The vapor flow rates are plotted in the abscissa at discrete values of 1 g/min, 2 g/min, and 3 g/min.

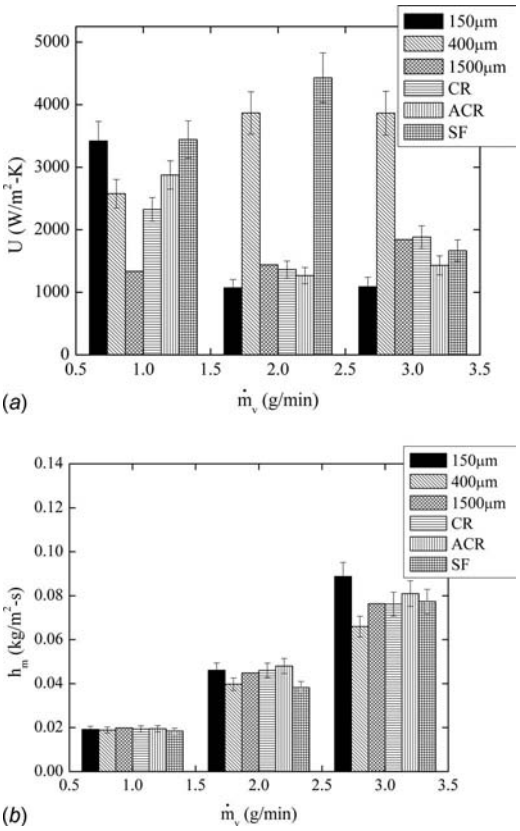

Fig. 6 Effect of the vapor flow rate on the absorber performance for various channel geometries and at a fixed inlet flow rate of 30 g/min: (*a*) overall heat transfer coefficient and (*b*) mass transfer coefficient. The nominal absorber pressure is 4.0 bars and X_{ws}=0.15. The vapor flow rates are plotted in the abscissa at discrete values of 1 g/min, 2 g/min, and 3 g/min.

flow rate of 3 g/min for all structured absorbers and the 1500 μm absorber resulted in incomplete absorption as indicated by visual observation at the exit of the absorber test section and hence data for these cases are not shown. The trend in U for the 400 μm absorber clearly stands apart; on average, over all vapor flow rates, a 270% increase in U is observed over the 150 μm absorber. The variation in U with the vapor flow rate variation is not significant for the 400 μm absorber, and the slight variations with the vapor flow rate are within the reported uncertainty. The CR and ACR absorbers, as well as the 150 μm and 1500 μm absorbers, show a gradual increase in U with increasing vapor flow rate. At the low vapor flow rate of 1 g/min, the CR absorber exhibits a 38% increase in U, and the 1500 μm absorber, a 48% increase in U, compared with the 150 μm absorber. In contrast, the U of the ACR absorber is slightly lower than that of the CR absorber and is approximately the same as that of the 150 μm absorber. This is a consequence of the smaller number of ribs in the ACR absorber, which results in a less frequent renewal of the hydrodynamic and thermal boundary layers on the heat transfer surface. The difference in U between these absorbers becomes negligible for the 2 g/min vapor flow rate.

For a given absorber geometry, with an increase in the vapor flow rate, the potential for vapor contact with the walls increases, thereby decreasing the heat transfer rate. At the same time, mixing is enhanced significantly due to the injection of more vapor into the absorber. For the 400 μm absorber, these competing effects seem to largely balance each other resulting in little variation with the vapor flow rate. However, the enhanced mixing seems to offset the reduction in the heat transfer area for the 150 μm, CR, and ACR absorbers, resulting in a net gradual increase in U with the vapor flow rate.

In contrast to the trends seen in the 150 μm, CR, and ACR absorbers, the U for the SF absorber is very large (2700 $\mathrm{W/m^2\,K}$) at a low vapor flow rate of 1 g/min and decreases dramatically to 950 $\mathrm{W/m^2\,K}$ at a vapor flow rate of 2 g/min. At the lower vapor flow rates, it is possible that the solution covered the side walls of the fins and the tip thereby increasing the surface area for heat transfer by as much as 15%. However, with an increase in the vapor flow rate, it is likely that the injected vapor progressively covered the sides and tips of the fins, thereby reducing the effective area for convective heat transfer and hence the solution-side and overall heat transfer coefficients. Note that at this low solution flow rate of 10 g/min, as well as at a larger vapor flow rate of 2 g/min, liquid inertia may have been insufficient to shear the vapor pinned to the sides or tips of the fins.

The effect of the vapor flow rate on the mass transfer coefficient for a weak solution flow rate of 10 g/min is shown in Fig. 5(*b*) for all absorbers. The mass transfer coefficient at the low vapor flow rate of 1 g/min is similar for all absorbers. With an increase in the vapor flow rate, the mass transfer coefficient of each absorber increases. Also, with an increase in the vapor flow rate, the difference between the mass transfer coefficient of the 150 μm and 400 μm absorbers increases. Because the vapor flux rate is fixed, this implies that ΔX_{lm} varies in inverse proportion to h_m for the absorbers.

Figure 6(*a*) shows the variation of U with vapor flow rates in a similar manner as shown in Fig. 5(*a*), but for a larger weak solution flow rate of 30 g/min. Data have also been obtained for a 20

g/min vapor flow rate but are not presented here for brevity; these data also show similar trends to that indicated in Fig. 6(*a*). At the outset, it is clear that the trend of the variation of U with the vapor flow rate for most absorbers is very different from that shown in Fig. 5(*a*) for the lower solution flow rate of 10 g/min. At a low vapor flow rate of 1 g/min, the 150 μm and SF absorbers exhibit the largest U, followed by the ACR, 400 μm, CR, and 1500 μm absorbers, in that order. This trend is to be expected for smooth-bottom-wall absorbers because at a low flux ratio of 1/30, the flow approaches a single-phase laminar flow; channels with smaller hydraulic diameters have larger heat transfer coefficients. However, the trend changes at a high vapor flow rate. For example, at 3 g/min, the 400 μm absorber has a U of 3750 $\mathrm{W/m^2\,K}$ as compared to 1200 $\mathrm{W/m^2\,K}$ for the 150 μm absorber. The substantial decrease in U of the 150 μm absorber can be attributed to the increase in the amount of vapor in contact with the heat exchange surface, as discussed previously in relation to the channel depth variation.

Also of interest is the insensitivity of U for vapor flow rates of 2 g/min and 3 g/min for the 150 μm and 400 μm absorbers. For the 400 μm absorber, the limiting resistances of the conduction across the stainless-steel wall material between the microchannel and coolant and the coolant side heat transfer could plausibly explain the constant high U value. On the other hand, U may be limited to a constant low value in the 150 μm absorber by the low absorber-side heat transfer coefficient.

Among the structured microchannels, the trend of U with the vapor flow rate for the SF channel is particularly worth mentioning. At 1 g/min, the U is the largest (along with the 150 μm absorber) among all absorbers. With an increase in the vapor flow rate to 2 g/min, U further increases to 4500 $\mathrm{W/m^2\,K}$, followed by a dramatic decrease to 1400 $\mathrm{W/m^2\,K}$ at a vapor flow rate of 3 g/min. It is likely that at the first two vapor flow rates, the inertia of the liquid flow is sufficient to shear the vapor bubbles that accumulate on the sides and tip of the ribs, whereas the vapor is pinned to the side and tip of the ribs for the last flow rate, reducing the heat exchange area, and hence, the heat transfer coefficient.

The ACR absorber U is 25% larger than the CR absorber at a low vapor flow rate of 1 g/min; however, the trend is reversed for the largest vapor flow rate of 3 g/min, where U for the ACR is 42% lower than that of the CR absorber. Both these absorbers show a substantial decrease in U with the increase in vapor flow rate from 1 g/min to 2 g/min and a very gradual increase from 2 to 3 g/min. One trend that remains consistent between the 10 g/min flow condition (see Fig. 5(*a*)) and the 30 g/min condition in Fig. 6(*a*) is that of the U variation for the 1500 μm absorber. At a vapor flow rate of 1 g/min, U is 1300 $\mathrm{W/m^2\,K}$, and it increases gradually to 2000 $\mathrm{W/m^2\,K}$ at a vapor flow rate of 3 g/min. Nevertheless, U for this absorber at any vapor flow rate is significantly lower than that of the 400 μm absorber.

Figure 6(*b*) presents the h_m variation with the vapor flow rate for a weak solution flow rate of 30 g/min for all the absorber geometries studied. The trends are similar to that seen in Fig. 5(*b*) for the 10 g/min weak solution flow rate. The values of h_m are lower for each absorber at any fixed vapor flow rate compared with Fig. 5(*a*) because the larger solution flow rate for identical vapor flow rates result in a lower ΔX_{lm}.

5.3 Source-to-Heat Rate Ratio Representation. In order to better understand the effect of the heat of absorption on the heat and mass transfer coefficients, it is instructive to plot these coefficients against a ratio of the source to heat rate, $\dot{s}/\dot{q}$. The term $\dot{s}$ refers to the source rate term, which accounts for the additional heat generation due to the heat of absorption within the hot side of the heat exchanger, and is estimated from thermodynamics to be [13]

$$\dot{s} = \dot{m}_v(h_v - h_{ws}) \tag{9}$$

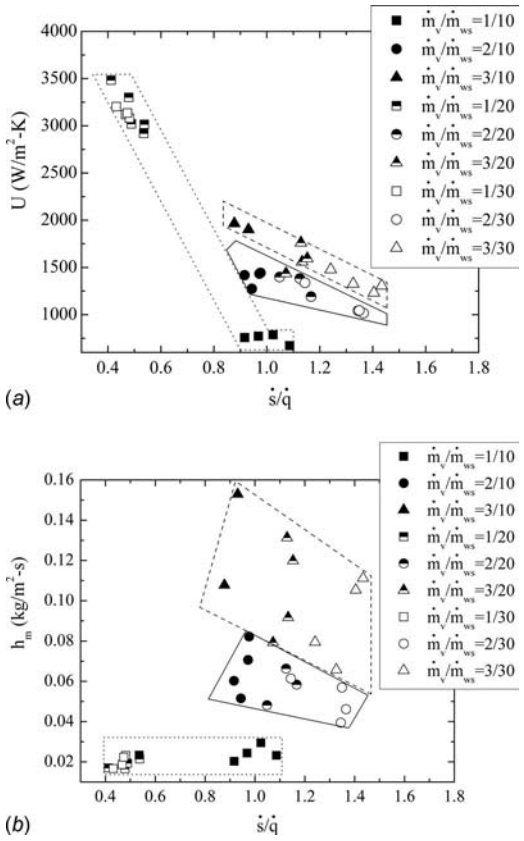

Fig. 7 Performance of the 150 μm absorber plotted against source to heat ratios: (*a*) overall heat transfer coefficient and (*b*) mass transfer coefficient. The system pressure is 2.5 bars.

A $\dot{s}/\dot{q}$ ratio less than unity implies that the amount of heat removed by the coolant was larger than that generated due to absorption heat release; consequently, the exit temperature was lower than the inlet temperature of the solution in the microchannel. In contrast, several cases in which the exit temperature was larger than the inlet temperature were observed in the experiments despite the removal of heat by the counterflowing coolant. Such experiments are characterized by a $\dot{s}/\dot{q} > 1$. Figure 7(*a*) shows a scatter plot of U against $\dot{s}/\dot{q}$ for the 150 μm absorber at a working pressure of 2.5 bars and for various flow rate ratios and inlet concentrations. It is clear that U has a large value of around 3000 $\mathrm{W/m^2\,K}$ for a low $\dot{s}/\dot{q}$; however, when this quantity approaches unity and beyond, U tends toward lower values. As expected, a large U is achieved for the lowest flow rate ratio cases, 1/20 and 1/30. For $\dot{s}/\dot{q} > 1$, with the exception of the flow rate ratio of 1/10, U is bounded between 1000 $\mathrm{W/m^2\,K}$ and 1700 $\mathrm{W/m^2\,K}$. For the 1/10 flow rate ratio, U is much lower than the 1/20 and 1/30 flow rate ratios because the high influx of vapor reduces the overall heat transfer area and because the solution flow rate is much lower. Figure 7(*b*) shows a scatter plot of h_m against $\dot{s}/\dot{q}$ for the 150 μm absorber. For a low $\dot{s}/\dot{q}$ value, h_m is quite low and is highest as $\dot{s}/\dot{q}$ approaches unity, coincidentally corresponding to the highest flow rate ratio cases. At any fixed solution flow rate, h_m increases with an increase in the vapor flow rate.

Groupings of U and h_m at fixed vapor flow rates are identified in Figs. 7(*a*) and 7(*b*). In Fig. 7(*a*), the slope of the low vapor flow rate grouping is largest, and this slope progressively decreases for the larger vapor flow rate groupings. Contrary to this trend the slope of the lowest vapor flow rate grouping is the smallest and vice versa in Fig. 7(*b*). By inspection of the two plots, it is evident that the favorable operating point for the absorber considering

both heat and mass transfer attributes is exhibited by the largest vapor flow rate grouping. In particular, the flow rate ratio of 3/10, which occurs at a $\dot{s}/\dot{q}$ of slightly less than unity, is seen to be the most favorable operating condition for this absorber among the flow conditions studied.

5.4 Final Remarks. The intent of this paper was to report a new design for an ammonia-water absorber. Whereas data presented in this paper are not at typical operating conditions of absorption systems, comparisons of various absorber geometries are made under identical conditions, and hence their trends can be expected to be relevant even at system conditions. An increase in pressure at a fixed temperature in the weak solution has been shown to increase absorption rates in this study, whereas an increase in solution, gas, and coolant inlet temperatures are expected to significantly reduce the rate of absorption. The microchannel bubble absorber presented in this paper can result in a compact absorber size. However, because the vapor needs to be bubbled through a porous plate, the vapor pressure in the evaporator is typically larger than that in a falling-film type absorber. In the experiments reported here, the ammonia gas pressure drop across the 0.5 μm sintered porous plate ranged between 0.32 bar for the 1 g/min vapor flow rate and 0.34 bar for the 3 g/min vapor flow rate. This resulted in an evaporator operating pressure of around 5.8 bars for an absorption system with a low side pressure of 5.5 bars. For the purpose of comparison, it is assumed that there is a zero pressure drop across the falling-film absorber. Assuming a 100% weight fraction of ammonia in the evaporator and a mass flow rate of ammonia of 5 g/s, there is only a 0.4% decrease in the cooling capacity of the evaporator and a negligible change in the absorber load because of the increased vapor pressure. Of significance, however, is the increase in the evaporator saturation temperature, which is at 8.3°C for the 5.8 bar evaporator, as opposed to 6.8°C for the 5.5 bar evaporator.

6 Conclusions

An experimental study of an ammonia-water binary mixture bubble absorption in a large aspect ratio microchannel is presented. Ammonia vapor is introduced into the channel through a porous channel wall. A counterflowing coolant in a minichannel removes the heat released due to the absorption of the injected vapor into a weak flowing solution. Six different microchannel geometries were studied—three smooth microchannels of 150 μm, 400 μm, and 1500 μm depth and three structured geometries: a cross-ribbed, a 45-deg angled cross ribbed, and a streamwise-finned microchannel. The varied flow conditions included the weak solution and ammonia gas mass flow rates at a fixed inlet mass concentration of 0.15. Within the range of parameters studied, the salient results are as follows.

(i) The 150 μm smooth microchannel exhibited the largest U for low flow rate ratios of 1/20 and 1/30; however, correspondingly, the lowest h_m existed for these flow cases. A compromise between high heat and mass transfer coefficients was achieved for a vapor to weak solution mass flow rate ratio of 3/10.

(ii) Channel depth variation studies showed that U decreased with an increase in the channel depth for the low flow ratio cases of 1/20 and 1/30, as would be expected for a single-phase flow. For higher flow rate ratios U increased from the 150 μm to 400 μm absorbers followed by a drop in U for the 1500 μm absorber, suggesting that there exists an optimum channel depth. For a fixed h_m the corresponding U was highest for the 400 μm absorber.

(iii) At the larger weak solution flow rate of 30 g/min, with an increase in the vapor flow rate, U decreased for the 150 μm and the three structured absorbers but increased for the 400 μm absorber. The U for the 150 μm and 400 μm absorbers tended toward limiting values at the higher vapor flow rates.

(iv) At a weak solution flow rate of 30 g/min, for low and moderate vapor flow rates of 1 g/min and 2 g/min, the streamwise-finned microchannels exhibited a high overall heat transfer coefficient; however, for the larger flow rate of 3 g/min, the performance of the streamwise-finned microchannel diminished substantially.

(v) Representation of the overall heat transfer and mass transfer coefficients against a ratio of the source rate to heat rate helps to identify the desirable operating points for the absorber.

Acknowledgment

Financial support provided by the U.S. Army (Technical Monitors: Jonathan Thorud and Frank Calkins, Ft. Belvoir) through Contract No. W909MY-05-C-0024 is greatly appreciated.

Nomenclature

A = heat exchange area (m^2)
A_{cs} = cross sectional area of the microchannel (m^2)
c_p = specific heat at constant pressure (J/kg K)
h = specific enthalpy of the fluid stream (kJ/kg)
h_m = mass transfer coefficient (kg/m^2 s)
H = microchannel depth (m)
L = length of the microchannel (m)
$\dot{m}$ = mass flow rate (kg/s, g/min)
P = pressure (Pa)
$\dot{q}$ = heat rate (W)
Re_{ws} = weak solution Reynolds number $\mathrm{Re}_{ws}=2\dot{m}_{ws}/\mu_{ws}[W+H]$ (unitless)
Re_v = Reynolds number for vapor $\mathrm{Re}_V=2\dot{m}_v/\mu_v[W+H]$ (unitless)
$\dot{s}$ = source rate (W)
T = temperature (K)
U = overall heat transfer coefficient (W/m^2 K)
V = velocity (m/s)
V_{LS} = superficial liquid velocity (m/s); $V_{LS}=\dot{m}_{ws}/\rho_L A_{cs}$
V_{VS} = superficial vapor velocity (m/s); $V_{VS}=\dot{m}_v/\rho_v A_{cs}$
W = width of the microchannel (m)
X = mass concentration (unitless)

Greek

ΔT_{lm} = log-mean temperature difference (K)
ΔX_{lm} = log-mean mass concentration difference (unitless)
μ = dynamic viscosity (kg/m s)
ρ = density of the fluid (kg/m^3)

Subscripts

abs = absorber
c = coolant
e = exit of the microchannel
g = gas
h = hot
i = inlet of the microchannel
l = liquid
m = mass transfer
mod = modified
s = superficial
ss = strong solution
v = vapor (anhydrous ammonia gas)
ws = weak solution

References

[1] Garimella, S., 2005, "Binary-Fluid Heat and Mass Transfer in Microchannel Geometries for Minuaturized Thermally Activated Absorption Heat Pumps," *Microscale Heat Transfer*, S. Kakac, L. L. Vasiliev, Y. Bayazitoglu, and Y. Yener, eds., Springer, Dordrecht, The Netherlands, pp. 339–368.

[2] Meachum, M. J., and Garimella, S., 2004, "Ammonia-Water Absorption Heat and Mass Transfer in Microchannel Absorbers With Visual Confirmation," ASHRAE Transactions: Symposia, Anaheim, CA, Jan. 24-28, pp. 525–532, Paper No. AN-04-7-4.

[3] Goel, N., and Goswami, D. Y., 2005, "A Compact Falling Film Absorber," ASME J. Heat Transfer, **127**, pp. 957–965.

[4] Goel, N., and Goswami, D. Y., 2007, "Experimental Verification of a New Heat and Mass Transfer Enhancement Concept in a Microchannel Falling Film Absorber," ASME J. Heat Transfer, **129**, pp. 154–161.

[5] Staicovici, M. D., 2000, "A Phenomenological Theory of Polycomponent Interactions in Non-Ideal Mixtures: Application to NH_3/H_2O and Other Working Pairs," Int. J. Refrig., **23**, pp. 153–167.

[6] Helbing, U., Würfel, R., and Fratzscher, W., 2000, "Comparative Investigations of Non-Adiabatic Absorption in Film Flow and Bubble Flow," Chem. Eng. Technol., **23**, pp. 1081–1085.

[7] Kang, Y. T., Atsushi, A., and Kashiwagi, T., 2000, "Analytical Investigation of Two Different Absorption Modes: Falling Film and Bubble Types," Int. J. Refrig., **23**, pp. 430–443.

[8] Lee, K. B., Chun, B. H., Lee, J. C., Hyun, J. C., and Kim, S. H., 2002, "Comparison of Heat and Mass Transfer in Falling Film and Bubble Absorbers of Ammonia-Water," Exp. Heat Transfer, **15**, pp. 191–205.

[9] Lee, K. B., Chun, B. H., Lee, J. C., Lee, C. H., and Kim, S. H., 2002, "Experimental Analysis of Bubble Mode in a Plate-Type Absorber," Chem. Eng. Sci., **57**, pp. 1923–1929.

[10] Jenks, J., and Narayanan, V., 2006, "An Experimental Study of Ammonia-Water Bubble Absorption in a Large Aspect Ratio Microchannel," Proceedings of the IMECE 2006, Chicago, IL, Nov. 5-10, Paper No. IMECE2006-14036.

[11] Ekkad, S., and Han, J.-C., 1997, "Detailed Heat Transfer Distributions in Two-Pass Square Channels With Rib Turbulators," Int. J. Heat Mass Transfer, **40**(11), pp. 2525–2537.

[12] Ibrahim, O. M., and Klein, S. A., 1993, "Thermodynamic Properties of Ammonia-Water Mixtures," ASHRAE Transactions: Symposia, Chicago, IL, Jan. 23-27, Vol. 21(2), p. 1495.

[13] Narayanan, V., Kanury, A. M., and Jenks, J., 2007, "Modified Heat Exchanger Analysis Accounting for Heat Generation," Proceedings of the 2007 ASME-JSME Thermal Engineering Summer Heat Transfer Conference, Vancouver, BC, Canada, July 8–12, Paper No. HT2007-33444.

[14] Figliola, R. S., and Beasley, D. E., 2000, *Theory and Design for Mechanical Measurements*, 3rd ed., Wiley, Hoboken, NJ.

[15] Jenks, J., 2007, "An Experimental Study of Ammonia-Water Bubble Absorption in a Constrained Microscale Film," MS thesis, Oregon State University, Corvallis, OR.

Stability and Convection in Impulsively Heated Porous Layers

M. J. Kohl[1]
Mem. ASME

M. Kristoffersen[2]
Mem. ASME
e-mail: mkristoffersen@mmm.com

F. A. Kulacki[3]
Fellow ASME
e-mail: kulacki@me.umn.edu

Department of Mechanical Engineering,
University of Minnesota,
Minneapolis, MN 55455

Experiments are reported on initial instability, turbulence, and overall heat transfer in a porous medium heated from below. The porous medium comprises either water or a water-glycerin solution and randomly stacked glass spheres in an insulated cylinder of height:diameter ratio of 1.9. Heating is with a constant flux lower surface and a constant temperature upper surface, and the stability criterion is determined for a step heat input. The critical Rayleigh number for the onset of convection is obtained in terms of a length scale normalized to the thermal penetration depth as $Ra_c = 83/(1.08\eta - 0.08\eta^2)$ *for* $0.02 < \eta < 0.18$. *Steady convection in terms of the Nusselt and Rayleigh numbers is* $Nu = 0.047 Ra^{0.91} Pr^{0.11} (\mu/\mu_0)^{0.72}$ *for* $100 < Ra < 5000$. *Time-averaged temperatures suggest the existence of a unicellular axisymmetric flow dominated by upflow over the central region of the heated surface. When turbulence is present, the magnitude and frequency of temperature fluctuations increase weakly with increasing Rayleigh number. Analysis of temperature fluctuations in the fluid provides an estimate of the speed of the upward moving thermals, which decreases with distance from the heated surface.*
[DOI: 10.1115/1.2957484]

Keywords: porous media, stability, turbulence, steady and transient convection

1 Introduction

This paper reports experiments on the transition to convection for impulsive heating and the resulting steady state heat transport in a saturated porous medium. While the stability problem and steady convection in such systems have an extensive literature, the situation considered here has received scant attention. Steady state heat transfer results include measurements of Nusselt number for a saturating fluid with a strongly temperature-dependent viscosity. For Rayleigh numbers well above the transition to convection, turbulence is observed, and we quantify fluctuating temperatures to estimate the velocity of thermals that contribute to eddy diffusivity for heat. Measurement and analysis of time-averaged temperature profiles provide insight on the large scale features of the flow in steady convection.

The critical Rayleigh number for marginal stability in fully saturated porous layers for a wide range of thermal boundary conditions has been determined [1–5]. Experiments verifying many of the analytical results have been reported as well [6,7]. These analyses predict the condition for the onset of convection when the initial temperature (conduction) gradient and thermal boundary conditions are independent of time. Much less work has been published when instability is driven by a transient conduction state.

Currie [8] modeled transient constant flux bottom heating in a semi-infinite porous layer by assuming a linear temperature profile between the surface and a thermal penetration depth, $\delta(t)$. His linear stability analysis with this approximate profile yields critical Rayleigh numbers as a function of the thermal penetration depth. An interesting result is that transition to convection can occur for Rayleigh numbers less than those obtained for the Rayleigh–Bénard problem in a saturated porous layer. Nield [9] extended Currie's analysis to porous layers of finite thickness with constant flux heating at both surfaces. The critical Rayleigh number in terms of the dimensionless thermal penetration length (diffusion boundary layer) is

$$\mathrm{Ra}_c = \frac{12}{3\eta - 2\eta^2} \tag{1}$$

Nield also found that transition to convection can occur at Rayleigh numbers lower than those obtained for a stationery conduction profile, i.e., for $\eta = 1$. More recent research has expanded and refined his results [10–13].

Once convection is established, characterization of convective heat transfer needs to be made. Many experiments have been performed on steady convection in porous layers heated from below, and the data for the overall heat transfer coefficient have a great deal of scatter, e.g., in a graph of overall Nusselt number versus Rayleigh number, which has been attributed to a neglect of the effects of layer aspect ratio, fluid inertia, and improper modeling of the overall thermal conductivity [14–24]. A few studies [21–23] report that the scatter can be reduced by taking into account the effects of fluid inertia essentially via a modified Prandtl number and the Kozeny–Carman number, K/bH [24]. Wang and Bejan [25] used scale analysis to argue for the dependence of the Nusselt on the Prandtl number and cited data from previous researchers to obtain a heat transfer correlation. However, Prasad et al. [26] argued that the dependence of the Nusselt number on the Prandtl number is unlikely and proposed use of an effective thermal conductivity based on an ad hoc iterative procedure to reduce scatter in the heat transfer data. Kladias and Prasad [27] found via numerical analysis that the fluid Prandtl number for sufficiently low Darcy number can affect the critical Rayleigh number. Lage et al. [28] successfully disputed this result and argued that the Prandtl number has no effect on the threshold of convection and only affects the intensity of convection. Further confirmation of Lage's result is given by Nield and Bejan [4].

To date no experimental work has appeared on the transition to convection in a saturated porous layer instantaneously heated, i.e.,

[1]Present address: Intel Corporation, Chandler, AZ 85226.
[2]Present address: 3M Company, St. Paul, MN.
[3]Corresponding author.

Contributed by the Heat Transfer Division of ASME for publication in the JOURNAL OF HEAT TRANSFER. Manuscript received June 21, 2007; final manuscript received April 13, 2008; published online August 28, 2008. Review conducted by Cholik Chan. Paper presented at the 2005 ASME Heat Transfer Summer Conference (HT2005), San Francisco, CA, July 15–22, 2005.

by a step heat input, from below at constant heat flux with an isothermal top. Likewise, neither numerical nor analytical studies directly address these boundary conditions. Based on the analysis that has been performed thus far, it is not clear whether a Prandtl number dependence on the onset of convection should be expected. Also, the validity of the piecewise linear temperature profile, which has been widely used for time-dependent heating, remains to be determined. This is an especially important issue because stability analyses based on this profile predict a critical Rayleigh–Darcy number lower than that in the case of a steady linear temperature profile across the entire layer [8,9,11]. Further, Jonsson and Catton [23] showed for steady convection that measured and calculated values of effective thermal conductivity of the porous medium can be drastically different. Improved models for effective conductivity may reduce the scatter in overall heat transfer coefficients for steady convection, and several studies have shown that accounting for the effect of fluid inertia can also reduce scatter [21–25].

2 Apparatus and Procedure

The apparatus is a well insulated acrylic cylinder with a constant heat flux lower plate and a constant temperature upper plate. The cylinder has a 20.3 cm ID, a height of 38.7 cm, and a wall thickness of 1 cm. The top plate is a water jacket with a hole through its center so that thermocouples can be located inside the test cell along its centerline. The lower plate utilizes a thin heating element and guard heater beneath it contained in an acrylic guard plate that is integrated with the base of the cylinder. An aluminum plate 1.55 mm thick with embedded Type E thermocouples covers this heater. One thermocouple is located at its center, and four equally spaced thermocouples are located on radii between the center and its outer edge. Temperatures are recorded from up to 36 thermocouples during each experiment: six in the aluminum plate above the primary heater, six below the guard heater, five in the water jacket plate, two at the water jacket inlet and exit temperatures, one on the outer surface of the test cell, and up to 16 inside the porous medium at various radial and axial locations. A set of thermocouples in the fluid across the cross section of the porous medium is suspended 3 cm above the heated surface attached with epoxy to a horizontal grid of monofilament nylon. Radial locations of these thermocouples are $r/r_0=0$, 0.259, 0.366, 0.499, 0.563, 0.707, and 0.753. Temperatures on the centerline are measured at $z/H=0.078$, 0.13, 0.18, 0.23, 0.40, 0.57, 0.74, and 0.90. All thermocouples are made of 40 Ga Type E wire with twisted and soldered junctions, and the time constant for these thermocouples is ~ 0.05 s. Additional details of the design and assembly are discussed elsewhere [29–31].

The porous medium comprises 6 mm DIA soda-lime-silicate glass spheres ($k_s=0.64$ W/m K and $\alpha_s=2.79\times10^{-7}$ m^2/s obtained by chemical analysis [31]) and either water or a glycerin-water solution comprising 70% glycerin and 30% water by volume. The bulk porosity is $0.395<\varepsilon<0.399$ over the 35 experiments in this study and is determined by measuring the volume of liquid required to fill the test cell after the glass spheres have been loaded into it. In all experiments great care is exercised to assure that the solid phase makes uniform contact with the upper surface with no air pockets between the spheres and the top plate.

Prior to each experiment, room temperature water is circulated through the water jacket, and temperatures are monitored to make sure that the system is in thermal equilibrium at the temperature of the cold upper surface, T_i. An experiment is initiated by supplying power to the primary heater and comprises the heat up phase, initiation of convection, attainment of steady convection, and measurement of temperatures in steady convection. The critical elements of data reduction are the heat flux into the porous medium at each stage of an experiment and the transition time to convection using temperature-versus-time data. At the start of each experiment, the primary heater in the lower plate is used with an inactive guard heater. Initially, heat penetrates into the guard plate and the porous medium above it, and both can be considered initially semi-infinite. With the heater-aluminum and the heater-guard plate interfaces initially at the same temperature, the relation between the heat flux into the porous medium and that into the guard plate when radial heat losses are negligible is

$$\frac{q_{0m}}{q_0}=\left(1+\frac{k_m}{k_s}\sqrt{\frac{\alpha_g}{\alpha_m}}\right)^{-1} \tag{2}$$

Equation (2) is valid up to the onset of convection.

To determine the heat flux into the porous medium during the conduction phase of the experiment, three methods are used: evaluation of Eq. (2), experimental data in conjunction with an analytical model, and experimental data in conjunction with a numerical model. For the numerical model, measured temperature histories in the aluminum top plate and at the guard heater are used as boundary conditions. The analytical model for heat transfer into the medium is based on the conduction solution for the temperature at $z=0$,

$$\theta_w\frac{k_m}{2}\sqrt{\frac{\pi}{\alpha_m}}=q_{0m}\sqrt{t} \tag{3}$$

Linear regression is used to obtain the heat flux entering the porous medium from a plot of the lower boundary temperature versus $t^{1/2}$. The three methods produce heat flux values in very good agreement, with an average difference of less than 11% over the entire data set and a 7.5% standard deviation in the fraction of main heater power delivered to the porous medium. The details and comparison of each method of heat flux evaluation are given by Kohl [29].

In steady convection, power input to the guard heater is manually adjusted so that its temperature is equal to that of the primary heater. This procedure eliminates the thermal gradient in the guard plate and ensures that the heat generated by the primary heater is nearly as possible directed into the porous medium above it. Once the guard heater has been adjusted, the system is monitored until stabilized, and the heat flux into the medium is simply the power supplied to the primary heater.

3 Transition to Convection

To determine the transition from conduction to convection, the temperature of the lower surface is plotted as a function of time and compared with the analytical solution for conduction heat transfer. The deviation of this temperature from the transient conduction solution signals the transition to convection, i.e., the breakdown of the diffusion boundary layer on the wall. Owing to the difficulty in resolving the temperature-versus-time data, the transition time can be accurately determined when the data are plotted in terms of stretched coordinates of the form $\mathrm{Nu}_\delta\cdot\mathrm{Ra}_\delta$ versus Ra_δ, where the diffusion length is taken for the length scale. For conduction into a semi-infinite domain, the temperature rise across the penetration depth is given by Eq. (3), and with $h=q_{0m}/\theta_w$, $\mathrm{Nu}_\delta=\pi/2$. Prior to the onset of convection, $\mathrm{Nu}_\delta\mathrm{Ra}_\delta=\mathrm{Ra}_\delta\pi/2$, and once convection begins, the data deviate from this line. For Fig. 1, the departure of the data from conduction solution, $\mathrm{Nu}_\delta\mathrm{Ra}_\delta=\mathrm{Ra}_\delta\pi/2$, was seen at ~ 140 s. A break in the slope is obtained at the intersection of the conduction solution and a regression line fit to the heat transfer data for $\mathrm{Ra}>50$.

Figure 2 presents the transition to convection in terms of Ra_c and η with properties evaluated at the average temperature across the layer, and the working fluid is water. The data trend is similar to that determined analytically by Nield [9] except that the measured values are higher. Also, Nield's result pertains to two constant heat flux boundaries for which $\mathrm{Ra}_c=12$. For the boundary conditions of the present study, the analytical result is $\mathrm{Ra}_c=27.1$. The magnitude of Ra_c observed in this study is much greater than the difference in the critical Rayleigh numbers that can be attributed to the effects of the thermal boundary conditions. This dif-

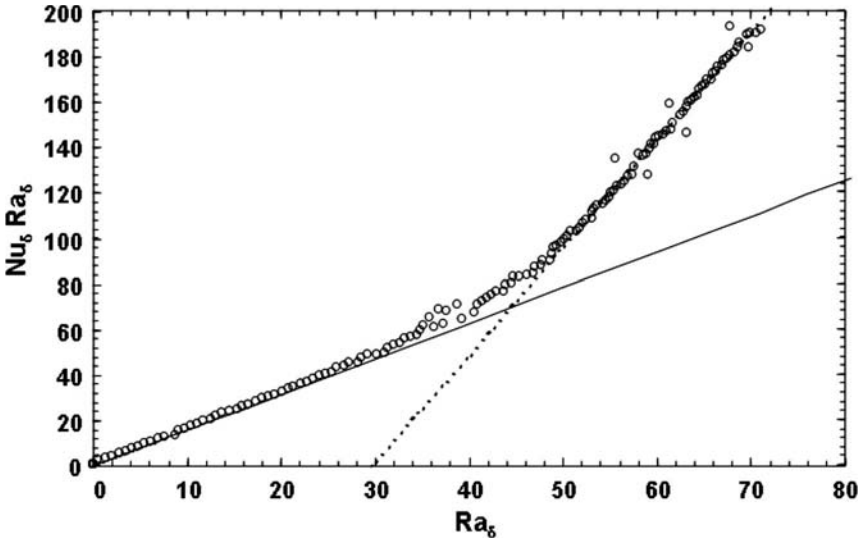

Fig. 1 Determination of transition to convection for water and 6 mm DIA glass spheres. Applied heat flux is q_{0m}=683.9 W/m^2. (—) Conduction solution; (- - -) regression fit.

ference is likely due to the differences in stability criteria created by the stationery piecewise linear temperature profile assumed by Nield and the true conduction profile. The increase in the conduction penetration depth with time in the present work has a stabilizing effect that is not possible to model with Nield's analysis and thus produces a different stability criterion. However, owing to the similarity between Nield's analytical result and the present experimental data, a correlation for the critical Rayleigh number of the form

$$\mathrm{Ra}_c = \frac{83}{1.08\eta - 0.08\eta^2} \tag{4}$$

is obtained by least-squares regression.

By noting the similarity of the penetration depth model used by Currie [8] and the linear temperature profile between the upper and lower boundaries used in the stability analyses mentioned earlier, $\delta(t)$ can be used as the length scale for the Rayleigh number. A plot of $\mathrm{Ra}_{\delta c}$ as a function of η is shown in Fig. 3 where $\mathrm{Ra}_{\delta c}$ remains relatively constant for $0.02 < \eta < 0.18$. The average $\mathrm{Ra}_{\delta c}$ over this range is 83 ± 8, where the uncertainty is the standard error times the student "t" value. Also shown in Fig. 3 is the critical Rayleigh number for the boundary conditions of the experiment, $\mathrm{Ra}_c = 27.1$, predicted by stability analysis for a stationary linear temperature profile between the upper and lower boundaries. Just as the measured value of Ra_c is greater than would be expected form theory, the data for $\mathrm{Ra}_{\delta c}$ are consistently greater than expected via this simple analogy. Also, it is interesting to see that the stability limit determined in terms of penetration depth appears not to be strongly dependent on either the temperature-dependent viscosity or the larger Prandtl number of the glycerin-water fluid phase.

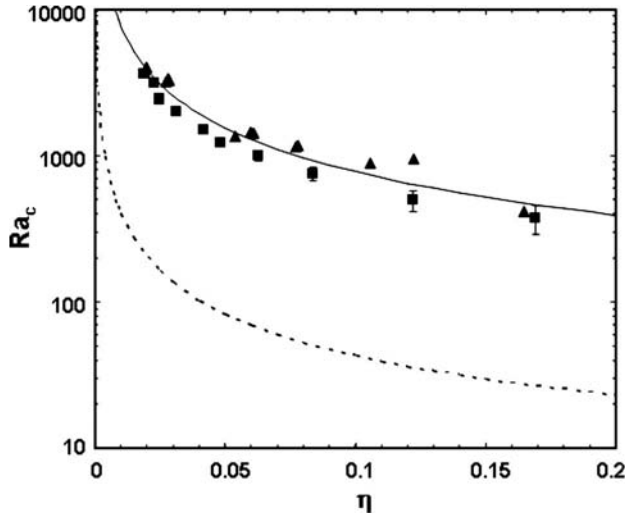

Fig. 2 Transition Rayleigh numbers in terms of normalized penetration depth. Thermal conductivity is evaluated as k_A, and viscosity is evaluated at the porous medium average temperature. (■) water-glass; (▲) glycerin-water-glass; (——) Eq. (4); (- - -) Eq. (1).

4 Steady State Heat Transfer

Overall Nusselt numbers are determined with water and a water-glycerin solution as the working fluids. Owing to the large variation of viscosity with temperature for the water-glycerin solution, property evaluation is critical to how the present data are presented. Sheely [32] reported the temperature dependence of viscosity for water-glycerin solutions from 293 K to 303 K, and because this temperature range does not cover the entire range required for the present study (302.2–313.8 K), an exponential form $\mu = (1.22 \times 10^{-8})\exp[4234.4/T]$ successfully extends the range of the data. Data from Raznjevic [33] are used to determine water viscosity. Reference values of the thermophysical properties are given in the Appendix for the benefit of comparison to future studies.

Steady heat transfer coefficients are well represented by a correlation that corrects for viscosity variation with a ratio of viscosity at the average layer temperature and that at $t=0$, or equivalently at the temperature of the upper (cold) boundary. Linear regression of reduced steady heat transfer data gives

$$\mathrm{Nu} = 0.047\mathrm{Ra}^{0.91}\mathrm{Pr}^{0.11}\left(\frac{\mu}{\mu_0}\right)^{0.72} \tag{5}$$

for which $r=0.946$. The properties of solid and fluid phases in Eq. (5) are evaluated at the average temperature across the height of the porous medium. Equation (5) is shown in Fig. 4 with data for both water and the water-glycerin solution as the fluid phases.

The present correlation is relatively insensitive to the method of evaluation of the effective stagnant conductivity of the porous

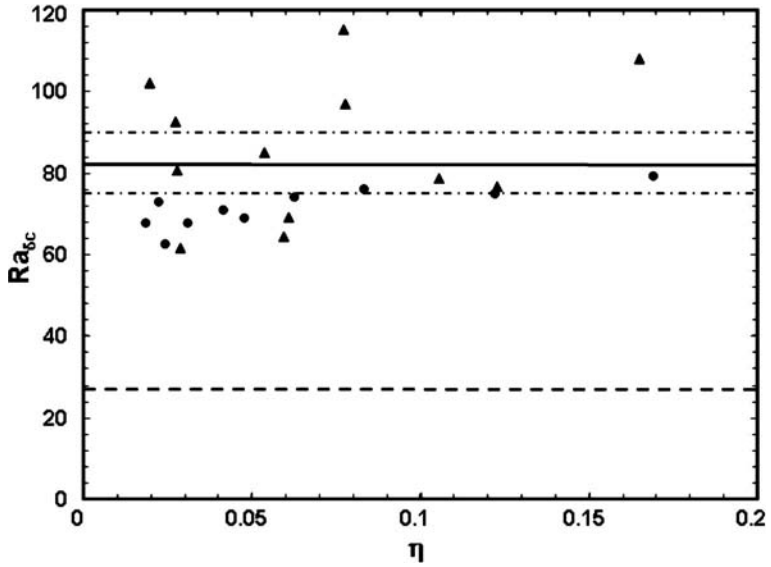

Fig. 3 Transition Rayleigh numbers scaled to penetration depth with uncertainty band on average value of 83. (●) water-glass; (▲) glycerin-water-glass; (- - -) linear stability theory.

medium. Owing to the level of the overall uncertainty in the measurements and with $k_s/k_f \sim 1$ over the range of mean temperature of the present data set, the series and parallel models of conductivity provide equally as good values ($k_m \approx 0.623$ W/m K) as those obtained from measurements of the true effective conductivity for the water-glass porous medium ($k_e = 0.61 \pm 0.09$ W/m K [29,30]). For the glycerin-water-glass porous medium, use of the two models introduces ~6% difference in the Rayleigh and Nusselt numbers ($k_A = 0.539$ W/m K versus $k_H = 0.506$ W/m K).

Elder [15] proposed a correlation for steady convection in the form Nu=Ra/40 for two constant temperature boundary conditions, and the Nusselt numbers given by Eq. (5) are in reasonably good agreement with this relation. However, by fitting the Nusselt number data to a linear expression, we obtain Nu=Ra/35 ($r = 0.945$), wherein the fluid properties are evaluated at the mean temperature of the porous medium. Equation (5) produces less scatter at low Rayleigh numbers, but the overall fit of this modified Elder-type relation is equally as good for engineering purposes.

5 Steady and Fluctuating Temperatures

Extensive measurements of time varying temperatures within the porous medium over the full extent of the heating schedule have been obtained for centerline and radial temperatures at $z/H = 0.078$ for $0 < t \sim 10^6$ s. Representative distributions are shown in Figs. 5–8 over the cross section and along the centerline.

All temperatures exhibit an initial growth period during which those on the heated surface and near to it grow in accordance with heat conduction theory. When a critical Rayleigh number is reached (Figs. 2 and 3), chaotic motion begins that signals the breakdown of the conduction layer and formation of large ther-

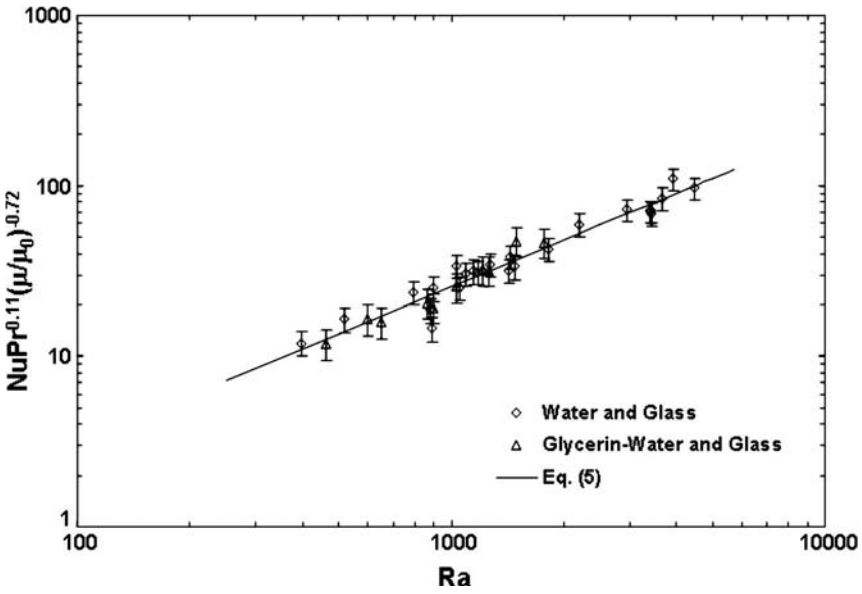

Fig. 4 Steady state Nusselt numbers and correlation, Eq. (5)

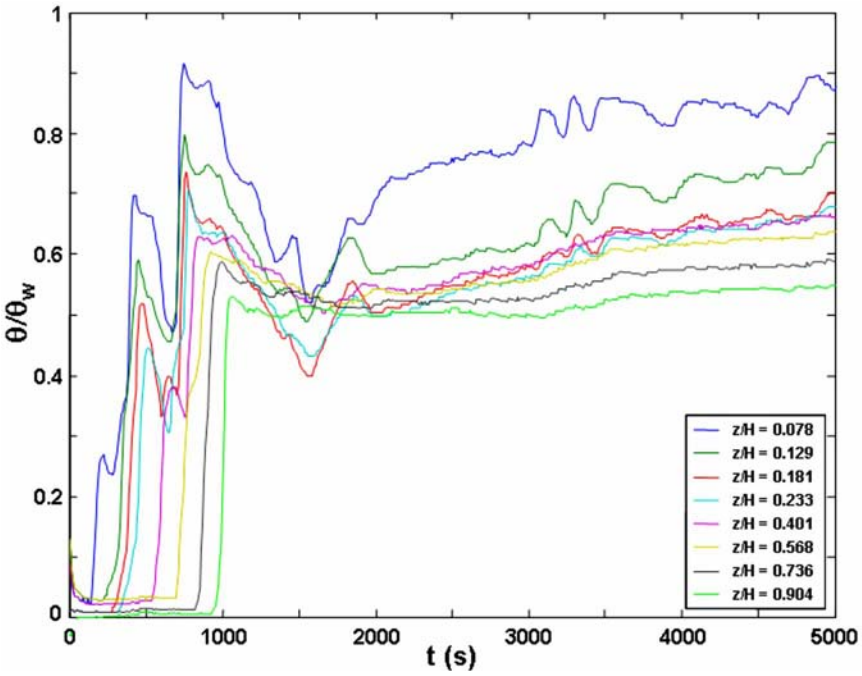

Fig. 5 Temperature traces for the water-glass porous medium along the centerline for the first 5000 s after the start of heating. Ra≈2700.

mals that rise into the overlying porous medium. In all experiments, this breakdown is accompanied by an initial fall in temperatures and then a recovery after which fluctuating temperatures are observed at all radii and heights above the heated surface. For example, Fig. 5 shows centerline temperatures for $0<t<5000$ s at Ra≈2700. The initial temperature excursion at $z/H=0.078$ appears well before excursions take place at locations much further removed from the heated surface. After $t\sim1000$ s, the entire system has transitioned to a chaotic state. When $t>4000$ s, the temperature profile appears established, and turbulent temperatures oscillate about well defined average values. An extensive set of temperature traces is available that supports these general observations [29,31].

It is also noteworthy that no correlation appears to exist in the fluctuations with respect to radial location in the present experiments. There is, however, observational evidence that large scale fluctuations have a spatial scale on the order of the diameter of the heated surface and that these temperature excursions above and below the temporal mean appear to have some relation to each other. This aspect of the data is interpreted to represent the flow of large eddies, or thermals, much the same as observed in turbulent Rayleigh–Bénard convection. These rising flows are essentially plumelike in character and represent up-welling motions leaving the heated surface from approximately its central region.

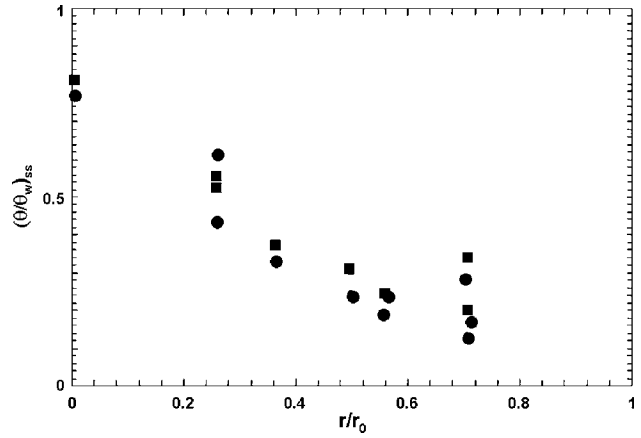

Fig. 6 Radial temperature distribution for steady convection with glycerin-water solution and an applied heat flux of ~900 W/m^2. Measurements are made at z=3 cm (z/H=0.078). Properties are evaluated at 293 K. (■) Ra=414. (●) Ra=429.

The time-averaged radial and centerline temperature profiles are of interest because they provide further insight on the structure of the flow field. Radial temperature profiles (Figs. 6 and 7) give an indication of the overall spatial structure of the buoyant convection. For both data sets, convection is dominated by upward flow in the center with colder fluid descending along the vertical walls of the enclosure. Upflow is confined to approximately one-third of the central area of the heated surface and thus represents a higher velocity on average than that of the downflow. With no evidence of a reversal in the temperature profile with radius from the center to the wall, these data imply a global flow structure comprising an axisymmetric cell, at least for the range of Rayleigh numbers attainable with the present apparatus. Additional temperature profiles are available over the range of Rayleigh numbers attainable with the apparatus [29,31].

Once steady turbulent convection is established, centerline and radial temperature profiles oscillate around mean values that appear to be related to the slow overturning of fluid within the system. Figure 8 shows centerline profiles obtained in time segments of 5000 s over 10^5 s for Ra≈2700. For $0<t<5000$ s, heat transfer develops from the initial conduction transient to turbulent convection. For $t>60,000$ s, steady turbulent convection is observed. Based on segmented time averaging, the profiles generally exhibit a reversal at midheights for $t>35,000$ s. Such a reversal is not steady owing to the flow structure resulting from the aspect ratio of the apparatus ($H/D=1.9$), and thus convection at these elevated Rayleigh numbers is quasistationary in nature.

Temperature-versus-time traces at steady state allow estimates of two important turbulent transport quantities, rms fluctuating

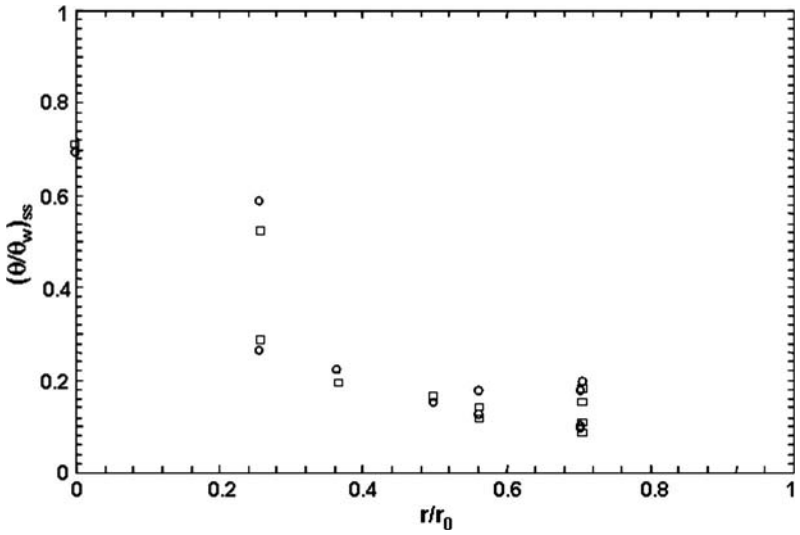

Fig. 7 Radial temperature distribution for steady convection with water and an applied heat flux of 1550 W/m^2. Measurements are made 3 cm above lower surface, $z/H=0.078$. Properties are evaluated at 293 K. (□) Ra =512. (○) Ra=525.

temperature and the speed with which an eddy rises. The rms fluctuating temperatures are obtained from the magnitudes of the point values of temperatures in steady convection over a sample size of 10^4. For $1300<\mathrm{Ra}<2200$, the dimensionless rms fluctuating temperature on the centerline over the eight measurement sites is ~0.045 K. Similar calculations for $r/r_0=0.366$ and 0.707 yield about the same order of magnitude of rms value but with slightly larger scatter for $1900<\mathrm{Ra}<2600$. A definitive relation between. rms temperatures and Rayleigh number is not possible with the present data set, but rms fluctuating temperatures appear to be weakly dependent on Rayleigh number and to increase over the range of Ra considered here. The rms fluctuating temperatures do not strongly depend on radius over ~70% of the cross sectional area over the heated lower surface (Figs. 9(*a*) and 9(*b*)).

Estimates of the vertical eddy speed along the centerline are obtained from analysis of the peaks in the temperature traces. With the locations of the temperature probes known, a time correlation is obtained by computing the elapsed time between peaks as the warm fluid moves up the cylinder from one thermocouple location to the next. In nondimensional terms, this characteristic rise time is $\tau=\tau\alpha_e/z^2$. Results are summarized in Table 1, and it can be seen that the warmer fluid loses both speed and temperature (energy) excess as it moves up the cylinder.

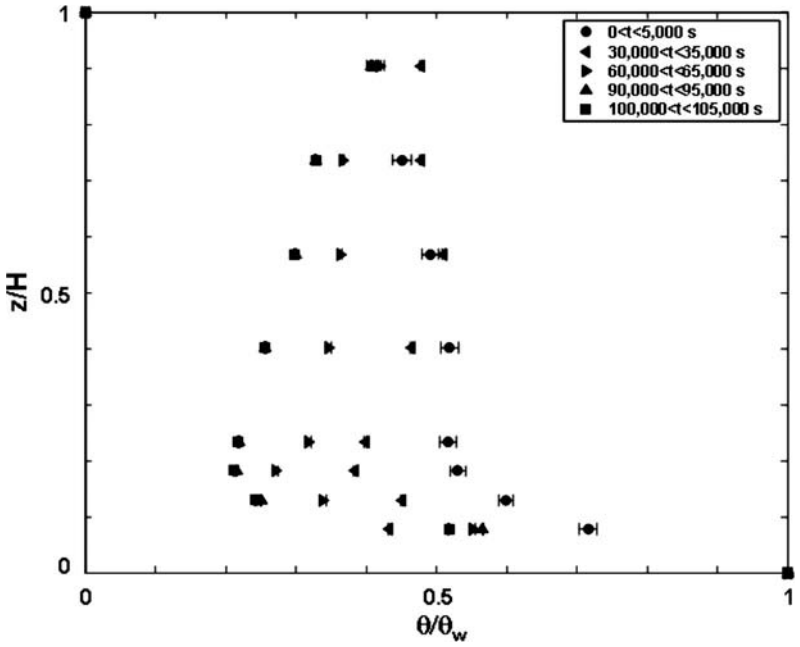

Fig. 8 Centerline temperatures averaged over 5000 s intervals at Ra ≈2700. For $0<t<5000$ s, flow develops from initial conduction transient to turbulent flow. For $t>60{,}000$ s, steady turbulent flow is observed. Temperatures profiles generally exhibit a reversal at midheights for $t>35{,}000$ s.

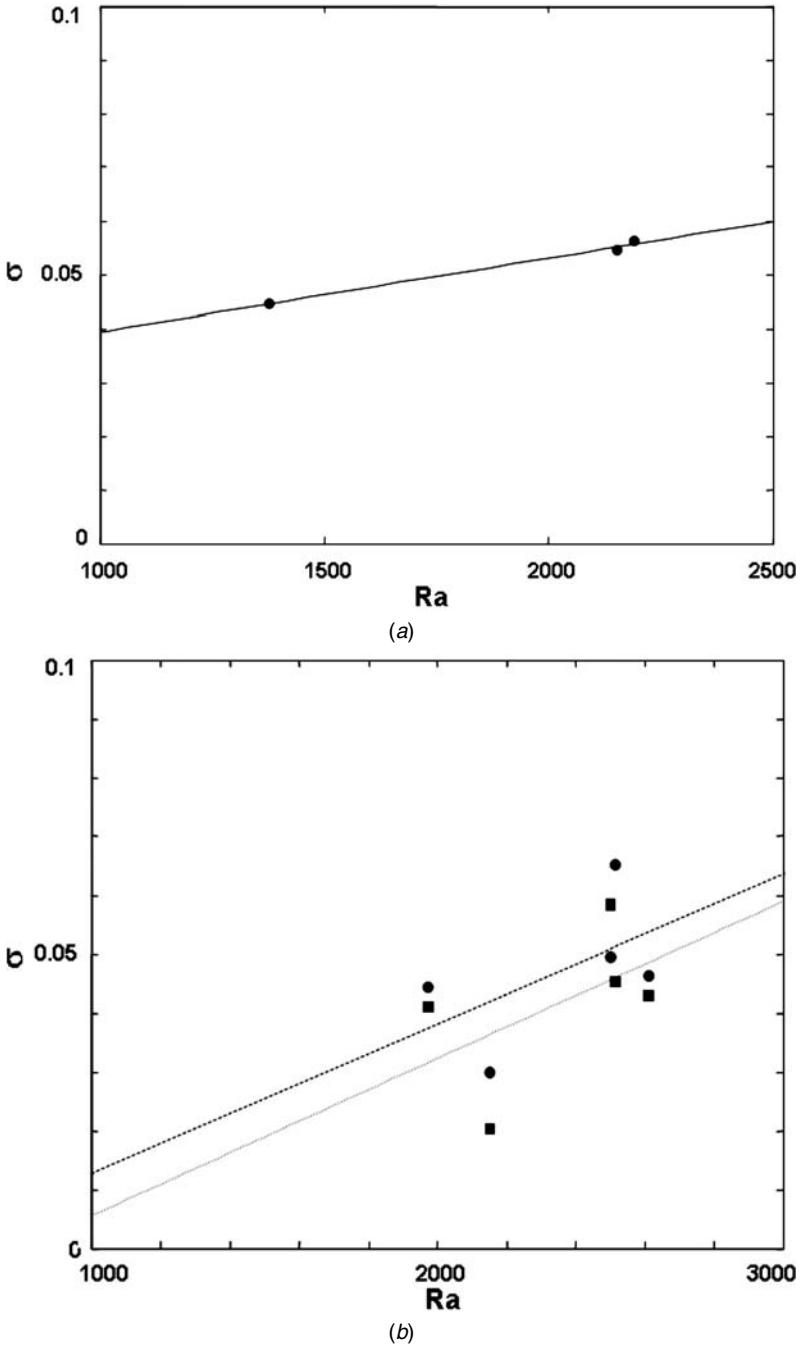

Fig. 9 rms fluctuating temperatures at $z/H=0.078$. (*a*) (●) $r/r_0=0$ and (——) regression line. (*b*) (●) $r/r_0=0.366$ and (——) regression line. (■) $r/r_0=0.070$ and (- - -) regression line.

6 Experimental Uncertainty

Based on the analysis of Aichlmayr and Kulacki [30] and present measurements, energy loss from the apparatus to the ambient environment during steady convection amounts to no more than 5–9% of energy input to the main heater in the lower surface, and heat flux delivered to the porous medium during the conduction phase is determined with an uncertainty of less than 1%. Data reduction and heat loss estimates are made on the basis of property values referenced to 293 K with their temperature dependency determined from the published database for each. The Appendix provides this information as a foundation for future applications and comparison to the present results.

Table 1 Mean temperature and velocity of warm fluid at different vertical locations

z/h	θ	t (s)	Eddy speed (cm/s)	τ
0.08	0.9157	740.0	NA	NA
0.13	0.7964	750.0	0.2	0.0009
0.18	0.7349	759.9	0.2	0.0009
0.23	0.7048	779.9	0.1	0.0011
0.40	0.6287	839.9	0.1	0.0010
0.57	0.6042	920.0	0.1	0.0009
0.74	0.5872	1000.0	0.1	0.0007
0.90	0.5310	1060.0	0.1	0.0006

Table 2 Experimental uncertainty in primary quantities

Quantity	Uncertainty	Source
q_0	$<1\%$	-
k_s	1%	Chemical analysis
Water properties	2%	[33]
Water-glycerin properties	2.5%	[32,33]
T	± 0.5 K	-
ε	$\ll 0.1\%$	-
t	± 0.5 s	-
Heat flux for conduction phase	$<1\%$ of Applied q_0	Computed
Heat flux for steady convection	<5–$<9\%$	Computed

Uncertainties in thermophysical properties, power input to the heating elements, and temperature measurements are summarized in Table 2. These values are taken from either primary sources as reported or estimated from zero-level uncertainties. The uncertainty in dimensionless groups is computed using the root sum of squares method for single sample experiments.

Total fractional uncertainty in Nusselt number ranges from 4% to 9%, and in Rayleigh number in steady convection, 5% or less. These estimates of uncertainty are due largely to the accuracy obtained in determining the net heat flux at the lower surface that is transferred into the porous medium [29]. Values of total uncertainty vary across the present data set, and the uncertainty in key dimensionless groups is discussed elsewhere [29,31].

Uncertainty in the transition time from conduction to convection is less than ± 5 s over all experiments for measured transition times of 72–5798 s. The fractional uncertainty in the transition time from conduction to convection varies from <0.01 to ~ 0.07. Rayleigh numbers at transition based on mean properties and the height of the test cylinder have fractional uncertainties ranging from 0.03 to 0.12. The Rayleigh number is evaluated in terms of θ_w, and thus the uncertainty in heat flux in steady convection is inconsequential with respect to this correlation parameter.

7 Conclusion

Measurements of time-dependent transition to turbulent buoyant convection for bottom heated porous layers are reported, and a correlation is developed for steady heat transfer that accounts for a larger viscosity variation than in the published database.

Results for the transition to convection are found to correlate well for critical Rayleigh numbers as a function of the nondimensional penetration depth for $0.02 < \eta < 0.18$. For the same penetration depth range, the onset of convection is also predicted by $\mathrm{Ra}_{\delta c} = 83 \pm 8$. When compared with theoretical stability predictions using approximate linear conduction temperature profiles, both Ra_c and $\mathrm{Ra}_{\delta c}$ are consistently greater. This result strongly suggests a stabilizing effect associated with the upward movement of the diffusion boundary layer, or penetration of the positively buoyant region on the lower surface into the stable overlying fluid, and the inadequacy of the linear temperature distributions used in available linear stability analyses [8,9].

Steady convection data are correlated well in terms of Ra, Pr, and a ratio of the viscosities at the upper and lower boundaries. The latter factor accounts adequately for the variation of viscosity that can result for fluids other than water, which is most frequently used in laboratory studies of the kind reported in this paper. It should be noted that the exponent on the Prandtl number in the correlation is found to be significant enough such that it cannot be neglected. Limitations on the present steady heat transfer correlation are $(k_f/k_s)_{\text{water-glass}} \sim 1$, $(k_f/k_s)_{\text{glycerin-glass}} \approx 0.8$, and $H/D = 1.9$. Experiments for a wider range of aspect ratios and an expanded property range for the fluid would extend the validity of the current correlation and perhaps add a factor related to the enclosure geometry for both heat transfer and transition to convection.

Time-averaged temperatures in steady convection indicate that the global structure of the flow is a single convection cell dominated by an upflow that occupies approximately one-third of the central region of the cylindrical test cell. At Rayleigh numbers $\sim 100\mathrm{Ra}_c$ and above, the upflow region appears to be sharply defined. Colder downflow occupies a larger outer annular area and thus has much reduced average velocities. Analysis of the temperature-versus-time traces along the centerline and at several radial locations at $z/H \approx 0.08$ reveals a weak dependence of the rms fluctuating temperatures on Rayleigh number. Additionally, time-averaged centerline temperature profiles reveal a reversal that appears to be quasisteady over experiments with duration of 10^6 s. Both of these features of the flow warrant further investigation both experimentally and theoretically, but as far as is known, rms fluctuating temperatures have hitherto not been reported in the open literature.

Nomenclature

b = inertial resistance coefficient, $0.0117d/(1-\varepsilon)$
c = specific heat, J/ kg K
d = bead diameter, m
D = test cell internal diameter, m
h = heat transfer, $\mathrm{W/m^2\ K}$
H = height of test cell, m
k = thermal conductivity, W/m K
K = permeability, m^2
Nu = Nusselt number, hH/k_m
Nu_δ = Nusselt number, $(h/k_m)\ (\pi\alpha_m t)^{1/2}$
Pr = Prandtl number, ν/α
Pr_m = porous medium Prandtl number, ν/α_m
q_0 = applied heat flux at boundary, $\mathrm{W/m^2}$
r = radial coordinate, m
r_0 = radius of porous medium, m
r = coefficient of linear regression
Ra = Rayleigh number, $\rho_f^2 c_f g \beta K \theta_{w,ss} H/\mu k_m$
Ra_δ = Rayleigh number, $\rho_f^2 c_f g \beta K \theta_w (\pi\alpha_m t)^{1/2}/\mathrm{mk}_m$
T = temperature, K
t = time, s
z = vertical coordinate, m

Greek Symbols

α = thermal diffusivity, $\mathrm{m^2}/s$
β = coefficient of thermal expansion, $\mathrm{K^{-1}}$
δ = thermal penetration length $(\pi\alpha_m t)^{0.5}$, m
ε = porosity
η = nondimensional penetration length, δ/H
μ = dynamic viscosity, $\mathrm{N\ s/m^2}$
ν = kinematic viscosity, $\mathrm{m^2/s}$
θ = temperature difference, $(T-T_i)$
ρ = density, $\mathrm{kg/m^3}$
σ = rms temperature fluctuation, K
τ = characteristic rise time, $\alpha_e t/z^2$

Subscripts

A = evaluated using $k_A = (1-\varepsilon)k_s + \varepsilon k_f$
c = critical
e = effective
f = fluid
g = guard plate
H = evaluated using $k_H^{-1} = (1-\varepsilon)/k_s + \varepsilon/k_f$
i = initial at $t=0$

Table 3 Reference property data at 293 K [32,33]

	Water	Glycerin	Glycerin (70%)-water (30%)	Units
k	0.597	0.286	0.3793	W/m K
α	1.34×10^{-7}	9.95×10^{-8}	1.09×10^{-7}	m^2/s
β	2.1×10^{-4}	5.0×10^{-4}	4.13×10^{-5}	K^{-1}
μ	9.93×10^{-4}	1.49	0.0229	N s/m^2
ρ	998.2	1264.0	1184.3	kg/m^3
c_p	4182	2386	2924.8	J/kg K

m = property of or relating to the porous medium
s = solid
ss = steady state
w = wall, $z=0$
δ = penetration depth

Appendix

Reference values (Table 3) for the thermophysical properties of the fluid phase and their variation with temperature are taken from Sheely [32] and Raznjevic [33]. Values at 293 K are given for completeness and future analysis and manipulation of the present data.

References

[1] Horton, C. J., and Rogers, F. T., Jr., 1945, "Convection Currents in a Porous Medium," J. Appl. Phys., **16**, pp. 367–370.
[2] Lapwood, E. R., 1948, "Convection of a Fluid in a Porous Medium," Proc. Cambridge Philos. Soc., **44**, pp. 508–521.
[3] Nield, D. A., 1968, "Onset of Thermohaline Convection in a Porous Medium," Water Resour. Res., **4**, pp. 553–660.
[4] Nield, D. A., and Bejan, A., 2000, *Convection in Porous Media*, 3rd ed., Springer-Verlag, New York.
[5] Wilkes, K. E., 1995, "Onset of Natural Convection in a Horizontal Porous Medium With Mixed Thermal Boundary Conditions," ASME J. Heat Transfer, **117**, pp. 543–547.
[6] Katto, Y., and Masuoka, T., 1967, "Criterion for the Onset of Convective Flow in a Fluid in a Porous Medium," Int. J. Heat Mass Transfer, **10**, pp. 297–309.
[7] Kaneko, T., Mohtadi, M. F., and Aziz, K., 1974, "An Experimental Study of Natural Convection in Inclined Porous Media," Int. J. Heat Mass Transfer, **17**, pp. 485–496.
[8] Currie, I. G., 1967, "The Effect of Heating Rate on the Stability of Stationary Fluids," J. Fluid Mech., **29**, pp. 337–347.
[9] Nield, D. A., 1975, "The Onset of Transient Convective Instability," J. Fluid Mech., **71**, pp. 441–454.
[10] Rudraiah, N., Veerappa, B., and Balachandra, S., 1980, "Effects of Nonuniform Thermal Gradient and Adiabatic Boundaries on Convection in Porous Media," ASME J. Heat Transfer, **102**, pp. 254–260.
[11] Vasseur, P., and Robillard, L., 1993, "The Brinkman Model for Natural Convection in a Porous Layer: Effects of Nonuniform Thermal Gradient," Int. J. Heat Mass Transfer, **36**, pp. 4199–4206.
[12] Caltagirone, J., 1980, "Stability of a Saturated Porous Layer Subject to a Sudden Rise in Surface Temperature: Comparison Between the Linear and Energy Methods," Q. J. Mech. Appl. Math., **33**, pp. 47–58.
[13] Kaviany, M., 1984, "Onset of Thermal Convection in a Saturated Porous Medium: Experiment and Analysis," Int. J. Heat Mass Transfer, **27**, pp. 2101–2110.
[14] Schneider, K. J., 1963, "Investigation on the Influence of Free Thermal Convection on Heat Transfer Through Granular Material," *Proceedings of the 11th International Congress of Refrigeration*, Pergamon, Oxford, pp. 247–253, Paper No. 11-4.
[15] Elder, J. W., 1967, "Steady Free Convection in a Porous Medium Heated From Below," J. Fluid Mech., **27**, pp. 29–48.
[16] Combarnous, M. A., and Bories, S. A., 1975, "Hydrothermal Convection in Saturated Porous Media," Adv. Hydrosci., **10**, pp. 231–307.
[17] Buretta, R. J., and Berman, A. S., 1976, "Convective Heat Transfer in a Liquid Saturated Porous Layer," ASME J. Appl. Mech., **43**, pp. 249–253.
[18] Yen, Y. C., 1974, "Effects of Density Inversion on Free Convective Heat Transfer in Porous Layer Heat From Below," Int. J. Heat Mass Transfer, **17**, pp. 1349–1356.
[19] Kaneko, T., Mohtadi, M. F., and Aziz, K., 1974, "An Experimental Study of Natural Convection in Inclined Porous media," Int. J. Heat Mass Transfer, **17**, pp. 485–496.
[20] Seki, N., Fukasako, S., and Inaba, H., 1978, "Heat Transfer in a Confined Rectangular Cavity Packed With Porous Media," Int. J. Heat Mass Transfer, **21**, pp. 985–989.
[21] Somerton, C. W., 1983, "The Prandtl Number Effect in Porous Layer Convection," Appl. Sci. Res., **40**, pp. 333–344.
[22] Georgiadis, J. G., and Catton, I., 1986, "Prandtl Number Effect on Bénard Convection in Porous Media," ASME J. Heat Transfer, **108**, pp. 284–290.
[23] Jonsson, T., and Catton, I., 1987, "Prandtl Number Dependence of Natural Convection in Porous Media," ASME J. Heat Transfer, **109**, pp. 371–377.
[24] Ergun, S., 1952, "Flow Through Packed Columns," Chem. Eng. Prog., **48**, pp. 89–94.
[25] Mingyu, W., and Bejan, A., 1987, "Heat Transfer Correlation for Bénard Convection in a Fluid Saturated Porous Layer," Int. Commun. Heat Mass Transfer, **14**, pp. 617–626.
[26] Prasad, V., Kulacki, F. A., and Keyhani, M., 1985, "Natural Convection in Porous Media," J. Fluid Mech., **150**, pp. 89–119.
[27] Kladias, N., and Prasad, V., 1989, "Natural Convection in Horizontal Porous Layers: Effects of Darcy and Prandtl Numbers," ASME J. Heat Transfer, **111**, pp. 926–935.
[28] Lage, J. L., Bejan, A., and Georgiadis, J. G., 1992, "The Prandtl Number Effect Near the Onset of Benard Convection in a Porous Medium," Int. J. Heat Fluid Flow, **13**, pp. 408–411.
[29] Kohl, M. J., 2000, "The Transition to Convection of Porous Layers Heated From Below," M.S. thesis, University of Minnesota, Minneapolis, MN.
[30] Aichlmayr, H. T., and Kulacki, F. A., 2006, "A Transient Technique for Measuring the Effective Thermal Conductivity of Saturated Porous Media With a Constant Boundary Heat Flux," ASME J. Heat Transfer, **128**, pp. 1217–1220.
[31] Kristoffersen, M., 2001, "Meta-Stable Convective Heat Transfer in Porous Media," M.S. thesis, University of Minnesota, Minneapolis, MN; Kristoffersen, M., and Kulacki, F. A., 2006, "Turbulence in a Porous Medium Heated From Below," *Proceedings of the 13th International Heat Transfer Conference*, G. de Vahl Davis and E. Leonardi, eds., Sydney, Vol. 13, Paper No. PRT-06 (CDROM).
[32] Sheely, M. L., 1932, "Glycerol Viscosity Tables," Ind. Eng. Chem., **24**, pp. 1060–1064.
[33] Raznjevic, K., 1976, *Handbook of Thermodynamic Tables and Charts*, McGraw-Hill, New York.

Magnetohydrodynamic Mixed-Convective Flow and Heat and Mass Transfer Past a Vertical Plate in a Porous Medium With Constant Wall Suction

O. D. Makinde
Faculty of Engineering,
Cape Peninsula University of Technology,
P. O. Box 652,
Cape-Town 8000, South Africa
e-mail: dmakinde@yahoo.com

P. Sibanda[1]
School of Mathematical Sciences,
University of KwaZulu-Natal,
Private Bag X01, Scottsville,
Pietermaritzburg 3209, South Africa
e-mail: sibandap@ukzn.ac.za

The problem of steady laminar hydromagnetic heat transfer by mixed convection flow over a vertical plate embedded in a uniform porous medium in the presence of a uniform normal magnetic field is studied. Convective heat transfer through porous media has wide applications in engineering problems such as in high temperature heat exchangers and in insulation problems. We construct solutions for the free convection boundary-layer flow equations using an Adomian–Padé approximation method that in the recent past has proven to be an able alternative to the traditional numerical techniques. The effects of the various flow parameters such as the Eckert, Hartmann, and Schmidt numbers on the skin friction coefficient and the concentration, velocity, and temperature profiles are discussed and presented graphically. A comparison of our results with those obtained using traditional numerical methods in earlier studies is made, and the results show an excellent agreement. The results demonstrate the reliability and the efficiency of the Adomian–Padé method in an unbounded domain. [DOI: 10.1115/1.2955471]

Keywords: MHD flow, mass transfer, vertical plate, porous medium, constant heat flux, Adomian–Padé method

1 Introduction

Convective boundary-layer flows that are subject to a chemical reaction have many applications in geophysics and engineering. Many of these applications, for example, in building structure insulation, food processing, and the spread of pollutants underground, involve the flow of a fluid over a porous matrix. Also, the past three decades have seen a tremendous interest in magnetohydrodynamic (hereinafter MHD) mixed convection from a vertical plate embedded in porous media, largely as a result of applications of such flows in industries involving heat exchanger design, petroleum production, filtration, chemical catalytic reactors, MHD accelerators and generators, and others. Examples of such theoretical studies include those of Sparrow and Cess [1], Bejan and Khair [2], and Magyari and Keller [3] (see also the references therein). Ahmed et al. [4] presented a theoretical study of steady MHD mixed-convective and mass transfer boundary layers of an electrically conducting fluid through a porous medium. Their study was an extension of earlier works by Raptis and Kafousias [5], Acharya et al. [6], Ahmed and Ahmed [7], and Ahmed et al. [8] to include the effects of a transverse magnetic field, a heat generating source, and Joule heating. However, in their study, Ahmed et al. [4] assumed small Eckert numbers in order to allow for asymptotic solutions to be constructed in terms of this small parameter. In this study we aim to improve on the scope and applicability of the results of Ahmed et al. [4] by using a novel numerical scheme that allows for the construction of boundary-layer solutions for all Eckert numbers and other parameter values.

The boundary-layer equations for mixed-convective flow through a porous medium constitute a nonlinear problem. The theory of nonlinear differential equations is quite elaborate, and their solutions are of practical relevance in the engineering sciences. Several numerical approaches have been developed in the past few decades, e.g., finite differences, spectral method, and shooting method, to tackle this problem. More recently, the ideas of classical analytical methods have experienced a revival in connection with the proposition of novel hybrid numerical-analytical schemes for nonlinear differential equations. One such trend is related to the Adomian–Padé method due to Adomian [9]. This approach, over the past few years, has proven itself as a powerful tool and a potential alternative to traditional numerical techniques in various applications in sciences and engineering. Successful applications of this technique can be found, for example, in recent studies by Makinde [10], Wazwaz [11], and Kechil and Hashim [12].

In the present study, we construct approximate solutions for mixed-convective boundary-layer equations for flow past a vertical porous plate embedded in a saturated porous medium with a constant heat flux and mass transfer in the presence of a magnetic field and with heat absorption or generation using the Adomian–Padé method. In this study we consider only the case of constant wall suction with heat absorption. The solutions for the region far downstream of the leading edge of the plate are presented and discussed qualitatively with respect to various parameters embedded in the problem.

2 Mathematical Formulation

Consider a steady convective flow of an incompressible and electrically conducting Newtonian fluid along an infinite vertical plate embedded in a porous medium. A uniform magnetic field with strength B_0 is imposed along the y-axis. Following Raptis and Kafousias [5], Brinkman [13], and Ahmed et al. [4], the governing boundary-layer equations are

[1]Corresponding author.

Contributed by the Heat Transfer Division of ASME for publication in the JOURNAL OF HEAT TRANSFER. Manuscript received December 11, 2007; final manuscript received March 11, 2008; published online September 3, 2008. Review conducted by Louis C. Burmeister.

$$-v_0\frac{\partial \bar{u}}{\partial \bar{y}} = \upsilon\frac{\partial^2 \bar{u}}{\partial \bar{y}^2} + g\beta(\bar{T}-\bar{T}_\infty) + g\bar{\beta}(\bar{C}-\bar{C}_\infty) + \frac{\upsilon}{\bar{K}}(\bar{U}-\bar{u}) + \frac{\sigma B_0^2}{\rho}(\bar{U}-\bar{u}) \tag{1}$$

$$-v_0\frac{\partial \bar{T}}{\partial \bar{y}} = \frac{\lambda}{\rho C_p}\frac{\partial^2 \bar{T}}{\partial \bar{y}^2} + \frac{\upsilon}{C_p}\left(\frac{\partial \bar{u}}{\partial \bar{y}}\right)^2 + \frac{\sigma B_0^2}{\rho C_p}(\bar{U}-\bar{u})^2 + \frac{Q}{\rho C_p}(\bar{T}_\infty - \bar{T}) \tag{2}$$

$$-v_0\frac{\partial \bar{C}}{\partial \bar{y}} = D\frac{\partial^2 \bar{C}}{\partial \bar{y}^2} \tag{3}$$

Here $\bar{x}$ and $\bar{y}$ are, respectively, the directions along and perpendicular to the surface, $\bar{u}$ is the velocity component along the tangential direction, $\bar{U}$ is the uniform freestream velocity,v_0 is the constant suction velocity, g is the acceleration due to gravity, and ρ, υ, λ, and σ are, respectively, the fluid density, coefficient of kinematic viscosity, thermal conductivity, and electrical conductivity. The temperature is $\bar{T}$, and $\bar{C}$ is the species concentration. The subscript ∞ denotes freestream conditions. The other parameters are the specific heat at constant pressure C_p, the coefficient of volume expansion for heat transfer β, the coefficient of volumetric expansion with respect to species concentration $\bar{\beta}$, the heat source term Q, and the molecular diffusivity D. The appropriate boundary conditions for this flow are

$$\bar{u}=0, \quad \frac{\partial \bar{T}}{\partial \bar{y}} = -\frac{\bar{q}}{\lambda}, \quad \bar{C}=\bar{C}_w \quad \text{at } \bar{y}=0 \tag{4}$$

$$\bar{u}\to\bar{U}, \quad \bar{T}\to\bar{T}_\infty, \quad \bar{C}\to\bar{C}_\infty \quad \text{as } \bar{y}\to\infty \tag{5}$$

We now introduce the following dimensionless variables and quantities into the governing momentum, energy balance, and concentration equations (see also Ahmed et al. [4]):

$$y=\frac{v_0\bar{y}}{\upsilon}, \quad u=\frac{\bar{u}}{v_0}, \quad U=\frac{\bar{U}}{v_0}, \quad \theta=\frac{\lambda v_0(\bar{T}-\bar{T}_\infty)}{\bar{q}\upsilon},$$

$$\phi=\frac{\bar{c}-\bar{c}_\infty}{\bar{c}_w-\bar{c}_\infty}, \quad G_r=\frac{g\beta\bar{q}\upsilon^2}{\lambda v_0^4}, \quad P=\frac{\upsilon\rho C_p}{\lambda}$$

$$G_m=\frac{\upsilon g\bar{\beta}(\bar{c}_w-\bar{c}_\infty)}{v_0^3}, \quad M=\frac{\sigma B_0^2\upsilon}{\rho v_0^2}, \quad \alpha=\frac{Q\upsilon^2}{\lambda v_0^2}, \tag{6}$$

$$K=\frac{v_0^2\bar{K}}{\upsilon}, \quad \mathrm{Ec}=\frac{\lambda v_0^3}{\bar{q}\upsilon C_P}, \quad \mathrm{Sc}=\frac{\upsilon}{D}$$

where α is the heat source term when the vertical wall temperature exceeds the freestream temperature, i.e., when $\bar{T}_\infty-\bar{T}<0$, and the heat sink term when $\bar{T}_\infty-\bar{T}>0$. Ec is the Eckert number, G_m and G_r are the Grashof numbers for mass and heat transfer, respectively, K is the porosity parameter, M is the Hartmann number, P is the Prandtl number, and Sc is the Schmidt number. Equations (1)–(5) now give the ordinary differential equations

$$-\frac{du}{dy} = \frac{d^2u}{dy^2} + G_r\theta + G_m\phi + M(U-u) + \frac{U-u}{K} \tag{7}$$

$$-\frac{d\theta}{dy} = \frac{1}{P}\frac{d^2\theta}{dy^2} + \mathrm{Ec}\left(\frac{du}{dy}\right)^2 + M\,\mathrm{Ec}(U-u)^2 - \frac{\alpha}{P}\theta \tag{8}$$

$$-\frac{d\phi}{dy} = \frac{1}{\mathrm{Sc}}\frac{d^2\phi}{dy^2} \tag{9}$$

$$u=0, \quad \frac{d\theta}{dy}=-1, \quad \phi=1 \quad \text{at } y=0 \tag{10}$$

$$u=U, \quad \theta=\phi=0 \quad \text{as } y\to\infty \tag{11}$$

When the Eckert number Ec=0, Eqs. (7)–(9) are all linear, and exact analytical solutions for $u(y)$, $\theta(y)$, and $\phi(y)$ can easily be found. Equation (9), subject to the boundary conditions (Eqs. (10) and (11)), admits the exact elementary solution

$$\phi(y)=e^{-\mathrm{Sc}\,y} \tag{12}$$

In the case of a heat sink ($\alpha>0$), the exact solutions that satisfy the boundary conditions (Eqs. (10) and (11)) are

$$u(y)=U(1-e^{-\xi y}) + \frac{G_r}{\omega(\omega^2-\omega-\gamma)}(e^{-\xi y}-e^{-\omega y}) + \frac{G_m}{\mathrm{Sc}^2-\mathrm{Sc}-\gamma}(e^{-\xi y}-e^{-\mathrm{Sc}y}) \tag{13}$$

$$\theta(y)=\omega^{-1}e^{-\omega y} \tag{14}$$

where $\xi=(1+\sqrt{4\gamma+1})/2$, $\gamma=M+1/K$, and $\omega=(P+\sqrt{P^2+4\alpha})/2$.

Equations (7)–(11) were solved numerically for all other Eckert numbers using the Adomian–Padé method. The exact solutions were used as a benchmark in evaluating the accuracy of the Adomian–Padé approximation scheme.

3 Computational Approach

In order to explicitly construct approximate nonperturbative solutions of the problem described by Eqs. (7)–(11), the Adomian–Padé method is employed and implemented in MAPLE (a symbolic algebra package) (see, for example, Heck [14]). We rewrite Eqs. (7)–(9) in the form

$$L_y u = -u_y - G_r\theta - G_m\phi - M(U-u) - \frac{U-u}{K} \tag{15}$$

$$L_y\theta = \alpha\theta - P\theta_y - P\,\mathrm{Ec}\,u_y^2 - PM\,\mathrm{Ec}(U-u)^2 \tag{16}$$

$$L_y\phi = -\mathrm{Sc}\,\phi_y \tag{17}$$

where the subscript y represents differentiation with respect to y and the differential operator employs the first three derivatives in the form $L_y=d^2/dy^2$. The inverse operator L_y^{-1} is considered to be a twofold integral operator defined by

$$L_y^{-1}=\int_0^y\int_0^y(\cdot)dydy \tag{18}$$

Applying L_y^{-1} to both sides of Eqs. (15)–(17) and using the boundary conditions in Eqs. (10) and (11), we obtain

$$u(y)=a_1y - L_y^{-1}(u_y) - G_rL_y^{-1}(\theta) - G_mL_y^{-1}(\phi) - ML_y^{-1}(U-u) - \frac{1}{K}L_y^{-1}(U-u) \tag{19}$$

$$\theta(y)=a_2 - y + \alpha L_y^{-1}(\theta) - PL_y^{-1}(\theta_y) - P\,\mathrm{Ec}\,L_y^{-1}(u_y^2) - PM\,\mathrm{Ec}\,L_y^{-1}(U-u)^2 \tag{20}$$

$$\phi(y)=1+a_3y - \mathrm{Sc}\,L_y^{-1}(\phi_y) \tag{21}$$

where $a_1=u_y(0)$, $a_2=\theta(0)$, and $a_3=\phi_y(0)$ are to be determined from the boundary conditions at infinity in Eq. (11). As usual, in the Adomian decomposition method the solutions of Eqs. (19)–(21) are approximated as an infinite series,

Table 1 Comparison between exact and Adomian–Padé approximate solutions for Ec=0, $G_r = G_m = 0.1$, $K = M = U = 1$, and $P = 0.71$

Sc	α	$u'(0)$ exact	$u'(0)$ (Adomian–Padé)	$\theta(0)$ exact	$\theta(0)$ (Adomain–Padé)	$\theta(0.5)$ (exact)	$\theta(0.5)$ (Adomain–Padé)
0.24	0.1	2.1464337	2.1444919	1.2042086	1.2041063	0.8869204	0.8756386
0.60	0.5	2.1031498	2.1030566	0.8724348	0.8724346	0.7408182	0.7401741
0.78	1.0	2.0854058	2.0853878	0.7061432	0.7061432	0.6770568	0.6769244
2.62	2.0	2.0472306	2.0472306	0.5515447	0.5515447	0.2698200	0.2698200

$$u(y) = \sum_{j=0}^{\infty} u_j, \quad \theta(y) = \sum_{j=0}^{\infty} \theta_j, \quad \phi(y) = \sum_{j=0}^{\infty} \phi_j \tag{22}$$

and the nonlinear terms are decomposed as

$$u_y^2 = \sum_{j=0}^{\infty} H_j, \quad (U-u)^2 = \sum_{j=0}^{\infty} G_j \tag{23}$$

where H_j and G_j are Adomian polynomials given by

$$H_j = \frac{1}{j!}\frac{d^j}{dh^j}\left[\left(\sum_{i=0}^{\infty} u_{yi}h^i\right)^2\right]_{h=0}, \quad G_j = \frac{1}{j!}\frac{d^j}{dh^j}\left[\left(U - \sum_{i=0}^{\infty} u_i h^i\right)^2\right]_{h=0} \tag{24}$$

We can thus identify

$$u_0 = a_1 y, \quad \theta_0 = a_2 - y, \quad \phi_0 = 1 + a_3 y \tag{25}$$

$$u_{j+1} = -L_y^{-1}(u_{yj}) - G_r L_y^{-1}(\theta_j) - G_m L_y^{-1}(\phi_j) - M L_y^{-1}(U - u_j) - \frac{1}{K} L_y^{-1}(U - u_j) \quad \text{for } j \geq 1 \tag{26}$$

$$\theta_{j+1} = \alpha L_y^{-1}(\theta_j) - P L_y^{-1}(\theta_{yj}) - P\,\mathrm{Ec}\, L_y^{-1}(H_j) - PM\,\mathrm{Ec}\, L_y^{-1}(G_j) \quad \text{for } j \geq 1 \tag{27}$$

$$\phi_{j+1} = -\mathrm{Sc}\, L_y^{-1}(\phi_{yj}) \quad \text{for } j \geq 1 \tag{28}$$

The MAPLE program was used to obtain a series solution up to $O(y^{20})$. For portability the Appendix gives only a sample of these terms up to $O(y^7)$. Let

$$W_L = \sum_{j=0}^{L} u_j, \quad A_L = \sum_{j=0}^{L} \theta_j, \quad \Phi_L = \sum_{j=0}^{L} \phi_j \tag{29}$$

represent the decomposition series partial sum obtained then

$$u(y) = \lim_{L\to\infty}(W_l), \quad \theta(y) = \lim_{L\to\infty}(A_l), \quad \phi(y) = \lim_{L\to\infty}(\Phi_l) \tag{30}$$

In general, the Adomian method yields rapidly convergent series solutions by using a few terms in the partial sum. However, in this particular problem the convergence of the series partial sum in Eq. (29) is enhanced using the Padé approximation technique. Furthermore, the undetermined values of $a_1 = u_y(0)$, $a_2 = \theta(0)$, and $a_3 = \phi_y(0)$ are calculated from the boundary condition at infinity in Eq. (11). The difficulty at infinity is overcome by employing the diagonal Padé approximants for W_L, A_L, and Φ_L. For instance, the series for the partial sums are transformed into diagonal Padé approximants as follows:

$$W_{L[n/n]}(y) = \frac{\sum_{i=0}^{n} b_i y^i}{\sum_{i=0}^{n} c_i y^i}, \quad A_{L[n/n]}(y) = \frac{\sum_{i=0}^{n} e_i y^i}{\sum_{i=0}^{n} d_i y^i},$$

$$\Phi_{L[n/n]}(y) = \frac{\sum_{i=0}^{n} r_i y^i}{\sum_{i=0}^{n} g_i y^i} \tag{31}$$

where $2(n+1)$ is the order of the series required for each approximant. In the MAPLE environment, the simultaneous evaluation of

$$\lim_{y\to\infty} W_{L[n/n]}(y) = U, \quad \lim_{y\to\infty} A_{L[n/n]}(y) = 0, \quad \lim_{y\to\infty} \Phi_{L[n/n]}(y) = 0 \tag{32}$$

for $n = 2, 3, 4, \ldots$ in Eq. (31) gives the numerical results for a_1, a_2, and a_3.

4 Numerical Results and Discussion

The governing equations (Eqs. (7)–(9)) subject to the boundary conditions (Eqs. (10) and (11)) were solved using the Adomian–Padé method, as described in Sec. 3. Solutions were obtained for

Table 2 Computations showing values of $u'(0)$ and $\theta(0)$ for Ec>0, $P = 0.71$, Sc=0.6, and $U = 1$

Ec	M	α	K	G_r	G_m	$-u'(0)$	$\theta(0)$
0.1	0.1	0.1	1.00	0.1	0.1	−1.828112255	1.2851345343
0.5	0.1	0.1	1.00	0.1	0.1	−1.854917600	1.6176927790
1.0	0.1	0.1	1.00	0.1	0.1	−1.889693729	2.0537260278
0.1	1.0	0.1	1.00	0.1	0.1	−2.135278993	1.3147140938
0.1	4.0	0.1	1.00	0.1	0.1	−2.886664516	1.3844156024
0.1	8.0	0.1	1.00	0.1	0.1	−3.616840018	1.4501453546
0.1	0.1	1.0	1.00	0.1	0.1	−1.777649653	0.7453369138
0.1	0.1	5.0	1.00	0.1	0.1	−1.753582381	0.3979437293
0.1	0.1	0.1	0.10	0.1	0.1	−3.786178510	1.3664985959
0.1	0.1	0.1	0.01	0.1	0.1	−10.54346651	1.6535961917
0.1	0.1	0.1	1.00	1.0	0.1	−2.660307295	1.3477368961
0.1	0.1	0.1	1.00	1.3	0.1	−2.965344337	1.3768728070
0.1	0.1	0.1	1.00	0.1	5.0	−5.756357713	1.8460335968
0.1	0.1	0.1	1.00	0.1	7.0	−7.374628261	2.2527584478

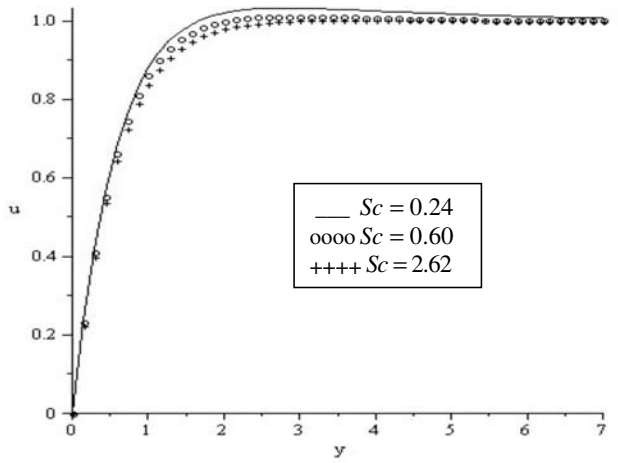

Fig. 1 Variation of the dimensionless velocity profiles along the plate with increasing Schmidt numbers when $G_r = G_m = 1$, $\alpha = \mathrm{Ec} = K = M = 1$, and $P = 0.71$

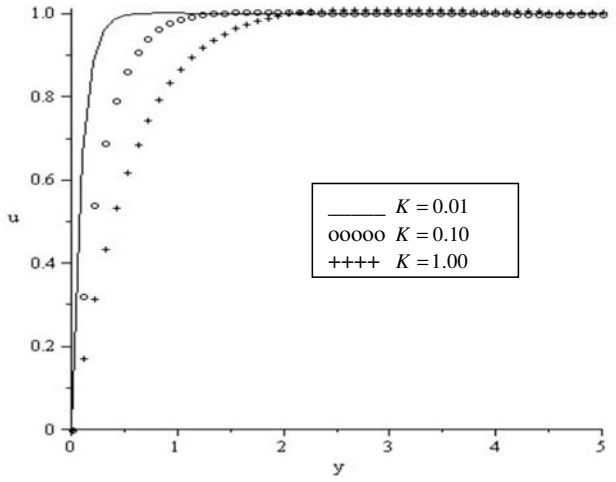

Fig. 3 The effect of surface porosity on the velocity profiles when $G_r = G_m = 0.1$, $\alpha = 1$, $\mathrm{Ec} = M = 1$, $P = 0.71$, and $\mathrm{Sc} = 0.60$

various values of the parameters embedded in the problem, as shown in Tables 1 and 2 and Figs. 1–11. Throughout this study the value of the Prandtl number was taken to be $P = 0.71$, which corresponds to air and the values of Sc were chosen in such a way that they represent diffusing chemical species of most common interest in air such as H_2, H_2O, NH_3, and propyl benzene whose Schmidt numbers are Sc = 0.24, 0.6, 0.78, and 2.62, respectively.

For Ec = 0, both the exact and the numerical results in Table 1 agree very well and serve as a benchmark in evaluating the accuracy of the Adomian–Padé approximation scheme. The results in Table 1 correspond to heat absorption ($\alpha > 0$) within the boundary layer. A similar trend is observed in the case of heat generation, $\alpha < 0$.

Other physical quantities of interest in this problem, namely, the skin friction, τ_w, and the local mass transfer rate at the surface characterized by the Sherwood number Sh, are easily computed. The local convective heat transfer rate at the surface (characterized by the Nusselt number, Nu) is constant. The dimensionless skin friction and Sherwood numbers are given by

$$\tau_w = -\left(\frac{\partial u}{\partial y}\right)_{y=0}, \quad \mathrm{Sh} = -\frac{1}{\mathrm{Sc}}\left(\frac{\partial \phi}{\partial y}\right)_{y=0} = -1 \tag{33}$$

Equation (33) shows that the local mass transfer rate at the surface remains constant at all times. The results in Table 2 reveal that the

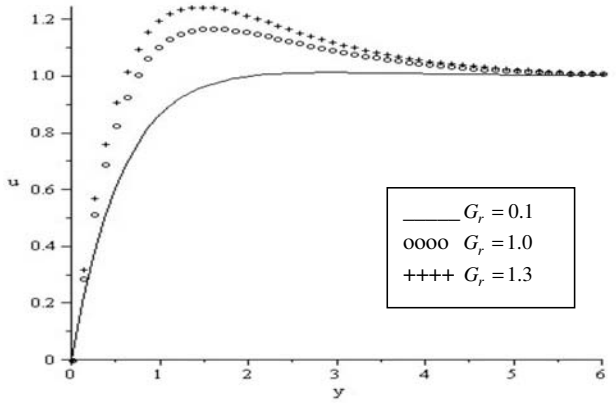

Fig. 4 Variation of the velocity profiles for increasing Grashof numbers when $G_m = 0.1$, $\alpha = 1$, $\mathrm{Ec} = K = M = 1$, $P = 0.71$, and $\mathrm{Sc} = 0.60$

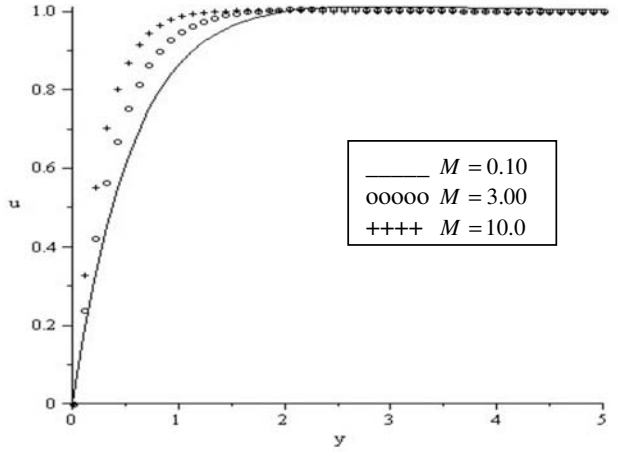

Fig. 2 Variation of the dimensionless velocity profiles with increasing magnetic field strength when $G_r = G_m = 0.1$, $\alpha = \mathrm{Ec} = K = 1$, $P = 0.71$, and $\mathrm{Sc} = 0.60$

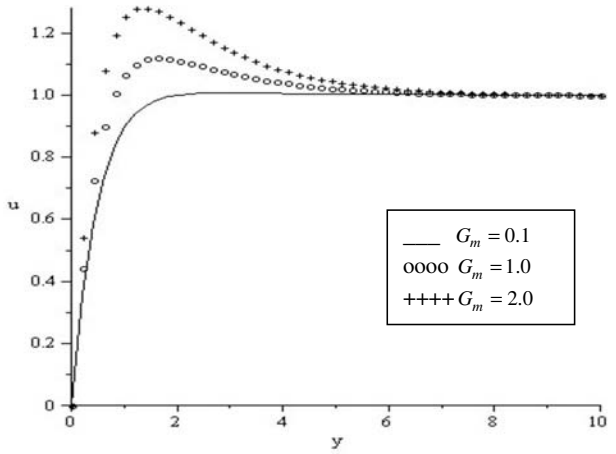

Fig. 5 Variation of velocity profiles with mass transfer Grashof numbers when $G_r = 0.1$, $\alpha = \mathrm{Ec} = K = M = 1$, $P = 0.71$, and $\mathrm{Sc} = 0.60$

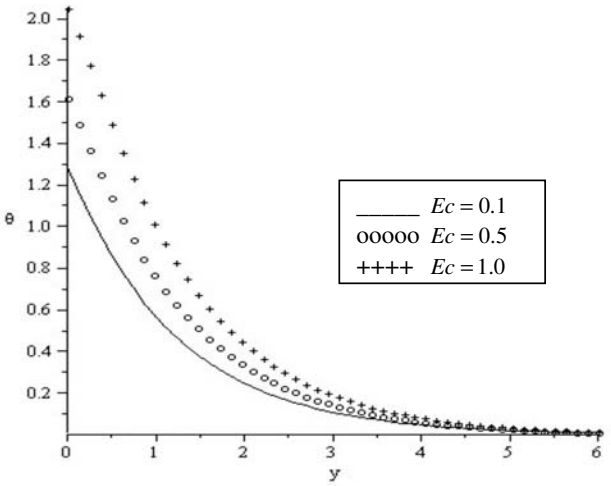

Fig. 6 Variation of boundary-layer temperature profiles with increasing Eckert numbers when $G_r = G_m = 1$, $\alpha = K = M = 1$, $P = 0.71$, and Sc = 0.60

skin friction decreases monotonically with increasing Eckert number Ec, Hartmann number M, and Grashof numbers G_r and G_m. In the linear case, Ec=0, and moderate values of the freestream velocity, Ahmed et al. [4] found that the skin friction increased with increases in M, whereas for nonzero values of Ec the skin friction decreased with increases in the Hartmann number. Similarly the skin friction increases with increases in the Schmidt number Sc, the porosity K, and the heat absorption term α.

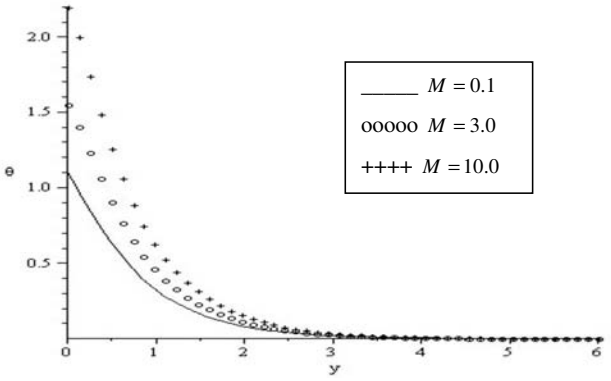

Fig. 7 Variation of temperature profiles with increasing magnetic field strength when $G_r = G_m = 1$, $\alpha = K = \mathrm{Ec} = 1$, $P = 0.71$, and Sc = 0.60

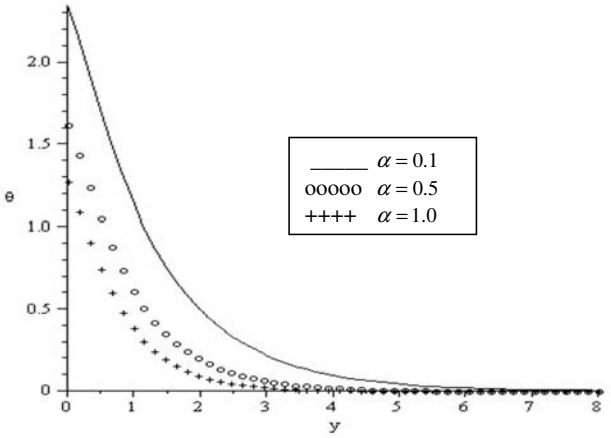

Fig. 8 The variation of the boundary-layer temperature profiles with increasing heat absorption when $G_r = G_m = 0.1$, $M = K = Ec = 1$, $P = 0.71$, and Sc = 0.60

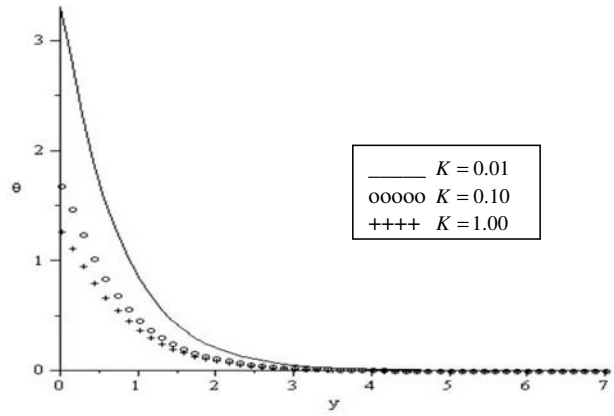

Fig. 9 The variation of the temperature profiles with increasing porosity when $G_r = G_m = 0.1$, $\alpha = \mathrm{Ec} = M = 1$, $P = 0.71$, and Sc = 0.60

A parametric study was carried out, and the results are shown in Figs. 1–11. Figures 1–5 show the variation of the boundary-layer fluid velocity profiles for different parameter values. Generally, the fluid velocity increases across the boundary layer, reaching its peak value, and then asymptotically approaches the freestream velocity value at a distance far from the plate.

Figure 1 shows the variation of the fluid velocity with Schmidt numbers when other physical parameters are fixed. Increasing Schmidt numbers leads to a reduction in the boundary-layer velocity.

Figure 2 shows the effect of increasing the magnetic field strength on the momentum boundary-layer thickness. It is now a well established fact that the magnetic field presents a damping effect on the velocity field by creating a drag force that opposes the fluid motion, causing the velocity to decrease. However, in this case an increase in the Hartmann number only slightly slows down the motion of the fluid away from the vertical plate surface toward the freestream velocity, while the fluid velocity near the vertical plate surface increases. The interaction of the magnetic field with the constant wall heat flux and freestream velocity may

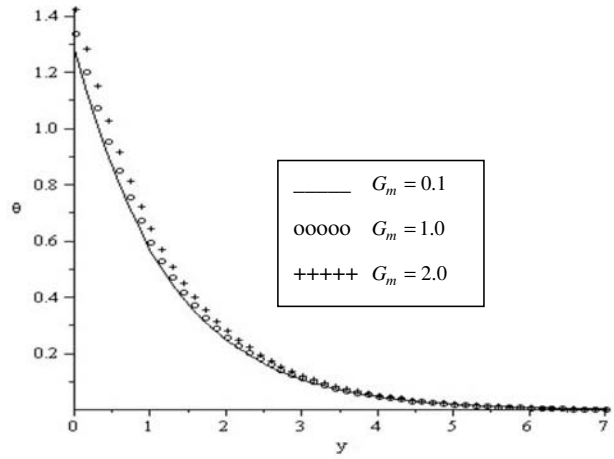

Fig. 10 Variation of the temperature profiles with increasing solutal Grashof numbers when $G_r = 0.1$, $M = \alpha = \mathrm{Ec} = K = 1$, $P = 0.71$, and Sc = 0.60

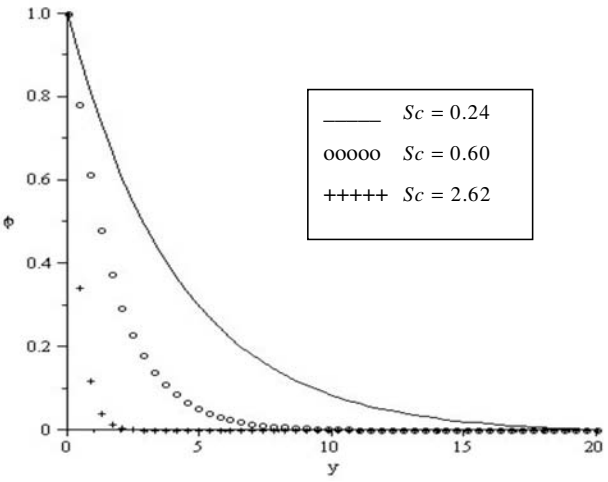

Fig. 11 Variation of species concentration profiles with increasing Schmidt numbers when $G_r = G_m = 0.1$, $M = \alpha = \mathrm{Ec} = K = 1$, and $P = 0.71$

account for this effect. As can be more clearly seen in Fig. 7, the extra resistive force causes the temperature to rise and the fluid to warm up. These results found using the Adomian–Padé approach are consistent with the earlier findings of studies that employed traditional numerical approaches, for example, Abo-Eldahad and El Aziz [15] on Joule heating effects on MHD free convection flows.

Figure 3 shows the effect of increasing surface porosity on the velocity. In practice porosity can be increased in one of two ways, either by increasing the pore area or by increasing the pore density, that is, the number of pores per mm^2 of surface. Numerical simulation shows that in the immediate vicinity of the vertical plate, the momentum boundary layer increases with increasing porosity. These results show that for low porosity when inertial effects are very significant, the momentum boundary layer decreases, agreeing with Vafai and Kim [16]. For the temperature profiles (Fig. 9), the fluid temperature reduces with increasing porosity as more heat is conducted away from the surface by the faster moving fluid. The study by Aduda and Rawlings [17] has, however, shown that the change in the velocity with increasing porosity is sensitive to endogenous factors such as the pore shape, size, and content. These factors have not been considered in this study.

Figures 4 and 5 show the variation of the boundary-layer velocity with the Grashof numbers G_r for heat transfer and G_m for mass transfer, respectively.

In both cases increasing the Grashof number causes an upward acceleration of the fluid in the vicinity of the vertical wall caused by increasing buoyancy. Further downstream the fluid motion decelerates to the freestream velocity for all Grashof numbers.

Increasing solute Grashof numbers causes an upward acceleration of the fluid motion near the wall.

The temperature profiles are depicted in Figs. 6–10 for different values of the important flow parameters. The fluid temperature attains its maximum value at the plate surface and then decreases gradually to the freestream zero value far away from the plate. Furthermore, it is observed that the fluid temperature increases with increasing values of Ec, M, and G_m and decreases with increasing values of K and α.

Figure 6 shows the variation of the temperature profiles with the Eckert number. The Eckert number characterizes dissipation, and, in general, at high Eckert numbers frictional and compression heating dominate the boundary-layer fluid temperature. However, in practice the effects of work done due to friction are dominant when the freestream velocity is comparable to the speed of sound. For $O(1)$ Eckert numbers and freestream velocity values in this study, the fluid temperature is seen to increase with increasing Eckert numbers.

Figure 7 shows the warming effect of the magnetic field. The viscous stresses caused by the decelerating motion of the fluid cause the heat to build up and the fluid temperature near the wall to increase.

The results depicted in Fig. 8 correspond to heat absorption within the boundary layer. In this case we have assumed that $T_w > T_\infty$ so that $\alpha > 0$ represents a heat sink. The effect of a heat sink is to reduce boundary-layer temperature profiles.

Figure 10 shows that larger Grashof numbers result in increased boundary-layer temperature profiles.

The fluid concentration profiles generally reveal an exponential decrease away from the plate surface, and Fig. 11 shows a significant thinning of the concentration profile with increasing Schmidt numbers. High Schmidt numbers are generally associated with, and have important implications for, turbulent mixing processes. The decrease in the concentration profiles with increasing Schmidt numbers is not unexpected since, for example, in the case of very large Schmidt numbers such as those appropriate for carbon dioxide in seawater ($\mathrm{Sc} \approx 700$), the concentration boundary-layer thickness is known to become very thin, resulting in steeper concentration gradients and greater diffusion and mixing with the surrounding fluid. However, Schmidt numbers used here are those that generally represent the diffusion of chemical species of interest in air. These results are in agreement with the earlier results by, for example, Anjali-Devi and Kandasamy [18], which indicate that the surface mass flux increases with increasing Schmidt numbers.

5 Conclusion

In this study we have employed the Adomian–Padé method to compute nonperturbative solutions for mixed-convective boundary-layer flow past a vertical porous plate embedded in a saturated porous medium with constant heat flux and mass transfer in the presence of a magnetic field. We have considered the effects of flow parameters such as the Eckert numbers, the Hartmann numbers, the porosity, and the Schmidt numbers on the flow characteristics and the dependence of fluid velocity, temperature, and concentration gradients on these physical parameters. We have extended the scope and applicability of the earlier small Eckert number studies by Raptis and Kafousias [5] and Ahmed et al. [4] to all Eckert numbers in an unbounded domain.

The results confirm earlier findings by, among others, Abel et al. [19] that, inter alia, increasing the Grashof number increases the fluid velocity and that the presence of heat absorption effects causes reductions in the fluid temperature and hence in the fluid velocity. The results demonstrate the reliability and the efficiency of the Adomian–Padé method in an unbounded domain as a viable alternative to the usual numerical schemes such as the boundary and finite element methods.

Acknowledgment

The authors thank the National Research Foundation and the NRF Thuthuka program for financial support. The input of the anonymous referees is also gratefully acknowledged.

Nomenclature

B_0 = magnetic field induction
C_p = specific heat at constant pressure
$\bar{C}$ = species concentration
D = molecular diffusivity
Ec = Eckert number $(\lambda \upsilon_0^3 / \bar{q} \upsilon C_p)$
G_m = Grashof number for mass transfer $(\upsilon g \bar{\beta}(\bar{c}_w - \bar{c}_\infty)/\upsilon_0^3)$
G_r = Grashof number for heat transfer $(g\beta\bar{q}\upsilon^2/\lambda\upsilon_0^4)$

g = acceleration due to gravity
K = porosity parameter ($v_0^2\bar{K}/\upsilon$)
M = Hartmann number ($\sigma B_0^2\upsilon/\rho v_0^2$)
Nu = Nusselt number ($-\theta'$)
P = Prandtl number ($\mu C_p/\lambda$)
Q = heat source/sink term
$\bar{q}$ = convective heat transfer rate
Sc = Schmidt number (υ/D)
Sh = Sherwood number
$\bar{T}$ = fluid temperature
$\bar{U}$ = dimensional freestream velocity
U = scaled freestream velocity ($\bar{U}/v_0$)
u = scaled streamwise velocity ($\bar{u}/v_0$)
v_0 = suction velocity
$\bar{x}$ = distance parallel to the plate surface
$\bar{y}$ = direction perpendicular to the plate surface
y = normalized distance in the $\bar{y}$ direction ($v_0\bar{y}/\upsilon$)

Greek Symbols

α = scaled heat source or sink term ($Q\upsilon^2/\lambda v_0^2$)
β = coefficient of volume expansion for heat transfer
$\bar{\beta}$ = coefficient of volume expansion for species concentration
θ = nondimensional temperature term $\lambda v_0(\bar{T}-\bar{T}_\infty)/\bar{q}\upsilon$
ϕ = nondimensional concentration term $(\bar{c}-\bar{c}_\infty)/(\bar{c}_w-\bar{c}_\infty)$
σ = electrical conductivity
ρ = fluid density
μ = coefficient of dynamic viscosity
υ = coefficient of kinematic viscosity (μ/ρ)
λ = thermal conductivity
τ_w = skin friction ($-u'(0)$)

Subscripts

∞ = freestream values
w = wall surface

Appendix

This appendix gives the truncated series solutions to Eqs. (7)–(9) obtained using the Adomian–Padé approximation method. Here we give solutions only up to $O(y^7)$,

$$\gamma = M + \frac{1}{K}$$

$$\delta_1 = PM\,\mathrm{Ec}$$

$$\delta_2 = G_r PM\,\mathrm{Ec} = \delta_1 G_r$$

$$\lambda_1 = \left(\alpha U^2 + 20a_1^2 + 5a_1 P - \frac{60a_1^3}{U^3}\right)$$

$$\lambda_2 = a_1 + a_2 G_r + G_m + \gamma U$$

$$\lambda_3 = 2a_1\lambda_2 P\,\mathrm{Ec}$$

$$\lambda_4 = \alpha a_2 + P(1 - \mathrm{Ec}\,a_1^2) - \delta_2 U^2$$

$$\lambda_5 = \lambda_4 - 2a_1^2\delta_2$$

$$u(y) = \frac{1}{360a_1^4}\delta_2 U^6 + \left(a_1 - \frac{1}{60a_1^2}\delta_1 U^5\right)y - \frac{1}{2}\left(a_1 + G_m - \frac{1}{12a_1^2}\delta_1 U^4 + 2\gamma U + G_r a_2\right)y^2 + \frac{1}{6}\left(a_1 - G_m a_3 + \gamma(a_1 + U) + G_r(1 + a_2) - \frac{1}{3a_1}\delta_1 U^3 + G_m\right)y^3 + \frac{1}{24}(G_m a_3 - \gamma a_1 - G_r\lambda_4 - \lambda_2\gamma + G_m\,\mathrm{Sc}\,a_3 - G_r)y^4 + \frac{1}{120}(-\gamma(-G_r + G_m a_3 - \gamma a_1) + \alpha G_r - 2a_1\delta_1 U)y^5 + \frac{1}{360}\delta_1 a_1^2 y^6 + O(y^7)$$

$$\theta(y) = a_2 - \frac{1}{360a_1^4}(\alpha U^2 + 6a_1 PU + 30a_1^2)\delta_2 U^4 + \frac{1}{60a_1^3}\lambda_1 y + \frac{1}{24}\left(12\alpha a_2 + 12P - \frac{\delta_2}{a_1^2}(\alpha U^4 + 12a_1^2 U^2 - 4PU^3 a_1) - 12P\,\mathrm{Ec}\,a_1^2\right)y^2 + \frac{1}{6}\left(\frac{1}{a_1}\left(2Ua_1^2 + \frac{1}{3}\alpha U^3\right)\delta_2 - \alpha(1 + a_2 P) - P(-a_1^2 P\,\mathrm{Ec} + 1 - \delta G_r^{-1}U^2) + \lambda_3\right)y^3 + \frac{1}{24}(\lambda_5 - 2a_1 P\,\mathrm{Ec}(G_r - a_3 G_m + a_1\gamma) + P(\alpha - a_1\delta_2) - 2\delta_2 U\lambda_2)y^4 + \frac{1}{120}(2a_1^2 P\delta_2 - \alpha(\alpha - 2a_1\delta_2) - 2\delta_2(G_r - G_m + a_1\gamma)U - 6a_1\lambda_2)y^5 - \frac{1}{360}(\alpha a_1^2\delta_2 + 4a_1\delta_2(G_r - a_3 G_m + a_1\gamma))y^6 + O(y^7)$$

$$\phi(y) = 1 + (y - \tfrac{1}{2}\mathrm{Sc}\,y^2 + \tfrac{1}{3!}\mathrm{Sc}^2 y^3 - \tfrac{1}{4!}\mathrm{Sc}^3 y^4 + \tfrac{1}{5!}\mathrm{Sc}^4 y^5 - \tfrac{1}{6!}\mathrm{Sc}^5 y^6)a_3 + O(y^7)$$

References

[1] Sparrow, E. M., and Cess, R. D., 1961, "Free Convection With Blowing or Suction," Int. J. Heat Mass Transfer, **83**, pp. 243–248.
[2] Bejan, A., and Khair, K. R., 1985, "Heat and Mass Transfer by Natural Convection in a Porous Medium," Int. J. Heat Mass Transfer, **28**, pp. 909–918.
[3] Magyari, E., and Keller, B., 2000, "Exact Solutions for Self-Similar Boundary-Layer Flows Induced by Permeable Stretching Walls," Eur. J. Mech. B/Fluids, **19**, pp. 109–122.
[4] Ahmed, N., Sarma, K., and Ahmed, S., 2007, "Free and Forced Convective MHD Flow and Mass Transfer Through a Porous Medium Bounded by an Infinite Vertical Porous Plate in the Presence of a Constant Heat Flux and Heat Source," *Proceedings of the 52nd Congress of ISTAM*, BNMIT, Bangalore, Dec. 14–17, pp. 152–160.
[5] Raptis, A., and Kafousias, N., 1982, "Magnetohydrodynamic Free Convective Flow and Mass Transfer Through a Porous Medium Bounded by an Infinite Vertical Porous Plate With Constant Heat Flux," Can. J. Phys., **60**, pp. 1725–1729.
[6] Acharya, M., Dash, G. C., and Singh, L. P., 2000, "Magnetic Field Effects on the Free Convection and Mass Transfer Flow Through Porous Medium With Constant Suction and Constant Heat Flux," Indian J. Pure Appl. Math., **31**(1), pp. 1–18.
[7] Ahmed, S., and Ahmed, N., 2004, "Two-Dimensional MHD Oscillatory Flow Along a Uniformly Moving Infinite Vertical Porous Plate Bounded by Porous Medium," Indian J. Pure Appl. Math., **35**(12), pp. 1309–1319.

[8] Ahmed, N., Sarma, D., and Sarma, K., 2006, "Free Convective MHD Flow Through a Porous Medium in the Presence of a Heat Source With Constant Heat Flux," *Proceedings of the 51st Congress of ISTAM*, Andhra University, Visakhapatnam, Dec. 18–21, pp. 73–81.
[9] Adomian, G., 1994, *Solving Frontier Problems of Physics: The Decomposition Method*, Kluwer, Boston, MA.
[10] Makinde, O. D., 2005, "Free-Convection Flow With Thermal Radiation and Mass Transfer Past a Moving Vertical Porous Plate," Int. Commun. Heat Mass Transfer, **32**, pp. 1411–1419.
[11] Wazwaz, A. M., 2006, "The Modified Decomposition Method and Padé Approximants for a Boundary-Layer Equation in Unbounded Domain," Appl. Math. Comput., **177**, pp. 737–744.
[12] Kechil, S. A., and Hashim, I., 2007, "Non-Perturbative Solution of Free-Convective Boundary-Layer Equation by Adomian Decomposition Method," Phys. Lett. A, **363**, pp. 110–114.
[13] Brinkman, H. C., 1947, "A Calculation of the Viscous Force Exerted by a Flowing Fluid on a Dense Swarm of Particles," Appl. Sci. Res., Sect. A, **A1**, pp. 27–34.
[14] Heck, A., 2003, *Introduction to Maple*, 3rd ed., Springer-Verlag, New York.
[15] Abo-Eldahad, E. M., and El Aziz, M. A., 2005, "Viscous Dissipation and Joule Heating Effects on MHD-Free Convection From a Vertical Plate With Power-Law Variation in Surface Temperature in the Presence of Hall and Ion-Slip Currents," Appl. Math. Model., **29**, pp. 579–595.
[16] Vafai, K., and Kim, S. J., 1989, "Forced Convection in a Channel Filled With a Porous Medium: An Exact Solution," ASME J. Heat Transfer, **111**, pp. 1103–1106.
[17] Aduda, B. O., and Rawlings, R. D., 1994, "An Acoustic-Ultrasonic Study of the Effect of Porosity on a Sintered Glass System," J. Mater. Sci., **29**(9), pp. 2297–2303.
[18] Anjali-Devi, S. P., and Kandasamy, R., 2002, "Analysis of Nonlinear Two Dimensional Laminar Natural Flow and Mixed Convection Over Variable Surface With Free Stream Conditions," J. Comput. Appl. Math., **3**(2), pp. 107–116.
[19] Abel, S., Prasad, K. V., and Mahaboob, A., 2005, "Buoyancy Force and Thermal Radiation Effects in MHD Boundary Layer Visco-Elastic Fluid Flow Over Continuously Moving Stretching Surface," Int. J. Therm. Sci., **44**, pp. 465–476.

Simulation of Laser-Induced Incandescence Measurements in an Anisotropically Scattering Aerosol Through Backward Monte Carlo

K. J. Daun[1]
e-mail: kjdaun@mme.uwaterloo.ca

K. A. Thomson

F. Liu

Institute for Chemical Process and Environmental Technology,
National Research Council of Canada,
1200 Montreal Road,
Ottawa, ON, K1A 0R6, Canada

Laser-induced incandescence (LII) measurements carried out in aerosols having a large particle volume fraction must be corrected to account for extinction between the energized aerosol particles and the detector, called signal trapping. While standard correction techniques have been developed for signal trapping by absorption, the effect of scattering on LII measurements requires further investigation, particularly the case of highly anisotropic scattering and along a path of relatively large optical thickness. This paper examines this phenomenon in an aerosol containing highly aggregated soot particles by simulating LII signals using a backward Monte Carlo analysis; these signals are then used to recover the soot particle temperature and soot volume fraction. The results show that inscattered radiation is a substantial component of the LII signal under high soot loading conditions, which can strongly influence properties derived from these measurements. Correction techniques based on Bouguer's law are shown to be effective in mitigating the effect of scatter on the LII signals. [DOI: 10.1115/1.2955468]

Introduction

Laser-induced incandescence (LII) is an established technique for measuring the properties of aerosols and is particularly well suited for characterizing soot within flames. In this procedure a nanosecond laser pulse energizes the particles contained within a small measurement volume to incandescent temperatures and the resulting radiance from these particles is measured using photodetectors, usually at several wavelengths in the near-infrared spectrum. The particle volume fraction within the measurement volume can then be inferred from the LII signal by comparing it to the signal obtained from an aerosol in which the particle volume fraction is known through an independent means, such as line-of-sight attenuation (LOSA) [1] or gravimetric sampling [2]. An alternative approach [3,4] is to first determine the particle temperature from the LII signals using multiwavelength pyrometry and then calculate the particle volume fraction by comparing the expected emission at that temperature to the observed incandescence signal. Because the particle cooling rate is inversely proportional to the specific surface area, the aerosol particle size distribution can also be found by deconvolving the time-resolved spectral incandescence intensity [5] or the pyrometrically defined temperature [6].

When the particle volume fraction is large, it is necessary to account for attenuation of the spectral incandescence due to extinction between the laser-energized aerosol particles and the detector; this effect is called *signal trapping* [7]. In combustion applications signal trapping is important in cases of high soot loading, such as flames in high ambient pressures [1] and buoyancy-driven turbulent flames [8], resulting in erroneous soot volume fraction measurements if the assumption of an optically thin medium does not hold [7]. Furthermore, since the extinction coefficients of soot-laden aerosols decrease with increasing wavelength, signal trapping causes pyrometrically defined temperatures to be underestimated [9,10], leading to errors in temperature, soot volume fraction, and temperature-based time-resolved LII particle sizing.

While it is becoming increasingly commonplace to correct the LII signal for trapping (e.g., Refs. [1,2,11–13]) most studies tacitly assume that the absorption coefficient is equal to the extinction coefficient, which in experiments involving soot-laden aerosols is usually justified by arguing that the primary particles act as independent Rayleigh scatters since their diameters almost always satisfy the required size parameter criterion [14]. While this treatment may be reasonable when the soot aggregates are very small, it is inappropriate for aerosols containing aggregates composed of large numbers of primary particles [15,16] typical in buoyant turbulent diffusion flames or carbon black reactors, for example. In these situations dependent scattering between primary particles is greatly enhanced and makes the scattering cross section of highly aggregated soot particles comparable in magnitude to the absorption cross section.

Accounting for signal trapping due to scattering is less straightforward than absorption alone, since the signal is simultaneously attenuated by outscattering and augmented by inscattered radiation along the path between the measurement volume and the detector; Murphy and Shaddix [17] and Liu et al. [9] show that, because of the highly forward scattering of soot aggregates, signal losses caused by outscatter are mitigated by inscatter. Due to the strong scattering of soot aggregates, Thomson et al. [18] raised the concern that in LII experiments in which a laser sheet is used instead of a beam inscattering of photons emitted from energized aerosol particles outside the detection volume could inflate the measured LII signal beyond the value one would expect without any scattering whatsoever. Nevertheless, to the best of the authors' knowledge no experimental LII study has yet to explicitly correct for the effect of in- and outscatter between the measurement volume and the detector.

[1]Corresponding author. Presently at Department of Mechanical and Mechatronics Engineering, University of Waterloo, 200 University Ave. W., Waterloo, ON, N2L 3G1, Canada.

Contributed by the Heat Transfer Division of ASME for publication in the JOURNAL OF HEAT TRANSFER. Manuscript received August 28, 2007; final manuscript received November 27, 2007; published online August 29, 2008. Review conducted by Walter W. Yuen. Paper presented at the 2007 ASME International Mechanical Engineering Congress (IMECE2007), Seattle, WA, November 10–16, 2007.

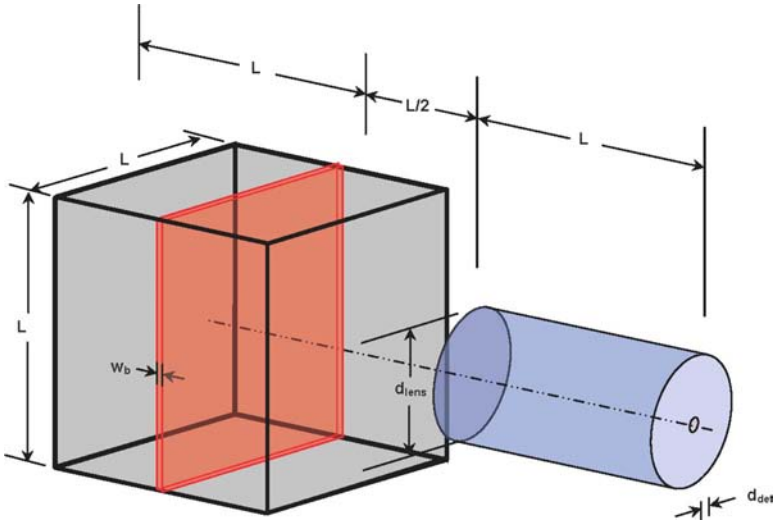

Fig. 1 Problem geometry for the sheet excitation case

This paper endeavors to elucidate the effect of in- and outscattering on LII measurement within aerosols containing highly aggregated soot particles, with a focus on the role inscattering plays when the aerosol particles are energized by a laser sheet instead of a beam. The analysis is done on a homogeneous aerosol containing soot aggregates typical of turbulent diffusion flames [8]. A backward Monte Carlo (BMC) analysis [19] is used to calculate the spectral incandescence measured by the simulated detector; this approach is well suited to this problem as it retains the accurate physics modeling associated with the standard Monte Carlo analysis but is far more efficient since only the photon bundles incident on the collection optics are traced to their emission locations. Although it has been used to simulate other types of optical measurement, to the authors' knowledge this is the first application of BMC to model LII.

The simulations show that outscattering is a major contributor to signal trapping, causing the pyrometric temperatures derived from LII signals to be underestimated, which in turn causes the soot volume fractions to be overestimated. This effect is less pronounced in the sheet excitation case since inscatter from aerosol particles within the sheet but outside the measurement volume offset signal losses due to trapping. We also evaluate several methods based on Bouguer's law [20], which are shown to be largely effective ways to account for signal trapping.

Problem Description

The analysis is carried out on a soot-laden aerosol at $T_g = 300$ K contained within a cubical enclosure having sides of length $L = 0.1$ m. The surroundings are also taken to be at 300 K. A spectral radiometer is located outside the enclosure and centered on the z-axis as shown in Fig. 1. Two excitation cases are considered: In the first case the aerosol particles are heated using a laser beam having a 2.5×2.5 mm^2 square profile, while in the second case a semi-infinite sheet having a 2.5 mm thickness is used to energize the particles. In both cases the particles within the beam reach a temperature, T_{beam}, of 3600 K. Figure 2 shows the details of the collection optics, consisting of a blackbody detector surface and a perfect lens. The detector surface has a diameter of 2.5 mm, while the lens has a diameter of 5 cm and a focal length of $L/2 = 5$ cm, which images the detector surface into the middle of the measurement volume. The intersection of the collection optics view angle and the laser beam or sheet carves out a roughly cylindrical measurement volume. The detection wavelengths are 400 nm and 780 nm, which are often used in real LII experiments.

The aerosol contains soot aggregates composed of various numbers of 30 nm diameter primary particles. The number of primary particles per aggregate obeys a log-normal distribution,

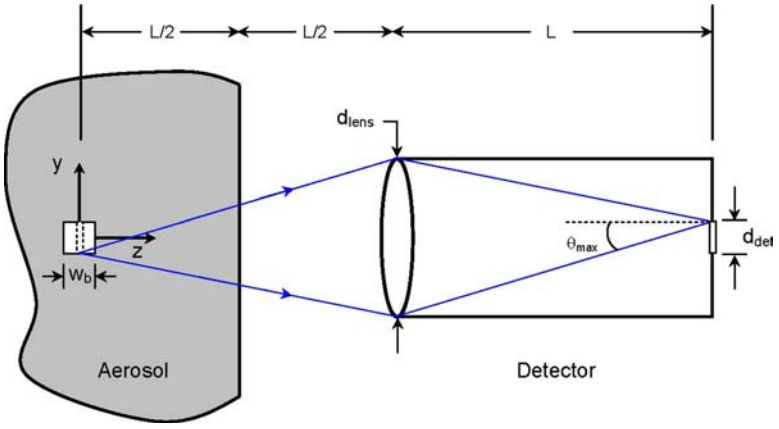

Fig. 2 Optics schematic shown for beam excitation case (not to scale)

$$P(N_p) = \frac{1}{N_p\sqrt{2\pi}\ln\sigma_g}\exp\left\{-\left[\frac{\ln(N_p/N_{p,g})}{\sqrt{2}\ln\sigma_g}\right]^2\right\} \quad (1)$$

where $N_{p,g}=200$ primary particles per aggregate and $\sigma_g=3$, parameters that are typical of soot in buoyant turbulent diffusion flames [8]. The aggregate structure is assumed to be mass fractal in nature, and the number of primary particles per aggregate is related to the radius of gyration, R_g, by [15,16]

$$N_p = k_g(2R_g/d_p)^{D_f} \quad (2)$$

where the fractal dimension and prefactor are set equal to $D_f=1.78$ and $k_g=2.3$, characteristic values for soot in flames [8]. The radius of gyration plays an important role in dependent scattering between the primary particles, which affects the aggregate scattering cross section and phase function as shown later.

The effects of scattering on the measured LII signal are evaluated at different soot loadings specified by the soot volume fraction, f_v, which is related to the aggregate number density, N_{agg}, by

$$N_{\text{agg}} = \frac{f_v}{\frac{\pi d_p^3}{6}\int_0^\infty N_p P(N_p)dN_p} = \frac{f_v}{\frac{\pi d_p^3}{6}\exp\{[N_{p,g}+(\ln\sigma_g)^2]/2\}} \quad (3)$$

Radiative Properties

Bulk radiative properties of the homogeneous medium are derived from the phase function and absorption and scattering cross sections of soot aggregates, which in turn are calculated using Rayleigh–Debye–Gans polyfractal aggregate (RDG-PFA) theory [8,15,16]. For independent primary particles, the absorption and scattering cross sections are obtained from Rayleigh theory [15,16]

$$C_a^p = \frac{4x_p^3 E(\mathbf{m})}{\pi\eta^2}, \quad C_s^p = \frac{8x_p^6 F(\mathbf{m})}{3\pi\eta^2} \quad (4)$$

where $E(\mathbf{m})=\text{Im}[(\mathbf{m}^2-1)/(\mathbf{m}^2+2)]$ is the complex absorption function, $F(\mathbf{m})=|[(\mathbf{m}^2-1)/(\mathbf{m}^2+2)]|$ is the complex scattering function, $\mathbf{m}=n+ik$ is the complex index of refraction of soot, $\eta=2\pi/\lambda$ is the wave number, and $x_p=\pi d_p/\lambda$ is the primary particle size parameter. The vertical and horizontal polarization cross sections of primary particles are given by

$$C_{vv}^p = \frac{x_p^6 F(\mathbf{m})}{\eta^2}, \quad C_{hh}^p = C_{vv}^p\cos^2\theta \quad (5)$$

where θ is the angle formed between the incident and the scattered radiation. (Both C_{hv}^p and C_{vh}^p are zero.)

Since primary particles are assumed to absorb and emit radiation independently, the absorption cross section of a soot aggregate containing N_p primary particles is simply

$$C_a^{\text{agg}} = N_p C_a^p \quad (6)$$

In contrast, since scattering by the primary particles within a soot aggregate is usually highly dependent, the aggregate scattering cross section can be much larger than the sum of primary particle scattering cross sections predicted by Rayleigh theory. The aggregate scattering cross section is given by [8]

$$C_s^{\text{agg}} = N_p^2 C_s^p g(\eta R_g, D_f) \quad (7)$$

where the aggregate total scattering factor, $g(\eta R_g, D_f)$, is equal to

$$g(\eta R_g, D_f) = 1 - 2(\eta R_g)^2/3, \quad (\eta R_g)^2 \le 3D_f/8 \quad (8)$$

in the Guinier regime and

Table 1 Radiative properties of the medium

	$\lambda=400$ nm	$\lambda=780$ nm
$\mathbf{m}$ [22]	$1.5+0.65i$	$1.63+0.49i$
$E(\mathbf{m})$	0.3170	0.2172
$F(\mathbf{m})$	0.4931	0.4546
$\bar{C}_a^{\text{agg}}$ ($\times 10^4$ nm^2)	7.67	4.31
$\bar{C}_s^{\text{agg}}$ ($\times 10^4$ nm^2)	2.70	0.69
$g_{\text{HG},\lambda}$	0.781	0.672

$$g(\eta R_g, D_f) = \frac{\beta}{2}(3-3\beta+2\beta^2) - \frac{(\eta R_g\beta)^2}{3}(3-4\beta+3\beta^2) + (2\eta R_g)^{-D_f}\left[\frac{3}{2-D_f} - \frac{12}{(6-D_f)(4-D_f)} - 3\beta^{1-D_f/2}\left(\frac{1}{2-D_f} - \frac{2\beta}{4-D_f} + \frac{2\beta^2}{6-D_f}\right)\right], \quad (\eta R_g)^2 > 3D_f/8 \quad (9)$$

in the power-law regime. The polarization cross section of the aggregate is

$$C_{vv}^{\text{agg}} = N_p^2 C_{vv}^p f(qR_g) = \frac{C_{hh}^{\text{agg}}}{\cos^2\theta} \quad (10)$$

where $q=2\eta\sin(\theta/2)$ is the modulus of the scattering vector and $f(q,R_g)$ is the form factor given by [21]

$$f(qR_g) = [1+8(qR_g)^2/(3D_f)+(qR_g)^8]^{-Df/8} \quad (11)$$

which applies over both the Guinier and power-law regimes.

Equations (4)–(11) provide the required equations to calculate the absorption, scattering, and polarization cross sections for a soot aggregate. When deriving the bulk radiative properties of the medium, however, it is necessary to account for the polydispersity of different-sized aggregates by calculating averaged cross sections using Eq. (1) [8],

$$\bar{C}_a^{\text{agg}} = \int_0^\infty C_a^{\text{agg}}(N_p)P(N_p)dN_p \quad (12)$$

with similar expressions for $\bar{C}_s^{\text{agg}}$ and $\bar{C}_{vv}^{\text{agg}}$, and again, $\bar{C}_{hh}^{\text{agg}}=\bar{C}_{vv}^{\text{agg}}/\cos^2\theta$. The absorption and scattering coefficients are then $\alpha_\lambda=N_{\text{agg}}\bar{C}_a^{\text{agg}}$ and $\sigma_{s\lambda}=N_{\text{agg}}\bar{C}_s^{\text{agg}}$, respectively, while the scattering phase function is given by

$$\Phi(\theta) = \frac{4\pi}{\bar{C}_s^{\text{agg}}}\frac{(\bar{C}_{vv}^{\text{agg}}+\bar{C}_{hh}^{\text{agg}})}{2} \quad (13)$$

Following the above calculations for soot aggregates at the detection wavelengths of 400 nm and 780 nm and assuming $\mathbf{m}=1.5+0.65i$ at $\lambda=400$ nm and $\mathbf{m}=1.63+0.49i$ at $\lambda=780$ nm [22] results in the average absorption and scattering cross sections in Table 1, and the phase functions shown in Fig. 3 evaluated at 181 angles evenly spaced between $0\le\theta\le\pi$. These values are closely interpolated by Heyney–Greenstein phase functions having the form

$$\Phi(\theta) = \frac{1-g_{\text{HG}\,\lambda}^2}{(1+g_{\text{HG}\,\lambda}^2-2g_{\text{HG},\lambda}\cos\theta)^{3/2}} \quad (14)$$

where the anisotropy factors, $g_{\text{HG},\lambda}$, determined by least-squares fitting are also included in Table 1.

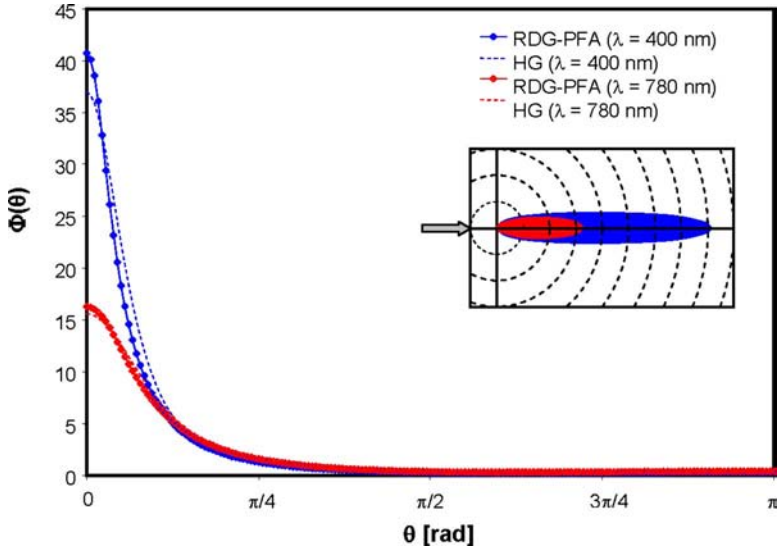

Fig. 3 Scattering phase functions

Radiation Analysis Through Backward Monte Carlo

The objective of this analysis is to evaluate how scattering affects LII measurements and soot volume fractions and pyrometric temperatures derived from these measurements, which requires calculation of the spectral radiant energy incident on the detector surface at the detection wavelengths. The radiation field is governed by the radiative transfer equation (RTE)

$$\mathbf{s}\cdot\nabla I_\lambda(\mathbf{r},\mathbf{s}) = -\kappa_\lambda I_\lambda(\mathbf{r},\mathbf{s}) + \alpha_\lambda I_{b\lambda}(\mathbf{r}) + \frac{\sigma_{s\lambda}}{4\pi}\int_0^{4\pi} I_\lambda(\mathbf{r},\mathbf{s}')\Phi_\lambda(\mathbf{s}',\mathbf{s})d\Omega \tag{15}$$

subject to

$$I_\lambda(\mathbf{r}_w,\mathbf{s}) = I_{\lambda w}(\mathbf{r}_w,\mathbf{s}) \tag{16}$$

where s is a unit vector, $\mathbf{r}$ is the position vector from the origin, $\mathbf{r}_w$ denotes a location on the boundary, $\kappa_\lambda = \alpha_\lambda + \sigma_{s\lambda}$, and $I_{b,\lambda}(\mathbf{r})$ is the blackbody intensity at $\mathbf{r}$ and λ. (Note that the radiative properties are homogeneous over the problem domain and are thus independent of $\mathbf{r}$.) The analysis is considerably simplified by neglecting the contributions of blackbody emission from the surroundings and the medium at 300 K at the detection wavelengths, which are small relative to the spectral blackbody intensity of the energized particles at 3600 K.

Despite this simplification solving the radiative transfer equation over the entire problem domain remains computationally expensive, particularly if the solution is carried out using a standard, or forward, Monte Carlo-type analysis. In its traditional implementation, photon bundles are emitted at various locations throughout the medium and ray traced to their termination. Since a very small fraction of these bundles would terminate on the detector surface, a large number of bundles would need to be emitted and ray traced to achieve an acceptable level of variance in the solution.

A more efficient approach is the BMC method presented by Modest [19] based on the reciprocity relation for the RTE derived by Case [23]. In this implementation, which uses pathlength-based energy partitioning [19,24], a bundle (say, the nth bundle) is ray traced backward from an absorption location on the detector surface given by

$$\mathbf{C}_0^n = r^n\cos\psi^n\hat{\mathbf{i}} + r^n\sin\psi^n\hat{\mathbf{j}} - 2L\hat{\mathbf{k}} \tag{17}$$

and in a direction

$$\mathbf{i}_0^n = \cos\phi^n\sin\theta^n\hat{\mathbf{i}} + \sin\phi^n\sin\theta^n\hat{\mathbf{j}} - \cos\theta^n\hat{\mathbf{k}} \tag{18}$$

The random deviates in Eqs. (17) and (18) are sampled from expressions derived from probability density functions,

$$r^n = \frac{d_{\text{det}}}{2}\sqrt{R_r^n}, \quad \psi^n = 2\pi R_\psi^n \tag{19}$$

and

$$\sin\theta^n = \sqrt{R_\theta^n}\sin\theta_{\max}, \quad \phi^n = 2\pi R_\phi^n \tag{20}$$

where R_r^n, R_ψ^n, R_θ^n, and R_ϕ^n are random uniform deviates. In Eq. (20) $\theta_{\max}$ is the maximum detector acceptance angle; although the detector surface acts as a blackbody, Fig. 2 shows that any ray passing from the aerosol through the lens can only reach the detector surface if $\theta^n < \tan^{-1}[(d_{\text{det}}+d_{\text{lens}})/2L]$, so $\theta_{\max}$ is set equal to this value to improve the efficiency of the simulation.

The nth bundle is then ray traced backward to its emission location through a series of random scattering events, the distance between scattering events being sampled from

$$l_s^{n,j} = \frac{1}{\sigma_{s\lambda}}\ln\frac{1}{R_\sigma^{n,j}} \tag{21}$$

starting at $j=0$. At each scattering event, a new scattering distance is sampled from Eq. (21) and a new random direction specified by polar and azimuthal angles, $\theta^{n,j}$ and $\phi^{n,j}$, measured relative to the prescattered direction is sampled according to

$$R_\theta^{n,j} = \int_o^{\theta^{n,j}}\Phi(\theta^*)\sin(\theta^*)d\theta^* \tag{22}$$

and $\phi^{n,j} = 2\pi R_\phi^{n,j}$. In the case of a Heyney–Greenstein phase function, Eq. (22) is equivalent to [25]

$$\cos\theta^{n,j} = \frac{1}{2g_{\text{HG},\lambda}}\left[1 + g_{\text{HG},\lambda}^2 - \left(\frac{1-g_{\text{HG},\lambda}^2}{1+g_{\text{HG},\lambda}-2g_{\text{HG},\lambda}R_\theta^{n,j}}\right)\right] \tag{23}$$

This process continues until the bundle reaches the boundary, at which point ray tracing terminates. Following this procedure results in a piecewise-straight bundle path l^n extending backward from the detector to the boundary, as shown in Fig. 4.

The intensity incident on the detector surface due to the nth bundle is then found by integrating the intensity forward along l^n

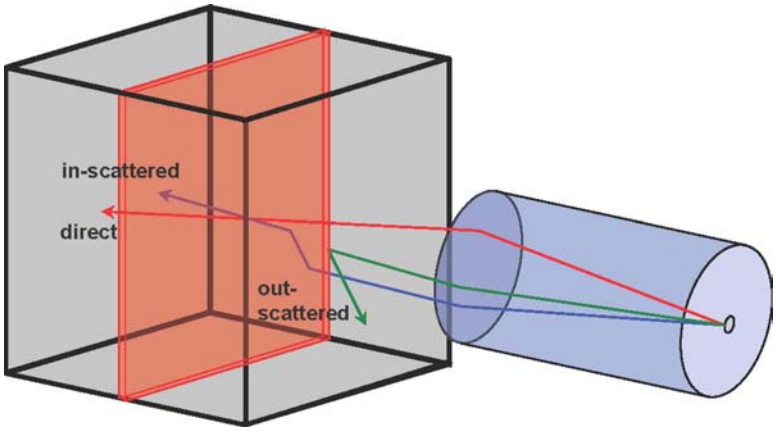

Fig. 4 Bundles emitted backward from the detector surface either travel directly to the beam are inscattered to the beam or outscattered away from the beam

from the domain boundary to the detector surface. Since the boundary is cold and black, this path integration simplifies to

$$I_\lambda^n = \int_0^{l^n} \alpha_\lambda I_{b\lambda}(\mathbf{r}')\exp[-\alpha_\lambda l'(\mathbf{r}')]dl' \tag{24}$$

(Note that the intensity along a ray traced through the perfect lens is conserved; a detailed proof is provided in Ref. [26].) Equation (24) is further simplified by splitting the path integral into two sets of m segments, the first containing m' segments that lie within the beam while the second set contains the remaining $m-m'$ segments that lie outside the beam. This latter set can be excluded from the integration since $I_{b\lambda}$ is negligible outside the beam, resulting in

$$l_\lambda^n = I_{b\lambda}(T_{\text{beam}})\sum_{j=1}^{m'} [\exp(-\alpha_\lambda l_{j,\text{in}}^n) - \exp(-\alpha_\lambda l_{j,\text{out}}^n)] \tag{25}$$

where $l^n{}_{j,\text{in}}$ and $l^n{}_{j,\text{out}}$ denote the distances along l^n from the detector surface to the location, where the jth segment enters and leaves the beam, respectively.

Finally, the spectral radiant heat absorbed by the detector is found by integrating the intensity from a large number of trial bundles

$$q_{\text{det},\lambda} = \int_0^{d_{\text{det}}/2}\int_0^{2\pi}\int_0^{\theta\,\max} I_{\lambda,\text{in}}(\theta,\phi)2\pi r\cos\theta\sin\theta d\theta d\phi dr$$

$$\approx \frac{\pi^2\sin^2\theta_{\max}d_{\text{det}}^2}{4N}\sum_{n=1}^{N} I_\lambda^n \tag{26}$$

Results and Discussion

The BMC simulation is performed on the problem at soot volume fractions over the range $10^{-8} \leqslant f_v \leqslant 10^{-5}$. (At this level of soot loading the aggregates are spaced sufficiently far apart so as to scatter independently [13].) When calculating $q_{\text{det},\lambda}$, bundles are continually ray traced from the detector surface in subsets of 100; and ray traced in subsets of 100; the total number of bundles is progressively doubled until the standard deviation of the mean in the spectral radiant energy absorbed by the detector, Eq. (26), is less than 1% of the average value. Each bundle emission has one of three outcomes corresponding to direct (unscattered) radiation, inscattered radiation, and outscattered radiation, as shown in Fig. 4: The bundle may travel directly from the detector to the measurement volume without undergoing a scattering event, be scattered from its original direction but still pass through the energized particles at some point along its path, or be scattered and intercept the domain boundary without passing through the energized zone.

The suitability of BMC to this application is first demonstrated by comparing the number of bundles that need to be emitted by the BMC technique to estimate the detector signal at 400 nm for the case of beam excitation at different soot volume fractions, compared to the number required by a forward, pathlength-based technique [24]. (The computational effort required to trace a ray path is similar for both techniques.) Figure 5 shows that the required number of bundles generally increases with soot loading in the BMC case since fewer of the bundles traced from the detector pass through the beam as f_v becomes large due to outscattering. Nevertheless, BMC requires far fewer bundles than the forward Monte Carlo (FMC) technique to obtain the same level of solution accuracy, and is consequently better suited to this problem.

Figure 6 shows the spectral radiant flux incident on the detector at 400 nm and 780 nm as a function of soot volume fraction. The straight lines on the log-log charts correspond to cases where extinction between the measurement volume and the detector surface is neglected and only direct emission from the energized particles is considered, in which case the spectral intensity incident on the detector due to measurement volume incandescence is

$$I_{\text{det},\lambda} \approx I_{b,\lambda}(T_{\text{beam}})[1-\exp(-w_b\alpha_\lambda)] \tag{27}$$

where w_b is the beam width. The detector incandescence is thus an exponential function of α_λ, which is directly proportional to f_v as expected from Eqs. (3) and (6). The actual detector signals initially follow the emission-only cases at low soot loadings but depart these trends as f_v becomes larger and signal trapping becomes more important. The signals at 400 nm depart from the emission-only line at lower values of f_v compared to the 780 nm signal because the extinction coefficients are larger at shorter wavelengths. The LII signals from sheet excitation are somewhat larger than those obtained using beam excitation due to inscatter from the energized particles located within the laser sheet but outside the measurement volume.

To further demonstrate the effect of inscatter on signal strength, the ratio of detector signal due to direct, nonscattered radiation to the total detector signal is plotted as a function of soot volume fraction in Fig. 7. At low soot loading the ratio is close to unity, indicating that the signal is almost entirely due to direct emission from the measurement volume. At higher soot loadings, however, inscatter makes up a larger portion of the signal. This effect is more pronounced at 400 nm than at 780 nm, and for sheet excitation compared to beam excitation for the reasons described above.

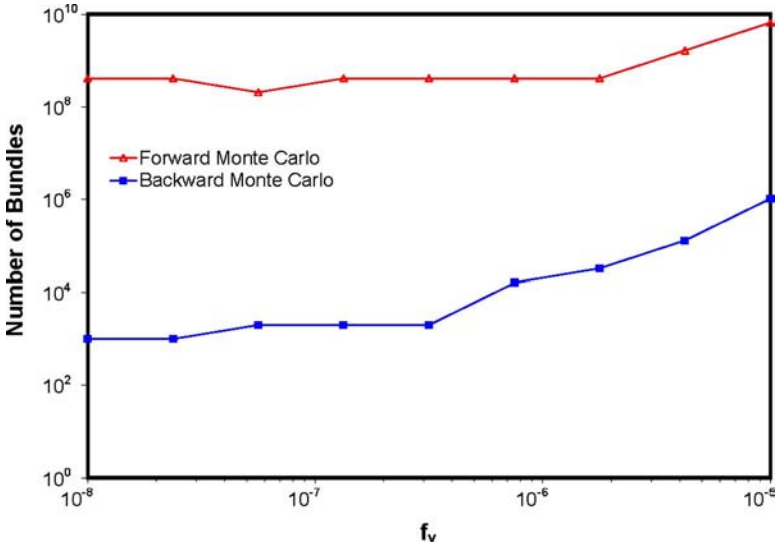

Fig. 5 Comparison of FMC and BMC efficiencies for the beam excitation case at λ_d=400 nm

We next investigate several corrections for signal trapping based on Bouguer's law [20] that have the form

$$q_{\mathrm{det},\lambda}^{\mathrm{corr}} = \frac{q_{\mathrm{det},\lambda}}{\exp(-\kappa_{\lambda,\mathrm{eff}} L/2)} \tag{28}$$

where $L/2$ is the distance between the measurement volume and the aerosol boundary as shown in Fig. 2 and $\kappa_{\lambda,\mathrm{eff}}$ is an effective spectral extinction coefficient. In many LII studies the scattering cross section is assumed to be negligible compared to the absorption cross section because the primary particle diameters satisfy the size parameter criterion for Rayleigh scattering. (While this is reasonable in some experiments, it is certainly erroneous for aerosols containing highly aggregated soot particles.) In these situations the extinction coefficient is set equal to the absorption coefficient, i.e., $\kappa_{\lambda,\mathrm{eff}}=\alpha_\lambda$, which in turn can be estimated using

$$\alpha_\lambda = \frac{6\pi E(\mathbf{m}_\lambda) f_v}{\lambda} \tag{29}$$

if the soot volume fraction is known a priori (e.g., Ref. [2]). In other cases, the extinction coefficient is inferred through supplemental LOSA experiments (e.g., Refs. [1,7,11–13]); in most LOSA experiments the optics are designed to exclude inscatter so the extinction coefficient likely to be measured approaches $\kappa_{\lambda,\mathrm{eff}} = \alpha_\lambda + \sigma_{s\lambda}$, even in aerosols that contain strongly forward scattering particles. As a final alternative, Liu et al. [9] adopt a modified extinction coefficient originally developed by Liu et al. [27] that accounts for inscatter using the Heyney–Greenstein anisotropy factor,

$$\kappa_{\lambda,\mathrm{eff}} = \alpha_\lambda + (1 - g_{\mathrm{HG},\lambda})\sigma_{s\lambda} \tag{30}$$

Figures 8 and 9 show detector signals obtained using the correction schemes, the uncorrected signal, and the emission-only case for beam and sheet excitations at 400 nm. (Signals at 780 nm follow the same trends but deviate less from the emission-only case since scattering is less pronounced at longer wavelengths.) Although setting $\kappa_{\lambda,\mathrm{eff}}=\alpha_\lambda$ is an improvement over the uncorrected signal it does not completely offset signal losses due to outscattering, particularly for the case of beam excitation. On the other hand, setting $\kappa_{\lambda,\mathrm{eff}}=\alpha_\lambda+\sigma_{s\lambda}$ overestimates the LII signals since this correction neglects inscattering contributions; this effect

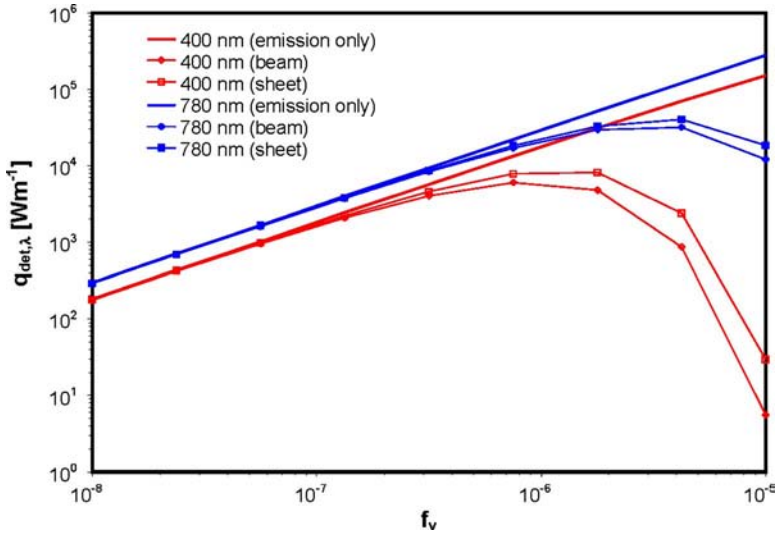

Fig. 6 Detector signal versus soot volume fraction

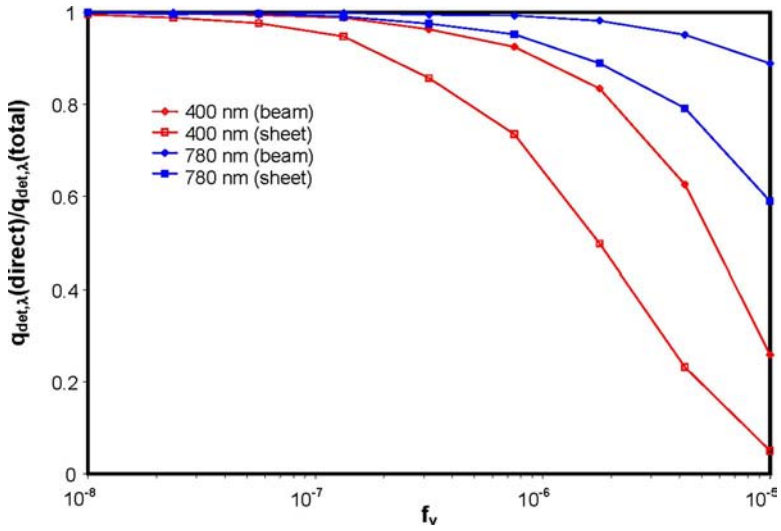

Fig. 7 Ratio of direct to total detector flux versus soot volume fraction

is most pronounced for sheet excitation at λ_d=400 nm. The best correction scheme is Eq. (30), although this technique also fails in the 400 nm beam excitation case at high soot loading. Furthermore, the anisotropy factor can only be determined if the scattering phase function is available, either by independent experimental measurement or if the soot morphology distribution parameters are known with certainty.

LII signals are often used to infer a pyrometric temperature and soot volume fraction. The impact of signal trapping on these measurements and the effectiveness of the correction schemes are assessed by calculating these parameters using the signals shown in Figs. 8 and 9. By invoking Wein's assumption, i.e., that $\exp(hc_0/\lambda k_B T_{\text{beam},m})$ is much larger than unity, the pyrometric beam temperature is found from Ref. [28]

$$T^w_{\text{beam},m} = \frac{\dfrac{hc_0}{k_B}\left(\dfrac{1}{\lambda_2}-\dfrac{1}{\lambda_1}\right)}{\ln\left[\dfrac{q_{\text{det},\lambda 1}}{q_{\text{det},\lambda 2}}\left(\dfrac{\lambda_1}{\lambda_2}\right)^6\dfrac{E(\mathbf{m}_{\lambda 1})}{E(\mathbf{m}_{\lambda 2})}\right]} \tag{31}$$

where h is Planck's constant, k_B is Boltzmann's constant, and c_0 is the speed of light. The error induced by Wein's approximation is then corrected using the iterative procedure of Levendis et al. [29],

$$T_{\text{beam},m} = \frac{\dfrac{hc_0}{k_B}\left(\dfrac{1}{\lambda_2}-\dfrac{1}{\lambda_1}\right)}{\ln\left[\dfrac{q_{\text{det},\lambda 1}}{q_{\text{det},\lambda 2}}\left(\dfrac{\lambda_1}{\lambda_2}\right)^6\dfrac{1-\exp(-hc_0/\lambda_1 k_b T^w_{\text{beam},m})}{1-\exp(-hc_0/\lambda_2 k_b T^w_{\text{beam},m})}\right]} \tag{32}$$

which usually provides a satisfactory result in a single iteration. Once the pyrometric temperature is known, the soot volume fraction can be calculated using the autocorrelated method of Snelling et al. [28],

$$f_{v,m} = \frac{q_{\text{det},\lambda}}{\Phi_p(T_{\text{beam},m},\lambda)M^2 A_{\text{detector}} A_{\text{lens}} w_b} 4\pi L^2 \tag{33}$$

where M is the magnification (equal to unity), A_{detector} and A_{lens} are the surface areas of the detector and lens, and Φ_p is the total radiated power per unit volume of particulate at detection wavelength λ,

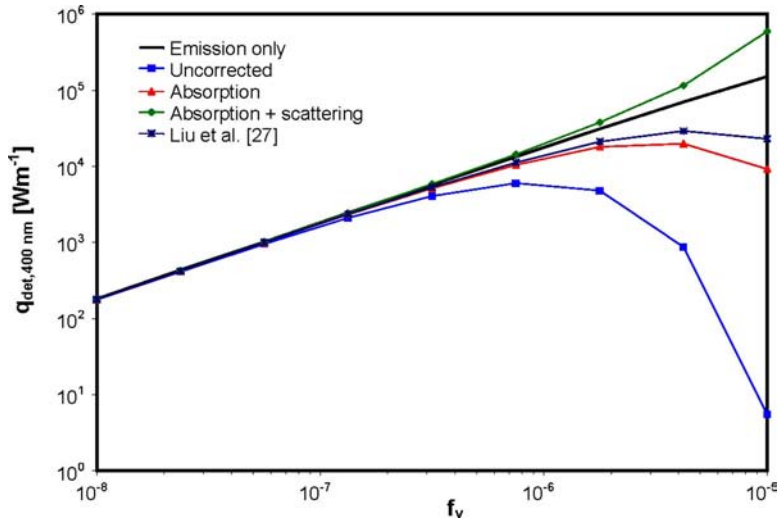

Fig. 8 Comparison of correction schemes for the beam excitation case at λ_d=400 nm

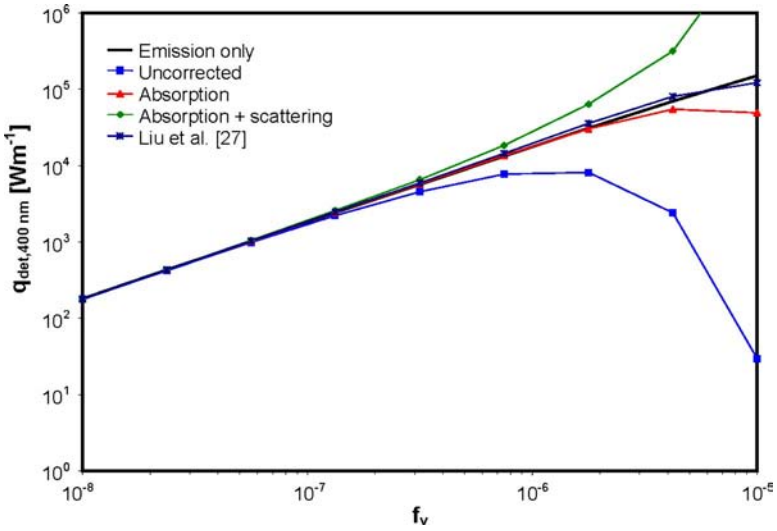

Fig. 9 Comparison of correction schemes for the sheet excitation case at λ_d=400 nm

$$\Phi_p(T_{\text{beam},m},\lambda) = \frac{48\pi^2 c_0^2 h}{\lambda^6}\left[\exp\left(\frac{hc_0}{\lambda k_B T_{\text{beam},m}}\right) - 1\right]^{-1} E(\mathbf{m}_\lambda) \tag{34}$$

The detection wavelength for Eqs. (33) and (34) is chosen to be 780 nm since this channel is least affected by signal trapping.

Figures 10 and 11 show the relative errors in the pyrometric temperatures for beam and sheet excitations, respectively. At higher soot loadings $T_{\text{beam},m}$ underestimates the actual beam temperature because the $q_{\text{det,400 nm}}$ is more strongly attenuated than $q_{\text{det,780 nm}}$, although this effect is somewhat offset by inscatter in the sheet excitation case. The correction schemes generally improve the accuracy of $T_{\text{beam},m}$, although as noted above setting $\kappa_{\lambda,\text{eff}}=\alpha_\lambda+\sigma_{s\lambda}$ overcompensates for outscatter and causes $T_{\text{beam},m}$ to be overestimated, particularly when sheet excitation is used. Figures 12 and 13 and inspection of Eqs. (33) and (34) show that underestimating the pyrometric beam temperature causes f_v to be overestimated except when $\kappa_{\lambda,\text{eff}}=\alpha_\lambda+\sigma_{s\lambda}$ in which case f_v is severely underestimated at high soot loadings, particularly in the case of sheet excitation. The correction proposed by Liu et al. [27] usually gives pyrometric temperatures and soot volume fractions that are closest to the actual values, although again this scheme can only be implemented if the scattering phase function is known.

Conclusions

This paper investigates how scattering influences LII measurements on aerosols containing highly aggregated particles, with a focus on the effect of inscattering when a laser sheet is used to energize the particles instead of a laser beam. The bulk radiative properties of the aerosol are derived from RDG-PFA theory and the radiation analysis is carried out through a BMC simulation. BMC is well suited to modeling LII signals since complex phenomenon such as anisotropic scattering is incorporated into the simulation with ease, and a performance comparison shows BMC to be much more efficient than the traditional FMC implementation for solving this problem.

The analysis shows that signal trapping has a strong effect on LII signals made on aerosols containing highly aggregated soot particles. This effect is most pronounced at short wavelengths due to the spectral dependence of the extinction cross section and increases with soot loading. Inscattering along the optical path

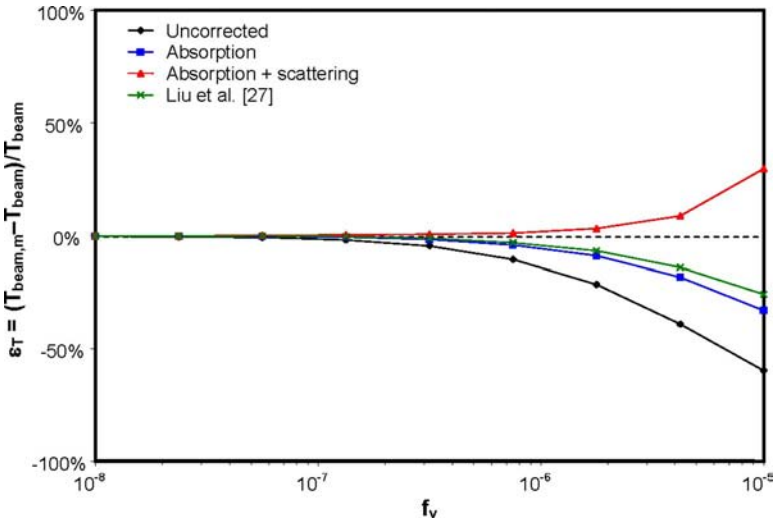

Fig. 10 Relative errors in beam temperature derived using beam excitation

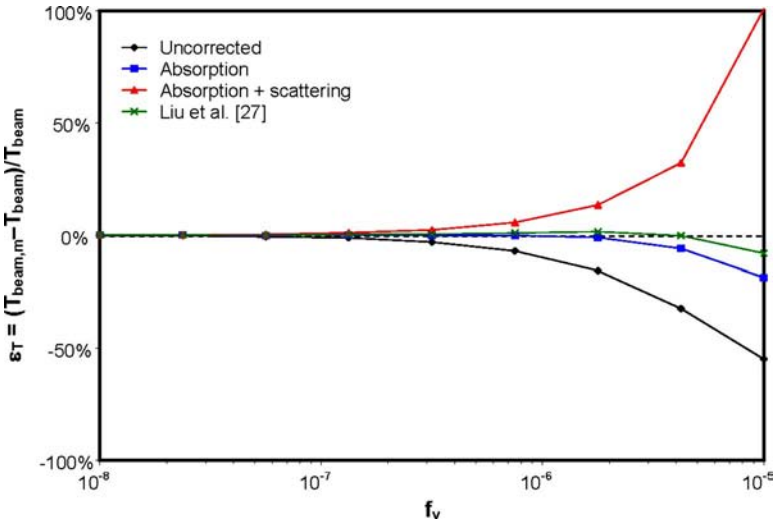

Fig. 11 Relative errors in beam temperature derived using sheet excitation

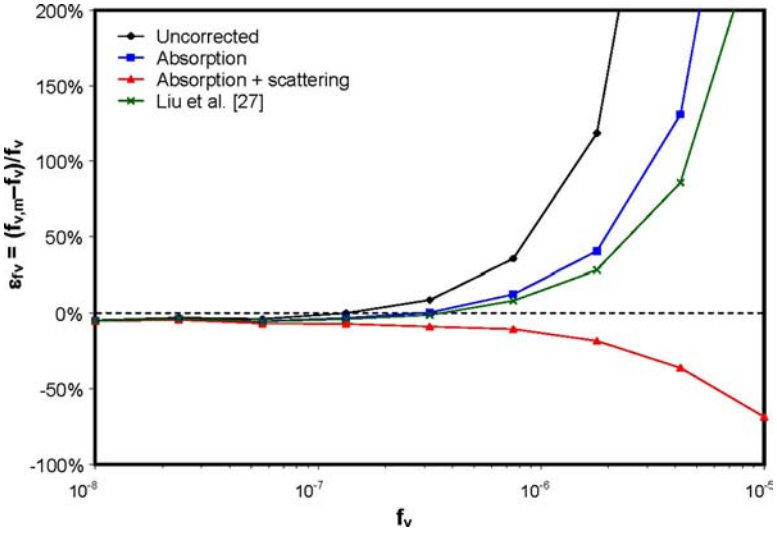

Fig. 12 Relative errors in soot volume fraction derived using beam excitation

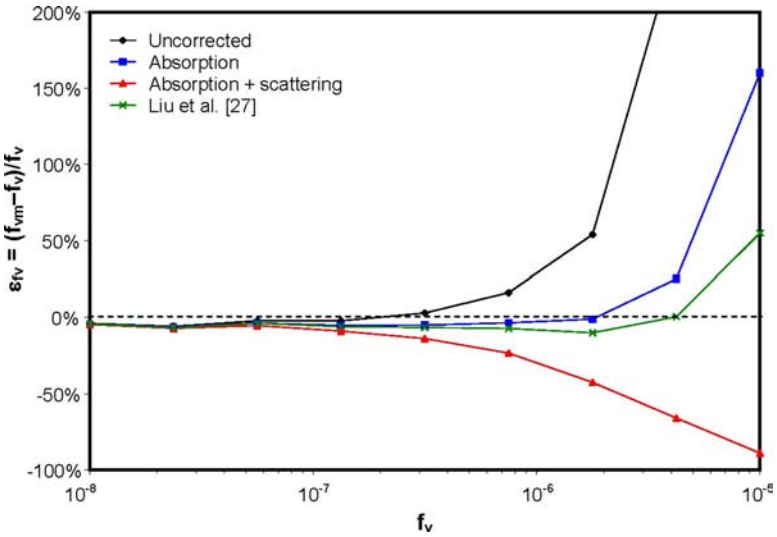

Fig. 13 Relative errors in soot volume fraction derived using sheet excitation

somewhat mitigates signal trapping, however, particularly in the case of sheet excitation. Signal trapping causes the pyrometric temperature derived using LII signals to be underestimated and the soot volume fraction to be overestimated when the latter is calculated using the autocorrelated technique of Snelling et al. [28].

Correction schemes based on Bouguer's law are, on the whole, effective in correcting for signal trapping and extend the range of soot loadings over which accurate LII measurements can be made. The best scheme is the one proposed by Liu et al. [27] that uses the Heyney–Greenstein anisotropy factor, although this parameter is usually available only if independent scattering measurements have been made on the aerosol or if particle morphology distribution parameters are known.

Nomenclature

C_a = absorption cross section, nm^2
C_s = scattering cross section nm^2
D_f = soot aggregate fractal dimension
d_p = primary particle diameter, nm
d_{det} = detector diameter, mm
d_{lens} = lens diameter, mm
$E(\mathbf{m})$ = complex absorption function
$F(\mathbf{m})$ = complex scattering function
f_v = Soot volume fraction
$g_{HG,\lambda}$ = Heyney–Greenstein anisotropy factor
$I_{b,\lambda}$ = blackbody spectral intensity, $W\ m^{-2}\ nm^{-1}\ sr^{-1}$
I_λ = spectral intensity, $W\ m^{-2}\ nm^{-1}\ sr^{-1}$
k_g = soot aggregate prefactor
L = aerosol dimension, m
l_s = distance between scattering events, m
$\mathbf{m}$ = complex index of refraction
N_{agg} = aggregate number density, particles m^{-3}
N_p = number of primary particles per aggregate
$N_{p,g}$ = geometric mean number of primary particles per aggregate
$q_{det,\lambda}$ = detector flux, $W\ m^{-1}$
R_g = radius of gyration, nm
$\mathbf{r}$ = position vector
T_{beam} = beam temperature, K
T_g = gas temperature, K
w_b = beam width, m
x_p = primary particle size parameter, $\pi d_p/\lambda$
α_λ = absorption coefficient, m^{-1}
ϕ = azimuthal angles, rad
$\kappa_{\lambda,}$ = extinction coefficient, m^{-1}
$\kappa_{\lambda,eff}$ = effective extinction coefficient, m^{-1}
λ = wavelength, nm
η = wave number, nm^{-1}
$\Phi(\theta)$ = phase function
θ = polar angle, rad
θ_{max} = maximum detector acceptance angle, rad
σ_g = geometric standard deviation
$\sigma_{s\lambda}$ = scattering coefficient, m^{-1}

Subscripts and Superscripts

a = absorption
agg = aggregate property
m = measured parameter
n = Monte Carlo trial index
p = primary particle
s = scattering

References

[1] Vander Wal, R. L., and Jensen, K. A., 1998, "Laser-Induced Incandescence: Excitation Intensity," Appl. Opt., **37**, pp. 1607–1616.

[2] Vander Wal, R. L., Zhou, Z., and Choy, M. Y., 1996, "Laser-Induced Incandescence Calibration via Gravimetric Sampling," Combust. Flame, **105**, pp. 462–470.

[3] Snelling, D. R., Smallwood, G. J., Liu, F., Gülder, Ö. L., and Bachalo, W. D., 2005, "A Calibration-Independent Laser-Induced Incandescence Technique for Soot Measurement by Detecting Absolute Light Intensity," Appl. Opt., **44**, pp. 6773–6785.

[4] De luliis, S., Cignoli, F., and Zizak, G., 2005, "Two-Color Laser-Induced Incandescence (2C-LII) Technique for Absolute Soot Volume Fraction Measurements in Flames," Appl. Opt., **44**, pp. 7414–7423.

[5] Roth, P., and Filippov, A. V., 1996, "In Situ Ultrafine Particle Sizing by a Combination of Pulsed Laser Heatup and Particle Thermal Emission," J. Aerosol Sci., **27**, pp. 95–104.

[6] Lehre, T., Jungfleisch, B., Suntz, R., and Bockhorn, H., 2003, "Size Distributions of Nanoscaled Particles and Gas Temperatures From Time-Resolved Laser-Induced-Incandescence Measurements," Appl. Opt., **42**, pp. 2021–2030.

[7] Choy, M. Y., and Jensen, K. A., 1998, "Calibration and Correction of Laser-Induced Incandescence for Soot Volume Fraction Measurements," Combust. Flame, **112**, pp. 485–491.

[8] Köylü, Ü. Ö., and Faeth, G. M., 1994, "Optical Properties of Overfire Soot in Buoyant Turbulent Diffusion Flames at Long Residence Times," ASME J. Heat Transfer, **116**, pp. 152–159.

[9] Liu, F., Thomson, K. A., and Smallwood, G. J., 2007, "Effects of Soot Absorption and Scattering on LII Intensities in Laminar Coflow Diffusion Flames," *Proceedings of the 5th International Symposium on Radiative Transfer*, Bodrum, Turkey, June 17–22.

[10] Chen, L. H., Garo, A., Cen, K., and Grehan, G., 2007, "Numerical Simulation of Soot Optical Diagnostics in Non-Optically Thin Media," Appl. Phys. B: Lasers Opt., **87**, pp. 739–747.

[11] Migliorini, F., De luliis, S., Cignoli, F., and Zizak, G., 2006, "Absorption Correction of Two-Color Laser-Induced Incandescence Signals for Soot Volume Fraction Measurements," Appl. Opt., **45**, pp. 7706–7711.

[12] Shaddix, C. R., and Smyth, K. C., 1996, "Laser-Induced Incandescence Measurements of Soot Production in Steady and Flickering Methane, Propane, and Ethylene Diffusion Flames," Combust. Flame, **107**, pp. 418–452.

[13] McCrain, L. L., and Roberts, W. L., 2005, "Measurement of the Soot Volume Field in Laminar Diffusion Flames at Elevated Pressures," Combust. Flame, **140**, pp. 60–69.

[14] Modest, M. F., 2003, *Radiative Heat Transfer*, 2nd ed., Academic Press, San Diego, CA.

[15] Dobbins, R. A., and Megaridis, C. M., 1991, "Absorption and Scattering of Light by Polydisperse Aggregates," Appl. Opt., **30**, pp. 4747–4754.

[16] Eymet, V., Brasil, A. M., El Hafi, M., Farias, T. L., and Coelho, P. J., 2002, "Numerical Investigation of the Effect of Soot Aggregation on the Radiative Properties in the Infrared Region and Radiative Heat Transfer," J. Quant. Spectrosc. Radiat. Transf., **74**, pp. 697–718.

[17] Murphy, J. J., and Shaddix, C. R., 2005, "Influence of Scattering and Probe-Volume Heterogeneity on Soot Measurements Using Optical Pyrometry," Combust. Flame, **143**, pp. 1–10.

[18] Thomson, K. A., Snelling, D. R., Smallwood, G. J., and Liu, F., 2006, "Laser Induced Incandescence Measurements of Soot Volume Fraction and Effective Particles Size in a Laminar Co-Annular Non-Premixed Methane/Air Flame at Pressures Between 0.5–4.0 MPa," Appl. Phys. B: Lasers Opt., **83**, pp. 469–475.

[19] Modest, M. F., 2003, "Backward Monte Carlo Simulations in Radiative Heat Transfer," ASME J. Heat Transfer, **125**, pp. 57–62.

[20] Siegel, R., and Howell, J. R., 2002, *Thermal Radiation Heat Transfer*, 4th ed., CRC Press, Boca Raton, FL, p. 423.

[21] Yang, B., and Köylü, Ü. Ö., 2005, "Soot Processes in a Strongly Radiating Turbulent Flame From Laser Scattering/Extinction Experiments," J. Quant. Spectrosc. Radiat. Transf., **93**, pp. 289–295.

[22] Chang, H., and Charalampopoulos, T. T., 1990, "Determination of the Wavelength Dependence of Refractive Indices of Flame Soot," Proc. R. Soc. London, Ser. A, **430**, pp. 570–591.

[23] Case, K. M., 1957, "Transfer Problems and the Reciprocity Principle," Rev. Mod. Phys., **29**, pp. 651–663.

[24] Farmer, J. T., and Howell, J. R., 1998, "Comparison of Monte Carlo Strategies for Radiative Transfer in Participating Media," Adv. Heat Transfer, **31**, pp. 333–429.

[25] Toublanc, D., 1996, "Henyey-Greenstein and Mie Phase Functions in Monte Carlo Radiative Transfer Computations," Appl. Opt., **35**, pp. 3270–3274.

[26] Smith, W. J., 1990, *Modern Optical Engineering: The Design of Optical Systems*, 2nd ed., McGraw-Hill, New York, pp. 211–212.

[27] Liu, F., Garbett, E. S., and Swithenbank, J., 1992, "Effects of Anisotropic Scattering on Radiative Heat Transfer Using the P_1-Approximation," Int. J. Heat Mass Transfer, **35**, pp. 2491–2499.

[28] Snelling, D. R., Smallwood, G. J., Liu, F., Gulder, O. L., and Bachalo, W. D., 2005, "A Calibration-Independent Laser-Induced Incandescence Technique for Soot Measurement by Detecting Absolute Light Intensity," Appl. Opt., **44**, pp. 6773–6785.

[29] Levendis, Y. A., Estrada, K. R., and Hottel, H. C., 1992, "Development of Multicolor Pyrometers to Monitor the Transient Response of Burning Carbonaceous Particles," Rev. Sci. Instrum., **63**, pp. 3608–3622.

Prediction of Thermal Emission and Exchange Among Neighboring Wavelength-Sized Spheres

Daniel W. Mackowski
Department of Mechanical Engineering,
Auburn University,
Auburn, AL 36849
e-mail: mackodw@auburn.edu

Michael I. Mishchenko
NASA Goddard Institute for Space Studies,
2880 Broadway,
New York, NY 10025

An analysis of radiative emission and radiative exchange among an ensemble of closely spaced, wavelength-sized spheres, in which each sphere in the ensemble is at a distinct and uniform temperature, is presented. We show that the rate of spectral emission from a specific sphere in the ensemble and the rate at which emission is exchanged between a pair of spheres can be deduced from the application of reciprocity and energy conservation principles to the solution of Maxwell's time harmonic wave equations for a sphere ensemble that is exposed to a plane wave incident field of wavelength λ. *We show that in the limit of* $d/\lambda \to 0$, *the emissive exchange between a pair of spheres becomes inversely proportional to the gap thickness d. We also show that when the spheres are in the mutual far-field zones of each other, the emissive exchange between the spheres can be well approximated by geometric configuration factors, with an effective area correction to account for finite wavelength effects.* [DOI: 10.1115/1.2957596]

Keywords: nanoscale heat transfer, electromagnetic scattering, spheres, radiative heat transfer

1 Introduction

The objective of this article is to develop an exact prediction of the thermal radiation heat transfer exchanged between small neighboring spheres. By "small" and "neighboring," we are referring to spheres that have radii comparable to the visible and IR wavelengths of thermal radiation and that are located in the mutual near-field zones that characterize the thermal radiation. Our motivation in addressing this topic is, to a large part, simply one of academic interest and academic continuity: a large body of work has been assembled on the plane wave scattering properties of multiple sphere systems, and we wish to extend this work to delineate the intersphere energy transport processes. The topic, however, is certainly relevant to a variety of situations in the emerging fields of nano- and microscale transport phenomena. In particular, a detailed understanding of the microscopic-level energy transport process in deposits of nanometer- and micrometer-sized particles—which is necessary for the prediction of the optical and photonic properties of the deposits—will require an improved ability to predict energy transfer on the individual-particle scale.

The wavelength-sized length scales of our system will certainly preclude the application of a macroscopic-level radiant exchange analysis. Our approach to the problem will be to employ solutions to Maxwell's macroscopic wave equations for multiple spheres to characterize the electromagnetic energy flow from and among the spheres that results from thermal emission. Beginning with the pioneering work of Brunning and Lo, a great deal of analytical and computational resources have been developed to determine the absorption and scattering properties of multiple sphere systems [1–3]. Even though the solution can identify the absorption cross section of individual spheres in the ensemble—for both fixed and random orientations relative to the incident wave—the prediction of thermal emission from individual spheres or the rate of intersphere energy transfer has not been addressed in these works.

An analysis of thermal emission from a micrometer-sized homogeneous and isothermal sphere was first examined by Kattawar and Eisner [4], who employed the Rytov model in which thermal emission is modeled as fluctuating electric polarization [5]. Their model provided a detailed confirmation of Kirchoff's law in that the spectral emission cross section of the sphere was shown to be equal to the absorption cross section as predicted by the Lorenz–Mie theory. The exchange of thermal radiation between a small spherical particle, modeled as an electric dipole, and a plane surface was formulated by Mulet et al., and their analysis shows that the coupling of evanescent waves can lead to a significant increase in heat transfer when the sphere is in the near-field zone of the surface [6]. More recently, Narayanaswamy et al. applied the Rytov model to predict the thermal emission exchange between a pair of arbitrarily sized spheres [7]. This analysis enabled, for the first time, an exact determination of intersphere thermal energy transfer for pairs of spheres that are separated by subwavelength distances. However, they report that their solution develops convergence problems as the two spheres approach contact. In addition, it is not obvious from their work how their solution corresponds or connects to the existing understanding of absorption and scattering by sphere clusters.

A key goal in the present work is to develop a general formulation for thermal emission by, and exchange among, the individual spheres in a multiple sphere ensemble. To this end, we will not model emission explicitly via the Rytov formulation. Rather, we will begin with the plane wave scattering formulation for the sphere cluster and develop, via equilibrium and reciprocity arguments, the formulas which predict the emissive flow of energy among the spheres.

2 Formulation

2.1 Definition of the Emission Cross Section. The model we use in our analysis is illustrated in Fig. 1, which consists of a

Contributed by the Heat Transfer Division of ASME for publication in the JOURNAL OF HEAT TRANSFER. Manuscript received August 22, 2007; final manuscript received January 11, 2008; published online September 3, 2008. Review conducted by Walter W. Yuen.

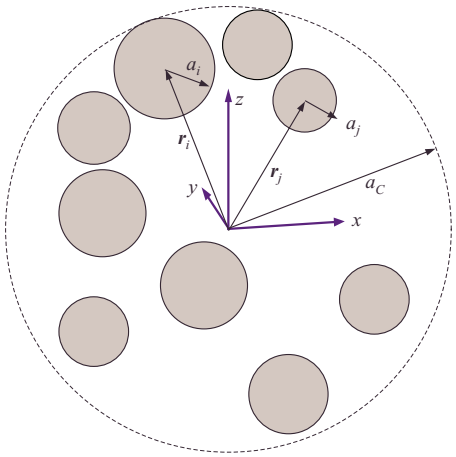

Fig. 1 Ensemble configuration

system of N_S spheres denoted by $i=1,2,\ldots,N_S$. Each sphere is characterized by a position $\mathbf{r}_i$ (relative to a common coordinate origin), a radius a_i, and a complex refractive index $\mathsf{m}_i=\mathsf{n}_i+\mathsf{i}\mathsf{k}_i$ (which, in general, will be dependent on the wavelength of radiation). The system is surrounded by a large (and black) environment.

In the most general case, we will take each of the spheres to be maintained, via some unseen means, at a distinct yet uniform temperature of T_i, and likewise the environment is at a temperature of T_e. One consequence of the isothermal-sphere model is that the spheres are assumed to be separated from their neighbors to avoid the existence of a discontinuous temperature jump at a contact point. We wish to predict the monochromatic power (or, synonymously, thermal radiative heat transfer) emitted from and absorbed by each of the spheres and to also identify the detailed exchange of thermal radiation among the spheres (i.e., the fraction of the power emitted by i, which is absorbed by j).

Our analytical route to this goal will begin with the observation that the net rate of monochromatic thermal *emission* from a sphere must be proportional to the spectral blackbody intensity $I_{b,\lambda}(T_i)$ evaluated at the sphere temperature. It is therefore consistent to state that

$$q_{i,\lambda}d\lambda = 4\pi C_{\text{emis},i} I_{b,\lambda}(T_i)d\lambda \tag{1}$$

where $q_{i,\lambda}$ denotes the heat transfer contained within the wavelength interval $d\lambda$ and $C_{\text{emis},i}$ denotes a monochromatic emission cross section for sphere i (units of area). This cross section would depend not only on the properties of sphere i, but also on the optical properties and positions of all the neighboring spheres in the system. However, since we are considering only spontaneous emission, the cross section will not be a function of the radiative field incident on the sphere; in particular, it would be decoupled from the temperatures of the surrounding spheres and the environment. Second, a detailed and identifiable accounting must exist for the radiation emitted from sphere i; a fraction of the radiation will be absorbed by sphere 1, a different fraction by 2, etc., and whatever is not absorbed by the spheres will be absorbed by the environment. Therefore, we can postulate the property of an exchange cross section $C_{\text{emis},i-j}$ so that $4\pi C_{\text{emis},i-j} I_{b,\lambda}(T_i)d\lambda$ is the power emitted from i and absorbed by j. Since all the radiation from i must end up somewhere, then

$$C_{\text{emis},i} = C_{\text{emis},i-e} + \sum_{\substack{j=1 \\ j\neq i}} C_{\text{emis},i-j} \tag{2}$$

in which subscript e denotes the environment. Note that by excluding $j=i$ from the sum, we imply that self-absorption is included into the definition of $C_{\text{emis},i}$ in Eq. (1). Third, thermodynamical considerations will prohibit the net exchange of heat between two sites i and j that are at the same temperature. This establishes the reciprocity condition of

$$C_{\text{emis},i-j} = C_{\text{emis},j-i} \tag{3}$$

For any particle, it is known that the absorption of thermal emission from the isothermal environment by the particle is equivalent to the absorption of unpolarized plane wave radiation having the same blackbody intensity and averaged over all incident directions [8]. This concept can also be extended to each subunit within the particle; for the problem at hand, the absorption by sphere i of thermal emission from the environment—which will be $4\pi C_{\text{emis},i-e} I_{b,\lambda}(T_e)d\lambda$—will be equal to the random-incidence plane wave absorption by the sphere. It follows that

$$C_{\text{emis},i-e} = \langle C_{\text{abs},i} \rangle \tag{4}$$

where $\langle C_{\text{abs},i} \rangle$ denotes the orientation-averaged absorption cross section of sphere i.

A well-developed formulation exists for the prediction of the absorption cross section of an individual sphere in an ensemble—in both fixed and random orientation—and this formulation will be reviewed in the following section. What has not been performed and what is presented here is a decomposition of the absorption cross section into components which account for the intersphere energy transfers implied in Eq. (2). In particular, we intend to identify the exchange cross sections so that

$$\langle C_{\text{abs},i} \rangle = C_{\text{emis},i-e} = C_{\text{emis},i} - \sum_{\substack{j=1 \\ j\neq i}} C_{\text{emis},i-j} \tag{5}$$

2.2 Multiple Sphere Scattering Formulation

2.2.1 Superposition Model and the Interaction Equations. Only those aspects of the multiple sphere scattering formulation which are directly relevant to the problem at hand will be presented here; the reader is referred to Refs. 2 and 9 for details. In the solution, the field external to the spheres is constructed from a superposition of the incident field and fields scattered from each sphere in the ensemble,

$$\mathbf{E}_{\text{ext}} = \mathbf{E}_{\text{inc}} + \sum_{i=1}^{N_S} \mathbf{E}_{\text{sca},i} \tag{6}$$

For each sphere, the incident and scattered fields can be represented by an expansion of vector spherical harmonics (VSH), centered about the origin of the sphere,

$$\mathbf{E}_{\text{inc},i} = \sum_{n=1}^{L_i} \sum_{m=-n}^{n} \sum_{p=1}^{2} p^i_{mnp} \mathbf{N}^{(1)}_{mnp}(\mathbf{r}-\mathbf{r}_i) \tag{7}$$

$$\mathbf{E}_{\text{sca},i} = \sum_{n=1}^{L_i} \sum_{m=-n}^{n} \sum_{p=1}^{2} a^i_{mnp} \mathbf{N}^{(3)}_{mnp}(\mathbf{r}-\mathbf{r}_i) \tag{8}$$

In the above, $\mathbf{N}_{mnp}$ denotes the VSH of either type 1 (regular, based on the spherical Bessel function $j_n(kr)$) or 3 (outgoing, based on the spherical Hankel function $h_n=j_n+\mathsf{i}y_n$) and of order n, degree m, and mode $p=1$ (TM) or 2 (TE). The order truncation limit L_i in Eq. (8) is chosen to provide an acceptable precision in the calculated scattering properties of the cluster; L_i can typically be set using the Lorenz–Mie criterion, although in certain cases the neighboring spheres can have a significant effect on the convergence of Eq. (8) [9].

The incident field coefficients p^i will depend on the propagation direction and polarization state of the incident field (which typically is a plane wave) and the relative position of origin i, whereas the scattering coefficients a^i are initially unknown and are sought from the analysis. A relationship between the incident and scattered field coefficients can be obtained via a generalized applica-

tion of the Lorenz–Mie theory for a sphere, in which the exciting field for a particular sphere includes the incident field as well as the fields scattered from all other spheres. This analysis leads to a set of interaction equations, the solution of which provides a linear relationship of the form

$$a^i_{mnp} = \sum_{j=1}^{N_S} \sum_{l=1}^{L_j} \sum_{k=-l}^{l} \sum_{q=1}^{2} T^{i-j}_{mnpklq} p^j_{klq} \tag{9}$$

in which the sphere-sphere T^{i-j} matrix is given by the solution to the following matrix interaction equations:

$$\frac{1}{\bar{a}^i_{np}} T^{i-j}_{mnpklq} - \sum_{\substack{j'=1 \\ j' \neq i}}^{N_S} \sum_{l'=1}^{L_{j'}} \sum_{k'=-l'}^{l'} \sum_{q'=1}^{2} H^{i-j'}_{mnpk'l'q'} T^{j'-j}_{k'l'q'klq} = \delta_{ij}\delta_{mk}\delta_{nl}\delta_{pq} \tag{10}$$

In the above, δ_{ij} is the Kronecker delta function, $\bar{a}^i_{np}$ denotes the Lorenz–Mie coefficients of the sphere and depends on the sphere size parameter $x_i = ka_i$ and the refractive index m_i, and the matrix H^{i-j} translates an outgoing VSH centered about origin j into an expansion of regular VSH centered about i. This translation matrix will be a function solely of the distance and direction between origins i and j, and the elements of H involve summations of the scalar harmonic $h_w(kr_{i-j})P^v_w(\cos\theta_{i-j})\exp(\mathrm{i}v\phi_{i-j})$ for $w = |n-l|, \ldots, n+l$.

The sphere-sphere T^{i-j} matrix describes the scattered field produced at sphere i due to an incident field at j. All the effects of multiple scattering on the coupling of the fields between j and i are embedded within the matrix. For equal-size spheres with equal truncation limits of $L_i = L_S$, Eq. (10) represents $2N_S L_S(L_S+2)$ linear equations for each column vector of T^{i-j}. The set of scattering coefficients obtained from Eq. (9), for a given incident field, provides a complete picture of the electromagnetic field in both the near- and far-field regions. In particular, the cross sections and the polarimetric scattering pattern can be obtained directly from the scattering coefficients.

For the application at hand—which deals with the exchange of thermal radiation—it will be necessary to identify the orientation-averaged absorption cross sections of the spheres. This can be done most effectively by utilizing the T matrix relationships, as described in Refs. 2 and 9. The relevant formula is

$$\langle C_{\mathrm{abs},i} \rangle = \frac{2\pi}{k^2} \sum_{\mu,\nu} \bar{b}^i_\mu \sum_{j=1}^{N_S} \sum_{j'=1}^{N_S} \sum_{\nu'} T^{i-j}_{\mu\nu'} J^{j-j'}_{\nu'\nu} (T^{i-j'}_{\mu\nu})^* \tag{11}$$

In the above and in what follows, Greek subscripts are shorthand for degree/order/mode, i.e., $\nu = (klq)$. The matrix J is referred to as the regular VSH (or plane wave) translation matrix; it has the same structure as H, except with basis functions involving the spherical Bessel functions $j_w(kr)$ as opposed to the Hankel functions $h_w(kr)$. Superscript * denotes complex conjugate, and $\bar{b}$ is a positive real-valued property solely of sphere i and is defined by

$$\bar{b}^i_{np} = -\mathrm{Re}\left(\frac{1}{\bar{a}^i_{np}} + 1\right) \tag{12}$$

2.2.2 Expansion of the Absorption Cross Section. The detailed transfer of radiant energy among the particles—which has been anticipated in Eq. (5)—should be embedded within the formula for $\langle C_{\mathrm{abs},i} \rangle$. This structure is not obvious in the definition given in Eq. (11), and an alternative definition is needed to elucidate the interactive form of the absorption cross section. The derivation makes use of the symmetry and contraction properties of the translation matrices, details of which are found in Refs. 2 and 10. The application of these properties ultimately leads to the relation

$$\langle C_{\mathrm{abs},i} \rangle = -\frac{2\pi}{k^2} \sum_{\mu} \bar{b}^i_\mu \left[\mathrm{Re}\, T^{i-i}_{\mu\mu} + \sum_{\nu} \bar{b}^i_\nu |T^{i-i}_{\mu\nu}|^2 + \sum_{\substack{j=1 \\ j\neq i}}^{N_S} \sum_{\nu} \bar{b}^j_\nu |T^{i-j}_{\mu\nu}|^2 \right] \tag{13}$$

We now submit that each of the terms appearing in this formula can be interpreted according to the exchange formula appearing in Eq. (5). When multiplied by $4\pi I_{b,\lambda}(T_i)d\lambda$, the sum of the first and second terms on the right represent the net emissive power from sphere i. The third term accounts for the absorption of the net emissive power from i by all the other spheres in the ensemble. Consequently, we have

$$C_{\mathrm{emis},i} = -\frac{2\pi}{k^2} \sum_{\mu} \bar{b}^i_\mu \left[\mathrm{Re}\, T^{i-i}_{\mu\mu} + \sum_{\nu} \bar{b}^i_\nu |T^{i-i}_{\mu\nu}|^2 \right] \tag{14}$$

$$C_{\mathrm{emis},i-j} = \frac{2\pi}{k^2} \sum_{\mu} \bar{b}^i_\mu \sum_{\nu} \bar{b}^j_\nu |T^{i-j}_{\mu\nu}|^2 \tag{15}$$

We will demonstrate in the following section that the formula for the exchange cross section is consistent with that obtained from a direct modeling of the emission mechanism. For now we note that the formulas have the required properties that were originally postulated for the cross sections. Due to the symmetry properties of T^{i-j}, the exchange emission cross sections in Eq. (15) will automatically satisfy the reciprocity condition in Eq. (3). When a sphere is nonabsorbing—which corresponds to $\bar{b}=0$ for the sphere—the exchange cross section to the sphere will be zero. For a single isolated sphere the self-interaction T matrix reduced to $T^{i-i}_{\mu\nu} \rightarrow \bar{a}^i_\mu \delta_{\mu\nu}$, and using

$$\bar{b}^i_\mu = -\frac{1}{|\bar{a}^i_\mu|^2} (\mathrm{Re}\, \bar{a}_\mu + |\bar{a}^i_\mu|^2) \tag{16}$$

it follows that

$$\begin{aligned} C_{\mathrm{emis},1}|_{N_S=1} &= \frac{2\pi}{k^2} \sum_{\mu} [-\mathrm{Re}\, \bar{a}^1_\mu - |\bar{a}^1_\mu|^2] \\ &= \frac{2\pi}{k^2} \sum_{n=1}^{L_1} \sum_{p=1}^{2} (2n+1)[-\mathrm{Re}\, \bar{a}^1_{np} - |\bar{a}^1_{np}|^2] \\ &= C_{\mathrm{ext},1} - C_{\mathrm{sca},1} = C_{\mathrm{abs},1} \end{aligned} \tag{17}$$

In other words, the emission cross section for an isolated sphere becomes identical to the absorption cross section for the sphere.

2.2.3 An Alternate Approach. The formula for the exchange cross section in Eq. (15) is not at all unexpected. Indeed, this formula could have been derived in a few lines solely from Eqs. (3), (9), and (11). The emission cross section in Eq. (14), on the other hand, is somewhat less intuitive. However, it would not be inappropriate to question the entire validity of the results because we have derived cross sections related to emission without dealing explicitly with the emission process. In this section, we will demonstrate—using a formulation that is realistic yet economical—that our derivation is consistent with an emission model.

We will begin with the exchange cross section in Eq. (15), which shows that the geometrical dependence on energy exchange is contained solely within $|T^{j-i}|^2$. We note again that the sphere-sphere T^{j-i} matrix describes the scattered field at j that results from the presence of the incident field at i. In a broader sense, the incident field at i could be generalized to include any form of external or internal excitation of the sphere, which results in an outgoing (i.e., scattered) wave from the sphere. The source of excitation will obviously have bearing on the overall "harmonic content" of the outgoing wave, yet the mechanism which carries

the energy of the wave to the surrounding spheres—and which is described by the T^{j-i} matrix—will be independent of the excitation source.

In this sense, we can separate the "source" and "transfer" mechanisms to predict the emissive power carried from sphere i to j. The latter will be a function entirely of T^{j-i}, whereas the former will depend only on the properties of the emitting sphere. We also note that the identification of the relevant source characteristics for the sphere need not begin with the fundamental Rytov formulation. This problem has already been solved, and the solution has demonstrated the equivalence between the emission and absorption cross sections of the sphere. We contend that this equivalence is sufficient to establish the necessary characteristics of thermal emission for our multiple sphere problem.

To demonstrate, we note that thermal emission by an isolated sphere can be modeled by a distribution of randomly oriented dipole point sources within the sphere. Each dipole radiates a field that is uncorrelated with all other dipoles. Because of the lack of correlation among the sources, interference among waves emitted from separate dipoles will have no net effect on the total power radiated from the sphere. Moreover, because of the random orientation, the net wave emitted will be unpolarized. It is therefore consistent to compute the net power of the field emitted from the entire distribution of dipoles by computing the power of the field produced by a single dipole and then averaging (i.e., integrating) the power over the volume of the sphere and the orientation of the dipole.

A single dipole, located at an arbitrary point $\mathbf{r}_d$ inside the sphere, will produce an outgoing wave from its origin. By using the addition theorem (applied with a propagation constant corresponding to the particle material, i.e., $k \to \mathsf{m}k$), the outgoing wave from the dipole can be transformed into an outgoing VSH expansion, centered about the sphere origin, that is convergent at the interior surface of the sphere. We will denote the VSH expansion coefficients of this wave as $d_{mnp}(\mathbf{r}_d)$.

Each internal wave component will generate an external, outgoing VSH wave component given by

$$a_{mnp} = \bar{d}_{np} d_{mnp}(\mathbf{r}_d) \tag{18}$$

where $\bar{d}_{np}$ denote the "transmission" coefficients of the sphere; these quantities are typically encountered in the solution for scattering by a layered sphere [11]. The total power radiated from the sphere will be $4\pi C_{\text{emis}} I_{b,\lambda} d\lambda$, with C_{emis} determined from integration of the Poynting vector over the surface of the sphere for the fixed dipole location $\mathbf{r}_d$, followed by integration of the dipole over volume and orientation. This results in

$$C_{\text{emis}} = -\frac{2\pi}{k^2} \sum_{n,m,p} \langle |a_{mnp}|^2 \rangle = -\frac{2\pi}{k^2} \sum_{n,m,p} |\bar{d}_{np}|^2 \langle |d_{mnp}(\mathbf{r}_d)|^2 \rangle \tag{19}$$

in which $\langle \cdots \rangle$ denotes integration over volume and orientation. The minus sign is included to make the cross section positive since power leaving the sphere would naturally be negative per our sign convention. We now use the fact that the emission cross section must equal the absorption cross section of the sphere, given by

$$C_{\text{emis}} = \frac{2\pi}{k^2} \sum_{n,m,p} |\bar{a}_{np}|^2 \bar{b}_{np} \tag{20}$$

In addition, the emitted intensity from the isothermal sphere must be isotropic, and this implies that the first, second, and higher directional moments of the volume-averaged Poynting vector—which would represent the coefficients in a Legendre polynomial expansion of the emitted intensity—must be zero. From this we can conclude that the volume and orientation averaging process must result in an orthogonal operation, so that

$$\langle d_{mnp}(\mathbf{r}_d) d^*_{klq}(\mathbf{r}_d) \rangle = \left| \frac{\bar{a}_{np}}{\bar{d}_{np}} \right|^2 \bar{b}_{np} \delta_{nl} \delta_{mk} \delta_{pq} \tag{21}$$

The orthogonality property identified in Eq. (21) is not explicitly needed to match Eqs. (19) and (20), yet it will play a role in the subsequent analysis.

We can now extend these results to the interaction matrix description of the scattered field. Since $a^j = T^{j-i} p^i$ describes the scattered field at j produced by an external plane wave (regular VSH) excitation at i, then $a^j = T^{j-i}(\bar{d}/\bar{a}) d^i$ will generate the scattered field due to an internal outgoing VSH excitation within i. Referring to Eq. (11), the absorption cross section at j, due to the power emitted at i, would therefore be

$$C_{\text{emis},j-i} = \frac{2\pi}{k^2} \sum_{\mu} \sum_{\nu,\nu'} \bar{b}^j_\mu T^{j-i}_{\mu\nu} \frac{\bar{d}^i_\nu}{\bar{a}^i_\nu} \left(T^{j-i}_{\mu\nu'} \frac{\bar{d}^i_{\nu'}}{\bar{a}^i_{\nu'}} \right)^* \langle d^i_\nu(\mathbf{r}_d) (d^i_{\nu'}(\mathbf{r}_d))^* \rangle$$

$$= \frac{2\pi}{k^2} \sum_{\mu} \sum_{\nu} \bar{b}^j_\mu |T^{j-i}_{\mu\nu}| \bar{b}^i_\nu \tag{22}$$

which is precisely the result obtained in Eq. (15). Likewise, the formula for the emission cross section, in Eq. (14), can be obtained via the dipole model by the calculation of the net power leaving sphere i.

2.3 Evaluation and Properties of the Emission and Exchange Cross Sections

2.3.1 Convergence. Narayanaswamy et al. observed that the convergence, in harmonic order, of their series expression for the radiative conductance between a pair of spheres is highly dependent on the gap distance $kd_{1-2} = k|\mathbf{r}_{1-2}| - ka_1 - ka_2$ separating the spheres [7]. In the limit of zero gap (i.e., spheres in contact), the series does not converge. This behavior can be anticipated by examining the properties of the interaction T^{i-j} matrix. Considering the specific case of two identical spheres, the T^{1-2} matrix will be given by the Born expansion of Eq. (10),

$$T^{1-2} = \bar{a} H^{1-2} \bar{a} + \bar{a} H^{1-2} \bar{a} H^{2-1} \bar{a} H^{1-2} \bar{a} + \cdots \tag{23}$$

in which matrix multiplication is implied. The above equation can now be substituted into Eq. (15), and the ratio test can be applied to determine the series convergence in harmonic order n since all of the terms in the series will be positive. After lengthy manipulations, it turns out that the ratio of the $n+1$ and n terms scale, in the limit of $n \to \infty$, as $(2x_S/(2x_S+kd))^4$. In the limit of $d \to 0$, we conclude that the series for the exchange cross section will not converge.

There is a simple physical explanation for this behavior. Our model takes the spheres to be at uniform yet distinct temperature, and heat transfer—via any mechanism—between two bodies at different temperatures will become infinite as the distance between the bodies vanishes. Narayanaswamy et al. suggested that the dielectric function would need to become a function of the wave vector to accurately model the radiative exchange for vanishing gap thicknesses [7]. Alternatively, we would submit that the model would need to incorporate finite-rate conductive heat transfer within each of the spheres to maintain temperature continuity at the contact point between the spheres. It is also important to remark that the gap-sensitive convergence behavior of the emission cross sections does not cross over to the absorption cross section. That is, even though $C_{\text{emis},1}$ and $C_{\text{emis},1-2}$ will become unbounded as the spheres approach contact, their difference—which is the absorption cross section of sphere 1—will remain finite. Furthermore, the absorption cross section will typically converge within the order limit prescribed by the Lorenz–Mie criterion for the individual spheres.

2.3.2 Calculation for Small Gap Thickness. An implication of the previous section is that the algorithms and codes that were

designed to calculate the plane wave absorption properties of the spheres cannot be blindly applied to the calculation of the emission and exchange cross sections for conditions of $kd \ll 1$. In such regimes the number of harmonic orders required for the convergence of the emission and exchange cross sections will significantly exceed the usual Lorenz–Mie truncation limit for the spheres [7]. The evaluation of the terms in Eq. (10), for such conditions, will require the calculation of Bessel and Hankel functions for orders that are significantly greater than the magnitude of their arguments; algorithms that are not specifically designed for such tasks are likely to fail due to overflow/underflow and/or loss-of-precision errors. In addition, the solution of Eq. (10) obviously becomes more difficult as the number of orders increases.

A computational strategy which circumvents these difficulties can be identified for the two-sphere case. We define a new interaction matrix Q via

$$Q_{\mu\nu}^{i-j} = (\bar{b}_{\mu}^{i})^{1/2} T_{\mu\nu}^{i-j} (\bar{b}_{\nu}^{j})^{1/2} \tag{24}$$

so that the exchange cross section is

$$C_{\text{emis},i-j} = \frac{2\pi}{k^2} \sum_{\mu} \sum_{\nu} |Q_{\mu\nu}^{i-j}|^2 \tag{25}$$

For the two-sphere case, and assuming that both spheres are identical, an interaction equation for Q^{1-2} can be obtained by combining Eq. (10) for $(i,j)=(2,2)$ and $(1,2)$ and eliminating T^{2-2} to yield

$$Q_{\mu\nu}^{1-2} - \sum_{\mu',\nu'} G_{\mu\mu'}^{1-2} G_{\mu'\nu'}^{2-1} Q_{\nu'\nu}^{1-2} = G_{\mu\nu}^{1-2} \bar{a}_{\nu} \bar{b}_{\nu} \tag{26}$$

with

$$G_{\mu\nu}^{i-j} = \bar{a}_{\mu} (\bar{b}_{\mu})^{1/2} H_{\mu\nu}^{i-j} (\bar{b}_{\nu})^{-1/2} \tag{27}$$

When both n and l are much greater than the translation distance $2x_S + kd$, we apply the large-order asymptotic limit to the Bessel and Hankel functions in the expansion for the translation matrix. The only significant terms for this case are for $p=q=1$. We can also align the spheres along a common z axis, for which the azimuthal degrees will become decoupled, i.e., $m=k$. These conditions result in

$$\begin{aligned} G_{mn1ml1}^{1-2} &\approx \tilde{G}_{mnl}^{1-2} \\ &= -(-1)^{m+n} \frac{(2n+1)(\epsilon-1)}{n(\epsilon+1)+1} \left(\frac{enl}{2\pi}\right)^{1/2} \left(2 + \frac{kd}{x_S}\right)^{-n-l-1} \\ &\quad \times \frac{(1+n+l)^{1+n+l}}{(2n+1)^{n+1/2}(2l+1)^{n+1/2}} \\ &\quad \times \frac{\Gamma\left(n+\frac{1}{2}\right)\Gamma\left(l+\frac{1}{2}\right)\Gamma(n+l+1)}{2\Gamma\left(n+l+\frac{3}{2}\right)} \\ &\quad \times (\Gamma(n+m+1)\Gamma(n-m+1)\Gamma(l+m+1) \\ &\quad \times \Gamma(l-m+1))^{-1/2} \end{aligned} \tag{28}$$

with

$$\tilde{G}_{mnl}^{2-1} = (-1)^{n+l} \tilde{G}_{mnl}^{1-2} \tag{29}$$

and

$$\bar{a}_{n1} \bar{b}_{n1} \approx \tilde{s}_n = -\frac{\mathrm{i}(2n+1)\epsilon''}{(\epsilon^* - 1)(1 + n(1+\epsilon))} \tag{30}$$

where $\epsilon = \mathrm{m}^2 = \epsilon' + \mathrm{i}\epsilon''$ is the complex permittivity of the sphere and $e = 2.71828$.

The procedure to calculate the emission cross sections is to first calculate $G_{mnp\ mlq}^{1-2}$ using the exact formulas up to an order n, $l = L_E$, and then use the approximate $\tilde{G}$ and $\tilde{s}$ formulas for higher orders. For a given order n, $\tilde{G}_{mnl}$ will be a maximum for $n=l$ and falls off rapidly in magnitude as $|n-l|$ increases; in this respect we found it necessary to include $\tilde{G}$ values only for $|n-l| \leqslant 100$. Equation (26) was then solved via the Born expansion per Eq. (23), and the exchange cross section was obtained from Eq. (25). Each multiplication stage in the Born expansion was carried to a maximum order n that satisfied a set convergence criterion for Eq. (25). The random-orientation absorption cross section of the spheres are calculated via Eq. (11)—for which the typical order truncation of $n = L_S \sim x_S$ is employed—and the emission cross section is obtained from the sum of the exchange and absorption cross sections.

2.3.3 Two-Sphere Case: Limiting Behavior for Small Gap Thickness. We can use the Born approximation in Eq. (23) and the asymptotic formulas in Eqs. (28) and (30) to develop an approximate formula for the exchange cross section for a pair of spheres in the limit of vanishing gap thickness. Key assumptions are that (1) the terms of order $n \approx x_S$ contribute a relatively small fraction to the summations in Eq. (25), so that the large-order approximations can be applied to all terms, and (2) only the first term in the Born series is retained. This results in

$$C_{\text{emis},1-2}(kd \ll 1) \approx \frac{2\pi}{k^2} \sum_{n=1}^{\infty} \sum_{l=1}^{\infty} \sum_{m=-(n,l)}^{(n,l)} |\tilde{G}_{mnl}^{1-2} \tilde{s}_n|^2 \tag{31}$$

The sum over m can be exactly represented by the generalized hypergeometric functions, which can then be approximated in terms of gamma functions for large n,l. Stirling's formula can then be applied to the gamma functions, and we again take the limiting forms of the resulting formula for large n,l. The substitution of $s=n+l$ and $t=n-l$ is then used to eliminate n and l, and the summations over s and t are approximated by integrals. The resulting formula is

$$\begin{aligned} C_{\text{emis},1-2}(kd \ll 1) \approx \frac{2\pi}{k^2} &\left(\frac{\epsilon''}{(\epsilon'+1)^2 + \epsilon''^2}\right)^2 \left(2 + \frac{d}{a}\right)^{-2} \\ &\times \left(\ln\left(\frac{2 + d/a}{2}\right)\right)^{-1} \end{aligned} \tag{32}$$

Taking the limit $kd \to 0$ yields the sought result of

$$C_{\text{emis},1-2}(kd \to 0) \approx \frac{\pi}{k^2} \left(\frac{\epsilon''}{(\epsilon'+1)^2 + \epsilon''^2}\right)^2 \frac{a}{d} \tag{33}$$

The $1/d$ dependence in Eq. (33) shows that emissive exchange, in the vanishing gap limit, is analogous to conductive heat transfer. Indeed, Narayanaswamy et al. [7] defined a thermal emission conductance via $\kappa_{\text{emis}} = q_{\text{emis},i-j} d/(T_1 - T_2)$ in the limit of $T_1 \to T_2$, and our analysis would indicate that this conductance would approach a constant as the gap approached zero. This behavior is consistent with the results shown in Ref. [7].

2.3.4 Two-Sphere Case: Limiting Behavior for Large Gap Thickness. In principle, the exchange of thermal radiation between two spheres that are separated by a sufficiently large distance can be described by radiative transfer theory. In this case, a sufficiently large distance would correpond to the situation in which each sphere is in the far-field zone of the radiation emitted from its neighbor. In addition, widely spaced spheres would have approximately equal emission and absorption cross sections because field interactions among the spheres would not significantly perturb the sphere properties from their single-scattering values. The exchange cross section would then be approximated by

$$C_{\text{emis},i-j} = \langle C_{\text{abs},i} \rangle F_{i-j} \frac{\langle C_{\text{abs},j} \rangle}{\pi a_j^2} \tag{34}$$

in which F_{i-j} is the geometrical radiative configuration factor from sphere i to j. This quantity describes the fraction of emitted energy from sphere i that intercepts sphere j assuming a geometrical limit. The presence in the formula of the absorption/geometrical cross section ratio of j—which defines the absorption

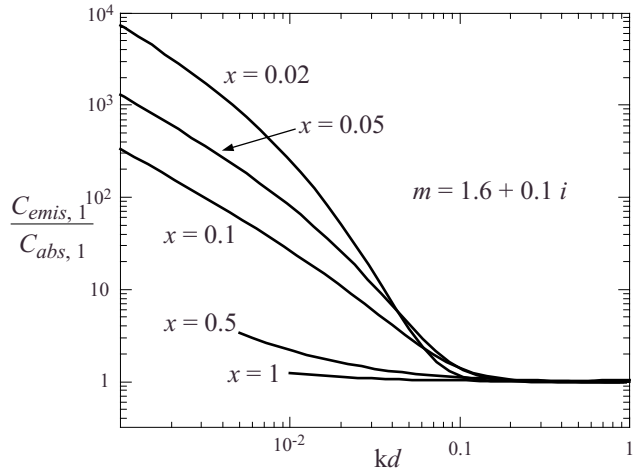

Fig. 2 Emission/absorption ratio for a sphere in a two-sphere cluster as a function of gap thickness *kd*

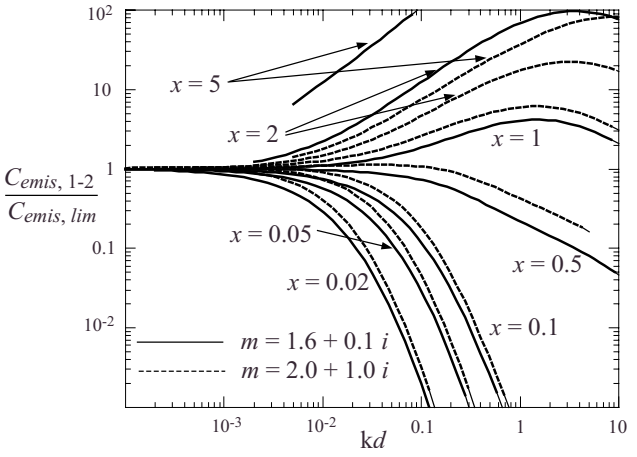

Fig. 3 Exchange cross section, scaled with a limiting value, as a function of gap thickness *kd*

efficiency factor $\langle Q_{\mathrm{abs},j}\rangle$—represents an ad hoc correction to account for the effect of finite wavelength.

3 Results and Discussion

Although we have derived general formulas for the emission and exchange among an arbitrary number of closely spaced spheres, we will present and discuss results only for the case of two identical spheres. We do this to minimize the parameter space so that the effects of sphere spacing on emission and exchange can be better isolated and—perhaps more importantly—because we are currently incapable of accurately solving the emission and exchange problem for more that two spheres. We will also present spectral as opposed to wavelength-integrated results; doing so allows us to treat refractive index as a free parameter and obviates the need to characterize the refractive index of a specific material.

We focus first on the emission behavior as the sphere pair approaches contact. Shown in Fig. 2 is the ratio of the emission and absorption cross section, $C_{\mathrm{emis},1}/\langle C_{\mathrm{abs},1}\rangle$, for the two-sphere cluster as a function of dimensionless gap distance kd. Per our discussion in Sec. 2, the quantity $C_{\mathrm{emis},1}/\langle C_{\mathrm{abs},1}\rangle$ can be interpreted as the ratio of the total emission from sphere 1 to the emission transferred from 1 to the environment. The refractive index of the spheres is $\mathsf{m}=1.6+0.1\mathrm{i}$, and curves are shown for size parameters ranging from 0.02 to 1. Regardless of the size parameter, the emission/absorption ratio approaches unity once kd exceeds around 0.1. As kd decreases from 0.1, the emission/absorption ratio increases at a rate that is highly dependent on the size parameter. This effect is due almost entirely to an increase in the emission cross section; the absorption cross section, for the particular value of m, is not strongly dependent on the separation distance.

The behavior seen in Fig. 2 illustrates the effects of evanescent field coupling between the spheres. The fact that the onset of the coupling effects, for the different x values, occurs for the same value of kd would indicate that the thickness of the evanescent field layer is the same for all sphere size parameters at around $\sim 0.1/k$. Likewise, the amplified effects of coupling for the smaller spheres would also suggest a constant-thickness evanescent field layer; the smaller spheres will have a larger fraction of their surface coupled to the layer as the spheres become closer, and this would result in a larger relative increase in the emission cross section. We have performed additional calculations for spheres with a refractive index of $\mathsf{m}=2+1\mathrm{i}$ (not shown), and the behavior of $C_{\mathrm{emis},1}/\langle C_{\mathrm{abs},1}\rangle$ with kd is similar to that in Fig. 2 in that onset of near-field coupling occurs around $kd\sim 0.1$.

The results in Fig. 2 indicate that the emission cross section approaches an inverse-linear relationship with kd as the gap approaches zero, which is consistent with our limiting-gap analysis. To examine this effect further, we show in Fig. 3 the exchange cross section scaled by the limiting form in Eq. (33) as a function of kd and with size and refractive index as parameters. For the particular refractive indices examined here, i.e., $\mathsf{m}=1.6+0.1\mathrm{i}$ and $2+1\mathrm{i}$, the exchange cross sections for $x\leqslant 1$ asymptote to the limiting approximation in Eq. (33) as $kd\ll 1$. The results for larger size parameters appear to have the same trends, yet we were not able to obtain a converged solution, for these x values, for the sufficiently small kd values needed to check the limit.

We have also performed limited calculations of the emission and exchange cross sections for highly conducting materials, such as gold. The results for these materials appear to follow the same general trends shown in Fig. 3—in that the exchange cross section becomes inversely proportional to kd for $kd\ll 1$—yet the conductivity value is somewhat different than that predicted in Eq. (33). That is, the curves in Fig. 3 for gold particles would asymptote to a constant other than unity. The inability of the limiting formula to accurately predict the behavior of metallic particles is likely a result of including only the first Born term in the approximation leading to Eq. (33). For the same reasons, we encountered significant numerical difficulties in finding converged solutions to Eq. (26) for metallic particles for small kd, and because of this we have put off the presentation of calculations for the metallic particles until we can resolve the numerical issues.

The last set of results will focus on the limiting behavior for $d/a\gg 1$, i.e., far-field exchange between the spheres. In Fig. 4 we plot $\pi a^2 C_{\mathrm{emis},1-2}/C^2_{\mathrm{abs},1}$ $(=Q_{\mathrm{emis},1-2}/Q^2_{\mathrm{abs},1}$, where Q denotes the efficiency factors) versus d/a for the same parameters in Fig. 3. We choose this scaling because, based on our analysis leading to Eq. (34), the quantity should become a function solely of d/a for $kd\gg 1$. The results in the plot show, for the parameters examined here, that this is indeed the case. We include in Fig. 4 the geometrical-optics configuration factor (labeled GO) calculated for a pair of identical spheres using a simple Monte Carlo algorithm. Note that all curves asymptote to the geometrical formula once d/a exceeds around $1/x$ or, equivalently, $kd\gg 1$.

The curves for $x\leqslant 0.1$ in Fig. 4 display a transitional region around $d/a\sim 10$, which is between the evanescent field and far-field regions. As x becomes smaller, the slopes in this region (note that the plot is on a log-log scale) appear to approach the value of -5, and the corresponding conductance between the spheres would have a dependence of d^{-6} in this region. It has been shown that the thermal emission conductance between two point dipoles scales as d^{-6}, and our results appear to be consistent with this

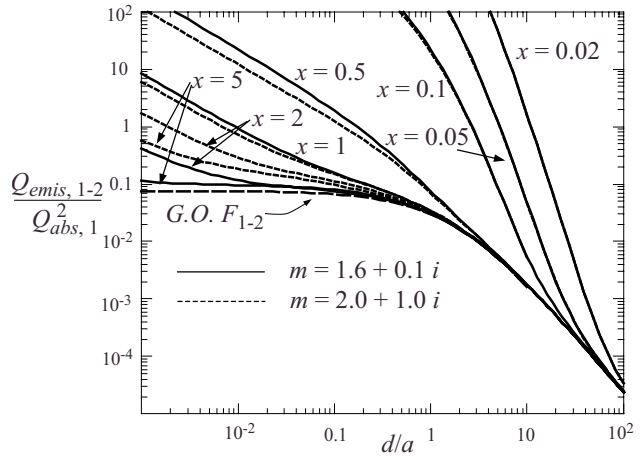

Fig. 4 Scaled exchange factor as a function of *d*/*a*

behavior for small x [7]. On the other hand, the results show that the region of the dipolelike behavior becomes increasingly small as the size parameters of the spheres increase.

4 Conclusions

We have presented an analysis of radiative emission and exchange among an ensemble of closely spaced, individually isothermal spheres. With regard to the theoretical framework of the problem, our analysis suggests that—for the case of neighboring spheres—the Rytov fluctuation-dissipation theory is not explicitly needed to identify the emission and exchange cross sections. Rather, these quantities can be deduced by the application of reciprocity and energy conservation principles to the solution to Maxwell's time harmonic wave equations for external (i.e., plane wave) excitation of the spheres. An asymptotic analysis of the exchange cross section indicates that the rate of emissive exchange between a pair of spheres becomes inversely proportional to d in the limit of $kd \to 0$.

Nomenclature

a = sphere radius
a^i_{mnp} = scattering expansion coefficient for sphere i
$\bar{a}_{np}$ = Lorenz–Mie coefficient
$\bar{b}_{np}$ = defined in Eq. (12)
C = cross section
d = gap distance between spheres, $=r_{1-2}-a_1-a_2$
$\mathbf{E}$ = electric field
G^{i-j} = scaled H^{i-j} matrix, Eq. (27)
H^{i-j} = outgoing VSH translation matrix
J^{i-j} = regular VSH translation matrix
k = $2\pi/\lambda$
m = refractive index, $=\mathsf{n}+\mathsf{i}\mathsf{k}$
Q = efficiency factor
Q^{i-j} = scaled T^{i-j} matrix, Eq. (24)
$\mathbf{r}$ = position vector
T_i = temperature of sphere i
T^{i-j} = interaction T matrix for spheres i and j
x_i = sphere size parameter, $=ka_i=2\pi a_i/\lambda$

Greek Symbols

ϵ = permittivity, $=\mathsf{m}^2=\epsilon'+\mathsf{i}\epsilon''$
λ = wavelength

References

[1] Brunning, J. H., and Lo, Y. T., 1971, "Multiple Scattering of EM Waves by Spheres. Part I. Multipole Expansion and Ray-Optical Solutions," IEEE Trans. Antennas Propag., **AP-19**, pp. 378–390.

[2] Mackowski, D. W., and Mishchenko, M. I., 1996, "Calculation of the *T* Matrix and the Scattering Matrix for Ensembles of Spheres," J. Opt. Soc. Am. A, **13**, pp. 2266–2278.

[3] Fuller, K. A., and Mackowski, D. W., 2000, "Electromagnetic Scattering by Compounded Spherical Particles," *Light Scattering by Nonspherical Particles: Theory, Measurements, and Applications*, M. I. Mishchenko, J. W. Hovenier, and L. D. Travis, eds, Academic, Chap. 8.

[4] Kattawar, G. W., and Eisner, M., 1970, "Radiation From a Homogeneous Isothermal Sphere," Appl. Opt., **9**, pp. 2685–2690.

[5] Rytov, S. M., 1959, *Theory of Electric Fluctuations and Thermal Radiation*, Air Force Cambridge Research Center, Bedford, MA.

[6] Mulet, J.-P., Joulain, K., Carminati, R., and Greffet, J.-J., 2001, "Nanoscale Radiative Heat Transfer Between a Small Particle and a Plane Surface," Appl. Phys. Lett., **78**, pp. 2931–2933.

[7] Narayanaswamy, A., Chen, D.-Z., and Chen, G., 2006, "Near-Field Radiative Energy Transfer Between Two Spheres," ASME Paper No. IMECE2006-15845.

[8] Mishchenko, M. I., Travis, L. D., and Lacis, A. A., 2006, *Multiple Scattering of Light by Particles: Radiative Transfer and Coherent Backscattering*, Cambridge University Press, Cambridge, England.

[9] Mackowski, D. W., 1994, "Calculation of Total Cross Sections of Multiple Sphere Clusters," J. Opt. Soc. Am. A, **11**, pp. 2851–2861.

[10] Mackowski, D. W., 2001, "An Effective Medium Method for Calculation of the *T* Matrix of Aggregated Spheres," J. Quant. Spectrosc. Radiat. Transf., **70**, pp. 441–464.

[11] Bohren, C. F., and Huffman, D. R., 1983, *Absorption and Scattering of Light by Small Particles*, Wiley, New York.

Development of a Transparent Heater to Measure Surface Temperature Fluctuations Under Spray Cooling Conditions

A. R. Griffin[1]
Department of Mechanical, Materials and Aerospace Engineering,
University of Central Florida,
Room 307,
Orlando, FL 32816
e-mail: al366353@ucf.edu

A. Vijayakumar
School of Electrical Engineering and Computer Science,
University of Central Florida,
Room 307,
Orlando, FL 32816

R.-H. Chen
Department of Mechanical, Materials and Aerospace Engineering,
University of Central Florida,
Room 307,
Orlando, FL 32816

K. B. Sundaram
School of Electrical Engineering and Computer Science,
University of Central Florida,
Room 307,
Orlando, FL 32816

L. C. Chow
Department of Mechanical, Materials and Aerospace Engineering,
University of Central Florida,
Room 307,
Orlando, FL 32816

A heater designed to monitor surface temperature fluctuations during pool boiling and spray cooling experiments while the bubbles are simultaneously being observed has been fabricated and tested. The heat source was a transparent indium tin oxide (ITO) layer commercially deposited on a fused quartz substrate. Four copper-nickel thin film thermocouples (TFTCs) on the heater surface measured the surface temperature, while a thin layer of sapphire or synthetic fused silica provided electrical insulation between the TFTCs and the ITO. The TFTCs were microfabricated using the lift-off process to deposit the nickel and copper metal films. The TFTC elements were 50 μm wide and overlapped to form a 25×25 μm^2 junction. A DAQ program recorded the TFTC voltages at a sampling rate of 50 kHz and sent a trigger to a high-speed camera to synchronize bubble images with the surface temperature data. As the bubbles and their contact rings grew over the TFTC junction, correlations between bubble behavior and surface temperature changes were demonstrated.
[DOI: 10.1115/1.2952761]

Keywords: thin film thermocouples, pool boiling, spray cooling, bubble nucleation

Introduction

Critical issues in pool boiling have been studied by analyzing the local heat fluxes and temperature fluctuations caused by bubble nucleation on a heated surface. These pool boiling bubbles can be observed in the isolated bubble regime, which occurs at low heat fluxes up to about 10% of the critical heat flux (CHF) [1]. At higher superheats closer to CHF, individual bubbles cannot be differentiated and monitored, and therefore correlating data between bubble behavior and local heat removal cannot be obtained.

Spray cooling can provide up to ten times higher CHF than that of pool boiling [2], and therefore can be used to remove heat from surfaces operating at much higher heat fluxes. Isolated bubbles have been observed in spray cooling at heat fluxes close to CHF [3], allowing bubble behavior over most of the heat transfer curve to be examined. An experimental device designed to study these bubbles and the corresponding surface thermal variations could provide details about the spray cooling heat transfer mechanism and address the unresolved issues that still exist for spray cooling conditions.

The need for a transparent heater to measure local temperature changes while simultaneously observing surface and secondary bubbles during spray cooling is evident. This study demonstrates the development of a transparent heater with a surface temperature resolution of 25×25 μm^2 that has been tested under FC-72 pool boiling conditions.

Background

Many measurement techniques have previously been used to look at local temperature and heat flux values under pool boiling and spray cooling conditions. In 1961, Moore and Mesler [4] used a flush-mounted surface thermocouple to look at the surface temperature fluctuations under a single pool boiling bubble on a nichrome heater. This surface thermocouple consisted of an alumel metal wire concentrically inserted through a chromel metal tube, with the wire electrically insulated from the tube. A thin nickel film deposited at one end of the tube connected the wire and tube to form a 127 μm diameter junction. In a follow up experiment [5], one photograph of the bubble during each bubble lifetime was taken from above the heater to determine the size of the bubble at a certain position on the surface temperature trace. Cooper and Lloyd [6] in 1969 developed a device with four germanium thin film thermometers, as small as 75×75 μm^2 each, which measured the surface temperatures as a single pool boiling bubble successively grew over each thermometer. A camera provided a side-view of the bubbles to observe bubble growth and departure and to interpret the simultaneous temperature fluctuations.

More modern fabrication techniques, as well as higher resolution data acquisition and imaging systems, have been used in the past decade to continue the examination of pool boiling and spray cooling heat transfer. Sako and Kikuchi [7] fabricated eight copper-nickel thin film thermocouples (TFTCs) to monitor the surface temperature fluctuations over a 10×10 mm^2 heated area. These TFTCs had a junction size of 50×200 μm^2. A nichrome film deposited on the bottom surface of the glass substrate completely covered the heated area, so bubbles were viewed from the side with a high-speed camera synchronized with the temperature fluctuations. Pool boiling experiments by Yaddanapudi and Kim [8], Demiray and Kim [9], and Myers et al. [10] used an array of

[1]Corresponding author.

Contributed by the Heat Transfer Division of ASME for publication in the JOURNAL OF HEAT TRANSFER. Manuscript received May 7, 2007; final manuscript received March 24, 2008; published online August 28, 2008. Review conducted by Minking Chyu. Paper presented at the 2007 ASME-JSME Thermal Engineering Conference and Summer Heat Transfer Conference (HT2007), Vancouver, British Columbia, Canada, July 8–12, 2007.

96 microheaters arranged in a 10×10 pattern to monitor the local heat flux under constant surface temperature conditions or the local surface temperature under constant surface heat flux conditions. These microheaters were platinum resistance heaters deposited on quartz and silica substrates. The entire heater array was 2.7×2.7 mm^2 when the microheaters were each 270×270 μm^2 [8] and 1×1 mm^2 when the microheaters were each 100×100 μm^2 [9,10]. These devices were considered to be semitransparent and allowed the bubble to be viewed from below the heater. A study by Moghaddam and Kiger [11] involved a heater comprised of layers of silicon, benzocyclobutene, resistance temperature detector (RTD) sensors, and a thin film heat source on the bottom of the substrate. The 44 temperature sensors were deposited 0.5 μm below the pool boiling surface in a radial pattern and had 22–40 μm spatial resolution. Temperature measurements were recorded under individual bubbles formed from artificial cavities on the heater surface while side-view images of the bubbles were taken with a high-speed camera. A different type of temperature sensor called a microthermocouple was used by Buchholz et al. [12] to measure surface temperature changes over the entire pool boiling curve. The two elements of the microthermocouples were a Constantan wire and a thin copper film that formed a 38 μm thermocouple junction. There were 36 microthermocouples placed in a 1 mm^2 area and positioned 3.6 μm below the surface of the copper heater.

In addition to the pool boiling experiments described above, a few studies have also looked at the surface temperature and heat flux distributions that exist in spray cooling. Guinn and Banerjee [13] fabricated chromel-alumel TFTCs on a silicon substrate in order to measure the temperature fluctuations that appeared while single spray droplets impacted the heated surface. The TFTC junctions were less than 50 μm wide and heaters with two to four TFTCs on the surface were tested. There were no images taken of the surface during this experiment. Another study of single droplet spray cooling was performed by Lee et al. [14] using a 96 microheater array like the one described above with a 270×270 μm^2 individual heater resolution [8]. Additional spray cooling experiments utilizing a single nozzle [15] and multiple nozzles [16] were completed with an overall array size of 7×7 mm^2 and an individual microheater size of 700×700 μm^2. These heater arrays were again semitransparent since the pattern of the platinum resistance heaters covered about 50% of the transparent silica substrate and allowed images to be taken of the surface from below the heater.

The measurement device that has been developed in this study is the first to be completely transparent, allowing clear bubble images to be obtained from below the heater and for bubble behavior to be closely observed. In addition, this experiment incorporates many of the advantages of the previous experiments described above. The thermocouple junctions are of a similar or smaller size than all of the preceding temperature sensors, providing excellent spatial resolution and fast response time. The data sampling rate and camera frame rate are as high, or higher, than the prior experiments in order to capture the details of the temperature fluctuations and corresponding bubble growth. This experiment is the first to record bubble images from underneath a transparent heater at high frame rates while simultaneously sampling small temperature sensors at a very high frequency.

Experimental Design

Heater. A 17×17 mm^2 transparent heater, seen in Fig. 1, was assembled in order to observe pool boiling and spray cooling bubbles on the top surface of the heater using a camera positioned below the heater. The base of the heater was a 0.5 mm thick fused quartz substrate. A transparent layer of indium tin oxide (ITO) was commercially deposited over the entire quartz substrate to provide heat to the surface of the heater. These ITO films had a sheet resistance of 64 Ω/sq. Two aluminum power pads that were 2.5 $\times10$ mm^2 and 100 nm thick were deposited on opposite sides of the heater. Power was supplied to the ITO by wires epoxied to these aluminum films. Layers of 0.2 mm thick sapphire or 0.1 mm thick synthetic fused silica were mounted to the top of the ITO with optical cement, covering the 12×17 mm^2 area between the aluminum power pads. These layers provided electrical insulation between the ITO and the TFTCs. This entire configuration of quartz, ITO, cement, and insulation layer was transparent below the heated area.

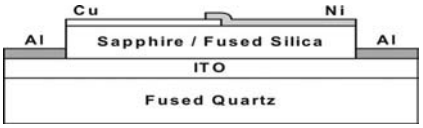

Fig. 1 Side-view cross section of the heater

Thin Film Thermocouples. TFTCs were designed to monitor the surface temperature fluctuations that occur during pool boiling and spray cooling. An overhead view of the heater can be seen in Fig. 2, where the arrows indicate the locations of the TFTC junctions. The four TFTCs, each composed of a copper and a nickel element, were deposited on top of the insulation layer. These TFTCs were fabricated in a clean room using a photolithography method called the lift-off process. The TFTCs were approximately 40 nm thick and 50 μm wide, and the two metal films overlapped to form 25×25 μm^2 offset junctions. A mask aligner was used to ensure a consistent junction size. The 2×2 mm^2 squares on the opposite sides of the heater from the power pads are the thermocouple pads. Thin copper and nickel wires were epoxied to these copper and nickel pads with an electrically conducting silver epoxy. An ice point dry well maintained the reference junction temperature at 0 °C. Before the heater was placed into the experiment, each TFTC was calibrated in an FC-70 constant-temperature bath. The TFTC calibration curves were stable and repeatable and corresponded to the known bulk wire copper-nickel temperature coefficient.

Experiment Setup. A diagram of the experiment setup used for this pool boiling study can be seen in Fig. 3. The heater was mounted on a pyramid-shaped platform in an elevated acrylic chamber that was entirely sealed with silicone. An opening was constructed at the top of the pyramid to create a viewing area under the heated portion of the heater. The heater was submerged in an FC-72 pool to about 3 cm beneath the liquid surface. A tubular heater surrounding the base of the pyramid heated the FC-72 to saturation and was regulated by a thermocouple in the liquid pool that was connected to a proportional-integral-

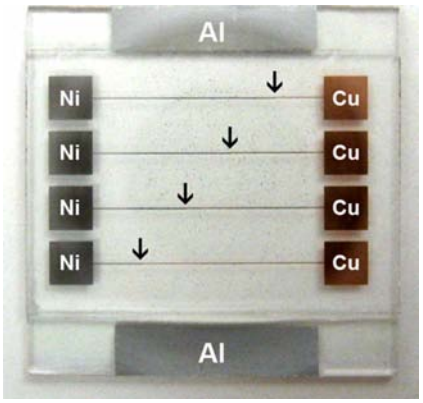

Fig. 2 Top-view photograph of the heater (arrows indicate TFTC junctions)

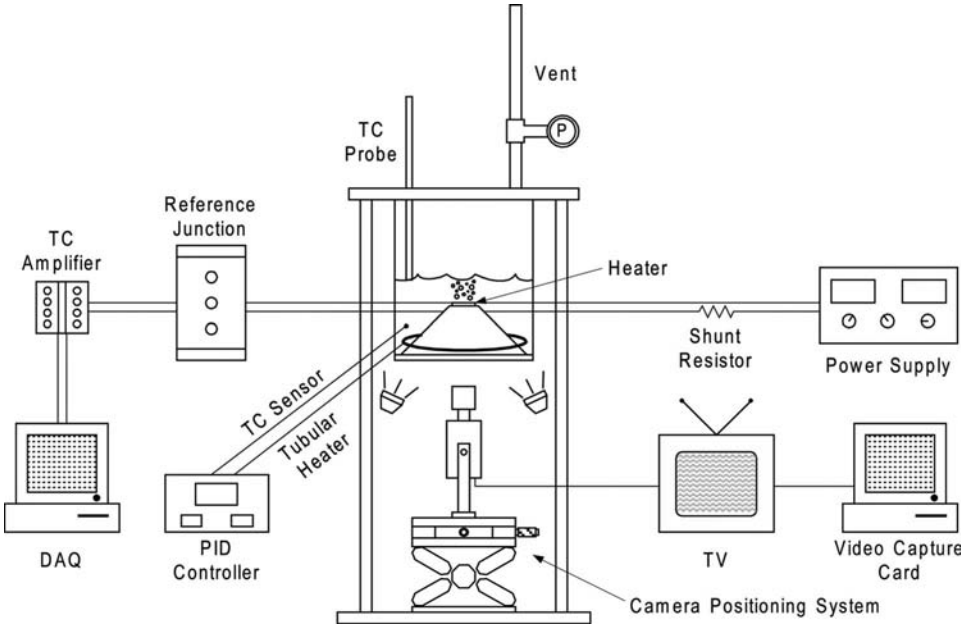

Fig. 3 Diagram of the experiment setup

derivative (PID) controller. An open vent at the top of the chamber maintained the experiment at atmospheric pressure. Dissolved gases escaped through this vent, made from a long copper tube, while the thin film heater as well as the tubular heater vigorously boiled the FC-72 during degassing. A thermocouple probe monitored the temperature of the liquid-vapor interface to ensure that the dissolved gas concentration was sufficiently low. This procedure is detailed by Rini et al. [17]. Power was supplied to the heater with a 1000 W (maximum) dc power supply. The current was calculated from the voltage measured across a low-resistance shunt resistor.

A programmable gain amplifier amplified the voltages produced by the TFTCs by a factor of 1000. A 200 kHz data acquisition card along with a LabVIEW program recorded these voltages. Four channels were used, one for each of the four TFTCs, and each channel was sampled at 50 kHz for 1 s. LabVIEW software was also used to digitally filter the voltages to reduce some of the noise components in the signal.

A high-speed charge coupled device (CCD) camera was mounted below the heater to observe the bubbles growing on the top surface of the heater. The camera was attached to an *xy*-stage, which allowed the camera position to be horizontally adjusted so that the entire heated surface could be scanned. The camera recorded bubble images at 2000, 4000, and 8000 frames per second. The images were viewed and measured from a television screen with the TFTC width serving as the reference length. The images were also examined frame by frame with a video capture card. A trigger incorporated into the LabVIEW program allowed the bubble images from the camera to be synchronized with the TFTC voltages from the heater.

Rini et al. [17] reported that FC-72 pool boiling bubbles at low heat fluxes had an 8–10 ms bubble lifetime and a 400–500 μm bubble departure diameter. It was important to confirm that the spatial resolution, temporal resolution, and camera frame rate were sufficient to capture the details of the bubble behavior and surface temperatures that occurred in this experiment. The TFTC junction size was 25×25 μm^2, significantly smaller than the bubble departure diameter and therefore able to capture localized temperature fluctuations during bubble growth. The 50 kHz sampling rate for each TFTC recorded 50 temperature values for each millisecond of the 8–10 ms bubble lifetime. In addition, the thermal response time of the TFTC was known to be less than 1 μs [18,19]. These values ensured that no details of the temperature fluctuations were overlooked. The camera simultaneously recorded 2 frames for every millisecond of the bubble lifetime at a 2000 frames per second frame rate, allowing the bubble and contact ring growth rates to be observed. Higher frame rates are available to extract additional data from higher heat flux pool boiling and from spray cooling.

Uncertainty Analysis. Not all of the power supplied to the ITO was concentrated between the two power pads in the area of interest; some of the power was conducted to the outer areas of the heater. An analysis of the current flow established that approximately 70% of the input power was conducted through the center area of the heater. At a low heat flux of 1 W/cm^2, the uncertainty was ±0.02 W/cm^2. At a higher heat flux of 6 W/cm^2, the uncertainty was ±0.12 W/cm^2.

The uncertainty in the temperature values measured by the TFTCs had many sources. The platinum resistance thermometer used during calibration (±0.018°C), the reference junction dry well (±0.02°C), the DAQ resolution (±0.11°C), the noise in the voltage signal (±0.2°C), and the interpolation from the calibration curve (±0.1°C) all contributed. The total uncertainty in the TFTC temperature values was calculated to be less than ±0.5°C.

Results

Observations of bubble images showed that while a bubble grew out over a TFTC junction, its contact ring enlarged and crossed over the junction. As the bubble began to depart, the contact ring grew smaller and crossed over the junction again. Both of these events were associated with surface temperature drops. A set of these temperature drops for one bubble lifetime, and the corresponding bubble images, is displayed in Fig. 4. These data are taken at approximately 1 W/cm^2. These images cover about a 1 $\times1$ mm^2 area of the heater surface. The vertical line in the pictures is one TFTC, and the slight offset in the line indicated by an arrow in each image is the TFTC junction formed where the copper and nickel films overlap. The bubble in these images emerged from a nucleation site located just below the TFTC junction. The darker shadow seen below this bubble is an already departed bubble from an adjacent nucleation site. These images were taken at 2000 frames per second, so there are 25 TFTC voltage values

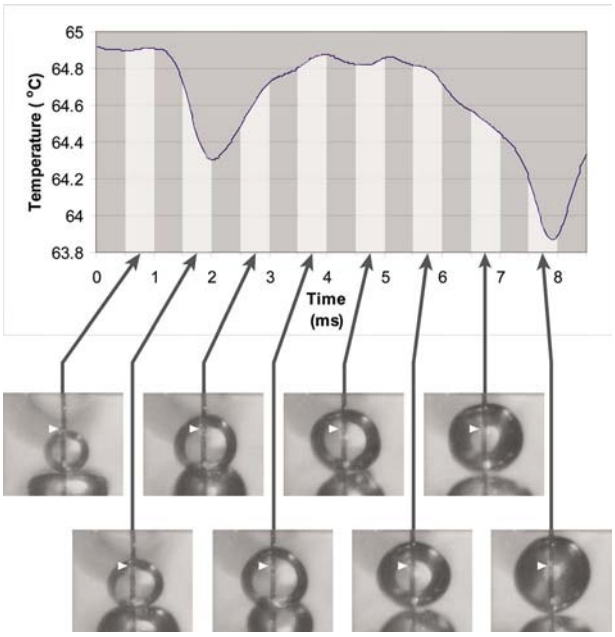

Fig. 4 Surface temperature and bubble images during one bubble lifetime (arrows indicate TFTC junction)

corresponding to every frame. This bubble had an 8.5 ms lifetime; therefore 17 frames exist between bubble emergence and bubble departure. Time on the temperature trace is shown in 0.5 ms increments, so there is one frame corresponding to every time increment. Eight of these frames are correlated to the surface temperature of the TFTC. The second image and the seventh image demonstrate the contact ring crossing over the TFTC junction during bubble growth and departure, respectively. It is apparent that the surface temperature drops are related to this movement of the contact ring. The first temperature drop that occurs while the contact ring is crossing the TFTC junction during bubble growth is about 0.6 °C and takes place over less than 1 ms. The second temperature drop, due to the contact ring crossing back over the TFTC junction during bubble departure, is about 1 °C and takes place over approximately 2 ms. These temperature drops occur more frequently at higher heat fluxes due to higher surface temperatures and an increase in the frequency and site density of the bubbles.

Conclusions

A heater with four TFTCs was developed to measure the surface temperature fluctuations that occur during pool boiling and spray cooling. The heater was transparent, which allowed high-speed images of the bubbles on the heater surface to be recorded from below the heater. The surface temperature and bubble images were taken simultaneously so that the temperature fluctuations could be correlated to bubble behavior. Initial pool boiling experiments observed that the surface temperature dropped when the bubble contact ring crossed over the TFTC junction during bubble growth and during bubble departure. The spatial and temporal resolution of this heater will be valuable in the continuing studies of pool boiling and spray cooling that investigate the local surface temperature and the heat flux behavior under bubbles.

References

[1] Incropera, F. P., and Dewitt, D. P., 2002, *Fundamentals of Heat and Mass Transfer*, Wiley, New York, Chap. 10, p. 598.
[2] Chow, L. C., Sehmbey, M. S., and Pais, M. R., 1997, "High Heat Flux Spray Cooling," Annu. Rev. Heat Transfer, **8**, pp. 291–318.
[3] Rini, D., Chen, R.-H., and Chow, L. C., 2002, "Bubble Behavior and Nucleate Heat Transfer in Saturated FC-72 Spray Cooling," ASME J. Heat Transfer, **124**, pp. 63–72.
[4] Moore, F. D., and Mesler, R. B., 1961, "The Measurement of Rapid Surface Temperature Fluctuations During Nucleate Boiling of Water," AIChE J., **7**(4), pp. 620–624.
[5] Rogers, T. F., and Mesler, R. B., 1964, "An Experimental Study of Surface Cooling by Bubbles During Nucleate Boiling of Water," AIChE J., **10**(5), pp. 656–660.
[6] Cooper, M. G., and Lloyd, A. J. P., 1969, "The Microlayer in Nucleate Pool Boiling," Int. J. Heat Mass Transfer, **12**, pp. 895–913.
[7] Sako, M., and Kikuchi, Y., 1997, "Bubble Growth and Transient Heat Transfer at the Onset of Boiling," Heat Transfer-Jpn. Res., **26**(7), pp. 484–492.
[8] Yaddanapudi, N., and Kim, J., 2001, "Single Bubble Heat Transfer in Saturated Pool Boiling of FC-72," Multiphase Sci. Technol., **12**(3–4), pp. 47–63.
[9] Demiray, F., and Kim, J., 2004, "Microscale Heat Transfer Measurements During Pool Boiling of FC-72: Effect of Subcooling," Int. J. Heat Mass Transfer, **47**, pp. 3257–3268.
[10] Myers, J. G., Yerramilli, V. K., Hussey, S. W., Yee, G. F., and Kim, J., 2005, "Time and Space Resolved Wall Temperature and Heat Flux Measurements During Nucleate Boiling With Constant Heat Flux Boundary Conditions," Int. J. Heat Mass Transfer, **48**, pp. 2429–2442.
[11] Moghaddam, S., and Kiger, K. T., 2006, "Microscale Study of the Boiling Process in Low-Surface-Tension Fluids," *Proceedings of ASME International Mechanical Engineering Congress and Exposition*, Chicago, IL.
[12] Buchholz, M., Auracher, H., Luttich, T., and Marquardt, W., 2006, "A Study of Local Heat Transfer Mechanisms Along the Entire Boiling Curve by Means of Microsensors," Int. J. Therm. Sci., **45**, pp. 269–283.
[13] Guinn, J. E., and Banerjee, D., 2006, "Experimental Study of Nanofluids for Droplet Cooling Applications Using Temperature Microsensors," *Proceedings of ASME International Mechanical Engineering Congress and Exposition*, Chicago, IL.
[14] Lee, J., Kim, J., and Kiger, K. T., 2001, "Time- and Space-Resolved Heat Transfer Characteristics of Single Droplet Cooling Using Microscale Heater Arrays," Int. J. Heat Fluid Flow, **22**, pp. 188–200.
[15] Horacek, B., Kiger, K. T., and Kim, J., 2005, "Single Nozzle Spray Cooling Heat Transfer Mechanisms," Int. J. Heat Mass Transfer, **48**, pp. 1425–1438.
[16] Horacek, B., Kim, J., and Kiger, K. T., 2004, "Spray Cooling Using Multiple Nozzles: Visualization and Wall Heat Transfer Measurements," IEEE Trans. Device Mater. Reliab., **4**(4), pp. 614–625.
[17] Rini, D., Chen, R.-H., and Chow, L. C., 2001, "Pool Boiling Characteristics Using FC-72," Exp. Heat Transfer, **14**, pp. 27–44.
[18] Zhang, X., Choi, H., Datta, A., and Li, X., 2006, "Design, Fabrication, and Characterization of Metal Embedded Thin Film Thermocouples With Various Film Thicknesses and Junction Sizes," J. Micromech. Microeng., **16**, pp. 900–905.
[19] Tong, H. M., Arjavalingam, G., Haynes, R. D., Hyer, G. N., and Ritsko, J. J., 1987, "High-Temperature Thin-Film Pt-Ir Thermocouple With Fast Time Response," Rev. Sci. Instrum., **58**(5), pp. 875–877.

Benchmark Studies for the Generalized Streamwise Periodic Heat Transfer Problem

Steven B. Beale
Fellow ASME
National Research Council of Canada,
Montreal Road,
Ottawa, ON, K1Y 0A5, Canada
e-mail: steven.beale@nrc-cnrc.gc.ca

This is a comparison of calculations performed with a scheme for handling streamwise-periodic boundary conditions with known solutions to the common problem of fully developed heat transfer in a plane duct. Constant value, constant flux, mixed boundary conditions, and linear wall flux (conjugate heat transfer) are all considered. Agreement is, in every case, near exact showing that the methodology may be applied with confidence to complex engineering problems with a variety of thermal wall boundary conditions. [DOI: 10.1115/1.2955477]

Keywords: computational fluid dynamics, periodic boundary conditions, heat transfer, plane duct

Introduction

Computational fluid dynamics has been used on occasion to improve the design of heat exchangers. Frequently, streamwise-periodic boundary conditions are employed to perform calculations for fully developed flow and heat transfer in situations where a single unit cell represents a geometry repeated numerous times in the flow direction over some characteristic length scale, l. Figure 1(a) illustrates one such example. Under the circumstances, suitably reduced or nondimensionalized pressure and temperature fields, asymptotically approach constant values. Patankar et al. [1] pioneered the development of methodologies for periodic heat transfer under conditions of either constant heat flux (Neumann) or constant wall temperature (Dirichlet) boundary conditions. These approaches were subsequently applied by numerous other researchers in numerical heat transfer work. The reader will note that the choice of state variable in Ref. [1] differs for the constant T_w and $\dot{q}''$ boundary value problems. For this reason the approach cannot readily be adopted for problems involving combinations of Neumann and Dirichlet boundary conditions, or for the intermediate linear (Robin) boundary value problem. Mixed boundary conditions arise naturally, e.g., within the passages of heat exchangers transferring energy between two working fluids.

Recently the present author [2] proposed a rationale, which could, in principle, be applied not only to the Dirchlet and Neumann problems, but also to the intermediate linear boundary value problem, as well as combinations of different wall boundary conditions. This is possible because primitive variables, temperature and pressure, were selected as state variables. However, the only example given in Ref. [2] was a 3D constant T_w offset-fin heat exchanger geometry. The purpose of this article is to present comparisons of the methodology [2] for a simple geometric case, namely, the fully developed Graetz problem, over a range of thermal boundary conditions, and to demonstrate that it is possible to obtain fully developed solutions under regularly repeating but arbitrary wall boundary conditions using a primitive-variable formulation, i.e., to validate the methodology. The deliberate choice of simplified geometry allows for exact comparison with data from the standard literature to be made without compromise in terms of the general nature of the methodology and its potential for practical application.

Contributed by the Heat Transfer Division of ASME for publication in the JOURNAL OF HEAT TRANSFER. Manuscript received October 15, 2007; final manuscript received March 4, 2008; published online August 29, 2008. Review conducted by Jayathi Murthy.

Periodic Boundary Conditions

The general details of how periodic boundary conditions are applied to the flow by means of a pressure jump or shock, were provided in Ref. [2]. Therefore only material related to heat transfer is provided below. The streamwise-periodic thermal condition may be expressed [3] as follows:

$$T(0) = c_1 T(l) + c_2 \tag{1}$$

with

$$c_1 = \frac{T_0(0) - T_w(0)}{T_0(l) - T_w(l)} \tag{2}$$

$$c_2 = T_0(0) - c_1 T_0(l) \tag{3}$$

where T_0 is a suitable reference, e.g., local bulk temperature. Thus, the temperature difference or jump between the given upstream and downstream values is $\Delta T=(c_1-1)T+c_2$, an expression, which will prove useful when prescribing periodic boundary conditions below. For $T_w \neq$ constant, the upstream wall values must be computed from those downstream

$$T_w(0) = \frac{T_0(0) + B(l)T_\infty}{1 + B(l)} \tag{4}$$

where the driving force [4] is

$$B = \frac{T_0 - T_w}{T_w - T_\infty} \tag{5}$$

and T_∞ is an ambient or external value. Periodicity is defined here as being the case if and only if the local heat transfer driving force is cyclic,

$$B(x + l, y) = B(x, y) \tag{6}$$

It being assumed that the upstream bulk value, $T_0(0)$, is prescribed a priori, whereas the downstream value $T_0(l)$ is computed iteratively at run time.

Benchmark Cases

The methodology was tested by obtaining performance calculations for fully developed flow and heat transfer in ducts, for which solutions are known for a variety of wall conditions. Table 1 shows the four cases considered.

(1) constant wall temperatures, T_1 and T_2 (Dirichlet)
(2) constant heat fluxes $\dot{q}_1''$ and $\dot{q}_2''$ (Neumann)
(3) one constant heat flux, $\dot{q}_1''$, and one constant temperature, T_2 (mixed)
(4) heat flux prescribed according to a linear rate equation (Robin), namely,

$$\dot{q}'' = U(T_\infty - T_w) \tag{7}$$

a physical interpretation being the transfer of heat to walls of overall heat transfer coefficients, U_1 and U_2, which in turn transfer heat to two reservoirs, at temperatures $T_{1\infty}$ and $T_{2\infty}$. Under the circumstance, a nondimensional wall resistance [5] is defined, for each wall, by

$$R_w = \frac{k}{UD_h} \tag{8}$$

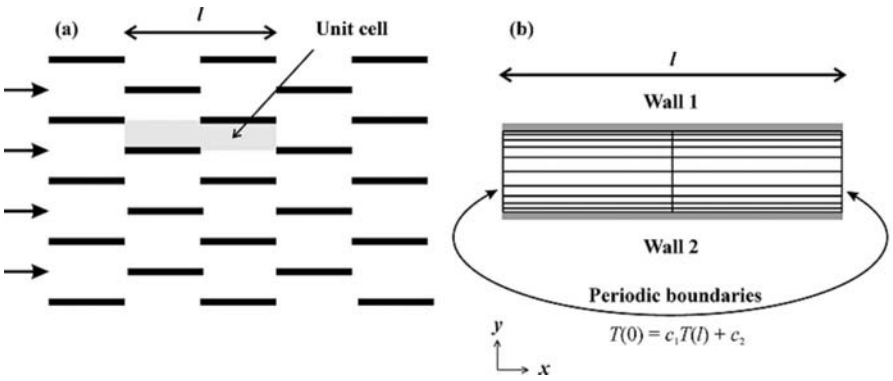

Fig. 1 Example of streamwise-periodic geometry showing unit cell geometry for (*a*) offset fin and (*b*) plane duct showing the mesh and boundary conditions

This is related to the Biot number according to $R_w = 1/(4\mathrm{Bi})$. Cases (1)–(4) in Table 1 summarize the performance of these four commonly encountered internal forced convection problems [6] in terms of the Nusselt number.

Implementation

In computational heat transfer codes based on the finite-volume method [7], a set of linear algebraic equations having the form

$$\sum a_{\mathrm{NB}}(T_{\mathrm{NB}} - T_P) + S = 0 \tag{9}$$

is solved for steady flow. T_P is the in-cell value of T at any given computational cell, with neighbors NB=W (west), E (east), S (south), and N (north). NB: With temperature, T, as state variable, the units of the linking neighbor coefficients, a_{NB}, are W/K as opposed to the more usual units of kg/s when enthalpy is dependent variable.

The wall boundary conditions in Eq. (9) are linearized according to

$$S = C(T_\infty - T_P) \tag{10}$$

where C is a source-term coefficient and T_∞ is a source-term value. Equation (10) follows the notation of Spalding [8], which is consistent with the zero-flux form of Eq. (9). Patankar [7] employed the form $S = S_C + S_P T_P$ with $S_C = CT_\infty$ and $S_P = -C$.

For Case (4), the source-term coefficient and wall value are computed using harmonic and arithmetic averaging [7],

$$\frac{1}{C} = \frac{\delta y}{kA_N} + \frac{1}{UA_N} \tag{11}$$

$$T_w = \frac{k/\delta y}{k/\delta y + U} T_P + \frac{U}{k/\delta y + U} T_\infty \tag{12}$$

As noted in Ref. [9], the Dirichlet and Neumann cases are easily constructed as limits of the linear Case (4). This is achieved by (i) setting the resistance, R_w, to a very small number, so that U and C are correspondingly large (Dirichlet), or (ii) by setting both R_w and $T_\infty = \dot{q}''/C$ to large numbers (Neumann).

Table 1 Benchmark problems and results

			Previous work		Present study			
			Nu_1	Nu_2	Nu_1	% error	Nu_2	% error
1.	T_1 / T_2	(a) $T_1 = T_2$	7.541	7.541	7.536	0.066	7.536	0.066
		(b) $T_1 \neq T_2$	4.000	4.000	4.000	0	4.000*	–
2.	$\dot{q}_1''$ / $\dot{q}_2''$	(a) $\dot{q}_1'' = \dot{q}_2''$	8.235	8.235	8.232	0.036	8.232	0.036
		(b) $\dot{q}_1'' = 0$	0.000	5.384	0	0	5.384	–
		(c) $\dot{q}_1'' \neq \dot{q}_2''$	Fig. 3		Fig. 3			
3.	$\dot{q}_1''$ / T_2	(a) $\dot{q}_1'' = 0$	0.000	4.861	0.000	0	4.860	0.020
		(b) $\dot{q}_1'' \neq 0$	4.000	4.000	4.000	0	4.000*	–
4.	$T_{1\infty}$ / U_1 / U_2 / $T_{2\infty}$	(a) $T_{1\infty} = T_{2\infty}$, $U_1 = U_2$	Fig. 4		Fig. 4			
		(b) $T_{1\infty} \neq T_{2\infty}$	4.000	4.000	4.001	0.025	4.001*	0.025

*For these cases, the temperature field is cyclic rather than periodic, hence $c_1 = 1$, $c_2 = 0$, and $T_0(0)$ is not prescribed.

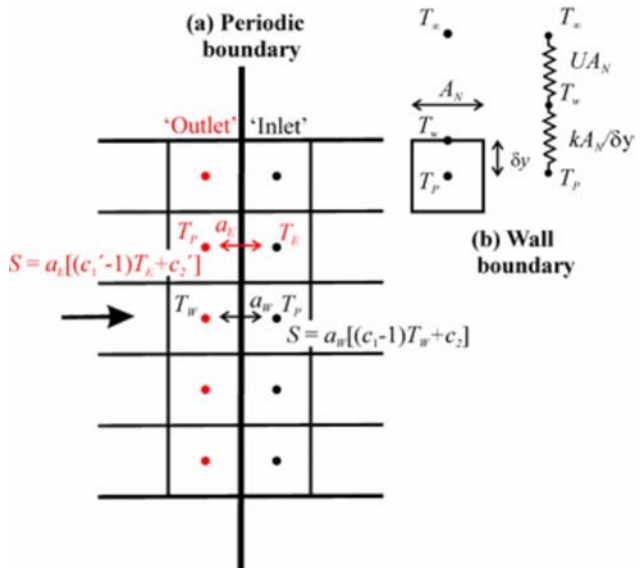

Fig. 2 Boundary condition implementation showing (*a*) jump boundary condition at the inlet/exit and (*b*) wall boundary notation

The streamwise-periodic boundary condition is prescribed [2] in two steps: (i) By activating true cyclic boundary conditions across the inlet/outlet in the streamwise direction, storage is assured for the missing streamwise linking coefficients, a_{NB}, in the energy and momentum equations at what would otherwise be the inlet and outlet of the domain, creating an endless flow loop. (ii) At the inlet a step or jump in the temperature field across the boundary is imposed by prescribing a line of source terms $S=a_W[(c_1-1)T_W+c_2]$ in computational cells immediately downstream of the periodic boundary, as shown in Fig. 2(*a*). Combining these with the terms $a_W(T_W-T_P)$ in Eq. (9) has the effect of replacing T_W with $c_1T_W+c_2$, from Eq. (1). For parabolic situations, such as considered here, no further considerations are required.

For elliptic problems, Eq. (1) may be rewritten in the form

$$T(l) = c_1'T(0) + c_2' \tag{13}$$

and a similar line of source terms $S=a_E[(c_1'-1)T_W+c_2']$ must be prescribed immediately upstream of the boundary at the outlet [10], as shown in Fig. 2. For the particular case of constant T_w, the present formulation is equivalent to that of Kelkar and Patankar [11]; however, it is more generally used for a wide range of thermal boundary conditions.

A staggered velocity scheme with hybrid differencing of convection and diffusion terms [7] was implemented in the PHOENICS code [12], which is based on a version of the SIMPLE algorithm [7,8,13]. Calculations were performed with meshes of both 2×100 and 10×100 cells in the x-y plane, similar to that shown Fig. 1(*b*), and concentrated by means of a geometric progression toward the walls where velocity and temperature gradients are maximum. (NB: A minimum of two cells in the x-direction is required for the present method.) Regardless of the number of cells in the x-direction, the values of local Nusselt numbers, Nu_1 and Nu_2, at the north and south walls, were observed to be invariant. These were obtained as follows:

$$\mathrm{Nu} = \frac{D_h}{k} C\left(\frac{T_P - T_\infty}{T_0 - T_w}\right) \tag{14}$$

where T_P is the in-cell value of T nearest the appropriate north or south wall, Fig. 2(*b*), and C is the source-term coefficient, from Eq. (10).

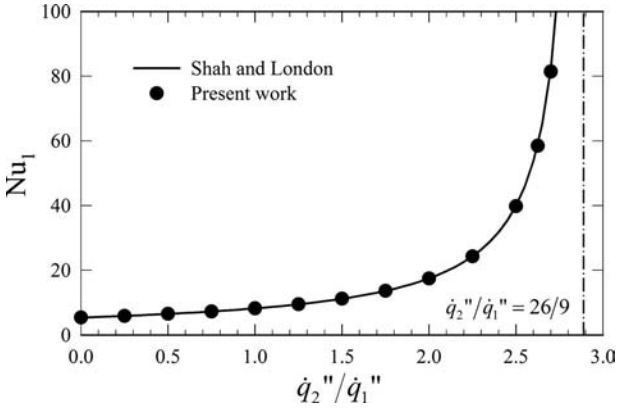

Fig. 3 Comparison of the present work with the expression of Shah and London [6] for Case 2(c)

Results

Table 1 provides a comparison of the present results, in terms of Nusselt numbers, with those of Shah and London [6] and others. These are discussed briefly below.

(1) *Dirichlet problem*. Agreement with analytical solutions is within 0.07% for (a) $T_1=T_2$ and (b) $T_1\neq T_2$.

(2) *Neumann problem*. (a) $\dot{q}_1''=\dot{q}_2''$ agreement is within 0.04%. (b) $\dot{q}_1''=0$ agreement is exact. (c) $\dot{q}_1''\neq\dot{q}_2''$. Figure 3 shows that agreement is excellent for this case. For $\dot{q}_2''=\dot{q}_1''\leqslant 2.5$ the present data agree with Ref. [6] to within 0.3%, and substantially better as $\dot{q}_2''=\dot{q}_1''\to 0$. Note that as $\dot{q}_2''=\dot{q}_1''\to 26/9$, $\mathrm{Nu}\to\infty$ because $T_1\to T_0$.

(3) *Mixed problem*. (a) $\dot{q}_1''=0$ agreement is within 0.02%. (b) $\dot{q}_1''\neq 0$ exact agreement is obtained.

(4) *Linear boundary values*. (a) $T_{1\infty}=T_{2\infty}$. Figure 4 is a comparison of the present results with those of Sideman et al. [5] in terms of Nusselt number as a function of wall resistance. Agreement is always within 0.07%. (b) $T_{1\infty}\neq T_{2\infty}$. The same result is obtained as for Cases 1(a) and 3(b), regardless of whether $U_1=U_2$ or not, showing these to be special cases of 4(b).

Discussion and Conclusion

Comparison of the present numerical work with previously obtained analytical and numerical results of others indicates that it is possible to prescribe fully developed streamwise-periodic boundary conditions under a range of thermal conditions. The results show that multiple wall temperatures/fluxes, a combination of constant temperature and constant flux, and linear wall conditions

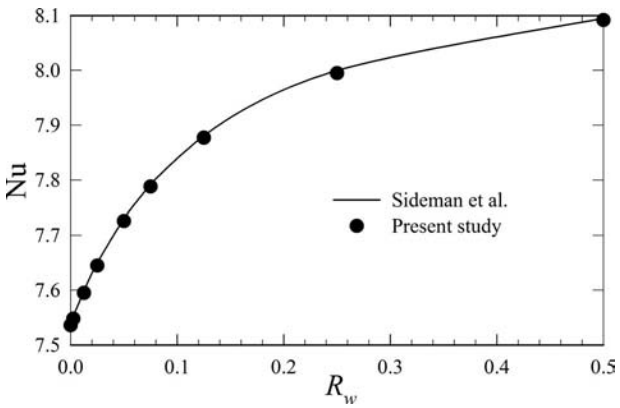

Fig. 4 Comparison of the present work with the data of Sideman et al. [5] for Case 4(a)

can all be handled by the methodology. Although only pairs of boundary values were considered for a plane duct, the extension to a manifold of boundary fluxes and temperatures, and/or complex geometries and recirculating flow regimes with or without mass transfer at the walls, is readily apparent. Performance calculations for such problems are generally correlated with empirical, rather than analytical data.

Cases 1(a), 2(a)–(c), 3(a), and 4(a) all admit fully developed solutions where the solution is independent of the inlet bulk temperature and heat is transferred to or from the working fluid. Cases 1(b), 3(b), and 4(b) only allow for cyclic solutions where no net heat is transferred to or from the working fluid, and the bulk temperature is simply a weighted average of wall values. It is important, when considering more complex geometries, to identify which class of problem is under consideration. For example, for crossflow in a bank of finned tubes, there may be temperature variations from fin tip to root, and a periodic solution still achieved; on the other hand, if alternate rows are at different temperatures, only a cyclic solution is possible. Nusselt number correlations for the former class of problem are, generally speaking, of more interest to the heat exchanger designer. It is also important to appreciate that not every problem involving regularly repeating geometry will necessarily admit a steady fully developed periodic solution [14].

In view of the wide range of Nusselt numbers observed in Figs. 3 and 4, the presumption of constant flux or constant temperature formulations for engineering problems will lead to substantial errors, when applied to periodic problems where these are, in fact, variable, and is neither recommended nor necessary. A conclusion of this study is that the primitive-variable streamwise-periodic formulation generates reliable results over a range of thermal boundary conditions, as verified by analytical and other data. Based on this observation, the methodology may be applied with confidence to performance calculations for complex periodic heat and mass transfer problems.

Nomenclature

a = linking coefficient, W/K
A_N = area of north face of computational cell, m^2
C = source-term coefficient, W/K
D_h = hydraulic diameter, m
k = thermal conductivity, W/(m K)
l = length, m
T = temperature, K
$\dot{q}''$ = heat flux, W/m^2
S = source term, W
U = overall heat transfer coefficient, $W/(m^2K)$
δy = cell half distance, m

Nondimensional Numbers

B = heat transfer driving force
Bi = Biot number
Nu = Nusselt number
R_w = thermal resistance

Subscripts

E, W, S, N = east, west, south, and north neighbors
NB = neighbor
P = nodal
w = wall
0 = reference, bulk
∞ = external, ambient

References

[1] Patankar, S. V., Liu, C. H., and Sparrow, E. M., 1977, "Fully-Developed Flow and Heat Transfer in Ducts Having Streamwise-Periodic Variations of Cross-Sectional Area," ASME J. Heat Transfer, **99**, pp. 180–186.
[2] Beale, S. B., 2007, "Use of Streamwise Periodic Conditions for Problems in Heat and Mass Transfer," ASME J. Heat Transfer, **129**, pp. 601–605.
[3] Beale, S. B., and Spalding, D. B., 1998, "Numerical Study of Fluid Flow and Heat Transfer in Tube Banks With Stream-Wise Periodic Boundary Conditions," Trans. Can. Soc. Mech. Eng., **22**, pp. 394–416.
[4] Spalding, D. B., 1963, *Convective Mass Transfer; An Introduction*, Arnold, London.
[5] Sideman, S., Luss, D., and Peck, R. E., 1964, "Heat Transfer in Laminar Flow in Circular and Flat With (Constant) Surface Resistance," Appl. Sci. Res., Sect. A, **14**, p. 1570171.
[6] Shah, R. K., and London, A. L., 1978, *Advances in Heat Transfer*, T. F. Irvine, and J. P. Hartnett, eds., Academic, New York.
[7] Patankar, S. V., 1980, *Numerical Heat Transfer and Fluid Flow*, Hemisphere, New York.
[8] Spalding, D. B., 1980, *Mathematical Modelling of Fluid-Mechanics, Heat-Transfer and Chemical-Reaction Processes: A Lecture Course*, Imperial College, University of London, London.
[9] Sparrow, E. M., and Patankar, S. V., 1977, "Relationships Among Boundary Conditions and Nusselt Numbers for Thermally Developed Duct Flows," ASME J. Heat Transfer, **99**, pp. 483–485.
[10] Beale, S. B., 1993, Ph.D. thesis, Imperial College of Science, Technology and Medicine, London.
[11] Kelkar, K. M., and Patankar, S. V., 1987, "Numerical Prediction of Flow and Heat Transfer in a Parallel Channel With Staggered Fins," ASME J. Heat Transfer, **109**, pp. 25–30.
[12] Spalding, D. B., 2006, "PHOENICS Overview (Version 3.6)," CHAM Ltd., TR001, London.
[13] Patankar, S. V., and Spalding, D. B., 1972, "A Calculation Procedure for Heat, Mass, and Momentum Transfer in Three-Dimensional Parabolic Flows," Int. J. Heat Mass Transfer, **15**, pp. 1787–1806.
[14] Beale, S. B., 2005, "Mass Transfer in Plane and Square Ducts," Int. J. Heat Mass Transfer, **48**, pp. 3256–3260.

Effects of Growth Temperature on Carbon Nanotube Array Thermal Interfaces

Baratunde A. Cola

Placidus B. Amama

Xianfan Xu

Timothy S. Fisher
e-mail: tsfisher@purdue.edu

School of Mechanical Engineering and Birck Nanotechnology Center,
Purdue University,
West Lafayette, IN 47907

Due to their excellent compliance and high thermal conductivity, dry carbon nanotube (CNT) array interfaces are promising candidates to address the thermal management needs of power dense microelectronic components and devices. However, typical CNT growth temperatures (~800°C) limit the substrates available for direct CNT synthesis. A microwave plasma chemical vapor deposition and a shielded growth technique were used to synthesize CNT arrays at various temperatures on silicon wafers. Measured growth surface temperatures ranged from 500°C to 800°C. The room-temperature thermal resistances of interfaces created by placing the CNT covered wafers in contact with silver foil (silicon-CNT-silver) were measured using a photoacoustic technique to range from approximately 7 $mm^2°C/W$ to 19 $mm^2°C/W$ at moderate pressures. Thermal resistances increased as CNT array growth temperature decreased primarily due to a reduction in the average diameter of CNTs in the arrays.
[DOI: 10.1115/1.2969758]

Keywords: carbon nanotube, thermal interface material, contact thermal resistance, plasma CVD, low temperature, photoacoustic

Introduction

As semiconductor technology continues to advance, resulting in progressive reductions of device feature sizes and expansion of application opportunities, ensuring reliable operation has become a growing challenge. The effective and efficient transfer of heat from a chip to a heat sink is a vital step in meeting this challenge. Advanced thermal management schemes that employ carbon nanotube (CNT) arrays as interface materials have been suggested as a means to dissipate high heat fluxes while maintaining low chip temperatures [1–6]. Under moderate pressure, CNT array interfaces have been reported to produce thermal resistances as low as 8 $mm^2°C/W$ for arrays grown on one side of the interface [6] and as low as 4 $mm^2°C/W$ for arrays grown on both sides of the interface [4]. However, the temperatures at which these CNT array thermal interfaces were grown (>800°C) are incompatible with the temperature-sensitive substrates used in standard semiconductor processes because the electrical performance of most metal contacts and interconnects degrades when exposed to temperatures up to 450°C for more than a limited time [7].

Contributed by the Heat Transfer Division of ASME for publication in the JOURNAL OF HEAT TRANSFER. Manuscript received July 6, 2007; final manuscript received June 17, 2008; published online September 2, 2008. Review conducted by Yogendra Joshi.

An insertable CNT array/foil material was recently suggested as a way to apply CNT arrays to an interface without exposing the mating materials to normal CNT growth temperatures, and resistances as low as 10 $mm^2°C/W$ were achieved under moderate pressure [5]. While this technique seems promising, progress in low-temperature synthesis has been reported [7–10], and these approaches may prove advantageous for their ability to offer seamless integration into existing manufacturing processes; yet, to the best of our knowledge, the literature reveals no studies on the effects of decreased growth temperature on the thermal performance of CNT array interfaces. In this Technical Brief, we report on studies of thermal conduction through CNT array interfaces grown at various temperatures, lower than those previously reported.

Experimental Methods

Sample Fabrication. Microwave plasma chemical vapor deposition (MPCVD) [11] and a shielded growth technique [10] were used to synthesize vertically oriented CNT arrays on polished silicon wafers (560 μm thick). Iron oxide (Fe_2O_3) nanoparticles were deposited as a catalyst via a dendrimer template [12] on a 30 nm titanium barrier layer deposited atop the silicon. The silicon wafers were elevated (catalyst side facing away from the plasma) on a 5.5 mm thick molybdenum puck by 1.2 mm thick ceramic spacers, and the puck was set in the growth chamber on a heated stage, as illustrated in Fig. 1. The stage temperature, T_{stage}, was set to 800°C, 700°C, 600°C, 500°C, 400°C, 300°C, and 200°C for different synthesis processes, and the catalyst was heated in nitrogen ambient. The plasma power ranged 400–500 W, and the growth chamber's pressure was 10 Torr. The MPCVD process gases were hydrogen (50 SCCM (SCCM denotes cubic centimeter per minute at STP)) and methane (10 SCCM), and growth was carried out for 20 min. Two separate runs were performed at each growth condition to test repeatability. A dual-wavelength pyrometer was aimed at the backside of the silicon wafers to measure their temperature, $T_{pyrometer}$, during growth and to quantify the significance of additional heating due to the plasma [13]. Because of the relatively low intrinsic thermal resistance of the silicon wafers, we expect the temperature at the catalytic surfaces to be nearer $T_{pyrometer}$ than to T_{stage}. Thus, we will refer to $T_{pyrometer}$ as the "growth temperature."

Sample Characterization. Figure 2 shows the scanning electron microscope (SEM) images that illustrate the results of CNT arrays grown at different temperatures. Figure 2(*a*) shows a vertically oriented CNT array grown at 806°C. Figures 2(*b*)–2(*h*) are SEM images of equal magnification that illustrate the CNT morphologies obtained from growth at 806–506°C, respectively. The CNTs in each sample were entangled near their free ends; yet, as illustrated in Fig. 2(*a*) and in the insets of Figs. 2(*c*)–2(*h*), the bulk of all CNT array samples were vertically oriented. A transmission electron microscope (TEM) was used to examine wall structure and revealed that nanotubes (as apposed to nanofibers) were grown at each temperature. The bottom inset in Fig. 2(*h*) contains a TEM image of a CNT grown at 506°C. Table 1 summarizes the morphological characteristics of the CNT arrays grown at each temperature. The data are characteristic of the CNT arrays produced from two growth experiments at each temperature; hence, redundant sample types were morphologically similar.

Raman spectroscopy was also used to characterize the CNT arrays grown at each temperature. Well defined *G* (indicating well ordered graphite) and *D* (indicating amorphous carbon and/or tube defects) bands were observed, and the band intensity ratios I_G/I_D were approximately 0.5 for each sample, indicating a similar quality of CNTs produced in this study. These results were somewhat unexpected, as the quality of CNTs can depend strongly on growth temperature; however, using the dendrimer-assisted catalysis technique, such control over CNT characteristics has been demon-

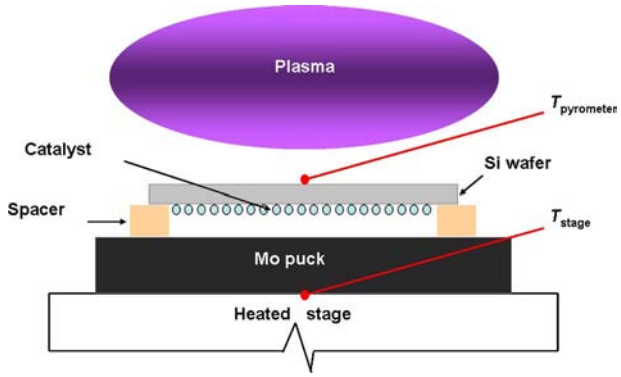

Fig. 1 Schematic of the sample configuration in the MPCVD chamber (not to scale)

strated in arrays grown at various temperatures [6,9].

The CNT diameter ranges displayed in Table 1 include two standard deviations from the mean, and the average is determined from diameters within the ranges. As growth temperature decreased, the CNT diameters decreased as expected because of the decrease in the mobility and/or aggregation of the catalyst nanoparticles [14]. For each sample, SEM images were analyzed to determine the density of CNTs by counting the number of CNTs per unit area. The mean CNT array heights were also estimated from SEM images. As growth temperature decreased, CNT density slightly decreased and mean array height decreased presumably because of a lower reaction energy that impedes the CNT growth process. At low growth temperatures, there is a decrease in surface diffusion of the catalyst nanoparticles, carbon solubility in the catalyst nanoparticles, and the diffusion of the carbon feedstock. All these factors play key roles during CNT growth especially the diffusion of carbon in the catalyst nanoparticles, which has been widely suggested as the rate-determining step.

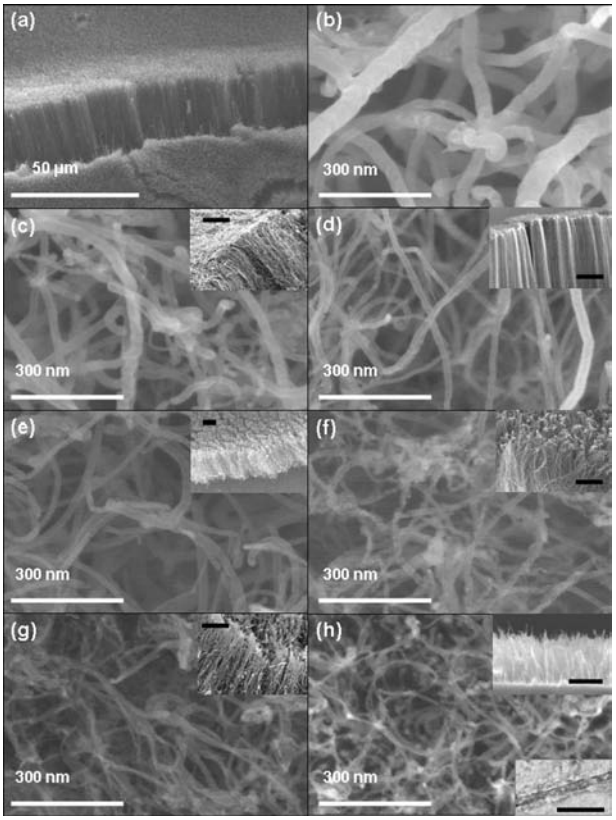

Fig. 2 SEM images of CNT arrays grown from 806°C to 506°C. (*a*) Vertically oriented CNT array grown at 806°C. (*b*) Higher magnification image of CNTs grown at 806°C. (*c*) CNTs grown at 737°C. The inset contains a lower magnification image that illustrates vertically oriented CNTs (scale bar is 5 μm). (*d*) CNTs grown at 707°C. The inset contains a lower magnification image (scale bar is 5 μm). (*e*) CNTs grown at 641°C (inset scale bar is 5 μm). (*f*) CNTs grown at 612°C (inset scale bar is 1 μm). (*g*) CNTs grown at 524°C (inset scale bar is 1 μm). (*h*) CNTs grown at 506°C. The top inset scale bar is 1 μm. The bottom inset contains a TEM image of a nanotube grown at 506°C (scale bar is 100 nm).

Thermal Resistance Measurement. The room-temperature thermal resistances of silicon-CNT-silver interfaces grown via MPCVD in the temperature range 806–506°C have been measured using a photoacoustic (PA) technique described in detail by Cola et al. [4]. Due to its transient nature, the PA technique can be used to measure multiple interface resistances as well as thermal diffusivity within layered materials such as CNT array interfaces [4]. The PA measurements were performed as a function of pressure in a range applicable to the thermal management of microprocessors, and relatively smooth silver foil (average peak-to-valley surface height of 0.4 μm) was used as the top interface substrate to enable precise PA measurements [4].

Results and Discussion

The average results from several PA measurements on each CNT array sample are illustrated in Fig. 3. Two separate samples were fabricated at each growth temperature and thermally tested. Figure 3 reveals exceptional consistency, both in terms of the repeatability of redundant samples and in terms of trends with respect to incremental variations in growth conditions. In fact, the thermal resistance values of the redundant samples significantly overlap considering the range of measurement uncertainty (± 0.5 mm^2°C/W). After testing, the interfaces were separated, and the CNTs remained well adhered to the silicon for each array, independent of growth temperature. The one-sided CNT array total thermal interface resistances R measured in this study are the sum of two local resistances (at the silicon-CNT interface and at the free CNT tip-silver interface) plus the intrinsic resistance of the CNT array. However, the local thermal resistances at the silicon-CNT interfaces were measured using the PA technique to be less than 1 mm^2°C/W and the resistances at the free CNT tip interfaces were measured to be approximately equal to the thermal resistances of the entire CNT array interface. Consequently, the contact of the CNTs to their growth substrate and the effective thermal conductivity of the CNT arrays had negligible effects on the total thermal resistances. Previous works [3,4] have also demonstrated that the thermal resistance at the interface to the free CNT tips dominates the resistance of one-sided CNT array interfaces.

As clearly illustrated in Fig. 3, the total thermal resistance R of the CNT array interfaces increases as CNT growth temperature decreases. We attribute this performance characteristic to the CNT array morphologies produced at different growth temperatures. As the growth temperature was decreased, the associated decreases in CNT density and average CNT diameter resulted in increased thermal resistance at the interface. Because the average peak-to-valley surface height of the silver foil (0.4 μm) is much less than the CNT array heights, we expect the variations in array height to have little effect on thermal resistance in this study [2]. For the most part, the CNT density and diameter changed simultaneously as array growth temperature changed; therefore, it is difficult to isolate the individual effects of these morphological characteristics on the associated changes in thermal interface resistance. However, the CNT densities varied by a much lesser percentage than the CNT diameters. Thus, we postulate that the changes in CNT diameter governed the changes in thermal resistance. This

Table 1 CNT morphologies for arrays grown at different temperatures

T_{stage} (°C)	800	700	600	500	400	300	200
$T_{pyrometer}$ (°C)	806	737	707	641	612	524	506
Plasma power (W)	400	400	400	500	500	500	500
Mean CNT array height (μm)	25	20	20	10	7	3	2
CNT density (%)	40–50	40–50	35–50	35–45	30–45	30–45	30–40
CNT diameter range (nm)	20–60	15–40	10–30	10–25	10–20	5–15	5–10
Average CNT diameter (nm)	40	30	23	15	15	10	8

performance characteristic is best illustrated through closer examination of the growth temperature ranges 641–524°C and 806–737°C, where the effects of CNT diameter are clearly distinguished.

When the CNT array growth temperature was reduced from 641°C to 612°C, the CNT density was slightly reduced, yet the average CNT diameter remained constant. As illustrated in Fig. 3, the thermal resistances produced by the 612°C arrays were approximately the same as the resistances produced by the 641°C arrays. When the growth temperature was reduced from 612°C to 524°C, the average CNT diameter in the arrays decreased from approximately 15 nm to 10 nm, yet the CNT density was approximately the same. In this case, the thermal resistances produced by the 524°C arrays were larger than the resistances produced by the 612°C arrays (Fig. 3). Additionally, when growth temperature was reduced from 806°C to 737°C, the average CNT diameter reduced while CNT density was approximately unchanged, and as illustrated in Fig. 3, interface resistance increased from the 806°C arrays to the 737°C arrays. These results are in support of the CNT array's average diameter having the dominate effect on the measured thermal resistances in this study.

Because the local resistances at the free CNT end dominates the total thermal resistances of the CNT array interface, changes in total resistance are due to changes in resistance at the free CNT end interface. At this interface, the characteristic contact size established between an individual CNT and the opposing silver substrate is at least an order of magnitude less than the room-temperature phonon mean free path of CNTs (approximately 150 nm [15]). Therefore, phonon transport through the contacts is ballistic [16,17], and the total thermal resistance at the free CNT ends interface, i.e., the total thermal resistance of the one-sided CNT array interface, can be represented as

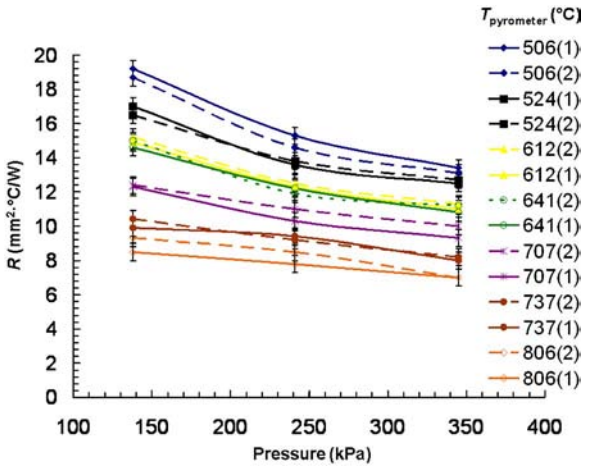

Fig. 3 Total thermal resistance *R* as a function of pressure for one-sided CNT array interfaces with arrays grown at various temperatures

$$R = R_b \cdot \frac{A}{A_r} \tag{1}$$

where R_b is the thermal resistance at individual CNT contacts, A_r is the real contact area established at the free CNT ends interface, and A is the apparent contact area. We postulate that changes in CNT diameter result in changes in A_r, which affects the total thermal resistance. Moreover, for the arrays in this study, we suggest that CNT diameter affects A_r primarily by influencing the effective hardness of the CNT array, which determines the number of CNTs that make contact with the opposing substrate. CNT coverage in this study only varied by a small percentage; consequently, as CNT diameter decreased, the total number of CNTs in the arrays increased. Hence, the smaller diameter CNTs were more closely packed (see Fig. 2). Presumably, as the smaller diameter CNT arrays deformed in the interface under the applied load, the close packing of CNTs promoted more tube-to-tube contact within the arrays, providing increased support for individual CNTs, such that the effective hardness of the arrays was increased and A_r was decreased, which is expected from traditional contact theory in which A_r is inversely proportional to hardness [18]. Therefore, as represented in Eq. (1), the total thermal resistance of the CNT array interfaces increases as A_r decreases.

Conclusions

The thermal resistances of CNT array interfaces grown in the temperature range 806–506°C were measured to range from 7 mm^2°C/W to 19 mm^2°C/W, respectively. These values comparable favorably to previously reported CNT array thermal interface resistances [1–6]. Moreover, it has been demonstrated that CNT arrays that provide good thermal interface conductance can be grown at reduced temperatures that allow integration with sensitive substrates (e.g., aluminum) that may be of particular interest to the heat transfer community. Thermal resistance was measured to increase as CNT array growth temperature decreased presumably due to an increase in the stiffness of the CNT arrays that reduced the amount of real contact area established in the interface. Further experiments and extensive modeling are still required to fully understand the contact mechanics in and the thermal transport through CNT array interfaces.

Acknowledgment

We gratefully acknowledge financial support from the National Science Foundation under grant CBET-0646015. The lead author is grateful for personal support from the Intel Foundation and the Purdue University Graduate School.

Nomenclature

A = apparent contact area, m^2
A_r = real contact area at the free CNT end interface, m^2
I_D = intensity of D band, a.u.
I_G = intensity of G band, a.u.
R = total thermal resistance of CNT array interface, mm^2°C/W

R_b = thermal resistance at individual CNT contacts, $mm^2 \cdot °C/W$

$T_{pyrometer}$ = temperature of silicon surface facing the plasma, °C

T_{stage} = temperature of the growth stage, °C

References

[1] Xu, J., and Fisher, T. S., 2006, "Enhanced Thermal Contact Conductance Using Carbon Nanotube Array Interfaces," IEEE Trans. Compon. Packag. Technol., **29**(2), pp. 261–267.

[2] Xu, J., and Fisher, T. S., 2006, "Enhancement of Thermal Interface Materials With Carbon Nanotube Arrays," Int. J. Heat Mass Transfer, **49**, pp. 1658–1666.

[3] Tong, T., Zhao, Y., Delzeit, L., Kashani, A., Meyyappan, M., and Majumdar, A., 2007, "Dense Vertically Aligned Multiwalled Carbon Nanotube Arrays as Thermal Interface Materials," IEEE Trans. Compon. Packag. Technol., **30**(1), pp. 92–100.

[4] Cola, B. A., Xu, J., Cheng, C., Hu, H., Xu, X., and Fisher, T. S., 2007, "Photoacoustic Characterization of Carbon Nanotube Array Thermal Interfaces," J. Appl. Phys., **101**, p. 054313.

[5] Cola, B. A., Xu, X., and Fisher, T. S., 2007, "Increased Real Contact in Thermal Interfaces: A Carbon Nanotube/Foil Material," Appl. Phys. Lett., **90**, p. 093513.

[6] Amama, P. B., Cola, B. A., Sands, T. D., Xu, X., and Fisher, T. S., 2007, "Dendrimer-Assisted Controlled Growth of Carbon Nanotubes for Enhanced Thermal Interface Conductance," Nanotechnology, **18**, p. 385303.

[7] Melechko, A. V., Merkulov, V. I., McKnight, T. E., Guillorn, M. A., Klein, K. L., Lowndes, D. H., and Simpson, M. L., 2005, "Vertically Aligned Carbon Nanofibers and Related Structures: Controlled Synthesis and Directed Assembly," J. Appl. Phys., **97**, p. 041301.

[8] Boskovic, B. O., Stolojan, V., Khan, R. U. A., Haq, S., and Silva, S. R. P., 2002, "Large-Area Synthesis of Carbon Nanofibers at Room Temperature," Nat. Mater., **1**, pp. 165–168.

[9] Hofmann, S., Ducati, C., Robertson, J., and Kleinsorge, B., 2003, "Low-Temperature Growth of Carbon Nanotubes by Plasma-Enhanced Chemical Vapor Deposition," Appl. Phys. Lett., **83**(1), pp. 135–137.

[10] Amama, P. B., Ogebule, O., Maschmann, M. R., Sands, T. D., and Fisher, T. S., 2006, "Dendrimer-Assisted Low-Temperature Growth of Carbon Nanotubes by Plasma-Enhanced Chemical Vapor Deposition," Chem. Commun. (Cambridge), **27**, pp. 2899–2901.

[11] Maschmann, M. R., Amama, P. B., Goyal, A., Iqbal, Z., Gat, R., and Fisher, T. S., 2006, "Parametric Study of Synthesis Conditions in Plasma-Enhanced CVD of High-Quality Single-Walled Carbon Nanotubes," Carbon, **44**, pp. 10–18.

[12] Amama, P. B., Maschmann, M. R., Fisher, T. S., and Sands, T. D., 2006, "Dendrimer-Templated Fe Nanoparticles for the Growth of Single-Wall Carbon Nanotubes by Plasma-Enhanced CVD," J. Phys. Chem. B, **110**, pp. 10636–10644.

[13] Teo, K. B. K., Hash, D. B., Lacerda, R. G., Rupesinghe, N. L., Bell, M. S., Dalal, S. H., Bose, D., Govindan, T. R., Cruden, B. A., Chhowalla, M., Amaratunga, G. A. J., Meyyappan, M., and Milne, W. I., 2004, "The Significance of Plasma Heating in Carbon Nanotube and Nanofiber Growth," Nano Lett., **4**(5), pp. 921–926.

[14] Meyyappan, M., Delzeit, L., Cassell, A., and Hash, D., 2003, "Carbon Nanotube Growth by PECVD: A Review," Plasma Sources Sci. Technol., **12**, pp. 205–216.

[15] Shi, L., 2001, "Mesoscopic Thermophysical Measurements of Microstructures and Carbon Nanotubes," Ph.D. thesis, University of California, Berkeley.

[16] Prasher, R., 2008, "Thermal Boundary Resistance and Thermal Conductivity of Multiwalled Carbon Nanotubes," Phys. Rev. B, **77**, 075424.

[17] Prasher, R., 2005, "Predicting the Thermal Resistance of Nanosized Constrictions," Nano Lett., **5**(11), pp. 2155–2159.

[18] Madhusudana, C. V., 1996, *Thermal Contact Conductance*, Springer-Verlag, New York.

Unsteady Hydromagnetic Generalized Couette Flow of a Non-Newtonian Fluid With Heat Transfer Between Parallel Porous Plates

Hazem Ali Attia

Mohamed Eissa Sayed-Ahmed

Department of Engineering Mathematics and Physics,
Faculty of Engineering,
Fayoum University,
63111 El-Fayoum, Egypt

The unsteady magnetohydrodynamics flow of an electrically conducting viscous incompressible non-Newtonian Casson fluid bounded by two parallel nonconducting porous plates is studied with heat transfer considering the Hall effect. An external uniform magnetic field is applied perpendicular to the plates and the fluid motion is subjected to a uniform suction and injection. The lower plate is stationary and the upper plate is suddenly set into motion and simultaneously suddenly isothermally heated to a temperature other than the lower plate temperature. Numerical solutions are obtained for the governing momentum and energy equations taking the Joule and viscous dissipations into consideration. The effect of the Hall term, the parameter describing the non-Newtonian behavior, and the velocity of suction and injection on both the velocity and temperature distributions are studied.
[DOI: 10.1115/1.2927392]

Keywords: MHD flow, heat transfer, non-Newtonian fluids, Hall effect, numerical solution

1 Introduction

The study of Couette flow in a rectangular channel of an electrically conducting viscous fluid under the action of a transversely applied magnetic field has immediate applications in many devices such as magnetohydrodynamics (MHD) power generators, MHD pumps, accelerators, aerodynamics heating, electrostatic precipitation, polymer technology, petroleum industry, purification of crude oil, and fluid droplet sprays. Channel flows of a Newtonian fluid with heat transfer have been studied with or without Hall currents by many authors [1–12]. These results are important for the design of the duct wall and the cooling arrangements.

The most important non-Newtonian fluid possessing a yield value is the Casson fluid, which has significant applications in polymer processing industries and biomechanics. Casson fluid is a shear thinning liquid, which has an infinite viscosity at a zero rate of shear, a yield stress below which no flow occurs, and a zero viscosity at an infinite rate of shear. Casson's constitute equation represents a nonlinear relationship between stress and rate of strain and has been found to be accurately applicable to silicon suspensions, suspensions of bentonite in water, and lithographic varnishes used for printing inks [13–15]. Many authors [16–18] studied the flow and/or heat transfer of a Casson fluid in different geometries.

Contributed by the Heat Transfer Division of ASME for publication in the JOURNAL OF HEAT TRANSFER. Manuscript received October 24, 2005; final manuscript received February 14, 2007; published online September 2, 2008. Review conducted by Yogesh Jaluria.

Tao [1] has studied the influence of an external applied uniform magnetic field on Couette flow without taking the Hall effect into consideration. Attia and Kotb [9] have studied the flow and heat transfer between stationary parallel plates in the presence of a uniform magnetic field by neglecting the Hall effect and considering variable viscosity. In Refs. [1,9], the flow was steady and the fluid was Newtonian. Attia [10] has studied the influence of the Hall current on the velocity and temperature fields of an unsteady Hartmann flow of a conducting Newtonian fluid between two infinite nonconducting horizontal parallel and porous plates. The effect of the ion slip on unsteady Couette flow with heat transfer in a Newtonian fluid was studied in Ref. [19]. The influence of an external uniform magnetic field on Couette flow of an Oldroyd non-Newtonian fluid has been studied by Hayat et al. [20] neglecting the Hall effect.

In the present paper, the hydromagnetic flow and heat transfer of a generalized Couette flow of a non-Newtonian Casson fluid are studied considering the Hall effect. The upper plate is moving with a uniform velocity while the lower plate is stationary. The fluid is acted upon by a constant pressure gradient, a uniform suction from above, and a uniform injection from below and is subjected to a uniform magnetic field perpendicular to the plates. The Hall current is taken into consideration, while the induced magnetic field is neglected by assuming a very small magnetic Reynolds number [5]. The two plates are kept at two different but constant temperatures. This configuration is a good approximation of some practical situations such as heat exchangers, flow meters, and pipes that connect system components. The Joule and viscous dissipations are taken into consideration in the energy equation. The governing momentum and energy equations are solved numerically using the finite difference approximations. The inclusion of the Hall current, the suction and injection, and the non-Newtonian fluid characteristics leads to some interesting effects on both the velocity and temperature fields.

2 Formulation of the Problem

The fluid is assumed to be laminar, incompressible, and obeying a Casson model and flows between two infinite horizontal plates located at the $y=\pm h$ planes and extend from $x=0$ to ∞ and from $z=0$ to ∞. The upper plate is suddenly set into motion and moves with a uniform velocity U_0 while the lower plate is stationary. The upper plate is simultaneously subjected to a step change in temperature from T_1 to T_2. Then, the upper and lower plates are kept at two constant temperatures T_2 and T_1 respectively, with $T_2 > T_1$. The fluid is acted upon by a constant pressure gradient dp/dx in the x-direction (as done by many authors [5–10,17–19]), and a uniform suction from above and injection from below, which are applied at $t=0$. A uniform magnetic field B_0 is applied in the positive y-direction and is assumed undisturbed as the induced magnetic field is neglected by assuming a very small magnetic Reynolds number. The Hall effect is taken into consideration and consequently a z-component for the velocity is expected to rise. The uniform suction implies that the y-component of the velocity is constant. Thus, the fluid velocity vector is given by $\mathbf{v}(y,t)=u(y,t)\mathbf{i}+v_0\mathbf{j}+w(y,t)\mathbf{k}$. The fluid motion starts from rest at $t=0$, and the no-slip condition at the plates implies that the fluid velocity has neither a z nor an x-component at $y=\pm h$. The initial temperature of the fluid is assumed to be equal to T_1. Since the plates are infinite in the x- and z-directions, the physical quantities do not change in these directions.

The flow of the fluid is governed by the momentum equation

$$\rho\frac{D\mathbf{v}}{Dt}=\nabla\cdot(\propto\nabla\mathbf{v})-\nabla p+\mathbf{J}\cdot\mathbf{B}_0 \tag{1}$$

where ρ is the density of the fluid and ∞ is the apparent viscosity of the model and is given by

$$\propto = \left[K_c + \left(\tau_0 / \sqrt{\left(\frac{\partial u}{\partial y}\right)^2 + \left(\frac{\partial w}{\partial y}\right)^2} \right)^{1/2} \right]^2 \tag{2}$$

where K_c^2 is Casson's coefficient of viscosity and τ_0 is the yield stress. If the Hall term is retained, the current density $\mathbf{J}$ is given by

$$\mathbf{J} = \sigma[\mathbf{v} \times \mathbf{B}_0 - \beta(\mathbf{J} \times \mathbf{B}_0)] \tag{3}$$

where σ is the electric conductivity of the fluid and β is the Hall factor [5]. Equation (3) may be solved in $\mathbf{J}$ to yield

$$\mathbf{J} \times \mathbf{B}_0 = -\frac{\sigma B_0^2}{1+m^2}[(u+mw)\mathbf{i} + (w-mu)\mathbf{k}] \tag{4}$$

where m is the Hall parameter and $m = \sigma\beta B_0$. Thus, the two components of the momentum equation (1) read

$$\rho\frac{\partial u}{\partial t} + \rho v_0 \frac{\partial u}{\partial y} = -\frac{dp}{dx} + \frac{\partial}{\partial y}\left(\propto \frac{\partial u}{\partial y}\right) - \frac{\sigma B_0^2}{1+m^2}(u+mw) \tag{5}$$

$$\rho\frac{\partial w}{\partial t} + \rho v_0 \frac{\partial w}{\partial y} = \frac{\partial}{\partial y}\left(\propto \frac{\partial w}{\partial y}\right) - \frac{\sigma B_0^2}{1+m^2}(w-mu) \tag{6}$$

The energy equation with viscous and Joule dissipations is given by

$$\rho c_p \frac{\partial T}{\partial t} + \rho c_p v_0 \frac{\partial T}{\partial y} = k\frac{\partial^2 T}{\partial y^2} + \propto \left[\left(\frac{\partial u}{\partial y}\right)^2 + \left(\frac{\partial w}{\partial y}\right)^2 \right] + \frac{\sigma B_0^2}{1+m^2}(u^2+w^2) \tag{7}$$

where c_p and k are, respectively, the specific heat capacity and the thermal conductivity of the fluid. The second and third terms on the right-hand side represent the viscous and Joule dissipations, respectively. We notice that each of these terms has two components. This is because the Hall effect brings about a velocity w in the z-direction. Assuming that the applied uniform magnetic field is undisturbed as a result of taking the magnetic Reynolds number to be very small [5], the initial and boundary conditions of the problem are given by

$$u = w = 0 \quad \text{at } t \le 0, \quad \text{and } w = 0 \quad \text{at } y = -h \quad \text{and } y = h \quad \text{for } t > 0$$

$$u = 0 \quad \text{at } y = -h \quad \text{for } t > 0, \quad u = U_0 \quad \text{at } y = h \quad \text{for } t > 0 \tag{8}$$

$$T = T_1 \quad \text{at } t \le 0, \quad T = T_2 \quad \text{at } y = h, \quad \text{and } T = T_1 \quad \text{at } y = -h \quad \text{for } t > 0 \tag{9}$$

It is expedient to write the above equations in the nondimensional form. To do this, we introduce the following nondimensional quantities:

$$\bar{x} = \frac{x}{h}, \quad \bar{y} = \frac{y}{h}, \quad \bar{z} = \frac{z}{h}, \quad \bar{t} = \frac{tU_0}{h}, \quad \bar{u} = \frac{u}{U_0}, \quad \bar{w} = \frac{w}{U_0},$$

$$\bar{p} = \frac{p}{\rho U_0^2}, \quad \theta = \frac{T - T_1}{T_2 - T_1}, \quad \bar{\propto} = \frac{\propto}{K_c^2}$$

$$\tau_D = \frac{\tau_0 h}{K_c^2 U_0} \quad \text{is the Casson number(dimensionless yield stress)}$$

$$\mathrm{Re} = \frac{\rho U_0 h}{K_c^2} \quad \text{is the Reynolds number}$$

$$S = \frac{\rho v_0 h}{K_c^2} \quad \text{is the suction parameter}$$

$$\mathrm{Pr} = \frac{\rho c_p U_0 h}{k} \quad \text{is the Prandtl number}$$

$$\mathrm{Ec} = \frac{U_0 K_c^2}{\rho c_p h (T_2 - T_1)} \quad \text{is the Eckert number}$$

$$\mathrm{Ha}^2 = \frac{\sigma B_0^2 h^2}{K_c^2} \quad \text{is the Hartmann number squared}$$

In terms of the above nondimensional variables and parameters, Eqs. (5)–(9) and (2) are, respectively, written as (where the hats are dropped for convenience)

$$\frac{\partial u}{\partial t} + \frac{S}{\mathrm{Re}}\frac{\partial u}{\partial y} = -\frac{dp}{dx} + \frac{1}{\mathrm{Re}}\left[\frac{\partial}{\partial y}\left(\propto \frac{\partial u}{\partial y}\right) - \frac{\mathrm{Ha}^2}{1+m^2}(u+mw) \right] \tag{10}$$

$$\frac{\partial w}{\partial t} + \frac{S}{\mathrm{Re}}\frac{\partial w}{\partial y} = \frac{1}{\mathrm{Re}}\left[\frac{\partial}{\partial y}\left(\propto \frac{\partial w}{\partial y}\right) - \frac{\mathrm{Ha}^2}{1+m^2}(w-mu) \right] \tag{11}$$

$$\frac{\partial \theta}{\partial t} + \frac{S}{\mathrm{Re}}\frac{\partial \theta}{\partial y} = \frac{1}{\mathrm{Pr}}\frac{\partial^2 \theta}{\partial y^2} + \mathrm{Ec} \propto \left[\left(\frac{\partial u}{\partial y}\right)^2 + \left(\frac{\partial w}{\partial y}\right)^2 \right] + \frac{\mathrm{Ha}^2 \mathrm{Ec}}{1+m^2}(u^2+w^2) \tag{12}$$

$$u = w = 0 \quad \text{for } t \le 0 \quad \text{and } u = w = 0 \quad \text{at } y = -1, \quad w = 0, \quad u = 1 \quad \text{at } y = 1 \quad \text{for } t > 0 \tag{13}$$

$$\theta = 0 \quad \text{for } t \le 0 \quad \text{and } \theta = 0 \quad \text{at } y = -1, \quad \theta = 1 \quad \text{at } y = 1 \quad \text{for } t > 0 \tag{14}$$

$$\propto = \left[1 + \left(\tau_D / \sqrt{\left(\frac{\partial u}{\partial y}\right)^2 + \left(\frac{\partial w}{\partial y}\right)^2} \right)^{1/2} \right]^2 \tag{15}$$

The shear stress at the two walls is given by

$$\tau_w = \left[\left(\left(\frac{\partial u}{\partial y}\right)^2 + \left(\frac{\partial w}{\partial y}\right)^2 \right)^{1/4} + \tau_D^{1/2} / \left(\left(\frac{\partial u}{\partial y}\right)^2 + \left(\frac{\partial w}{\partial y}\right)^2 \right)^{1/4} \right]^2 \Big| y = \pm 1$$

The Nusselt numbers at the stationary wall and the upper moving wall are, respectively, given by

$$\mathrm{Nu}_1 = \frac{2\left.\frac{\partial \theta}{\partial y}\right|_{y=-1}}{-\theta_m}, \quad \mathrm{Nu}_2 = \frac{2\left.\frac{\partial \theta}{\partial y}\right|_{y=1}}{1-\theta_m}$$

3 Numerical Solution

Equations (10), (11), and (15) represent coupled system of nonlinear partial differential equations, which are solved numerically under the initial and boundary conditions (13) using the finite difference approximations. A linearization technique is first applied to replace the nonlinear terms at a linear stage, with the corrections incorporated in subsequent iterative steps until convergence is reached. Then, the Crank–Nicolson implicit method is used at two successive time levels [21]. An iterative scheme is used to solve the linearized system of difference equations. The solution at a certain time step is chosen as an initial guess for the next time step and the iterations are continued till convergence, within a prescribed accuracy. Finally, the resulting block tridiagonal system is solved using the generalized Thomas algorithm [21]. The energy equation (12) is a linear inhomogeneous second-order ordinary differential equation, whose right-hand side is known from the solutions of the flow equations (10), (11), and (15) subject to the condition (13). The values of the velocity components are substituted in the right-hand side of Eq. (12), which is solved numerically with the initial and boundary conditions (14) using central differences for the derivatives and Thomas algorithm for the solution of the set of discritized equations. Finite difference equations relating the variables are obtained by writing the equa-

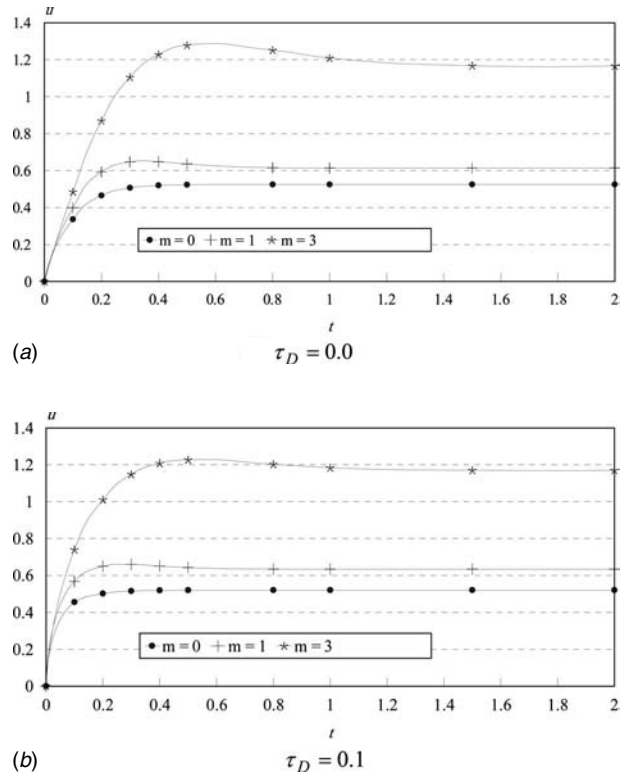

Fig. 1 Effect of the Hall parameter *m* on the time development of *u* at *y*=1 for *S*=1 and Ha=3

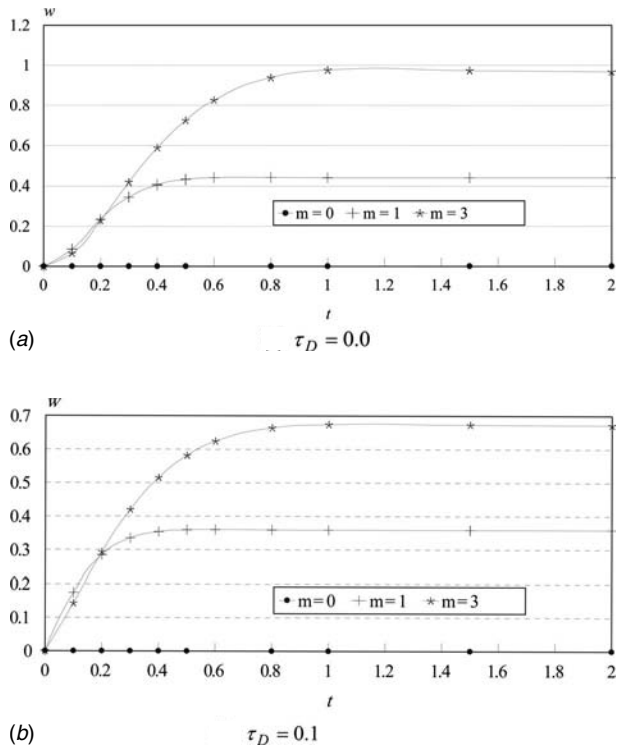

Fig. 2 Effect of the Hall parameter *m* on the time development of *w* at *y*=1 for *S*=1 and Ha=3

tions at the midpoint of the computational cell and then replacing the different terms by their second-order central difference approximations in the y-direction. The diffusion terms are replaced by the average of the central differences at two successive time levels. Computations have been made for $dp/dx=5$, Pr=1, Re =1, and Ec=0.2. Grid-independence studies show that the computational domains $0<t<\infty$ and $-1<y<1$ can be divided into intervals with step sizes $\Delta t=0.0001$ and $\Delta y=0.005$ for time and space, respectively.

4 Results and Discussion

Figures 1–3 depict the variation of the velocity components u and w and the temperature θ at the center of the channel ($y=0$) with time, respectively, for various values of the Hall parameter m and for $\tau_D=0.0$, 0.05, and 0.1. In these figures, Ha=3 and $S=1$. Figure 1 shows that u increases with increasing m for all values of τ_D as the effective conductivity ($=\sigma/(1+m^2)$) decreases with increasing m, which reduces the magnetic damping force on u. It is observed also from the figure that the time at which u reaches its steady state value increases with increasing m while it decreases when τ_D increases. The effect of τ_D on u becomes more pronounced for large values of m. In Fig. 2, the velocity component w increases with increasing m as w is a result of the Hall effect. On the other hand, at small times, w decreases when m increases. This happens due to the fact that, at small times, w is very small and then the source term of w is proportional to $(mu/(1+m^2))$, which decreases with increasing $m(m>1)$. This accounts for the crossing of the curves of w with t for all values of τ_D. Figures 1 and 2 indicate also that the influence of τ_D on u and w depends on m and becomes clearer when m is large. An interesting phenomenon is observed in Figs. 1 and 2, which is that, when m has a nonzero value, the component u and, sometimes, w overshoot. For some times, they exceed their steady state values and then go down towards steady state. This may be explained by stating that with the progress of time, u increases and consequently w increases according to Eq. (11) until w reaches its maximum value. The increase in w results in a small decrease in u according to Eq. (10). This reduction in u may, in turn, result in a decrease in w

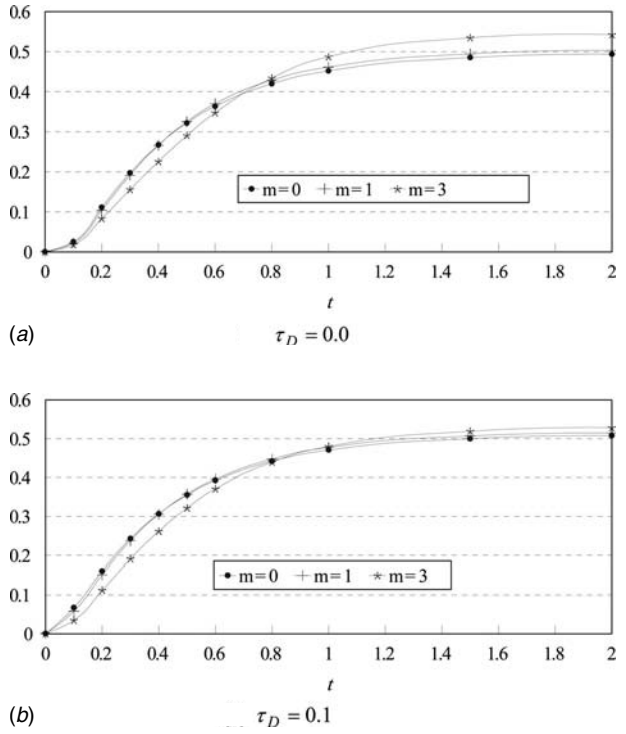

Fig. 3 Effect of the Hall parameter *m* on the time development of θ at *y*=1 for *S*=1 and Ha=3

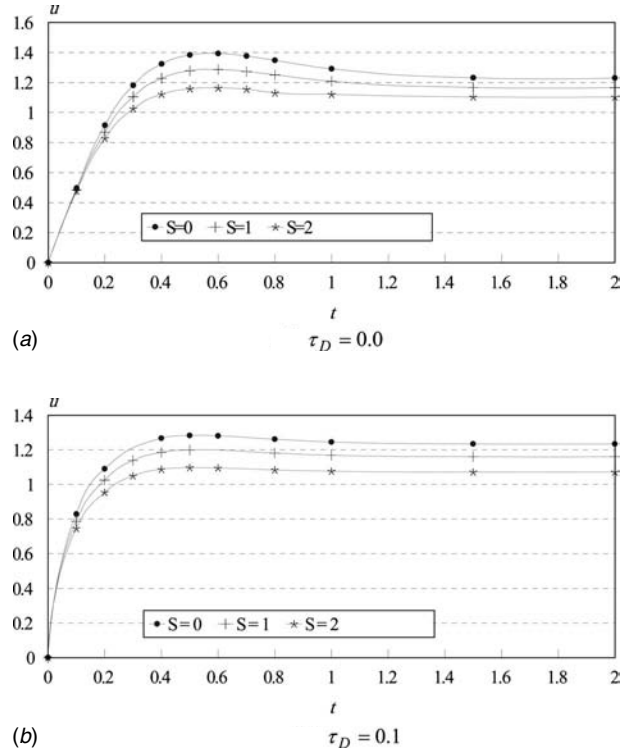

Fig. 4 Effect of the suction parameter *S* on the time development of *u* at *y*=1 for *m*=1 and Ha=3

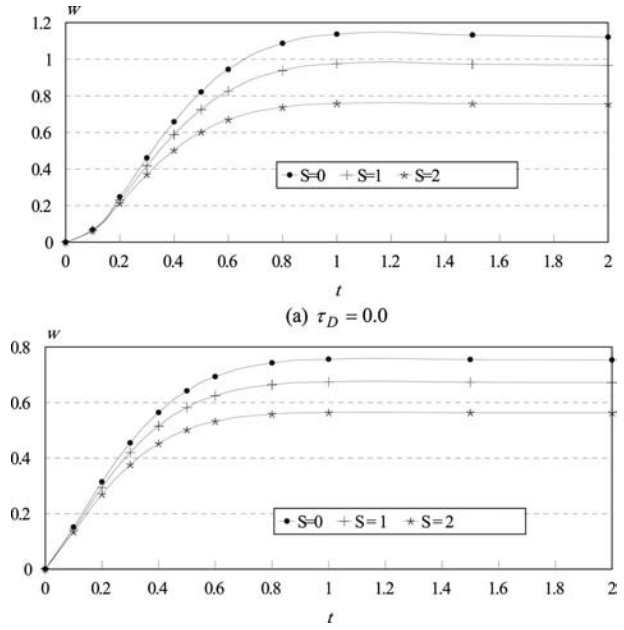

Fig. 5 Effect of the suction parameter *S* on the time development of *w* at *y*=1 for *m*=1 and Ha=3

according to Eq. (11), which explains the reduction after the peaks. The time at which overshooting occurs decreases with increasing τ_D. Figure 3 shows that the influence of m on θ depends on t. Increasing m decreases θ at small times and increases it at large times. This is due to the fact that, for small times, u and w are small and an increase in m increases u but decreases w. Then, the Joule dissipation, which is also proportional to $(1/1+m^2)$, decreases. For large times, increasing m increases both u and w and, in turn, increases the Joule and viscous dissipations. This accounts for the crossing of the curves of θ with time for all values of τ_D. It is also observed that increasing τ_D increases the temperature θ for small t, but decreases it for large t. This is because increasing τ_D decreases both u and w and their gradients, which decreases the Joule and viscous dissipations.

Figures 4–6 show the effect of the suction parameter S on the time development of the velocity components u and w and the temperature θ at $y=0$ with time, respectively, for various values for $\tau_D=0.0$, 0.05, and 0.1. In these figures, Ha=3 and $m=3$. Figure 4 shows that u at the center of the channel decreases with increasing S for all values of τ_D due to the convection of the fluid from regions in the lower half to the center, which has higher fluid speed. Figure 5 shows that w decreases with increasing S for all values of τ_D as a result of decreasing u, which affects the source term of w. The figure presents also the influence of S on the reduction of the overshooting in w especially for small values of τ_D. Figure 6 indicates that increasing S decreases the temperature at the center of the channel for all values of τ_D. This is due to the influence of the convection in pumping the fluid from the cold lower half towards the center of the channel.

5 Conclusions

The transient Couette flow of a Casson non-Newtonian fluid under the influence of an applied uniform magnetic field is studied considering the Hall effect. The effects of the Casson number τ_D, the Hall parameter m, and the suction parameter S on the velocity and temperature distributions are studied. The Hall term affects the main velocity component u in the x-direction and gives rise to another velocity component w in the z-direction. An overshooting in the velocity components u and w with time due to the Hall effect is observed for all values of τ_D. The flow index τ_D has an apparent effect in controlling the overshooting in u or w and the time at which it occurs. The results show that the influence of the parameter τ_D on u and w depends on m and becomes more apparent when m is large. It is found also that the effect of m on w depends on t for all values of τ_D, which accounts for a crossover in the w-t graph for various values of m. The effect of m on the

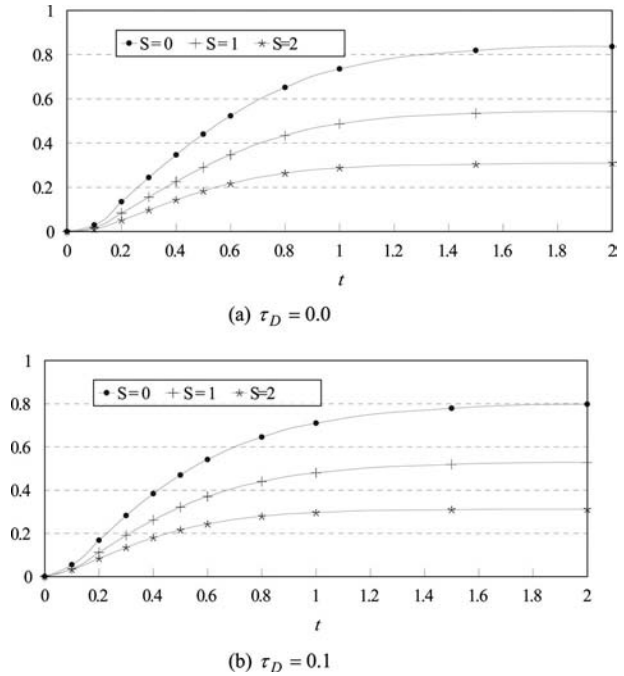

Fig. 6 Effect of the suction parameter *S* on the time development of θ at *y*=1 for *m*=1 and Ha=3

magnitude of θ depends on n and becomes more pronounced in case of small τ_D. The time at which u and w reach the steady state increases with increasing m, but decreases when τ_D increases. The time at which θ reaches its steady state increases with increasing m while it is not greatly affected by changing τ_D.

References

[1] Tao, I. N., 1960, "Magnetohydrodynamic Effects on the Formation of Couette Flow," J. Aerosp. Sci., **27**, pp. 334–347.

[2] Nigam, S. D., and Singh, S. N., 1960, "Heat Transfer by Laminar Flow Between Parallel Plates Under the Action of Transverse Magnetic Field," Q. J. Mech. Appl. Math., **13**, pp. 85–97.

[3] Alpher, R. A., 1961, "Heat Transfer in Magnetohydrodynamic Flow Between Parallel Plates," Int. J. Heat Mass Transfer, **3**, pp. 108–117.

[4] Tani, I., 1962, "Steady Motion of Conducting Fluids in Channels Under Transverse Magnetic Fields With Consideration of Hall Effect," J. Aerosp. Sci., **29**, pp. 287–299.

[5] Sutton, G. W., and Sherman, A., 1965, *Engineering Magnetohydrodynamics*, McGraw-Hill, New York.

[6] Soundalgekar, V. M., Vighnesam, N. V., and Takhar, H. S., 1979, "Hall and Ion-Slip Effects in MHD Couette Flow With Heat Transfer," IEEE Trans. Plasma Sci., **PS-7**(3), pp. 178–182.

[7] Soundalgekar, V. M., and Uplekar, A. G., 1986, "Hall Effects in MHD Couette Flow With Heat Transfer," IEEE Trans. Plasma Sci., **PS-14**(5), pp. 579–583.

[8] Abo-El-Dahab, E. M. H., 1993, "Effect of Hall Currents on Some Magnetohydrodynamic Flow Problems," Master thesis, Department of Mathematics, Faculty of Science, Helwan University, Egypt.

[9] Attia, H. A., and Kotb, N. A., 1996, "MHD Flow Between Two Parallel Plates With Heat Transfer," Acta Mech., **117**, pp. 215–220.

[10] Attia, H. A., 1998, "Hall Current Effects on the Velocity and Temperature Fields of an Unsteady Hartmann Flow," Can. J. Phys., **76**(9), pp. 739–746.

[11] Attia, H. A., 2003, "Steady Hartmann Flow With Temperature Dependent Viscosity and the Ion Slip," Int. Commun. Heat Mass Transfer, **30**(6), pp. 881–890.

[12] Lahjomri, J., Zniber, K., Oubarra, A., and Alemany, A., 2003, "Heat Transfer by Laminar Hartmann's Flow in Thermal Entrance Region With Uniform Wall Heat Flux: The Graetz Problem Extended," Energy Convers. Manage., **44**(1), pp. 11–34.

[13] Casson, N., 1959, "A Flow Equation for Pigment Oil-Suspensions of the Printing Ink Type," *Rheology of Disperse Systems*, C. C. Mill, ed., Pergamon, London, p. 84.

[14] Tamamashi, B., 1968, "Consideration of Certain Hemorheological Phenomena From the Standpoint of Surface Chemistry," *Hemorheology*, A. L. Copley, ed., Pergamon, London, p. 89.

[15] Walawander, W. P., Chen, T. Y., and Cala, D. F., 1975, "An Approximate Casson Fluid Model for Tube Flow of Blood," Biorheology, **12**, pp. 111–124.

[16] Batra, R. L., and Jena, B., 1991, "Flow of a Casson Fluid in a Slightly Curved Tube," Int. J. Eng. Sci., **29**, pp. 1245–1261.

[17] Das, B., and Batra, R. L., 1993, "Secondary Flow of a Casson Fluid in a Slightly Curved Tube," Int. J. Non-Linear Mech., **28**(5), pp. 567–578.

[18] Sayed Ahmed, M. E., and Attia, H. A., 1998, "Magnetohydrodynamic Flow and Heat Transfer of a Non-Newtonian Fluid in an Eccentric Annulus," Can. J. Phys., **76**, pp. 391–404.

[19] Attia, H. A., 2005, "Unsteady Couette Flow With Heat Transfer Considering the Ion Slip," Turk. J. Phys., **29**(6), pp. 379–388.

[20] Hayat, T., Khan, M., and Ayub, M., 2004, "Couette and Poiseuille Flows of an Oldroyd 6-Constant Fluid With Magnetic Field," J. Math. Anal. Appl., **298**, pp. 225–244.

[21] Antia, M., 1991, *Numerical Methods for Scientists and Engineers*, Tata McGraw-Hill, New Delhi.

Multiobjective Optimization of a Microchannel Heat Sink Using Evolutionary Algorithm

Afzal Husain
Department of Mechanical Engineering,
Graduate School of Inha University,
253 Yonghyun-Dong, Nam-Gu, Incheon 402-751,
Republic of Korea
e-mail: afzal19@inhaian.net

Kwang-Yong Kim[1]
Professor
Department of Mechanical Engineering,
Inha University,
253 Yonghyun-Dong, Nam-Gu, Incheon 402-751,
Republic of Korea
e-mail: kykim@inha.ac.kr

A multiobjective performance optimization of microchannel heat sink is carried out numerically applying surrogate analysis and evolutionary algorithm. Design variables related to microchannel width, depth, and fin width are selected, and two objective functions, thermal resistance and pumping power, are employed. With the help of finite volume solver, Navier–Stokes analyses are performed at the design sites obtained from full factorial design of sampling methods. Using the numerically evaluated objective function values, polynomial response surface is constructed for each objective functions, and multiobjective optimization is performed to obtain global Pareto optimal solutions. Analysis of optimum solutions is simplified by carrying out trade-off with design variables and objective functions. Objective functions exhibit changing sensitivity to design variables along the Pareto optimal front. [DOI: 10.1115/1.2969261]

Keywords: microchannel, electronic cooling, numerical simulation, evolutionary algorithm, multiobjective optimization

1 Introduction

The limitations of space in microelectromechanical systems (MEMSs) and power to drive cooling devices used in electronics robotics, avionics, and medicine industry have opened the doors for optimization. Following the pioneering work of Tuckerman and Pease [1], who carried out silicon-based microchannel heat sink experimentation, many researchers have analyzed microcooling phenomena and conducted parametric and optimization studies. Kawano et al. [2] carried out experiments for microchannel heat sink and found Navier–Stokes solutions for these experiments well within the experimental uncertainties. Some analytical studies [3–5] are devoted to analyze the fluid flow and heat transfer to optimize the microchannel heat sink.

Kim [6] and later Liu and Garimella [7] derived the analytical models based on various assumptions and compared these models with the robust three-dimensional numerical model and optimized the microchannel heat sink. Although the numerical optimization of the rectangular microchannel heat sink has been carried out to minimize thermal resistance at constant pumping power [8,9], there is scarcity of literature related to the full model microchannel heat sink optimization for a wide range of pumping source.

Evolutionary algorithms have been used as effective tools for generating Pareto optimal solutions in various engineering designs. Foli et al. [10] performed the shape optimization of microheat exchanger and obtained the Pareto optimal solutions using a fast and elitist nondominated sorting genetic algorithm (NSGA-II) in combination with the analytical and computational fluid dynamics (CFD) analysis.

The present work deals with the multiobjective optimization of microchannel heat sink, which involves the usage of hybrid multiobjective evolutionary approach [11] in combination with three-dimensional Navier–Stokes analysis. As a surrogate model, response surface approximation is used to evaluate objective function values required by NSGA-II to search optimal solutions. The global Pareto optimal front is explored to get inside of the trade-off analysis between the competing objectives.

2 Microchannel Model and Numerical Methods

The dimensions of the microchannel heat sink shown in Fig. 1 are $10\times10\times0.42$ mm^3. It has been found that thermal resistance decreases with an increase in the aspect ratio (H_c/W_c) [8,10], and therefore $H_c=370$ μm is kept constant for all optimization cases in order to assess the effect of the microchannel and fin widths on the thermal resistance and pumping power. The steady, incompressible, and fully developed laminar flow is assumed and uniform heat flux is applied at the bottom of the heat sink with constant fluid (water) properties at 27°C. Governing equations for conservation of mass and momentum are solved with the following energy equations for conjugate heat transfer:

$$\bar{V}\cdot\nabla(\rho_f C_{p,f} T_f)=\nabla\cdot(k_f\nabla T_f) \quad \text{(for the fluid)} \tag{1}$$

$$\nabla\cdot(k_s\nabla T_s)=0 \quad \text{(for the substrate conduction)} \tag{2}$$

These governing equations are solved using commercial code ANSYS CFX-10.0 [12]. The code uses finite volume solver based on the SIMPLE algorithm [13]. Due to the symmetry of the problem, half of the single microchannel is selected as computational domain, as shown in Fig. 2. The silicon part of the heat sink at the inlet and outlet of the channel is maintained as an adiabatic boundary. No-slip condition is applied at the interior walls of the channel, i.e., $\bar{V}=0$. The thermal conditions in the z-direction are

$$-k_s\frac{\partial T_s}{\partial z}=q \quad \text{at} \quad z=0 \quad \text{and} \quad k_s\frac{\partial T_s}{\partial z}=0 \quad \text{at} \quad z=L_z$$

3 Optimization Techniques

3.1 Design Variables and Objective Functions. Out of four geometric parameters, which affect the performance of microchannel heat sink, three design variables, $W_c/H_c(=\theta)$, $W_w/H_c(=\phi)$, and $W_b/W_c(=\eta)$, are formed for the optimization and design points are selected using three-level full factorial design in

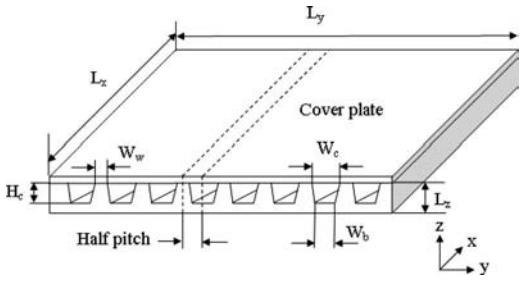

Fig. 1 Schematic of microchannel heat sink

[1]Corresponding author.

Contributed by the Heat Transfer Division of ASME for publication in the JOURNAL of HEAT TRANSFER. Manuscript received March 14, 2007; final manuscript received April 18, 2008; published online September 4, 2008. Review conducted by Yogendra Joshi.

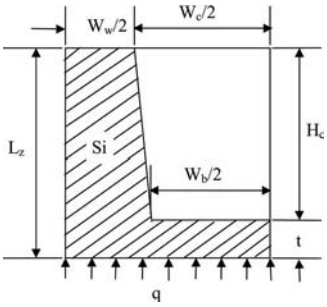

Fig. 2 Computational domain

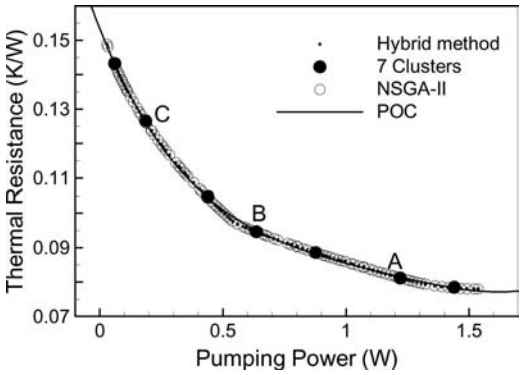

Fig. 3 Pareto optimal solutions using hybrid multiobjective evolutionary approach, NSGA-II, seven clusters, and global POC

the ranges 0.1–0.25, 0.02–0.1, and 0.5–1.0, respectively, which covers both rectangular ($W_b/W_c=1$) and trapezoidal ($0.5<W_b/W_c<1$) cross sections of the microchannel.

Two objective functions are employed to optimize the microchannel heat sink; one is the thermal resistance related to the heat transfer performance and the other is the pumping power to drive the coolant through the microchannel. The thermal resistance is defined by

$$R_{\text{th}} = \frac{\Delta T_{\max}}{qA_s} \tag{3}$$

The pumping power required to drive the fluid through the microchannel heat sink can be evaluated as

$$\bar{P} = Q \cdot \Delta p \tag{4}$$

3.2 Surrogate Construction and Multiobjective Evolutionary Algorithm. In the present study, response surface approximation (RSA) [14] method is applied to construct response functions for the two objectives under study. In a hybrid multiobjective evolutionary approach, first, approximate Pareto optimal solutions are obtained using real coded NSGA-II. These solutions are then refined by searching a local optimal solution for each objective function over the whole NSGA-II obtained optimal solutions using sequential quadratic programming (SQP) with NSGA-II solutions as initial guesses. To perform local search, the first objective is optimized and the second objective is treated as equality constraint. The local search is repeated for the second objective function treating the first as equality constraint. This process gives two new sets of optimal solutions, which are then merged with the NSGA-II solutions. From these solutions, first, dominated solutions are discarded and then duplicate solutions are removed to get global Pareto optimal solutions.

4 Results and Discussion

The numerical results were validated with the analytical and experimental results and reported in a previous work by Husain and Kim [9], where the analysis methods same as in this work were employed. Initially 27 design points are chosen by full factorial design and the objective functions are calculated numerically at these points. In the RSA method, an analysis of variance (ANOVA) and a regression analysis, provided by *t*-statistics [14], are implemented to measure the uncertainty in the set of coefficients in the polynomial. The values of R^2, R^2_{adj}, and PRESS for thermal resistances are 0.979, 0.966, and 0.008, respectively, while for pumping power the values are 0.982, 0.977, and 0.086, respectively. These values are reliable in reference to the value of $0.9<R^2_{\text{adj}}<1.0$ suggested by Guinta [15] for accurate prediction of the response surface model.

A real coded NSGA-II is invoked to obtain well spread approximate Pareto optimal solutions with 200 populations and 500 generations. The crossover and mutation probabilities are set to 0.9 and 0.25, respectively. The crossover and mutation parameters are decided as 20 and 200, respectively. These parameters are adjusted one by one to suit the nature of the problem. After a local search, there are 415 optimal solutions, which are called as global Pareto optimal solutions. *K*-mean clustering is performed to find a representative solution for a group of solutions. Seven representative clusters are formed, as shown in Fig. 3. Three of these clusters are reproduced numerically and the values of objective functions and corresponding design variables are presented in Table 1 along with the reference [2] solution.

The shape of the Pareto optimal front suggests that the two objective functions are convex in nature, and for every fixed value of one objective there is one optimum value of the other objective function. Due to the conflicting nature of the objective functions, which was presumed before obtaining the Pareto optimal front, improvement of one objective leads to deterioration of other objective. Here, it can be noticed that no solution out of 415 optimal solutions is superior to other in both objectives since each solution is global Pareto optimal solution.

The trade-off analysis shows that at point A, lower thermal resistance is obtained at the expense of higher pumping power, whereas at point C, thermal resistance is higher at lower pumping power. The Pareto optimal front changes its gradient significantly near point B. A designer can pick optimal solution according to the pumping power available to drive the fluid or thermal resis-

Table 1 Predicted results of optimum designs with their CFD computed results and comparison with reference geometry

		Design variables			MOEA prediction		CFD calculation	
Optimal points		θ	ϕ	η	R_{th} (K/W)	$\bar{P}$ (W)	R_{th} (K/W)	$\bar{P}$ (W)
Reference [2]		0.154	0.116	1.000	0.199	0.050	0.192	0.050
MOEA	A	0.100	0.022	0.773	0.081	1.220	0.084	1.213
	B	0.100	0.086	0.946	0.095	0.636	0.098	0.627
	C	0.146	0.098	0.971	0.127	0.187	0.127	0.180

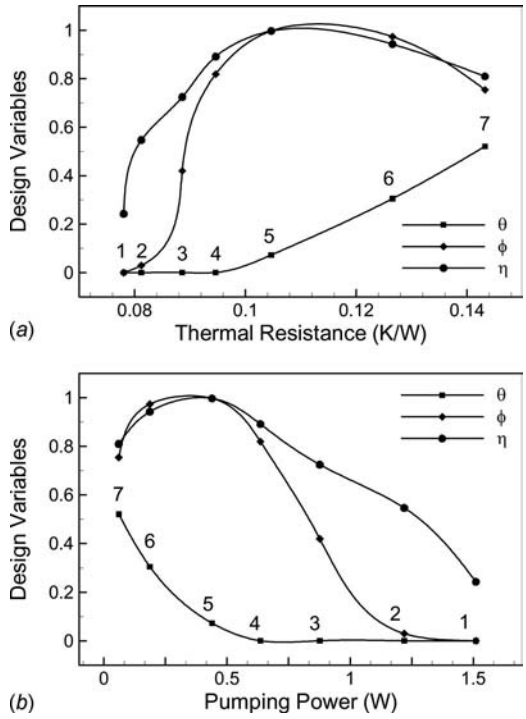

Fig. 4 Distribution of design variables over Pareto optimal front with objective functions: (*a*) thermal resistance and (*b*) pumping power

tance required. Pareto optimal curve (POC) is obtained by fitting a fourth order polynomial for two objectives representing thermal resistance as a function of pumping power, as shown in Fig. 3. Only the extent of POC bounded by global Pareto optimal solutions represents global Pareto optimal front. The trend of POC shows that thermal resistance and its gradient decrease with increasing pumping power.

A deeper insight of the Pareto optimal solutions can be attained by analyzing the variation of design variables along the Pareto optimal front. This analysis gives the designer a freedom to choose economic combination from the design and manufacturing points of view. The distribution of design variable over the Pareto optimal front is studied by plotting these against both thermal resistance and pumping power corresponding to the seven clusters of Pareto optimal solutions, as shown in Fig. 4. It is observed that θ increases continuously while ϕ and η show the alternating increasing and decreasing characteristics along the optimal front moving from point 1 toward point 7, which is the direction of increasing thermal resistance and decreasing pumping power.

5 Conclusion

The present study demonstrates multiobjective optimization of microchannel heat sink with the help of hybrid multiobjective evolutionary approach. Global Pareto optimal solutions are obtained using NSGA-II in combination with a local search strategy. All the three design variables have significant effect on the thermal performance of microchannel heat sink. Pareto optimal front reveals the existing trade-off between the thermal resistance and the pumping power to optimize the microchannel heat sink. The optimum design variables are sensitive to pumping power within the design space and show an alternating behavior with change of pumping power.

Acknowledgment

This work was supported by Inha University Research Grant.

Nomenclature

A_s = surface area of substrate base
C_p = specific heat
H_c = microchannel depth
k = thermal conductivity
L_x, L_y, L_z = length, width, and height of heat sink, respectively
$\bar{P}$, p = pumping power and pressure drop, respectively
q = heat flux
Q = coolant flow rate
R^2 = coefficient of multiple determination
R^2_{adj} = adjusted value of R^2
R_{th} = thermal resistance
T, t = temperature and thickness of the base of microchannel, respectively
$\bar{V}$ = velocity vector
W_b, W_c, W_w = widths of bottom, top, and fin of microchannel, respectively
x, y, z = orthogonal coordinate system

Greek Symbols

Δ = change in value
ϕ, η, θ = design variables, W_w/H_c, W_b/W_c, and W_c/H_c, respectively
ρ = density

Subscripts

f, s = fluid and substrate, respectively
max = maximum value

References

[1] Tuckerman, D. B., and Pease, R. F. W., 1981, "High-Performance Heat Sinking for VLSI," IEEE Electron Device Lett., **EDL-2**, pp. 126–129.
[2] Kawano, K., Sekimura, M., Minakami, K., Iwasaki, H., and Ishizuka, M., 2001, "Development of Micro Channel Heat Exchanging," JSME Int. J., Ser. B, **44**(4), pp. 592–598.
[3] Knight, R. W., Hall, D. J., Goodling, J. S., and Jaeger, R. C., 1992, "Heat Sink Optimization With Application to Microchannels," IEEE Trans. Compon., Hybrids, Manuf. Technol., **15**(5), pp. 832–842.
[4] Wei, X., and Joshi, Y., 2003, "Optimization Study of Stacked Micro-Channel Heat Sinks for Micro-Electronic Cooling," IEEE Trans. Compon. Packag. Technol., **26**(1), pp. 55–61.
[5] Fisher, T. S., and Torrance, K. E., 2001, "Optimal Shapes of Fully Embedded Channels for Conjugate Cooling," IEEE Trans. Adv. Packag., **24**(4), pp. 555–562.
[6] Kim, S. J., 2004, "Methods for Thermal Optimization of Microchannel Heat Sinks," Heat Transfer Eng., **25**(1), pp. 37–49.
[7] Liu, D., and Garimella, S. V., 2005, "Analysis and Optimization of the Thermal Performance of Microchannel Heat Sinks," Int. J. Numer. Methods Heat Fluid Flow, **15**(1), pp. 7–26.
[8] Li, J., and Peterson, G. P., 2006, "Geometric Optimization of a Micro Heat Sink With Liquid Flow," IEEE Trans. Compon. Packag. Technol., **29**(1), pp. 145–154.
[9] Husain, A., and Kim, K. Y., 2007, "Design Optimization of Micro-channel for Micro Electronic Cooling," The Fifth International Conference on Nanochannels, Microchannels and Minichannels, Puebla, Mexico, June 18–20, Paper No. ICNMM2007-30053.
[10] Foli, K., Okabe, T., Olhofer, M., Jin, Y., and Sendhoff, B., 2006, "Optimization of Micro Heat Exchanger: CFD, Analytical Approach and Multi-Objective Evolutionary Algorithms," Int. J. Heat Mass Transfer, **49**, pp. 1090–1099.
[11] Deb, K., and Goel, T., 2001, "A Hybrid Multi-Objective Evolutionary Approach to Engineering Shape Design," *Proceedings of Evolutionary Multi-Criterion Optimization Conference*, Zurich, March 7–9, pp. 385–399.
[12] CFX-10.0 Solver Theory, 2005, ANSYS.
[13] Patankar, S. V., 1980, *Numerical Heat Transfer and Fluid Flow*, McGraw-Hill, New York, pp. 124–134.
[14] Myers, R. H., and Montgomery, D. C., 1995, *Response Surface Methodology: Process and Product Optimization Using Designed Experiments*, Wiley, New York.
[15] Guinta, A. A., 1997, "Aircraft Multidisciplinary Design Optimization Using Design of Experimental Theory and Response Surface Modeling Methods," Ph.D. thesis, Virginia Polytechnic Institute and State University, Blacksburg.

Simulation of Thermal Fluid Flow Transport in a Channel Containing Slot-Perforated Flat Plates

Shuichi Torii
Department of Mechanical System Engineering,
Kumamoto University,
2-39-1 Kurokami,
Kumamoto 860-8550, Japan
e-mail: torii@mech.kumamoto-u.ac.jp

Wen-Jei Yang
Department of Mechanical Engineering,
University of Michigan,
Ann Arbor, MI 48109
e-mail: wjyang@engin.umich.edu

A numerical study is performed to investigate unsteady, two-dimensional, incompressible laminar flow over both sides of a slot-perforated flat surface in a pulsating channel flow. Consideration is given to the effects of the pulsating Strouhal number fSr, the Reynolds number Re, and the blockage factor, i.e., the ratio of plate thickness, δ, to channel width, W, on the heat-transfer performance and the velocity and thermal fields. It is found from the study that (i) time-averaged Nusselt number at the rear plate is amplified with Re, (ii) in contrast, the corresponding performance is attenuated with an increase in the blockage factor, whose effect becomes larger in the lower region of the Reynolds number, i.e., Re = 100, and (iii) enhancement of the Nusselt number causes an increase in fSr, whose effect becomes minor near in the region of Re = 100. [DOI: 10.1115/1.2970077]

Keywords: heat transfer, perforated plate, alternate crossing of flow, numerical simulation, blockage factor, pulsating Strouhal number

1 Introduction

Perforated plates may be employed as an extended surface for internal cooling of turbine blades. They are compact and high in heat-transfer performance induced by boundary layer interruption due to perforations without the salient penalty of the form drag [1–6]. Liang et al. [7] investigated the flow characteristics and the mechanisms of plate vibration and noise, induced by the shedding of vortices from perforated holes. Furthermore, Liang et al. [7] and Liang [8] studied the effects of geometry and arrangement of the perforations on fluid flow behavior and disclosed that the ratio of slot length, in the flow direction, to its thickness plays a very important role in flow behavior. In order to investigate the effects of the Reynolds number and the ratio of the slot width, d, to the plate thickness, δ, on the velocity field, the corresponding numerical analysis was carried out by Torii and Yang [9]. They reported that the flow pattern between two plates placed in a freestream or two-dimensional channel can be classified into four categories depending on the combination of Re and d/δ. In particular, at a certain combination of Re and d/δ, an alternating crossing of flow of the fluid streams takes place through the slot from one side to the other side of the plate in the flow direction so that the heat-transfer performance from a surface wall of the rear plate is intensified [10]. Amon and Mikic [11] performed numerical investigation of the flow pattern and forced convective heat transfer in slotted channels, in which numerical results are compared with the results in a plane-channel flow. They disclosed that over a certain Reynolds number the flow exhibits laminar self-sustained oscillations, which cause significant heat-transfer enhancement. Suzuki et al. [12] and Nigen and Amon [13] dealt with thermal-fluid flow transport phenomenon in a plane channel with an in-line fin array and in a grooved channel, respectively. They reported that heat-transfer performance is induced due to the self-sustained oscillatory flow.

The present study investigates unsteady thermal and fluid flow transport phenomena over both sides of a slot-perforated surface in a pulsating channel flow. Emphasis is placed on the effects of the blockage factor, k_q, Reynolds number, Re, and pulsating Strouhal number, fSr, on heat-transfer performance and velocity and thermal fields. In this study the flow is assumed to be two dimensional to keep the computational time manageable.

2 Conservation Equations and Numerical Procedure

The present study deals with a forced flow over a single slot-perforated surface heated with constant wall temperature in the channel, which consists of two plain straight plates (i.e., the front and rear plates), of length, L, and thickness, δ, aligned in the flow direction with a spacing of d. Here two plates are set at $y = W/2$. Here the proposed physical model and the coordinate system are the same as Ref. [10]. The following assumptions are imposed in the formulation of the problem: incompressible, laminar, unsteady flow; constant fluid properties; uniform inlet velocity and uniform inlet fluid temperature; and negligible axial conduction (due to the high Peclet number). Under these assumptions, the simplified governing equations for mass, momentum, and energy read as follows:

$$\frac{\partial U_i}{\partial_{xi}} = 0 \tag{1}$$

$$\frac{\partial U_i}{\partial t} + U_j \frac{\partial U_i}{\partial_{xj}} = -\frac{1}{\rho}\frac{\partial P}{\partial_{xi}} + \nu \frac{\partial}{\partial_{xj}}\left(\frac{\partial U_i}{\partial_{xj}}\right) \tag{2}$$

and

$$\frac{\partial T}{\partial t} + U_j \frac{\partial T}{\partial_{xj}} = \alpha \frac{\partial}{\partial_{xj}}\left(\frac{\partial T}{\partial_{xj}}\right) \tag{3}$$

respectively. Initially, the fluid is quiescent and a uniform temperature at $T = T_{\text{inlet}}$. Then, the plate surface temperature is suddenly changed to $T = T_w$ and the flow velocity in the channel is given at U ($= u_m + u_b \sin \omega t$). Nonslip condition is employed at the perforated-plate and channel-wall surfaces. At the exit, the boundary conditions for the dependent variables are obtained by setting the first derivatives in the axial direction equal to zero. This is because the same use in other flow conditions is permissible for computational convenience if the outlet boundary is located in a flow region, which is sufficiently far downstream from the region of interest. Notice that the above boundary condition at the exit is strictly valid only when the flow is fully developed. The discretization method employed in the present study uses a finite difference formulation [14,15]. The grid system is changed from 200 $\times$ 400 ($= W \times B$) to 400 $\times$ 800 to obtain a grid-independent solution. Numerical computation was performed on a personal computer at time interval $\Delta t = 0.00001$ s. Here, the maximum time interval employed is determined to ensure the numerical stability. In the present study, $u_b/u_m = 0.20$ is fixed because the effect of pulsation amplitude on heat-transfer enhancement is not considered. L/δ and d/δ are fixed at 2 and 3, respectively, while the Reynolds number (Re) is varied from 100 to 1100, k_q is varied

Contributed by the Heat Transfer Division of ASME for publication in the JOURNAL OF HEAT TRANSFER. Manuscript received September 8, 2007; final manuscript received April 4, 2008; published online September 4, 2008. Review conducted by Gautam Biswas. Paper presented at the 2007 International Electronic Packaging Technical Conference and Exhibition (IPACK2007), Vancouver, British Columbia, Canada, July 8–12, 2007.

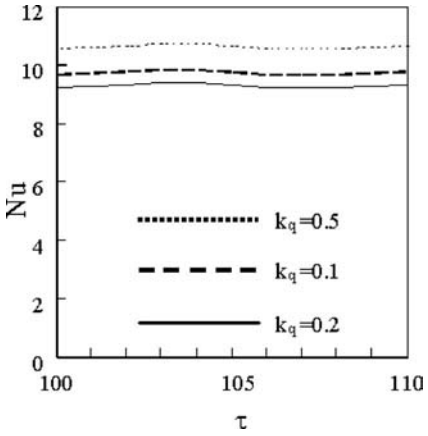

Fig. 1 Timewise variation of Nusselt numbers at the rear plate for Re=120

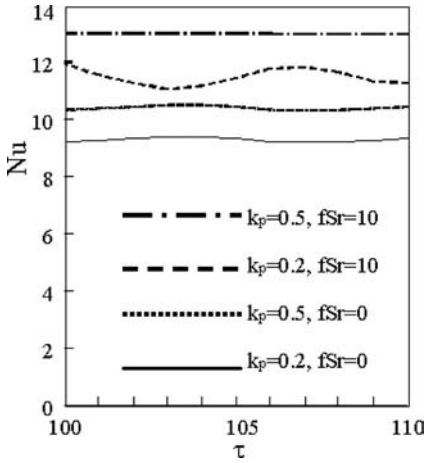

Fig. 2 Timewise variation of Nusselt numbers at the rear plate for Re=120

from 0.05 to 0.50, and pulsating Strouhal number, fSr, is varied from 0 to 10. Note that for $d/\delta=3.0$, the alternating change in the fluid flow disturbs the thermal boundary layer formed along the plate and induces mixing of the upper and lower streams of the plate downstream from the slot, resulting in an amplification of heat-transfer performance [16].

In order to confirm the numerical cord developed here, numerical calculation was performed on the heat transfer between an incompressible fluid and a blunt flat plate with constant wall temperature, whose experimental data were obtained by Marty et al. [17]. Here numerical result was compared with the Nusselt number Nu along the plate at Re=240, which corresponds to Fig. 12(a) in Ref. [17]. Numerical prediction showed that the asymptotic behavior appears in the downstream region and Nu approaches about 2.4 whose value is in good agreement with the experiment [17]. Note that the plate thickness is employed as the characteristic length in Nu and Re. Furthermore, simulations with grids of various degrees of coarseness, as mentioned earlier, were conducted to determine the required resolution for grid-independent solutions. Throughout the Reynolds number range considered here, the maximum relative error was estimated to be about 2% by comparing the solutions on regular and fine grids with twice the grid points. Although a few solutions were computed with half the time step to ensure consistency and time-step independence, there was no substantial discrepancy between two different time intervals.

3 Results and Discussion

Figure 1 illustrates the time history of the Nusselt number, Nu, at one sidewall of the rear plate. Note that numerical results during arbitrary dimensionless time interval, i.e., of $\tau=100$ to $\tau=110$, are depicted at Re=120 in the figure because the thermal transport phenomenon, from the calculation results, becomes periodic after about $\tau=80$. Here, Nu implies the averaged Nusselt number over one sidewall of the plate at each time, τ. The oscillation of the heat-transfer rate with time is caused by the alternating changes in the fluid flow across the slot, as mentioned in the following. This mechanism of heat-transfer enhancement is described in Ref. [16]. The Nusselt number is suppressed by a decrease in the channel width, i.e., an increase in the blockage factor, because the alternating changes in the fluid flow across the slot are attenuated due to the presence of the channel walls. In contrast, heat-transfer rate is intensified in the narrow channel due to the substantial flow acceleration, in spite of the suppression of the alternating changes in the fluid flow. Furthermore, the oscillation of the heat-transfer rate with time disappears in comparison with the wider channel flow case, as seen in Fig. 1.

Figure 2, for Re=120, illustrates the time records of the Nusselt number, Nu, at one sidewall of the rear plate in the same form as Fig. 1. The Nusselt number at $k_q=0.2$ oscillates with time and is substantially enhanced. This trend is induced by the presence of the pulsation of the fluid stream, i.e., fSr=10. The oscillation of the heat-transfer rate with time is caused by the alternating changes in the fluid flow across the slot. The enhanced heat transfer due to the flow pulsation also appears at $k_q=0.5$. Notice that the oscillation of the heat-transfer rate with time is suppressed, while heat-transfer rate is substantially increased. In other words, Nu is always constant as time progresses and this level is amplified with an increase in fSr. This is because the dynamic behavior due to the pulsation of the fluid stream is interacted with the flow acceleration in the narrow channel, resulting in suppression of the alternating change in the flow direction across the slot.

Figure 3 illustrates the time-averaged Nusselt number, Nu, versus the Reynolds number, Re, at fSr=1 for different values of blockage factor k_q. Although the Nusselt number is attenuated with an increase in the blockage factor, heat-transfer performance is intensified in the substantially narrow channel, i.e., for $k_q=0.5$. This trend becomes larger in the lower Reynolds number region plotted. In other words, the effect of the blockage factor on heat-transfer performance becomes minor in the higher Reynolds number region. It is found that (i) as the channel width becomes narrow, an alternating change in the velocity and temperature fields is suppressed, resulting in deterioration of heat-transfer performance, and (ii) however, heat-transfer enhancement is stimulated for larger blockage factor due to local acceleration at the minimum cross-sectional area in the channel. Notice that for larger

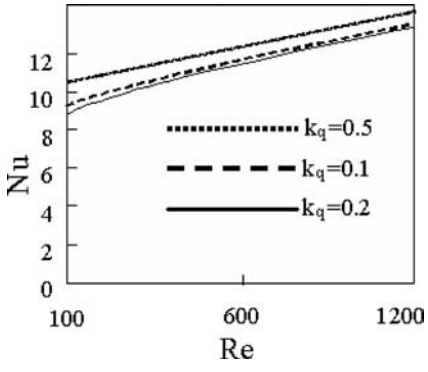

Fig. 3 Time-averaged Nusselt numbers for different blockage factors, fSr=1

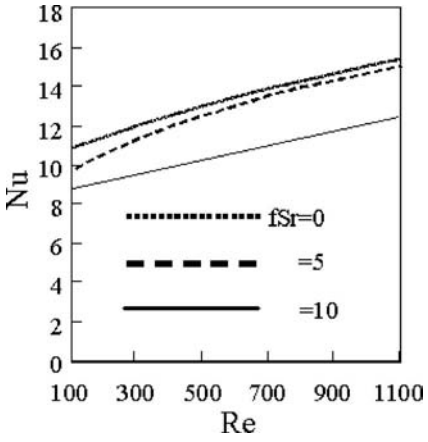

Fig. 4 Time-averaged Nusselt numbers for different pulsating Strouhal numbers, *f*Sr, for *kq*=0.1

blockage factor, the substantial pressure drop is needed to obtain the accelerated flow effect, that is, the pressure loss increases.

The effect of the pulsation of the fluid stream on the time-averaged Nusselt number is illustrated in Fig. 4, in the same form as Fig. 3. The Nusselt number, for $k_q=0.1$, is intensified with increasing pulsation of the fluid stream, i.e., fSr. This trend becomes greater in the higher Reynolds number region plotted. In other words, the effect of the pulsation frequency of the fluid stream on an enhancement of heat-transfer performance becomes minor in the lower Reynolds number region. Notice that even if the value of fSr increases substantially over 10, heat-transfer enhancement is only slight at higher Reynolds number region plotted.

4 Summary

A numerical study has been performed on unsteady thermal-fluid flow over a perforated plate (consisting of two plates spaced at an interval of d in the flow direction) installed in channels with different widths. Consideration was given to the roles of the blockage factor, k_q, Reynolds number, Re, and pulsating Strouhal number, fSr on the flow and temperature fields. The following were found.

1. Heat-transfer enhancement is stimulated for larger blockage factor due to local acceleration at the minimum cross-sectional area in the channel, whose trend becomes larger in the lower Reynolds number region, i.e., Re=100.
2. Heat-transfer performance is intensified with an increase in fSr, whose trend becomes larger in the higher Reynolds number region, i.e., Re=1100.

Nomenclature

B = channel length, m
d = slot width, m
$f\mathrm{Sr}$ = pulsating Strouhal number, $w\delta/2\pi u_m$
h = heat-transfer coefficient on the plate, $\mathrm{W/m^2\,K}$, $=\lambda[\partial T/\partial y]/T_w-T_{\mathrm{inlet}}$
k_q = blockage factor, δ/W
L = length of plate, m
Nu = Nusselt number on the plate, $h\delta/\lambda$
Re = Reynolds number, $u_m\delta/\nu$
t = time, s
T = temperature, K
Δt = time interval, s
U = velocity component in the x direction
V = velocity component in the y direction
U_i = velocity component in the j direction
u_b = amplitude of oscillating free-flow velocity, m/s
u_m = cycle-averaged velocity of pulsating free flow, m/s
x_i = i coordinate, m
x,y = coordinate, m
W = channel width, m
α = thermal diffusivity, $\mathrm{m^2/s}$
δ = plate thickness, m
ρ = density, $\mathrm{kg/m^3}$
ν = molecular viscosity, $\mathrm{m^2/s}$
λ = thermal conductivity, W/m K
θ = dimensionless temperature, $\theta=(T-T_{\mathrm{inlet}})/(T_w-T_{\mathrm{inlet}})$
τ = dimensionless time, tu_m/δ
ω = scillation, 1/s

Subscripts

inlet = inlet
i,j = i and j directions, respectively
m = mean
w = wall surface of the plate

References

[1] Liang, C. Y., and Yang, W.-J., 1975, "Heat Transfer and Friction Loss Performance of Perforated Heat Exchanger Surface," *ASME Heat Transfer Conference*, San Francisco, CA, August, Vol. 97, pp. 9–15.
[2] Liang, C. Y., and Yang, W.-J., 1975, "Modified Single Blow Technique for Performance Evaluation on Heat Transfer Surface," *ASME Heat Transfer Conference*, San Francisco, CA, August, Vol. 97, pp. 16–21.
[3] Liang, C. Y., Yang, W.-J., and Hung, Y. Y., 1977, "Perforated-Fin Type Compact Heat Exchangers for Gas Turbines," *1977 Tokyo Joint Gas Turbine Congress*, Tokyo, Japan, May, pp. 77–85.
[4] Lee, C. P., and Yang, W.-J., 1978, "Augmentation of Convective Heat Transfer From High-Porosity Perforated Surfaces," *Heat Mass Transfer 1978*, Toronto, ON, August, Vol. 2, pp. 589–594.
[5] Fujii, M., Seshimo, S., and Yamanaka, G., 1988, "Heat Transfer and Pressure Drop of Perforated Surface Heat Exchanger With Passage Enlargement and Contraction," Int. J. Heat Mass Transfer, **31**(1), pp. 135–142.
[6] Hwang, G. J., Wu, C. C., Lin, L. C., and Yang, W.-J., 1996, "Investigation of Flow Drag and Forced Convective Heat Transfer in Perforated Coolant Channels," *Transport Phenomena in Combustion*, Vol. 2, Taylor & Francis, London, pp. 1747–1758.
[7] Liang, C. Y., Lee, C. P., and Yang, W.-J., 1976, "Visualization of Fluid Flow Past Perforated Surfaces," *Proceedings of the Japanese Fourth Symposium on Flow Visualization*, Tokyo, Japan, October, pp. 69–73.
[8] Liang, C. Y., 1975, "Heat Transfer, Flow Friction, Noise and Vibration Studies of Perforated Surface," Ph.D. thesis, University of Michigan, Ann Arbor, Michigan.
[9] Torii, S., and Yang, W.-J., 1998, "Flow Over a Slot-Perforated Flat Surface Between Two Parallel Plates," *Proceedings of the Eighth International Symposium of Flow Visualization*, Sorrento, Italy, September, Vol. 6, pp. 1–8.
[10] Torii, S., Yang, W.-J., and Umeda, S., 1998, "Flow Visualization and Transport Phenomena Over a Slot-Perforated Flat Surface Between Two Parallel Plates," J. Flow Visualization Image Process., **5**, pp. 63–80.
[11] Amon, C. H., and Mikic, B. B., 1991, "Spectral Element Simulations of Unsteady Forced Convective Heat Transfer: Application to Compact Heat Exchanger Geometries," Numer. Heat Transfer, Part A, **19**, pp. 1–19.
[12] Suzuki, K., Xi, G. N., Inaoka, K., and Hagiwara, Y., 1994, "Mechanism of Heat Transfer Enhancement Due to Self-Sustained Oscillation for In-Line Fin Array," Int. J. Heat Mass Transfer, **37**, pp. 83–96.
[13] Nigen, J. S., and Amon, C. H., 1994, "Time-Dependent Conjugate Heat Transfer Characteristics of Self-Sustained Oscillatory Flows in a Grooved Channel," ASME J. Fluids Eng., **116**, pp. 499–507.
[14] Harlow, F. H., and Welch, E. J., 1965, "Numerical Calculation of Time-Dependent Viscous Incompressible Flow of Fluid With Free Surface," Phys. Fluids, **8**, pp. 2182–2189.
[15] Hirt, C. W., Nichols, B. D., and Romero, N. C., 1975, "SOLA-A Numerical Solution Algorithm for Transient Fluid Flows," LASL Report No. LA-5852.
[16] Torii, S., and Yang, W.-J., 2002, "Thermal Transport Phenomena Over a Slot-Perforated Flat Surface in Pulsating Free Stream," Int. J. Therm. Sci., **41**, pp. 241–252.
[17] Marty, Ph., Michel, F., and Tochon, P., 2008, "Experimental and Numerical Study of the Heat Transfer Along a Blunt Flat Plate," Int. J. Heat Mass Transfer, **51**, pp. 13–23.

Definition and Evaluation of Mean Beam Lengths for Applications in Multidimensional Radiative Heat Transfer: A Mathematically Self-Consistent Approach

Walter W. Yuen
Department of Mechanical Engineering,
University of California at Santa Barbara,
Santa Barbara, CA 93106

A set of mathematically self-consistent definitions of mean beam length is introduced to account for surface-surface, surface-volume, and volume-volume radiative exchanges in general three-dimensional inhomogeneous medium. Based on these definitions, the generic exchange factor (GEF) formulated by the recently introduced multiple-absorption-coefficient-zonal-method (MACZM) can be written in an equivalent one-dimensional form. The functional behavior of the proposed mean beam lengths is shown to be readily correlated by either simple algebraic relations or neural network based correlations. They can be implemented directly with MACZM in general computational code to account for the radiation effect in complex three-dimensional systems. In addition, these definitions of mean beam length can also be used to assess the accuracy of the conventional mean beam length concept currently used by the practicing engineering community. [DOI: 10.1115/1.2969752]

Introduction

The concept of mean beam length (MBL) was originally formulated by Hottel [1,2] over 50 years ago. It was introduced as a length scale to account for the effect of geometry in the evaluation of radiative heat transfer between an isothermal gas volume and its boundary. Specifically, if $q_{\lambda i,k}$ is the radiative heat flux incident on a surface A_k from a radiating volume V with A_k being all or a part of its boundary, the traditional definition of the MBL, L_e, is defined as

$$q_{\lambda i,k} = (1 - e^{a_\lambda L_e}) e_{\lambda b,g} \tag{1}$$

where $e_{\lambda b,g}$ is the blackbody emissive power evaluated at a specific wavelength and the medium's temperature and a_λ is the corresponding absorption coefficient. Physically, MBL can be interpreted as the required radius of an equivalent hemisphere of a medium such that the flux received by the center of its base is equal to the average flux radiated to the area of interest by the actual volume of the medium.

For an isothermal nongray gas volume with arbitrary optical thickness, a number of works were reported [3–6] suggesting that the "exact" MBL can be approximated by

$$L_e = C L_{e,0} \tag{2}$$

where C is estimated to be in the range 0.8–1.0, and $L_{e,0}$ is the optically thin limit of the MBL given by

$$L_{e,0} = \frac{4V}{A} \tag{3}$$

with V and A being the volume and boundary of the medium, respectively. The applicability of Eq. (2) for isothermal media has been verified for different geometric configurations [7,8].

For radiative heat transfer in inhomogeneous, nonisothermal, and nongray media, However, the MBL concept is generally not applicable mathematically. But due to the difficulty in performing accurate multidimensional nongray calculation, Eq. (2) is still widely used by many engineering designers and commercially available computational fluid dynamics (CFD) codes as a basis to estimate the multidimensional effect of thermal radiation. This approach, however, is generally done without mathematical validation and it has led to much uncertainty in determining the importance of radiative heat transfer effect in practical engineering application scenarios. The objective of this work is to develop a more general set of length scales, which are mathematically correct and physically consistent in application for general radiative heat transfer.

Based on the generic exchange factor (GEF) concept introduced by the recently developed multiple-absorption-coefficient-zonal-method (MACZM) [9], the present work will show that six separate independent definitions of the MBL (two transmission MBLs, two emission MBLs, and two absorption MBLs) are needed to characterize the transmission, emission, and absorption processes of general three-dimensional radiative exchange. Simple correlations of the six MBLs are generated. The two transmission MBLs are shown to have simple functional behavior and can be readily correlated with a simple algebraic expression. The two absorption MBLs are shown to be effectively equivalent to the two emission MBLs. The two emission MBLs have complex functional behavior. However, they can be correlated by simple algebraic expressions generated by neural network.

In addition to serve as length scales for the various radiative heat transfer processes, the six correlated MBLs reduce the surface-surface, volume-surface, and volume-volume GEFs to simple 1D expressions. These MBL correlations eliminate the need to evaluate GEFs numerically in an actual calculation and MACZM can thus be implemented accurately and efficiently in CFD codes.

Concepts of GEF and the Basic Geometry

In the formulation of the MACZM [9], the three basic radiative exchange processes (surface-surface, surface-volume, and volume-volume) are shown to be characterized completely by three two-component GEFs, $s_1 s_{2,pp}$ $s_1 s_{2,pd}$; $g_1 s_{2,pp}$, $g_1 s_{2,pd}$; $g_1 g_{2,pp}$ and $g_1 g_{2,pp}$ and $g_1 g_{2,pd}$. As shown in Ref. [9], the radiative exchange between arbitrary volumes and surfaces in a three-dimensional inhomogeneous nonisothermal medium can be generated based on the superposition of these GEFs.

In the definition of GEFs, the emitting volume (surface) $V_1(A_1)$ and the absorbing volume (surface) $V_2(A_2)$ and their relative geometry are shown in Fig. 1. For the parallel (pp) component, A_1 is a square area with dimension D parallel to the x-y plane situated at the $z=0$ plane with one corner at the origin while V_1 is a cubical volume with dimension D and A_1 being its top surface area. For the perpendicular (pd) component, A_1 is a square area with dimension D parallel to the y-z plane situated at the $x=0$ plane with one corner at the origin while V_1 is a cubical volume with dimension D and A_1 being its surface area on the right. For all six GEFs, the absorbing area A_2 is a square area with dimension D parallel to the x-y plane and the absorbing volume V_2 is a cubical volume with dimension D and A_2 being its bottom surface. The position of the absorbing volume (area) $V_2(A_2)$ related to A_1 is specified by the coordinate at its lower left corner ($n_x D$, $n_y D$, $n_z D$) as shown in Fig. 1.

Contributed by the Heat Transfer Division of ASME for publication in the JOURNAL OF HEAT TRANSFER. Manuscript received June 19, 2007; final manuscript received June 4, 2008; published online September 5, 2008. Review conducted by Jayathi Murthy.

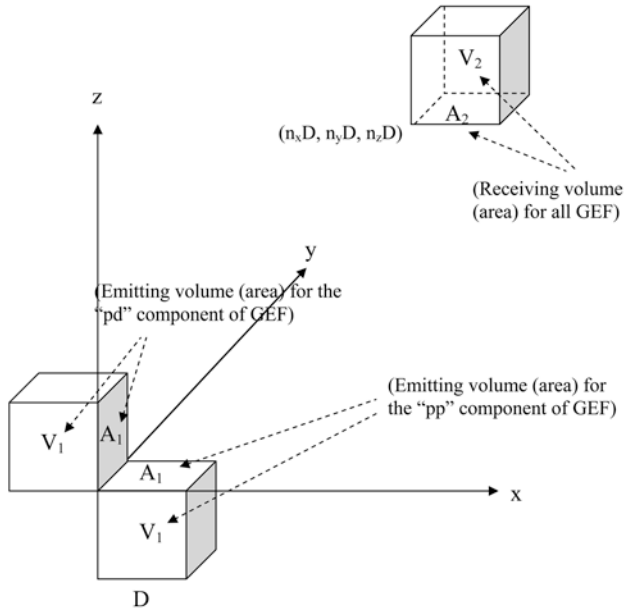

Fig. 1 Geometry of the emitting volume (area) and receiving volume (element) used in the definition of the two components of the GEF and the associated coordinate system

Mathematically, the two surface-surface GEFs $s_1s_{2,pp}$ and $s_1s_{2,pd}$ correspond to the actual exchange factors between the two square surfaces A_1 and A_2. For the four volume-surface and volume-volume GEFs $g_1s_{2,pp}$, $g_1g_{2,pd}$, $g_1g_{2,pp}$ and $g_1s_{2,pd}$, the exchange factors include only the portion of the radiation emitted by V_1 through the surface A_1. For the two volume-volume GEFs $g_1g_{2,pp}$ and $g_1g_{2,pd}$, the exchange factor is further limited by including only the radiation received by the volume V_2 through the surface A_2.

Actual volume-surface and volume-volume exchange factors are generated from the six GEFs by superposition. The detail of the superposition is presented in Ref. [9] and will not be repeated here. It should be noted that by restricting the emission/absorption through specific areas in the definition of the three basic GEFs, the MACZM approach can simulate accurately the variation of optical properties in an inhomogeneous medium, particularly in a region of large discontinuity in optical properties (e.g. a continuously changing 3D solid/liquid/gas phase boundary). The six GEFs are the basis for the definition of six corresponding MBLs in the present work.

The Concepts of Transmission, Absorption, and Emission Mean Beam Length

Mathematically, the two surface-surface GEFs $s_1s_{2,pp}$ and $s_1s_{2,pd}$, normalized by the area D^2, depend only on the optical thickness, and the relative orientation between the two areas as specified by (n_x, n_y, n_z). The optical thickness τ_{12} is evaluated along the line of sight between the center-point of the two areas. The two transmission MBLs are defined by

$$\frac{s_1s_{2,xx}}{D^2} = F_{12,xx}(n_x,n_y,n_z)e^{-a_mL_{t,xx}}, \quad xx = pp,pd \tag{4}$$

In the above expressions, $F_{12,xx}(n_x,n_y,n_z)$, $xx=pp,pd$ are the view factors between the two areas for the two configurations. The average absorption coefficient between the two surfaces, a_m, is

$$a_m = \frac{\tau_{12}}{L_c} \tag{5}$$

with L_c being the distance between the center of the two surfaces.

The concept of emission MBL is introduced based on the volume-surface exchange process characterized by the two GEFs, $g_1s_{2,pp}$ and $g_2s_{2,pd}$, with the emitting volume V_1 and absorbing area A_2 as shown in Fig. 1. As an extension to Eq. (4), the emission MBLs for the two configurations are defined by

$$\frac{g_1s_{2,xx}}{D^2} = F_{12,xx}(n_x,n_y,n_z)(1-e^{-a_1L_{\mathrm{em},xx}})e^{-a_mL_{t,xx}}, \quad xx = pp,pd \tag{6}$$

where a_1 is the absorption coefficient of the emitting medium in volume V_1. The two emission MBLs $L_{\mathrm{em},pp}$ and $L_{\mathrm{em},pd}$ are functions of the two absorption coefficients a_1 and a_m, as well as the geometrical configuration represented by (n_x, n_y, n_z).

Finally, the concept of absorption MBL is introduced based on the volume-volume exchange GEFs $g_1g_{2,pp}$ and $g_1g_{2,pd}$, with the emitting volume V_1 and absorbing volume V_2 as shown in Fig. 1. Generalizing the mathematical expression introduced by Eq. (6), the absorption MBLs for the two components are given by

$$\frac{g_1g_{2,xx}}{D^2} = F_{12,xx}(n_x,n_y,n_z)(1-e^{-a_1L_{\mathrm{em},xx}})(1-e^{-a_2L_{a,xx}})e^{-a_mL_{t,xx}}, \quad xx = pp,pd \tag{7}$$

where a_2 is the absorption coefficient of the medium in volume V_2. The two absorption MBLs $L_{a,pp}$ and $L_{a,pd}$ are functions of the three absorption coefficients a_1, a_2, and a_m, as well as the geometrical configuration represented by (n_x, n_y, n_z).

It is important to note that, together, the three MBLs (absorption, emission, and transmission MBLs) in its two-component are a set of path lengths, which reduce the six GEFs to equivalent one-dimensional expressions (Eqs. (4), (6), and (7)). Since these path lengths are introduced to account for the three distinct physical processes, their mathematical behaviors are influenced most strongly by the absorption coefficient associated with the specific process. The geometric effect is largely accounted for by the view factor and, therefore, the dependence of the MBLs on (n_x, n_y, n_z) is generally weak. The one-dimensional form of the GEFs can potentially serve as a basis for further development of additional engineering correlation to account for the nongray effect of multidimensional radiative heat transfer.

The Transmission Mean Beam Length, $L_{t,pp}$ and $L_{t,pd}$

Numerical data show that for two disjoint surfaces, the two transmission MBLs $L_{t,pp}$ and $L_{t,pd}$ are generally independent of optical thickness and can be approximated accurately by the corresponding center-to-center distances $L_{c,pp}$ and $L_{c,pp}$. One exception is that the pd component with $(n_x,n_y,n_z)=(0,0,1)$, when A_1 and A_2 are two perpendicular square surfaces with a common edge. For this case, the transmission MBL can be correlated by

$$\frac{L_{t,pd}}{L_{c,pd}} = 0.78 - 012\tau_{12} + 0.0093\tau_{12}^2 \quad (n_x,n_y,n_z) = (0,0,1) \tag{8}$$

The Emission Mean Beam Length $L_{\mathrm{em},pp}$ and $L_{\mathrm{em},pd}$

Physically, the behavior of the emission MBL for the case with the absorbing surface in contact with the emitting volume (the pp component with $(n_x,n_y,n_z)=(0,0,0)$) is expected to differ from cases in which the absorbing area and the emitting volume are disjoint. Different correlations are thus needed for the two possibilities. Specifically, the GEF $g_1s_{2,pp}$ with $(n_x,n_y,n_z)=(0,0,0)$ corresponds to the actual exchange factor between a cubical volume and one of its bounding surface. The transmission MBL is zero. The emission MBL is tabulated and shown in Fig. 2(*a*). The conventional MBL, given by Eq. (2) with $C=0.9$, is shown in the same figure for comparison. The corresponding prediction for the exchange factor is shown in Fig. 2(*b*). The conventional MBL is clearly not an accurate approximation of the emission MBL. The

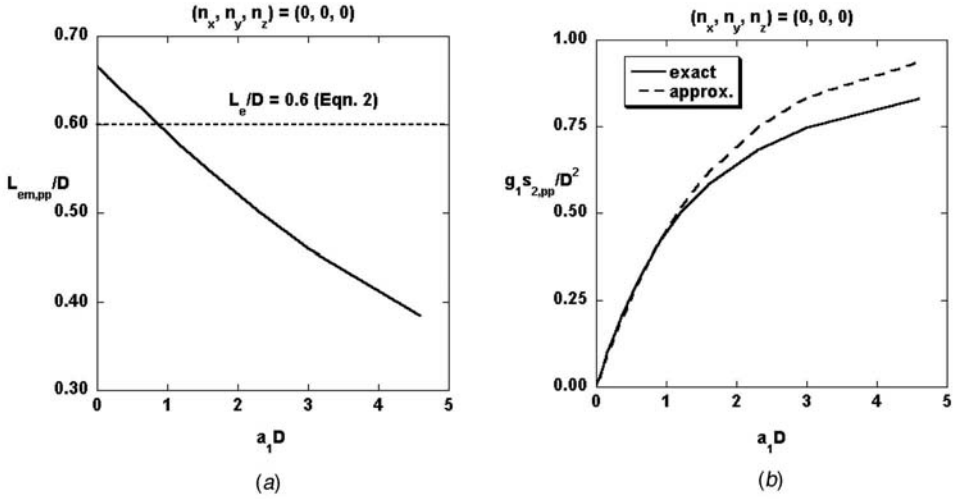

Fig. 2 Comparison of the emission MBL and the conventional MBL and the corresponding exchange factor for the $g_1 g_{2,pp}$ exchange factor with $(n_x, n_y, n_z)=(0,0,0)$

discrepancy in the exchange factor prediction is large in the limit of an optically thick emitting volume (i.e., large $a_1 D$). The numerical data presented in Fig. 2(a) can be correlated by

$$\frac{L_{\mathrm{em},pp}(0,0,0)}{D} = 0.67 - 0.081 a_1 D + 0.0043 (a_1 D)^2 \tag{9}$$

For cases in which the emitting volume and the absorbing area are disjoint, the emission MBLs are influenced strongly by the two optical thicknesses $a_1 D$ and τ_{12} and geometry (n_x, n_y, n_z). Since algebraic correlations are difficult to obtain, a neural network is created to provide a simple mathematical correlation. The capability of using neural networks to correlate experimental or numerical data accurately is well documented [10]. Specifically, using a two-layer neural network as shown in Fig. 3, neural network correlations are developed for the two emission MBLs. For $L_{\mathrm{em},pp}$ in ranges of $0 \le n_x \le 7$, $0 \le n_y \le 7$, $1 \le n_z \le 7$, $0.01 \le a_1 D \le 4.6$, and $0 \le \tau_{12} \le 4.6$, the numerical data can be correlated with the following equation:

$$z = \sum_{i=1}^{18} \left\{ \tanh\left[\left(\sum_{j=1}^{5} W_{1,ij} p_j \right) + b_{1,i} \right] \right\} W_{2,i} + b_2 \tag{10}$$

where $\boldsymbol{p}$ is a normalized input vector with components $\bar{n}_x$, $\bar{n}_y$, $\bar{n}_z$, $\overline{a_1 D}$, and $\bar{\tau}_{12}$ and $z = \overline{L_{\mathrm{em},pp}/L_{c,pp}}$ is the normalized output. All normalized variables are generated by a linear transformation from its range of value to the common range of -1 to 1. Numerical values for the network elements $\hat{W}_1$, $\boldsymbol{b}_1$, $\boldsymbol{W}_2$, and b_2 are available upon request to the author. The accuracy of the neural network prediction is illustrated for some typical data with $n_z=1$ in Fig. 4. The conventional MBL, given by Eq. (2) with $C=0.9$, is shown in the same figure to demonstrate the general inaccuracy of the conventional MBL concept.

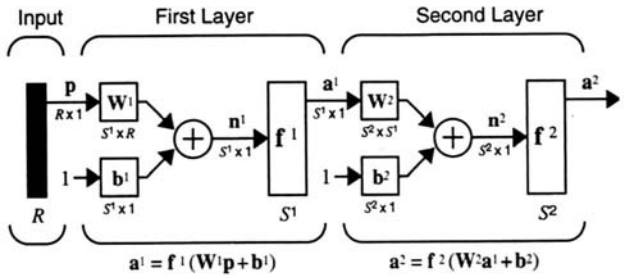

Fig. 3 Schematic of a two-layer neural network used in generating the correlation for the emission MBL

Because of the more complex mathematical behavior of $L_{\mathrm{em},pd}$, two separate neural network correlations are generated to simulate the numerical data. For $0 \le n_x \le 5$, $1 \le n_z \le 7$, $0.01 \le a_1 D \le 4.6$, and $0 \le \tau_{12} \le 4.6$ with $n_y=0$, the data are correlated by the following equation:

$$z = \sum_{i=1}^{13} \left\{ F\left[\left(\sum_{j=1}^{4} W_{1,ij} p_j \right) + b_{1,i} \right] \right\} W_{2,i} + b_2 \tag{11}$$

with

$$F(x) = \frac{1}{1+e^{-x}} \tag{12}$$

The normalized vector $\mathbf{p}$ is a vector with components $\bar{n}_x$, $\bar{n}_z$, $\overline{a_1 D}$, and $\bar{\tau}_{12}$ Note that $z = L_{\mathrm{em},pd}/L_{c,pd}$ is normalized to be within the range 0–1, which is the range of the "log-sigmoid" transfer function as represented by Eq. (12).

For cases with $1 \le n_y \le 6$, a second network is generated to correlate the numerical data as follows:

$$z = \sum_{i=1}^{21} \left\{ F\left[\left(\sum_{j=1}^{5} W_{1,ij} p_j \right) + b_{1,i} \right] \right\} W_{2,i} + b_2 \tag{13}$$

with $\boldsymbol{p} = (\bar{n}_x, \bar{n}_y, \bar{n}_z, \overline{a_1 D}, \bar{\tau}_{12})$. Detailed numerical data of the two networks are available upon request to the author. The accuracies of the two neural network correlations are illustrated for some selected geometry with $n_z=1$ in Fig. 5. The conventional MBL, given by Eq. (2) with $C=0.9$, is again shown in the same figure to demonstrate the inaccuracy of the conventional MBL concept.

It should be noted that the numerical data and the associated neural network correlation for the emission MBLs $L_{\mathrm{em},pp}$ and $L_{\mathrm{em},pd}$ are generated only for a finite range of the input variables $a_1 D$, τ_{12}, n_x, n_y, and n_z. Since the emitting volume is expected to approach a blackbody in the limit of a large emission optical thickness ($a_1 D$) and GEF is generally small (approaches zero) in the limit of a large distance between the emitting volume and the absorbing surface, the accuracy of the emission MBL is less critical in those limits. For the optically thick limit $a_1 D > 4.6$ and/or $\tau_{12} > 4.6$, it is sufficient to use the corresponding emission MBL evaluated at $a_1 D = 4.6$ and/or $\tau_{12} = 4.6$. For a geometric configura-

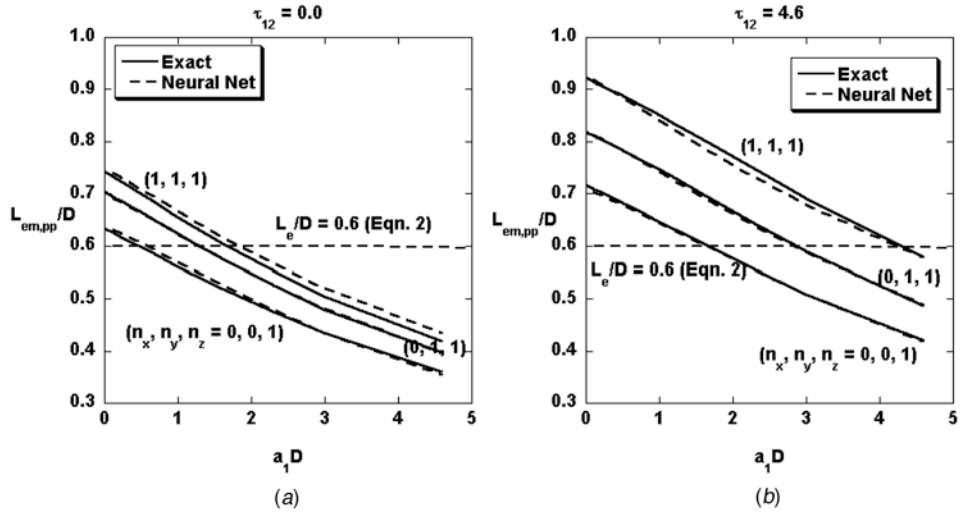

Fig. 4 Comparison between the neural network prediction of the emission MBL, $L_{em,pp}$, for different geometric configurations with n_z=1

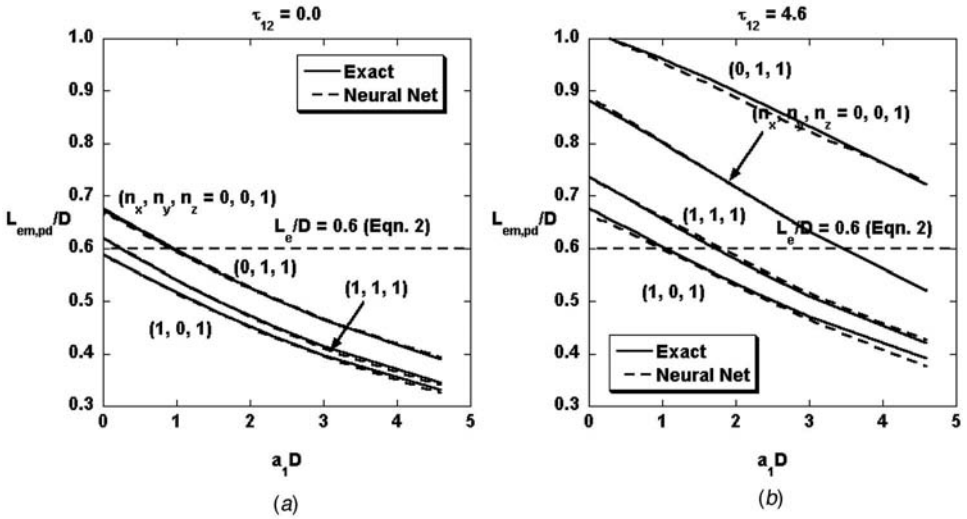

Fig. 5 Comparison between the neural network prediction of the emission MBL, $L_{em,pd}$, for different geometric configurations with n_z=1

tion with (n_x, n_y, n_z) outside of the specified range, the normalized emission MBL can be taken to be the value evaluated at a configuration with the closest distance.

Absorption Meam Beam Length, $L_{a,pp}$ and $L_{a,pd}$

Numerical data show that, in general, the absorption MBL is effectively independent of the optical properties of the emitting volume and can be taken to be the same as the emission MBL evaluated at the optical property of the absorbing volume. Due to the selection of the x-direction as the orientation of A_1 in the definition of the pd component of the GEF, the equivalence between the pd component of the absorption MBL and the mission MBL would require an exchange in the value of n_x and n_z as follows:

$$L_{a,pp}(n_x,n_y,n_z,a_1D,a_2D,\tau_{12}) = L_{\mathrm{em},pp}(n_x,n_y,n_z,a_2D,\tau_{12}) \tag{14a}$$

$$L_{a,pd}(n_x,n_y,n_z,a_1D,a_2D,\tau_{12}) = L_{\mathrm{em},pd}(n_x-1,n_y,n_x+1,a_2D,\tau_{12}) \tag{14b}$$

Nomenclature

- a_1 = absorption coefficient of the emitting volume V_1
- a_2 = absorption coefficient of the absorbing volume V_2
- a_λ = absorption coefficient at wavelength λ
- a_m = average absorption coefficient of the medium between surfaces A_1 and A_2
- A = surface area
- C = constant used in the definition of the conventional mean beam length, Eq. (2)
- D = characteristic dimension used in the definition of GEF
- $e_{\lambda b}$ = blackbody emissive power

F_{ij} = view factor between surfaces A_i and A_j
$g_1g_{2,xx}$ = the xx component of the volume-volume GEF, $xx=pp,pd$
$g_1g_{2,xx}$ = the xx component of the volume-surface GEF, $xx=pp,pd$
L_e = conventional mean beam length introduced by Hottel
L_a = absorption mean beam length, Eq. (7)
L_{em} = emission mean beam length, Eq. (6)
L_c = center-to-center distance between surfaces A_1 and A_2
$L_{e,0}$ = optically thin limit of the conventional mean beam length, Eq. (3)
L_t = transmission mean beam length, Eq. (4)
n_x = discretized x-coordinate of A_2 relative to A_1 in the definition of GEF
n_y = discretized y-coordinate of A_2 relative to A_1 in the definition of GEF
n_z = discretized z-coordinate of A_2 relative to A_1 in the definition of GEF
$q_{\lambda i,k}$ = incident radiative heat flux on surface A_k
$s_1s_{2,xx}$ = the xx component of the surface-surface GEF, $xx=pp,pd$
S = distance
V = volume

Greek Symbols

λ = wavelength
θ = angular coordinate
τ_{12} = optical thickness between areas A_1 and A_2

Subscripts

i = the ith volume (or surface)
pp = parallel component
pd = perpendicular component

References

[1] Hottel, H. C., 1954, "Radiant-Heat Transmission," *Heat Transmission*, 3rd ed., W. H. McAdams, ed., McGraw-Hill, New York, Chap. 4.
[2] Hottel, H. C., and Sarofim, A. F., 1967, *Radiative Transfer*, McGraw-Hill, New York.
[3] Olfe, D. B., 1961, "Mean Beam Length Calculations for Radiation From Non-Transparent Gases," J. Quant. Spectrosc. Radiat. Transf., **1**, pp. 169–176.
[4] Dunkle, R. V., 1964, "Geometric Mean Beam Lengths for Radiant Heat Transfer Calculations," ASME J. Heat Transfer, **86**(1), pp. 75–80.
[5] Tien, C. L., and Wang, L. S., 1965, "On the Calculation of Mean Beam Length for a Radiating Gas," J. Quant. Spectrosc. Radiat. Transf., **5**, pp. 453–456.
[6] Mandell, D. A., and Miller, F. A., 1973, "Comparison of Exact and Mean Beam Length Results for a Radiating Hydrogen Plasma," J. Quant. Spectrosc. Radiat. Transf., **13**, pp. 49–56.
[7] Wassal, A. T., and Edwards, D. K.,1976, "Mean Beam Lengths for Spheres and Cylinders," ASME J. Heat Transfer, **98**, pp. 308–309.
[8] Anderson, K. M., and Hadvig, S., 1989, "Geometric Mean Beam Lengths for a Space Between Two Coaxial Cylinders," ASME J. Heat Transfer, **111**(3), pp. 811–813.
[9] Yuen, W. W., 2006, "Development of a Multiple Absorption Coefficient Zonal Method for Application to Radiative Heat Transfer in Multi-Dimensional Inhomogeneous Non-Gray Media," Numer. Heat Transfer, Part B, **49**(2), pp. 89–103.
[10] Hornik, K. M., Stinchcombe, M., and White, H., 1989, "Multilayer Feedforward Networks are Universal Approximators," Neural Networks, **2**, pp. 359–366.

Demonstration of Heat Transfer Enhancement Using Ferromagnetic Particle Laden Fluid and Switched Magnetic Fields

Mark M. Murray
Department of Mechanical Engineering,
United States Naval Academy,
Annapolis, MD 21402
e-mail: mmmurray@usna.ed

A convective heat transfer enhancement technique and the experimental methods used to quantify the improvement in heat transfer and subsequent differential pressure are introduced. The enhancement technique employed time varying magnetic fields produced in a pipe to cause the ferromagnetic particles of a particle laden fluid (mineral oil and iron filings) to be attracted to and released from a heated pipe wall. The ferromagnetic particles acted not only to advect heat from the pipe wall into the bulk fluid but they also significantly modified the flow field, disrupted the boundary layer, allowed cooler fluid to reach the high temperature pipe wall, increased thermal energy transfer directly to the fluid, and contributed to the overall improvement in heat transfer rate. The experimental method utilized to quantify an increased effectiveness of convective heat transfer used an apparatus designed to replicate an internally cooled fin, whose surface temperature was measured with an IR camera. These temperature measurements were utilized to calculate the convective heat transfer coefficient (h) of the fluid within the pipe. The enhancement technique demonstrated a 267% increase in heat transfer coefficient with only a corresponding 48% increase in flow differential pressure for an electromagnetic switching frequency of 2 Hz. It is also found that there were optimum magnetic field switching frequencies for both enhancement and differential pressure magnitudes.
[DOI: 10.1115/1.2970064]

Keywords: convection, enhancement, magnetic field, particle laden fluid

1 Introduction

To increase the effectiveness of convective heat transfer, there have been many enhancement techniques developed. Single-phase forced convective enhancement techniques can be classified into two general categories: passive enhancement and active enhancement [1]. The general mechanisms utilized by the majority of single-phase forced convection passive enhancement techniques are to increase the heat transfer surface area and/or promote mixing in the boundary layer. Another passive enhancement technique recently investigated by several researchers is the addition of nanoparticles to liquids to increase the overall fluid thermal conductivity and potentially increase the heat transfer characteristics [2–4].

Active enhancement techniques are also utilized to increase heat transfer in single-phase forced convection but require external power. Active techniques range from methods as basic as mechanically stirring the fluid to more exotic methods such as applying electrostatic fields to the fluid [1]. One of the less common methods of active enhancement is the use of external magnetic fields to improve the heat transfer characteristics of the flow. The majority of research in magnetic field convective heat transfer enhancement is focused on the hydrodynamic manipulation of magnetorhetrological fluids (ferrofluids). Much of the numerical and theoretical investigation in this area centers on the disruption of the boundary layer through the use of a steady magnetic field acting on a homogeneous ferrofluid [5,6].

An area of convective heat transfer enhancement utilizing magnetic fields that varies significantly from ferrofluid manipulation was proposed by Hishida and Maeda and claimed a 60% increase in local heat transfer rates [7]. The technique involved a solid-gas two phase flow that utilized soft magnetic particles as the solid. The magnetic particles were attracted to a heated wall by a steady magnetic field, heated above the particle Curie point, removed from the wall by fluid dynamic forces, and then carried away by the flow. To obtain a significant increase in heat transfer rate, a very high particle mass loading (ratio of solid to gas) of 1.6 was needed. The local enhancement was attributed to the particle direct contact conduction, particle motion in the thermal boundary layer, and turbulence promotion. The research presented in this paper had similar physical phenomenon inducing enhancement but utilized a switching of magnetic fields instead of Curie point transition to release particles and a liquid-solid mixture with significantly smaller particle mass fraction.

2 Enhancement Technique Description

The basic principle of the enhancement technique is to combine the thermal conductivity (k) characteristics of certain solids with the high specific heat (c_p) values of appropriate fluids to improve the overall heat transfer characteristics of a heat exchanger. By attracting the highly conductive particles directly to the solid surface, heat can be effectively transferred to the particles with minimal thermal resistance. Releasing the particles into the bulk fluid allows the heat to be transferred to the high specific heat fluid very effectively because of the large total surface area of the particles when mixed within the bulk fluid. The attracting and releasing of the particles from the solid surface has the additional advantage of breaking up the boundary layer and allowing the fluid from the core bulk flow to come into more direct contact with the wall. The relative importance of these two resultant consequences of particle manipulation has not been fully investigated, although the combined effect has been shown to be significant.

For the experimental procedure presented in this paper, the above was achieved by utilizing a particle laden flow consisting of iron filings and mineral oil. A time varying magnetic field produced in the fluid channels of a heat exchanger caused the ferromagnetic particles to be attracted to the wall. With a magnetic field utilized as the particle manipulative motive force, particle removal was enhanced by energizing the magnetic field that is offset and out of phase with the field that initially attracted the particle to the wall. Although the particles can be removed from the wall by the hydrodynamic forces of the flowing fluid, the use of a separate magnetic field helps ensure the effective removal of particles from the solid surface.

Figure 1 illustrates the agglomerated ferromagnetic particles attracted to the pole pairs of one of the left (Fig. 1(a)) and right (Fig. 1(c)) electromagnets as they were alternately energized. The intermediate picture (Fig. 1(b)) shows the transition of particles when the electromagnets were switched from left to right. The 2% by weight iron filing/mineral oil mixture utilized for the visual demonstration flowed from top to bottom in transparent 1.4 cm diameter glass tubing (for comparison, the particle weight fraction utilized for the heat transfer experimental portion of this work was 5%). The images suggest the significant modification to flow that even a small weight percentage of particulate can have on the flow when agglomeration occurs at the wall. The formation and dissolution of the agglomerations resulted in the disruption of the es-

Contributed by the Heat Transfer Division of ASME for publication in the JOURNAL OF HEAT TRANSFER. Manuscript received August 6, 2007; final manuscript received June 7, 2008; published online September 5, 2008. Review conducted by Gautam Biswas. Paper presented at the 2007 ASME-JSME Thermal Engineering Conference and Summer Heat Transfer Conference (HT2007), Vancouver, BC, Canada, July 8–12, 2007.

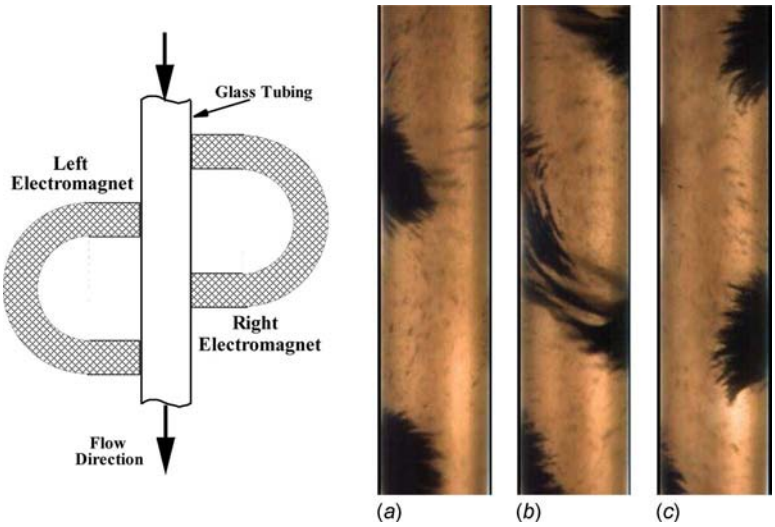

Fig. 1 High speed camera images of iron filings alternately attracted to (*a*) left and (*c*) right energized electromagnets in transparent glass tubing

tablished boundary layer through the entrainment of fluid, which led to increased fluid mixing near the wall. When formed, the agglomerations also acted as fins and turbulence promoters further enhancing heat transfer.

3 Experimental Overview

The purposes of the experimental procedures were to quantify the improvement in heat transfer and determine the relative increase in differential pressure when the magnetically manipulated particle laden enhancement technique was utilized. An internally cooled fin configuration was developed for the experimental procedure. An IR camera was utilized to extract surface temperature measurements from which heat transfer coefficients were calculated utilizing the axial temperature profile of the test section.

To help ensure the validity of the ratio of the calculated heat transfer coefficients, the experimental procedure was designed to have minimal axial variations in the heat transfer coefficient in the test section. The major constraints to ensure minimal variations in heat transfer coefficient (h) included the minimization of fluid temperature increase through the test section, the establishment of the hydrodynamic steady flow boundary layer prior to flow entering the test section, and minimization of external heat transfer. It was assumed that the heat transfer coefficient remains constant over the length of the test section through the implementation of these constraints. With the Prandtl number of 350 and Reynolds number of 140 for pure mineral oil at testing temperatures, the calculated theoretical change in Nusselt over the test section was 15%. It was also assumed that there is not significant convective heat transfer from the outer surface of the test section tube (calculations show that for the worse case of natural convection, the exterior heat transfer rate is between one and two orders of magnitude less than the heat transfer at the interior of the pipe) or significant conduction to the thermally insulated magnets. Therefore, the temperature of the fin material (copper pipe) was assumed to decay exponentially by the function

$$\theta = \theta_b \exp(-mx), \quad m = \left(\frac{hp}{kA_c}\right)^{1/2} \tag{1}$$

where θ is the excess temperature function where $\theta(x) = T(x) - T_\infty$, k is the thermal conductivity of the copper, A_c is the cross-sectional area of the copper tubing, p is the inside perimeter of the pipe, h is the convective heat transfer coefficient, and x is the axial distance down the pipe. By fitting the axial surface excess temperature profile obtained by the IR camera to a decaying exponential, the value of the coefficient (m) was determined and the average convective heat transfer coefficient was calculated knowing the physical parameters of the pipe.

4 Experimental Apparatus and Procedure

The experimental apparatus used to determine the coefficient of heat transfer provided a constant heat flux source, a constant temperature heat sink, and a constant fluid flow rate to make the most accurate comparison between the heat transfer coefficients of the test section when there is no magnetic field applied (nonenhanced case) and when an alternating magnetic field is applied (magnetically enhanced case). The apparatus consisted of mechanical and electrical components. The mechanical components included a pump, a connector tubing, heat exchanger, a heated copper tubing, a recirculating chiller bath, connectors, and the heat transfer fluid (a mixture of 5% mass fraction of 300 iron filings and mineral oil). The electrical components consisted of a function generator, amplifiers, electromagnets, and heaters.

The half inch type-L copper tubing (ID=1.38 cm and OD =1.59 cm) section of the experimental apparatus was designed to have a 74 cm total length of vertical pipe with an initial 46 cm heated upstream section and a 28 cm test section. The tubing had the lowest flow velocity in the system and was placed in a vertical orientation, with flow from top to bottom, to minimize possible gravitational particle settling. The extended entrance region was designed to ensure that the flow profile was fully established prior to the test section where the temperature measurements were made. The calculated bulk fluid temperature increase over the total length of the pipe was 1.8°C with a small percentage of the rise occurring over the test section. The measured magnetic field at the tip of the U-shaped electromagnets when energized at maximum amplifier current (2.6 A) was determined utilizing a Telatomic magnetic field sensor model TEL-M111 to be approximately 90 mT.

5 Results

A series of trials was made to compare the difference in heat transfer coefficient between the magnetically enhanced and nonenhanced cases. To ensure that the different sets were being compared accurately, all other controllable parameters of the experiment were held constant. The effect of varying some of these other parameters will be the subject of future research by this investigator. Most of the controllable parameters were set as a "best guess" to help ensure that the differences in heat transfer

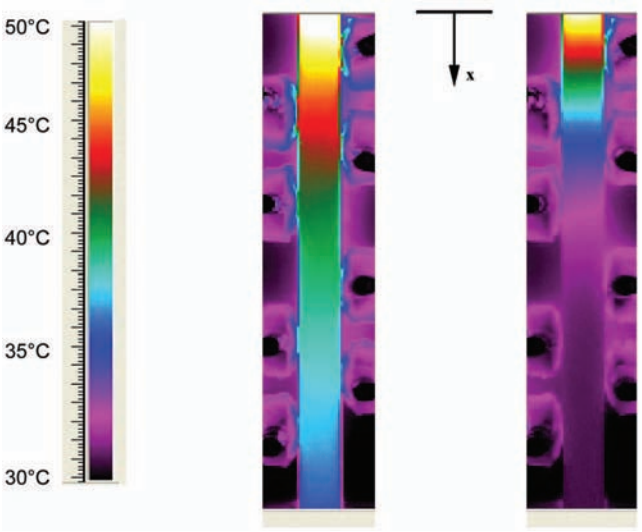

Fig. 2 IR camera images of test section without enhancement (left) and with magnetic field enhancement (right)

rates could be easily demonstrated. It was experimentally determined that a 2 Hz was optimum for enhancement and was therefore utilized. The corresponding 0.5 s period is significantly larger than the 0.13 s required for the flow to advect a magnetic pole pair in the pipe. The apparatus was alternately switched from magnetically enhanced to nonenhanced modes allowing sufficient thermal stabilization time prior to IR image capture. Figure 2 shows a representation of the data capture of the pipe's test section (internally cooled fin) for both the nonenhanced (left) and magnetically enhanced (right) cases.

The images in Fig. 2 show, qualitatively, the dramatic effect that the enhancement technique has on the temperature distribution of the test section. The temperatures of the magnetically enhanced pipe were significantly lower than those of the nonenhanced pipe. It was also observed that the rate of temperature decrease near the top portion of the pipe (considered an internally cooled fin) was much greater for the magnetically enhanced pipe. The pole pairs of the two sets of the electromagnets can also be seen to the left and right of the test section, to give the reader a general idea of the location of the electromagnets.

The data for each magnetically enhanced case were alternately tested with a nonenhanced case and allowed to stabilize. The image data were downloaded into a MATLAB script, which converted it to temperature data utilizing a daily determined calibration curve. The surface temperature was averaged in the circumferential direction. The decay constant was roughly determined by best fitting the axially decaying temperature distribution to an exponential curve. The heat transfer coefficient (assumed to be constant for the length of the test section) was determined utilizing Eq. (1).

The data for the nonenhanced case produced a mean value for the heat transfer coefficient of 57.7 W/m^2 K with a standard deviation of 8.3 W/m^2 K. The data for the magnetically enhanced case produced a mean value for a heat transfer coefficient of 205.8 W/m^2 K, with a standard deviation of 15.0 W/m^2 K. This corresponded to a 267% increase in heat transfer coefficient. The corresponding increase in differential pressure measured for the 2 Hz switching frequency was 48% with a standard deviation of 12%. Other investigators comparing smooth and internally finned tubes, at Reynolds numbers similar to this study, have reported the experimental heat transfer augmentation ratios of 103% [8] with associated increase in flow resistance of 140% [8] and increases of 2.8-fold in the Nusselt number [9] with 1.7-fold increase in friction factor [9].

The percent increase in differential pressure across the test section was also measured for various frequencies above and below 2 Hz. The results of percent increase in pressure drop across the test section as a function of electromagnetic switching frequency showed a relative minimum occurring at 4 Hz corresponding to a 28% increase in pressure drop. As with all active enhancement techniques, a power cost was incurred, which must be accounted for when quantifying enhancement. This currently nonoptimized technique required significant electrical power for the oversized electromagnets. For the presented experiment, the electromagnets consumed approximately 45 W. Most of this power was dissipated in the resistive load of the electromagnetic windings.

6 Conclusions

A method of active convective heat transfer augmentation utilizing ferromagnetic particle laden fluid and oscillating magnetic fields was introduced. A simple experimental method using IR camera measurements of an internally cooled fin was utilized to determine the relative increase in the heat transfer coefficient. The experimental results demonstrated a significant increase in the heat transfer coefficient in the pipe, an average increase of over 267%, with a corresponding increase of differential pressure of 48% for the parameters tested. This enhancement and subsequent increase in differential pressure compares very favorably to the increases in the heat transfer coefficient and pressure drop measured by other researchers for internal finned tubes when compared with unfinned tubes in laminar flow.

Further investigation needs to be performed, specifically the scaling and nondimensionalizing appropriate parameters with experimental validation. The experimental apparatus used in future experimental investigations will be modified to include embedded thermocouples, integral heaters, and multiple electromagnet geometries. Future investigation will include parametric searches for the most effective magnetic switching frequency and pulse type, particle size, composition, concentration, flow Reynolds number, and pipe size.

Acknowledgment

The author would like to acknowledge the support of this research by the Naval Academy Research Council (NARC) under Grant No. N00014-02-WR20325 and Army Research Office (ARO) under Grant No. MIPR6MUSNAR137, which supported this work.

Nomenclature

A_c = cross-sectional area of tubing
c_p = specific heat of fluid
D = inside pipe diameter
h = heat transfer coefficient
k = thermal conductivity of fluid
L = length of pipe
m = excess temperature exponential constant, $(hp/kA_c)^{1/2}$
p = inside perimeter of pipe
Re = Reynolds number, $\rho Dv/\mu$
Pr = Prandtl number, $\mu/\rho/\alpha$
T = temperature
v = mean velocity of fluid
x = axial distance on pipe
θ = excess temperature function
μ = absolute viscosity

References

[1] Webb, R. L., 1994, *Principles of Enhanced Heat Transfer*, Wiley, New York.
[2] Eastman, J. A., Choi, S. U. S., Yu, W., and Thompson, L. J., 2001, "Anomalously Increased Effective Thermal Conductivities of Ethylene Glycol Based Nanofluids Containing Copper Nanoparticles," Appl. Phys. Lett., **78**(6), pp. 718–720.

[3] Xuan, Y., and Li, Q., 2003, "Investigation on Convective Heat Transfer and Flow Features of Nanofluids," J. Heat Transfer, **125**, pp. 151–155.
[4] Eastman, J. A., Phillpot, S. R., Choi, S. U. S., and Keblinski, P., 2004, "Thermal Transport in Nanofluids," Annu. Rev. Mater. Res., **34**, pp. 219–246.
[5] Ganguly, R., Sen, S., and Puri, I. K., 2004, "Heat Transfer Augmentation Using a Magnetic Fluid Under the Influence of a Line Dipole," J. Magn. Magn. Mater., **271**, pp. 63–73.
[6] Tangthieng, C., Finlayson, B. A., Maulbetsch, J., and Cader, T., 1999, "Heat Transfer Enhancement in Ferrofluids Subjected to Steady Magnetic Fields," J. Magn. Magn. Mater., **201**, pp. 252–255.
[7] Hishida, K., and Maeda, M., 1994, "Enhancement and Control of Local Heat Transfer Coefficients in a Gas Flow Containing Soft Magnetic Particles," Exp. Heat Transfer, **7**, pp. 55–69.
[8] Li, L. J. et al., 2005, "Heat Transfer Augmentation in 3D Internally Finned and Microfinned Helical Tube," Int. J. Heat Mass Transfer, **48**(10), pp. 1916–1925.
[9] Liao, Q., and Xin, M. D., 1995, "Experimental Investigation on Forced Convective Heat Transfer and Pressure Drop of Ethylene Glycol in Tubes With Three-Dimensional Internally Extended Surface," Exp. Therm. Fluid Sci., **11**(4), pp. 343–347.

An Experimental Investigation of Sorption Process in Fluidized Bed With Cooling Pipe

Akihiko Horibe
e-mail: horibe@mech.okayama-u.ac.jp

Syahrul Husain

Hideo Inaba

Naoto Haruki

Ping Tu

Department of Mechanical Engineering,
Faculty of Engineering,
Graduate School of Natural Science and Technology,
Okayama University,
Tsushimanaka 3-1-1,
Okayama 700-8530, Japan

An experimental investigation of a fluidized bed with multiple cooling pipes was conducted to study adsorption characteristics of a new organic sorbent desiccant material (HU300P) for a new air conditioning system. The mass ratio of the present sorbent desiccant powder type is from 1.3 to 2.3 times greater than that of silica gel. The sorption rate of the water vapor in the sorbent bed was measured under various conditions. It was found that the sorption rate is highly dependent on the effect of cooling pipes. The sorption ratio increases and the completion time for the sorption process decreases by using multiple cooling pipes.
[DOI: 10.1115/1.2970076]

Keywords: sorption polymer, fluidized bed, cooling pipe

1 Introduction

The utilization of sorbent/desiccant for cooling and dehumidification systems has increased in the past several years because of the possible utilization of low grade thermal energy such as solar energy or waste heat energy. An application of the sorbent in solar or waste heat powered sorption refrigeration has been reported in literature [1–3]. Henning et al. [2] discussed the experiences achieved in a coupled system, which is the combination of a solar collector in a desiccant cooling cycle. Shu et al. [3] presented a locomotive cabin adsorption air-conditioner powered by waste heat from the exhaust of the diesel engine, and it has been successfully run for two years. Solid particle adsorption systems are being developed up to now and are still at the research and development stage [1–4].

A bridged complex of sodium polyacrylate (HU300P) is one of the new sorption polymers used as an organic sorbent. This bridged complex containing the carboxyl group as the water sorption site has a larger sorption capacity per unit mass compared with the silica gel adsorbent [1]. The dynamic sorption characteristics of the organic sorbent have been previously investigated in our laboratory for the fibrous type sorption material [1] and for the powder type sorption material [4], respectively.

Contributed by the Heat Transfer Division of ASME for publication in the JOURNAL OF HEAT TRANSFER. Manuscript received September 4, 2007; final manuscript received April 12, 2008; published September 5, 2008. Review conducted by Louis C. Chow.

In order to improve the performance of the desiccant air conditioning system, a new bed configuration should be developed. Hamed [5] investigated an inclined fluidized bed with a desiccant and reported that a regeneration temperature as low as 90°C was satisfactory. Most recently, Moskal and Nastaj [6] considered introducing electromagnetic induction to generate heat inside a modified sorbent bed for the desorption process. Heating can be applied to a recovering sorbent bed after the adsorption step. This method of regeneration has several advantages (e.g., high capacity of internal volumetric heat source, simplicity of heating system control) [6].

Differently from the previous work, the objective of this experimental study is to investigate the effect of cooling pipe (single and multiple pipes) in a fluidized bed of sorption material (HU300P). In this respect, this article is concerned in the sorption process of the sorbent bed with the mass transfer aspect for multiple cooling pipes.

2 Experimental Apparatus and Procedure

The schematic of the experimental apparatus is shown in Fig. 1. The experimental apparatus consists of an air compressor, an aftercooler, a filter, a membrane dryer, a humidifier and a temperature controller, a heater, a flowmeter, the batch vessel packed bed with the test sorption material, and the cooling water circulation section.

The test section is made of transparent acrylic fiber in order to make visualization possible. It is a rectangular container that is 130 mm in width and 200 mm in height. The polyflon filter no. 10 (in microns) is set up in both the inlet and outlet of the test section to distribute the air flow uniformly and to prevent the leakage of sorbent particles. There are nine cooling pipes, as shown in Fig. 1, which are arranged in two lines: five pipes in the lower line and four pipes in the upper line with a horizontal interval of 26 mm at a vertical position of 20 mm and 40 mm from the air filter, respectively. The cooling pipe made of copper is a double tube structure. The inner pipe with an outer diameter 6 mm and a wall thickness of 1 mm is inserted into the outside pipe with an outer diameter of 13 mm and a wall thickness of 1 mm. A copper wire that is 1 mm in diameter is installed into the outside pipe, and the wire is rolled spirally 60 times to increase the overall heat transfer from the sorbent material to the cooling water.

First of all, the processing air is compressed at a desired pressure by an air compressor. The air passes through the aftercooler to eliminate the heat generated by the air compressor. The air purifier system is composed of an air filter and a micromist filter having the capacity to get rid of dust over 0.01 μm in diameter. In order to reduce humidity, the air is blown through the membrane dryer.

The humidifier in the air moisture control unit is made up of a cylinder stainless steel vessel equipped with an air bubble distributor. The air humidity is controlled by the air bubbling operation through the air bubble distributor, and the air temperature is also adjusted by the input control of electric heater in the humidifier.

The flow rate of air controlled at a desired temperature and humidity is adjusted to a given value by using a flow rate control valve and a flow rate meter (with a measuring range of 0.83–8.3 m^3/s, a measuring accuracy of ± 0.01 m^3/s for a low flow rate, and a measuring accuracy of ± 0.05 m^3/s for a high flow rate). Furthermore, in the air controller, the inlet air temperature (10–60°C) and the inlet air relative humidity (5–80% RH) have become possible to ventilate the air in the test section. The air pressures at the inlet and outlet of the test section are measured by pressure gauges with a measuring accuracy of ± 0.5 Pa.

The temperature profile of the test powder sorbent layer was obtained by using *K* type thermocouples (0.32 mm in diameter and with a measuring accuracy of ± 0.1°C). One of them was set at the center position of the upper line pipe and the other two were set at an interval of 26 mm in the center position of the lower line

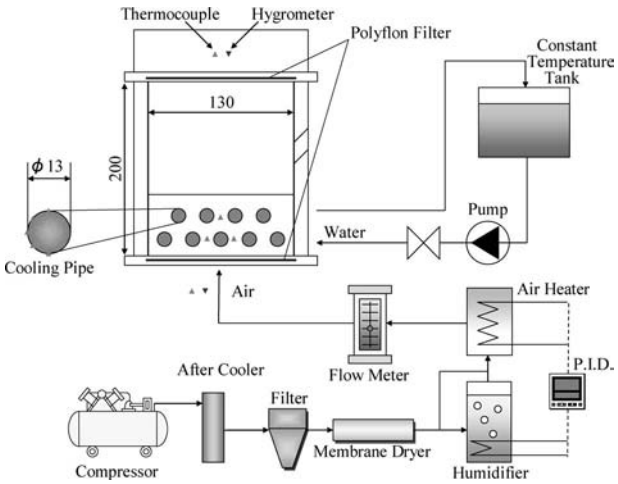

Fig. 1 Schematic of the experimental apparatus

pipe. The temperature and humidity at the inlet and outlet of the test section were obtained by using *K* type thermocouples (0.1 mm in diameter and with a measuring accuracy of ±0.1 °C) and static electricity type hygrometers (measuring accuracy of ±2% RH). The amount of water vapor adsorbed into the test powder sorbent was measured with an electric balancer (with a measuring range of 3000 g and with a measuring accuracy of ±0.01 g) by taking samples transiently from the test section.

3 Results and Discussion

The proposed sorption material is a powder type sodium polyacrylate (HU300P) to be used as a new organic sorption polymer. The physical properties of the organic sorbent (HU300P) are: the diameter of the particle is between 90 μm and 160 μm, the density is 600 kg/m^3, the effective thermal conductivity is 0.076 W/K, and the specific heat is 1.4 kJ/kg K. Figure 2 presents the sorption isotherm of the powder sorbent HU300P for various temperatures, which were obtained from our previous paper [7] by the salt saturation method. Where ψ means the relative humidity and m_w/m_0 means the mass ratio of the sorbed water vapor, m_w, to the dried polymer sorbent, m_0. In Fig. 2, it can be noticed that the mass ratio of the present powder type sorbent is 1.3–2.3 times greater than that of silica gel. The mass ratio m_w/m_0

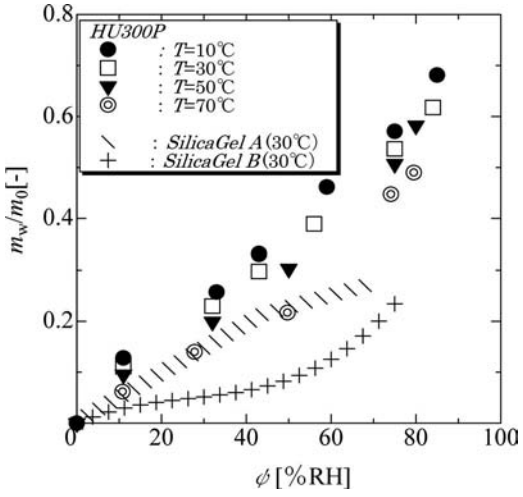

Fig. 2 Sorption isotherm of HU300P

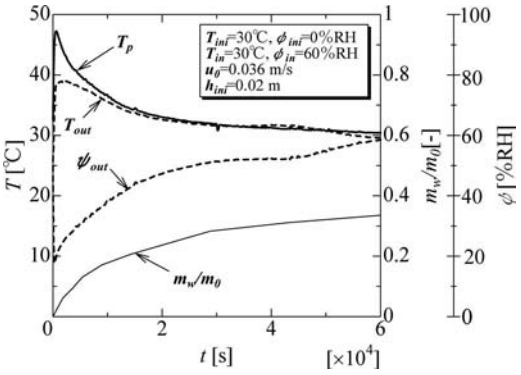

Fig. 3 Time histories without the cooling pipes

of the present powder type sorbent is higher for the lower initial material temperature. It can also be seen that the data of m_w/m_0 increases with an increase in relative humidity.

The following correlation equation of m_w/m_0 was derived in terms of the relative humidity and the temperature ratio within the relative deviation of 13% with the least-squares method.

$$(m_w/m_0) \cong 0.759 \times (\psi/100)^{0.89} \times \left(\frac{T+T_0}{T_0}\right)^{-1.19} \quad (1)$$

Applicable ranges are as follows: $10 < \psi < 85\%$ RH and $10 < T < 70$ °C, where T is the sorption material temperature and $T_0 = 273.15$ K.

The experimental examinations have been carried out to investigate the heat and mass transfer behavior in the sorption process. First of all, the experiment is conducted without any cooling pipes in order to investigate the difference with the case in which cooling pipes are inserted in the fluidized bed. Test conditions are the inlet air temperature $T_{in}=30$ °C, the inlet air relative humidity $\psi_{in}=60\%$ RH, the initial sorption material temperature $T_{ini}=30$ °C, the sorption material, which is absolute dry packed, has an initial bed height $h_{ini}=0.02$ m, and the sorption experiment is done for the inlet air velocity $u_0=0.035$ m/s. Furthermore, the experiment with cooling pipes are performed for a single cooling pipe and for multiple cooling pipes with a circulating water whose temperature T_{wat} is 23 °C and whose flow rate q_{wat} is 0.006l/s. The error of experimental results of the amount of water vapor adsorbed, the inlet air velocity, the relative humidity, and the temperature is ±0.005 g, ±0.0005 m/s, ±1%, and ±0.05 °C, respectively.

Figure 3 presents the relation between the test sorbent temperature T_p, the relative humidity of moist air ψ, and the amount of nondimensional sorbed water vapor m_w/m_0 with time without a cooling pipe. It is found that with the temperature profile of the test sorbent layer there is a considerable increase in the temperature of the sorbent from 30 °C to 47 °C in a couple of minutes after starting the experiment due to the heat generated by the water vapor sorption phenomenon. After reaching a maximum temperature, the inside layer temperature decreases until its balance with the entrance air temperature of 30 °C. The relative humidity of moist air at the outlet of the test section increases by sorption processing until its approach to the inlet air relative humidity ψ_{in}.

The temperature variations of the test sample and the relative humidity of moist air with time in the case of the sorption experiment with a cooling pipe inside the sorbent layer, as shown in Fig. 4, are similar to the sorption experiment without a cooling pipe. However, the maximum temperature of the sorption material is 10 °C lower than the maximum temperature found in the sorption experiment without a cooling pipe. Both the temperature of mate-

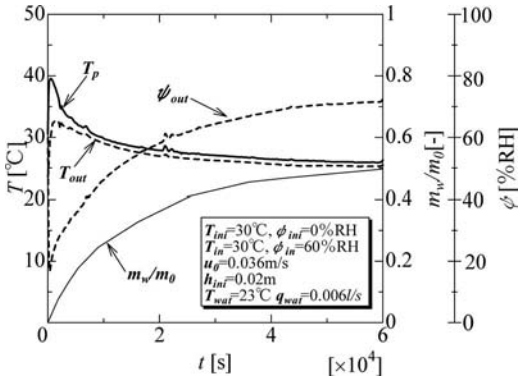

Fig. 4 Time histories with a cooling pipe

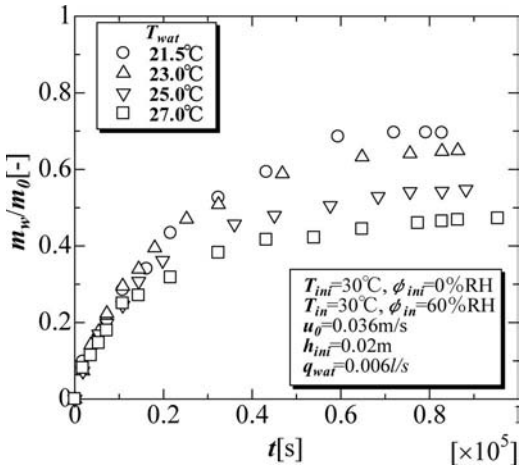

Fig. 6 Effect of cooling water temperature on the sorption ratio

rial and the outlet air decrease until they reach the temperature balance with the inlet cooling water temperature and the inlet air temperature.

Figure 5 presents the mass ratio of sorbed water vapor to the dried powder organic sorbent for the cases without the cooling pipes and with the cooling pipe (single and multiple/nine pipes) as a function of time. Shown as the dimensionless sorption ratio, the vapor sorption behavior is different from each other. If there is no cooling pipe, the dimensionless sorption ratio m_w/m_o reaches 0.33 at the equilibrium level, while it increases to 0.48 and 0.60 for the cases with a single cooling pipe and with multiple cooling pipes, respectively. Furthermore, the time period for reaching 90% of the whole sorbed water vapor mass under the sorption equilibrium condition is defined as the sorption completion time t_f, and the results are plotted in Fig. 5. The sorption completion times are $t_f=0.53\times10^5$ s, $t_f=0.47\times10^5$ s, and $t_f=0.41\times10^5$ s for the cases without cooling pipes, with a single cooling pipe, and with multiple cooling pipes, respectively. The sorption process with multiple cooling pipes progresses rapidly. Consequently, we concentrate on the experiment with multiple cooling pipes, and the results are indicated in the following.

Figure 6 shows the effect of cooling water temperature on the sorption ratio. The cooling water temperature is in the range of $T_{\text{wat}}=21.5-27°\text{C}$. As indicated in Fig. 6, the amount of nondimensional sorption ratio increases with decreasing the cooling temperature T_{wat}. During the sorption process, cooling sorbent particles contribute to their sorption capacity, as shown in Fig. 2. Meanwhile, the cooling air flow causes an increase in its relative humidity. Consequently, both of the above phenomena bring about a higher sorption ratio. Cooling of the sorbent bed during the sorption process increases the sorption ratio.

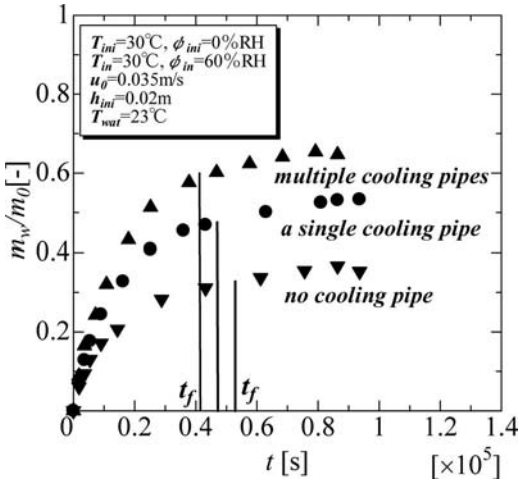

Fig. 5 Effect of multiple cooling pipes on the sorption ratio

4 Conclusions

An experimental investigation was carried out to observe the sorption characteristic of the organic powder type sorbent composed of the bridged complex of sodium polyacrylate (HU300P) as a new kind of sorption material. The amount of water vapor sorption of the present sorbent desiccant is 1.3–2.3 times greater than that of silica gel. The sorption process in the fluidized bed with a single cooling pipe and with multiple cooling pipes is researched in this study. The measured result revealed that the sorption process was accelerated and the water uptake ability was improved by the cooling effect of water flowing through multiple pipes.

Nomenclature

h = bed height, m
m = mass, kg
m_w/m_0 = dimensionless sorption ratio
q = flow rate, l/s
T = temperature, °C
T_0 = absolute temperature, K
t_f = completion time, s
u_o = inlet air velocity, m/s

Greek

ψ = relative humidity, % RH

Subscripts

in = inlet
out = outlet
ini = initial
p = particle
wat = water

References

[1] Inaba, H., 1998, "Heat and Mass Transfer Characteristics of New Adsorption Polymers for Advanced Adsorption Cycle," Therm. Sci. Eng., **6**(1), pp. 11–18.
[2] Henning, H. M., Erpenbeck, T., Hindenburg, C., and Santamaria, I. S., 2001, "The Potential of Solar Energy Use in Desiccant Cooling Cycles," Int. J. Refrig., **24**, pp. 220–229.
[3] Shu, J., Ruzhu, W., Yunzhuang, L., and Jingyi, W., 2006, "Operational Aspects of Adsorption Air-Conditioner Used in Diesel Locomotive," Int. J. Energy Res., **30**, pp. 1377–1390.

[4] Inaba, H., Horibe, A., Kameda, K., Haruki, N., and Kida, T., 2000, "Heat and Mass Transfer of a Fluidized Bed Packed With Organic Powder Type Adsorption Material," *Proceedings of the Symposium on Energy Engineering in the 21st Century*, Hongkong, Jan. 9–13.
[5] Hamed, A. M., 2005, "Experimental Investigation on the Adsorption/Desorption Processes Using Solid Desiccant in an Inclined Fluidized Bed," Renewable Energy, **30**, pp. 1913–1921.
[6] Moskal, F., and Nastaj, J. F., 2007, "Internal Heat Source Capacity at Inductive Heating in Desorption Step of ETSA Process," Int. Commun. Heat Mass Transfer, **34**, pp. 579–586.
[7] Horibe, A., Husain, S., Inaba, H., and Haruki, N., 2008, "Sorption Characteristics of Organic Powder Sorption Material in Fluidized Bed With a Cooling Pipe," J. Thermal Science and Technology, **3**(2), pp. 207–218.